AD NUMBER

AD480862

NEW LIMITATION CHANGE

TO

Approved for public release, distribution unlimited

FROM

Distribution authorized to U.S. Gov't. agencies and their contractors; Administrative/Operational Use; Sep 1965. Other requests shall be referred to Air Force Materials Lab., Wright-Patterson AFB, OH 45433.

AUTHORITY

USAFML ltr, 29 Mar 1972

COATINGS FOR REFRACTORY METALS
IN AEROSPACE ENVIRONMENTS

R. A. Perkins
C. M. Packer

Lockheed Missiles & Space Company

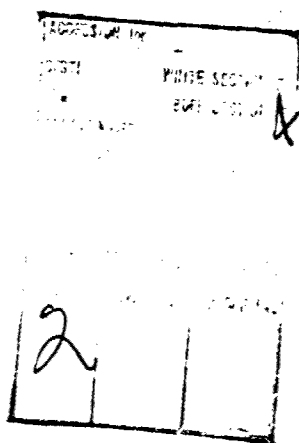TECHNICAL REPORT AFML-TR-65-351

September 1965

Air Force Materials Laboratory
Research and Technology Division
Air Force Systems Command
Wright-Patterson Air Force Base, Ohio

NOTICES

When Government drawings, specifications, or other data are used for any purpose other than in connection with a definitely related Government procurement operation, the United States Government thereby incurs no responsibility nor any obligation whatsoever; and the fact that the Government may have formulated, furnished, or in any way supplied the said drawings, specifications, or other data is not to be regarded by implication or otherwise as in any manner licensing the holder or any other person or corporation, or conveying any rights or permission to manufacture, use, or sell any patented invention that may in any way be related thereto.

COATINGS FOR REFRACTORY METALS
IN AEROSPACE ENVIRONMENTS

R. A. Perkins
C. M. Packer

(See form 1473)

ii

ABSTRACT

The behavior of 8 commercially coated refractory metal systems in various aerospace conditions was evaluated: PFR-6, Disil, and Durak-B coated TZM; PFR-32, CrTiSi, and Vought IV coated Cb-752; CrTiSi coated B-66; and Sn-Al coated Ta-10W. Environmental and performance requirements for aerospace applications of coated refractory metals were analyzed. Model environmental conditions for typical lifting reentry missions were derived, and the results used in determining time, temperature, and pressure for experimental phases of the program. Experimental equipment and evaluation procedures for studying the behavior of coated refractory metal systems in aerospace environments were developed. Initially the maximum temperature for a given useful lifetime up to 4 hr in slowly moving air was determined for each system at pressures of 0.01 to 50 mm Hg. Subsequently, the effects of such variables as Mach 3 air flow, vacuum exposure, temperature and pressure cycling, and acoustic irradiation were evaluated in terms of deviation from the performance in slowly moving air. The tolerance of the systems to various defects was studied, and in-field patch repair processes and compatibility with other high-temperature materials were explored. A detailed metallographic study was also conducted for each coating system. The behavior under various conditions was thus explained, and recommendations for additional applications and development were made. The following conclusions were drawn: the 8 coating systems have good utility over a broad range of aerospace applications; the oxidation resistance of all silicide-base coatings (including CrTiSi) and Sn-Al coatings is degraded at reduced pressure; in lifting reentry applications, temperature limits will probably be determined by the performance capabilities of the interior surfaces, where pressures will be lower.

CONTENTS

ILLUSTRATIONS

ILLUSTRATIONS (cont'd)

ILLUSTRATIONS (cont'd)

ILLUSTRATIONS (cont'd)

ILLUSTRATIONS (cont'd)

xiii

ILLUSTRATIONS (cont'd)

ILLUSTRATIONS (cont'd)

TABLES

TABLES (cont'd)

TABLES (cont'd)

NOMENCLATURE

$\dot{q}$ heat flux

R radius

d diffusion distance

h enthalpy

T temperature

P pressure

u velocity in the longitudinal direction

v velocity in the traverse direction

ν Prandtl-Meyer turning angle

M Mach number

C concentration

Q diffusion rate

t time

S distance from leading edge of wing

t time for dissociation or recombination

K rate constant for dissociation of oxygen

K rate constant for recombination of oxygen

D diffusion constant

Y fraction of molecules dissociated

ρ density

α angle of attack

Λ sweep angle

ϵ emissivity

θ angle between free stream and a line tangent to body surface

γ ratio of specific heats

Γ parameter which indicates catalytic efficiency of surface

Subscripts

c circular

o sea level

s stagnation point

sl stagnation line

e edge of boundary layer

w wing surface

FP flat plate

D dissociation

R recombination

O_2 molecular oxygen

O atomic oxygen

d diffusion

av average

L laminar

T turbulent

∞ free stream

Section I

INTRODUCTION

BACKGROUND

A number of promising coatings for protecting refractory metals from oxidation are available commercially or are in an advanced state of development. Useful data on performance are meager, however, and drawing sound conclusions regarding the relative merits of different coating systems for a specific application is difficult. Performance data have been obtained for a wide variety of samples exposed to relatively simple laboratory screening tests. Results of independent studies have shown considerable variation in coating life and in some cases have been contradictory. Often, even the simple limits of time and temperature within which a coating of specified thickness will protect the substrate are not known with certainty. Accumulation of design and performance data in terms of more precise parameters presents a formidable problem to the potential user.

These problems are of particular concern in aerospace applications, where performance and reliability must be considered from two points of view:

- Environmental factors that govern the degree of protection afforded
- Preexposure factors that may degrade the coating and reduce reliability

Important environmental factors include temperature, gas pressure, mass flow rate, thermal and pressure cycling, gas temperature, applied stress, and sonic vibration. Many of these have not been included in the majority of coating evaluation programs conducted to date. The importance of reduced air pressure as a factor governing useful coating life has been shown by pioneering work conducted in the LMSC Independent Research Program (1). The preexposure factors that may degrade coatings are the defects that result from processing and assembly or develop during launch, sustained orbital or space flight, and repetitive use. Such defects may be caused by tensile or compressive strain, sonic vibration, impact, heating in vacuum, or metallurgical and structural changes resulting from diffusion, alloying, or chemical reaction. Achieving compatibility between dissimilar materials in contact with coatings may be a problem. Overall reliability and tolerance for various types of defects must be established.

Many problems in obtaining more useful engineering data on coating performance for aerospace application are apparent. Simulation of the precise environment in a laboratory test is difficult, costly, and, in some cases, virtually impossible. The number of significant factors is large, and a detailed experimental study would be a monumental task. Yet, if any measure of reliability and basis for selection are to be achieved, the relative importance and possible interactions of significant variables

1

must be established. The complexity of the problem requires a careful analysis of variables and a systematic experimental investigation to provide useful results. The program conducted under this contract has been designed with these basic factors in mind.

OBJECTIVES AND SCOPE

The objectives of this program were as follows:

- To characterize, on a laboratory scale, the utility of advanced coatings for refractory metals in a broad range of anticipated environmental conditions and performance requirements for aerospace vehicles
- To obtain sufficient data to permit reasonable forecasts of reliability under varying conditions of exposure
- To determine the susceptibility for defect formation in use and the feasibility of improving reliability by control or removal of defects

Environmental conditions and performance requirements for aerospace applications of coated refractory metals were analyzed. Major consideration was given to sheet materials for use in heat shields of lifting reentry vehicles. Model environmental conditions for typical lifting reentry missions were derived. Secondary consideration was given to applications of sheet in liquid-fuel rocket engines. The results of this analysis were used as a guide in determining the time, temperature, and pressure to be used in experimental phases of the program.

Eight commercial or advanced pilot-scale coating systems were selected for testing and evaluation: TZM/PFR-6 (Pfaudler), TZM/Durak B (Chromizing), TZM/ Disil (Boeing), Cb 752/PFR-32 (Pfaudler), Cb 752/Vought IV (Vought Astronautics), Cb 752/CrTiSi (TRW), B-66/CrTiSi (TRW), and Ta-10W/Sn-Al (GT & E). First, the relative effect of pressure on the performance capabilities of each coating system in slowly moving air was investigated. The maximum temperature for coating lifetimes of 30, 60, 120, and 240 min in air at 0.01, 0.1, 1.0, 5, 20, and 50 mm Hg pressure was determined. These data provided a baseline of oxidation behavior (Baseline Studies). The effect of all other environmental parameters and preexposure conditions on coating performance was assessed in terms of deviations from baseline behavior.

Tests were conducted in air flowing over the surface at Mach 3 velocity to determine the effect of mechanical forces superimposed on oxidizing systems (Gas Velocity Studies). The potential contribution of ionization effects in high-velocity tests was also evaluated by plasma-arc tests at reduced pressure. The contribution of heating in high vacuum to degradation of structure and properties was investigated (Vacuum Volatility Studies). Tests were conducted under dynamic conditions to determine the effect of various environments and multiple-mission use on performance capabilities (Temperature and Pressure Cycling Studies). The ability to predict performance of heat-shield components in model reentry missions was evaluated by conducting stepwise oxidation tests according to calculated reentry profiles (Kinetic Model Tests).

2

It is anticipated that defects introduced in the manufacture, assembly, and use of coating systems will have a major influence on performance and reliability. The contribution of the types and severity of coating defects to degradation or variability of performance was investigated (Defect Tolerance Studies). This phase of the program also included an assessment of the relative resistance to formation of defects by mechanical strain and impact. A special case of defect formation resulting from vibration during use was studied in still another phase of the program (Vibration Studies). The ability to restore performance in defect areas by available repair techniques was also investigated (Coating Repair Studies). A small but important phase was an exploration of potential materials compatibility problems in aerospace applications (Compatibility Studies). The interaction of couples of different coating systems and of coating systems with various insulation materials was investigated.

The behavior of each coating system was investigated independently, and detailed results for each system are presented in this report. In each case, an attempt was made to characterize behavior in terms of the structure and composition of the system. A comparative analysis of the results for all systems is given in the last section of the report.

Section II

ENVIRONMENTAL ANALYSIS

GENERAL CONSIDERATIONS

Lifting Reentry Systems

Leading edges and heat shields for lifting reentry vehicles constitute one of the most important applications of coated refractory metal sheet in aerospace structures. Lifting reentry vehicles are designed essentially to operate beyond the sensible limit of the earth's atmosphere (400,000 ft). They are being considered for a variety of missions in orbit around the earth and in outer space. Such vehicles differ markedly from the present generation of satellites and manned spacecraft in that forces of aerodynamic lift are used during descent to the earth (reentry) for maneuverability and deceleration. This in turn results in relatively low rates of heating (heat flux) compared with ballistic reentry and generates surface temperatures that can be accommodated by refractory metal structures.

The size and shape of these vehicles may vary widely, depending upon the mission. The most common concept is that of a winged glider with vertical fins, as shown in Figure 1. The vehicles may range in length from 6 to 60 ft with a maximum wingspread of 4 to 24 ft and heights of 2 to 10 ft. They can be divided into three major classifications based on velocity at the start of atmospheric reentry: suborbital (18,000 to 24,000 ft/sec), orbital or circular (24,000 to 26,000 ft/sec), and super-orbital (36,000 ft/sec). The superorbital vehicles which reenter the earth's atmosphere from lunar or deep-space missions present the most critical high-temperature materials problems. The instantaneous heat flux, time for reentry, and total heat input are the highest for any class. Leading edges and other surfaces must accommodate relatively long periods of heating at very high temperatures compared with the length of time for suborbital or orbital vehicles.

Coatings for refractory metals perform their function only when heated in an oxidizing environment, and hence primary consideration usually is given to the reentry phase of flight. However, it must be remembered that structures or components using these materials pass through preliminary phases of manufacturing, transportation, pre-launch handling, launching and ascent, and orbital or space flight before performing their primary function. Any alteration or damage of the coating at any time in this sequence of events may seriously impair the ability of the coating to provide adequate protection from oxidation. The effect of natural environments associated with ascent, flight, and reentry is of vital concern with respect to overall coating performance.

The environmental factors most likely to affect the performance of coatings are temperature, pressure, mass flow, gas states and temperature, strain, vibration, shear, and impact or abrasion. Calculated data are being gathered at a rapid rate, but to

5
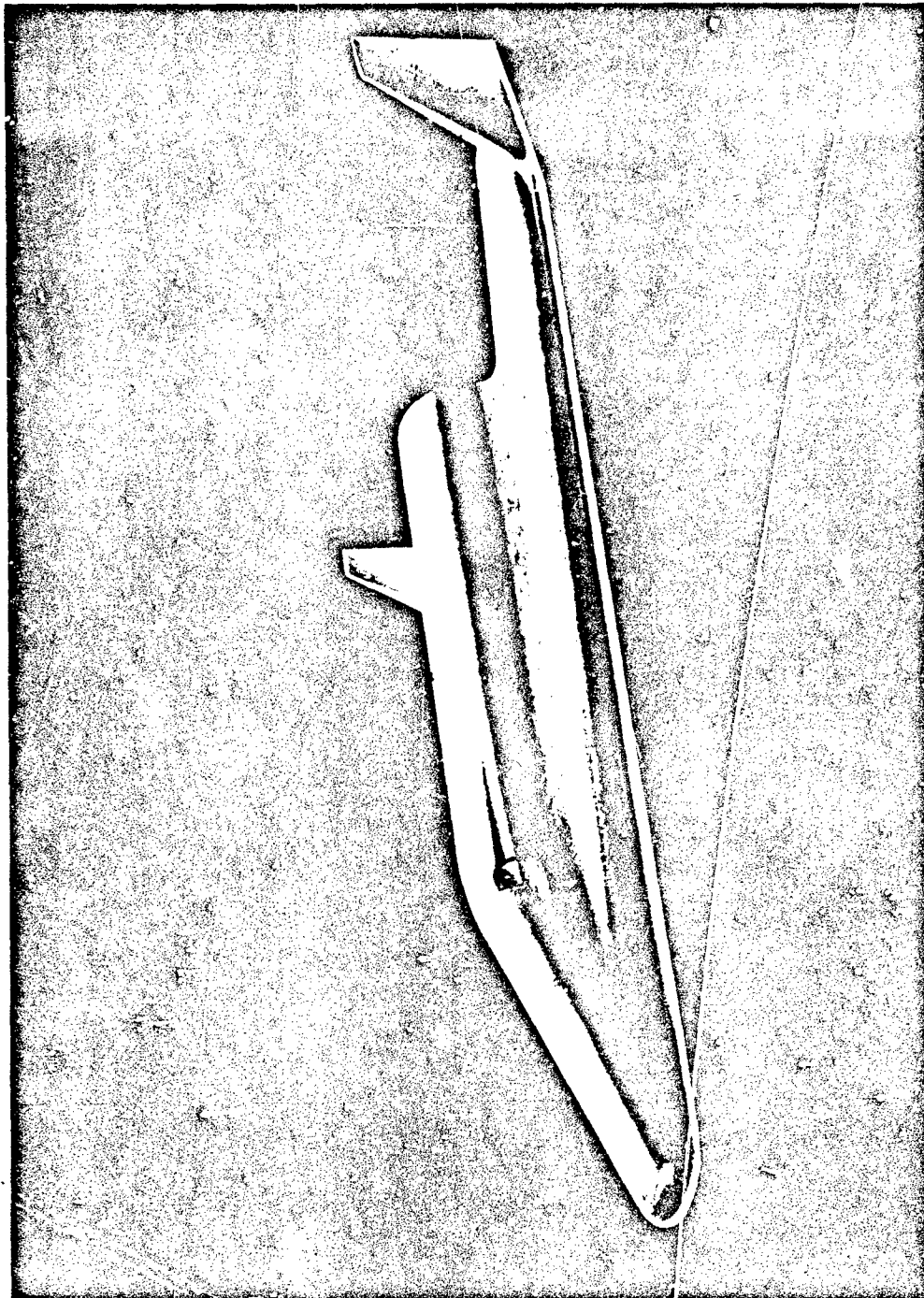
Figure 1 Lifting Reentry Vehicle, Medium Wing Load

date lifting reentry vehicles have been launched only on suborbital flights to measure the precise value of factors such as temperature, pressure, and stress. Hence, for the present, the environmental analysis must be based on data obtained from largely theoretical calculations or extrapolations.

The time variation of all important variables can be calculated for any given vehicle and flight trajectory or mission. By plotting several variables on a common time axis or by cross-plotting at equal time intervals, the interrelation and simultaneous occurrence of important factors can be studied. Since each variation in vehicle design and trajectory gives rise to a different set of data, it is impossible to define the range and interrelation of environmental factors with any degree of exactness for all types of vehicles. Such a detailed presentation is beyond the scope of this program. The approach, therefore, is to treat environmental factors in a generalized way, giving typical ranges or values that can be obtained from the literature. However, a detailed analysis of the time variation of parameters for a model vehicle following one trajectory in lifting reentry will be made to illustrate precise interactions and to serve as a basis for experimental verification of predicted coating behavior.

Ascent environment. During ascent out of the earth's atmosphere, the vehicle is exposed simultaneously to aerodynamic heating, reduced air pressure, mass flow and shearing forces, vibration, shock, and acceleration loads. The magnitude and the time variation of these parameters are dictated by the exact booster-vehicle combination and trajectory employed during ascent. Since most of the performance and trajectory data for large boosters are classified, little information on which to base an analysis of important factors is available in the open literature. Furthermore, theoretical models of behavior in the ascent environment are difficult if not impossible to formulate, since the complexity of both the environment and materials systems prevents their reduction to mathematical statements (2). Known behavior, therefore, has been established largely by testing and experimentation.

Although calculated and experimental information often do not agree very closely, it is evident from either source that very high temperatures are reached in short periods of time. Maximum skin heating for Agena ascent trajectories, for example, produces a temperature of 1400° F in about 170 sec after launch (3). Czarnecki and Braun (4) indicate peak temperatures ranging from 1100 to 2500° F on the skin of lifting reentry vehicles during boost. Peak heating occurs at about 8 min after liftoff with a total time at temperatures in the 1000 – 2200° F range of about 6 min. These calculations are based on an ascent time of 10 min, which is stated to be compatible with most of the current boosters (4).

The rapid rise in temperature during ascent is accompanied by a very rapid reduction in air pressure as the vehicle moves out through the atmosphere and into space. By the time the vehicle reaches 400,000 ft, ambient air pressure has dropped from 760 mm Hg at sea level to 10^{-5} mm Hg. Czarnecki and Braun (4) estimate the range of pressures at different points on the vehicle to be 5 mm Hg to 10^{-5} mm Hg at the time of peak heating on ascent. The rapid decrease in pressure accompanied by a high temperature may induce included gases or high vapor pressure constituents to escape, resulting in serious degradation or loss of coatings. The mechanism for potential

damage to coatings during ascent is significantly different from that which may reduce coating life during reentry. In reentry, accelerated rates of oxidation are found in critical low-pressure areas; in ascent, oxygen or oxidation do not necessarily play a significant role. The problem will be one of dissociation and volatilization on heating to moderately high temperatures in high vacuum. The extent of damage will depend on the precise combination of high temperature and low pressure that develops and the time that surfaces are exposed to vacuum before sufficient cooling occurs to stop volatilization. Although times of exposure are short, 1 to 2 min at temperatures above $2000°F$ and pressures of 10^{-5} or less could cause serious damage. For example, a Sn-Al coating on tantalum could be completely destroyed at temperatures of 2000 to $2400°F$ and pressures of 10^{-4} to 10^{-5} mm Hg in 15 to 45 sec by vaporization of tin and aluminum. If this occurred on boost, the coating might not be able to protect the substrate during the reentry phase. Thus vacuum volatility of coatings is an important consideration in determining overall suitability for aerospace use.

Of the mechanical factors in the ascent environment that may affect coatings, vibration and shock appear to be likely sources of difficulty. It has been established that satellite components and flight systems have been damaged or destroyed as a result of excessive g forces or sinusoidal vibration prior to or during flight (5). Vibration and shock inputs arise from booster ignition, engine acoustic pressures, aerodynamic forces, and stage separation. A typical pattern of vibration history during ascent is as follows:

- At time of ignition, the intense acoustic field created by the booster engine exhaust reverberates from the ground to the vehicle components; the aft portions of the vehicle are most affected. Vibration from this source diminishes rapidly as altitude is gained.
- When sonic velocity is approached, excitation increases sharply and reaches a maximum in the transonic region followed by an equally rapid decay.
- Finally, at stage separation and second-stage ignition, shocks are sensed throughout the vehicle.

Typical values cited for an Able-Star second stage on a Thor Booster gave overall vibration values of 7.5 g for 6 to 7 sec on ignition, 16 g for 10 to 20 sec at sonic, and a very short peak of 15 g at second-stage ignition (5). The estimated trend indicates a decrease in vibration with increased payload weight. Assuming that 10% of static thrust goes into a periodic component of vibration, vibration decreases from 10 g at 100 lb (Jupiter C and Explorers I – IV) to about 1 g at 8,000 lb (Centaur) (5).

Two types of vibration are noted: random levels at 0 to 2,000 cycles/sec and sinusoidal at 100 to 1,200 cycles/sec. Levels for ICBM boosters range from 4 g for random to 2 g for sinusoidal in forward instrument compartments (5). Vibration and shock that occur at time of ignition and upon exceeding sonic velocity are more likely to be damaging to coated refractory metals, since virtually no heating has occurred. Vibration at stage separation would be less damaging because structures are hot. Although vibration times are short, the level of vibration might be sufficient to introduce coating defects.

8

Other mechanical variables in the ascent environment should have little effect on coating systems. High shearing forces, which occur early in flight, reach a maximum and decay before appreciable temperatures are attained. Strains from aerodynamic loading are held to very low values in the elastic range by design; however, some knowledge of the sensitivity of coatings to defect formation on elastic straining must be made available.

Orbital or space flight environment. Of the total aerospace environment, the portion that is associated with orbital or space flight is considered least likely to have any detrimental effect on oxidation-resistant coating systems. The four major factors to be considered are: (1) temperature, (2) vacuum, (3) meteoroids, and (4) radiation. Average surface temperatures are likely to range between -150 and +400° F, with cyclic variations from highs to lows during orbital flight. Cracking or spalling of brittle coatings upon cycling to subzero temperatures might be encountered. Although high surface temperatures are not realized, loss of material by direct evaporation at the extremely low pressures should be considered. Pressure in near-earth orbit will range from 10^{-6} to 10^{-7} mm Hg, whereas pressure at altitudes beyond 2,500 miles will be less than 10^{-12} mm Hg. Evaporation rates of most coating constituents at temperatures to 400° F are exceedingly small (e.g., 1×10^{-7} in./yr for aluminum and 1×10^{-18} in./yr for titanium). Recent tests have shown W-3 coated Mo-0.5Ti and Vought IV coated Cb-1Zr to be relatively unaffected after 30 days at 1000° F and 10^{-7} mm Hg (6). Degradation was observed at higher temperatures. Problems with respect to direct evaporation are not anticipated in the use of coated structures in lifting reentry vehicles during orbital or space flight.

Coating degradation by sputtering probably will not occur within any reasonable time of flight. Sputtering is the removal of surface atoms by high-energy atomic or molecular particles that strike the surface. It is one of the least understood and least explored areas. An order of magnitude estimate is that one atom will be lost from the surface per 10^{+4} impacts. For a vehicle in circular orbit at 250 miles, the rate of removal is roughly 1 Å (3.94×10^{-9} in.)/hr (7). Under such conditions, 5 to 10 years of continuous exposure would be required to produce any significant change in coatings of 1- to 3-mil thickness. The rate of erosion due to micrometeorite bombardment is of the same order of magnitude. Conservative estimates indicate that erosion caused by meteoroids is negligible for periods up to 1 year (8). More recent studies show that the time for complete erosion of a 2200Å (0.87×10^{-5} in.) layer of aluminum on a 100-ft sphere by a combination of sputtering and micrometeorite impingement is about 3 years (9).

The physical impact phenomena more likely to cause damage in a reasonable period of time are those associated with the larger (penetrating) meteorites. High-impact collisions that can cause puncture are treated as a statistical probability. There is a high degree of uncertainty in data on frequency of impact and damage, since sizes, masses, and densities of particles have to be deduced. The physical relationships and mathematical theory that are used rely on estimates, assumptions, and empirical derivations; hence, a great range of predictions exists. The physical properties of meteoroids are essentially unknown because they are destroyed upon entering the earth's atmosphere. Fragments that have reached the earth vary in density from 2 to 8 gm/cc, but these are not thought to be representative of those in space; a density of 0.05 gm/cc

9

has been proposed for these same meteoroids in space (10). At this density, a 1-gm particle would have a diameter of about 3.37 cm. The total flux of such particles is estimated to be 2.5×10^{-5} meteoroids per square meter per year. If Whipple's 1958 summary of meteorite data is used, the rate of impact on 1 m^2 of area as a function of particle diameter is one hit per 1.2 hr for 0.1 mm, one per 12 days for 1 mm, and one per 160 years for 10 mm. A 0.1-mm-diameter particle would have a mass of about 5×10^{-8} gm, compared with about 5×10^{-2} gm for a 10-mm particle.

Although average particle mass is small, the kinetic energy of meteoroids is considerable. Absolute velocity varies from 7 to 26 miles/sec, and the average relative velocity in the vicinity of the earth is about 19 miles/sec. Calculations indicate that particles of 1.6×10^{-8} gm (about 0.1-mm diameter) traveling at 9.3 miles/sec could penetrate 3.98×10^{-3} in. of aluminum or 2.21×10^{-3} in. of steel (11) and could damage sensitive coatings or materials. Any damage, however, would be localized in random areas owing to the relatively low flux of particles having sufficient kinetic energy to cause damage. To evaluate potential damage, knowledge of the behavior of coatings in hypervelocity impact is required.

Metals (and probably intermetallic coatings) present little if any radiation damage problems in orbital or space flight. No appreciable degradation is to be expected from the various sources and types of radiation encountered beyond the atmosphere.

Reentry environment. Upon reentry a vehicle may follow a number of possible trajectories within a flight corridor defined in terms of altitude versus velocity contours. The boundaries of a corridor are selected on the basis of peak allowable heating rates and temperature at various points on the vehicle, deceleration loads on equipment and personnel, and the maximum lift coefficient (C_L max). A wide variation in environmental factors is possible within a given flight corridor.

The most important factor in reentry is the time variation of temperature and pressure. The critical peak heating period occurs upon descent from 400,000 to 100,000 ft. The temperature of exposed surfaces increases rapidly to a peak value within the first 1 to 10 min and then may hold at a nearly constant high value for the next 15 to 30 min, followed by a more gradual drop to low values during the final portion of descent (1, 4, 12). The temperature depends upon the position of a given structural element in the vehicle. It will be highest at the stagnation line of the leading edge surfaces and lowest on the upper wing and body surfaces. Peak stagnation temperatures on wing leading edges range from 2500 to 3500° F in several typical designs. In general, it can be concluded that temperatures for refractory metal components are determined primarily by materials capabilities. They will range from 1800 to 3000° F for the present substrate/coating combinations, with an increase to 3500° F or higher when improved materials are developed.

A time variation of pressure occurs simultaneously with that of temperature during reentry. Static air pressure increases from 1.35×10^{-5} mm Hg at 400,000 ft to 8.29 mm Hg at 100,000 ft. This pressure, dependent upon venting and design, could exist on all internal surfaces and structural members. Thus one requirement is for coating stability at temperatures of 1800 to 3000° F in relatively static air at pressures

10

of 10^{-5} to 10 mm Hg for times of 15 to 60 min. The outer surfaces are exposed to high-velocity air and encounter a correspondingly higher pressure at any given instant. Air pressure during descent to 100,000 ft may range from 10^{-2} to 100 mm Hg (1, 4).

In addition to temperature and pressure, other factors in the environment such as gas states, mass flow and shearing forces, strain, and vibration must be considered. The composition of the earth's atmosphere remains relatively constant at 20.95% O_2 and 78.09% N_2 to an altitude of 50 miles (264,000 ft) (13). Molecular oxygen starts to dissociate above this altitude and is about 50% dissociated at 65 miles (343,000 ft). Oxygen is totally dissociated above 90 miles (475,000 ft). Nitrogen begins to dissociate above 60 miles (315,000 ft). In addition to these four species, ozone occurs in a band from 5 to 30 miles above the earth, with the largest concentrations at 12 to 18 miles (63,400 to 95,100 ft). Since most of the deceleration and resultant aerodynamic heating occurs upon descent from 400,000 to 100,000 ft, O_2, O, N_2, and N will be the major gas species encountered. The ratio of atomic to molecular species decreases rapidly during descent, and the atomic species disappears in 1 to 2 min. It is relatively safe to assume, therefore, that the dissociated gases which exist at high altitudes will not play a significant role in the oxidation behavior of coated refractory metals during reentry. However, if thermal dissociation occurs in heated boundary layers, surfaces could be exposed to atomic species for longer periods. This type of dissociation could have significant environmental effects in terms of heat transfer and surface chemistry(14).

Air passing through the bow shock wave in the region of the wing stagnation line does not become heated sufficiently to cause dissociation. This is due to the large sweep angle. As the air expands around the leading edge, the temperature tends to drop in the inviscid portion of the flow field and the air remains undissociated at the edge of the boundary layer. Within the boundary layer, however, temperatures can reach 7200°R during reentry. This is sufficient to dissociate oxygen but probably will not result in significant dissociation of nitrogen. Thus, O_2, O, and N_2 will comprise the major gaseous species in the boundary layer for a significant portion of the total reentry time. Since temperature is not constant within the boundary layer, species concentration will vary through the thickness of the layer and in the plane of the boundary layer. In assessing the importance of this environmental factor, it is necessary therefore to estimate the species concentration at the metal surface for any given location as a function of reentry time. Czarnecki and Braun indicate that dissociated oxygen will exist in frozen flow during all but the last 5 to 10 min of reentry (4). However, the availability of this species at the surface for chemical reaction will depend on recombination and diffusion rates and temperature changes as the gas flows over the wing. Calculations of this nature are not available and should be made.

Shearing forces are induced by gas flowing over exposed surfaces at high velocity. These may be of sufficient magnitude to wash liquid or viscous coatings or oxide films off the surface. This factor may be critical in the performance of liquid-phase coatings (i.e., Sn-Al) or silicide coatings at very high temperature. The tensile or compressive strains resulting from deceleration and other forces are kept within the elastic region insofar as possible by proper design and should not materially affect coating behavior. High strains are not encountered until the vehicle enters a denser atmosphere. Maximum strains up to 0.1% will occur, however, while the materials are at peak temperature. Vibration loads generally will be encountered only at lower

11

altitudes, where buffeting occurs, and in the transonic region. By this time, structures will be relatively cool, and any defects will affect coating performance only upon reuse of the vehicle for other missions.

Liquid-Fuel Rocket Engines

Liquid-fuel chemical rockets have been used widely as "work horse" propulsion systems for large booster vehicles and spacecraft. High-temperature materials are required in the hot-gas turbine that drives the fuel and oxidizer pumps; the combustion or thrust chamber, including the fuel injection system and igniter; and the nozzle and exit skirt. The ability to cool regeneratively the nozzle and thrust chamber with liquid fuel or oxidizer reduces the operating temperature to levels where conventional high-temperature alloys can be used. In typical large boosters, the hot-gas turbine is made from investment cast iron-, nickel-, or cobalt-base alloys. Fuel injection and ignition components, thrust chambers, nozzles, and skirts are produced from similar materials in sheet or tubular form.

Demands for increased performance and new applications for low-thrust orbital or space maneuvering engines have created a need for materials of construction with increased temperature capability (15). Several methods of increasing the efficiency and performance capabilities of liquid-fuel engines are being used. The first approach is the use of new fuels and oxidizers to increase specific impulse. In most of the older propulsion systems, liquid oxygen was used as an oxidizer and RP-1 (kerosene-base) as a fuel. Combustion temperatures in the neighborhood of $5000-6000°F$ were realized. With regenerative cooling, operating temperatures of metal parts in combustion chambers were below $1500°F$. In the years ahead, combustion temperatures for more advanced fuel-oxidizer systems, including liquid hydrogen—liquid oxygen, may be lower. The one exception is liquid fluorine and hydrazine or liquid hydrogen, which yields theoretical temperatures of $7000-8000°F$. Corrosion and toxicity problems in handling liquid fluorine, however, have retarded the development of practical systems. In general, changes in fuels and oxidizers within the next few years should have little effect on high-temperature strength requirement for materials. However, they may have a pronounced effect on materials performance owing to chemical reaction with products of combustion.

A second approach to increased performance is to raise chamber pressure. As will be shown, this has a pronounced effect on operating temperatures of the thrust chamber, nozzle, and skirt. Consideration is being given to the use of coated refractory metals in critical components to take advantage of potential gains in performance by this means.

A third approach to increased efficiency and performance consists of using radiative cooling for all or part of the engine to reduce engine weight. This is particularly important in upper stage engines or space systems, where each pound of weight adds substantially to booster requirements or subtracts from payload capabilities. The high-expansion-ratio nozzles required for upper stage or spacecraft engines are prohibitive in weight if total regenerative cooling is used. Radiative- or ablative-cooled exit skirts are used in most systems today. All-metallic radiative-cooled skirts weigh less than ablative systems and represent a potential use of coated refractory metals.

12

The major demand for refractory metals, however, is for use in small, low-thrust orbital or space-maneuvering engines, designed for cyclic (start-stop) use with a short "on" time but a long cumulative burning time. These engines are entirely radiative cooled to provide minimum weight and maximum efficiency and reliability. Coated molybdenum-base alloys have been used successfully in experimental tests of engines operating with the combustion chamber at temperatures over 3000°F. The engines are made of fabricated sheet alloys and must be coated to resist the corrosive action of combustion products. Also basic materials must be resistant to thermal shock, plastic deformation, and erosion.

Although products of combustion primarily are reducing in nature, significant amounts of oxygen and water vapor are present in most exhaust gases. Other gases that may present corrosion problems include oxides of carbon and nitrogen, hydrocarbons, and hydrogen. The potential for chemical attack is sufficiently great to present a serious corrosion problem for refractory metals. Coatings are required to protect refractory metals, not only from oxidation but also from reaction with carbon, hydrogen, and nitrogen. Protection from hydrogen and nitrogen may be particularly critical for columbium- and tantalum-base alloys.

The nature of the corrosive environment is determined by temperature, gas composition, pressure, and velocity. Temperature is determined by the balance of heat input and heat loss: heat input resulting from convective heat transfer from the exhaust gases, and heat loss resulting from radiation and from heat transfer through the structure. Heat input is a function of the convective heat transfer coefficient h_g, gas temperature T_g, metal temperature T_s, and area of heat transfer A :

$$\dot{q} = h_g A (T_g - T_s) \tag{1}$$

The convective heat transfer coefficient is a complex function of at least 11 variables, including gas viscosity and heat capacity, pressure, and velocity. Gas pressure is a most significant variable in that small increases in chamber pressure produce significant increases in heat transfer coefficient. In a simple case where most of the heat loss occurs by heat transfer through the structure (i.e., heat sink or regenerative cool principals), the heat loss is given by

$$\dot{q} = \frac{A(T_g - T_a)}{R} \tag{2}$$

where T_a is the ambient temperature on the cold side and R is the resistance to heat flow through the structure. Resistance to heat flow is a function of the convective heat transfer coefficient h_g, the design, and the heat transfer properties of the structure, including the coolant if any.

Maximum temperature is attained at steady state, where heat input equals heat loss. By equating Equations (1) and (2) for a very simplified case, it can be shown that the maximum temperature is

$$T_s = T_g - f\left(\frac{T_g}{h_g R}\right)$$
(3)

Thus, maximum surface temperature is equal to the combustion or gas temperature less some function of the gas temperature divided by the convective heat transfer coefficient and the resistance to heat flow. Relatively minor changes in engine design, fuel-oxidizer system, chamber pressure, and burning time have significant effects on the total operational environment for metallic components.

These relations, coupled with wide variations in exhaust gas chemistry, are so complex that no generalizations of environmental conditions can be made. Each engine presents unique environmental characteristics, dependent upon design, fuel-oxidizer combination, and operational characteristics. Laboratory simulation of environmental conditions is difficult, if not impossible. In most cases, the only satisfactory test is subscale motor firing.

Perhaps the only common factor in all applications is the time or use cycle. All engines have relatively short burning times, ranging from a few seconds to perhaps 3 min. Large boosters on second-stage engines have a single use cycle. However, recoverable boosters or upper stages may cause multiple use to become important. For some upper stage engines and orbital or space maneuvering engines, stop and start recapability with multiple use cycles is a requirement. Total accumulated burning time may run up to 5 hr or more in radiative-cooled maneuvering engines. These engines are unique in that, after combustion, heated surfaces are exposed briefly to the high vacuum of deep space ($< 10^{-9}$ mm Hg). Repetitive cycles could produce some coating degradation as a result of low-pressure degradation during cooling at the end of each combustion cycle.

CALCULATED REENTRY ENVIRONMENTS

Methods of Analysis

Model reentry system. The operational environment (heat flux, temperature, gas pressure, etc.) is determined by the following:

- Lift-to-Drag Ratio at the Specific Mach Number (L/D) — upper limit of this factor fixed by vehicle shape; lower limit determined by angle-of-attack or attitude. Values for lifting reentry vehicles range from 0.2 to 3.0.
- Ballistic Reentry Factor ($W/C_D A$ where W = total weight, C_D = drag coefficient, A = wing loading area) — also fixed by vehicle shape and angle-of-attack. Values for lifting reentry vehicles range from 30 to 200 lb/ft^2.
- Reentry Angle (γ_E) — the angle defining the lower boundary of a reentry corridor; determined by the maximum tolerances for heating and deceleration.
- Reentry Velocity (V_E) — velocity at start of reentry, 26,000 ft/sec for reentry from orbit and 36,000 ft/sec for superorbital reentry.

14

The numerical values of these factors are used with four partial differential equations of motion to define precisely the altitude-velocity contours (flight path). The time variation of heat flux, temperature, pressure, and gas velocity can be calculated from these data for any desired point on the surface of a vehicle.

The vehicle selected for the model reentry system is a medium-wing-load glider similar to that shown in Figure 1. Details of the plan, side elevation, and front view are given in Figure 2. This design is from an Air Force program on development of a frontal section for superorbital lifting reentry vehicles (12). The external nose structure (not shown) is attached at a droop angle of 20 deg from the body centerline. It is an ellipsoid of revolution (oblate spheroid), with a ratio of semiminor to semimajor axes b/a equal to 0.4 and an effective radius of curvature at the stagnation point of 2.48 ft.

The wing leading edges have an effective radius of curvature of 0.5 ft. A flat plate lower wing surface is incorporated, and a diamond-shaped chamber is provided on the upper surface. Three representative locations on the wing were selected for analysis of environmental conditions: the stagnation line of the leading edge and two points 10 ft back from the leading edge, one on the upper surface and one on the lower surface. All points are sufficiently remote from the nose stagnation point so that nose flow effects over the wing are not encountered.

Two reentry trajectories were selected for analysis: one superorbital at a reentry velocity of 36,000 ft/sec and the other orbital at a velocity of 25,500 ft/sec. The variation in altitude and velocity as a function of reentry time is given in Figures 3 and 4. These trajectories were calculated using the LMSC "Five-Degree-of-Freedom Lifting Point Mass" computer program on an IBM-7090 computer. The vehicle was designed primarily for superorbital use, but it can be used for either type of mission. The two trajectories selected are considered to be reasonable flight paths for reentry from orbit or space for this vehicle. The purpose of analyzing two cases is to show the drastic change in environment as a function of mission requirements. Both trajectories have three distinct phases: (1) a constant L/D pullup from reentry into the atmosphere, commencing at 400,000 ft, until a horizontal (constant-altitude) flight path is achieved. (2) a constant-altitude deceleration with a constant L/D using a roll program in the superorbital case to control the vertical component of lift, and (3) final descent at constant L/D with constant roll angle terminated at a recovery altitude of 50,000 ft. Basic aerodynamic parameters are: L/D, 2; $W/C_D A$, 200; angle-of-attack, +22 deg; and reentry angle, -5.6 deg.

Heat flux. For the purposes of this analysis, the wing can be considered to have a cross section as shown in Figure 5. The laminar stagnation-point heating rate to a cylinder normal to the flow may be obtained by a coordinate transformation of a sphere in three dimensions to a cylinder in a two-dimensional system. Lees (16) points out that this entails merely multiplying the heat flux to a sphere by $2^{-0.5}$. The wing leading edge is not normal to the flow, however, and additional geometric considerations for wing sweep and angle-of-attack must be applied.

15

Figure 2 Configuration of Medium-Wing-Load Glider for Lifting Reentry Model

16

Figure 4 Model Trajectory for Superorbital Reentry

Figure 3 Model Trajectory for Orbital Reentry

17

BODY-WING INTERSECTION

SHOCK

α

BOUNDARY LAYER

SECTION A - A
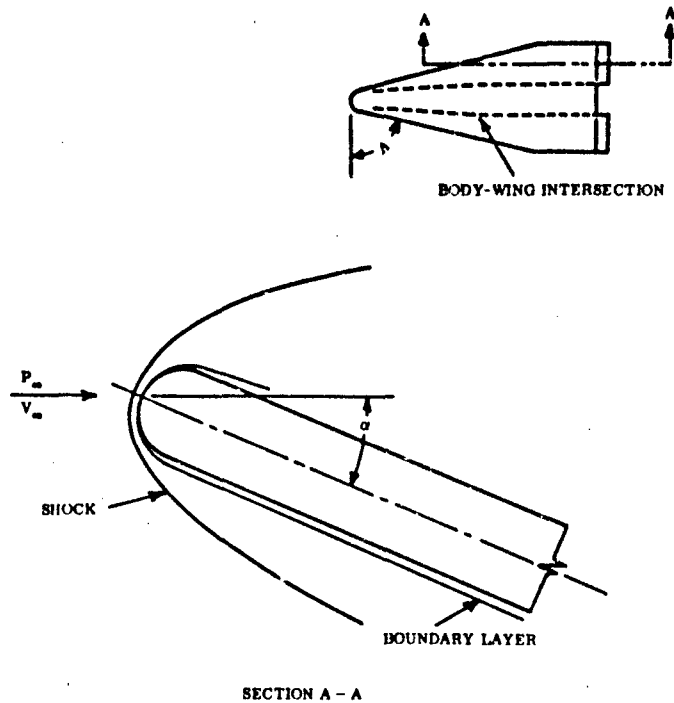
Figure 5 Flow Model for Lifting Reentry Vehicle

The relationship used to obtain the stagnation-point heat flux (17) was*

$$\dot{q}_s = \frac{17,600}{\sqrt{R}} \sqrt{\frac{\rho_\infty}{\rho_0}} \left(\frac{u}{u_c}\right)^{3.15} \left[\frac{h_{se} - h_{sw}}{h_{se} - (h_{sw})_{300}}\right] \tag{4}$$

If u_c = circular orbital velocity = 26,000 ft/sec and ρ_0 = density at sea level = 0.002377 lb sec^2/ft^4, the equation reduces to

$$\dot{q}_s = 17,800 \left(\frac{u}{10^4}\right)^{3.15} \sqrt{\frac{\rho_\infty}{R}} \left[\frac{h_{se} - h_{sw}}{h_{se} - (h_{sw})_{300}}\right] \tag{5}$$

for the trajectories considered, the assumption being that $h_{se} \gg h_{sw}$ will give temperature predictions slightly on the high side. In other words, a cold-wall assumption will be made, which is conservative, and for the purpose of this study is sufficiently accurate. Equation (5), reduces, therefore, to

$$\dot{q}_s = 17,800 \left(\frac{u}{10^4}\right)^{3.15} \sqrt{\frac{\rho_\infty}{R}} \tag{6}$$

---

*A nomenclature is given at the end of Section II.

18

By multiplying by $2^{-0.5}$, as mentioned previously, Equation (6) will give the heat flux to a cylinder normal to the flow. Therefore,

$$\dot{q}_{\Lambda=0} = \frac{17,800}{\sqrt{2}} \left(\frac{u}{10^4}\right)^{3.15} \sqrt{\frac{\rho_\infty}{R}} \tag{7}$$

If the wing has sweep, the above expression is corrected by multiplying by $\cos \Lambda$. When a delta wing is pitched to an angle-of-attack, the effective sweep is decreased and the local angle-of-attack or effective angle-of-attack relative to the leading edge increases. From purely geometrical considerations, the correction equation for sweep and angle-of-attack (18) can be expressed as

$$\frac{\dot{q}_\Lambda}{\dot{q}_{\Lambda=0}} = [1 - \sin^2 \Lambda \cos^2 \alpha]^n \tag{8}$$

The exponent n is an experimental correction factor and can vary between 1.5 and 1.0. For this study, $n = 1.0$ was used (18).

The heat flux at the point on the bottom surface of the wing 10 ft back from the leading edge was calculated by assuming the wing to be a flat plate. This is a reasonable assumption because 10 ft back from the cylindrical leading edge the induced pressure, caused by the blunted wing, is for all practical purposes not effective. In this study, simplified equations for flat-plate heating at a positive angle-of-attack were used (18): for laminar heating,

$$\frac{(\dot{q}_{FP})_L}{\dot{q}_s} = 0.0292 \left(\frac{R_o}{x}\right)^{0.5} \alpha^{2/3} \tag{9}$$

for turbulent heating,

$$\frac{(\dot{q}_{FP})_T}{\dot{q}_s} = 0.0666 \left(\frac{R_o}{x}\right)^{0.2} \frac{\alpha}{\left(1 + \frac{11}{3}\frac{h_w}{h_s}\right)} \tag{10}$$

The location 10 ft from the leading edge on the upper surface of the wing is affected by the induced pressure caused by the blunt leading edge of the wing. The experimental results of Bogdonoff and Vas (19) indicate that the pressure on the upper wing surface is approximately equal to free-stream pressure. Therefore, free-stream flow properties were used for determining the heat transfer to the upper surface of the wing. Eckert's reference enthalpy method (20) was used for determining the heat flux to the wing surface.

19

Temperature. Materials for lifting reentry gliders must be able to withstand the environment that will exist when a radiation-cooling technique is used for thermal protection. This implies that the heat flux from aerodynamic heating will be dissipated to the atmosphere and space by means of radiation. Therefore,

$$\dot{q}_{convective} = \dot{q}_{radiative} \tag{11}$$

The radiative flux can be calculated by the simplified Stefan-Boltzmann equation, expressed as

$$\dot{q}_{radiative} = 0.478 \; \epsilon \left(\frac{T_w}{10^3}\right)^4 \tag{12}$$

where $\dot{q}_{radiative}$ is expressed in Btu/ft^2-sec and T_w in °R .

The wall temperature was calculated from Equation (12). Actually, there is an additional energy term due to internal radiation between the various surfaces. This effect will tend to equalize the temperature of the various surfaces. In this study the internal radiation term was not considered, and skin temperatures will therefore be slightly on the high side.

Pressure. The pressure at the stagnation line of the wing will be determined by the Newtonian Flow Theory. Therefore,

$$P_{SL} = P_\infty + \rho_\infty u_\infty^2 \cos^2 \theta \tag{13}$$

The pressure on the bottom surface of the wing 10 ft from the leading edge was determined from Creager's results (21). Creager's paper presents curves for obtaining surface pressures over blunt delta wings at positive angles-of-attack.

The pressure on the top surface of the wing 10 ft from the leading edge was based on Bogdonoff and Vas experimental results (19). These results showed that the pressure on the upper wing surface is approximately equal to the free-stream pressure. In this study, free-stream pressure was assumed to be acting on the upper wing surface and on all internal surfaces.

Boundary-layer species. Because of the large sweep angle of the wing, the temperature of the air passing through the bow shock wave in the region of the wing stagnation line does not increase enough to cause dissociation. As the sweep angle increases, the normal component of the velocity vector relative to the shockwave decreases. Thus, the larger the sweep angle, the lower the temperature of the air downstream of the bow shock. As the air expands around the leading edge, its temperature tends to drop in

20

the inviscid portion of the flow field. Therefore, conditions at the edge of the boundary layer remain undissociated. Within the boundary layer, the temperature of the air will be high enough to cause dissociation. The temperature within the boundary layer may become as much as 18 times as high as the temperature at the edge of the boundary layer; if the temperature at the edge is 400°R, a temperature of 7200°R may be reached within the boundary layer during portions of the trajectory. Dissociation of oxygen can occur as a function of gas temperature by the reaction

$$O_2 = K_D \, 2(O) \tag{14}$$

The pressure of molecular oxygen (14) is given by

$$P_{O_2} = P_T \left[1 - \frac{2}{(1 + 4P_T/K_D)^{1/2} + 1} \right] \text{atm} \tag{15}$$

where K_D, the dissociation constant for oxygen, is $e^{16.1} e^{-122,000/RT}$. Using this relation, it can be shown that, for a total oxygen pressure of 0.076 mm Hg, atomic oxygen will exist in significant amounts above about 3200°F (3660°R). The temperature for significant dissociation at 7.6 mm O_2 pressure is about 4100°F (4560°R). Thus, since a temperature as high as 7200°R might occur in the boundary layers, it is reasonable to assume that significant amounts of oxygen will be dissociated during reentry. The effects of dissociation of nitrogen will not be considered, since in most cases it does not affect the chemical reactions at the wall surface. In addition, the equations that will be used to determine oxygen species concentration are practically independent of the nitrogen species concentrations, providing that the temperature is lower than the temperature at which nitrogen starts to dissociate (i.e., 7500°R).

The Reynolds number at the edge of the boundary layer will indicate whether a laminar or turbulent boundary layer exists at the wing location being considered. If a laminar boundary layer exists, the following approximate procedure can be used for determination of the oxygen species concentration at the wing surface.

The rate of change of concentration of the molecular oxygen to atomic oxygen as the gas enters the boundary layer from the inviscid flow field can be expressed as

$$\frac{dC_{O_2}}{dt} = - K_D \left[C_{O_2} \right]^2 \tag{16}$$

where C_{O_2} is concentration of molecular oxygen.

As the air dissociates within the boundary layer, the opposite process of recombination will occur simultaneously. Thus, Equation (16) can be expressed in the more general form

$$\frac{dC_{O_2}}{dt} = -K_D\left[C_{O_2}\right]^2 + K_R\left[C_O\right]^2\left[C_{O_2}\right] \tag{17}$$

The maximum rate of dissociation will occur when only molecular oxygen exists. Dr. N. Kulgein of LMSC has supplied the complete reaction rate in a form convenient for numerical computations:

$$\frac{dC_{O_2}}{dt} = W = \frac{276}{\bar{T}^5}\left(\frac{1 - Y_{AV}}{1 + Y_{AV}}\right)P^3\left[\frac{4Y_{AV}^2}{(1 + Y_{AV})^2} - \left(\frac{1 - Y_{AV}}{1 + Y_{AV}}\right)\frac{1.54 \times 10^6\,\bar{T}e^{-59/\bar{T}}}{P}\right] \tag{18}$$

where

$\bar{T}$ = T/1000, temperature in °K
P = atmospheres
Y = fraction of dissociated oxygen molecules

Equation (16) corresponds to Equation (18) when Y_{AV} is equal to zero and yields the maximum dissociation rate. The temperature at which the reaction occurs must be known. E. R. Van Driest (22) determined temperature and velocity profiles for laminar flow over a flat plate for Mach numbers up to 20. His solution is based on a Prandtl number of 0.75 and on Sutherland's rule for viscosity-temperature variation. His results can be used for a first approximation of the maximum temperature in the boundary layer. The temperature will be on the high side because he did not include dissociation effects; an approximation of the degree of dissociation can be made on the basis of the temperature he predicted.

To estimate the degree of dissociation, the air entering the boundary layer at the leading edge will be assumed to remain at the maximum temperature within the boundary layer. Thus, the minimum time required for a unit volume of air to be completely dissociated, along a streamline, is

$$t_c = \frac{\rho}{\left(dC_{O_2}/dt\right)} \tag{19}$$

where (dC_{O_2}/dt) is evaluated by Equation (18). The time available for this air to traverse the wing from the leading edge to a point on the wing is

$$t_w = \frac{s}{u} \tag{20}$$

If $(t_c/t_w) \gg 1$, then no appreciable dissociation occurs. Thus, the boundary layer is essentially undissociated, and only molecular oxygen can exist at the wall. If

22

$(t_c/t_w) \ll 1$, then significant dissociation occurs, and reevaluation of the temperature at which it occurs will be necessary. This temperature can be approximated by solving the following total enthalpy equation for the streamline being considered

$$h = \int_{T_0}^{T} C_p \, dT + Yh_D + \frac{u^2}{2g} \qquad (21)$$

where velocity u is selected from Van Driest's results, corresponding to the initial temperature estimated; C_p is expressed as a function of T; and T_0 is the reference temperature, usually taken as $0°K$. The total enthalpy h can be expressed as a function of u by assuming that Schmidt No. $\cong$ Prandtl No. $\cong 1$, which leads to the Crocco relationship

$$\frac{h - h_w}{h_e - h_w} = \frac{u}{u_e} \qquad (22)$$

The value of h_w is estimated by assuming a value of Y at the wall. This assumption can later be checked for correctness with a calculated value. The value of h can be determined from Equation (22) in terms of u. Substituting this result into Equation (21) results in an equation with temperature unknown. Solving for T will result in a more realistic value than the approximations using Van Driest's results. Equations (18), (19), and (20) can then be reevaluated.

If $(t_c/t_w) \ll 1$, an estimate must be made of whether the dissociated oxygen in the boundary layer will diffuse to the wing surface, and also if the oxygen atoms reaching the surface will recombine at the surface. Comparison of the recombination time normal to the streamlines with the diffusion time for the oxygen atoms to reach the surface will indicate whether frozen flow, equilibrium flow, or nonequilibrium flow exists in the boundary layer. For $(t_c/t_w) \ll 1$, complete dissociation will be assumed to exist at the streamline within the boundary layer that has the maximum static temperature. The recombination time can be determined by using Equation (18) to evaluate (dC_{O_2}/dt), and then using Equation (19) to calculate the recombination time t_c. The density ρ and temperature of the gas can be evaluated at the wall surface. Actually, an average temperature and density should be used in Equations (18) and (19), respectively. However, to obtain the most conservative estimate of whether frozen flow exists, the temperature and density of the gas at the wall should be used.

The diffusion rate can be expressed as

$$\dot{Q} = \rho v = \rho D \frac{dC_{O_2}}{dy} \qquad (23)$$

23

which reduces to

$$v = D \frac{dC_{O_2}}{dy}$$ (24)

By definition,

$$v = \frac{d}{t_D}$$ (25)

Substituting Equation (24) into Equation (25) yields

$$t_D = \frac{d}{D\left(\frac{dC_{O_2}}{dt}\right)}$$ (26)

If $(t_c/t_D) \gg 1$, frozen flow will exist within the boundary layer. The following equation can be used for determination of Y at the wall only if frozen flow exists:

$$\left(\rho D \frac{dC_{O_2}}{dy}\right) = \frac{350}{\sqrt{T_w}} \Gamma P \frac{Y_w}{1 + Y_w}$$ (27)

where Γ is a measure of the ability of the wall to act as a catalyst. Equation (27) was supplied by N. Kulgein of the LMSC Aerophysics group. The value of Y_w determined from Equation (27) can be compared with the assumption of Y_w used in evaluating h_w. If the difference is significant, a new estimate of Y_w must be made and the calculations repeated. If $(t_c/t_D) \ll 1$, equilibrium conditions will exist within the boundary layer. The species concentration at the wall can be simply determined from equilibrium air tables knowing the temperature of the wing and the local air pressure. For equilibrium conditions, the species concentration at the wing surface is obviously independent of the catalytic efficiency Γ of the wing surface.

If $(t_c/t_D) \cong 1$, nonequilibrium conditions exist within the boundary layer. This requires a complete solution of the governing differential equations. The laminar boundary layer for flow around a blunt body of revolution has been analyzed and presented in the open literature, but a literature search has not revealed a solution for the flat-plate problem. Therefore, if the flow is laminar on the wing, results for frozen or equilibrium conditions can only be presented.

N. Kulgein has developed a computer program for calculating the species concentration on a flat plate for a nonequilibrium turbulent boundary layer (23). This computer program can be used when the Reynolds number indicates turbulent flow conditions. It will not be necessary to calculate whether equilibrium or frozen flow exists because these are just special cases of nonequilibrium flow. A detailed discussion of this computer program is beyond the scope of this report. The program calculates for any

24

point on the trajectory the fraction of gas that is dissociated at the surface. In addition, by assuming a reasonable catalytic efficiency Γ of the wall, it is possible to calculate the net heat transfer of the wall. Since gaseous dissociation and recombination affect the heat balance, a more realistic heat-transfer value and corresponding surface temperature are obtained when these effects can be considered.

Model Environments

The time variations of heat flux, temperature, external pressure, and internal pressure have been calculated for one boost and two reentry trajectories. A hypothetical boost trajectory was derived for a single-stage booster capable of lifting the vehicle to 400,000 ft, at which time a second-stage booster would be used to accelerate the vehicle to orbital or escape velocity. No calculations were made for the second stage of ascent, since negligible heating would occur during acceleration above 400,000 ft. The two reentry trajectories, already described, consist of three distinct phases:

- Phase I — Constant L/D initial reentry into the atmosphere from 400,000 ft with pullup until a horizontal flight path is achieved at 226,000 ft (L/D = 2.0, α = +22 deg, γ = -5.6 deg)
- Phase II — Constant-altitude (226,000 ft) deceleration at constant L/D using a roll program upon superorbital reentry to control the vertical component of lift
- Phase III— Final descent, at constant L/D, with constant roll angle, terminated at a recovery altitude of 50,000 ft

The choice of constant L/D during Phase I accrues the major benefits of reduced acceleration and heating without the added complexity of density-dependent lift programs. The constant L/D, with roll programming to control the vertical component of lift during Phase II, allows for simple analytical analysis of the phase and is adaptable to a wide variety of maneuvering techniques. The final descent (Phase III) is very gradual, approaching an equilibrium glide, since the vertical forces are initially in equilibrium.

Three representative locations on the wing at a section sufficiently removed from the nose to preclude "nose effects" in the environmental calculations were analyzed: (1) the stagnation line at the leading edge, (2) a point 10 ft back from the leading edge on the bottom surface, and (3) a point 10 ft back from the leading edge on the upper surface. These locations represent the complete spectrum of conditions important to the use of coated refractory metals. The leading edge gives information concerning the high limits of temperature and pressure; the two locations back from the leading edge give information on the low limits of pressure and temperature that the wing surfaces may experience.

Ascent environment. The ascent trajectory and calculated time variation of surface temperature and external pressure at the stagnation line of the wing leading edge are shown in Table I and Figure 6. For this single-stage boost to 400,000 ft, a maximum surface temperature of 1040° F is attained at 1-1/2 min after liftoff. At this time, air pressure is 25 mm Hg on the external surface. Peak temperature is sustained for

Table I. Calculated Model Ascent Environment (Leading Edge Stagnation Line)

Time (min)	Altitude (ft)	Velocity (ft/sec)	Heating rate (Btu/ft^2-sec)	Surface temp. (°F)	External pressure (mm Hg)
0.25	3,000	400	0.005	10	—
0.50	12,000	800	0.05	190	500
0.75	26,000	1,200	0.165	435	327
1.00	43,000	1,800	0.45	680	160
1.25	66,000	2,700	1.20	930	68
1.50	94,000	3,800	1.44	1040	25
1.75	125,000	4,600	1.24	985	8
2.00	158,000	5,300	1.025	915	2.7
2.25	186,000	5,800	0.835	845	1.3
2.50	215,000	6,300	0.66	770	4×10^{-1}
2.75	240,000	6,900	0.505	695	1.7×10^{-1}
3.00	266,000	7,700	0.36	600	5×10^{-2}
3.25	294,000	8,600	0.23	485	1.3×10^{-2}
3.50	320,000	9,600	0.145	375	8×10^{-3}
3.75	346,000	10,900	0.10	300	6×10^{-3}
4.00	371,000	12,300	0.075	260	4×10^{-3}
4.25	397,000	13,900	0.065	235	—
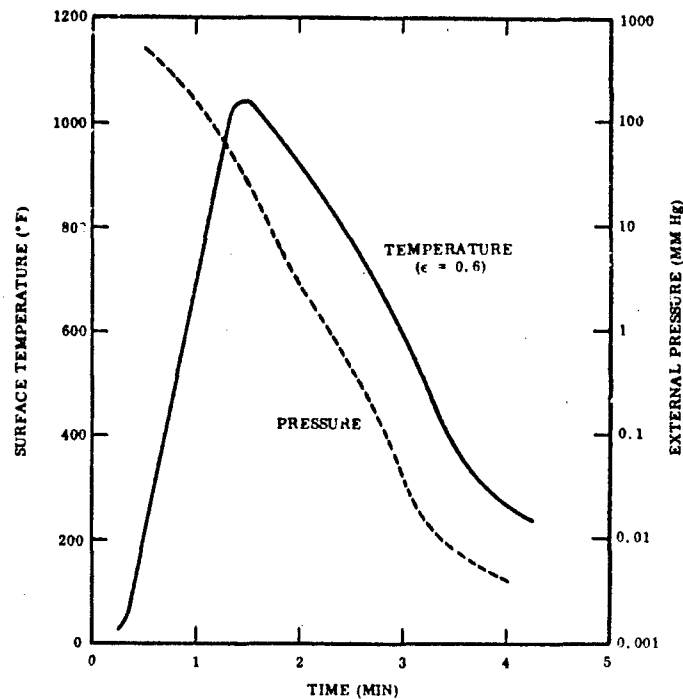
Figure 6   Time Variation of Temperature and Pressure at Stagnation Line of Leading Edge During Ascent to Orbit

only a few seconds and decays rapidly as the vehicle gains altitude. The time variation of temperature and pressure indicates that no degradation of coating systems would occur in this hypothetical model. This is not to say, however, that the ascent environment will not present problems, for in other cases dependent on vehicle design and booster characteristics much higher peak temperatures may be attained. The model merely serves to illustrate the relation of environmental factors that is characteristic of an ascent trajectory.

Reentry environment. The reentry trajectories and calculated model environments for superorbital and orbital reentry are presented in Tables II and III and Figures 7 and 8. The highest temperatures occur at the stagnation line of the leading edge. A peak temperature of 200° F is attained 1 min after reentry at superorbital speeds with a corresponding peak of 3460° F at 4 min in the orbital reentry case. Considering the orbital model in which coated refractory metals could be used in the wing leading edge, temperatures above 2000° F must be sustained for 29 min with external air pressure in the range of 0.5 to 12 mm Hg. Pressure on the internal surfaces varies from 10^{-3} to 0.6 mm Hg during this period.

As shown in Figure 8, temperatures on the upper and lower surfaces of the wing at a point 10 ft back from the leading edge during superorbital reentry are relatively low. The upper surface panels do not exceed 1050° F and hence would not require coated refractory metals. Lower surface panels are exposed to a peak temperature of 2810° F at 2 min, and to temperatures above 2000° F for 13 min at external pressures of 3 to 7 mm Hg. Internal pressure during this time is relatively constant at 0.02 to 0.06 mm Hg. Model environments for the upper and lower surface panels were not calculated for the orbital cases, since peak temperature would be below the range in which coated refractory metal structures would be used.

Boundary layer effects. A boundary-layer analysis and variation of gaseous species concentration at the surface during reentry were considered for a panel on the lower surface of the wing 10 ft back from the leading edge during superorbital reentry. The Reynolds number was found to range from 400,000 to 450,000, indicating a transition region between laminar and turbulent flow. Laminar flow was assumed for the first approximation of boundary-layer composition, and a very lengthy hand calculation was made for one point at 20 min on the reentry trajectory. The calculated value of t_c/t_w (ratio of time for air to dissociate to time for air stream to traverse wing) was 1.05×10^{-2}, indicating that oxygen in the boundary layer was dissociated. Temperatures, however, were not sufficient for nitrogen to dissociate. The subsequent calculation of t_c/t_D (ratio of time for recombination to time for diffusion to the wall) yielded a value of 0.4, indicating a nonequilibrium condition in which flow is not frozen and is not equilibrium. Under these conditions, no further calculations can be made, since the basic method of deriving species concentration applies only to the limiting frozen or equilibrium flow conditions.

Since the Reynolds number approached that for turbulent flow (500,000), calculation of boundary-layer composition could be made by the computer program for turbulent flow. The extent of oxygen dissociation at the metal surface has been calculated for turbulent flow conditions at a point on the lower surface of the wing 10 ft back from the leading edge (superorbital reentry). Calculations were made by a computer

27

Table II. Calculated Model Reentry Environment — Superorbital Velocity

Time (min)	Altitude (ft)	Velocity (ft/sec)	Static pressure (mm Hg)	Stagnation line			Lower surface			Upper surface		
				Heating rate (Btu/ft² sec)	Surface temperature (°F)	External pressure (mm Hg)	Heating rate (Btu/ft² sec)	Surface temperature (°F)	External pressure (mm Hg)	Heating rate (Btu/ft² sec)	Surface temperature (°F)	External pressure (mm Hg)
0	400,000	36,000	1.4×10^{-5}	—	—	—	—	—	—	—	—	—
1	245,000	36,000	2×10^{-2}	209	5200	19.9	33.7	2300	3	1.05	925	2×10^{-2}
2	226,000	34,700	6×10^{-2}	201	5000	19.5	31.5	2810	7	1.55	1055	6×10^{-2}
3		33,500		176	4670	17.8	28.0	2700	6.2	1.45	1030	
4		32,300		155	4430	16.5	25.0	2610	5.8	1.33	1000	
5		31,200		137	4220	15.2	22.5	2530	5.4	1.23	970	
6		30,100		123	4070	14.2	20.0	2450	5.0	1.14	945	
7		29,100		111	3940	13.3	18.1	2370	4.7	1.05	920	
8		28,200		100	3820	12.4	16.3	2300	4.4	0.98	895	
9		27,400		91	3720	11.7	14.8	2220	4.2	0.91	875	
10		26,600		83	3640	11.1	13.5	2160	3.9	0.85	855	
11		25,800		76	3570	10.4	12.3	2090	3.7	0.79	830	
12		25,100		70	3500	9.9	11.3	2030	3.5	0.74	815	
13		24,500		64.5	3430	9.4	10.3	1980	3.4	0.70	795	
14		23,800		59.5	3360	9.0	9.5	1920	3.2	0.66	780	
15		23,200		54.5	3280	8.5	8.7	1870	3.0	0.63	760	
16		22,600		50	3200	8.1	8.0	1820	2.8	0.60	745	
17		22,100		46	3120	7.8	7.3	1780	2.7	0.57	735	
18		21,500		42	3030	7.4	6.7	1740	2.6	0.54	720	
19		21,000		39	2950	7.0	6.3	1700	2.4	0.52	710	
20		20,500		36.5	2890	6.7	5.9	1670	2.3	0.50	700	
21		20,100		34	2840	6.4	5.6	1640	2.2	0.48	690	
22		19,700		32.5	2800	6.1	5.3	1620	2.1	0.47	680	
23		19,300		31	2770	6.0	5.1	1590	2.1	0.46	670	
24	225,000	18,900	7×10^{-2}	30	2740	6.0	4.9	1570	2.2	0.44	663	7×10^{-2}
25	222,000	18,500	8×10^{-2}	29	2720	6.3	4.7	1550	2.3	0.43	660	8×10^{-2}
26	219,000	18,000	9×10^{-2}	28	2700	6.7	4.6	1530	2.5	0.42	655	9×10^{-2}
27	216,500	17,530	1×10^{-1}	27.5	2680	7.5	4.5	1520	2.7	0.42	650	1×10^{-1}
28	213,500	17,100	1.2×10^{-1}	27	2660	8.0	4.4	1500	2.8	0.41	650	1.2×10^{-1}
29	210,000	16,600	1.3×10^{-1}	26.5	2620	8.4	4.2	1480	3.0	0.41	650	1.3×10^{-1}
30	207,000	16,100	1.5×10^{-1}	25.5	2590	8.8	4.0	1460	3.1	0.41	645	1.5×10^{-1}
31	204,000	15,500	1.7×10^{-1}	24	2530	9.2	3.8	1440	3.3	0.41	640	1.7×10^{-1}
32	200,500	15,000	2.0×10^{-1}	22.5	2500	9.6	3.6	1410	3.4	0.41	635	2.0×10^{-1}
33	197,000	14,300	2.3×10^{-1}	21	2450	9.9	3.4	1390	3.6	0.41	625	2.3×10^{-1}
34	193,000	13,700	2.7×10^{-1}	19	2390	10.2	3.1	1350	3.7	0.40	620	2.7×10^{-1}
35	189,000	13,000	3.1×10^{-1}	17.5	2330	10.5	2.8	1320	3.9	0.39	610	3.1×10^{-1}
36	185,000	12,300	3.7×10^{-1}	15	2230	10.9	2.5	1280	4.0	0.39	600	3.7×10^{-1}
37	180,000	11,600	4.5×10^{-1}	13	2170	11.2	2.1	1230	4.2	0.37	590	4.5×10^{-1}
38	174,500	10,830	5.3×10^{-1}	11	2070	11.6	1.8	1170	4.3	0.35	580	5.3×10^{-1}
39	159,000	10,100	6.9×10^{-1}	9	1980	12.0	1.5	1100	4.5	0.33	570	6.8×10^{-1}
40	163,000	9,200	8.6×10^{-1}	7.5	1870	12.4	1.2	1020	4.7	0.32	555	8.6×10^{-1}
41	156,500	8,300	1.1	6.5	1750	12.9	1.0	930	5.0	0.30	545	1.1
42	150,000	7,300	1.5	5	1610	13.4	0.8	820	5.3	0.28	530	1.5
43	142,000	6,100	2.0	4	1480	13.9	0.7	700	5.8	0.25	513	2.0
44	134,000	5,300	2.8	3	1320	14.5	0.5	560	6.3	0.22	500	2.8
45	126,000	4,500	3.9	2	1140	15.3	0.4	380	6.9	0.19	490	3.9
46	118,000	3,800		1	950	16.5	0.3	180	7.8	0.16	450	

Table III. Calculated Model Reentry Environment – Orbital Velocity

Time (min)	Altitude (ft)	Velocity (ft/sec)	Static pressure (mm Hg)	Stagnation line		
				Heating rate (Btu/ft^2 sec)	Surface temperature (° F)	External pressure (mm Hg)
0	400,000	25,500	1.4×10^{-5}	–	–	–
1	335,000	25,450	8×10^{-5}	3	1400	0.01
2	290,000	25,400	1.5×10^{-3}	16.5	2200	0.5
3	248,000	25,350	1.6×10^{-2}	59	3100	4.3
4	226,000	25,000	6×10^{-2}	67	3460	9.8
5	226,000	24,200		65	3410	9.8
6	226,000	23,600		59.5	3310	9.1
7	226,000	23,000		54.5	3220	8.6
8	226,000	22,500		49.5	3130	8.1
9	226,000	21,900		45.5	3050	7.7
10	226,000	21,400		42	2980	7.3
11	226,000	20,900		39	2930	6.9
12	226,000	20,500		36	2870	6.6
13	226,000	20,000		34	2820	6.4
14	226,000	19,600		32	2770	6.1
15	226,000	19,200		30.5	2740	6.0
16	224,000	18,800	6.4×10^{-2}	29.5	2720	6.1
17	221,000	18,400	7.4×10^{-2}	29	2700	6.4
18	218,000	18,000	8.4×10^{-2}	28	2680	6.9
19	216,000	17,600	9×10^{-2}	27.5	2660	7.4
20	213,000	17,100	1×10^{-1}	27	2630	8.1
21	209,000	16,500	1.25×10^{-1}	26	2600	8.6
22	206,000	16,000	1.4×10^{-1}	24.5	2560	8.9
23	203,000	15,400	1.6×10^{-1}	23.5	2520	9.3
24	199,000	14,900	1.85×10^{-1}	22	2480	9.6
25	195,000	14,100	2.2×10^{-1}	20.5	2420	10.0
26	191,000	13,500	2.5×10^{-1}	18.5	2360	10.3
27	187,000	12,800	2.9×10^{-1}	16.5	2290	10.6
28	183,000	12,200	3.3×10^{-1}	14.5	2220	11.0
29	178,000	11,300	4×10^{-1}	12.5	2140	11.4
30	173,000	10,600	4.8×10^{-1}	11	2050	11.8
31	167,000	9,800	5.8×10^{-1}	9	1950	12.2
32	161,000	8,800	7.3×10^{-1}	7.5	1840	12.7
33	154,000	7,900	9.4×10^{-1}	6	1720	13.1
34	146,000	6,900	1.3	4.5	1580	13.6
35	139,000	5,900	1.7	3.5	1430	14.2
36	131,000	5,100	2.3	2.5	1280	14.7

Figure 8   Time Variation of Temperature and Pressure on the Upper and Lower Surfaces of the Wing During Reentry From Superorbital Velocity

Figure 7   Time Variation of Temperature and Pressure at Stagnation Line of Leading Edge During Reentry

30

program devised by LMSC for predictive species concentration on a flat plate for a nonequilibrium turbulent boundary layer (23). Gas entering the boundary layer is assumed to be 100% molecular oxygen. Since nitrogen does not dissociate at the temperatures reached but otherwise physically behaves like oxygen in the boundary layer, results (total fraction dissociated) can be transposed to give the fraction of oxygen dissociated in air. For example, 21% dissociation of oxygen in an oxygen boundary corresponds to 100% dissociation of oxygen in an air boundary (21% O_2, 78% N_2).

As shown in Table IV, the oxygen in an air boundary layer at the metal surface was calculated to be 100% dissociated during the first 6 min of reentry. The extent of dissociation decreased rapidly with time beyond 6 min but remained at a significantly high level during the period of peak heating (1 to 10 min).

Table IV. Boundary Layer Species Concentration in Turbulent Flow

Reentry time (min)	Altitude (ft)	Approx. fractional composition (%)					
		Atmosphere			Boundary layer at wing surface		
		O	O_2	N_2	O	O_2	N_2
0	400,000	20	9	70	—	—	—
1	335,000	9	14	76	23	0	76
2	290,000	0	21	78	21	0	78
3	248,000	0	21	78	21	0	78
4	226,000	0	21	78	21	0	78
5	226,000	0	21	78	21	0	78
6	226,000	0	21	78	21	0	78
7	226,000	0	21	78	16.2	4.8	78
8	226,000	0	21	78	7.55	13.45	78
9	226,000	0	21	78	3.61	17.35	78
10	226,000	0	21	78	2.73	18.27	78
11	226,000	0	21	78	2.06	18.94	78
12	226,000	0	21	78	1.78	19.22	78
13	226,000	0	21	78	1.22	19.78	78
14	226,000	0	21	78	0.99	20.01	78
15	226,000	0	21	78	0.80	20.20	78
20	226,000	0	21	78	0.34	20.70	78
25	222,000	0	21	78	0.17	20.87	78
30	207,000	0	21	78	0.08	20.92	78
35	189,000	0	21	78	0.02	20.98	78

Since the time of exposure to atomic oxygen is relatively short (less than 7 min for high concentrations), it is unlikely that dissociation per se will have any great effect on the oxidation behavior of coated refractory metals. The major effect of this environmental factor will be to alter heat transfer and hence the wall temperature. Its effect on oxidation, therefore, will be indirect but may be of great importance if a significant change in wall temperature results.

All temperatures reported as requirements for heat shields on lifting reentry vehicles are calculated from theoretical models. The theory for such calculations is well developed and believed to yield fairly accurate predictions based on results of experimental studies and experience in ballistic reentry. One of the most important factors in determining the temperatures attained is the nature of the flow over a surface, i.e., laminar or turbulent. Turbulent flow results in higher rates of heat transfer and hence higher radiation equilibrium temperatures over the entire trajectory. This is illustrated in Table V and Figure 9, where time variation of surface temperature at a point on the lower surface of the wing has been calculated for laminar and turbulent flow conditions on the same trajectory. It can be seen that the peak temperature under turbulent flow conditions is about 800° higher than that under laminar flow conditions (2810 versus 3614° F). Coated refractory metals could be used for this portion of the vehicle in one case but not in the other. Not only is the peak temperature higher in turbulent flow, but peak heating also occurs later in the trajectory and for a longer period. Flow at this point on the vehicle on the given flight trajectory is in a transition region between laminar and turbulent. To be conservative in design and to provide an adequate safety factor, turbulent flow conditions probably would be assumed. The model environments presented in Table II are based on laminar flow and, as such, represent a more optimistic prediction of typical environments.

Table V. Effect of Boundary Layer and Flow Conditions on Wall Temperature (Lower Surface of Wing, Superorbital Reentry)

Time (min)	Dissociation of O_2 (%)	Surface temperature (° F)		
		Laminar flow	Turbulent flow	
			No dissociation	Dissociation
1	100	2,300	3,500	2,650
2	100	2,810	3,568	3,055
3	100	2,700	3,610	3,083
4	100	2,610	3,614	3,096
5	100	2,530	3,550	3,102
6	100	2,450	3,435	3,102
7	77	2,370	3,320	3,093
8	36	2,300	3,200	3,073
9	17.2	2,220	3,080	3,020
10	13.0	2,160	2,975	2,940
11	9.8	2,090	2,880	2,855
12	7.5	2,030	2,790	2,775
13	5.8	1,980	2,710	2,694
14	4.7	1,920	2,638	2,615
15	3.8	1,870	2,574	2,547
20	1.55	1,670	2,322	2,250
25	0.88	1,550	2,138	2,051
30	0.40	1,460	2,059	1,939
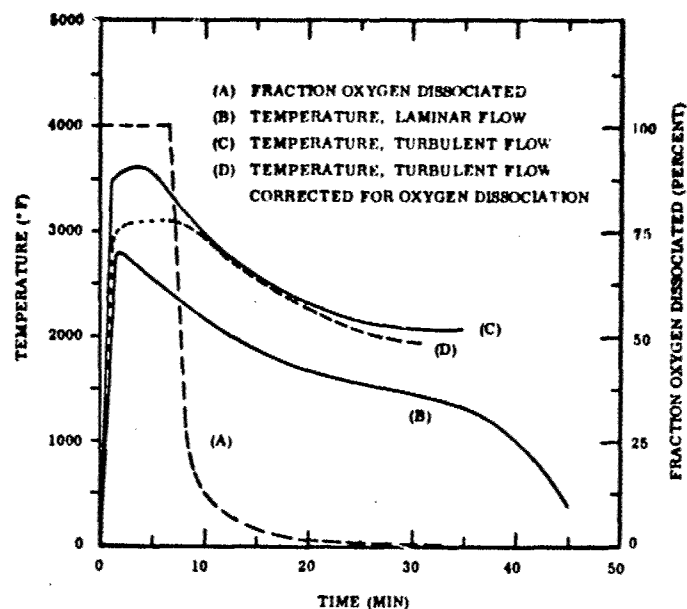
Figure 9   Time Variation of Temperature on Wing
Lower Surface During Reentry as
Influenced by Boundary Layer and Flow
Conditions

The effect of dissociation in the boundary layer on heat transfer and wall temperatures generally is not taken into consideration in the calculation of thermal environment. Dissociation of gas in the boundary layer absorbs heat and, if recombination does not occur at the wall, results in a reduction in heat transfer and wall temperatures. If, however, atomic species recombine at the metal surface, energy is released and an increase in heat transfer and temperature could result. Thus, the tendency for recombination at the surface is an important factor in heat-transfer calculations where dissociation effects are taken into consideration. The catalytic wall efficiency Γ is used as a measure of tendency to recombine, with low values of Γ favoring retention of atomic species at the wall.

The effect of dissociation in the boundary layer on wall temperatures has been calculated for the turbulent flow model developed by assuming a catalytic wall efficiency of 10^{-4}. This is the value for glass and was selected because silicide coatings form a glassy SiO_2 surface upon oxidizing. This low value of Γ implies that little if any recombination of atomic species to molecular species occurs on the metal surface. Thus, the full effect of dissociation in the boundary layer upon reducing heat flux is realized.

The results as shown in Table V and Figure 9 reveal significant decrease in peak temperature as a result of oxygen dissociation. In turbulent flow, peak temperature is

33

reduced from 3614 to 3102° F, a drop of 500°. Thus, the increased severity of temperature due to turbulent flow (+ 800°) is largely offset by the decreased severity of temperature (- 500°) due to dissociation effects. In this model, coated refractory metals could be used on the vehicle if the flow is laminar or if the flow is turbulent with the estimated degree of dissociation in the boundary layer. These calculations serve to illustrate that the most significant effect of dissociation is likely to be a reduction in peak operating temperature. The importance of this variable probably lies in the more accurate prediction of thermal environment than in any direct effect of atomic species on oxidation behavior per se.

Section III

MATERIALS, EQUIPMENT, AND PROCEDURES

MATERIALS

Substrate/Coating Systems

Based on current and projected usage of coated refractory metals in aerospace applications, the state of commercial development, and demonstrated performance capabilities, eight coating systems were selected for evaluation. Four substrate alloys – TZM, Cb-752, B-66, and Ta-10W – were selected to represent the basic classes of refractory metal sheet alloys that are being used in or considered for use in reentry and propulsion applications. Nominal 0.020-in.-thick sheet representative of current commercial or pilot-scale production was procured. Composition and identification of the sheet are given in Table VI.

* All material was in the cold-rolled and stress-relieved condition. The microstructure of each alloy in the longitudinal and transverse directions (relative to final rolling direction) is shown in Figures 10 and 11. The TZM and Ta-10W sheet have heavily cold-worked structures with no trace of recrystallization (Figure 10). The two Cb-base alloys (Figure 11) were partially recrystallized, indicating a high-temperature stress-relief treatment. The Cb-752 and Ta-10W had heavily banded structures, probably indicative of the dendritic coring commonly found in solid-solution alloys containing large amounts of tungsten. The Cb-752 and B-66 sheet also contained fine precipitates, randomly dispersed (Figure 11), which are probably compounds of zirconium and residual interstitial elements (C, O, N) in the alloys.

Microhardness traverses were made on longitudinal and transverse (relative to final rolling direction) cross sections to obtain baseline data on hardness before coating. The hardness of all alloys was comparatively uniform from surface to center, as shown in Figure 12. Some scatter in hardness, particularly in transverse sections, was observed. The average hardness of B-66 and Ta-10W was higher in the transverse section, whereas that of TZM and Cb-752 was higher in the longitudinal section. The Cb-752 sheet exhibited the least directionality for hardness. Average hardness in the longitudinal plane was used as a baseline value for all systems except the Ta-10W alloy. Samples were cut with the short axis (specimen width) parallel to the rolling direction of the sheet. The short axis of specimens of the Ta-base alloy was oriented 90 deg to the rolling direction so that transverse hardness data applied.

Coatings selected for application to the substrates are shown in Table VII. Selection was based on the state of commercial development, demonstrated performance capabilities, and current or projected aerospace applications. In addition, coatings were selected to permit evaluation of a broad spectrum of coating compositions and coating deposition processes on the same, as well as different, substrates.
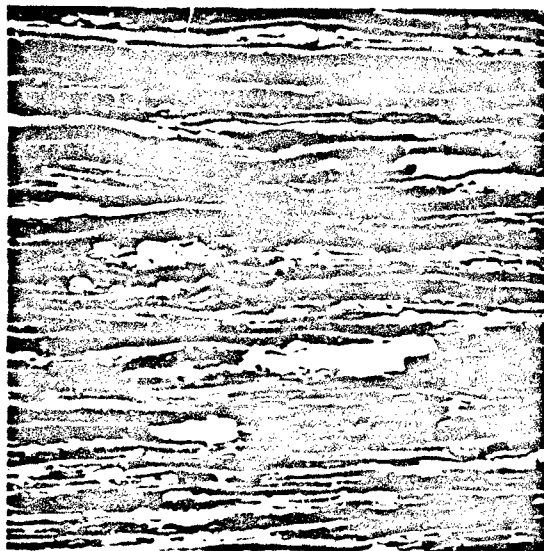
M4895   ×1000 · M4894   ×1000
        LONGITUDINAL   TRANSVERSE

TZM
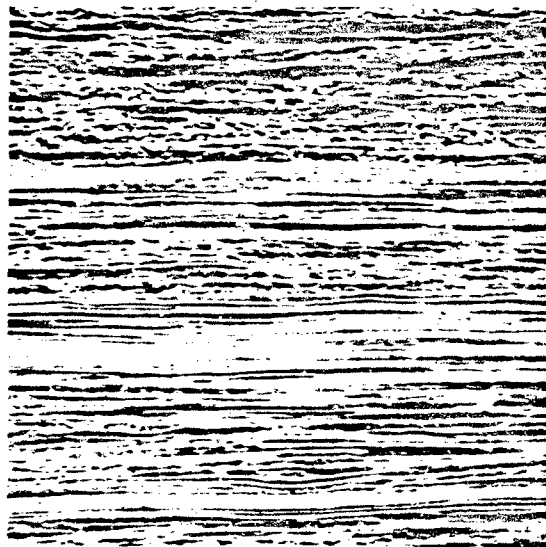
M4899   ×1000   M4898   ×1000
        LONGITUDINAL   TRANSVERSE

Ta-10W
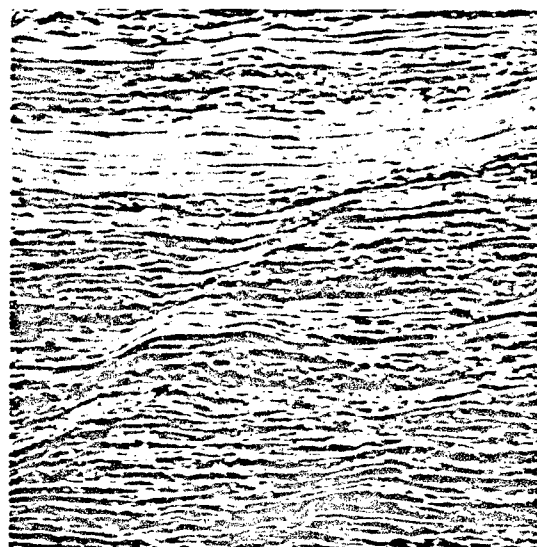
Figure 10 Microstructure of As-Received Sheet Alloys — Mo and Ta Base
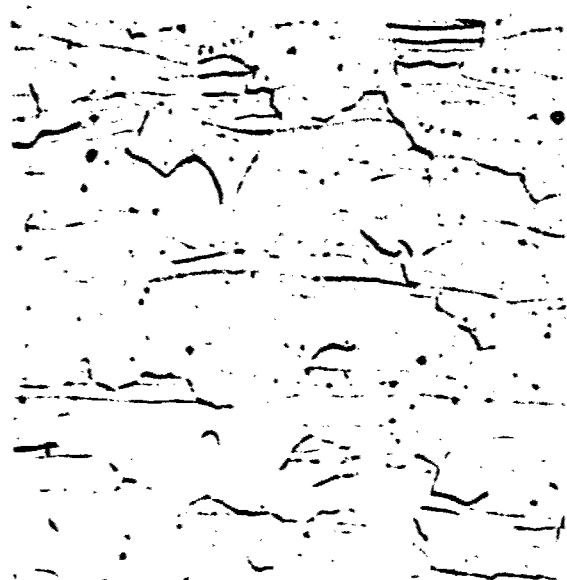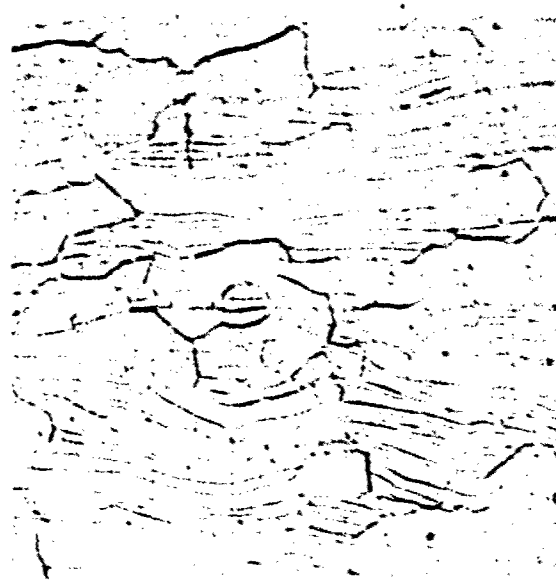
36

M5071   ×1000   M5070   ×1000

LONGITUDINAL   TRANSVERSE

Cb-752

M5073   ×1000   M5072   ×1000

LONGITUDINAL   TRANSVERSE

B-66

Figure 11 Microstructure of As-Received Sheet Alloys – Cb Base
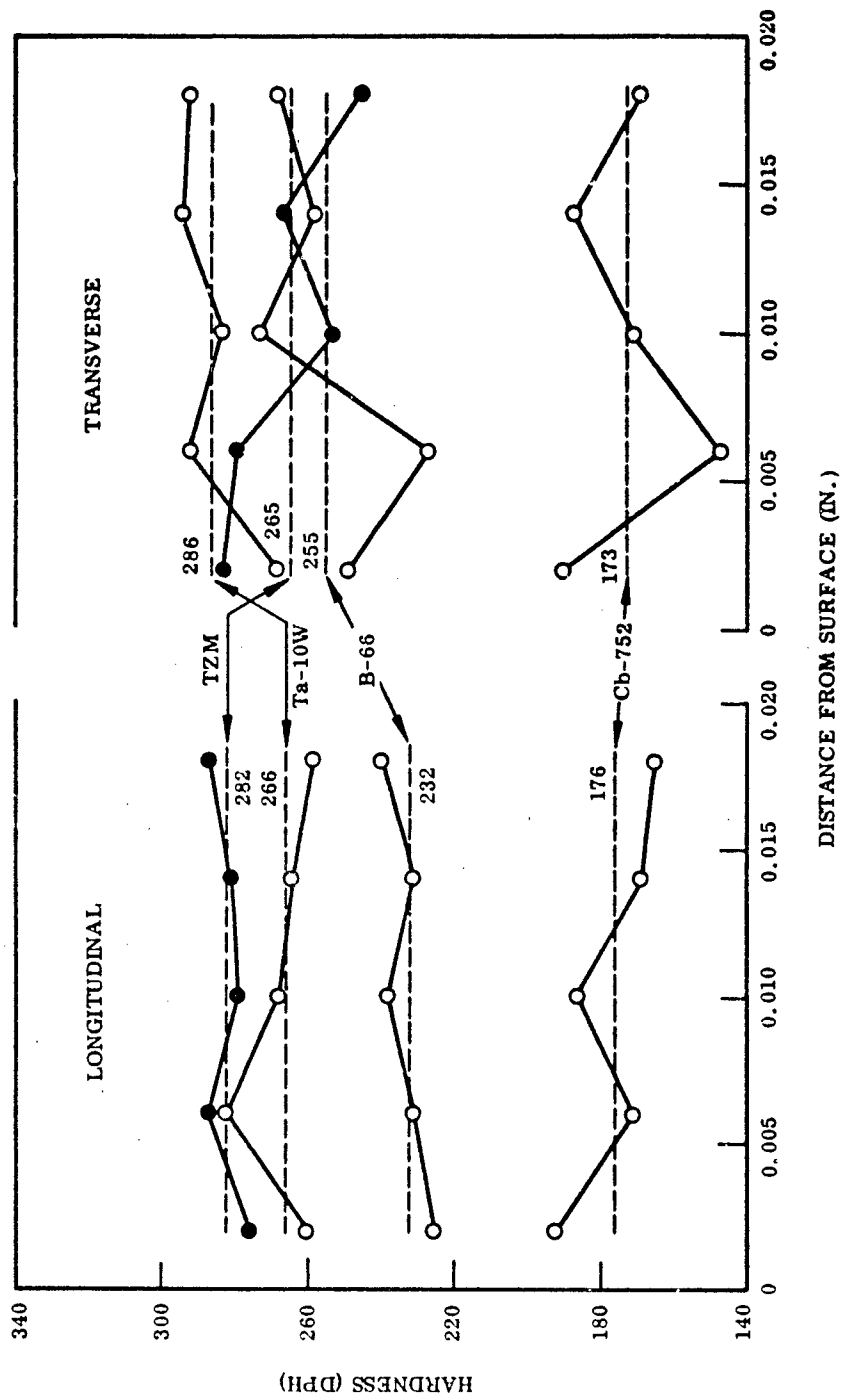
Figure 12 Hardness of As-Received Substrate Alloys, Cross-Section Traverse

38

Table VI.   Composition of Substrate Alloys

Alloy	Heat no.	Supplier	Chemical composition(a)										
			Mo (%)	Ti (%)	Zr (%)	Cb (%)	W (%)	V (%)	Ta (%)	C (ppm)	O (ppm)	H (ppm)	N (ppm)
TZM	KDTZM-1154-C	Universal-Cyclops Steel Corp.	Bal.	0.49	0.10	—	—	—	—	300	14	3	14
Cb-752	52165	Union Carbide Stellite Co.	—	—	2.80	Bal.	9.75	—	—	33	75	11	10
B-66	DX-605-3	Westinghouse Electric Co.	5.20	—	0.91	Bal.	—	4.70	—	33	148	—	93
Ta-10W	5-4179	Wah Chang Corp.	—	—	—	—	8.30	—	Bal.	30	90	4	16

(a) Heat analysis, supplied by material vendor.

39

Table VII. Substrate/Coating Systems

Trade designation	Supplier	Type	Deposition process	Substrate			
				TZM	Cb-752	B-66	Ta-10W
Durak-B	Chromizing Corp.	Silicide (modified)	Pack–double cycle	X			
PFR-6	Pfaudler Corp.	Silicide	Pack–single cycle	X			
Disil	Boeing Co.	Silicide	Fluidized bed–single cycle	X			
PFR-32	Pfaudler Corp.	Silicide	Pack–single cycle		X		
Vought IV	Vought Astronautics	Silicide (modified)	Pack–double cycle		X		
CrTiSi	Thompson Ramo Wooldridge (TRW)	CrTiSi	Vacuum pack–double cycle		X	X	
Sn-Al	General Telephone and Electronics (Sylcor)	Aluminide (Sn–Al)	(a) Slurry dip (b) Spray coat				

40

Three coatings were selected for application to the TZM alloy: Disil, PFR-6, and Durak-B. The Disil coating is a straight silicide ($MoSi_2$) applied by a single-cycle fluidized bed process. PFR-6 is a modified $MoSi_2$ coating produced by a single-cycle pack cementation process, the modification consisting of adding finely divided columbium to the pack. In recent studies using electron-probe techniques, however, columbium could not be detected in the PFR-6 coating, indicating that less than 0.2% may have been picked up. Spectrochemical analysis indicated a residual of 0.05% Cb in the coating (24). Durak-B is a highly modified $MoSi_2$ coating deposited in a two-cycle pack cementation process. Its composition, which is proprietary (Chromizing Corporation), has been reported to be essentially the same as that of the W-3 coating produced by Chromalloy. These three coatings on TZM represent a broad spectrum of $MoSi_2$-base coatings for molybdenum, permitting evaluation of the effects of coating composition and deposition processes on performance capabilities.

Three coatings were selected for application to the two Cb-base alloys: PFR-32, CrTiSi, and Vought IV. PFR-32 is a slightly modified $CbSi_2$ coating applied in a single-cycle pack process. Vought IV is a highly modified $CbSi_2$ coating applied by a two-cycle pack process. CrTiSi is a complex mixed silicide – intermetallic coating produced by a two-cycle vacuum pack process. All three coatings were applied to the Cb-752 alloy to permit evaluation of the effects of coating composition and structure on performance for a given substrate material. In addition, the CrTiSi coating was applied to the B-66 Cb-base alloy to permit evaluation of the influence of substrate composition on the performance of a given coating system.

The Sn-Al coating was selected for the Ta-base alloy because of (1) being one of the more promising coatings for this class of materials and (2) permitting comparison of the environmental effects on aluminide-base coatings and on silicide-base coatings. This coating consists of 90% (75% Sn – 25% Al) and 10% $TaAl_3$. It is applied as a slurry, dried, and then heat treated to form a tantalum – aluminide diffusion zone. Two methods for application of the coating were employed: slurry dip and slurry spray. The spray process is comparatively new and gives a more uniform coating without the tear-drop effect encountered in dip coating. This permits evalution of the effects of coating processes in the performance of a given system.

Sample Preparation

The configuration of test specimens used in the program is shown in Figure 13. The baseline and compatibility test specimens (Type A) and the defect tolerance specimens (Type C) were tested in radiation-heated furnaces. The four corners of these samples are broken with a 0.125-in. radius to minimize localized failures at these points. The baseline specimens (Type B) and hot-flow specimens (Type D) were heated by direct resistance. Because the ends were held in water-cooled copper grips and therefore were not tested, rounding of the corners was not required. Both ends of the hot-flow specimen (Type D) are flanged 90 deg, with a 0.125-in. bend radius for mounting in the test fixture.

All of Cb-752, B-66, and Ta-10W alloy test specimens were blanked by cold shearing. The TZM specimens were prepared by chemical blanking to minimize the possibility of delamination. Chemical blanking was done by Chemical Milling International, El Segundo, Calif. The corners of Type A and C specimens were rounded by clamping several pieces in a tool steel guide jig and hand-grinding on a water-cooled 120-grit

41

TOP

15/16 IN.

◄───────── 3 IN. ─────────►

SIDE   1/8 IN. R

5/8 IN.
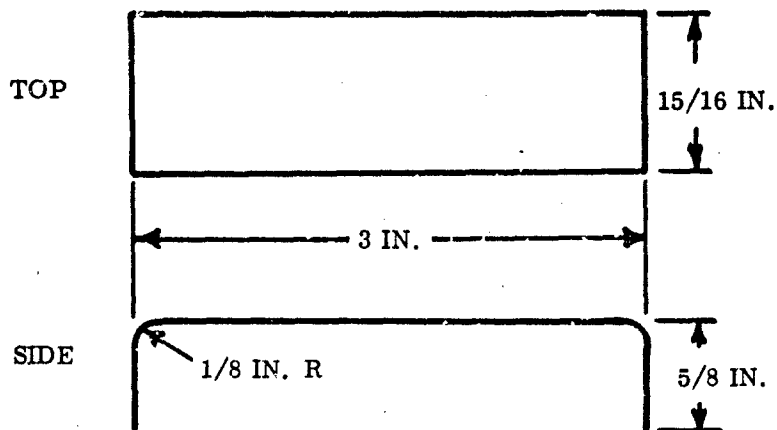
Type D: Hot-Flow Test

◄───────── 3 IN. ─────────►

1/4 IN.
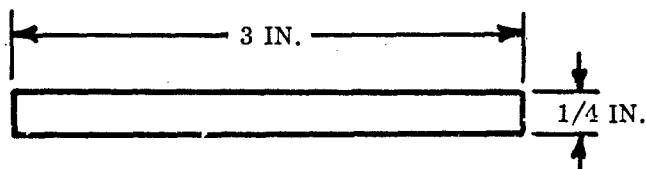
Type B: Baseline, Resistance Heated

◄─ 1 IN. ─►

1/8 IN.
R   1/2 IN.
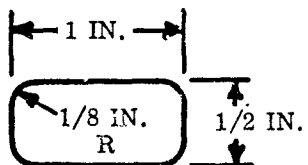
Type C: Defect Tolerance

3/4 IN.

1/8 IN.   1/2 IN.
R
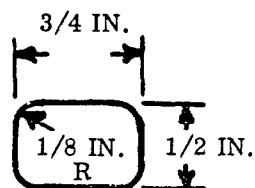
Type A: Baseline, Com-
         patability Test,
         Resistance Heated

Figure 13   Configuration of Test Specimens

abrasive belt. Knife edges on the chemical blanked TZM specimens were removed in the same manner. A 0.060-in.-diameter hole was punched in one end of each Ta-10W alloy specimen as required for dip coating. The edges of all specimens were rounded by vibratory finishing at the Hoyt Abrasive Company, Cupertino, Calif. This method of edge preparation was recommended by all the vendors of silicide-base coatings. Although edge finishing was stated not to be required for the Slycor Sn-Al coating on Ta-10W, these samples were finished the same as the others. The nominal edge radius was 3 to 4 mils after vibratory finishing for all materials.

All coatings were applied by the vendor or coating developer (as indicated in Table VII) in accordance with practices considered by these sources to be optimum for the system The procedures for sample preparation and the thickness of coating for each substrate/ coating system were also based on vendor recommendations, to assure that the test specimens would be representative of the best practices available for each coating system.

The average thickness and weight of baseline samples were measured before and after coating. One hundred samples of the substrate alloy were selected at random from the lot for each system and measured prior to coating. After coating, 100 more randomly selected samples were measured. The average thickness and weight and the standard deviations in thickness and weight were calculated from the measured values and are summarized in Tables VIII and IX. The actual coating thickness measured on cross sections of randomly selected samples is also indicated. In all cases, the average of values measured on cross-sectioned samples was taken as the thickness representative of that system. The results of these evaluations are discussed in the sections on the individual coating systems.

EQUIPMENT

Because the majority of the analyses pursued in this investigation required unique combinations of high temperatures and reduced pressures, special furnaces and associated equipment had to be designed and constructed. For some experimental phases (e.g., studies of gas velocity effects and acoustic irradiation of materials), existing equipment was modified; some apparatus was constructed or modified for the analytical phases. Equipment used in conjunction with the metallographic analyses is described in Appendix I, Metallographic Procedures.

Furnace Design Considerations

The bases for the design of furnaces included, of course, the program requirements and experience gained in related experimentation. Naturally, furnaces should provide appropriate temperatures, pressure, and flow ranges, combined with convenience and reliability. Beyond these general considerations, emphasis was placed on two very significant features — the capability to measure and control true temperature and the minimization of chemical reactions between specimens and support or furnace materials.

Measurement of true temperature by a thermocouple that is adjacent to but does not contact the specimen is possible only if blackbody conditions are maintained in the

Table VIII. Statistical Average and Standard Deviation of Thickness, Baseline Test Specimens

System	Before coating			After coating			Thickness increase/ side (mils)	Measured coating thickness/side(a)		
	Average thickness (in.)	Standard deviation (in.)	Percent within ±2σ	Average thickness (in.)	Standard deviation (in.)	Percent within ±2σ		Av. (mils)	Min. (mils)	Max. (mils)
TZM/Durak-B	0.0204	0.000696	99	0.0231(b) / 0.0193(c)	0.000744 / 0.000875	99 / 98	1.35(b) / (c)	2.35(b) / 1.70(c)	— / 1.50	— / 1.80
TZM/Disil	0.0204	0.00068	96	0.0227	0.000751	98	1.15	2.10	1.70	2.60
TZM/PFR-6	0.0204	0.000744	97	0.0268	0.001827	97	3.20	2.09	1.70	2.30
Cb-752/CrTiSi	0.0206	0.000532	96	0.0240	0.000634	97	1.80	1.86	1.70	2.00
Cb-752/PFR-32	0.0207	0.000442	96	0.0261	0.000961	99	2.70	2.65	2.55	2.70
Cb-752/Vought IV	0.0206	0.000412	98	0.0257	0.000863	96	2.55	2.65	2.50	2.80
B-66/CrTiSi	0.0219	0.00036	96	0.0246	0.000447	97	1.35	1.63	1.50	1.70
Ta-10W/Sn-Al	0.0203	0.000365	98	0.0343	0.001335	98	7.00	4.20	2.70	5.70

(a) Measured on a cross section of one sample.
(b) First coating.
(c) Recoated.

Table IX. Statistical Average and Standard Deviation of Weight, Baseline Test Specimens

System	Before coating			After coating				Average surface area/side (cm²)	Average weight increase (gm/cm²)
	Average weight (gm)	Standard deviation (gm)	Percent within ±2σ	Average weight (gm)	Standard deviation (gm)	Percent within ±2σ	Weight increase/side (gm)		
TZM/Durak-B	1.12	0.0514	95	1.16[a] / 0.936[b]	0.0647 / 0.0553	97 / 97	0.020[a] / [b]	2.50 / —	0.?8
TZM/Disil	1.11	0.0518	97	1.11[c]	0.0530	100	—	—	—
TZM/PFR-6	1.11	0.0548	99	1.15	0.0608	99	0.020	2.50	0...8
Cb-752/CrTiSi	1.01	0.0341	97	1.08	0.0343	94	0.035	2.50	0.045
Cb-752/PFR-32	1.01	0.0261	97	1.08	0.0307	98	0.035	2.50	0.045
Cb-752/Vought IV	1.01	0.0280	96	1.12	0.0347	96	0.055	2.50	0.022
B-66/CrTiSi	1.03	0.0230	98	1.08	0.0312	97	0.025	2.50	0.010
Ta-10W/Sn-Al	1.95	0.0452	97	2.20	0.0587	96	0.125	2.50	0.060

(a) First coating.
(b) Recoated.
(c) Additional edge preparation by Boeing resulted in apparent low weight (av.) after coating.

45

hot zone. Conversely, under nonblackbody conditions, the couple and sample cannot be assumed to be at the same temperature. A complete heat-transfer calculation would be required to establish the temperature relationships.

The first step, therefore, was to analyze radiant-heated tube furnaces to determine the furnace conditions necessary for a blackbody situation. The blackbody quality Q* of a hot zone is the ratio of actual heat flux to blackbody heat flux. A minimum value of 0.95 for Q* is adequate in most cases to assure blackbody conditions. By assuming this value, the length of hot zone having this quality can be determined from the following equation:

$$Q^* = 1 - 4a \left[\frac{\iint \frac{4c^2\, dxdy}{[(x-y)^2 + R^2C]^2}}{\iint \frac{c^2\, dxdy}{[(x-y)^2 + R^2C]^2}} \right] \tag{28}$$

where:

Q^* = blackbody quality (0.95)
y = half-length of heated length of tube
x = half-length of blackbody zone in heated length
R = inside radius of tube
C = average integrated value of $1 - \cos(\phi - \theta)$, where θ and ϕ are the angles between a perpendicular to the tube axis and arbitrary locations on the inner surfaces of dx and dy, respectively.

It can be seen that the length of a blackbody zone of a given quality is a function of the inside diameter and the heated length of the tube.

Equation (28) was solved for a hot-zone tube having a 2-1/2-in. i. d. and 20-in. length. The results indicated a 2-in.-long zone with a Q* of 0.95 in the midsection of the tube. After construction of furnaces, the validity of this calculation was verified experimentally by two methods. First, the melting point of gold was measured with a calibrated optical pyrometer. The melting point at 1945° F was observed at an optical reading of 1943° F, indicating close-to-unity emittance and relatively good blackbody conditions. Second, a blackbody cavity was formed in a hairpin-shaped ribbon of molybdenum. Optical readings at the surface and at the base of the blackbody hole agreed within ±5° F from 2200 to 2600° F, yielding calculated normal spectral emittances of 0.97 to 1.0 for the surface.

As a rule, blackbody conditions can be assumed to exist for a short length in the center of a hot zone of any tube furnace when the ratio of the length of the hot zone to the inside diameter is approximately 10:1 or greater.

Compatibility with support and materials of furnace construction is the other major consideration in the design of test furnaces. In atmospheric testing of coating refractory metals, it is common practice to support test samples on refractory oxides, usually high-purity alumina. Experience has shown, however, that in testing at high temperatures a severe reaction may occur between silicide coatings and refractory oxides. This can lead to errors in evaluation of coating performance and to contamination or deterioration of furnace components. Therefore, in the design of the test furnaces, particular attention was given to means of (1) preventing the test specimens from contacting the furnace refractories and (2) permitting the use of various support materials as required for compatibility for each coating system.

Low-Pressure Oxidation Furnaces

Radiation furnaces. Two different designs for radiation furnaces were developed. An existing 4-kW Sentry Model V furnace was modified for low-pressure use. This furnace consisted of a horizontal mullite tube having a 1-3/4-in. o.d., 1-3/8 in. i.d., and 30-in. length, closed at one end with a removable sight port, gas inlet, and vacuum-sealed push-rod assembly. The other end was connected to a vacuum pumping system capable of evacuating to 10^{-5} mm Hg pressure. The tube was heated by four SiC "Globar" elements, which extend the length of the tube. The heated length was approximately 16 in. At temperatures of 2000 to 2600° F, a 2-in.-long hot zone existed within which the temperature was ±25° F of the control point. A blackbody quality of better than 0.95 was observed in this zone, based on optical measurement of the gold melting point. Temperature was controlled with Pt - Pt 10% Rh thermocouples, which were enclosed in an alumina sheath. All temperature measurements, however, were based on optical readings in the blackbody zone of the furnace. Movement of heated specimens along the floor of the furnace was found to be impractical because of the thermal shock sensitivity of the mullite tube. A "fork-lift" device consisting of two 5-in. alumina tubes mounted in a water-cooled copper push rod was used to transport specimens in and out of the hot zone. The specimen and a supporting pedestal were carried to and from the hot zone without contacting the mullite tube.

The advantages of this furnace were the following:

- Blackbody conditions in the hot zone
- Uniform and reproducible specimen temperature
- Simplicity of construction, operation, and repair

The disadvantages were the following:

- The maximum temperature was about 2700° F when the heating elements were new but only about 2600° F after the elements had been used for a few days.
- The sag — resulting from the creep of the ceramic furnace tube — caused difficulties during loading and unloading operations.
- The tube was susceptible to thermal shock in spite of all precautions.
- Repair and maintenance costs were high.
- The furnace would accommodate only one specimen at a time.

47

Two other radiation furnaces were built which were so versatile that they were used more extensively than any other equipment. A schematic of the second model developed is presented in Figure 14. The furnace wall was a high-purity alumina tube having a 2-in. i.d., 2-1/4-in. o.d., and 30-in. length. The wall was sealed with epoxy to water-cooled brass fittings at each end. Again, the dimensions were appropriate for blackbody conditions. Inside this tube was another alu ina tube, which was used as a sacrificial liner — to minimize the possibility of thermal-shock damage to the furnace wall and to prevent specimen decomposition products that might be harmful to alumina from reaching the wall. This sacrificial liner served no structural purpose. A third alumina tube (2-1/2-in. i.d., 3-in. o.d., 30-in. length) was concentric with the furnace tube. Molybdenum wire (0.080in. in diameter) was wound around the outside of this larger tube. The furnace tube and molybdenum winding were surrounded with alumina bubble grain insulating material and enclosed in a 12-in.-diameter water-cooled copper cylinder. The top of this cylinder was equipped with flanges, water and gas fittings, and a bellows system to allow for expansion and contraction of the furnace tube.

The unique feature of this furnace was a dual-chamber construction in which different atmospheres could be maintained at balanced pressures. In the outer chamber (furnace shell), a nitrogen -5% hydrogen gas (forming gas) atmosphere was provided to protect the molybdenum windings. Shell pressure was maintained at about 1 mm Hg, and gas was flushed continuously through the shell. An air atmosphere was maintained at 0.01 to 50 mm Hg in the inner chamber (oxidation test section). The two sections were isolated from each other by O-ring seals and operated on independent vacuum pumping systems. This design feature was incorporated to minimize the pressure differential across the wall of the main alumina tube, thereby permitting operation to 3100°F without collapse or rupture of the main tube.

As shown in the sketch (Figure 14), the furnace was connected to a specimen loading chamber and the vacuum system by a large gate valve, which permitted the test section of the furnace to be sealed off at low pressure when specimens were being inserted or removed. This isolation valve was not included in the first furnace constructed, and exposure of the furnace tube to atmospheric pressure during loading and unloading contributed to tube failures by stress-rupture and thermal shock. The second furnace was equipped with the isolation valve, and no difficulties were encountered; it has operated continuously for more than 2000 hr at temperatures of 2600 to 3000°F and pressures of 0.01 to 50 mm Hg.

A water-cooled copper T-section was designed and constructed for use as a loading and viewing chamber, support rod assembly, and vacuum system connection. A vacuum system consisting of a fore and roughing pump and an oil-diffusion pump was connected to the side of this fitting. An opening was provided on the front of the tee to serve as an access port for loading specimens and as a viewing port. A prism was located in line with the viewing port so that specimens could be observed during all phases of operation. Two water-cooled copper push rods were mounted in the base of the tee. These could be moved upward and downward through vacuum-tight O-ring seals. Guide tubes extended downward to prevent lateral movement of the push rods.

48
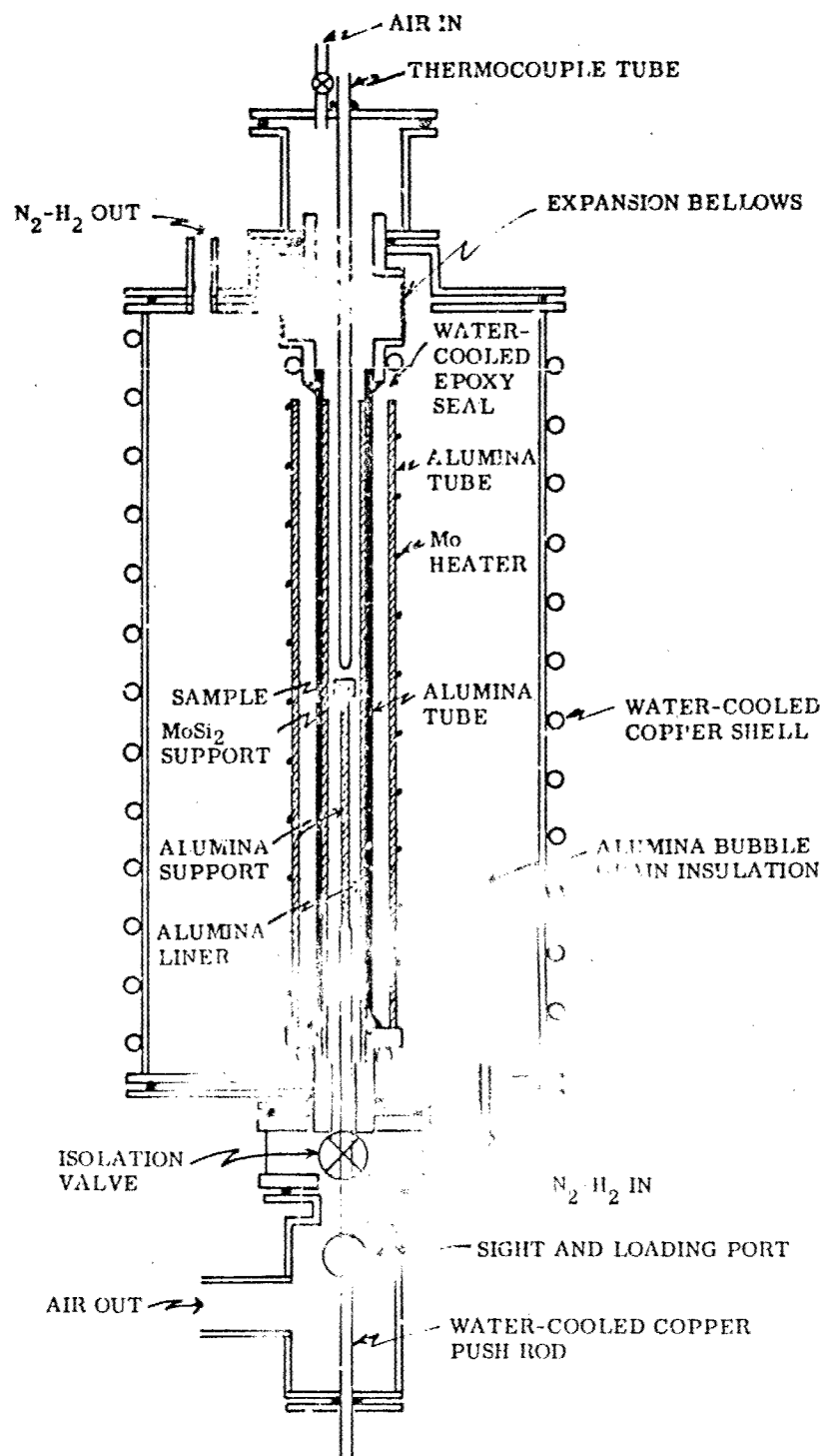
Figure 14 Schematic of 3100° F Molybdenum-Wound Tube Furnace

49

Alumina tubes were added as extensions to the copper push rods using bayonet fittings. The specimens were held by $MoSi_2$ cylinders about 1/2 in. long and 1/8 in. in diameter, which were supported in the top ends of the alumina extension rods. Use of the $MoSi_2$ specimen supports was an important feature of these furnaces: of the high-temperature materials, $MoSi_2$ was found to be the most compatible with coated refractory metal systems. (Details of compatibility studies are presented in other sections of this report.)

Temperature was controlled by a Pt - 6Rh/Pt - 30Rh thermocouple, which was enclosed in a 3/8-in.-diameter alumina tube supported at the top of the furnace. The thermocouple junction was about 1/4 in. from the specimen position at the centerline of the hot zone. The uniform-temperature zone of the furnace was 2 to 3 in. in length. The protection tube was vented to the furnace atmosphere to provide a balanced pressure across the tube wall. Prior to venting, considerable difficulty was encountered with stress-rupture failure of thermowells.

Pressures of $<10^{-5}$ mm Hg to 50 mm Hg could be maintained within the reaction zone at temperatures up to 3100° F. Use at temperatures above 3000° F was possible, however, only in the initial few weeks of operation. Contamination of the high-purity alumina with volatile metals or oxides from test samples (notably boron oxides) reduced the softening temperature and contributed to rupture at low stress levels. With a 3000° F limitation, however, and proper operational care, continuous service was obtained for 2000 to 3000 hr without failure.

The principal advantages of vertical radiant tube furnaces for low-pressure oxidation tests were:

- Known true temperature; no emittance correction
- Flexible sample size and geometry
- Multiple sample tests possible
- Uniform temperature over all sample surfaces
- Ease of temperature and pressure cycling

Disadvantages of the Mo-wound low-pressure test furnace were:

- High cost of maintenance and repair
- Materials compatibility problems
- Limited visual observation during test
- Difficulty in simulating complete trajectory profiles

The most serious limitation of these furnaces is related to high repair costs. Small leaks in the main alumina tube reduce the life of the Mo windings. All furnace failures occurred by this mechanism. In each case, all three high-purity alumina tubes had to be replaced and a new winding installed. This required 2 weeks of down time for rebuilding and 2 weeks for heatup and recalibration after rebuilding.

Resistance Furnaces. Because of the adverse effect of temperatures greater than 3000° F on the lifetime of the radiation furnace components and the high-temperature reactions between coatings and support material, it was necessary to heat specimens by direct resistance at higher temperatures. The cold-wall resistance furnace represented schematically in Figure 15 and used in previous low-pressure oxidation studies (1) was selected for use in this investigation.

Specimens 3 by 1/4 by 0.020 in. were heated by direct resistance using an ac transformer and a saturable core reactor. Temperature was measured optically and controlled manually by varying the dc input to the saturable core reactor. The specimen was held in slotted copper grips which were free to slide in the water-cooled electrodes, thus preventing any buckling as the result of expansion during heating. A fairly uniform temperature (±30° F) hot zone 1/4 to 1/2 in. long in the specimen could be maintained at temperatures of 3000 to 3500° F. Beyond this zone, the temperature fell off sharply.

The advantages of this furnace were:

- No limit in test temperature to specimen melting point
- No chance for reactions between specimens and support material
- Simple operation and maintenance
- Capability for simulating complex reentry profiles
- Close visual observation during test

Disadvantages were as follows:

- No blackbody conditions; true temperature not known
- Nonuniform temperature distribution in the specimen
- Rapid catastrophic failure after first failure at a defect due to localized overheating

High Gas Velocity Tunnel

A Mach 3 flow tunnel was used for studies of the effect of gas velocity on coating performance at high temperature and low pressure. This apparatus (Figure 16) consisted of a high-pressure (up to 2,500 psi) gas preparation section; a low-pressure, high-velocity test section; and a low-pressure exhaust section. Oxygen and nitrogen could be mixed in the preparation section to form any desired O_2N_2 ratio. The high-pressure gas was expanded through a two-dimensional nozzle into the test section and then exhausted by a system of vacuum tanks and vacuum pumps.

A specimen 0.020 by 15/16 by 3 in. was mounted in the test section with the length parallel to the gas flow. The specimen was the floor of the test section; thus, the gas flowed over the upper surface only. It was mounted in water-cooled copper grips and heated by direct resistance using alternating current from a variable-output transformer. The specimen could be observed during an experiment through quartz windows on the top and sides of the test section.

51

1 Rod or Sheet Sample
2 Pressure-Gage Port
3 Water-Cooled Electrode
4 Access Door
5 Water-Cooled Reaction Chamber
6 Observation Port (3)
7 Measuring Telescope
8 Gas-Inlet Diffuser
9 Inlet for Gasdynamic Studies
10 Selector Valves
11 Leak-Rate Control Valve
12 Flowmeter
13 Molecular-Sieve Gas Drier
14 Gas Inlet
15 High-Vacuum Valve
16 Roughing Valve
17 Fore Line
18 Diffusion Pump

Figure 15 Cold-Wall Resistance-Heated Test Furnace

52
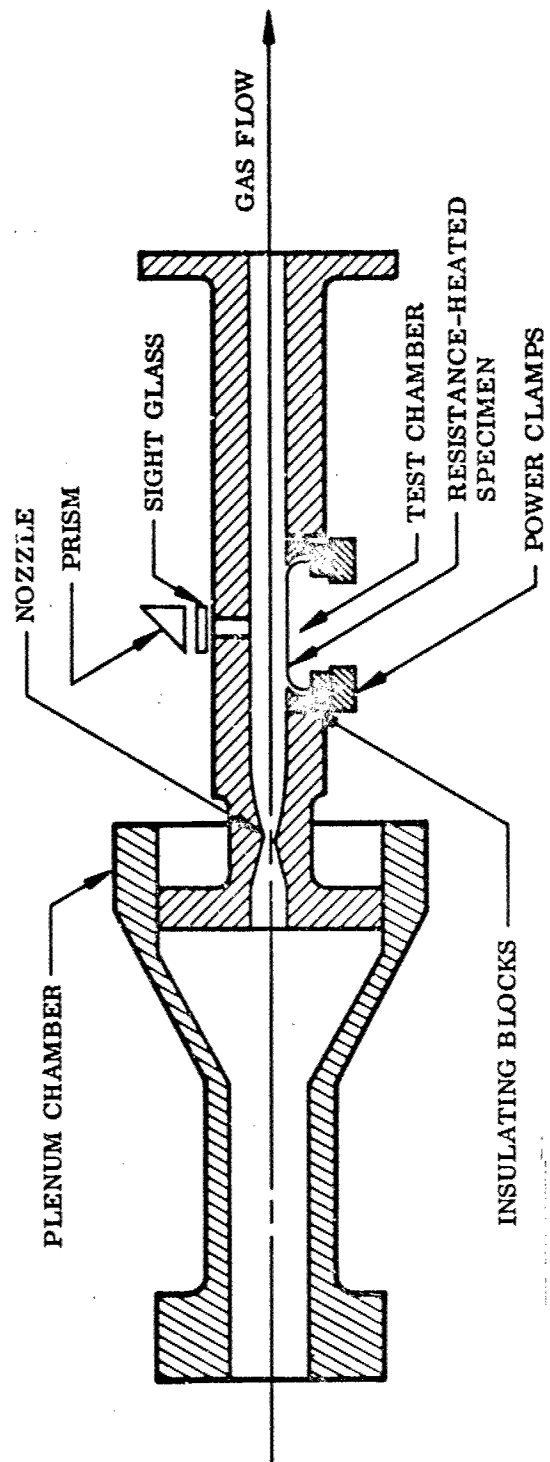
Figure 16 Hot Flow Tunnel

Temperature was controlled manually and measured with an L&N optical pyrometer. Static pressure in the test section was controlled by adjusting the upstream pressure and could be maintained as low as 20 mm Hg at a velocity of Mach 3.0.

Vacuum Volatility Furnace

A cold-wall resistance furnace with tantalum heating element was constructed for vacuum volatility studies. Specimens were heated by radiation from a resistance heated Ta element enclosed in a water-cooled Pyrex chamber. Temperatures up to 4200° F were obtained at pressures as low as 10^{-6} mm Hg with heating or cooling rates of about 1500° F/min. Specimens were supported in a slotted Ta rod in the center of the hot zone. Temperature was measured by sighting with a calibrated L&N optical pyrometer on a blackbody hole in a Ta rod adjacent to the specimen.

Instrumentation

Temperature. Thermocouples were used to control and indicate temperature in all the radiation furnaces. Calibrated Pt versus Pt - 10Rh thermocouples were used in the Sentry furnace where the maximum temperature was 2700° F. Temperatures in the two 3100° F vertical furnaces exceeded the recommended limit for Pt versus Pt - 10Rh, and it was therefore necessary to find a system that would perform reliably at temperatures up to 3100° F in vacuum. The requirement for performance in vacuum was necessary because the end of the thermocouple protection tube near the specimens reacted with various products coming off the specimens and tended to develop leaks when the interior of the tube was at atmospheric pressure. This was prevented by venting the tube to the furnace atmosphere.

On the basis of some of these criteria, a Pt - 6Rh versus Pt - 30 Rh thermocouple was selected. Little information on the effect of environment on the thermoelectric characteristics of this system existed; therefore, the couple was calibrated regularly by comparison of temperature indicated by the thermocouple with that indicated by an optical pyrometer sighted on the thermowell. In Figure 17 a curve is presented to show the change in temperature indicated by the thermocouple with time at a true temperature of 2800° F. The indicated temperature was nearly constant for about 1000 hr but decreased rapidly on continued exposure beyond this time. A spectrographic analysis of the wire after 2,500 hr at 2500 to 3000° F indicated only Fe in addition to Pt and Rh. It was concluded that Pt - 6Rh versus Pt -30Rh thermocouples were appropriate for use at temperatures up to at least 2800° F in air at reduced pressure or in vacuum for about 1,000 hr and then changes in the thermoelectric behavior became appreciable because of a change in either the Fe content or the Pt/Rh ratio or both.

The thermocouple for each furnace was connected to an L&N Speedomax H temperature controller-recorder and an L&N potentiometer. The latter was used for all temperature measurements.

54
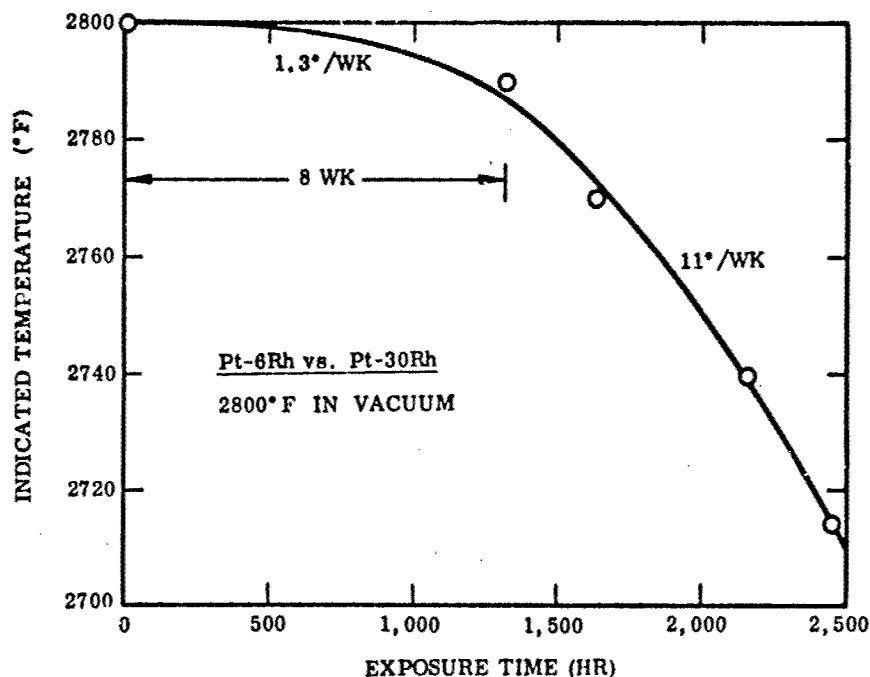
Figure 17 Calibration Stability of Pt-6Rh Versus Pt-30Rh Thermo-
couple in Air at Reduced Pressure

The thermocouple calibration was checked daily with a Micro Optical Pyrometer (Pyro-
meter Instrument Co., Inc.) sighted on the end of the alumina protection tube. The
pyrometer was calibrated monthly using a Pyrometer Test Stand (Pyrometer Instrument
Co., Inc.); the light source was a tungsten-filament lamp calibrated and certified by
the National Bureau of Standards.

Temperature in the resistance furnace was measured with a Micro Optical Pyrometer
and/or a Thermoscope (Milletron, Inc.), the latter a self-calibrating, two-color optical
pyrometer.

An L&N optical pyrometer was used to measure temperatures in the gas-velocity phase
of the program. This pyrometer was also calibrated on the Optical Pyrometer Test
Stand.

Pressure. Pressure-measurement devices were selected on the basis of precision and
ability to provide continuous indication of and rapid response to pressure change. The
devices selected and the pressure ranges measured were as follows: 5×10^{-3} mm Hg
and less, ion gages (National Research Corp. or Consolidated Vacuum Corp.); 0.01 to

55

0.1 mm Hg, Pirani gages (Consolidated Vacuum Corp.); 0.1 to 3 mm Hg, Decker Absolute Pressure Meters; 3 to 20 mm Hg, Dubrovin Vacuum Gauges (Welch Scientific Co.); >20 mm Hg, Bourdon pressure gages (Wallace and Tiernan). In experiments conducted in the high-velocity apparatus, pressure was measured by Pitot tubes and Bourdon gages.

The pressure-measurement devices were calibrated as follows: ion gages by a Hexow Co. Electrometer Calibrator; Pirani, Decker, and Dubrovin gages by a Universal Vacuum Gauge (Todd Scientific Co.); Bourdon gages by secondary standards. All pressure-measurement gages which operate electronically required weekly calibration.

PROCEDURES

Preexposure Evaluation

Average coating thickness and substrate hardness were determined for each coating system by direct measurement of randomly selected samples. Samples were cross-sectioned, mounted in bakelite, and prepared for metallographic examination. Coating thickness was measured at 10 locations on each surface using a millimeter scale at 1000× magnification. Substrate hardness was measured with a Leitz microhardness tester using a 250-gm load. Readings were taken in a thickness traverse at 0.005-in. increments from the coating-metal interface to the sample centerline. Several samples were measured for each system to obtain representative averages of coating thickness and substrate hardness.

Each sample prior to test was weighed on an analytical balance. Sample thickness was measured with a micrometer at four locations. All samples were examined under a binocular microscope for general surface and edge condition. Samples having obviously bad edge, corner, or surface defects were rejected.

Environmental Exposure

Temperature calibration. Throughout this program an extensive effort was directed toward either measurement of true temperature or calculation of true temperature on the basis of observed temperatures and accurately determined correction factors. Knowledge of true temperature is important because, of all the environmental factors that affect the performance of coating/substrate systems, temperature has the greatest effect on useful life. In general, coating life decreases exponentially with increasing temperatures. A coating that can survive 10 to 20 hr at 2700° F may fail in less than 1 hr at 3000° F. A variation of as little as ±50° F from a given true temperature could produce a significant change in behavior. It is believed that much of the variability in performance and contradictory data reported in recent years can be attributed to inadequate knowledge and control of temperature. This is not to say that the measured temperature has been controlled inaccurately; the problem is, rather, one of knowing the precise relation between measured temperature and true temperature of the sample at all times during an experiment. It is the true temperature and not necessarily an indicated

temperature that governs coating life. For this investigation to provide data on which to base reasonable forecasts of reliability, experiments had to be conducted at accurately known and controlled values of specimen temperature.

True temperature was selected as the basis for all test work because this is a universal factor that will permit the greatest use of the data obtained. The other alternative was to express performance in terms of heat flux, which is the factor that generates temperature. Measurement of radiant energy and controlling power input to attain a specific heat flux (q̇) is a valuable technique for screening and final evaluation of a coated structure to be used in a well-defined mission. The structure will approach an equilibrium temperature dependent on structural design, method of heating, and emittance characteristics of the surface. The data obtained, however, have very limited applicability and cannot always be used to predict the performance of the material in other applications, even though the applications may be similar. Furthermore, testing on this basis relies on the assumption that all heat transfer occurs by radiation. At pressures above about 10 μ Hg, gaseous conduction may be important and will introduce errors if not corrected. Nevertheless, testing on a heat flux basis may prove to be the best method for the final evaluation of coated structures in applications where it is not possible to measure or predict the true temperature accurately. For this program, however, where it was desired to characterize the basic behavior of various coating systems in terms of significant environmental variables, true temperature was considered the most useful basis for measurement.

In the vertical molybdenum-wound radiation furnaces, blackbody conditions existed and there was no problem in determining the true temperature of samples. In the resistance furnaces and the high gas velocity tunnel, however, blackbody conditions did not exist and true temperature could not be determined directly.

The consequences of the lack of blackbody conditions are worthy of some discussion. Under nonblackbody conditions, the true temperature (T) must be calculated from an apparent brightness temperature (θ) which is measured by an optical pyrometer. These two temperatures are related by the spectral hemispherical emittance ϵ_λ:

$$\ln \epsilon_\lambda = \frac{C_2}{\lambda} \left[\frac{1}{T} - \frac{1}{\theta}\right] \tag{29}$$

or

$$T = \frac{\theta}{1 + \frac{\lambda}{C_2} \theta \ln \epsilon_\lambda} \tag{30}$$

The constant λ/C_2 has a value of 1.04×10^{-4} for a pyrometer wavelength λ of 0.65. Under equilibrium conditions, the true temperature T is a function of two variables, power input P and total hemispherical emittance ϵ_H:

$$T = \left(\frac{P}{\sigma \epsilon_H}\right)^{1/4} \tag{31}$$

57

where σ is the Stefan-Boltzmann constant. By combining Equations (29) and (31), it can be seen that the apparent temperature θ is a function of three variables, P, ϵ_H, and spectral hemispherical emittance ϵ_λ:

$$\ln \epsilon_\lambda = \frac{C_2}{\lambda}\left[\left(\frac{P}{\sigma \epsilon_H}\right)^{1/4} - \frac{1}{\theta}\right] \tag{32}$$

Furthermore, since the surface is viewed normally in taking optical readings, the normal spectral emittance $\epsilon_{N,\lambda}$ is used in place of spectral hemispherical emittance in calculating true temperature.

The assumptions made in using Equation (30) or (31) to calculate temperature are that $\epsilon_H = \epsilon_\lambda$ and $\epsilon_{N,\lambda} = \epsilon_\lambda$ under the conditions of testing. These are good approximations for black surfaces that approach graybody conditions. A further assumption that the equivalence of emittance values is maintained when a change in emittance occurs during test must also be made in calculating temperature. None of these assumptions is particularly safe in the case of coated refractory metal sheet and can introduce significant errors in temperature measurement. A second, and perhaps more significant, source of error is that brightness temperature is determined by three variables, only two of which (P and ϵ_H) determine true temperature. Thus, a change in apparent temperature does not necessarily indicate a proportional change in true temperature and in some cases may occur with little, if any, change in true temperature.

These relations were shown more clearly by a number of calculations and observations. Consider a sample with a spectral hemispherical emittance of 0.7 running at a temperature of 2000°K (3150°F) at a given power input. According to Equation (29), the brightness temperature θ would be 1860°K (2900°F). Next, assume a line voltage variation that decreases power input and hence reduces true temperature to 1977°K ($\Delta T = -23$°C, -41°F). If the emittance remains constant, then, from Equation (29), brightness temperature will decrease to 1840°K ($\Delta \theta = -20$°C, -36°F). In general, for small temperature changes, true and apparent temperature will change in about a 1:1 ratio as a result of power fluctuations, all other factors remaining constant.

Tests were made of the power supply proposed for use in the experiments to determine the cyclic variations and drift in power input that reasonably could be expected. Using uncoated molybdenum (stable emittance) at "constant power" over a 2-hr period, the average brightness temperature was 1833°K with a random cyclic variation of 1823 to 1838°K ($\Delta \theta = +5$°, -10°C; +9°, -12°F). The corresponding true temperature would be 1993° with cyclic variation from 1985 to 1999°K ($\Delta T = +6$°, -8°C; +11°, -14°F). No drift in average temperature was observed in tests to 4 hr in length. Thus, at constant power input, a reasonable variation of ±15°F at a temperature of 3100°F could be expected as a result of line voltage fluctuations.

From experience, it is known that emittance will change during test. For MoSi$_2$ on Mo, values between 0.7 and 0.9 ($\epsilon_{N,\lambda}$) have been measured, with the amount and direction of change dependent on time, temperature, and pressure. Assume a sample with $\epsilon_\lambda = 0.7$ at a true temperature of 2000°K (3150°F). The corresponding brightness temperature

would be 1860°K (graybody assumption). If emittance were to increase to 0.9, the true temperature according to Equation (31) would decrease to 1880°K (ΔT = 120°K, 216°F). The new brightness temperature from Equation (29) would be 1840°K ($\Delta\theta$ = -20°K, 36°F), and the ratio of ΔT to $\Delta\theta$ would be 6:1. A number of such calculations in the range of emittances expected indicate that any change in true temperature as a result of emittance change at constant power input would be about 4 to 6 times the change in observed brightness temperature.

In this example, if the power is increased slightly to readjust the brightness temperature to its original value of 1860°K ($\Delta\theta$ = +20°C, 36°F), the true temperature would increase to 1901°K (ΔT = +21°C, 38°F). By adjusting power to maintain a constant brightness temperature, the net effect of an emittance change from 0.7 to 0.9 would be to decrease the true temperature from 2000 to 1901°K (ΔT = -99°C, 178°F). The basic problem arises from not knowing if an observed temperature change is due to an emittance change or to a power fluctuation or to both. If a change in observed temperature due to an emittance increase is assumed to be the result of a power fluctuation, the sample could be running at a temperature much lower (or, in the reverse situation, much higher) than believed. Temperature errors of 50°F or greater restrict the utility of the data obtained.

One method by which these errors can be reduced is to measure emittance as a function of time, temperature, and pressure and use an average value for calculations. For example, the following data were obtained on $MoSi_2$-coated Mo exposed to air at 50 mm Hg pressure. Brightness temperature was held constant at 1650°C (3002°F).

Time (min)	Measured $\epsilon_{N,\lambda}$	Calculated T
15	0.76	1696°C (3082°F)
60	.70	1711°C (3112°F)
180	.65	1725°C (3134°F)

True temperature increased by 52°F in a 3-hr test as a result of an emittance change. By selecting the emittance value at the 1-hr point ($\epsilon_{N,\lambda}$ = 0.70) and setting the brightness temperature to give a "true temperature" of 1711°C (3112°F) from start to finish, the temperature would be 30°F low at the start of the test and 22°F high at the end of the test. Thus, by knowing the magnitude of emittance change expected and assuming an average value, the accuracy of temperature measurement and control can be improved.

This procedure had been used effectively in all previous LMSC work on direct resistance heating. Samples of Mo/$MoSi_2$ and Cb/$CbSi_2$ were exposed to various oxidizing conditions, blackbody holes were drilled in the specimens, and the specimens were reheated in an inert environment. The true temperature and brightness temperature were measured, and emittances and correction factors were calculated.

Unfortunately, because the materials under investigation in this program were in the form of sheet, it was impossible to drill blackbody holes. Therefore, other procedures for determining true temperature were followed.

For temperature measurements in the self-resistance furnace, a "Therm-O-Scope" two-color pyrometer was selected because it indicates true temperature if graybody

conditions exist. To determine whether graybody conditions existed in the oxidation experiments, rods of $Cb/CbSi_2$ and $Mo/MoSi_2$ were heated under various oxidizing conditions and the temperature was measured simultaneously using a Micro Optical Pyrometer and the two-color pyrometer. Correction factors from the previous work described were applied to the temperature indicated by the Micro Optical Pyrometer, and the corrected temperature was compared with that indicated by the two-color pyrometer. The comparisons were good, and it was apparent that a two-color pyrometer would indicate true temperature with reasonable accuracy during these experiments. It remained, however, to confirm the suitability of the two-color pyrometer for measuring the temperature of the specific materials under investigation. Also, it was necessary to determine emittance, or at least calibration curves giving true temperature versus apparent temperature for the various materials under selected experimental conditions. This was required for the high gas velocity experiments where the two-color pyrometer was unavailable.

For the TZM/PFR-6, TZM/Disil, and Cb-752/PFR-32 systems, temperature calibration entailed the use of a novel method. These systems have as their coatings disilicide phases which are not greatly complicated by alloying additions. Consequently, the intermediate silicides which form during high-temperature exposures are not complex and are characterized easily using metallographic techniques. It was shown that the growth rate of one of these intermediate silicide phases, Mo_5Si_3, could be used as an index of the temperature during the growth of that phase. For example, the rate curve for the growth of Mo_5Si_3 in TZM/PFR-6 (Figure 18) was determined by (1) heating specimens isothermally at each of several temperatures for 30 min and (2) measuring the thickness of the Mo_5Si_3 zone. The heat treatment, of course, was conducted in the vertical radiation furnaces where there were blackbody conditions. Similar specimens were heated in the same temperature range in the resistance furnace. Temperature was measured with the two-color pyrometer and the Micro Optical Pyrometer. When the growth rates of Mo_5Si_3 in these specimens were determined, the two-color pyrometer was found to be measuring true temperature and the specimen emittance behavior was similar to that previously determined for $Mo/MoSi_2$.

Similar results were obtained with the TZM/Disil and Cb-752/PFR-32 systems. All of these experiments justified the use of a two-color pyrometer, provided curves for true temperature versus apparent temperature, and, perhaps of greater importance, demonstrated the usefulness of this method for temperature measurement.

Temperature calibrations of this nature were less quantitative for the other systems because of the complexity of the coating structure and the consequent difficulty in characterizing any given phase. Duplicate experiments were conducted, however, with one specimen heated under blackbody conditions and the other heated by self-resistance. For the self-resistance heating, the two-color pyrometer and the Micro Optical Pyrometer were used so that emittance correction factors could be determined for these materials. The structures of the duplicate specimens were found to be identical. It is interesting that the emittance correction factors and therefore the emittance of all the systems except Ta-10W/Sn-Al were very similar.

60
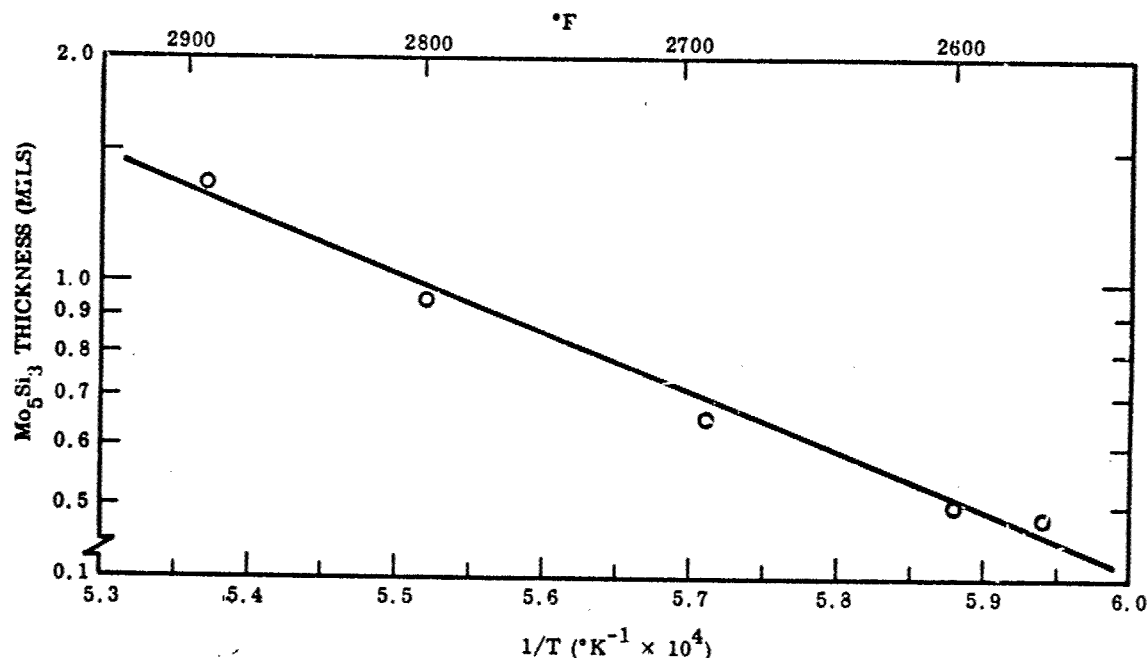
Figure 18 Temperature Calibration Curve for TZM/PFR-6 System — Mo_5Si_3 Layer Method (30 min, 20 mm Hg Air Pressure)

Because the Ta-10W/Sn-Al system is unique and its structure cannot be def ied clearly, some special procedures were required for temperature calibration. The true tempera- ture-apparent temperature relationship was established for uncoated Ta-10W rods using the blackbody hole technique. Then specimens of Ta-10W/Sn-Al were oxidized under selected baseline conditions. The coating was removed from small areas of these specimens, and the specimens were reheated in an inert atmosphere. The temperature obtained by observation of coated material was compared with the corrected temperature of the uncoated material, and correction factors for the coated material were obtained.

It is clear that extensive care was given to determination of true temperature and mini- mization of error in temperature measurement. As a result, the error in all tempera- tures reported is probably less than 25° F. Errors in reported data were decreased further by conducting many duplicate tests and overlapping experiments.

Baseline behavior. As mentioned previously, the study of baseline behavior was a key phase of this investigation. Here an evaluation was made of substrate/coating perform- ance under conditions of high temperature, reduced pressure, and slowly moving air. The baseline results served as a basis for comparison of all the other experimental phases; i.e., the results of the other phases were expressed in terms of degree of deviation from baseline behavior.

61

Specimens were exposed to elevated temperatures at six different air pressure levels — 0.01, 0.1, 1.0, 5, 20, and 50 mm Hg. In general, the time for each exposure was 30, 60, 120, or 240 min. For each substrate/coating system at each pressure level, exposures were conducted at appropriate temperatures and times so that boundaries between passing and failing regions on a time versus temperature plot could be defined clearly. Several experiments — including many duplications — were conducted at each pressure level. When more than one mode of heating was necessary in a series of experiments, overlapping experiments were conducted to ensure that no artifact was introduced. The performance data were further supported by plotting maximum temperature for a given lifetime versus pressure and checking any inconsistencies by conducting additional experiments.

The same procedure was followed for baseline exposures in all radiation furnaces. The specimens and supports (two specimens from a single system in the vertical furnaces and one specimen in the horizontal furnace) were mounted on the push rods, and the furnace was closed and evacuated to $<10^{-3}$ mm Hg. The furnace temperature was adjusted to within $\pm 5°F$ of the desired value, and the pressure was increased to the appropriate level by balancing a controlled gas leak against the vacuum pumping system. For exposures at 0.01 mm Hg the leak was balanced against an oil diffusion pump, and at higher pressures it was balanced against a mechanical pump. Micrometer leak inlet valves and vacuum-line throttling valves were used to adjust pressure and flow. The gas-flow rates were measured by flowmeters on the high-pressure (inlet) side.

When experimental conditions were stabilized, specimens from a single system were moved into the hot zone and a timer was started. Temperature stabilized at the set point within 3 min after insertion of specimens. In the vertical furnaces, one of the two specimens was lowered to the loading chamber after a prescribed time and the other was left in the hot zone for a longer time. Thus, in each run two specimens were exposed for different lengths of time under otherwise identical conditions. After the second specimen was withdrawn from the hot zone, the furnace and/or loading chamber was brought to atmospheric pressure to allow removal and introduction of specimens.

Tests were run at predetermined intervals (30, 60, 120, or 240 min). However, if premature failure or severe reaction was noted, tests were terminated early to prevent complete destruction of the specimen.

In the resistance furnace, the procedure was only slightly different. In this case, the specimen was clamped in the slotted copper specimen holders which in turn were inserted in the electrodes. The desired pressure was established by balancing the air leak against a vacuum pump, and the temperature of the specimen was then increased to the desired value using manual control of current. Test temperature was attained in less than 1 min. Upon completion of the test, the power was shut off and the specimen cooled to a black heat in less than 1 min. The time of test was taken as the interval between attaining of the desired temperature and shut off of the power.

Specimens were observed continuously throughout the test. At the first visible sign of failure, the run was terminated; testing beyond this point generally resulted in complete destruction of the sample due to localized overheating at failure sites. Where no failures were observed, tests were run to the desired exposure time (30, 60, 120, or 240 min).

Gas velocity. In this phase, the effect of high gas velocity, Mach 3, was assessed in terms of deviation from baseline behavior. Two pressure levels were selected and appropriate temperatures and exposure times were determined on the basis of baseline results. Values of these parameters were chosen so that a shift of the coating lifetime curve on a plot of temperature versus time could be detected.

The two pressure levels selected were 5 and 20 mm Hg. It was possible to use air for the 20 mm Hg experiments, but, because the lowest attainable static pressure was 20 mm Hg, a mixture of $N_2:O_2::19:1$ (oxygen partial pressure equal to that at an air pressure of 5 mm Hg) was used for experiments that corresponded to the baseline – the 5 mm Hg experiments. This, of course, was based on the assumption that in this pressure range the coating performance is dependent on oxygen partial pressure rather than total pressure. The validity of this assumption was verified by a series of tests with each substrate/coating system in the baseline furnaces using $19:1::N_2:O_2$ mixtures at 20 mm Hg pressure. In each case, it was found that the behavior was the same as that observed in air at 5 mm Hg. Details of these experiments are discussed in the section on results for each system.

Before any experiments were performed, a series of temperature and pressure calibrations was conducted.

Several pressure probes were mounted in a dummy specimen, and the upstream pressure level for each desired static chamber pressure was established. These predetermined values were used to regulate pressure in all subsequent tests, since pressure in the test cell could not be monitored during a test.

Temperature was measured by a microoptical pyrometer. A two-color direct-reading instrument was not available when these tests were conducted. Two methods were used for determining true temperature from observed optical reading. Samples for each system were preoxidized in the direct-resistance furnace at the temperature, pressure, and time desired for high-velocity tests. A hole was then ground through the coating to the substrate at the center of the specimen. Simultaneous optical readings were taken of the substrate and coating surface upon reheating to test temperature in argon. These data, combined with true versus apparent (optical) calibration curves for the substrate alloy, were used to calculate appropriate temperature corrections. Corrections obtained for the three silicide-coated TZM systems by this method were found to be in excellent agreement with calibration data previously obtained on preoxidized $MoSi_2/Mo$ and $CbSi_2/Cb$ systems using blackbody hole procedures. As a further check on temperature calibration, measurements were made of the thickness of the Mo_5Si_3 diffusion layers found during test in systems where well-defined zones were developed. Using the procedure previously described, true temperatures calculated from diffusion-zone thickness measurements were found to be within $\pm 1\%$ of the true temperature predicted by the primary method of temperature calibration. This remarkable agreement increases considerably the confidence in temperature measurement during high-velocity tests.

Once the system was calibrated satisfactorily, the experimental procedure was straightforward. Specimens were examined, measured for thickness, and placed in the copper grips. The system was evacuated and then the flow was initiated. After the flow was equilibrated at the proper velocity and static pressure, the specimen was heated to the

63

desired temperature. During the test, the specimen was observed constantly. At any indication of failure – hot spots, holes, or general failure – the test was aborted: specimens that did not show signs of failure were held at temperature for 1 hr.

Vacuum volatility. Vacuum volatility studies were conducted for four temperatures – 2600, 2800, 3000, and 3200° F – in the pressure range of 10^{-5} to 10^{-6} mm Hg. The experimental procedure was as follows.

A specimen of known weight and thickness was placed within the tantalum heating element of the cold-wall furnace. The system was evacuated to 10^{-5} to 10^{-6} mm Hg, and the temperature of the specimen was increased to the desired value. Two to 3 min were required to reach temperature. Four runs were made, at 30, 60, 120, and 240 min, with one specimen at one temperature to establish a volatilization rate curve. After each exposure period, the specimen was cooled rapidly, removed from the furnace, measured for thickness, and weighed.

Weight changes, in grams per square centimeter, were plotted against time on both log-log and linear graphs, and the resulting curves were analyzed to interpret the mechanisms and rate-controlling steps involved in the volatilization process. All interpretations were supported by careful metallographic analyses.

Temperature – pressure cycling. The effect of cyclic variations in temperature and pressure on performance capabilities was assessed in terms of deviations from baseline behavior. In each case, a pressure-temperature-time condition close to the limit of performance capability for a given system in static tests was selected as the baseline of comparison. The 30-min-life random failure boundary was used as the baseline of performance. The actual temperature-pressure-time parameters for each phase of the cycle were selected to represent the sequence of typical environmental conditions during atmospheric reentry. This was done to determine if the results of baseline studies could be used to predict performance under the dynamic environmental conditions characteristic of reentry.

Analysis of the environmental models developed in Section II.indicated that conditions were either too severe or too mild compared with the measured performance capabilities of the coating systems to be used as a guide. For example, in Figure 7, peak temperatures of 3460 to 5200°F at the stagnation line exceeded the melting point of all the silicide systems. In Figure 8, temperature – pressure history calculated for the lower surfaces did not present a sufficiently severe environment to be used for this phase of the investigation.

Other available data, therefore, were reviewed to find a more appropriate model for use in temperature-pressure cycling experiments. The model selected was based on an environmental analysis of the lower wing surface for a high L/D (~ 3.0) reentry vehicle in suborbital flight. The temperature-pressure history for the boost and reentry phase is shown in Figure 19. The vehicle is boosted to a 220,000-ft altitude and then reenters the earth's atmosphere at a velocity of 20,000 ft/sec. Lateral maneuvers conducted during the initial phase of reentry account for the variations in temperature and pressure during the first 7 min of reentry. This type of vehicle and reentry history represent a new class of lifting-reentry vehicles having broad maneuverability capabilities. Such vehicles are being considered for future missions and, as such, the profile

64
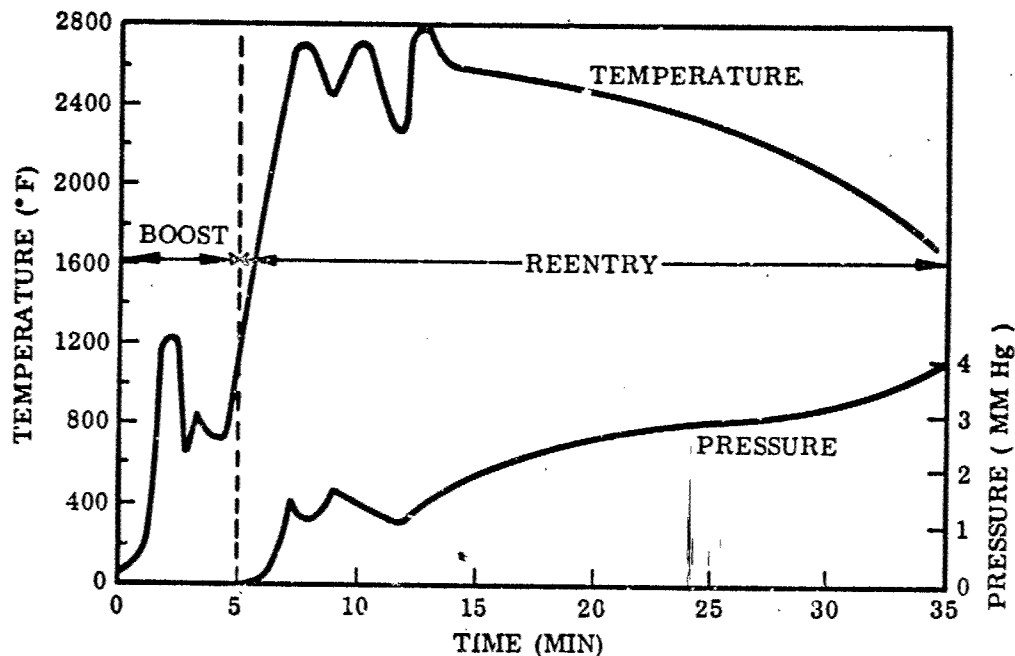
Figure 19 Temperature/Pressure History of Lower Surface of High L/D Vehicle
During Boost and Reentry

data selected are representative of the environmental conditions that may be encountered
by actual flight hardware in the future.

Two types of temperature-pressure-time cyclic experiments were designed on the basis
of this model (Figure 19). The baseline phase of the cyclic experiments was selected
to represent the average initial heat pulse during early stages of reentry. This consti-
tutes the more drastic performance requirements for coated refractory metals. The
second phase of the cycle was selected to represent the long-time, low-altitude glide
portion of reentry, which, in terms of temperature and pressure, is not as severe.
Performance of both external and internal surfaces was evaluated in two series of experi-
ments by changing the pressure levels between which samples were cycled. The actual
cyclic conditions imposed were as follows:

(1) External Surfaces
       Baseline Phase − 2600 - 2800° F, 1 mm Hg, 7 min per cycle
       Second Phase   − 2200 - 2400° F, 3 mm Hg, 21 min per cycle
(2) Internal Surfaces
       Baseline Phase − 2600 - 2800° F, 0.01 mm Hg, 7 min per cycle
       Second Phase   − 2200 - 2400° F, 0.1 mm Hg, 21 min per cycle

65

Samples were cycled from the baseline phase to the second phase until failure occurred or until total accumulated time at the baseline phase was 28 min (4 cycles). Actual temperature in the baseline phase was selected as the maximum temperature for a 50-min life (random failure boundary, baseline tests) in slowly moving air at 1 mm Hg or 0.01 mm Hg pressure for each system. Thus, if four cycles were accomplished without random failures, no degradation in baseline behavior occurred as a result of temperature-pressure cycling. It can be seen that, using this approach, the number of cycles achieved without failure also gives an approximation of the number of flights or missions that might be accomplished successfully according to the model reentry profile under ideal conditions.

In these experiments, both temperature and pressure were varied in each phase of the cycle. A third type of experiment was designed in which samples were cycled at constant temperature from vacuum to air at reduced pressure. The environmental conditions for the vacuum exposure test were as follows:

First Phase: 2600°F, 10^{-5} mm Hg, 30 min
Baseline Phase: 2600°F, 1 mm Hg, 240 min

The primary purpose of this experiment was to determine if short-time exposure to high vacuum at high temperature seriously degraded performance capabilities in air at reduced pressure. The 4-hr random failure boundary at 1 mm Hg pressure was selected as the baseline of comparison. The 30-min preexposure at 2600°F, 10^{-5} mm Hg, was selected to permit a correlation of the results with previously established effects of vacuum exposure on structure and composition of the coatings. The time-temperature-pressure conditions for these experiments were selected to explore possible degradation effects due to vacuum exposure rather than to analyze performance capabilities in potential applications. This type of exposure, however, might occur on internal surfaces or structures of reentry vehicles or in various space propulsion devices. The time of exposure in each phase for such applications, however, would be much less per cycle than the times used in this test. Test results, however, might be indicative of a total cumulative exposure, i.e., 15 – 30 cycles.

All experiments were conducted in the vertical, molybdenum-wound resistance furnaces using procedures similar to the baseline procedures. Pressure changes were made by adjusting the air flow with the micrometer leak valve. Temperature was adjusted simultaneously by moving the push rod up or down to change the position of the sample in the hot zone. Temperature profiles along the length of the hot zone were made for various maximum hot-zone temperatures to establish the proper push-rod position for each temperature. Both temperature and pressure could then be changed rapidly upon moving from phase to phase of the cycle.

Acoustic irradiation. The purpose of the acoustic irradiation studies was to evaluate the effect of sonic vibration on coating behavior. Specimens 1 in. long were clamped at each end under a strip of cork on a wood frame (Figure 20). The frame was placed under a 2 by 2 by 9 ft exponential horn. The following additional equipment was used: a Ling Tempco-Vought electropneumatic transducer, a General Radio random noise generator, a McIntosh power amplifier, and a Hewlett Packard signal generator. The electropneumatic transducer modulated the flow of nitrogen through the horn.

66
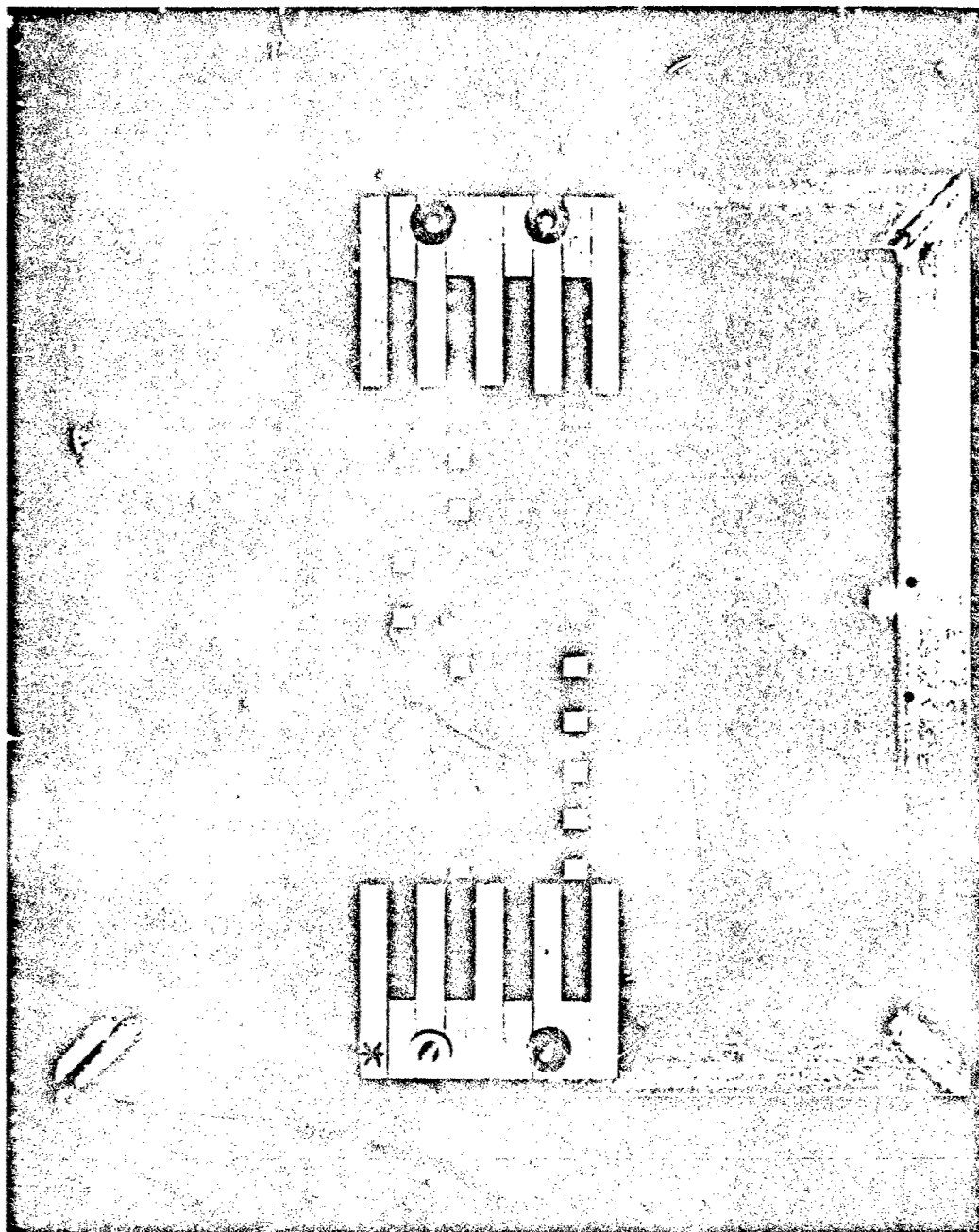
Figure 20 Test Specimen Setup for Acoustic Irradiation Studies

Specimens were divided into two groups, each group containing five samples each of the eight substrate/coating systems. One group was subjected to 60 sec of random noise (30–1,500 cycles/sec) at a sound pressure level (SPL) 159.5 dB; the other was subjected to a sine-wave sound environment, sweeping in frequency from 50 to 1,500 cycles/sec and hitting a peak SPL of 172.5 dB at 510 cycles/sec. The frequency was increased in steps of 100 cycles/sec and held constant at each pressure level for 10 sec. This procedure was repeated once so that the specimens were irradiated for a total of 20 sec at each pressure level to the sine-wave conditions.

All specimens were examined visually for any damage, and representative samples were examined metallographically. Four specimens of each system from each group were exposed to selected baseline conditions to determine any deterioration in oxidation resistance. Experimental procedures were identical to those used in the baseline oxidation testing phase of the program.

Defect tolerance. The objectives of defect tolerance studies were to determine (1) the effect of various types of controlled defects on the performance capabilities of coating systems and (2) the resistance of various coating systems to formation of defects. The initial studies were directed to formation of controlled defects similar to the naturally occurring defects found in coated samples (Figure 21). These are V-shaped or hairline fissures that penetrate to various depths. Attempts were made to produce similar defects of varying depth and severity by three methods: cyclic fatigue, hardness indentation, and simple bending. Of these, only bending was found suitable for creating crack defects.

A Man Labs, Inc., Fatigue Precracker was used to develop cracks in the coating by high cycle fatigue. Samples 1.0 by 0.5 by 0.020 in. were loaded as a simple beam and flexed in one direction at 1,750 cycles/min until cracking occurred. Deflection per cycle was increased if cracking did not occur within 30 min. In all tests of coated Mo alloys, complete fracture of the specimen occurred when the coating cracked. With Cb-base alloys, severe spalling occurred on the compression side of the sample.

In a second study, a Vickers-Dyamond Pyramid hardness tester was used to create coating fractures by indentation or scratch methods. Loads from 0.1 to 5 kg were applied to produce defects. Both single and multiple indentation techniques were used. In a few tests, the sample was traversed under load to produce a scratch. In all cases, spalling or chipping occurred when defects of sufficient depth to be of interest were produced. Although fine cracks could be made at lighter loads, the results were not reproducible and the size and nature of the defects could not be controlled.

Simple bending was found to be a suitable method for introducing fine hairline cracks (fissures). However, large cracks could not be produced in any of the silicide systems without spalling on the compression side of bend samples. (See Figure 22.) Fine hairline cracks similar to those present in as-coated samples could be produced on the tension side. However, continued bending to propagate and enlarge the cracks caused pieces of the coating to be spalled off the compression side and the edges.

All bend tests were conducted in a 200-lb-capacity Instron machine using simple 3-point bending. Samples were loaded at a cross-head rate of 1 in./min at temperatures

68

M5916   ×500

TZM/PFR-6

M6846   ×500
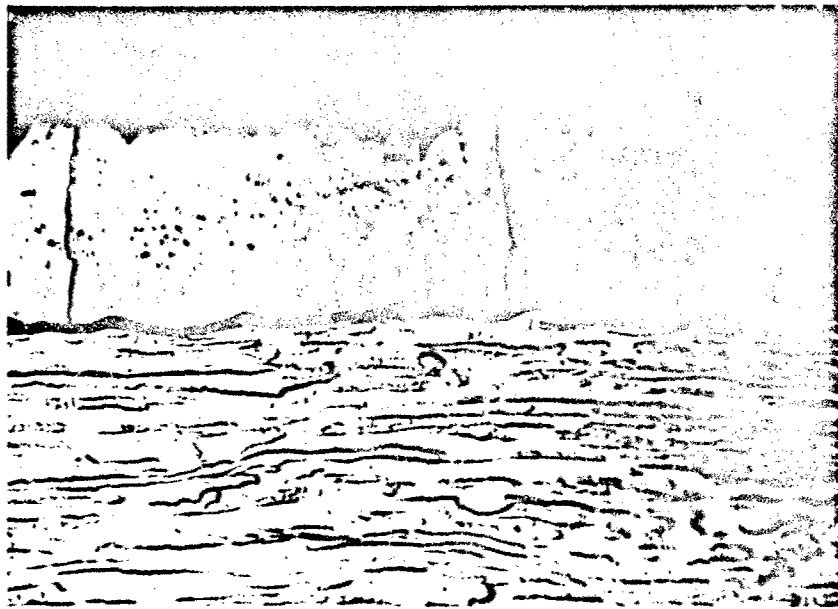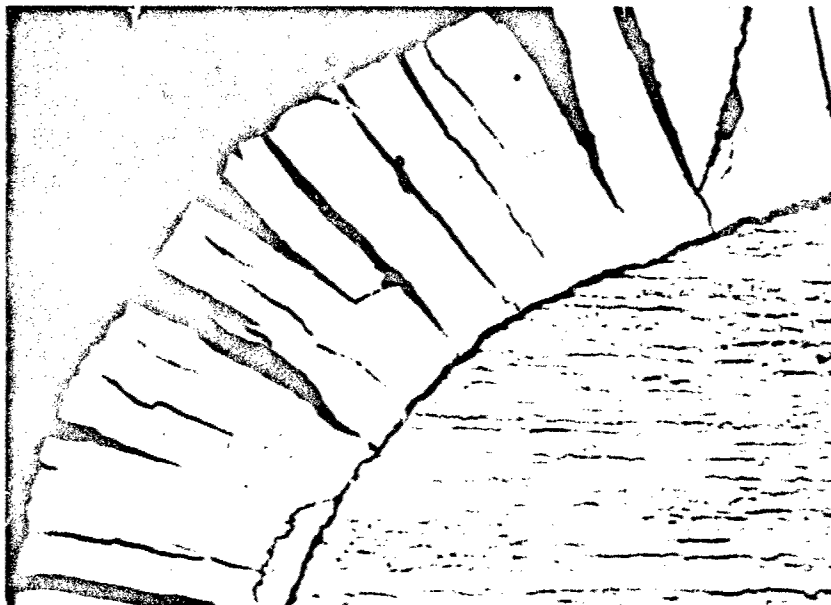
TZM/Disil

Figure 21 Natural Crack-Type Defects in Silicide-Coated TZM

69
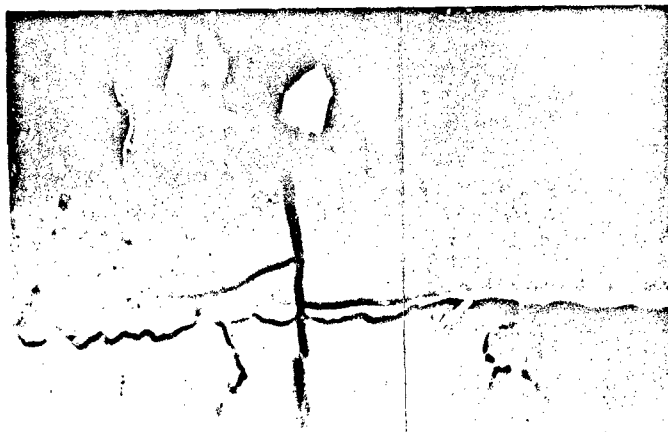
M6970 ×1000

(A) Tension Side, Hairline Crack
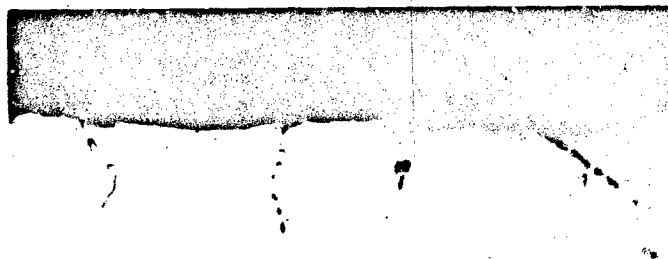
M6971 ×1000

(B) Compression Side, Spalled Coating

Figure 22 Artificial Coating Defects Produced by Simple Bending at Room
Temperature, Cb-752/CrTiSi

of 75 to 300° F. A 3t-radius punch was used after preliminary tests indicated that a punch radius as large as 10t had little effect on compression-side spalling. Load-deflection curves were recorded autographically for all tests.

Typical behavior in bending is illustrated for three different silicide coatings on Cb-752 alloy in Figure 23. Upon loading, samples sustained a 20 – 25 deg bend before major fracture of the coating occurred. In this region, small fissures were created near the surface. When major fracture occurred, large cracks propagated to the substrate on the tension side, pieces of the coating spalled off on the compression side, and a sharp drop in load resulted. Three types of behavior were then observed. Below the ductile-brittle temperature, cracks from the coating propagated through the substrate, resulting in complete fracture of the specimen (PFR-32 on Cb-752). In the ductile-brittle transition zone, cracks propagated part-way through the substrate and complete fracture occurred upon continued bending a few more degrees (Vought IV on
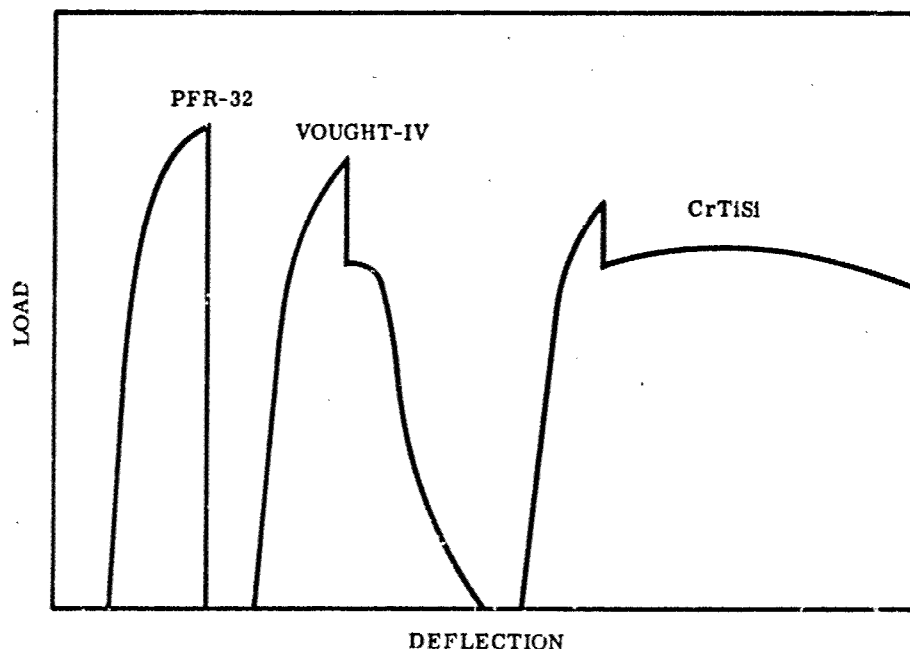
Figure 23   Load-Deflection Curves for Room-Temperature
Bending of Coated Cb-752

Cb-752). Above the ductile-brittle transition, cracks stopped just below the coating metal interface and a ductile 90-deg bend could be made (CrTiSi on Cb-752). This effect is shown in Figure 22 where the crack from the coating extends into the substrate for a short distance but did not propagate through the substrate.

The effect of fine hairline fissures on performance was evaluated by oxidation testing of specimens bent just short of major cracking. Test specimens were bent to within 1 – 2 deg of the point of major coating fracture and then unloaded. Samples containing

71

such defects were tested under baseline conditions to determine whether any degradation of performance occurred. The bend angle at which gross fracture of the coating (room temperature, 3t, 1.0 in./min bend) was taken as a measure of the resistance to formation of defects.

Ballistic impact was used as another method of evaluating the resistance to formation of defects. A facility in which projectiles of known kinetic energy could be impacted against coated specimens was constructed. A Crossman 0.22-caliber air rifle was modified to accept a high-pressure gas line. This permitted the gas pressure, and consequently the projectile velocity, to be controlled. A pipe 2-1/2 ft long was aligned in front of the rifle, and specimens were mounted on either steel or rubber backing at the end of this pipe. The projectiles were standard lead pellets weighing an average of 0.002 lb.

To determine impact energies, measurement of projectile velocity was accomplished as follows. A chronograph was assembled by mounting two polar coordinate graphs 6 in. apart on a shaft which was rotated at constant angular velocity by an electric motor. The shaft was positioned parallel to the rifle barrel, and an 0.88-gm lead pellet was shot through the two graphs. By measuring the angular difference between the holes in the polar graphs and knowing the angular velocity of the shaft, the instantaneous velocity of the pellet could be calculated. The gas pressure in the rifle was varied to develop a range of velocities of 105 to 273 ft/sec. The range of projectile kinetic energy corresponding to these velocities is 0.3 to 2.3 ft-lb. Calibration data are shown in Table X.

Table X. Calibration of Ballistic Impact Facility

Gas Pressure (psi)	Chart Angle(a) (deg)	Pellet Velocity (ft/sec)	Kinetic Energy (ft-lb)
60	73	105	0.32
70	55	137	0.57
80	50	153	0.71
100	41.5	184	1.02
120	35	218	1.53
140	–	235	1.66
200	29	264	2.09
300	28	273	2.25

(a) Angle in degrees between holes in chart paper, 6-in. spacing between charts, 2,250 rpm. Speed of rotation.

72

Specimens of each substrate/coating were mounted on a 1/2-in.-thick hardened steel plate or a 1-in.-thick soft rubber stopper and impacted over a range of impact energies sufficient to provide a determination of the energy level required to produce (1) coating cracking, (2) coating spalling, and (3) substrate cracking. The rubber backup permitted some deformation of the sample upon impact, as might be encountered by unsupported light-gage materials. The steel backup did not permit deformation and is representative of heavy-gage or rigidly supported material behavior. Multiple experiments were conducted in most cases.

Specimens after impact were examined under a binocular microscope. Those exhibiting coating fracture and/or minor spalling were tested by exposure to selected baseline conditions of high temperature and low pressure. Coating cracks that were not discernible at 60× magnification were assumed to be capable of self-healing; therefore, specimens with no apparent defects were not oxidation tested. The highest value of impact energy at which a given type of failure did not occur and the lowest value at which it did occur on both steel and rubber backups were taken as a measure of relative resistance to defect formation for all coating systems.

Two other methods of introducing major defects in coating systems were developed to determine (1) the effect of the depth of defects on performance capabilities and (2) the feasibility of patch repair of major coating defects. A grit-blasting technique, using an S. S. White Air Brasive unit, was first employed to prepare a slot 6 mils wide by 60 mils long at various depths in different coating systems. Fine Al_2O_3 grit was propelled through a nozzle 5 mils wide by 60 mils long using nitrogen gas under high pressure. Samples were mounted perpendicular to the nozzle, and the size and depth of cut were controlled by the sample-to-nozzle distance and time of exposure. Examples of defects produced in TZM/PFR-6 specimens by this method are shown in Figure 24 A. The major problem in this approach was control of defect depth and shape. Repetition of the tests in attempts to produce defects either one-half or three-fourths of the coating thickness indicated poor reproducibility. Defects were rounded at the bottom, and depth was difficult to control. This method was used, however, to prepare samples in which defects penetrated well into the substrate. Sufficiently accurate control was available for preparation of the totally defective specimens that were used in coating repair studies.

An electric discharge spark machining technique was developed for producing controlled defects of varying depth. A Servo Met Spark Machine, Type SMD (Metals Research, Ltd., England) was used for this work. This machine has an extrasensitive servomechanism that maintains an ultrafine spark and prevents damage due to contact between the tool and workpiece. It has an automatic range selector pulse-time circuit that adjusts the range during cutting according to a preset schedule to make controlled, reproducible cuts.

Specimens were mounted on a flat brass plate and immersed in kerosene for cutting. Tungsten sheet was used for the cutting electrode. The sheet was thinned by etching in HNO_3-HF until the size was suitable for production of a cut of the desired width.

The electrode was then dressed by polishing until the cutting surface was flat and square with all edges, and it was frequently redressed to maintain the flat cutting face. The electrode was aligned parallel to the specimen surface with a feeler gage and then clamped in a copper electrode attached to the servo system.

73
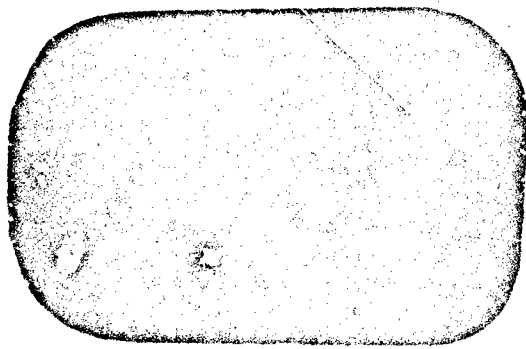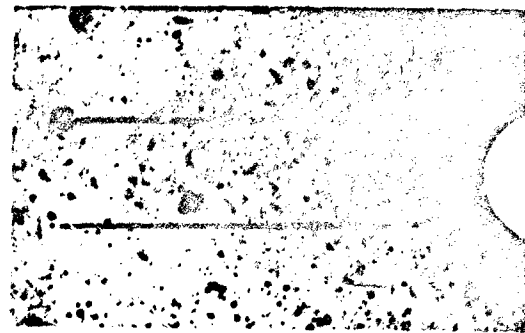
M7647   3 MILS WIDE   ×4   M8578   6 MILS WIDE   ×2
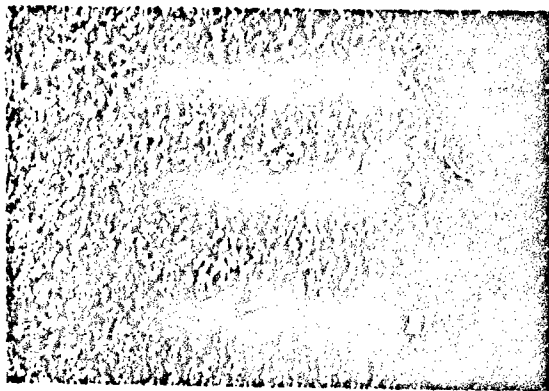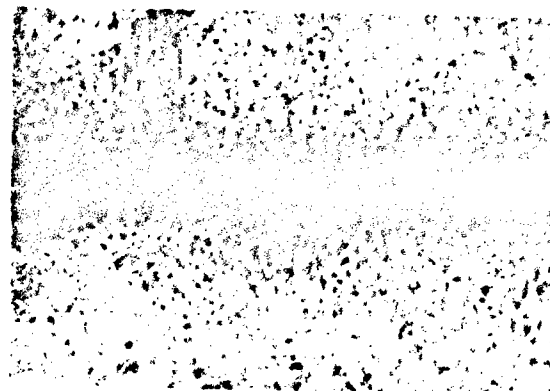
M7648   3 MILS WIDE   ×40   M8580   6 MILS WIDE   ×30
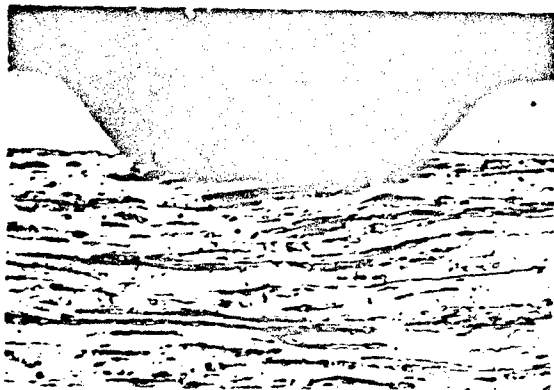
M7740   3 MILS WIDE   ×600 M8355   1 MIL WIDE   ×500
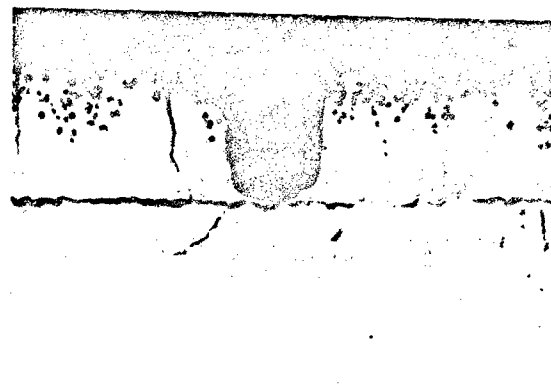
(A) Air Abrasive Method   (B) Spark Discharge Method
    TZM/Disil   Cb-752/CrTiSi

Figure 24 Gross Coating Defects Produced by Air Abrasive
           and Spark Discharge Methods

74

For any given range setting, the volume of coating removed was a linear function of time. For constant time, therefore, the depth of cut is proportional to the length and width of the cutting electrode. More important, however, uniformity of depth is a direct function of uniformity of thickness and flatness of the electrode. Hence, close control of the contour of the electrode and frequent redressing are critical in creating uniform, reproducible defects.

The defects produced by this method are illustrated in Figure 24 B. Straight-sided cuts of uniform width and depth were produced in silicide coatings on Mo- and Cb-base alloys. For example, in 24 defects produced in Cb-752/CrTiSi samples with the goal of achieving slots 6 mils wide by 4 mils deep by 3/4 in. long, the overall range of dimensions for all samples was 5.91 to 6.50 mils in width and 3.15 to 4.92 mils in depth, based on measurements at the center and at each end for each defect. Variations in depth were due largely to bowing (lack of flatness) of the as-coated samples.

Electric spark discharge machining was used to prepare all samples for defect tolerance testing. In these tests, two slots were machined across the entire width of baseline (Type A) test specimens. The slots were produced on opposite sides of the specimens near the ends. One slot penetrated through one-half of the coating thickness, and the other through three-fourths of the thickness. Depth and time for machining the defects are given in Table XI.

Table XI. Data on Spark Discharged Machined Defects

System	Av. coating thickness (μ)	Depth of Defect (μ)		Cutting Time (sec)	
		1/2 t	3/4 t	1/2 t	3/4 t
TZM/PFR-6	48	24	36	60	90
TZM/Durak-B	41	20	30	30	45
TZM/Disil	50	25	38	30	45
Cb-752/PFR-32	64	32	48	75	120
Cb-752/CrTiSi	34	17	26	30	45
B-66/CrTiSi	40	20	30	30	45

Width of the defects was measured on a Lietz microhardness tester using the calibrated eyepiece. Depth was measured using a microscope focused on the specimen surface and on the bottom of the defect using a focus control calibrated directly in microns. The specimens were then tested at selected baseline conditions. Performance in the defect areas was compared with that of the good portions of the sample. The defect tolerance limit was taken as the maximum depth of defect (1/2 or 3/4 t) for which no degradation from baseline behavior was observed. This was reported as < 1/2 t, > 1/2 t but < 3/4 t, or > 3/4 t.

At the request of the Air Force, similar defects were prepared in 60 samples of CrTiSi-coated Cb-752 for evaluation in the Asset program. Two parallel defects, 3/4 in. long and 1/4 in. apart, were machined in each specimen by the spark discharge method. Defects were 6 mils wide and either 1 mil or 4 mils deep. The cutting time was 3.5 min each for defects 6 mils by 1 mil by 3/4 in. and 40 min each for defects 6 mils by 4 mils by 3/4 in. The width and depth of each defect were measured at the center and each end. Results are presented in Appendix II.

75

Coating repair. The objective of this phase of the program was to assess the feasibility of repairing coating defects by "in-field" patch-repair techniques. Techniques of this nature obviate a commonly used repair method of stripping and recoating or reprocessing of defective parts. The investigation was concerned with an evaluation of various procedures which currently are being used or considered for use in small patch-type repair of defective areas in components or assemblies. The basic requirement is for a repair mix (slurry, paste, etc.) that can be applied to defective areas and cured or fired in situ by localized application of heat to produce an oxidation-resistant patch.

Coating vendors were requested to describe what patch-repair procedures, if any, were available for use with each of the eight coating systems under investigation. Suggested procedures are summarized in Table XII.

Table XII. Survey of Available Techniques for
Patch Repair of Coating Defects

System	Supplier	Recommended Patch-Repair Technique
TZM/PFR-6	Pfaudler Co.	None
TZM/Durak B	Chromizing Corp.	None
TZM/Disil	Boeing Co.	$MoSi_2$-Synar
Cb-752/PFR-32	Pfaudler Co.	None
Cb-752/CrTiSi (Tapco)	Thompson Ramo Wooldridge, Inc.	Duplex Slurry Pack
Cb-752/Vought IV	Vought Aeronautics	Slurry Pack
B-66/CrTiSi (Tapco)	Thompson Ramo Wooldridge, Inc.	Duplex Slurry Pack
Ta-10W/Sylcor	Sylvania Electric Products, Inc.	None

All vendors indicated that the only completely satisfactory method for repair would be either to strip and recoat or to reprocess the defective part. This approach, however, does not meet the basic requirements of a patch-repair technique. Boeing indicated that some success had been realized in tests of $MoSi_2$ powder suspended in a colloidal silica binder (Synar) as a patch repair for Disil-coated TZM (25). The mix is air dried at room temperature or 200° F and the repaired part used directly without the need for a high-temperature cure. TRW recommended the use of a duplex slurry pack repair process for CrTiSi-coated Cb alloys that had been developed by Solar (26). In this process, a slurry pack of Cr, Ti, and NaF is applied, dried at 200° F, and fired at 2200° F. Silicon is then deposited from a second pack slurry of Si and NaF which is dried at 200° F and fired at 2200° F. LTV recommended a one-cycle slurry pack repair process for Cb-752/Vought IV in which a slurry of the pack composition was applied and dried in air. An encapsulating slip was used to protect the patch while the repair area was heated to 3000° F for firing. The slip and spent pack were removed after cooling. GT&E stated that effective patch repairs could be made in Sn/Al-coated Ta alloys. However, they requested that defective samples be returned to GT&E for repair and did not recommend a procedure for use in the field.

Based on these replies, the Boeing $MoSi_2$/Synar and the Solar Slurry Pack repair procedures were selected for evaluation on coated TZM and Cb-base alloys, respectively. The LTV repair for Vought IV was not evaluated because of the high susceptibility of the

available test samples to random defect failures under all conditions of test. It was believed that meaningful or conclusive results could not be obtained with this particular batch of coated specimens.

Since the number of recommended techniques for patch repair was quite limited, consideration was given to the evaluation of a third procedure which was being investigated at LMSC in an Independent Research study. This procedure was based on the use of low melting point alloy braze materials which on fusion with the coating would produce an oxidation-resistant alloy patch of high melting point. The process was designed for repair of small cracks, fissures, or chip-type defects by gas-torch brazing techniques. Repair compositions were based on alloys of Cu, Ag, Au, and Si, $CbSi_2$, or $MoSi_2$ in varying proportions. Paste mixtures of the powders were applied to defective regions and fused in air with an oxyacetylene torch.

Standard defect samples were prepared for all tests. Slot-type defects 6 mils wide by 60 mils long were produced by the air abrasive cutting process. Defects were of sufficient depth to expose completely the substrate, and in many cases extended well into the substrate (Fig. 24 A). Two parallel defects, 1/8 in. apart, were machined near each end on opposite surfaces of the specimen. Thus, the repair of four defects was evaluated in each test, giving an indication of the reproducibility of the repair process with respect to effectiveness in restoring oxidation resistance.

Each of the four defects in a given sample was repaired by one procedure. Details for each of the three patch repair techniques evaluated are as follows:

(1) MoSi2/Synar. Synar (silica powder plus Synar binder) was obtained from the Penn Salt Chemical Corporation. The silica powder was reground to - 200 mesh and then blended with - 325 mesh $MoSi_2$ powder. Three mixes were prepared: 25/75, 50/50, and 75/25 silica/$MoSi_2$. Synar binder was added after mixing to form a thick paste. This material was troweled into the defects and air dried overnight at 200° F. Only small batches were prepared at one time since the Synar binder sets up solid in about 30 min on exposure to air.

(2) CrTiSi duplex slurry pack. A blend of 60% Cr (- 150 + 325 mesh) and 40% Ti (- 325 mesh) was prepared and mixed with 10% (by weight) of NaF. After mixing, sufficient glycerin was added to form a thick paste. The paste was troweled into the defect and the sample was fired for 1 hr at 2200° F in slowly moving argon. After firing, the spent bisque was removed and the surface brushed clean. A second paste composed of 90% Si (- 325) and 10% NaF in glycerin was troweled on and the sample refired for 1 hr at 2200° F in argon. The spent bisque was removed and the sample brushed clean. Argon heat treatments were conducted in a tube furnace. (For field repair, the process developed by Solar employs a tungsten strip heater in a box furnace which is placed over the repair area. An argon purge is used for atmosphere protection.)

(3) Braze repair procedure. Braze alloy compositions were prepared by blending metal powders (- 325 mesh) in a ball mill. The five compositions indicated in Table XIII were prepared for evaluation. The alloy powder blends were mixed

77

with Handy and Harmon "Handy Flux for Low Temperature Brazing" contain-
ing a 10%-by-weight addition of NaOH. Sodium hydroxide was added to promote
wetting of the braze alloy. A thick paste was formed which then was troweled
into the defect. Samples were heated in air with an oxyacetylene torch until
the braze alloy melted and flowed over the surface. Samples were cleaned by
brushing in hot running water. An invention disclosure on the braze alloy and
paste compositions developed under this program has been submitted.

Table XIII. Braze Repair Alloy Compositions

Braze Alloy Number	Composition (wt %)					
	Cu	Ag	Au	Si	$MoSi_2$	$CbSi_2$
1	25	55	–	20	–	–
2	25	55	–	–	20	–
3	21	51.7	2.3	25	–	–
4	21	51.7	2.3	5	20	–
5	25	55	–	–	–	20

Samples repaired by all three techniques were evaluated by metallographic examination
of cross sections through repaired defects before and after oxidation tests under
selected baseline conditions. Test procedures were the same as those used in baseline
studies.

Materials compatibility. The objective during this phase of the program was to evaluate
the chemical compatibility of the eight coating/substrate systems with one another and
with other high-temperature materials. Experiments with high-temperature materials
were necessary early in the program to select suitable materials with which to support
specimens during testing.

The high-temperature materials selected for compatibility tests with the coated materials
were Al_2O_3, ZrO_2, ThO_2, SiO_2, and $MoSi_2$. Coated samples were mounted in slotted
cylinders of each of these materials and this assembly was supported by the Al_2O_3
extension rods which were part of the radiation furnace push rods. These compatibility
couples were tested in air at temperatures of 2500 to 3000° F and pressures of 0.01 to
1.0 mm Hg for times of 30 to 240 min. Performance was evaluated by visual and metal-
lographic examination at points of direct contact.

To investigate possible reactions between different substrate/coating systems, two
specimens of dissimilar systems were placed with their surfaces in intimate contact in
slotted $MoSi_2$ specimen supports and tested under selected baseline conditions. Again
the evaluation was dependent primarily on metallographic analyses of cross sections
through the contact region and on visual examination.

Kinetic model tests. One objective of the overall program was to determine if reasonable
forecasts of reliability under the dynamic conditions characteristic of atmospheric
reentry could be based on static test data combined with an understanding of coating system

behavior. The approach employed to determine the feasibility of predicting performance in a dynamic environment was as follows:

(1) Environmental parameters were defined for heat-shield panels on a hypothetical vehicle during atmospheric reentry.

(2) Baseline data were analyzed to determine performance capabilities and limitations of a given system with respect to the various combinations of temperature, pressure, and time that would be encountered.

(3) The effect of other environmental and preexposure conditions on baseline performance in this environment was considered.

(4) Basic modes of failure as influenced by various environmental factors were delineated.

(5) Performance under dynamic conditions in terms of the ability to complete one or more missions was predicted on the basis of this analysis.

(6) Predictions were checked experimentally in pseudokinetic tests in which reentry profiles were simulated by step-wise variations of temperature and pressure.

The reentry profile for the high L/D vehicle previously described was selected for the kinetic model tests. Time variation of temperature and pressure is shown in Figure 19. Temperature and pressure plateaus were constructed for time intervals ranging from 1 to 8 min to approximate the smooth reentry profiles in a step-wise manner. These step functions, shown in Table XIV, provided the basis for simulated reentry environment tests in the laboratory.

All tests were conducted by direct resistance heating in the cold-wall furnace. Samples were brought to the temperature and pressure values indicated at the start of each time interval, held constant for 1 min, and then adjusted rapidly to new values (if so indicated) at the start of the next time interval. All tests were conducted in slowly moving air. Samples were cooled to room temperature and visually examined after test. Tests were repeated in a cyclic (multiple-mission) manner until failure occurred or until a selected number of missions without failure was attained. Final performance was evaluated by visual observation and metallographic study of sectioned samples.

Postexposure Analysis

Performance criteria and evaluation. The criteria for evaluating, rating, and reporting the performance of the coated refractory metals under investigation were established on the basis of several considerations. First, the general behavioral trends and failure modes of the various materials were analyzed and compared. The objective here was to design a general performance classification system mutually applicable to all materials and independent of specific chemical reactions and mechanisms of protection or failure. The second major requisite for a performance classification system was that it provide the greatest possible use of the generated data. That is, it should permit broad applicability of the result for prediction of performance in aerospace components or systems. The application of the results of this program toward a more complete understanding of the structure and chemistry of each coating system is also important. This, however, must be done on an individual coating system basis or, at least, within a family of the

79

Table XIV. Stepwise Time Variation of Temperature
and Pressure for Kinetic Model Test[a]

Time interval (min)	Temperature (°F)	Pressure (mm Hg)
0 - 1	1400	$< 10^{-3}$
1 - 2	2000	0.4
2 - 3	2625	1.4
3 - 4	2500	1.4
4 - 5	2650	1.4
5 - 6	2650	1.4
6 - 7	2300	1.4
7 - 8	2750	1.4
8 - 9	2600	1.8
9 - 10	2550	1.8
10 - 11	2550	2.3
11 - 12	2550	2.3
12 - 13	2500	2.3
13 - 14	2500	2.7
14 - 15	2450	2.7
15 - 16	2450	2.7
16 - 17	2400	2.7
17 - 18	2400	2.7
18 - 19	2350	2.7
19 - 20	2350	3.0
20 - 21	2250	3.0
21 - 22	2250	3.0
22 - 23	2150	3.0
23 - 24	2150	3.0
24 - 25	2050	3.0
25 - 26	2050	3.0
26 - 27	1950	3.0
27 - 28	1850	3.0
28 - 29	1800	3.5
29 - 30	1700	3.5
30 - 31	1600	3.5

(a) Lower surface heat-shield panel on high L/D vehicle, suborbital reentry from 220,000 ft at 20,000 ft/sec.

same types of coatings. It is impossible to generalize in this respect for all of the materials of this investigation.

Throughout all phases of the program, the principal criterion for evaluation was that a "passing" rating should be assigned to any specimen where the substrate was unaffected – aside from purely thermal effects such as grain growth or recrystallization, or both. A "failure" was recorded when there was any indication of substrate oxidation. If there were only random point failures on a specimen, a "random failure" rating was assigned that specimen. If there were more than four such point failures per specimen or an obviously general failure of the coating, a "total failure" was recorded. This distinction between random and general attack is useful in the application of results of this program to the design of coated parts. It is conceivable that in some requirements for coated components, random failures may be tolerable and the design should be limited only by the time required for a general failure to occur. It must be remembered, however, that the distinction between random and general failure limit in this program is purely an arbitrary distinction based on the relative number of failure sites.

A further distinction in the failure classification was made because of the geometry dependence of coating performance. In some cases, failure – both random and general – was predominant on specimen edges long before the coating on flat surfaces failed. Also, there were a few cases where the converse was true. Consequently, failures were designated as either surface or edge failures. Again, this distinction will be useful in the application of the results of this program. There will be some components with all radii of curvature much greater than those of the test specimens. Surface performance will be the primary criterion for predicting the useful lifetimes of these components. In others, the radii of curvature will be smaller and edge performance data will be of greater value.

There were a few specimens which failed because of chemical reactions between the specimens and the support materials. A further classification, "support reaction," was assigned to these specimens. These failures were easily recognized and no artifacts were introduced as a result of any incompatibilities between specimens and support materials. Where such failures were encountered, new support materials were employed to prevent such reactions in continued tests.

A summary of the various categories of coating performance and the appropriate coding follows:

A   Passing
B-1 Random surface failure
B-2 Total surface failure
C-1 Random edge failure
C-2 Total edge failure
D   Total failure (edge and surface)

Examples of these ratings for Mo-base-alloy systems are shown in Figure 25. Passing specimens may have a slightly crazed surface but contain no holes or other serious defects.

81

M6377   Type A: Pass   6x   M6380 Type B1: Random Surface 6x   M6416 Type B2: Total Surface 6x
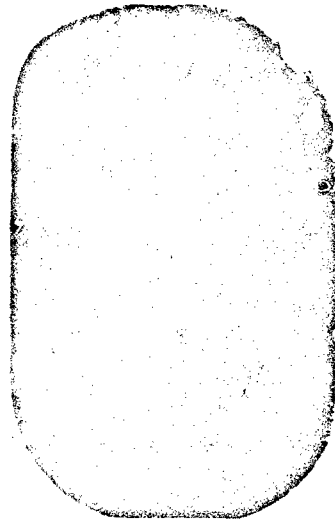
M6290   Type C1: Random Edge   4x   M6378   Type C2: Total Edge   4x

Figure 25 Examples of Basic Performance Ratings of Mo–Base Alloy

82

Random failures were the most difficult to detect after low-pressure tests. When pinhole failures occurred and the underlying metal was oxidized, the oxide, being volatile, escaped through the pinhole. The coating remained intact as a shell. If pinholes or bulges in the coating were discovered during macroscopic examination, a sharp steel pick was used to remove the coating and reveal failures. Often, as shown in Figure 25, large holes on the edge or surface were found. General edge or surface failures were more readily detected and were manifested by a spongy surface condition with general attack of the substrate metal apparent. Whenever there was doubt as to the performance rating after macroscopic examination, specimens were sectioned for metallographic examination. During microscopic examination the major failure criterion, again, was the loss of substrate material through volatilization of MoO_3.

The primary indication of failure in Cb- and Ta-base alloy specimens was embrittlement of the substrate caused by internal oxidation. Examples of typical failures as revealed by ductility tests are shown in Figure 26. Tested specimens were bent by hand 90 deg over a radius of 4t (t = specimen thickness). Passing specimens withstood a 90-deg bend with no substrate cracking. Random failures were readily detected because the cracking was confined to the point of failure. Apparently the oxygen diffusivity was sufficiently low to limit substrate embrittlement to the region of failure. Random failures were differentiated from general failures by making additional bends. If the sample cracked at the edge or surface on each bend, Type B-2 or C-2 ratings were assigned. In most cases of total failure, Type D, the specimen broke with a glass-brittle fracture.

The limitations of ductility testing as a sole criterion of performance for Cb and Ta alloys were recognized. First, there are factors other than oxidation that can affect ductility. These include changes in grain size or texture, redistribution of solute atoms, and possibly structural changes in the coating. Interdiffusion of coating and substrate may promote brittleness in some alloy systems. In others, growth of more ductile phases at the interface may reduce rates of crack propagation (crack arrestor) and hence change the ductile phase to brittle behavior in bending coated samples. Also, the initial ductile-brittle temperature of the substrate before testing may be substantially below room temperature for one system and near room temperature for another. If the postoxidation ductility tests are conducted at room temperature, failure might be observed in one system but not in the other depending on the relative increase in ductile-brittle transition as a result of substrate oxidation in the initial phase of coating failure. Obviously results of ductility tests must be qualified and supplemented with metallographic analyses or other types of analyses.

For the Cb-base alloy substrates, the baseline data served to qualify bend tests as accurate indicators of performance. Some lifetime curves were established on the assumption that ductility results were valid; then a selected datum point was analyzed. For example, consider a point which is in the passing region but near a failure boundary on a time-versus-temperature graph. Raising the temperature or increasing the time slightly to cross the failure curve always resulted in embrittlement. The changes in temperature or time were sufficiently small so that it was improbable that the sudden embrittlement could be attributed to other factors. In addition, data points at one pressure level were compared with similar data points (same time and temperature) which lay on the opposite side of failure boundaries

83
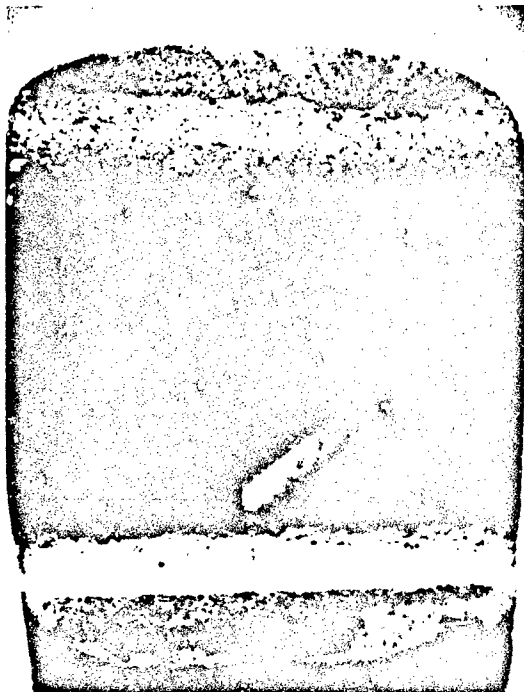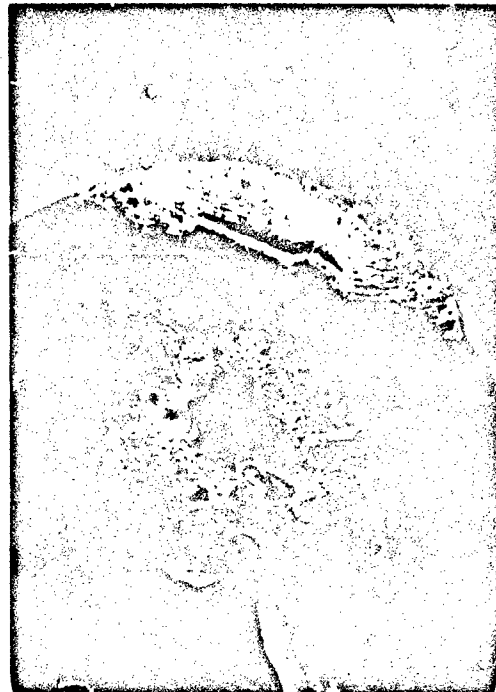
M6375   Type A: Pass   6×   M6381   Type B1: Random Surface   6×

M6374   Type C1: Random Edge   6×   M6224   Type D: Total   4×
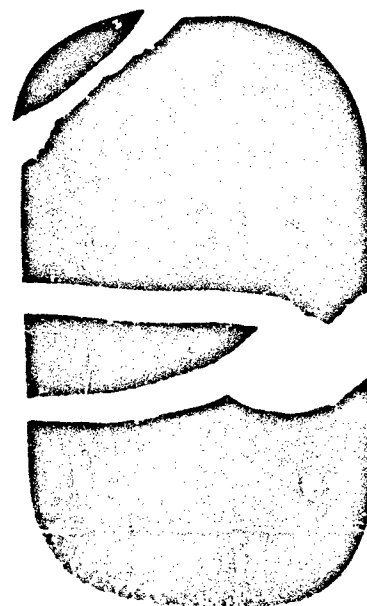
Figure 26   Examples of Basic Performance Ratings of Cb- and Ta-Base Alloys

at other pressure levels. Specimens exposed at higher pressures and higher temperatures or longer times which were passing and ductile were compared with corresponding specimens at lower pressures. The results consistently verified the assumption concerning the validity of ductility tests. In fact, ductility tests were shown to be more sensitive to performance in some cases than metallographic analyses. Embrittlement was apparent before oxides could be detected at magnifications up to 3000×.

Specimens with Cb-752 as a substrate material were bent over a radiused machinist vise at room temperature. It was necessary to heat coated B-66 specimens above 250° F for bend tests because of the higher initial ductile-brittle transition temperature of this system. A special bending device was built for these tests. It was a three-point loading apparatus with a spring-loaded plunger. Specimens were deformed in a silicone oil bath at a controlled temperature of 325 ± 1° F under easily reproducible conditions. In the Ta-10W/Sn-Al system, general failure was recognized readily by glass-brittle fracture of specimens. Lesser degrees of failure were more difficult to recognize. Sometimes cracks created in the brittle aluminide layer at the surface during bending propagated deeply into the substrate without any evidence of coating failure or substrate oxidation. It was necessary with this system to supplement ductility tests with light microscopy and microhardness surveys on virtually all samples. A diamond pyramid indenter with a 200-gm load was used with a Leitz Miniload Hardness Tester. Hardness surveys were made longitudinally along a specimen and across the thickness. Generally the hardness of passing specimens was from 200 to 300 DPH. Regions exceeding 350 DPH were assigned failure ratings.

The weight and thickness changes of each specimen in all phases of this program were measured. It was found that these values were generally not indicative of performance. Except in cases of gross failures, there was no consistent trend in the weight or thickness changes.

The surface color and finish were recorded and served as a useful basis of comparison when different heating modes were necessary. For example, when it became necessary in the baseline tests to use resistance-heated instead of radiation-heated samples, duplicate tests were conducted and surface conditions were compared. This was used in addition to normal methods of temperature calibration as a further check on the validity of these data.

In summary, the primary performance criteria were (a) loss of Mo substrate in TZM systems; (b) loss of bend ductility in Cb-752 (room temperature) and B-66 (325° F); and (c) loss of bend ductility (room temperature) and/or increase in substrate hardness above 350 DPH in Ta-10W. All evaluations were supported with metallographic examinations, and weight and thickness changes were recorded.

RESULTS

In this section, the results of all tests and evaluations are presented and discussed independently for each coating system. A more complete understanding of the performance capabilities and general behavior of each system as influenced by the interrelation of structure, composition, and various environmental factors is afforded by this method of presentation. A summary of the behavior of all systems, including an analysis of important factors governing performance, is presented in Section V.

TZM/PFR-6

Material Evaluation

The PFR-6 coating is essentially $MoSi_2$ applied by a single-cycle pack process. Columbium is added to the pack and appears as a trace element in the coating (24). The basic coating process was developed by the Pfaudler Corporation, Rochester, N.Y.

The as-coated specimens had a rough, granular surface, as shown in Figure 27. Color and texture were comparatively uniform, although some mottling in surface coloration was noted. Plane surfaces appeared to be free of cracks or fissures. The general edge condition was good, although some edge fissures were evident. They tended to be short in length and were randomly distributed.

The rough, granular nature of the surface is shown more clearly in Figure 28. A relatively porous, irregular surface layer about 1 mil thick was observed on all samples. Below this layer, the bulk of the coating was dense and relatively free of defects. Fine hairline fissures extended from surface to substrate. Edge defects were typical V-notch fissures extending to a depth of one-half to three-fourths of the coating thickness. Similar defects were observed at the four corners of all cross-sectional specimens examined during the test program, indicating a more gross defect condition than was evident from preliminary visual examinations.

Structural details at high magnification are shown in Figure 29. A thin layer, 0.01 to 0.03 mil thick, of Mo_5Si_3 existed at the substrate/coating interface. This layer was not uniform and continuous, however, and in some areas could not be detected at 3000× magnification (Figure 29B). Where the Mo_5Si_3 zone was present, fine hairline fissures extending inward from the surface were arrested at the $MoSi_2/Mo_5Si_3$ interface. No tendency for horizontal branching along the interface was noted. However, where the Mo_5Si_3 layer was less than 0.01 mil thick or was not observed, the cracks branched into transverse fissures that extended along the substrate/coating interface (Figure 29 B).

87
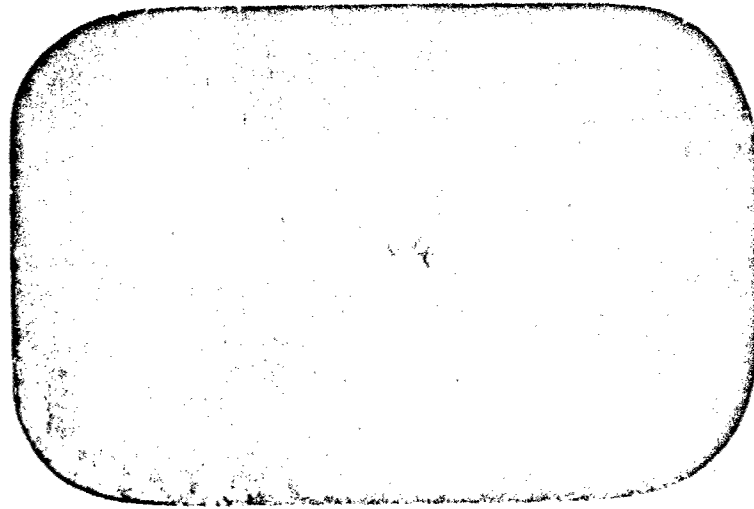
M9964   (A) Surface   ×6
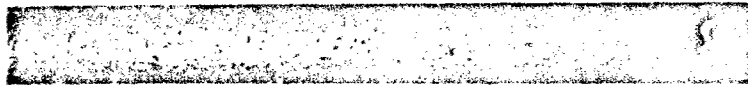
M5605   (B) Edge and Surface   ×18

Figure 27 General Appearance of As-Coated TZM/PFR-6

88
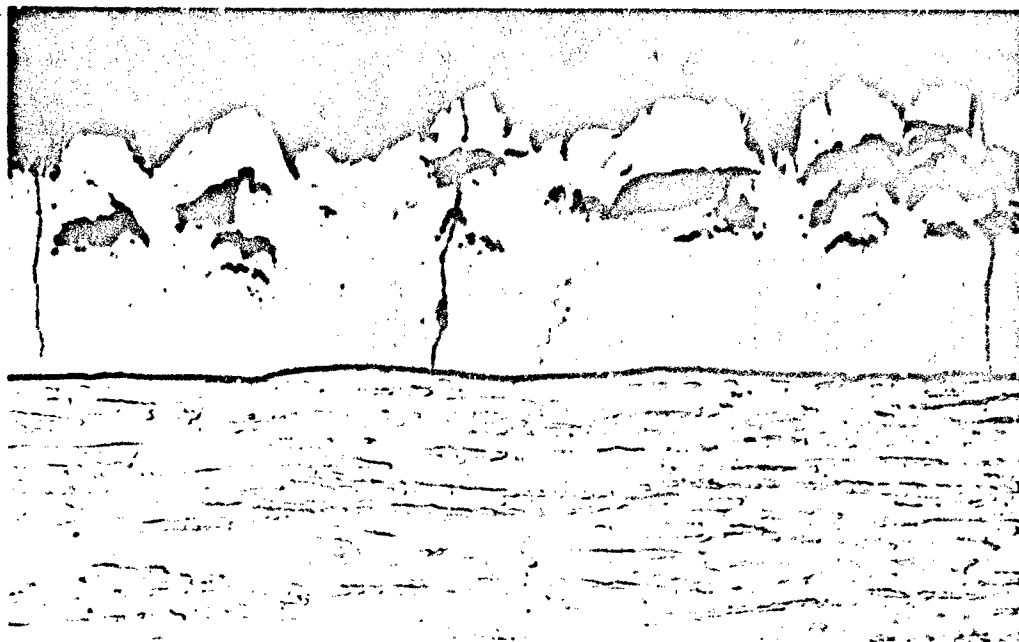
M8304   (A) Plane Surface   ×500

M8305   (B) Edge   ×500

Figure 28 General Structure of As-Coated TZM/PFR-6

89
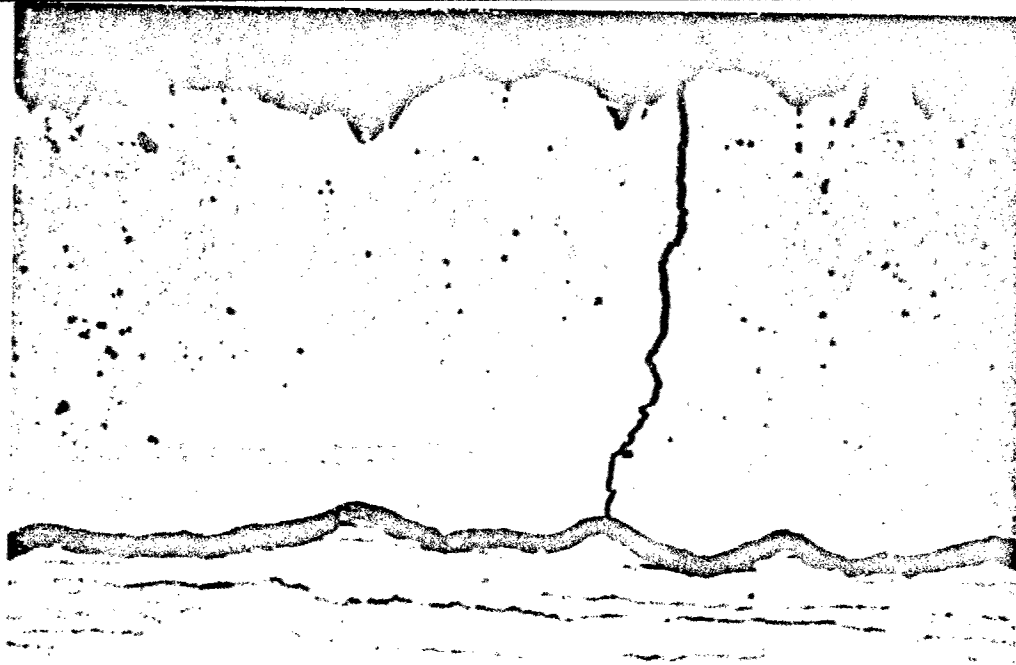
M5916   (A) Mo_5Si_3 Diffusion Zone   ×1000
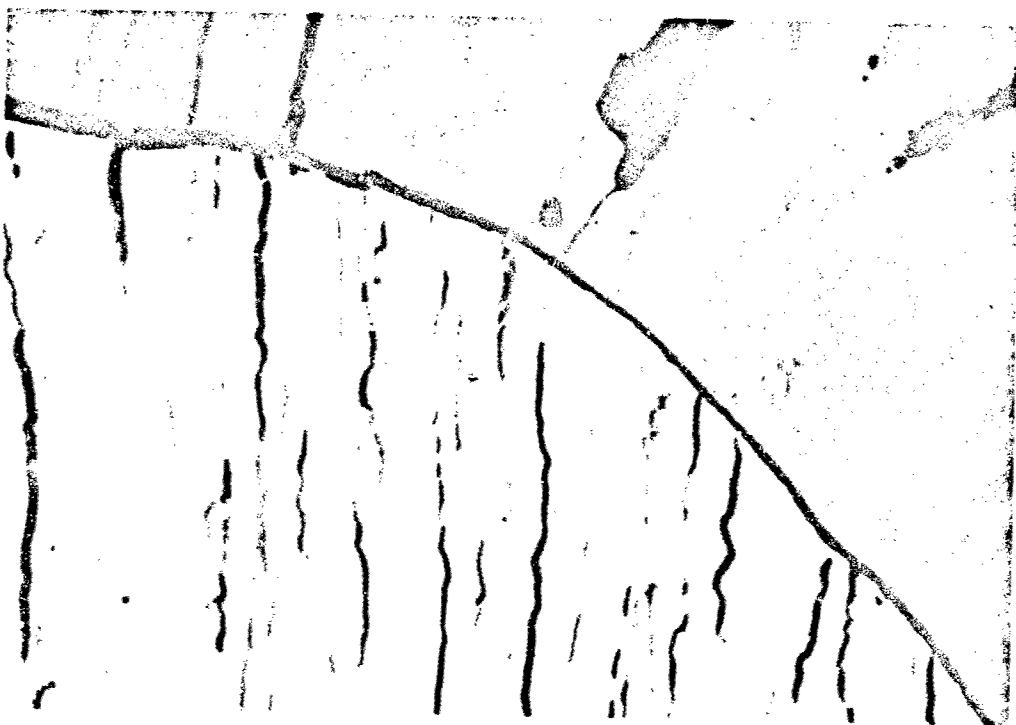
M8307   (B) No Mo_5Si_3 Diffusion Zone   ×3000

Figure 29 Structural Details of As-Coated TZM/PFR-6

90

As will be discussed in the following sections, this type of interfacial defect is a source for random defect failures in low-pressure oxidation. Formation of such defects can be prevented by adjustment of the coating process to create a Mo_5Si_3 diffusion zone at least 0.01 mil thick. It is believed that such fissures are formed from thermal stresses induced during the cooling phase of the deposition process. To prevent transverse branching, the thin Mo_5Si_3 zone must be formed during the coating process, not by subsequent heat treatment. The feasibility of this is demonstrated by the presence of crack-arresting diffusion layers in all the as-coated samples (Figure 29A), but the uniformity or continuity of this zone should be improved.

The coating above the Mo_5Si_3 zone consisted of coarse columnar grains of $MoSi_2$. Hairline fissures tended to follow the columnar grain boundaries, although some cleavage fractures were observed. Spectrographic analysis indicated that Mo and Si are the major elements in the coating. Traces of Ti and Zr were also detected; columbium was not detected. Since the coating was formed by reacting Si with the TZM substrate, it was expected that both Ti and Zr would be present as trace impurities in the coating. The $MoSi_2$ portion of the coating was single phase.

The TZM substrate was not altered significantly by the coating process. As shown in Figures 28 and 29, the cold-worked, elongated grain structure characteristic of the uncoated TZM sheet was retained. Substrate hardness averaged 296 DPH after coating, which is essentially the same as the uncoated average hardness of 284 DPH. No evidence of softening or recrystallization was found. As shown in Figure 30, substrate hardness decreased to 210 DPH after complete recrystallization upon oxidation testing for 4 hr at 2700° F. In all cases, substrate hardness was uniform from the coating interface to the centerline of the sheet.

Coated specimens were brittle in bending at room temperature but could be bent 90 deg without specimen fracture at 250° F. At 250° F, bends of 30 to 35 deg were possible before fracture and spalling of the coating occurred. The existence of a low ductile-to-brittle transition temperature and the ability to deform plastically without serious coating fracture are important considerations in manufacture and assembly of coated hardware. It is significant that coated TZM sheet can be as ductile as coated Cb-alloy sheet above about 200° F. The low-temperature brittleness of coated TZM is related to a notch sensitivity effect in which cracks initiated in the coating propagate through the substrate. This type of behavior is similar to that observed in other silicide-coated TZM and Cb-base alloy systems and is discussed in detail in the section on Cb-752/PFR-32. It is anticipated, of course, that the ductile-brittle transition temperature of coated TZM in bending will be increased significantly after complete recrystallization of the substrate. Thus, brittleness at low temperature would be expected after oxidation testing. As will be discussed, PFR-32 coated Cb-752 shows an opposite effect due to resolutioning of a precipitate responsible for low-temperature brittleness in this particular system.

Measurement of the average coating thickness and uniformity proved difficult because of surface roughness and granularity. Coating thickness measured directly on two cross-sectional samples was found to be 2.09 and 2.25 mils. The maximum and minimum
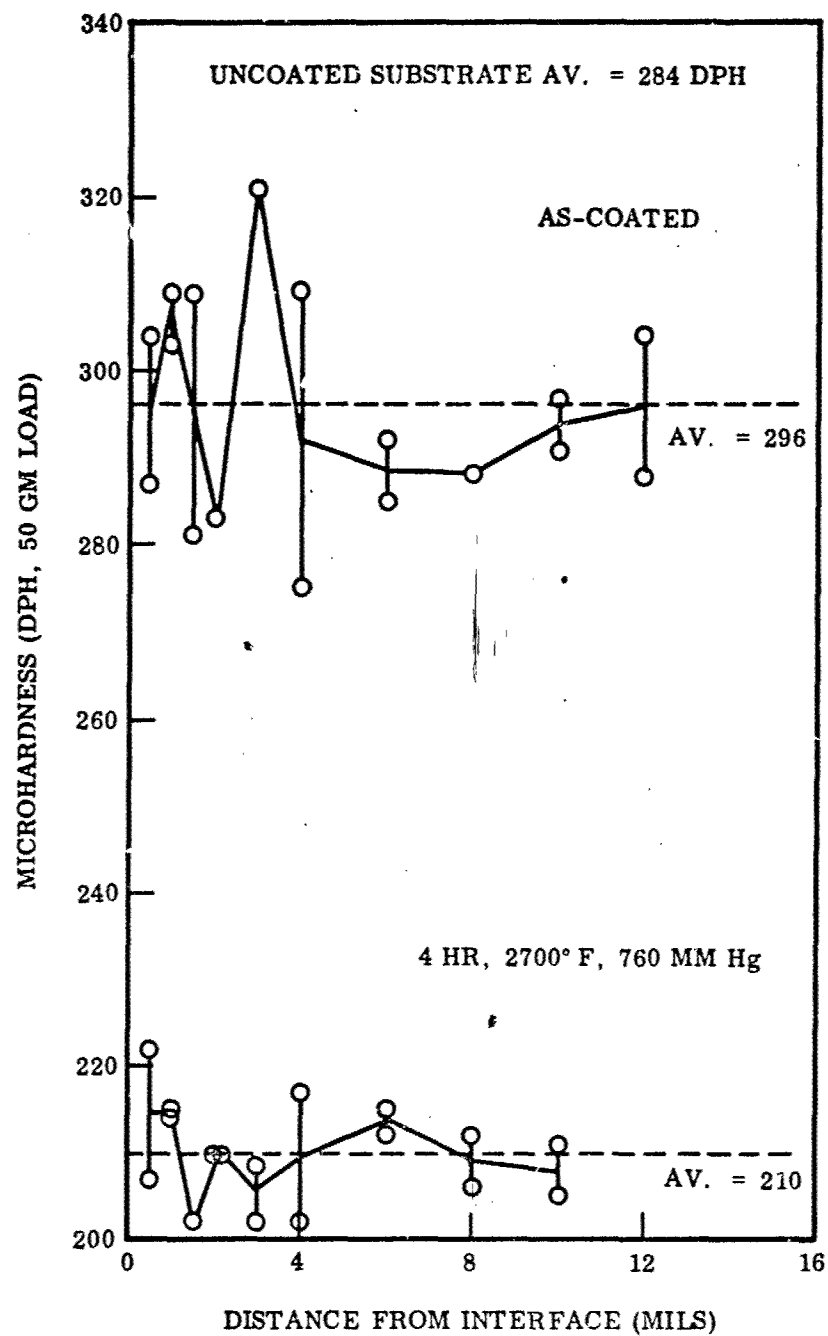
Figure 30 Results of Substrate Hardness Traverse, TZM/PFR-6

thickness noted were 1.69 and 3.07 mils, respectively. Based on these measurements, the average thickness is about 2.15 mils.

Reasonable estimates of coating thickness could not be calculated from thickness or weight increases of the substrate. The frequency distribution of total thickness for a lot of 100 random samples before and after coating is shown in Figure 31. Considerable variability in thickness of both uncoated and coated sheet is indicated. Thickness of the coated sheet averaged 26.8 mils; 95% of the samples were between 23.0 and 30.5 mils thick ($\pm 2\sigma$ limits). Based on molecular weight and density considerations, about 0.4 mil of Mo is consumed in making 1 mil of $MoSi_2$. Thus, for a 2.5-mil-thick coating, about 1 mil per side of the substrate is consumed. The average coating thickness calculated from the difference in corrected initial and final thickness measurements is 4.2 mils per side. This is significantly greater than values measured on sample cross sections. Since total thickness was measured by micrometer, the excessive roughness of the samples introduced a large error in coating thickness calculations.

Calculations based in weight change indicate a comparatively low average thickness, on the other hand. Average weight increased 0.04 gm. From density and molecular weight considerations and the assumption that the weight increase was due to silicon pickup, this corresponds to 0.1086 gm of $MoSi_2$. Average surface area was 4.9 cm^2, from which coating thickness is calculated to be 1.4 mils per side. The low value in this case is attributed again to the excessive surface porosity and roughness of the coated samples.

It is concluded that direct measurement of sectioned couples provided the best estimate of coating thickness. An average thickness of 2.25 mils has been assumed for samples of the TZM/PFR-6 systems. All measurements and calculations indicate considerable sample-to-sample and in-sample variation of coating thickness.

Baseline Behavior

The results of the baseline evaluations are presented in Figure 32 in the form of lifetime versus temperature curves at each pressure level. The details of the experimental conditions and postoxidation observations are tabulated in Appendix III. The ease with which boundaries separating the various performance regions could be established is evidence of the consistency of the data. It is clear that these regions are well defined at all pressures except 50 mm Hg. Here the total failure boundary was not established because of the high temperatures and the necessity for resistance-heating specimens. When a single, random failure formed, the loss of Mo was so great that the specimen resistance increased rapidly. Temperatures increased sharply and rapid destruction of the sample occurred. The boundary cannot be far above 3300° F, however, because the $MoSi_2 - Mo_5Si_3$ eutectic melts at about 3400° F.

The width of the random-failure region varies from 50 to 100° F throughout the pressure range of interest. Both random-edge and random-surface failures occurred at all pressure levels, but random-edge failures predominated at 1.0 mm Hg and below.

The influence of reduced pressure is perhaps more vividly shown by presenting the data on graphs of limiting temperature versus air pressure for a given lifetime. In Figure 33 it is apparent that the maximum useful temperature decreases rather sharply with

93
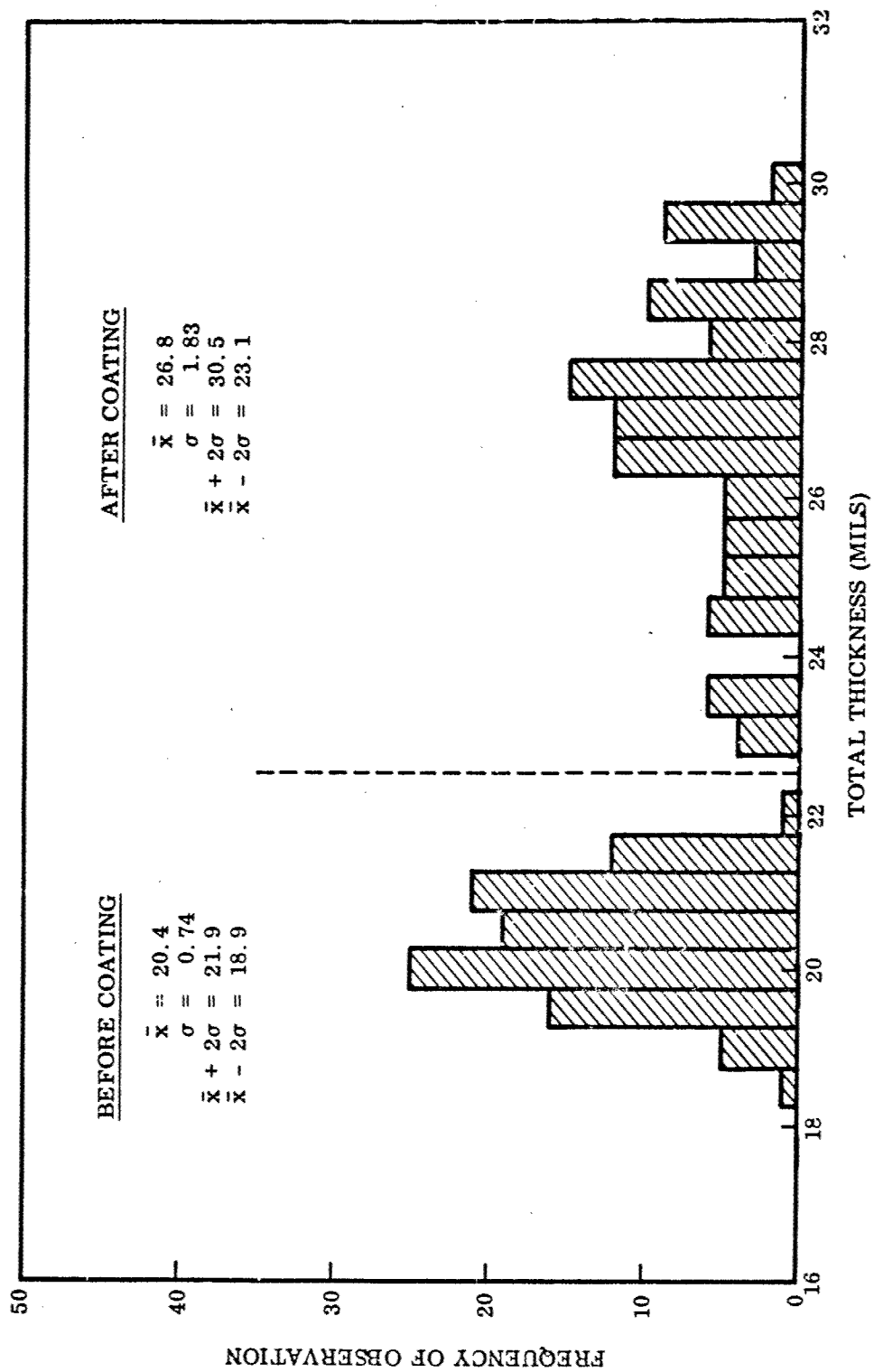
Figure 31 Frequency Histogram of Thickness Measurements, TZM/PFR-6 Before and After Coating

94

decreasing pressure down to about 1 mm Hg. At this pressure and below, the tempera-
ture for any given lifetime is relatively insensitive to pressure. Another interesting
feature of the curves of Figure 33 is the small spread in maximum temperatures for
different lifetimes. For example, temperatures for 30- and 240-min lifetimes do not
differ by more than 200°F except at very low pressures. Again, these curves illustrate
the general consistency of the data. The data shown in Figure 33 are also presented
in Table XV for convenience.

Table XV. Maximum Temperatures for Various
Lifetimes of TZM/PFR-6

Air pressure (mm Hg)	Maximum temperature at			
	30 min	60 min	120 min	240 min
	Random failure limits (°F)			
50	3225	3205	3180	3145
20	3050	3000	2990	2975
5	2900	2865	2825	2775
1	2800	2720	2650	2625
0.1	2825	2760	2710	2660
0.01	2790	2730	2670	2625
	Total failure limits (°F)			
50	>3300	>3300	>3200	>3200
20	3125	3105	3080	3050
5	2975	2925	2875	2825
1	2825	2790	2750	2725
0.1	2875	2825	2775	2725
0.01	2925	2820	2725	2675

At the higher pressures — above 1 mm Hg—all failures originated at defect sites, and
there were no cases of failure due to general coating recession. Conversely, at the
lower pressures, not only random failures but also general attack and surface
recession were observed; in fact, on some specimens the coating was totally consumed.

The surface conditions of several specimens tested for 4 hr in the baseline phase of
the program are shown in Figure 34. At the higher pressures (5 mm Hg and above),
glass was readily discernible on the surface of the specimens. The glass was not
smoothly or uniformly distributed but was rough and in some cases "foamy" in appear-
ance. The foamlike texture was caused by glass bubbles which formed, burst, and
reformed during testing. Some photographs of this interesting effect are presented
in Figures 35 and 36, which are typical of what was observed throughout the tests at
these pressures. Certainly, this effect is an indication of the fluidity of the glass at
these temperatures and suggests potential difficulties under conditions of high velocity
(as will be discussed later in the section on high gas velocity). The fact that the
bubbles did not form at the lower pressure may indicate the existence of a glass of a
different nature or simply that the internal bubble pressure was too great to form a
stable bubble.

95
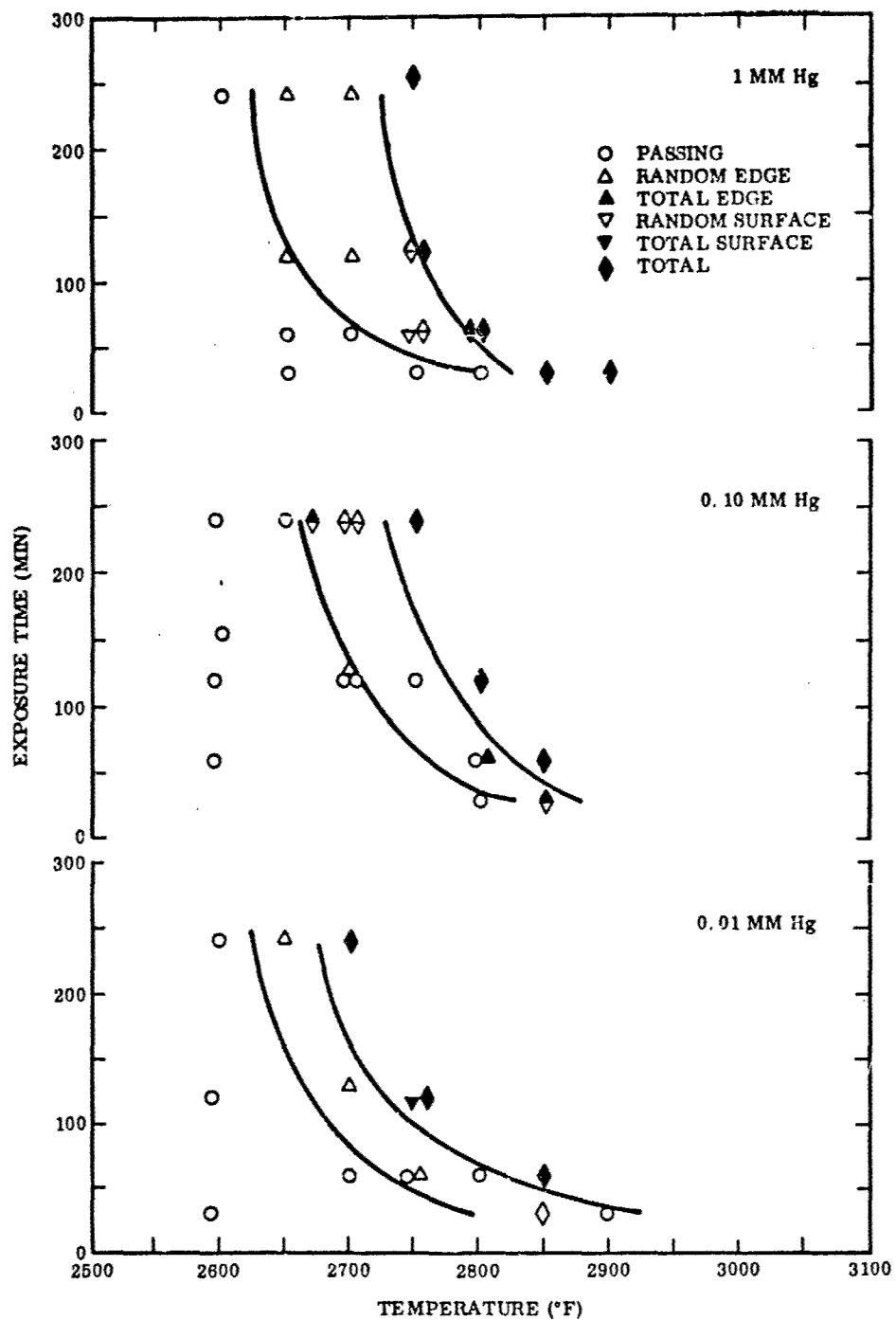
Figure 32 Results of Baseline Tests, TZM/PFR-6

96
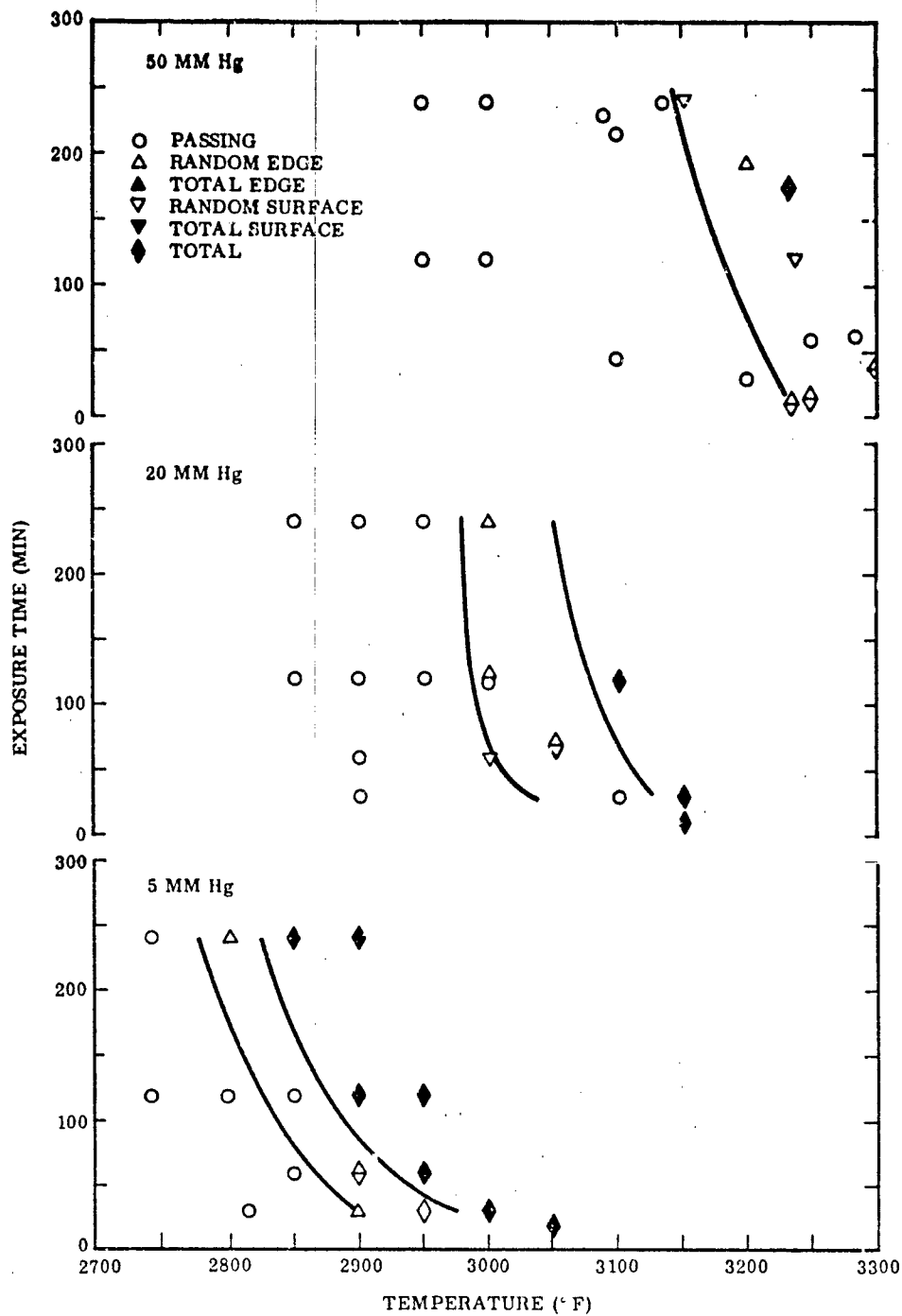
Figure 32 Results of Baseline Tests; TZM/PFR-6 (cont'd)

97
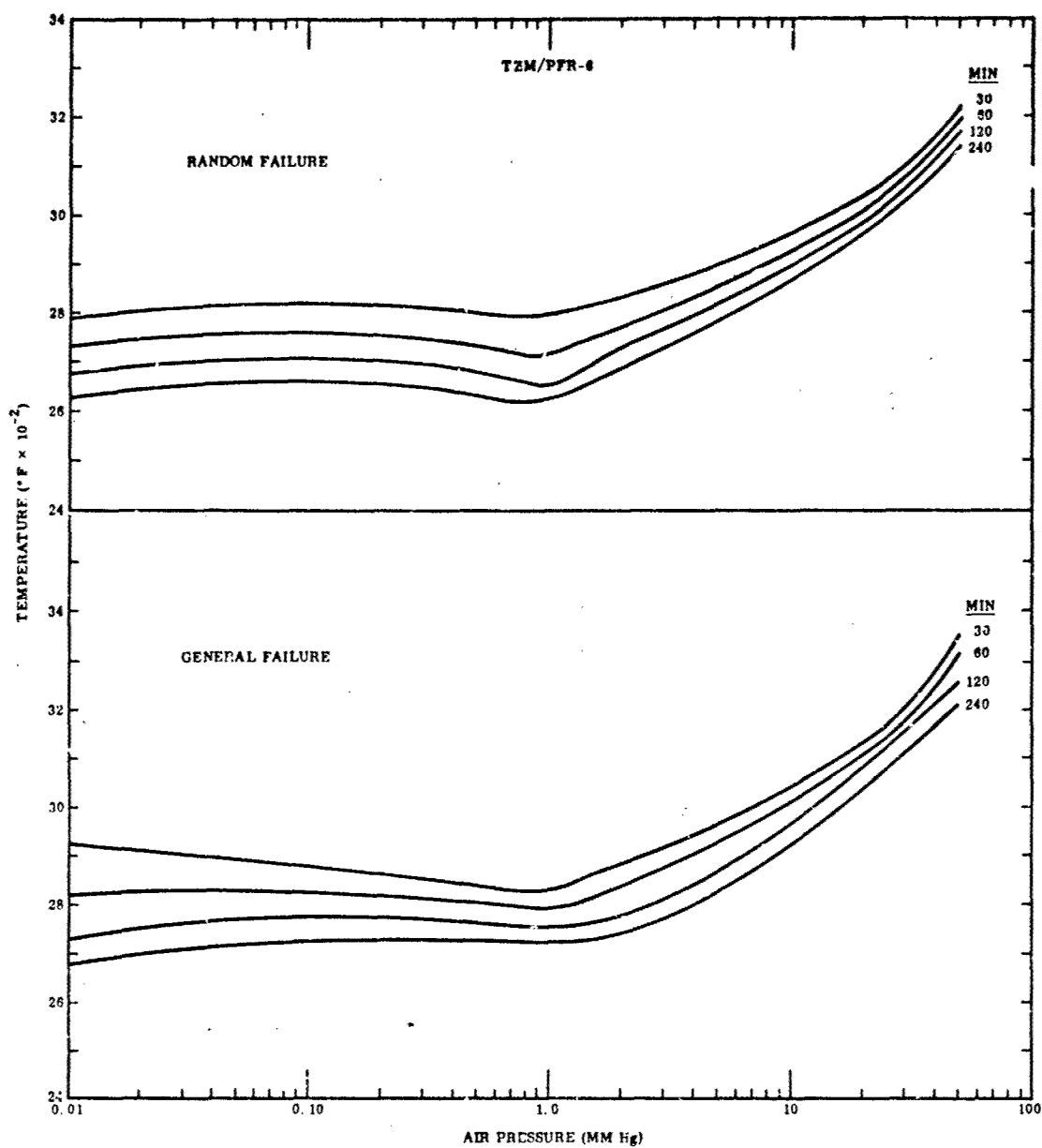
Figure 33 Baseline Failure Limits, TZM/PFR-6

98
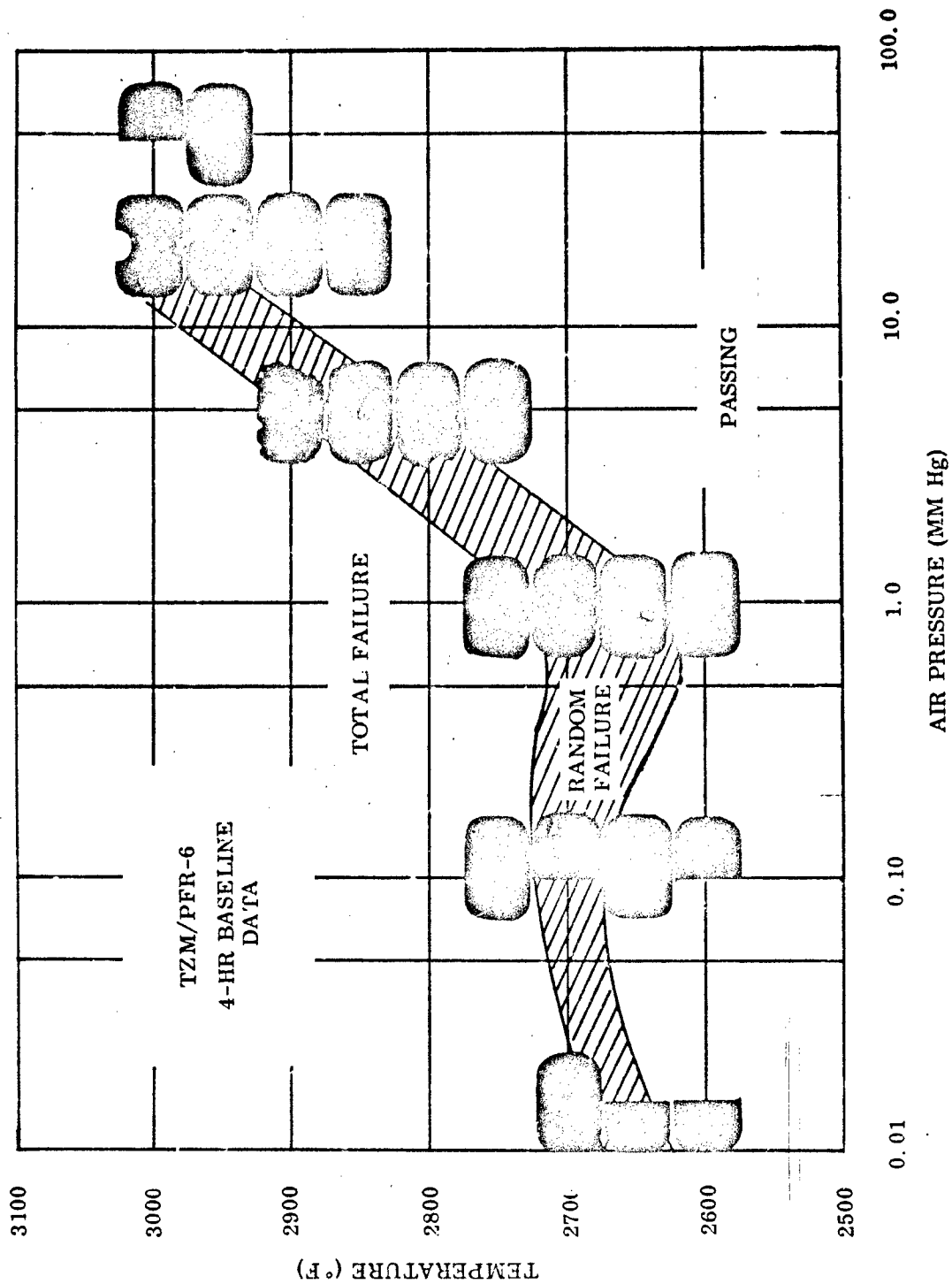
Figure 34 TZM/PFR-6, 4-hr Baseline Test Specimens

M7650   Figure 35 Bubble Formation on TZM/PFR-6 Specimen During
Testing at 2850° F, 20 mm Hg Pressure
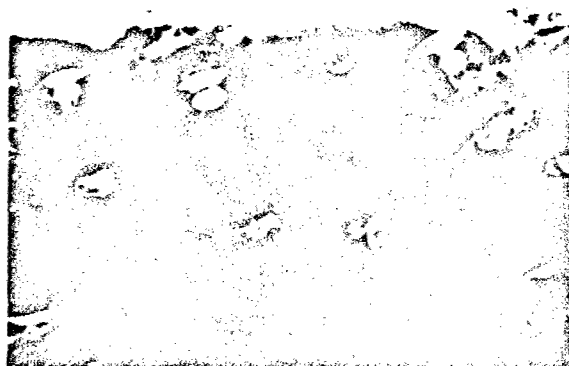
M7743   ×24

Figure 36 Glass Bubbles on TZM/PFR-6 Specimen After 4-hr
Exposure to Air at 2850° F, 20 mm Hg

100

Defect sites were probably the origin of the bubbles; since fine hairline cracks in the coating were the most common defects, these must be suspect. Candidate gases within the bubbles were MoO_3, SiO, or Si. The vapor pressure of Si at these temperatures is considerably less than 5 mm Hg, and therefore it is doubtful that Si vapor could support a bubble. Silicon monoxide could have formed as a result of the reaction of Si and SiO_2. The pressure of SiO at these temperatures could support bubbles. Traces of MoO_2 were found in the glass of the bubbles, and it is possible that MoO_3 formed by oxidation of Mo, Mo_3Si, Mo_5Si_3, or MoO_2 was the cause of bubble formation.

Random failure sites on the higher pressure specimens were often apparent only as slight bulges or pinholes or were not evident at all. It was frequently necessary to detect the random failures by probing the surface with a sharp tool.

After baseline exposures to lower pressures the specimens had a rough, powderlike, matte finish, and any glass present was not apparent under macroscopic inspection. Failures, both random and total, were more difficult to detect than those at higher pressures because when they occurred, much less Mo was lost through the volatilization of MoO_3. In severe failure specimens, oxidized substrate could be seen through failed areas of the coatings. Generally, however, it was necessary to cross-section specimens to characterize the performance.

During all baseline tests, two principal phenomena influenced the microstructure of this coating system. First, because of silicon diffusion into the substrate there was a disproportion of $MoSi_2$ to the lower silicides, Mo_5Si_3 and Mo_3Si, which was a thermally activated process and probably diffusion controlled. The disproportion was relatively insensitive to environment. Second was the oxidation of coating components (of course, highly dependent on environment) and, in cases of failure, oxidation of the substrate.

The general effect of air pressure in the range 5 − 760 mm Hg on the structure of the PFR-6 coating on TZM is illustrated in Figure 37 . As has already been described, in the as-received material, the coating was primarily $MoSi_2$ with a thin layer of Mo_5Si_3 at the substrate/coating interface. During exposure to air at 2700°F, 760 mm Hg, for 4 hr, a perceptible layer of Mo_3Si formed between the TZM and Mo_5Si_3. The Mo_5Si_3 layer has grown to the extent that the coating consists mainly of this phase. A layer of $MoSi_2$ remains above the Mo_5Si_3, and on the surface is some Mo_5Si_3 and a glass which may be SiO_2 with minor stoichiometric or other chemical deviations. It is well known, of course, that this glass forms as the result of selective oxidation of silicon in the coating and constitutes the protective layer for the underlying material (27). The general structural aspects remain the same down to about 1 mm Hg, except that more lower silicides formed on the surface with decreasing pressure (Figure 37B) because of the increased loss of silicon to the atmosphere at lower pressures.

At a pressure of 1 mm Hg, the behavior of this system changed, as reflected in the performance curves of Figure 33 and also in the coating microstructure. Figures 38A and B are photomicrographs of the two types of structure found in specimens tested at 1.0 mm Hg. Both types of structure were present in a random distribution on the surface of a given specimen. The structure shown in Figure 38A is similar to that of higher pressure specimens, whereas the structure of Figure 38B is typical of specimens tested at 0.1 and 0.01 mm Hg. For example, compare Figures 38B and C. Probably

101

M6154   ×1000   P657   ×1000
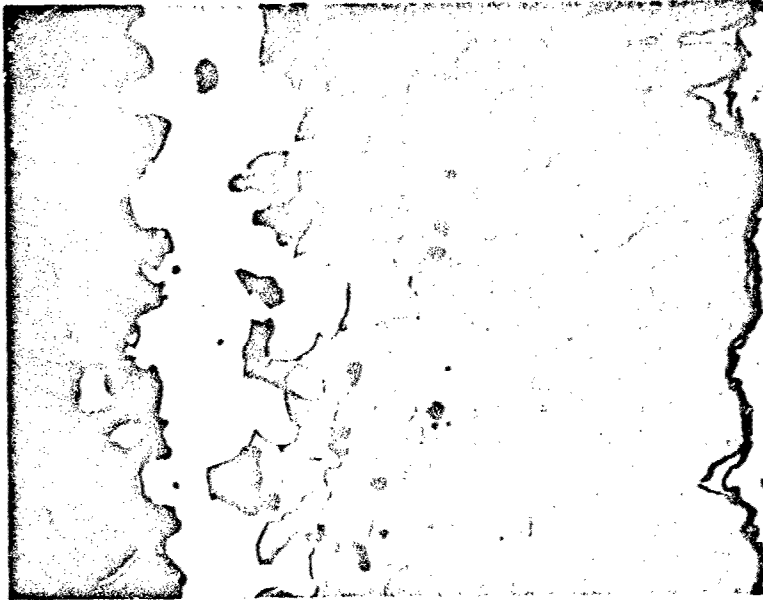
(A) 760 mm Hg, 2700° F, 4 hr   (B) 5 mm Hg, 2700° F, 4 hr

Figure 37 TZM/PFR-6 Structure After Exposure to Air at 760 and 5 mm Hg at a Temperature of 2700° F

102
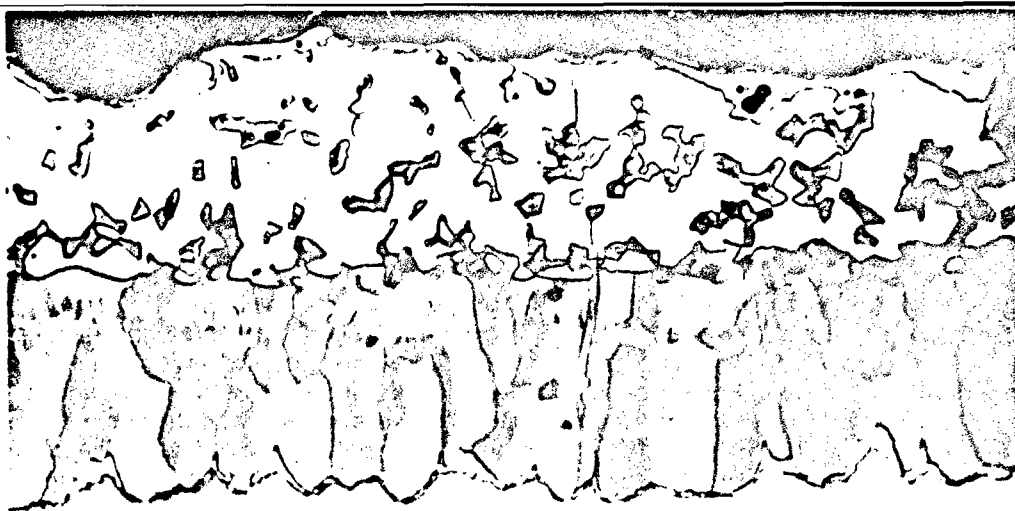
P434   (A) 1.0 mm Hg, 2850° F, 30 min   ×1000

P431   (B) 1.0 mm Hg, 2850° F, 30 min   ×1000
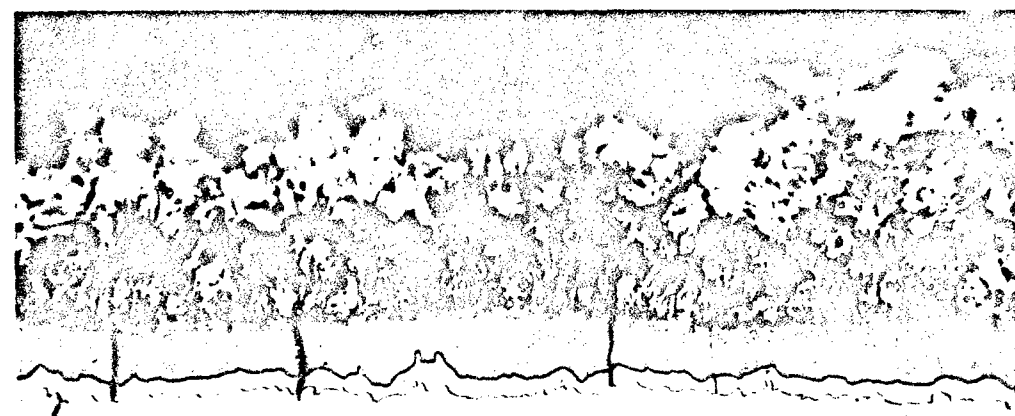
P696   (C) 0.01 mm Hg, 2850° F, 30 min   ×1000

Figure 38 Effect of Low Pressure on TZM/PFR-6 Structure

103

subtle deviations in the structure or composition of the coating from point to point are responsible for the difference in behavior along the surface of a given specimen.

At the lower pressures, the same silicide disproportion reactions resulting from diffusion of Si into the substrate occurred, but the oxidation effect was quite different. In Figures 38B and C a spongy mixture of phases can be seen on the surface. This is a mixture of a glassy oxide of silica and MoO_2, Mo_3Si, and Mo, resulting from the increased loss of silicon to the atmosphere at lower pressures. The silicon was lost through the reaction $Si + SiO_2 \rightarrow 2SiO \uparrow$ or by direct formation of SiO gas. The former is more likely because glass was always observed under the microscope, indicating that the rate of formation of SiO_2 was greater than the rate of loss of SiO. This loss of SiO causes a dynamic situation where Si from the coating is continually consumed and lower silicides are formed and even reduced to Mo. As long as this spongy mixture remains continuous along the substrate, the coating is effective and the substrate is protected; as soon as the reservoir of Si in the coating is expended, the coating fails.

So far, only general life-limiting processes have been discussed. These would be useful in predicting the performance of ideal, defect-free coatings. At pressures above 1 mm Hg, ideal coatings should remain protective, at least until the $MoSi_2$ is converted to Mo_5Si_3 and probably even longer, since Mo_5Si_3 is only passively attacked under most of the baseline conditions. (That is, Si is selectively oxidized to form SiO_2, as opposed to simultaneous oxidation of Mo and Si.) At lower pressures, the coating should remain protective until most of the Si and SiO_2 have been consumed. Unfortunately, defects do exist in all coatings and have a great influence on coating lifetime. At pressures greater than 1 mm Hg, the existing defects (generally in the form of fine hairline cracks) tend to be healed by glass which flows over or into the defects and decreases the rate at which oxygen reaches the substrate or the less-oxidation-resistant, lower silicides. Over this pressure range, the coating performance is quite pressure sensitive and, as shown in Figure 33, the maximum temperature for a given lifetime decreases markedly. This is not a result of changes in silicide structure within the coating, since the silicide structure is relatively insensitive to pressures from 5 to 760 mm Hg. Two effects, or a combination of these, are suggested as being responsible for the decrease in the protective capabilities in this pressure range. First, the air pressure within cracks may decrease to less than 1 mm Hg as the ambient pressure decreases. If so, the interior of the crack is exposed to low-pressure oxidation and, hence, to accelerated attack. Second, the glass may change chemically so that oxygen diffuses through the glass formed at lower pressures more rapidly, or the glass itself may become more corrosive to certain materials in the coating or substrate.

An example of different glass-coating interactions is presented in Figure 39. Glass has filled the edge crack on the 5 mm Hg sample, and the coating has remained protective. On the 1 mm Hg specimen the coating is still protective, but there is less glass and the glass has attacked the Mo_5Si_3 in the coating. In addition, traces of MoO_2 are evident in the glass. Enrichment of the glass with oxides of molybdenum is generally observed. This may be an important factor governing the protective capabilities of the glassy layer. Also, oxides of molybdenum may render the glass more corrosive to the coating.

104

(B) 1 mm Hg, 2740°F, 240 min   ×1000
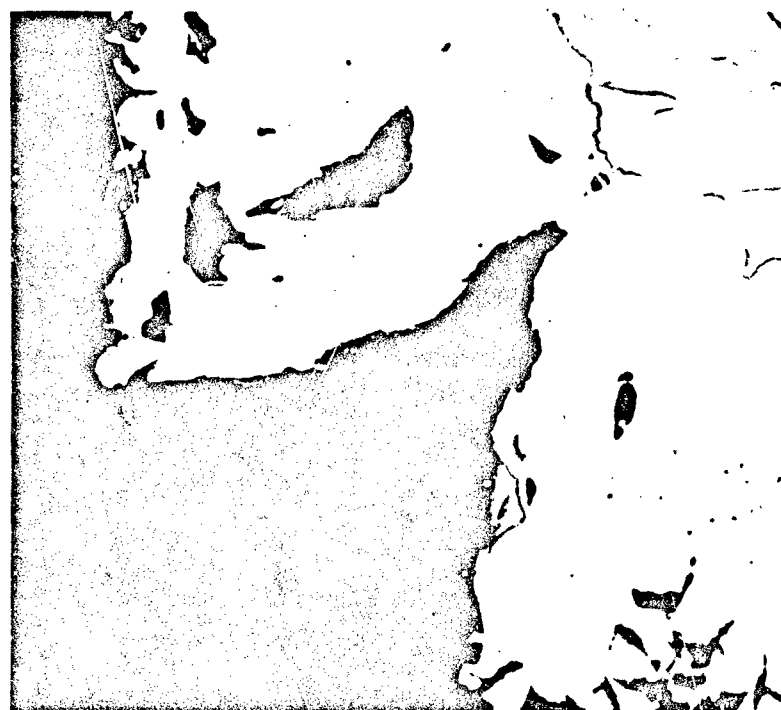
P519

(A) 5 mm Hg, 2700°F, 240 min   ×1000

P518

Figure 39 Effect of Pressure on Protective Glass. Note attack of coating near root of crack at right

105

At the lower pressures, defects still shorten the lifetime of the PFR-6 coating, but their effect is not as significant because there is a more rapid general attack. In fact, more premature edge failures at lower pressures are due to defects; i.e., there are more and larger cracks on the edges, the effective coatings thickness is less, and the general consumption of the coating is therefore quicker. Again referring to Figure 33, it is apparent that performance is generally insensitive to pressure below 1 mm Hg. One explanation for this is that, whereas the rate of volatilization is increasing with decreasing pressure, the rate of oxidation decreases (less oxygen) and the two factors tend to counteract each other. Actually, the portions of the curves between 0.01 and 1 mm Hg in Figure 33 represent a lower plateau in pressure. At pressures below 0.01 mm Hg, the curves will eventually turn upward because of lower oxidation rates.

Gas Velocity

The purpose of this phase, described in detail previously, was to evaluate the effects of air moving at a velocity of Mach 3 on the performance capabilities of PFR-6 on TZM. Prior to the gas velocity tests, experiments were conducted in the baseline apparatus to determine any effects resulting from the use of 19:1 $N_2:O_2$ at 20 mm Hg total pressure in lieu of air at 5 mm Hg. Two specimens were tested at 2850° F for 1 hr − one specimen in air and the other in 19:1 $N_2:O_2$ at equivalent oxygen partial pressures The specimens were examined carefully, and no difference in exterior appearance, microstructure, or glass formation was detected. The microstructures of the specimens are compared in Figure 40, and the similarity is obvious. This also suggests that the coating performance is dependent on oxygen partial pressure, rather than simply on total pressure.

The necessity of measuring and controlling the temperature of gas-velocity tests using an optical pyrometer and appropriate temperature calibration curves was discussed earlier. The calibration curve determined by blackbody hole techniques is presented in Figure 41. A further check on temperature calibration and measurement is provided by an Arrhenius curve based on the growth of the Mo_5Si_3 zone (Figure 18). The specimens on which Mo_5Si_3 zone measurements were made were heat-treated under blackbody conditions where temperatures were measured with certainty. This curve was used throughout the program as a check on temperature calibration by measuring the thickness of Mo_5Si_3 zones and using Figure 18 to estimate true temperature.

The results of the gas-velocity tests are summarized in Table XVI. Although the results reveal a degradation of performance capabilities as a consequence of high velocity, they also show that the system is not totally unusable under these conditions. For example, the conditions for the passing specimen at 2900° F, 20 mm Hg, for 60 min were only 100° F lower than the random failure boundary of Figure 32.

Considering the baseline results and the ensuing analyses of the mechanism of protection and failure, it is not surprising that the performance capabilities are degraded by high gas flow. It might be expected that the glass would be washed along the specimen surface, baring any crack in the coating. Careful examination of the specimens revealed that this is indeed the case. Figure 42 shows the effect. In Figure 42A, the

106
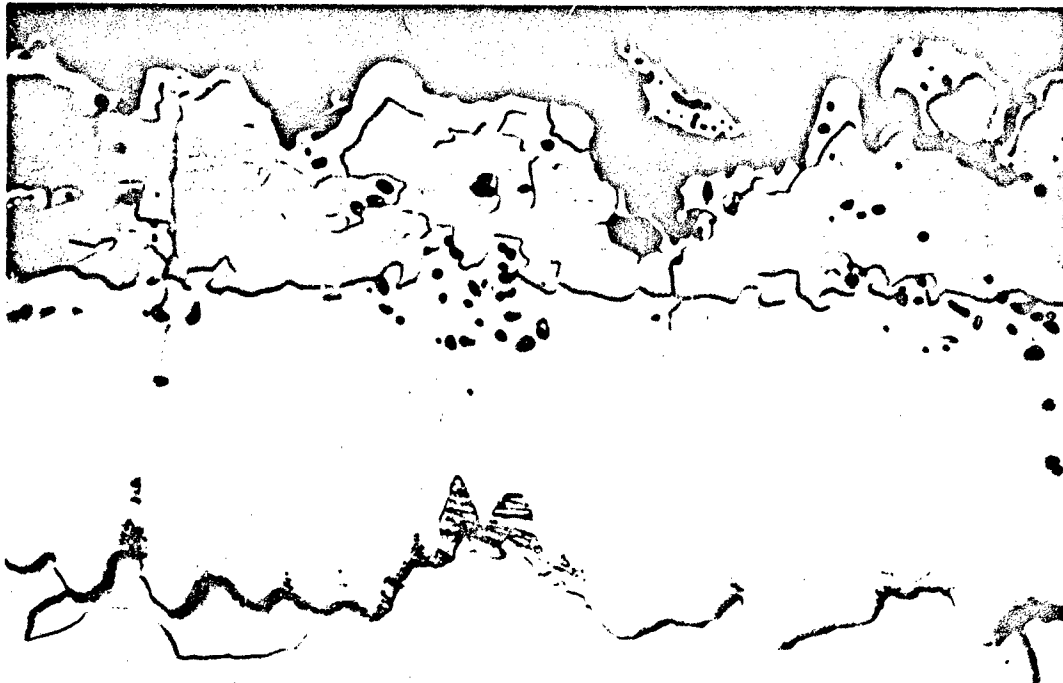
M9229   (A) 2850° F, 60 min, 20 mm Hg, 19:1 N_2:O_2 Mixture   ×1000

M9231   (B) 2850° F, 60 min, 5 mm Hg, Air   ×1000

Figure 40 TZM/PFR-6 Structures After Exposure in N_2:O_2 Mixture and Air

107
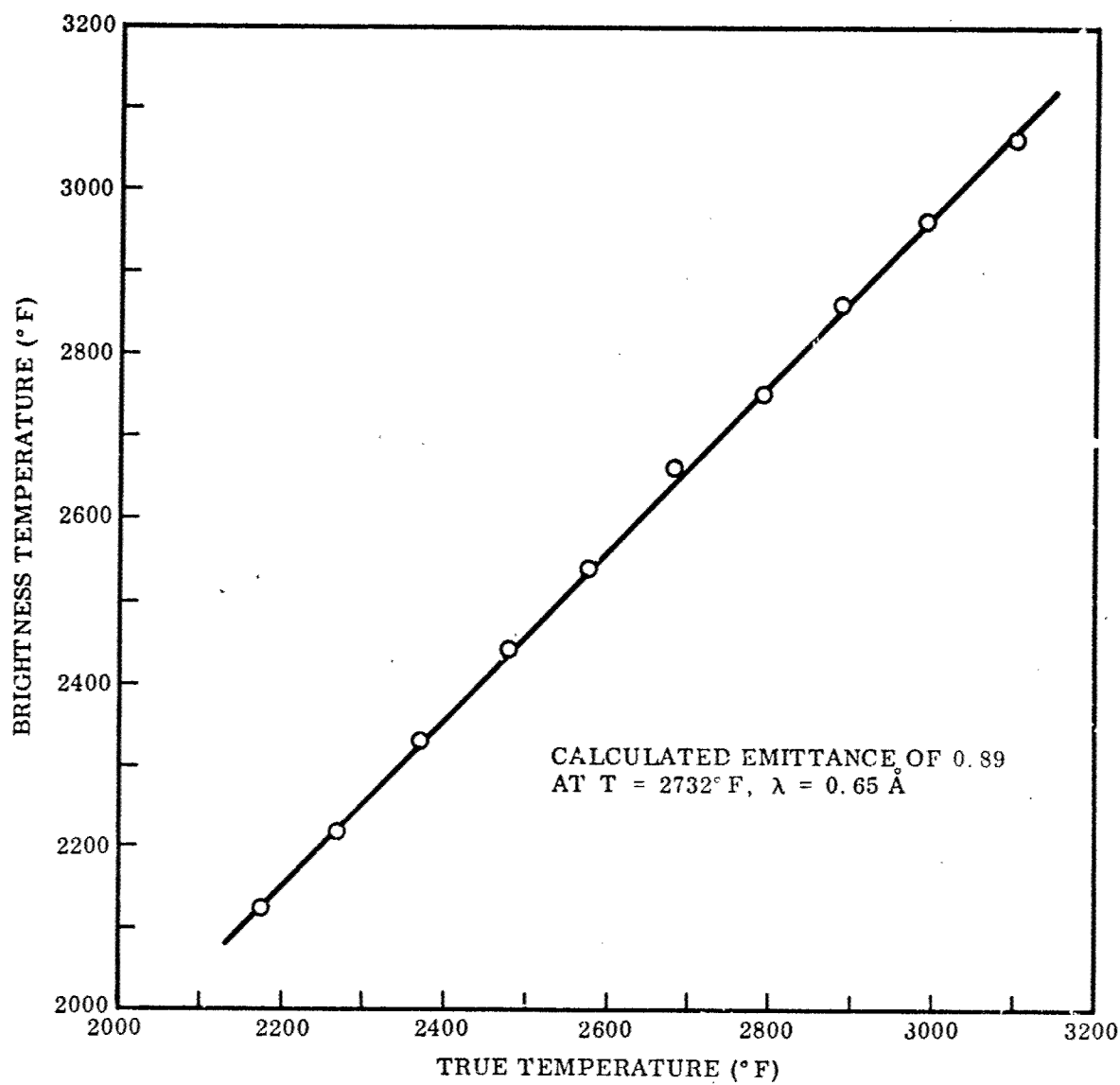
Figure 41 Emittance Calibration Curves for TZM/PFR-6, Preoxidized, 5 min, 2700°F, 1 mm Hg, Air

108

M9119   ×1000
(A) "Flow Side"

M9117   ×1000
(B) "Static Side"
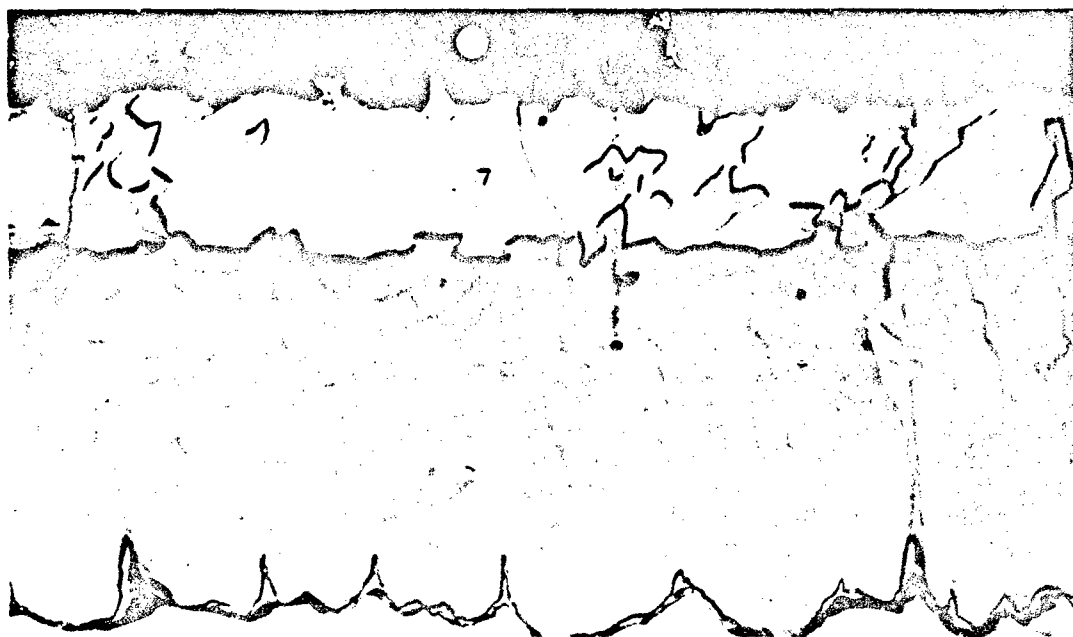
Figure 42 Structure of TZM/PFR-6 Tested at 2850° F, 5 mm Hg Equivalent Air
Pressure, Mach 3 Velocity

109

Table XVI. Summary of TZM/PFR-6 Mach 3 Velocity Studies

Temp. (°F)	Atmosphere	Pressure (mm Hg)	Equivalent air pressure (mm Hg)	Time (min)	Performance	Baseline time to failure (min)	
						Random	Total
2900	Air	20	20	60	Passing	> 240	> 240
2950	Air	20	20	54	Random surface failure	> 240	> 240
3000	Air	20	20	30	Total failure	60	> 240
2850	$N_2:O_2::19:1$	20	5	60	Random surface failure	80	170

flow side has failed at a defect site and, although some glass is present in the defect, there is little on the surface. Figure 42B is the static side directly opposite the region photographed in Figure 42A. The difference in coating condition is evident: a substantial thickness of glass is present on the coating surface. The spherical particles (probably copper oxide from the copper electrodes) are embedded in this glass. This is typical of what was observed on all specimens that were not totally destroyed during testing.

In every specimen, premature failures occurred on the flow side, and the static side reacted similar to the baseline specimens. It is concluded that, although Mach 3 air flow does have a deteriorating effect on PFR-6 coating performance capabilities, the difficulties are not insurmountable; i.e., the coating will survive exposures up to 1 hr at 2850 to 2900° F.

Gas Temperature

During this phase of the program, efforts were directed toward an evaluation of the effects of a plasma arc on TZM/PFR-6 at temperatures and pressures similar to those of the baseline tests. This evaluation was conducted with several PFR-6-coated TZM leading-edge models which the Plasmadyne Corporation exposed to a plasma for the Air Force. Tested samples were submitted to LMSC for metallurgical evaluation of performance.

The plasma arc impinged upon the surface perpendicularly, and the test area was a curved surface 4 in. wide with the convex surface exposed to the plasma. The heat-affected area was about 4 in. in diameter. Photomacrographs of a tested model are shown in Figure 43. The objectives of the evaluation were (1) to characterize the performance of this coating, (2) to compare the performance with that predicted on the basis of baseline studies, and (3) to determine the actual temperature profile during the tests making use of the kinetic data on the growth of Mo_5Si_3.

The test conditions, results, and appropriate baseline results are summarized in Table XVII. A distinction was made between the behavior of the coating on the outside (convex surface) and on the inside because of the significant difference in pressure. The results are in good agreement with the baseline data, especially considering the possible errors in the determination of the temperature and pressure of these tests.

110

M8012   ×3/4
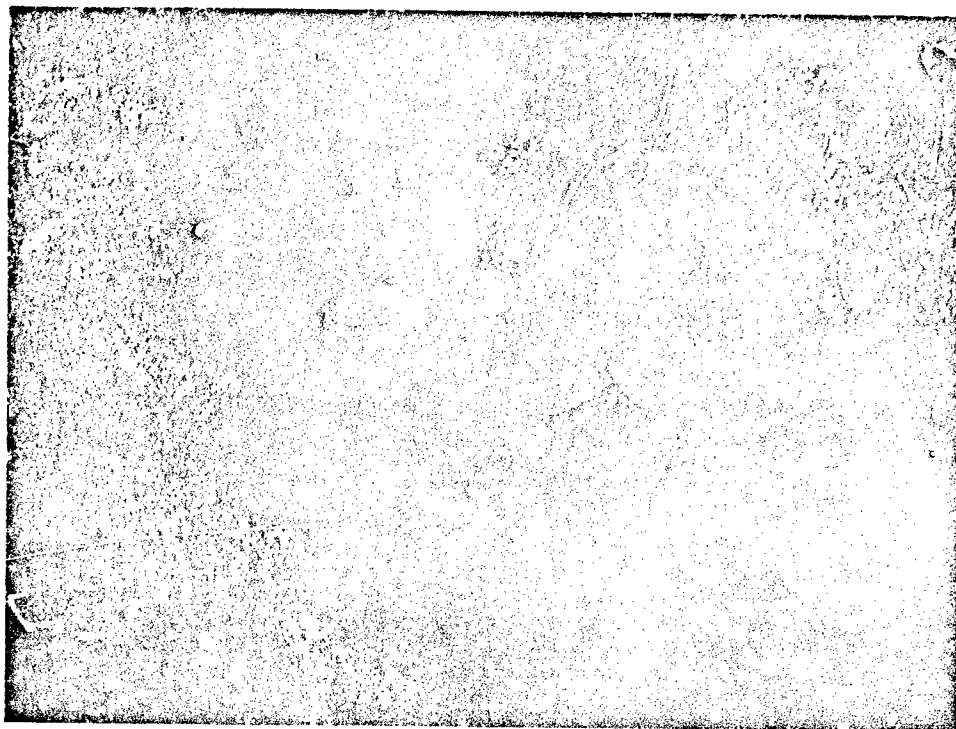
M8028   ×8

Figure 43 Test Area of Leading Edge Model 508

111

Table XVII. Test Conditions and Results for TZM/PFR-6 Leading Edge Models Tested in Plasma Arc by Plasmadyne Corporation

Model No.	Temperature (°F)			Pressure (mm Hg)		Time (min)		Performance		Baseline time to failure			
	Optical	True(a)	True(b)	External(c)	Internal(d)	Heatup	Hold	Outside	Inside	Outside		Inside	
										Random	Total	Random	Total
508	2770	2890	2887	4.6	1.2	17	31	Random surface failure	Passing	40	100	<30	<30
509	2790	2910	2942	9.5	1.2	4	30	Passing	Random surface failure	60	240	<30	<30
510	2890	3020	2992	9.6	1.4	6	30	Passing	Total failure	<30	60	<30	<30
511	2970	3100	>2992	9.6	1.0	3	13	Passing	Total failure	<30	<30	<30	<30
512	3070	3210	—	9.6	1.1	3	7	Total failure	Total failure	<30	<30	<30	<30
513	3080	3215	—	9.8	1.2	4	4	Passing	Passing	<30	<30	<30	<30
514	2750	2865	2922	23.8	1.8	4	30	Passing	Passing	>240	>240	<30	<30
515	2470	2560	2542	2.1	1.1	10	30	Passing	Passing	>240	>240	>240	>240

(a) Determined from LMSC emittance correction data.
(b) Determined from LMSC Mo_5Si_3 growth kinetic data.
(c) Stagnation pressure.
(d) Pressure on concave side of model.

In general, the inside surface were similar to corresponding baseline specimens and exhibited no unexpected effects. Traces of glass bubbles were observed. The outside surfaces were somewhat similar in appearance to the high-velocity flow specimens in that there was some smoothing of the glass due to the flow of gas. To illustrate the general structural effects, the microstructures of the coating on the external and internal surfaces of one of the models, No. 509, are shown in Figure 44. The plasma arc had no special effect on the external surface of the coating; except for smoother glass, and the absence of bubbles, the coating structure and the condition of the glass are what would be found after exposure to slowly moving air at similar temperatures, pressures, and times. On the interior side, the accelerated oxidation typical of lower-pressure environments is evident.

The coating behavior on the other models was, in general, also similar to that of the baseline specimens. A special effect was observed during the evaluation of one of the leading-edge models (No. 508): in some areas, the coating had extraordinary large cracks and had separated from the substrate (e. g. , the area shown in Figure 43). This condition was studied thoroughly and was correlated conclusively with the structure of the coating in the as-coated condition. If, during the coating process, a zone of Mo_5Si_3 formed between the disilicide and the substrate, any crack in the disilicide perpendicular to the substrate would terminate at the Mo_5Si_3 zone. If, however, no Mo_5Si_3 zone formed, the crack could propagate along the substrate/coating interface and the coating would part from the substrate. For example, consider the structures shown in Figures 45 through 47. In Figure 45, there is a continuous zone of Mo_5Si_3 and the cracks in the Mo_5Si_3 layer terminate at the Mo_5Si_3 substrate interface. In the absence of Mo_5Si_3, the crack continues along the $MoSi_2$-substrate interface, as seen in Figure 46. The separation of the coating from the substrate as a result of the lack of a continuous Mo_5Si_3 zone is shown in Figure 47. Actually, the absence of a Mo_5Si_3 zone was observed only on leading-edge model 508 and not on any of the other models or on the specimens used in the other phases of this program. Obviously, the most important conclusion from these observations is that care must be taken during the coating process to ensure the formation of a continuous zone of Mo_5Si_3.

True temperature-profile determinations were limited to the specimens that were exposed to the plasma arc for 30 min. As described earlier, the determinations were made on the basis of Mo_5Si_3 zone growth and the kinetic data of Figure 18. The temperature profiles are presented in Figure 18. The results demonstrate the usefulness of this novel method of temperature determination.

In summary of the activities and observations with TZM/PFR-6 during these two phases of the program, it is concluded that (1) high velocity gas flow parallel to the surface of PFR-6 coated TZM does have an adverse effect on coating lifetime and (2) a plasma arc impinging normally on the surface of coated material has no special effect; i. e. , the coating performance is similar to that of specimens tested by radiation or resistance heating in slowly moving air. In addition, the importance of a continuous zone of Mo_5Si_3 at the substrate/coating interface was clearly shown.

113

M8167   ×500

(A) External Side, 9.5 mm Hg

M8166   ×500

(B) Internal Side, 1.2 mm Hg

Figure 44 External and Internal Sides of Model 509   at 2940° F for 30 min

114
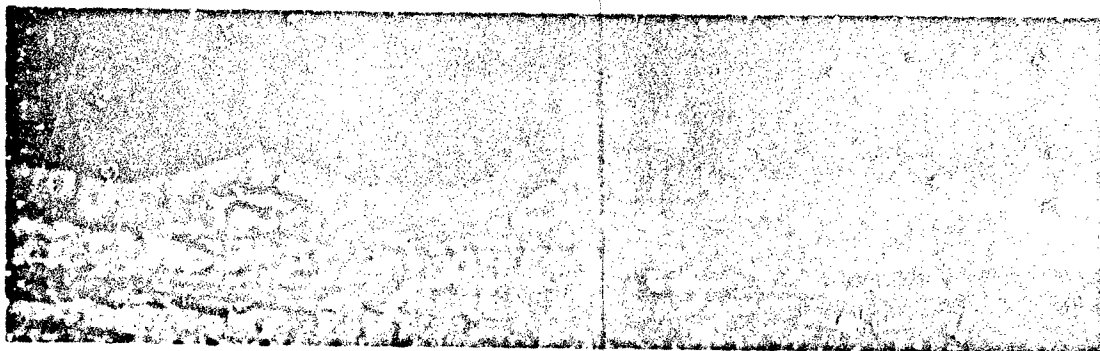
M7937   Figure 45 Termination of a Crack by the Mo_5Si_3 Zone   ×3000
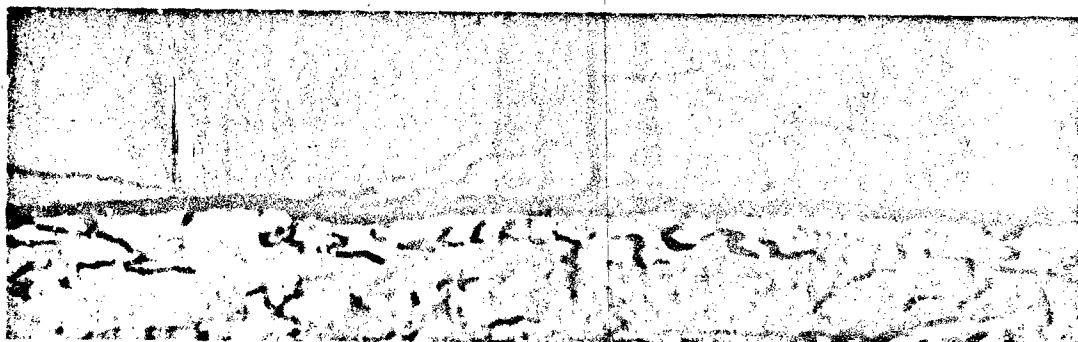
M7941   Figure 46 Propagation of a Crack Along Substrate/Coating Interface   ×3000
When No Mo_5Si_3 Exists

M8059   Figure 47 Results of the Absence of a Continuous Mo_5Si_3 Zone   ×500
During Oxidation Exposure

115
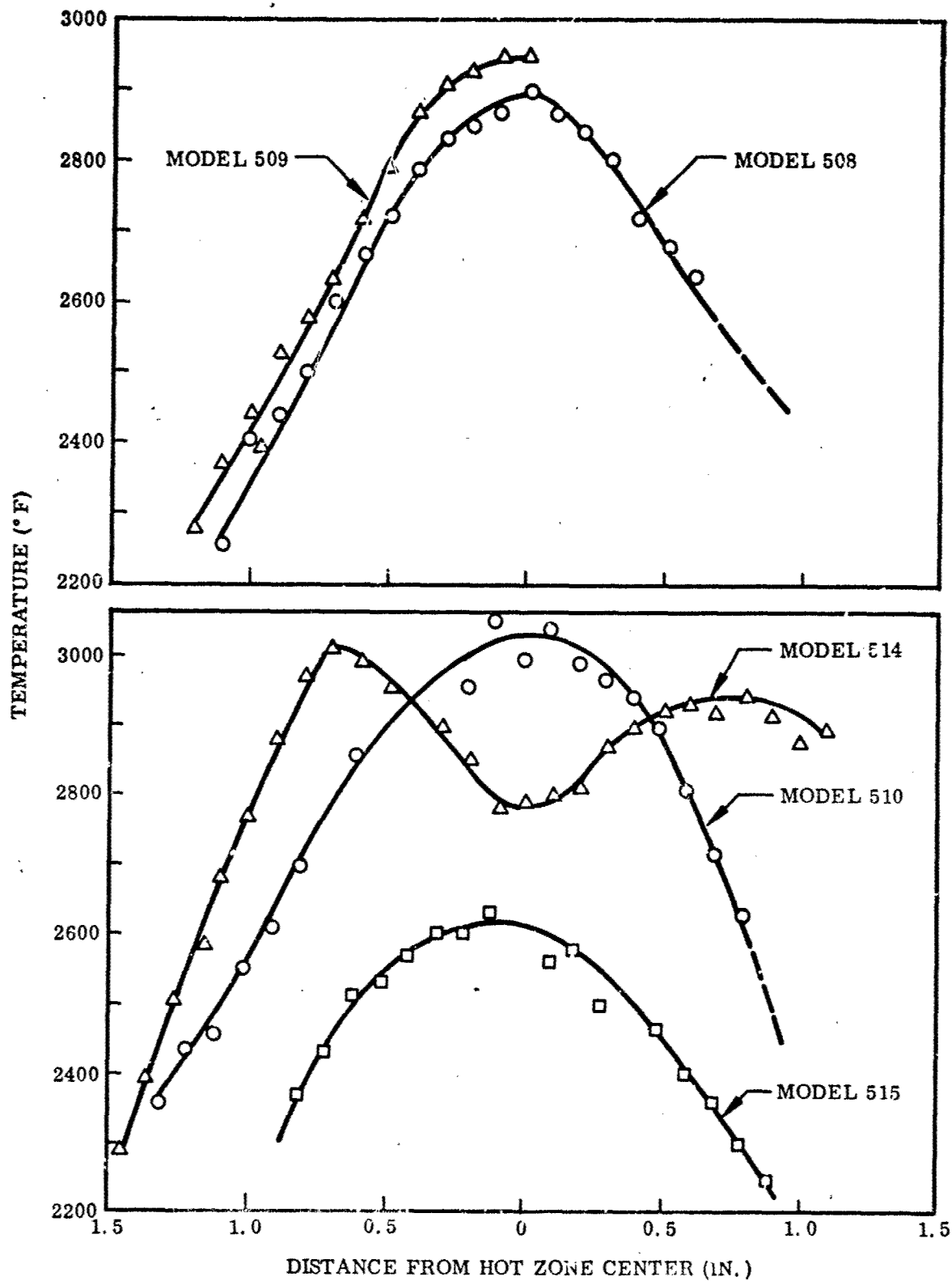
Figure 48 True Temperature Profiles Across Leading-Edge Models Tested in Plasma Arc

116

Vacuum Volatility

The TZM/PFR-6 vacuum volatility results are presented in Table XVIII and Figure 49. The weight loss data were computed on the basis of the planar area of the substrate rather than the absolute area of the coating-environment interface because of the defect nature of the coating and the consequent difficulty in determining the absolute surface area. The results in this form satisfy the purposes of this investigation but would be inappropriate for use in a quantitative, kinetic study of processes occurring during exposure to vacuum.

Although there are nonlinear portions of both the 2800 and the 3000°F curves of Figure 49, a square-root-of-time dependence and a diffusion-controlled process are indicated. Silicon is lost at the surface by volatilization and the $MoSi_2$ disproportionates to Mo_5Si_3. Of course, disproportionation occurs on the substrate side also. With continued loss of silicon, Mo_5Si_3 disproportionates to Mo_3Si and, in turn, the Mo_3Si is converted to Mo. The overall process is controlled by diffusion of Si through the various silicides. When either a new silicide forms or one is completely consumed and the Si diffusivity in these phases is substantially lower than that of the other existing silicides, the reaction rate of the vacuum volatility process will change. The nonlinear portions of the 2800 and 3000° F curves are the results of this effect.

An example of the microstructural change of the PFR-6 coating during a 4-hr exposure to vacuum at 3000°F is presented in Figure 50. The coating is primarily Mo_5Si_3 with a zone of Mo_3Si at the substrate interface. There is a nearly continuous layer of Mo_3Si along the outer surface of the Mo_5Si_3, and there is some Mo (light areas) outside the Mo_3Si. In addition to the microstructural effects, the general recession of the coating and the marked widening of cracks are evident.

The oxidation-resistance capabilities of the PFR-6 coating subsequent to vacuum exposure can be degraded for three reasons: (1) There is general surface recession; (2) cracks are broadened considerably, and consequently the effective coating thickness is reduced; and (3) the lower silicides are much less oxidation-resistant than $MoSi_2$. Probably vacuum exposures of 30−60 min at 2600−2800° F will not seriously degrade subsequent oxidation resistance. However, after higher temperatures or longer times in vacuum, the coating performance would be expected to be affected adversely.

Temperature and Pressure Cycling

As shown in Table XIX, cycling the temperature and pressure to 2200°F and 3 mm Hg did not seriously degrade the PFR-6 performance capabilities at 2700 or 2800°F and 1 mm Hg. Also, a short-time exposure in vacuum at 2600°F before oxidation exposure did not have a significant effect on the coating performance in air at 1 mm Hg. Comparisons with the temperature for random and total failure for a given exposure time are better indexes of the latter conclusion than the time to failure at a given temperature. For example, the postoxidation test was run at 2600°F and the temperature for random failure in 240 min at 1 mm Hg was only 20°F higher than the actual test temperature. (See Figure 32.)

117

Table XVIII. Vacuum Volatility Data, TZM/PFR-6

Temp. (°F)	Pressure (mm Hg)	Time (hr)	Thickness			Weight		Weight change (grm/cm2)(a)
			Initial (mils)	Final (mils)	Thickness decrease (mils/side)	Initial (gm)	Final (gm)	
2600	1 × 10-5	0.5	26.0	25.6	0.3	1.1564	1.1486	0.00159
	1 × 10-5	1.5		25.1	0.5		1.1447	0.00239
	5 × 10-6	3.5		25.0	0.5		1.1406	0.00323
	1 × 10-5	4		24.9	0.6		1.1392	0.00351
2800	1 × 10-5	0.5	24.6	23.4	0.5	1.1264	1.1115	0.00304
	9 × 10-6	1		23.2	0.7		1.1047	0.00443
	7 × 10-6	2		22.8	0.9		1.0975	0.00590
	5 × 10-6	4		22.6	1.0		1.0959	0.00623
3000	1 × 10-5	0.5	28.0	26.3	0.8	1.2476	1.2154	0.00657
	1 × 10-5	1		25.9	1.1		1.2101	0.00765
	1 × 10-5	2		25.9	1.1		1.2076	0.00817
	1 × 10-5	4		25.5	1.3		1.2052	0.00866
3200	1 × 10-5	0.5	28.9	26.2	1.4	1.2630	1.2233	0.00790
	9 × 10-6	1		25.8	1.6		1.2207	0.00864
	6 × 10-6	2		25.6	1.7		1.2147	0.00987
	4 × 10-6	4		23.4	2.8		1.2069	0.01143

(a) Per unit area of substrate.
Average Area = 4.9 cm2.

118
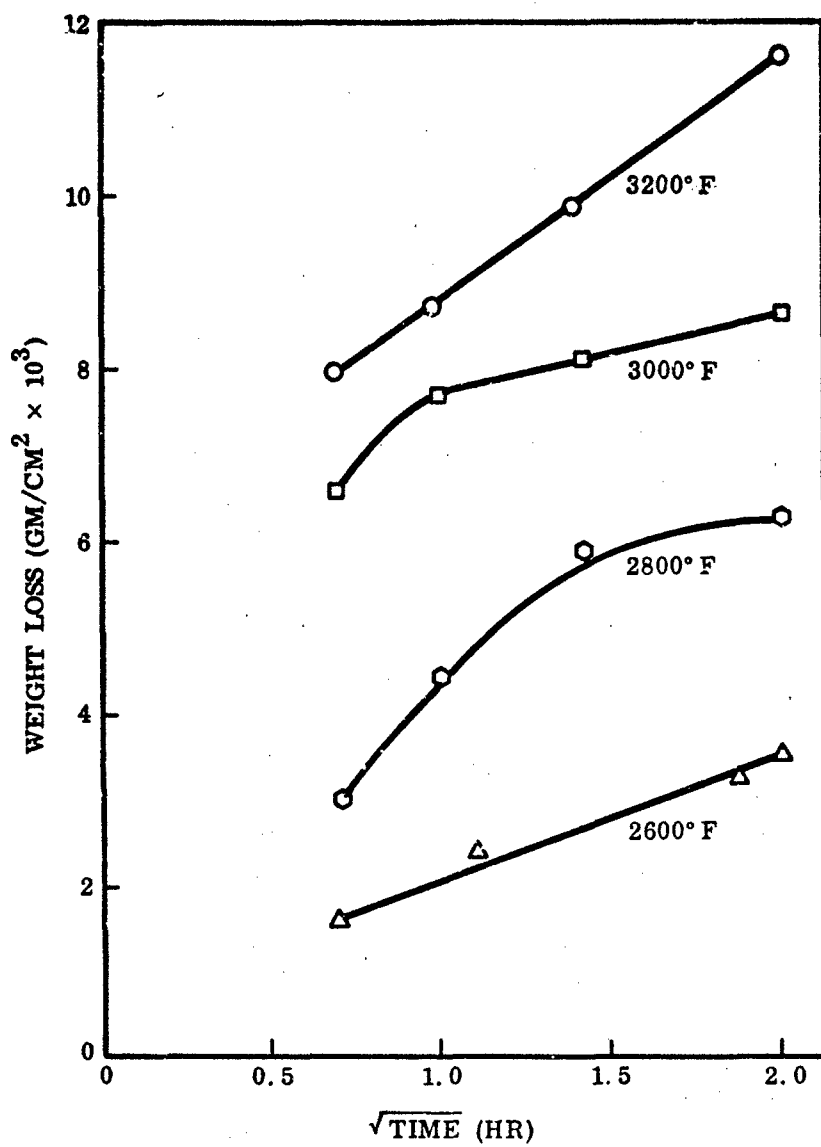
Figure 49 Vacuum Volatility Rate Curves, TZM/PFR-6

119
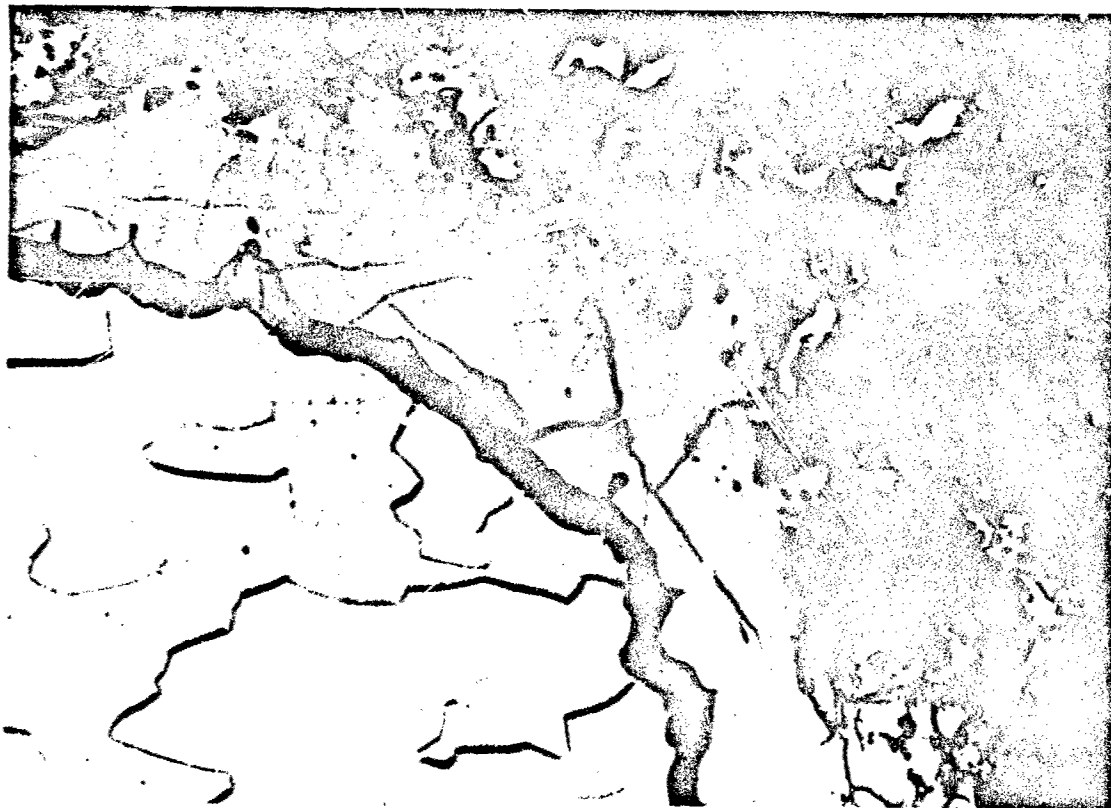
M6924   ×500

Figure 50 TZM/PFR-6 After 4 hr at 3000° F in Vacuum (10^{-5} mm Hg)

120

Table XIX. Results of Temperature and Pressure Cycling, TZM/PFR-6

Phase of cycle	Test conditions			No. of cycles	Total time (min)	Performance rating	Baseline time to failure (min)	
	Temp. (°F)	Pressure (mm Hg)	Time (min)				Random	Total
1st (baseline)	2700	1	7	5	35	Passing	60	>240
2nd	2200	3	21		105		–	–
1st (baseline)	2800	1	7	4	28	Passing	30	50
2nd	2200	3	21		84		–	–
1st (baseline)	2800	0.01	7	4	28	Passing	40	80
2nd	2400	0.1	21		84		–	–
1st	2600	10^{-5}	30	1	30	Passing	–	–
2nd (baseline)	2600	1	240		240		>240	>240

121

The results are significant per se, and they have additional significance in demonstrating the usefulness of the baseline data in predicting the lifetime of the PFR-6 coating under cyclic conditions. To make predictions, the cumulative time at the higher temperature and lower pressure phase of the cycle should be compared with the appropriate baseline data. It should be noted, however, that temperature cycling was from high to low and samples were not cooled below 2000° F in all cases. When cycling to room temperature is used, thermal shock may induce defects that can degrade baseline performance.

Acoustic Vibration

Specimens of TZM/PFR-6 which had been acoustically irradiated were examined metallographically and oxidation-tested under baseline conditions. No unusual cracking or any other effect was observed in the specimens. In the high-temperature oxidation test results presented in Table XX, it is apparent that exposure to acoustic vibration had no effect on the coating performance.

Table XX. Results of Acoustic Vibration, TZM/PFR-6

Vibration mode	Exposure conditions	Oxidation test conditions			Perf. rating	Baseline time to failure (min)	
		Temp. (° F)	Pressure (mm Hg)	Time (min)		Random	Total
Random	60 sec, 30−1500 cps, 159.5 dB	2650	1.0	60	Passing	120	>240
		2850	20	60	Passing	>240	>240
Sine	50−1500 cps, 20 sec at 100 cps intervals, 172.5 dB peak at 510 cps	2650	1.0	60	Passing	120	>240
		2850	20	60	Passing	>240	>240

To check for any cracking along the substrate/coating interface resulting from acoustic vibration, specimens were exposed to 900° F, 760 mm Hg air pressure, for 3 hr. Self-healing of cracks does not occur at this temperature, and any oxidation of the substrate will spall the coating. Again, acoustic irradiation had no adverse effect on coating performance, which further supports the conclusion that the acoustic irradiation had no effect on the TZM/PFR-6 system.

Defect Tolerance and Repair

A series of experiments was conducted to evaluate the TZM/PFR-6 capability to tolerate defects that might result from assembly or handling. Also, techniques for making "in-field" repair of defects were investigated.

Defects were introduced by bending specimens using three-point loading. Specimens were bent 28−30 deg (just short of coating and substrate fracture), metallographically

inspected, and oxidation-tested. The crack density on the tension side was 10 times that of the as-coated material. The compression side was unaffected. These cracks, similar to those of the as-received material, were normal to the substrate and penetrated the Mo_5Si_3 zone. They terminated at the Mo_5Si_3-TZM interface and did not propagate along this interface. The oxidation test was conducted under the following conditions:

Temperature (°F)	Pressure (mm Hg)	Time (min)	Performance	Baseline time to failure (min) Random	Total
2675	1.0	60	Passing	100	>240

The additional defects had no significantly adverse effect on performance. As discussed earlier, coating performance at 1 mm Hg is characterized both by the defect-controlled failures typical of higher pressures and by the general attack of the coating typical of lower pressures. The cracks introduced by bending were adequately protected by glass and were narrow enough so that the effective coating thickness was not decreased.

The high-velocity impact tests were conducted to introduce defects and to characterize the resistance of the TZM/PFR-6 system to ballistic impact. The results, presented in Table XXI, indicate the low resistance to impact — particularly when the backup material was rubber. A specimen that had been impacted by a projectile having a kinetic energy of 0.3 ft-lb was oxidation-tested. The conditions were identical to those for the oxidation test of the specimen in which cracks were introduced by bending. The specimen failed along the cracks created during impact. The results significantly show that the system is susceptible to impact damage and that this damage is extremely deleterious to the oxidation-resistant capabilities of the system. This is due to the fact that cracks introduced on impact propagate into the substrate.

Table XXI. Results of High-Velocity Impact Tests, TZM/PFR-6

Backup material	Kinetic energy (ft-lb)[a]					
	Spalling		Coating fracture		Substrate fracture	
	Pass	Fail	Pass	Fail	Pass	Fail
Rubber	0.3	0.6	<0.3	0.3	0.3	0.6
Steel	1.7	2.3	1.7	2.3	1.7	2.3

(a) Calculated from projectile mass and velocity at time of impact.

Defects in the form of slots (0.005 in. wide by one-half or three-fourths of the coating thickness in depth) were introduced in several specimens, and these specimens were oxidation-tested. The results are presented in Table XXII. Specimens were tested under the conditions of the passing and random failure regions of the baseline curves. A failure occurred only at 3050° F, 20 mm Hg, in a defect that was three-fourths of the coating thickness in depth. The conclusions are that the protective glass can protect 5-mil-wide defects up to three-fourths of the coating thickness in depth in this pressure range at temperatures as high as 3000°F.

123

Table XXII. Defect Tolerance Results (Defects in the form of slots 0.005 in. by 1/2 or 3/4 of coating thickness), TZM/PFR-6

Temperature (°F)	Pressure (mm Hg)	Time (min)	Results		Baseline time to failure (min)	
			1/2 t	3/4 t	Random	Total
2650	1.0	30	Pass	Pass	160	>240
2650	1.0	60	Pass	Pass	160	>240
2750	1.0	60	Pass	Pass	40	125
2750	1.0	120	Pass	Pass	40	125
2400	20	60	Pass	Pass	>240	>240
2900	20	30	Pass	Pass	>240	>240
2900	20	60	Pass	Pass	>240	>240
3000	20	60	Pass	Pass	120	>240
3050	20	72	Pass	Fail	30	240

The repair studies with TZM/PFR-6 yielded some encouraging results, as can be seen in Table XXIII. The Cu-Ag-Si repair alloys were 100% effective at 20 mm Hg and 1 mm Hg and at temperatures and times near the random-failure boundaries of the baseline curves. The Cu-Ag-MoSi$_2$ alloys, however, were only 50% effective at 20 mm Hg and completely ineffective at 1 mm Hg. The Cu-Ag-Si alloy wet both the PFR-6 coating and the substrate well and reacted with the substrate to form silicides. The microstructure of the repair area is shown in Figure 51. There is a layer of Mo$_5$Si$_3$ on the substrate and within this layer an unidentified phase. There is Mo$_3$Si on the Mo$_5$Si$_3$ and a glass layer on the Mo$_3$Si. The protective coating in the repaired area is thin, but it is protective and shows promise for this approach to repairing defects. Certainly, more research on this subject is required, and it is concluded that these results will provide a useful basis for further work.

Table XXIII. Results of Repair Studies, TZM/PFR-6

Repair Technique	Test conditions			Performance rating	Baseline time to failure (min)	
	Temp. (°F)	Pressure (mm Hg)	Time (min)		Random	Total
Cu-Ag-Si[a]	2700	1	60	4 passing	70	>240
Cu-Ag-Si	2900	20	60	4 passing	>240	>240
Cu-Ag-MoSi$_2$	2700	1	60	4 failures	70	>240
Cu-Ag-MoSi$_2$	2900	20	60	2 failures, 2 passing	>240	>240

(a) A powder mixture of these materials was applied to defects and heated until melting with an oxyacetylene torch.
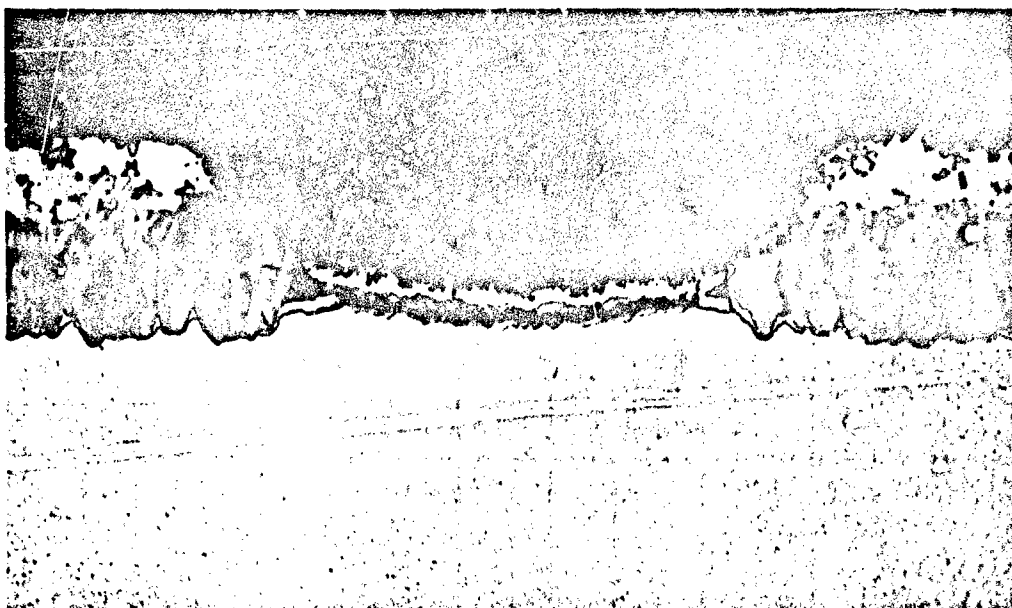
M9318   ×400

M9315   ×2000

Figure 51 TZM/PFR-6 Repaired With Cu-Ag-Si and Oxidation Tested at 2900° F, 20 mm Hg, 60 min

Materials Compatibility

Compatibility evaluations were made at high temperatures and low pressures with
TZM/PFR-6 and dissimilar coated refractory metal systems and with selected other
high-temperature materials. The results are summarized in Table XXIV.

Table XXIV. Results of Compatibility Studies, TZM/PFR-6

Contact material	Test conditions			Performance rating	Baseline time to failure (min)	
	Temp. (°F)	Pressure (mm Hg)	Time (min)		Random	Total
TZM/Durak B	2525	1	45	Passing	>240	>240
Cb-752/CrTiSi	2525	1	45	Passing	>240	>240
B-66/CrTiSi	2525	1	45	Passing	>240	>240
Cb-752/PFR-32	2525	1	45	Passing	>240	>240
Ta-10W/Sn-Al	2525	1	45	Failing	>240	>240
$MoSi_2$	Compatible under all baseline conditions					
SiO_2	Compatible under all baseline conditions					
Al_2O_3	Compatible under baseline conditions up to 2700° F					

The TZM/PFR-6 system was compatible with all other coating systems evaluated
except Ta-10W/Sn-Al. While no oxidation of the TZM occurred in the couple with
Ta-10W/Sn-Al, liquid Sn-Al did attack the PFR-6 coating, lifting portions of the
coating from the substrate, creating a complex structure, and causing minor
recession of the substrate surface. The only major effect of the other contact mate-
rials including $MoSi_2$ and SiO_2 was masking of the TZM/PFR-6. With the Al_2O_3,
especially above 2700° F, attack of the TZM/PFR-6 increased.

TZM/DISIL

Material Evaluation

The Disil coating is an unmodified $MoSi_2$ coating applied in a fluidized bed using a single-cycle process. Samples were coated by the Boeing Company, Seattle, Wash., in a 17-in.-diameter bed that was used for coating refractory metal components of the X-20 vehicle. Boeing engineers were of the opinion that the edge condition of samples prepared by LMSC was not satisfactory for the Disil process, and all edges were refinished by the Boeing Company in a vibratory finishing machine. Samples were coated using the same procedures as those developed for TZM components of the X-20 vehicle. Samples were coated in two batches, with half the total quantity in each batch.

Test coupons were run with each batch for evaluation of coating quality by Boeing. These were tested for 30 min in still air at 2700° F. Inspection revealed random edge failures on the coupons. All coated parts from both batches were subjected to a colorimetric inspection. Experience has shown that parts that pass this inspection will not fail prematurely in oxidation tests at 2700° F in air. A total of 196 of 318 baseline and defect-tolerance specimens failed the test. All the resistance and hot flow specimens passed.

The 196 defective samples were returned to the vibratory finisher to remove the coating and more of the base metal. The samples then were recoated in the X-20 facility and inspected again. Of these, 77 still had probable edge defects. These were vibratory finished again to clean edges and were recoated for a second time using the Boeing 8-in.-diameter bed. (The X-20 facility had been shut down by this time.) The samples still had defects and further rework was not attempted.

Because of the complex process history, it was decided to use only the 122 baseline and defect tolerance samples which were coated only once and had passed the colorimetric test. The 119 specimens that passed this test after refinishing and recoating appeared to be of poor quality. Surfaces of many had a high density of wide cracks in a crazed pattern, and edge coverage was not uniform. It was believed that use of these samples would introduce a new variable and distort test results. The 77 specimens that still had defects after being reworked twice were discarded. All the resistance and hot-flow specimens that passed the first inspection were of good quality and were used in the test program.

Initially, it was intended that an emittance control topcoat be applied to these specimens. Boeing had achieved some success in the use of a TiC topcoat on Disil-coated TZM for this purpose (28). However, Boeing engineers stated that the process had not been qualified for the X-20 vehicle. Since it was desired that these studies be conducted on materials representative of those used in the X-20, the TiC topcoat was not applied to the samples.

As shown in Figure 52, the samples had a very smooth surface of uniform texture and color. Many of the samples were banded with 1 to 3 stripes, however (Figure 52A). These bands were darker or, in some cases, lighter in color than the rest of the

M6816   ×4

(A) Surface

M6814, 6815   ×18

(B) Edge and Surface

Figure 52 General Appearance of TZM/Disil, As-Coated

128

surface. Slight blistering was noted in the bands, and in some areas surface layers of the coating flaked off. Few cracks were visible on the surfaces at low power magnification. In general, edge coverage appeared to be good, although long continuous fissures and cracks occurred on all edges (Figure 52B). Approximately 10% of the baseline samples were rejected upon visual examination at LMSC because of questionable edge quality (wide, long fissures).

The coating was fine-grained $MoSi_2$ (Figure 53). A continuous layer of Mo_5Si_3 about 0.05 to 0.1 mil thick had formed below the $MoSi_2$ coating. This layer tended to become thinner at the corners. Fine hairline cracks extended from the surface into the Mo_5Si_3 diffusion zone. No transverse branching of the cracks was evident. A heavy concentration of very deep but narrow fissures was found on all corners. Many of these extended to the substrate and were potential failure sites.

Banded areas observed on the surface could not be correlated with any underlying microstructural features. Transverse laminations existed in the coating near the surface in these regions. However, general structural details were identical to those in surrounding areas. The coating was very dense compared with the PFR-6 coating on TZM and had a fairly smooth surface. Spectrographic analysis indicated the presence of Mo, Si, Ti, and Zr as major elements. No other tramp impurities were detected.

The substrate had a wrought structure and no trace of recrystallization was found. Hardness was uniform across the section and averaged 305 DPH. Hardness of the uncoated substrate was 282 DPH. The minor difference in hardness is probably due to sample-to-sample variation within the lot of TZM specimens.

Coating thickness measured on the cross section of two samples averaged 2.31 and 1.90 mils. Individual readings ranged from 1.7 to 2.7 mils, and the overall average was 2.11 mils. The average thickness increase after coating was 1.15 mils per side (Figure 54). As discussed in the section on TZM/PFR-6, about 0.4 mil of Mo is consumed to produce 1.0 mil of $MoSi_2$. Thus, for a 2-mil coating, 0.8 mil per side of the substrate is removed. Calculated coating thickness, therefore, would be 1.95 mils per side, which is in good agreement with measured values. From the σ values in Figure 54, the standard deviation of coating thickness would be 0.16 mil per side. Thus, 95% of the samples would be expected to have a coating between 1.63 and 2.27 mils, with an average thickness of 1.95 mils (2σ limits). Weight change data could not be used to calculate approximate coating thickness, since sample edges were refinished by Boeing after weighing at LMSC, and corrected weights were not determined.

For purposes of this program, the average coating thickness is assumed to be 2.0 mils. Good uniformity of thickness within a sample and from sample to sample was indicated by the total thickness measurements. As shown in Figure 54, dispersion of total thickness values was increased very little upon application of the Disil coating. It is interesting that the coated and uncoated frequency distributions overlap, with a few of the as-coated samples being thinner than some of the uncoated sheet specimens. This is due to the large dispersion of thickness values (sample-to-sample variation) within the sheet of TZM procured for this program.

P914   ×500

(A) Surface

M6846   ×500
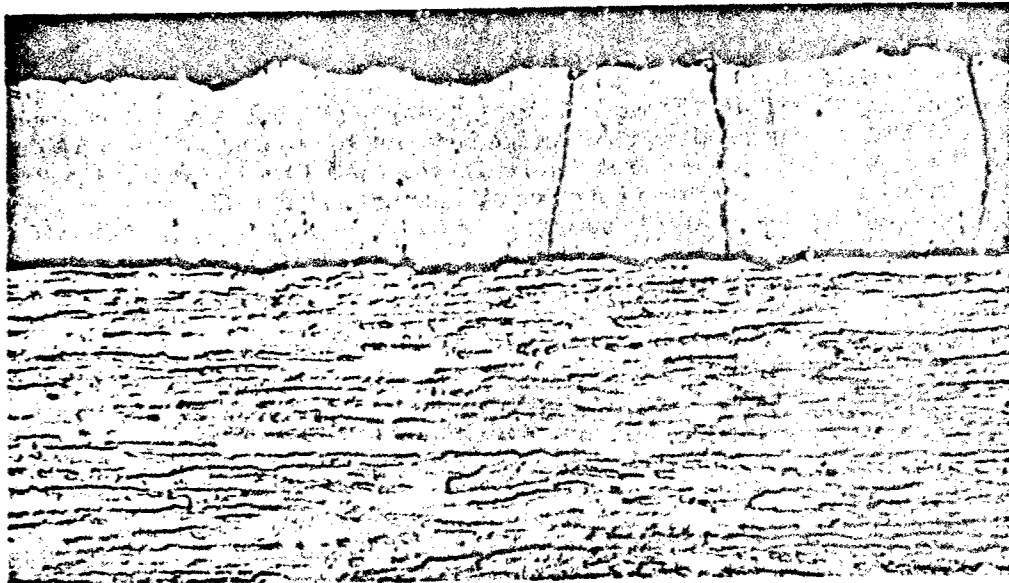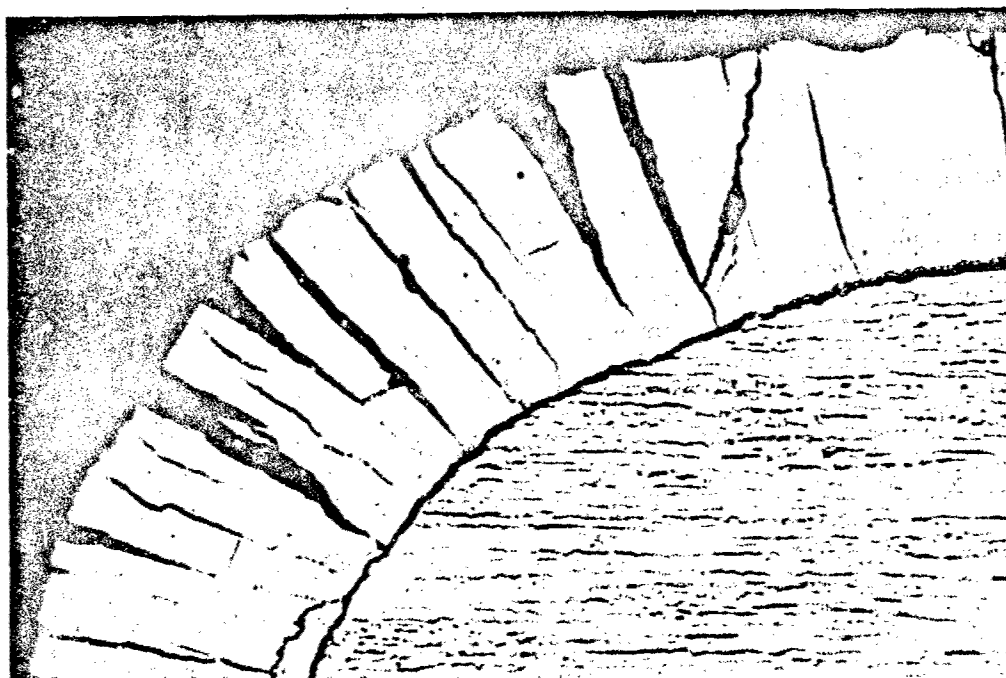
(B) Edge

Figure 53 Microstructure of TZM/Disil, As-Coated

130
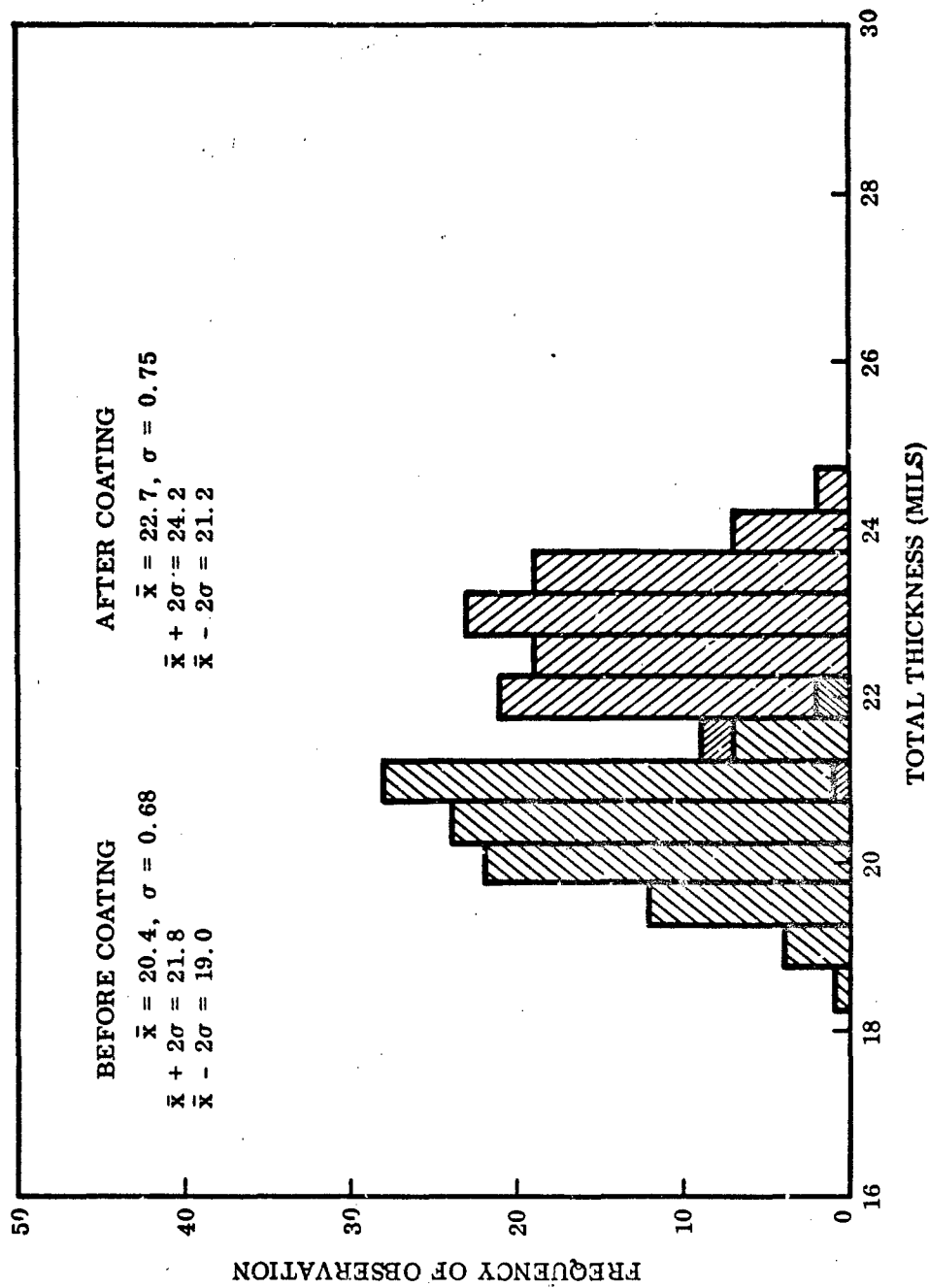
Figure 54 Frequency Histogram of Total Thickness Before and After Coating, TZM/Disil

131

Baseline Behavior

The results of the baseline evaluations are presented in Figure 55, and the complete data are tabulated in Appendix III. The pressure dependence of the performance capabilities is shown in Figure 56. In this plot, only the total failure limits are presented. At the lower pressures, there were no temperature-time regions of random failure, and at higher pressures there were so many random edge failures that the random failure boundaries were not defined.

Poor edge protection, particularly on the 1/2- by 3/4-in. specimens tested, resulted in an abundance of random edge failures in spite of careful screening of samples before testing. Generally there were fewer than four failure sites per specimen, but, because of molybdenum oxidation characteristics, large holes developed in the substrate at these points. As seen in Figure 55, edge failures were encountered more frequently at 5 mm Hg and above. It should be noted that, although the edges of these specimens were not well protected in this pressure range, there was good surface protection, and consequently few surface failures occurred.

There were some inconsistencies in the data; i.e., in some cases at 0.01 and 0.1 mm Hg, specimens exhibited only random surface failure or no surface failure at temperatures above the level where other specimens exhibited total surface failures. Nevertheless, the trend of the data was clear, and the adverse effect of low pressures on oxidation resistance was well demonstrated. There was a strong pressure dependence of the performance down to 0.1 to 1.0 mm Hg, but at lower pressures the performance was considerably less sensitive to pressure. Actually, as in similar coating systems, the pressure level 0.01 to 1.0 mm Hg probably represents a lower plateau in performance curves.

In addition to the decrease of the maximum useful temperature with decreasing pressure, another pressure-sensitive effect occurred. Again referring to the curves of Figure 55, it can be seen that a marked change in the slope of the failure boundaries occurred with decreasing pressure. At 5 mm Hg, and probably at higher pressure levels, the slope of the curve was higher and the coating performance was strongly temperature dependent. At the lower pressures, 0.01 to 1.0 mm Hg, the relative importance of temperature as a variable was less than at higher pressures.

After exposure to baseline conditions, the specimens were smooth and gray in color. In only one case, 5 mm Hg at 3000°F (in the total failure region), was bubbling on the glassy oxide observed during testing, and there was no evidence of bubble formation on other specimens. The stripes observed on the as-coated samples were still apparent as slightly darker, rougher regions. In a few cases, these were sites of local failure. The coating usually remained intact around random failure sites, and it was occasionally necessary to probe the specimens with a sharp tool to detect these failures.

As previously mentioned, the TZM/Disil and TZM/PFR-6 systems and other systems with slightly modified or unmodified $MoSi_2$ coatings on Mo-base alloys have similar microstructures. It was not unexpected, therefore, that the microstructural behavior of TZM/Disil was nearly identical to that of TZM/PFR-6.

132

Within the coating the silicide disproportion reactions resulting from silicon diffusion into the substrate were the same as in the TZM/PFR-6 system. (See the TZM/PFR-6 results section for a more detailed discussion of these phenomena.) The kinetics were also the same, and as a consequence it was possible to use the Arrhenius curve of Figure 18 as a basis for temperature calibrations for the TZM/Disil/system.

Glass formation and the interaction of the glass with coating defects were generally similar to what was found with TZM/PFR-6 — with the notable exception that there was little bubble formation on Disil. Again, with decreasing pressure from 50 to 1 mm Hg, the glass became less effective in protecting defects. The transition in the mode of oxidation of the coating from defect control to surface recession control took place at about 0.1 mm Hg. This, of course, accounts for the change in slope of the failure boundaries. At the higher pressures, the protective capabilities of the glass apparently are decreased sharply within a rather narrow temperature range. The decreased temperature sensitivity of the coating at pressures below 1 mm Hg probably reflects a change in the characteristics of the glass.

In Figure 57 the microstructures resulting after exposures at 1 atm and 0.1 mm Hg are contrasted. The structures shown in Figures 57B and 57C are in different regions on the same specimen. In Figure 57A are the following: a thin layer of Mo_3Si of varying thickness at the substrate/coating interface; next, a layer of Mo_5Si_3; and, finally, on the coating surface, $MoSi_2$ with islands of Mo_5Si_3. In Figure 57B, there is again a layer of Mo_3Si, and the coating is mostly Mo_5Si_3. (The increased thickness of the inner Mo_5Si_3 zone is due to higher temperature.) The significant feature, of course, is the existence of Mo_5Si_3 on the surface as the result of loss of Si to the environment. The light-colored phase is the remaining $MoSi_2$. Figure 57C illustrates the attack characteristic of low pressures and the formation of the spongy mixture of glass, oxides, lower silicides, and molybdenum.

Although, as mentioned, this system and the TZM/PFR-6 system were generally similar, there were a few marked differences. First, the tendency for bubble formation was less in the TZM/Disil system. This may have been in some way a consequence of the less porous, smoother Disil coating. More likely, there was some difference — perhaps subtle — in the composition of the glass. The transition to the low-pressure mode of attack occurred at 0.1 mm Hg in TZM/Disil and at 1.0 mm Hg in TZM/PFR-6. This seemed to have little effect on the overall performance, as it was generally equivalent for the two systems in this pressure range. However, if would appear that the TZM/Disil system does not lose silicon as readily as does TZM/PFR-6 at equivalent temperatures and pressures and consequently remains slightly more stable at all pressure levels. Again, this may be the result of greater surface area due to roughness and porosity in the PFR-6 coating, rather than the result of any compositional differences.

The three inconsistencies in the baseline data at 0.01 and 0.1 mm Hg (i.e., total surface failures occurring at lower temperatures than some random surface failures or passing surfaces) were studied in detail. Specimens exhibiting total surface failures were characterized by an extraordinarily high density of surface cracks in a crazed pattern. It is possible that three recoated samples were inadvertently used for these tests.
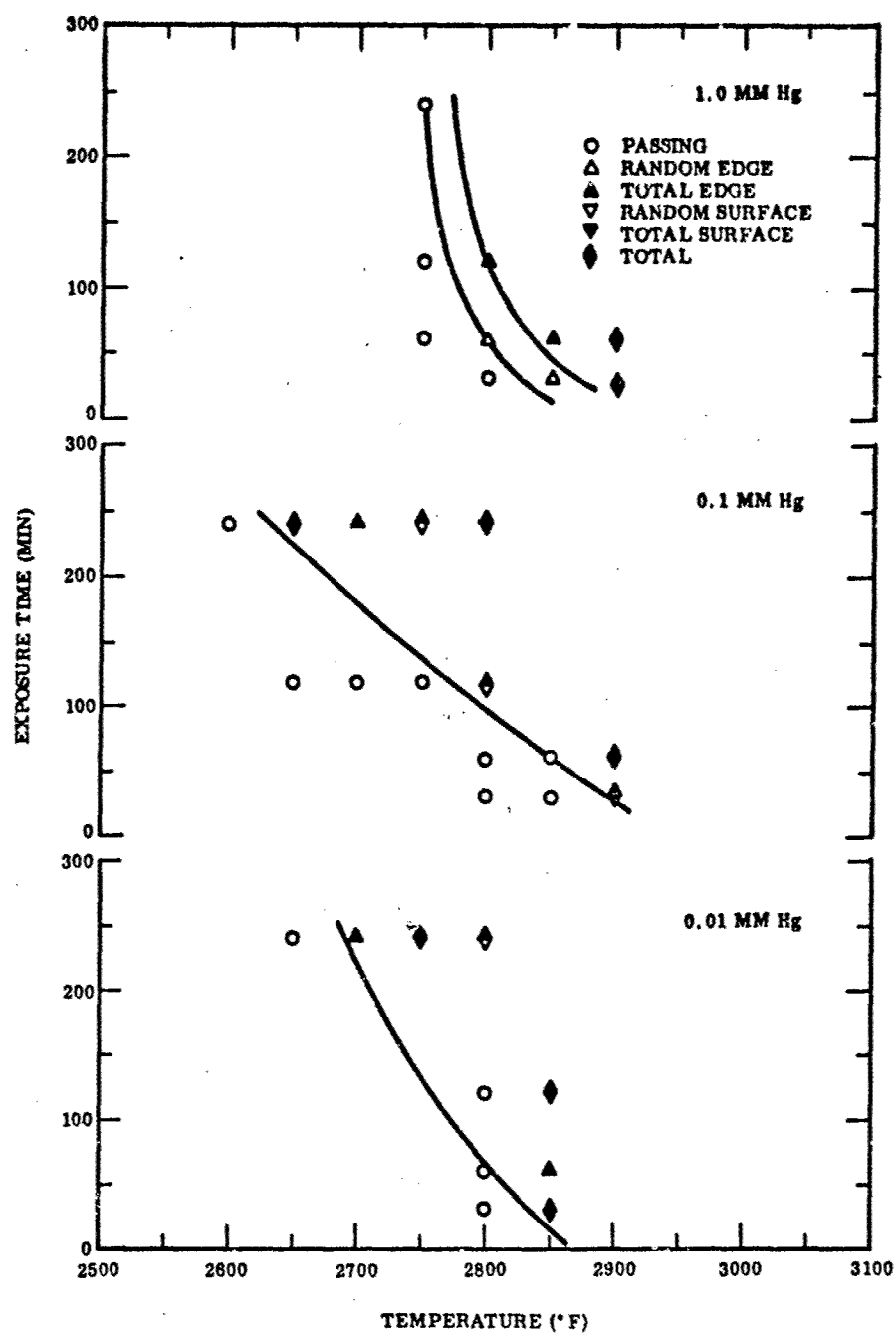
133

Figure 55 Results of Baseline Tests, TZM/Disil

134
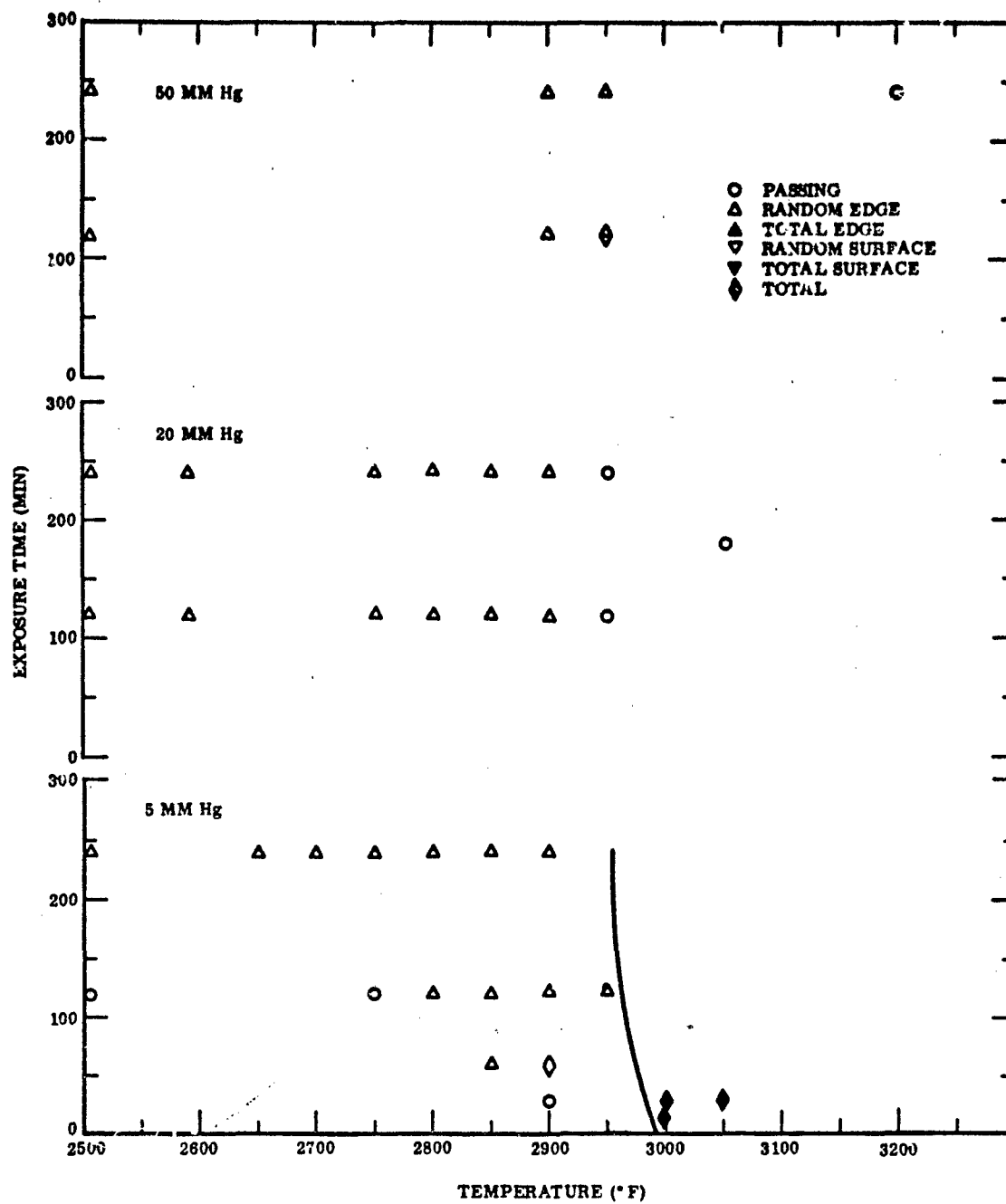
Figure 55 Results of Baseline Tests, TZM/Disil (cont'd)

135
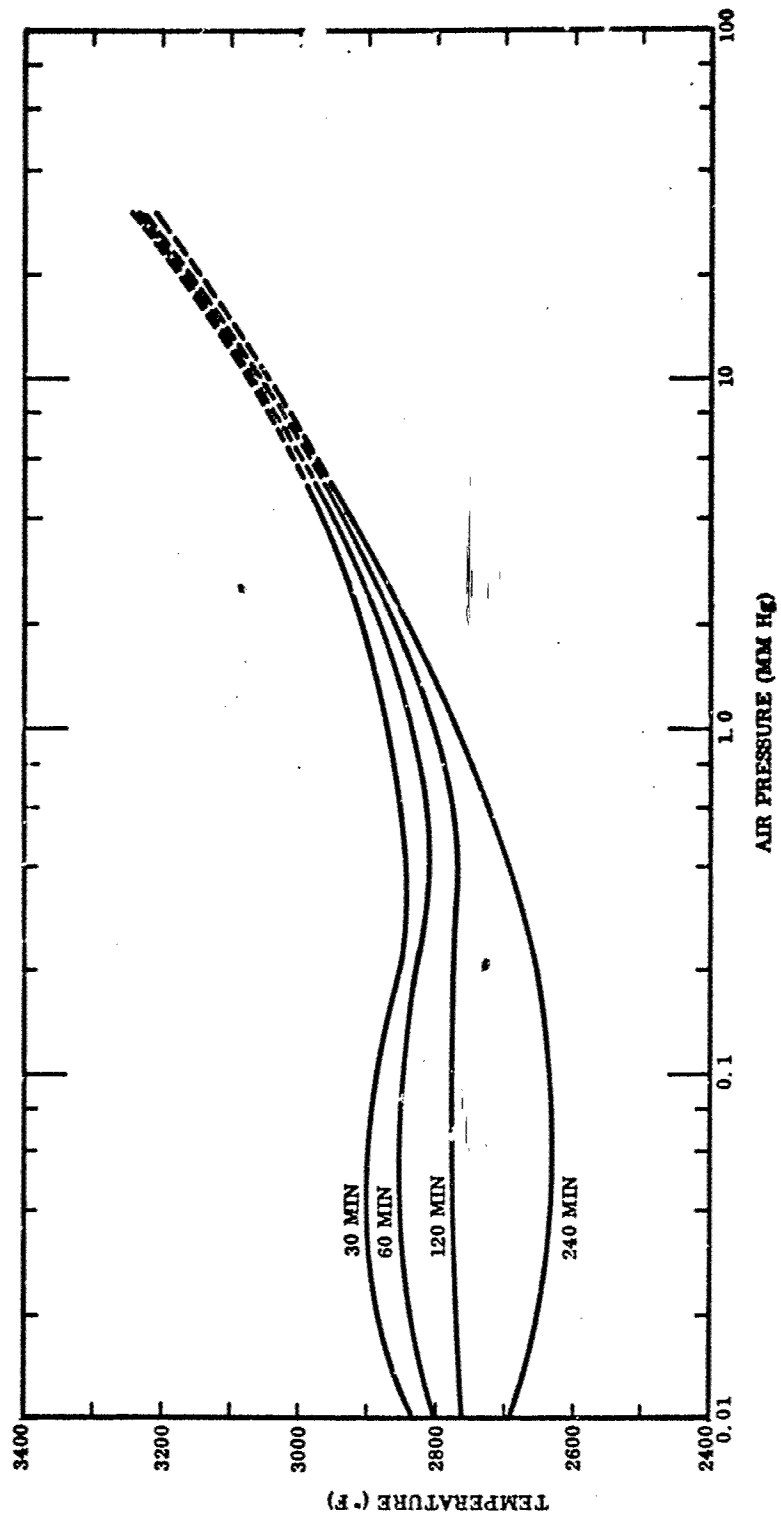
Figure 56   Baseline Failure Limits, TZM/Disil

136

M6790   ×1000   M6878   ×1000

(A) 2650° F, 760 mm Hg   (B) 2750° F, 0.1 mm Hg

M6879   ×1000

(C) 2750° F, 0.1 mm Hg

Figure 57 Effect of Pressure on TZM/Disil Structure (4 hr exposure)

137

Gas Velocity

During the gas-velocity tests, the temperature was measured and controlled using the same procedures and calibration data that had been used with TZM/PFR-6. Comparisons of the Mo_5Si_3 growth on gas-velocity specimens with the growth on baseline specimens served as checks on temperature. There was consistently good agreement between the true temperature measured and that indicated by Mo_5Si_3 growth. The fact that the same correction data could be used on both TZM/Disil and TZM/PFR-6 indicated a similarity in the emittances of the two systems — at least under the test conditions of this phase of the program. Actually, in view of the foregoing discussions on the structures of TZM/Disil and TZM/PFR-6, the most likely factor which might result in significantly different emittance values was the difference in surface roughness. Apparently, there was enough smoothing due to oxidation and formation of glass during both baseline and gas-velocity testing to negate the influence of any difference in surface roughness.

The results are presented in Table XXV. There was some degradation in performance capabilities with the adverse effect of high gas-velocity increasing with increasing temperature.

Table XXV. Results of Mach 3 Flow Tests, TZM/Disil

Test conditions					Performance rating	Baseline time to failure	
Temp. (°F)	Total pressure (mm Hg)	Atmosphere	Equivalent air pressure (mm Hg)	Time (min)		Random (min)	Total (min)
2900	20	Air	20	60	Passing[a]	—	> 240
3000	20	Air	20	60	Passing	—	> 180
3100	20	Air	20	60	Passing[a]	—	—
3200	20	Air	20	60	Total surface failure	—	—
2800	20	19:1 N_2O_2	5	60	Passing[b]	..	> 240
2900	20	19:1 N_2O_2	5	60	Random surface failure[c]	—	> 240

(a) Edge failure in the curved region of the specimen.
(b) Random surface failure on static side of specimen in stripe.
(c) Failure in stripe in cooler region of specimen.

At both 2900 and 3000°F and 20 mm Hg air pressure, the microstructure on the flow side resembled that on the static side after a 1-hr exposure. At 3100°F, however, there was a 25% decrease in coating thickness on the flow side as compared with the static side. Also there was some evidence of attack of the Mo_5Si_3 on the flow side but not the static side. At 3200°F there was sufficient degradation to cause total surface failure on the flow side. At an equivalent air pressure of 5 mm Hg and 2800°F,

138

there was attack of the Mo_5Si_3 on the flow side (much less on the static side) but no marked thinning of the coating. At 2900°F there was more attack of the Mo_5Si_3 on the flow side, 10 to 15% reduction in coating thickness, and random failures. It must be noted, however, that these failures occurred in the stripes in cooler regions of the specimen.

The edges on the gas-velocity specimens were greatly superior to the edges on the baseline specimens. A few edge failures occurred in curved regions of the specimens, but there were no edge failures in the test section.

It is concluded that whereas the glass was softened under all test conditions, it is sufficiently viscous to resist extensive flow until temperatures near the baseline failure boundaries were approached. In spite of greater surface recession, performance was still defect-controlled and hence not greatly different from baseline behavior.

Vacuum Volatility

The TZM/Disil vacuum volatility results are presented in Figure 58 and Table XXVI. Again, the weight loss data were computed on the basis of the planar area of the substrate rather than the absolute area of the coating-environment interface.

Table XXVI. Vacuum Volatility Data, TZM/Disil

Temp. (°F)	Pressure (mm Hg)	Time (hr)	Thickness Initial (mils)	Thickness Final (mils)	Thickness decrease (mils/side)	Weight Initial (gm)	Weight Final (gm)	Weight change (gm/cm^2)[a]
2600	7×10^{-6}	0.5	22.0	21.9	0.05	1.0806	1.0784	0.000449
	6×10^{-6}	1		21.7	0.15		1.0764	0.000857
	5×10^{-6}	2		21.6	0.2		1.0731	0.00153
	4×10^{-6}	4		21.4	0.3		1.0676	0.00265
2800	6×10^{-6}	0.5	22.9	22.4	0.25	1.1361	1.1253	0.00222
	5×10^{-6}	1		22.0	0.45		1.1196	0.00337
	4×10^{-6}	2		21.9	0.5		1.1144	0.00422
	3×10^{-6}	4		21.7	0.6		1.1134	0.00463
3000	1×10^{-5}	0.5	24.1	22.9	0.6	1.1625	1.1420	0.00418
	6×10^{-6}	1		22.7	0.7		1.1399	0.00462
	5×10^{-6}	2		—	—		1.1387	0.00486
	4×10^{-6}	4		22.6	0.75		1.1371	0.00518
3200	9×10^{-6}	0.5	23.9	22.6	0.65	1.1804	1.1551	0.00516
	8×10^{-6}	1		22.5	0.7		1.1528	0.00563
	7×10^{-6}	2		22.5	0.7		1.1487	0.00647
	5×10^{-6}	4		22.5	0.7		1.1426	0.00772

Average Area = 4.90 cm^2.
(a) Per unit area of substrate.

139
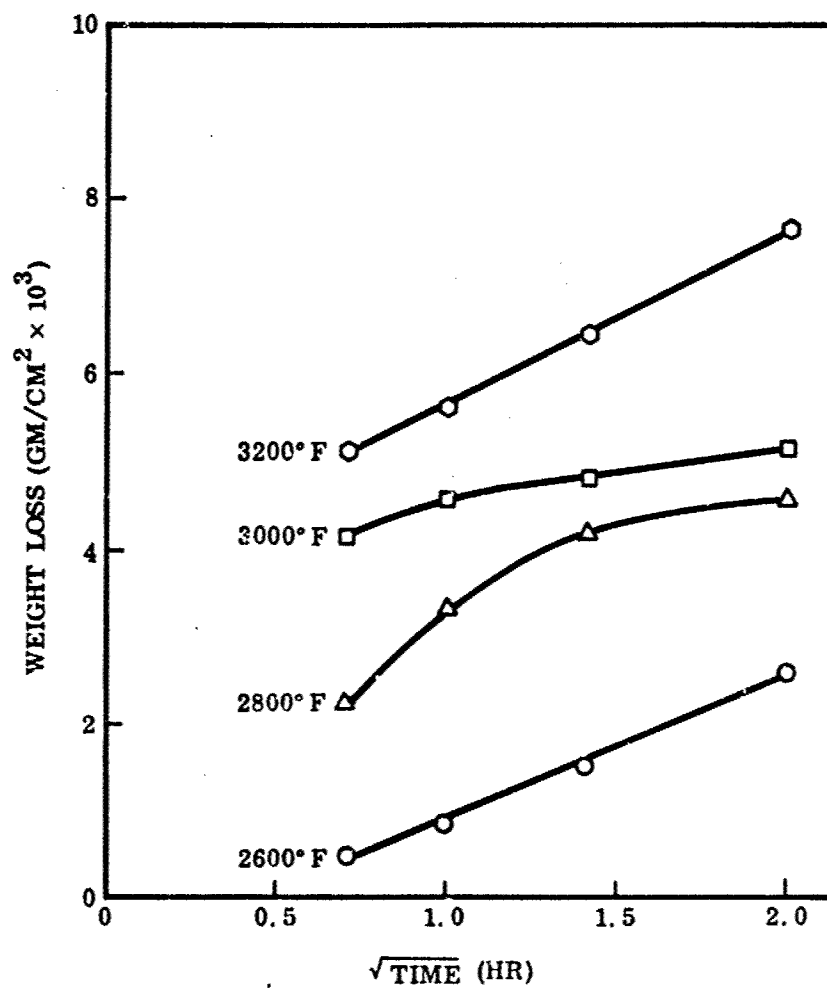
Figure 58 Rate Curves, Vacuum Volatility of TZM/Disil System

140

The basic mechanisms entailed in the vacuum volatility process are the same as those of the TZM/PFR-6 system and reference is made to the discussion of TZM/PFR-6 vacuum volatility results for a detailed analysis and description of this process. The structure of the Disil coating after vacuum exposure at various temperatures is shown in Figure 59.

The slopes of the TZM/Disil curves are nearly identical to the slopes of the TZM/PFR-6 curves in Figure 49; however, the PFR-6 curves reflect higher weight-loss values for a given set of conditions. This is a consequence of the roughness and porosity of the PFR-6 coating. The absolute surface area on the PFR-6 coating is much greater than that of the Disil coating, and, as a result, more Si is lost.

As with similar systems, the oxidation-resistant capabilities of the Disil coating subsequent to vacuum exposure can be degraded for three reasons: (1) there is general surface recession; (2) cracks are broadened considerably, and consequently the effective coating thickness is reduced; and (3) the lower silicides are much less oxidation resistant than $MoSi_2$. Probably vacuum exposures of 30-60 min at 2600-2800° F will not seriously degrade subsequent oxidation resistance. However, after higher temperatures or longer times in vacuum, the coating performance would be expected to be affected adversely.

Temperature-Pressure Cycling

At the time these tests were conducted, all of the original lot of 122 good specimens had been used. It was necessary to use recoated samples for the cycling tests. Results of one cyclic experiment are shown below.

Phase of cycle	Test conditions			No. of cycles	Total time (min)	Performance rating	Baseline time to failure	
	Temp. (°F)	Pressure (mm Hg)	Time (min)				Random (min)	Total (min)
1st (Baseline)	2700	1	7	4	28	Random edge failure	> 240	> 240
2nd	2200	3	21		84		–	–

This system has been shown to be similar in most respects to the TZM/PFR-6 system. Consequently, it is felt that the performance of this system under cyclic conditions should be equivalent to the TZM/PFR-6 performance. Because the latter system was not degraded under these conditions, it is believed that the premature failure in the TZM/Disil system was a result of the poor condition of the recoated specimens. No further tests were conducted because of lack of suitable specimens.

Acoustic Vibration

Again it was necessary to use some of the defective specimens, i.e., those that were coated, found by colorimetric tests to be defective, and were recoated. The specimens

141
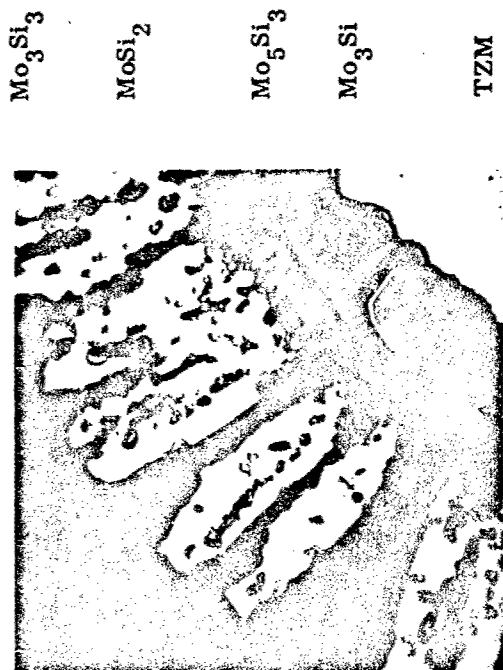
Mo₅Si₃ ... MoSi₂ ... Mo₅Si₃ ... Mo₃Si ... TZM

(A) 2600° F ×1000 M6850

Mo₅Si₃ ... Mo₃Si ... TZM

(B) 2800° F ×1000 M6883

Mo₃Si ... Mo₅Si₃ ... Mo₃Si ... TZM

(C) 3000° F ×1000 M6943
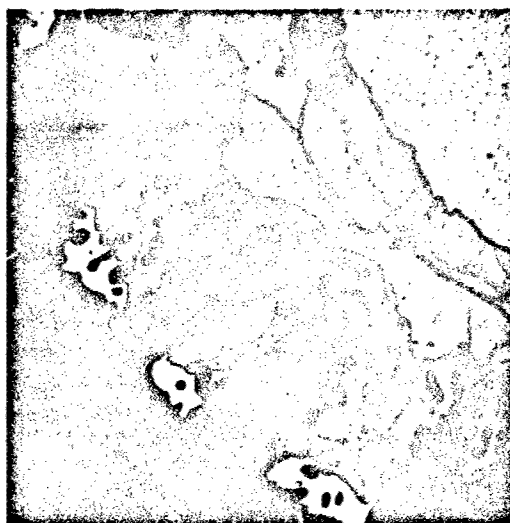
Mo ... Mo₃Si ... Mo₅Si.₃ ... Mo₃Si ... TZM

(D) 3200° F ×1000 M6852

Figure 59 Structure of TZM/Disil After 4-hr Exposure at 10^{-5} mm Hg

142

that were acoustically irradiated were examined before and after irradiation and no effect was found. One specimen which was exposed to a sine vibration mode was oxidation-tested at 20 mm Hg, 2750° F, for 60 min. The performance was rated as passing.

On the basis of the observations during this phase of the program and also those made during the similar evaluation of TZM/PFR-6, it was concluded that acoustic vibration of the nature used in this investigation has no effect on the performance of the TZM/Disil system.

Defect Tolerance and Repair

An evaluation was made of this system's capability to resist or tolerate defects which might arise during handling, assembly, or service. In addition, an investigation was made of the feasibility of using the Boeing $MoSi_2$-Synar Binder Coating Process (25).

Initially the ability to withstand any defects created by bending was assessed. Specimens were bent 30 deg over a 3t radius using three-point loading in the controlled bend-test apparatus. Any further bending resulted in substrate cracking. One of these specimens passed an oxidation test at 2750° F, 1.0 mm Hg air pressure, for 60 min. The baseline time to random failure at this temperature is 240 min but at 60 min the random failure boundary is only 50 deg higher at 2800° F. This indicates this system's ability to survive rather severe deformation with little or no loss in oxidation resistance.

The ballistic impact results are presented in Table XXVII. It is clear that there is low impact resistance but, of course, considering the fact that the substrate is brittle at room temperature at low strain rates, this is not too surprising.

Table XXVII. Results of High-Velocity Impact Tests, TZM/Disil

Backup material	Kinetic energy (ft-lb)[a]					
	Spalling		Coating fracture		Substrate fracture	
	Pass	Fail	Pass	Fail	Pass	Fail
Rubber	<0.3	0.3	<0.3	0.3	<0.3	0.3
Steel	1.7	2.3	1.7	2.3	1.7	2.3

(a) Calculated from projectile mass and velocity at time of impact.

The results of the oxidation studies with specimens containing defects 0.005 in. wide by either one-half or three-fourths of the coating thickness are presented in Table XXVIII. Unfortunately, it was again necessary to use some recoated samples and consequently relatively low temperatures and exposure times were selected for the 20 mm Hg specimen to avoid complete destruction of the specimen. Nevertheless, the results were significant. It is noted that at 1.0 mm Hg the 2750° F specimens were only 50 deg from the random failure boundary and the 2800° F specimen was on the random failure

143

Table XXVIII. Defect Tolerance Results (Defects in the form of slots 0.005 in.
by 1/2 or 3/4 of coating thickness), TZM/Disil

Temp. (°F)	Pressure (mm Hg)	Time (min)	Results		Baseline time to failure	
			1/2 t	3/4 t	Random (min)	Total (min)
2750[a]	1.0	30	Passing	Passing	240	>240
2750[a]	1.0	240	Passing	Passing	240	>240
2800[a]	1.0	120	Passing	Passing	60	120
2550[a]	20	30	Passing	Passing	—	—

(a) Recoated samples − although defects passed, there were edge and surface
failures.

boundary, yet all of the defect regions were passing. Also at 20 mm Hg there were
failures in the coating elsewhere but the defects were passing. Obviously natural
defects in the coating that are the cause of random failures are greater than three-
fourths of the coating thickness in depth.

Only the Boeing repair technique was evaluated with this system as there was a
shortage of suitable specimens. Also it is felt that for the other techniques evaluated
in this program, the TZM/PFR-6 system is representative of this TZM/Disil system
and that the response to a given repair process would be equivalent in both systems.

The results of repair studies are presented in Table XXIX. The technique appears to
be rather pressure-sensitive since it was 100% effective at 1.0 mm Hg and only one
mixture of $MoSi_2$-Synar yielded any protection at all at 20 mm Hg. In one case
(50 wt % $MoSi_2$-50 wt % Synar, 1 mm Hg), microscopic examination revealed the
formation of Mo_3Si around the defect and an excess of glass within the defect. In
other cases there was only a layer of glass above the substrate material. It would
appear from these limited studies that the 50-50 mixture is the best. Certainly it is
clear that further work is required to evaluate and develop this repair technique.

Materials Compatibility

Again the short supply of good specimens limited experimental activities, but it was
found that the TZM/Disil system was compatible with SiO_2 and, of course, $MoSi_2$ up
to 3000° F. It can also be said with certainty that the TZM/PFR-6 system is repre-
sentative of TZM/Disil and that those observations made with TZM/PFR-6 will be
equally applicable to TZM/Disil.

144

Table XXIX. Results of Repair Studies, TZM/Disil

Repair technique[a]		Test conditions			Performance rating	Baseline time to failure	
wt % MoSi$_2$	wt % Synar binder	Temp. (°F)	Pressure (mm Hg)	Time (min)		Random (min)	Total (min)
50	50	2700	1.0	60	4 passing	>240	>240
25	75	2700	1.0	60	4 passing	>240	>240
75	25	2700	1.0	60	4 passing	>240	>240
50	50	2900	20	60	2 failing 2 passing	—	>240
25	75	2900	20	60	4 failing	—	>240
75	25	2900	20	60	4 failing	—	>240

(a)Boeing MoSi$_2$-Synar Binder repair coating process (25).

TZM/DURAK-B

Material Evaluation

Durak-B is a modified $MoSi_2$ coating applied by a two-cycle pack process The coating is a product of Chromizing Corporation (a subsidiary of Chromalloy), Hawthorne, Calif., and is identical to the W-3 coating for TZM that is produced by Chromally. The composition and process history of the coating are proprietary.

The first batch of tabs coated by Chromizing Corporation proved to have a bad edge condition. Samples failed consistently in tests at 2700° F in air at 760 mm Hg and reduced pressure. This was believed to be the result of too sharp an edge radius Chromizing Corporation stripped the coating and reground the edges by hand on a rubber-bonded abrasive wheel. Edges were contoured to a smoothly rounded configuration and the specimens were recoated. No edge failures were encountered after testing these samples for 4 hr at 2700° F in air at 1 atm.

The general appearance of the initial and recoated tabs is shown in Figure 60. The initial tabs had a flat edge with rounded corners. On a cross section, four distinct "corners" were evident. The rounded edge on the recoated tabs was a bullet-nose configuration, and only two distinct "corners" were evident on the cross section. It should be noted that this edge configuration is quite different from that on the TZM/PFR-6 and TZM/Disil test specimens.

The effect of geometry on edge defect patterns is clearly shown in Figure 60. Flat-edged samples (Fig. 60B) had wide fissures which were continuous along the entire length of the edge. Fissures on the rounded edge samples, on the other hand, were short or discontinuous and much narrower.

Recoated samples had a smooth surface of uniform texture and color. Samples were a dark blue-gray with no variations in the appearance of the surface of a given sample. There was some color variation from sample to sample, from light to dark blue-gray.

The microstructure of the TZM/Durak-B specimens is shown in Figure 61. The change in edge condition as a result of the refinishing and recoating process is clearly shown. Recoated samples had narrower edge fissures and in general a more uniform edge coverage. Little tendency for growth of "unicorn" edges like those shown in Figure 61A was observed.

The coating on flat surfaces of recoated tabs was slightly thinner than that on the original set of samples. The structure of the coating was also slightly different from that of the first set. Fine hairline cracks extended from the surface to the interfacial zone. No tendency for transverse or lateral branching at the interface was noted. These fissures on the recoated tabs had a widened section in the central region of the coating. Also, the second phase in the coating was distributed along this central section in the recoated tabs. No evidence of substrate recrystallization wa. found. Substrate hardness averaged 283 DPH in the initial lot and 308 in the recoated lot. Hardness

146
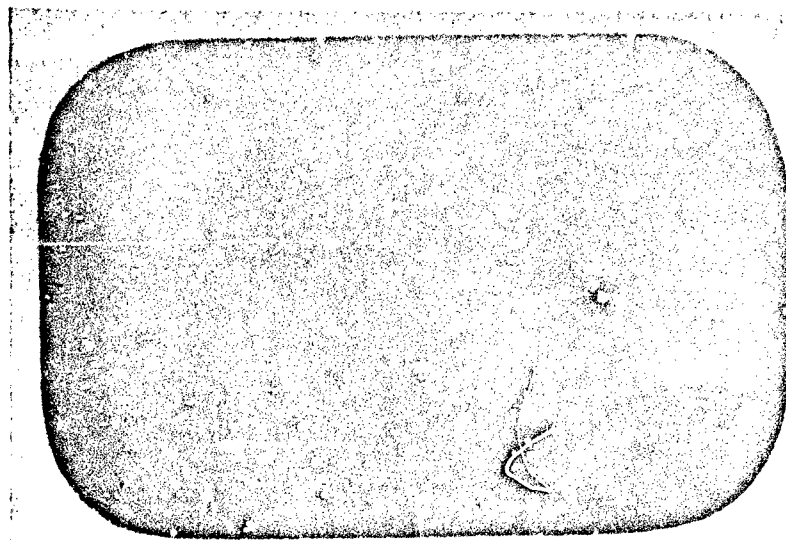
M9971   (A) Surface, Recoated   ×18

M5370   ×18   M6811, M6817   ×18

(B) Edge and Surface,   (C) Edge and Surface,
      First Coating   Recoated

Figure 60   General Appearance of TZM/Durak-B, As-Coated
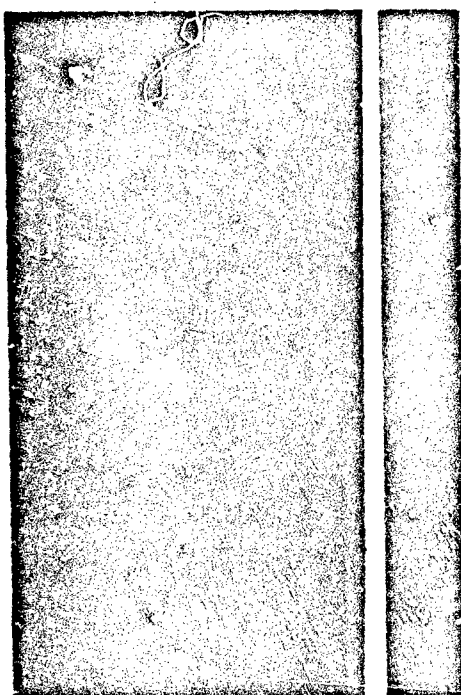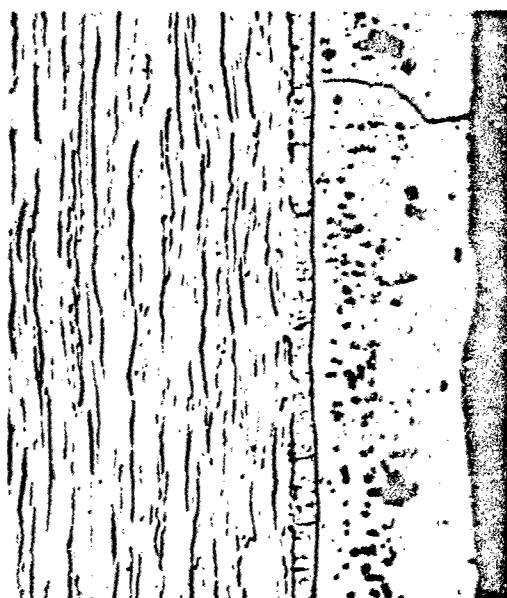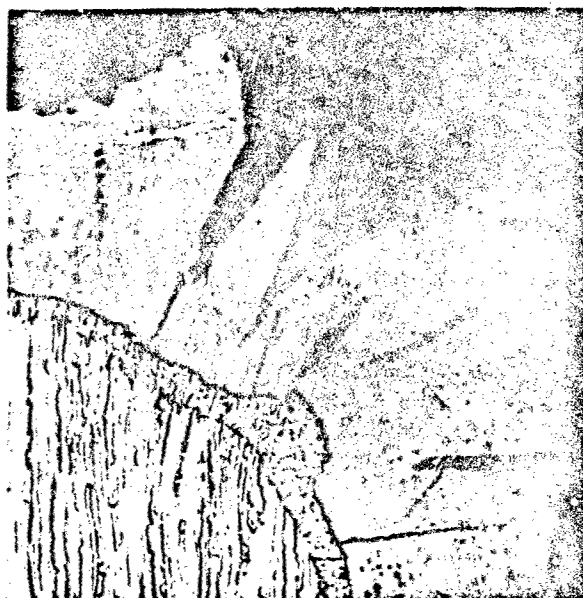
M5530 ×500 M5529 ×500

(A) Edge and Surface, First Coating
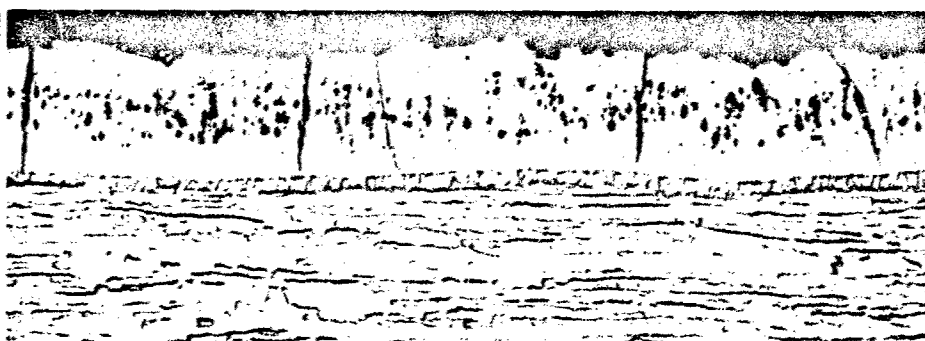
P912
×500
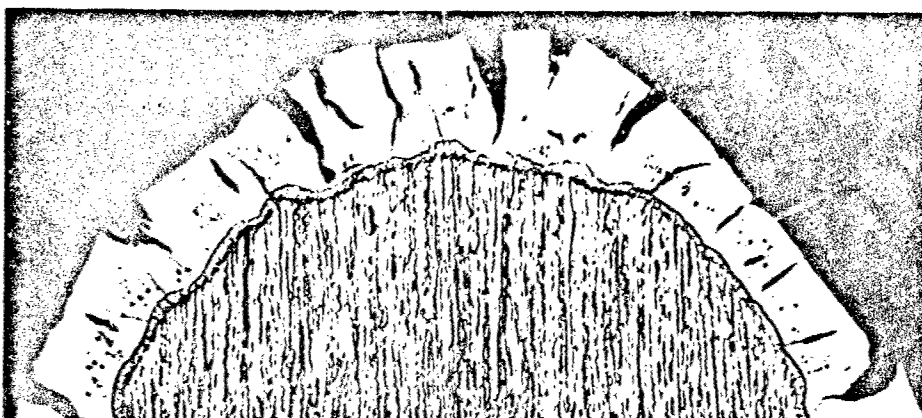
P915
×500

(B) Edge and Surface, Recoated

Figure 61 Microstructure of TZM/Durak-B, As-Coated

148

was uniform across the section. After 4 hours at 2700° F in air at 1 atm, complete recrystallization occurred and hardness decreased to 205 DPH.

Microstructural details of the Durak-B coating are shown in Figure 62. The coating is predominantly $MoSi_2$, with a second phase (gold colored) segregated in vertical stringers along the midsection of the disilicide layer. A thin diffusion zone, believed to be Mo_5Si_3, was evident between the $MoSi_2$ and an unidentified interfacial phase. The interfacial zone appeared to have a duplex structure, one phase of which appeared to be continuous with the Mo_5Si_3. The other phase in this zone had an appearance similar to that of the gold-colored segregates in the disilicide phase. Spectrographic analysis indicated Mo, Si, Ti, Zr, and B as major constituents of the coating.

The coating was dense and comparatively uniform in thickness. The average thickness on flat surfaces was measured as 1.7 mils, with a range of values between 1.6 and 1.8 mils. Because of the refinishing and recoating processes, total thickness and weight change measurements could not be used for calculating average coating thickness. Samples were not measured and weighed after the first coating was removed and the edges reground. For purposes of this program, the average coating thickness was assumed to be 1.75 mils.

TZM/Durak-B was brittle in bending at room temperature. However, at 250° F the substrate did not fracture after bending, indicating a ductile to brittle transition temperature below this value. Bend angles of 35 to 40 deg were required to produce major cracking and spalling of the coating at 250° F. Appreciable deformation is possible at comparatively low temperatures, permitting some flexibility in assembly of coated parts.

Testing of the TZM/Durak-B system at reduced pressure often caused failure of alumina furnace components, including the furnace tube. These failures were probably due to softening of the alumina components as the result of reactions between boron oxide (boron from the Durak-B) and the alumina. Liquid phases are present in the Al_2O_3-B_2O_3 system at temperatures as low as 1890° F (29).

To avoid furnace failures, the scope of less critical experimental activities was abridged. Nevertheless, the performance of the system was well-characterized and, equally important, the behavior was sufficiently similar to that of the other coated TZM systems to be representative of this system in areas where the number of experiments was limited.

Baseline Behavior

The results of the baseline studies with TZM/Durak-B are presented in Figure 63 and are tabulated in Appendix III. Figure 64 illustrates the pressure dependency of this system. The results were consistent at 20 mm Hg and lower, and failure boundaries were established with certainty. The consistency in the data is further reflected in the curves of Figure 64.

149
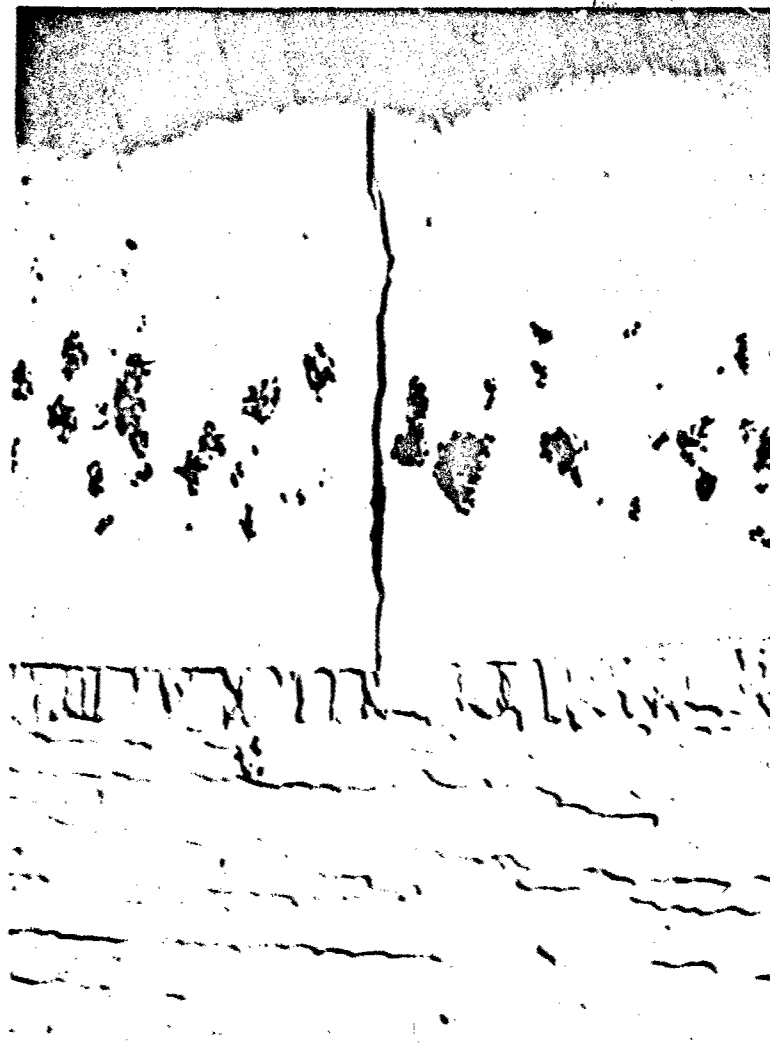
P913   ×2000

Figure 62 Microstructural Details of TZM/Durak-B, As-Coated

150

There was a tendency toward random failure at the higher pressure levels. As with similar systems, this coupled with the high Mo oxidation rate at the temperatures used prevented a clear definition of performance boundaries at 50 mm Hg. Up to 3200° F at this pressure level, the failures were random-edge in nature and the surface performance was passing, which gives an indication of the potential of this system at 50 mm Hg.

The maximum useful temperature for a given lifetime decreased as pressure decreased down to a pressure level of 0.1 to 1.0 mm Hg. At lower pressures, this temperature was relatively insensitive to pressure. As in similar systems, the range of pressure from about 0.01 to about 1.0 mm Hg probably represents a lower plateau for coating performance. As reflected in the slopes of the failure boundaries, coating performance was highly temperature dependent at higher pressures, whereas at the lower pressures the relative importance of temperature was less. This is similar to what was observed with the TZM/Disil system; a discussion of this effect is given in the results section for TZM/Disil.

During testing, the formation of glass bubbles on the specimen surfaces was observed only at 50 mm Hg. This is in contrast to TZM/Disil, where they were observed once at 5 mm Hg and to TZM/PFR-6 where they were observed over the pressure range 5 to 50 mm Hg. Bubble formation is illustrated and discussed in the TZM/PFR-6 results section. The differences in the tendency toward bubble formation may be either the result of chemical differences in the glass or differences in the surfaces of the various systems.

After exposure to baseline conditions, the specimens were generally a dark gray color and all had a crazed surface. There was a layer of glass which varied in thickness — thicker, of course, on specimens at the higher pressure.

Although the previously mentioned unidentified interfacial phase existed in the coating, the basic microstructural effects during testing were the same as for TZM/PFR-6 and TZM/Disil. There was silicon diffusion into the substrate with the resultant growth of the Mo_5Si_3 phase. With decreasing pressure, more silicon was lost from the coating surface and consequently lower silicides, mostly Mo_5Si_3, formed on the surface.

The transition in the mode of attack from defect-controlled to general surface recession took place between 0.1 and 1.0 mm Hg, although defects played a much more significant role in governing performance at the lower pressures in this system. The outer one-half to two-thirds of nearly all fissure-type defects was widened during testing at all pressures. This effect is evident in Figure 65, which illustrates the structures of coatings exposed at different pressures. It is clear that the localized attack at defects and resultant structure are unique among the coated TZM systems evaluated. Also, it is apparent that these widened cracks are the cause of the crazed surface noted earlier.

It is postulated that the glass that forms on the Durak-B coating was less viscous because it contained boron, and although the glass wet the interior surfaces of the crack it did not completely fill the cracks. Furthermore, communication between the
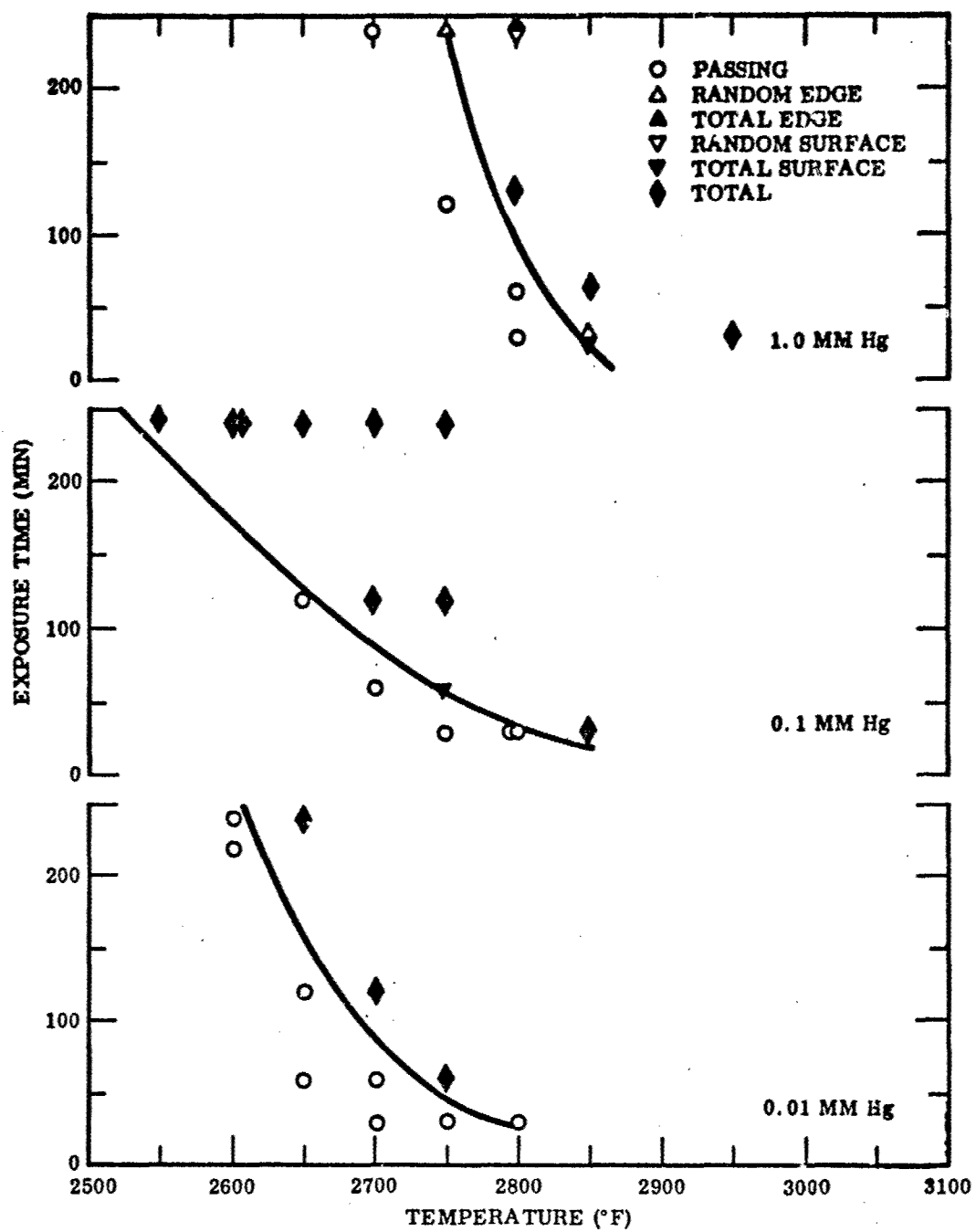
151

Figure 63 Results of Baseline Tests, TZM/Durak-B

152
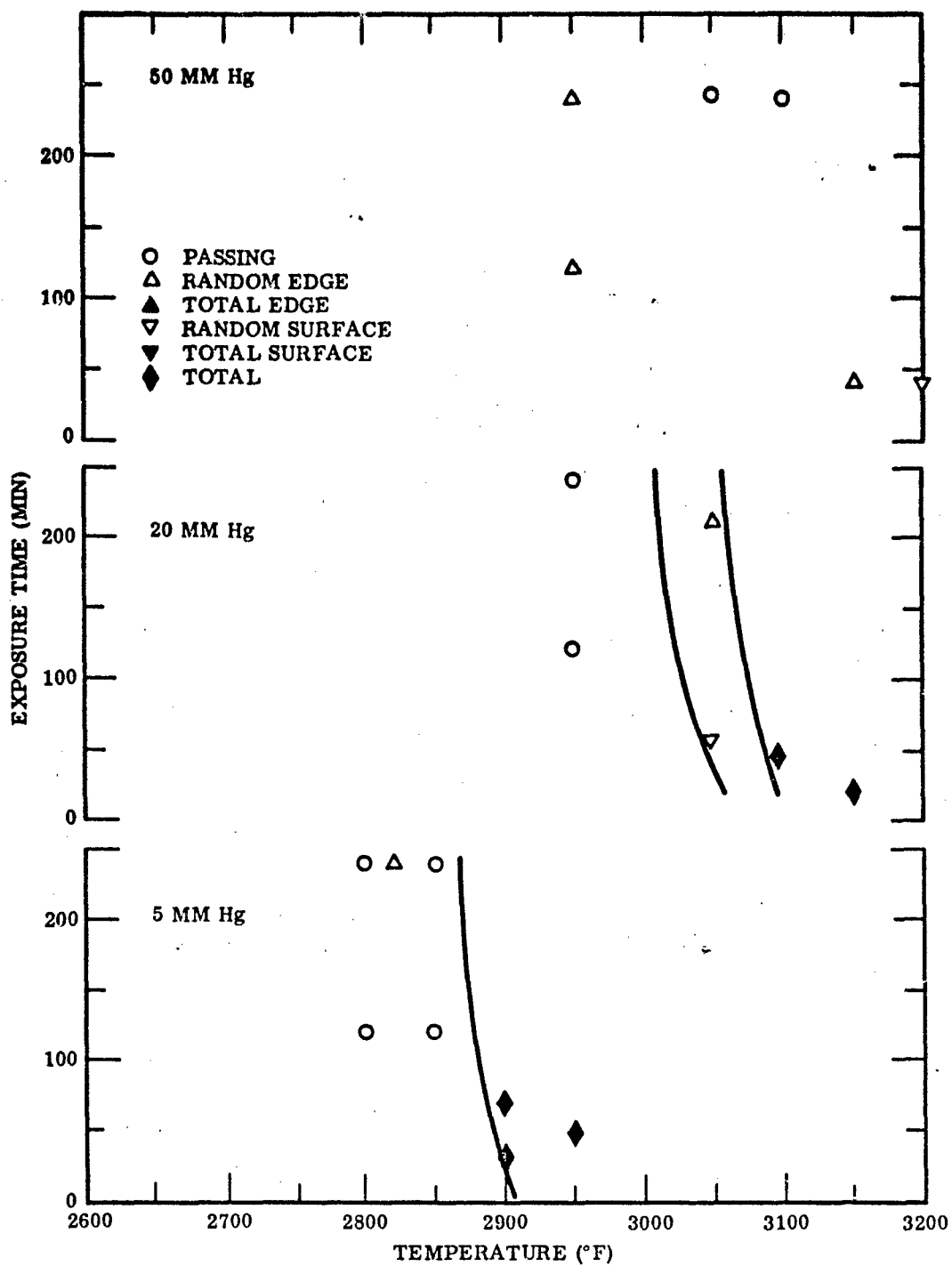
Figure 63 Results of Baseline Tests, TZM/Durak-B (cont'd)

153
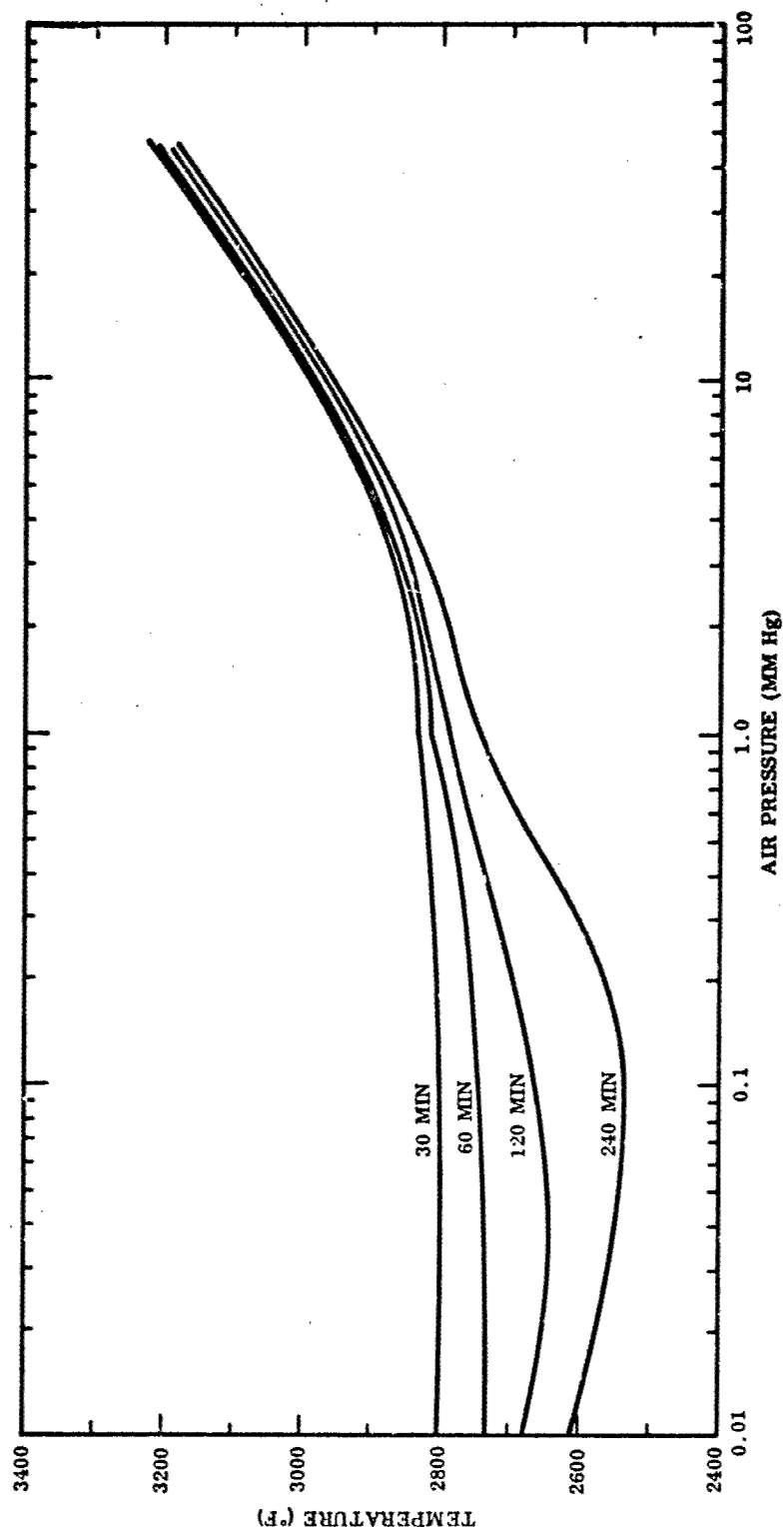
Figure 64 Baseline Total Failure Limits, TZM/Durak-B

154

P986   (A) 760 mm Hg, 2700° F, 240 min   ×500
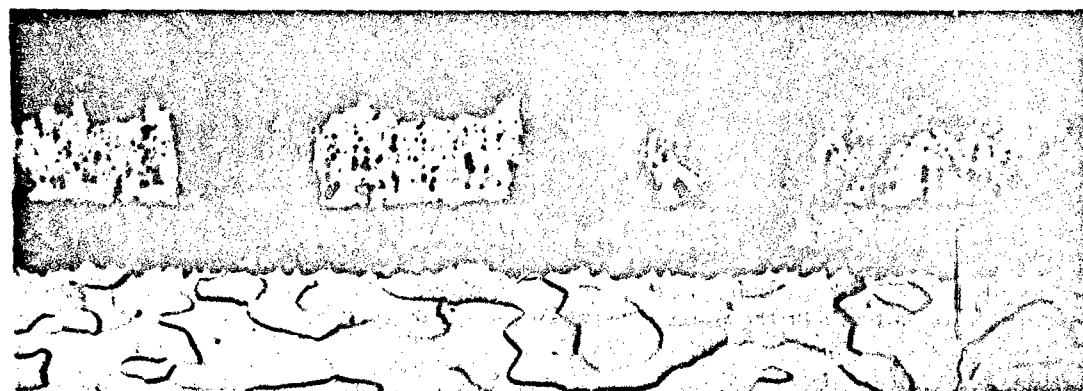
P924   (B) 1 mm Hg, 2800° F, 30 min   ×500

P985   (C) 0.1 mm Hg, 2700° F, 240 min   ×500

Figure 65   Effect of Pressure on TZM/Durak-B Structure

155

interior of the cracks and the environment was limited, and the oxygen partial pressure was reduced inside the cracks. Consequently, the interior of the cracks (i.e., that portion not filled with glass) underwent low-pressure oxidation with resultant widening of the crack. Consider Figure 65A. Here the environmental air pressure was 760 mm Hg and there were only a few patches of Mo_5Si_3 on the specimen surface, yet there is a continuous layer of Mo_5Si_3 around the widened portion of each crack. This is certainly strong evidence for accelerated, low-pressure attack at the inner surfaces of cracks. Of course, as the environmental air pressure decreases, the corresponding pressure within the cracks decreases and there is intensified attack of the crack surfaces. See, for example, Figure 65B. Because cracks were widened and more severe attack occurred around cracks, the effective coating thickness was reduced. When specimens were exposed to lower pressures where the mode of oxidation entailed general surface recession, coating failure occurred sooner than would have been the case if the density of cracks were less. Defects therefore had a greater relative effect in TZM/Durak-B at low pressures than in other systems. Interestingly, however, the overall performance was comparable to that of the other systems.

The fact that bubble formation was observed only at 50 mm Hg may be further evidence of a more fluid glass than, say, TZM/PFR-6 where bubbling was observed from 5 to 50 mm Hg. That is, with TZM/Durak-B a higher ambient pressure may be required to stabilize a bubble. Of course, bubble formation was observed only in an isolated case with TZM/Disil; on the basis of this and the high-velocity flow results, the glass on TZM/Disil appeared to be the most viscous of the three systems.

Gas Velocity

The emittance values and temperature correction curves used in studies with the other TZM systems were also assumed for TZM/Durak-B. To support this assumption, the growth rates of Mo_5Si_3 in high-velocity specimens were compared with those in corresponding baseline specimens where the temperature was known with certainty. There was good agreement, and it was concluded that the emittances of the three coated TZM systems were, indeed, equivalent.

The results of these studies are presented in Table XXX. It is clear that the high-velocity gas flow had little, if any, effect on the performance of this system. In view of the discussion on the fluidity of the glass, this might seem unusual. However, since the performance of this system was so highly keyed to the oxidation behavior within the cracks and since the interior of the cracks was unaffected by high-velocity flow, the performance under the flow conditions should not be seriously degraded. The more fluid glass may be washed from the surface by flowing air, with some increase in surface recession, but performance still is governed by reactions occurring within coating defects.

Vacuum Volatility

The results of the vacuum volatility studies with TZM/Durak-B are presented in Figure 66 and Table XXXI. The general behavior was similar to that of TZM/PFR-6 and TZM/Disil. The specific weight-loss values corresponded more closely to the weight loss of TZM/Disil, which is consistent with observations concerning the smoother surface of these two systems compared with that of TZM/PFR-6. A more detailed discussion of the vacuum volatility processes is given in the results sections for the other TZM systems.

156

Table XXX. Results of Mach 3 Flow Tests, TZM/Durak-B

Temp. (°F)	Total Pressure (mm Hg)	Atmosphere	Equivalent Air Pressure (mm Hg)	Time (min)	Performance Rating	Baseline Time to Failure (min)	
						Random	Total
3000	20	Air	20	60	Passing	>240	>240
3100	20	Air	20	44	Total Surface Failure	<30	30
3200	20	Air	20	26	Total Surface Failure	<30	<30
2750	20	$19:1::N_2:O_2$	5	60	Passing	>240	>240
2800	20	$19:1::N_2:O_2$	5	60	Passing	>240	>240
2900	20	$19:1::N_2:O_2$	5	45	Total Surface Failure	30	30
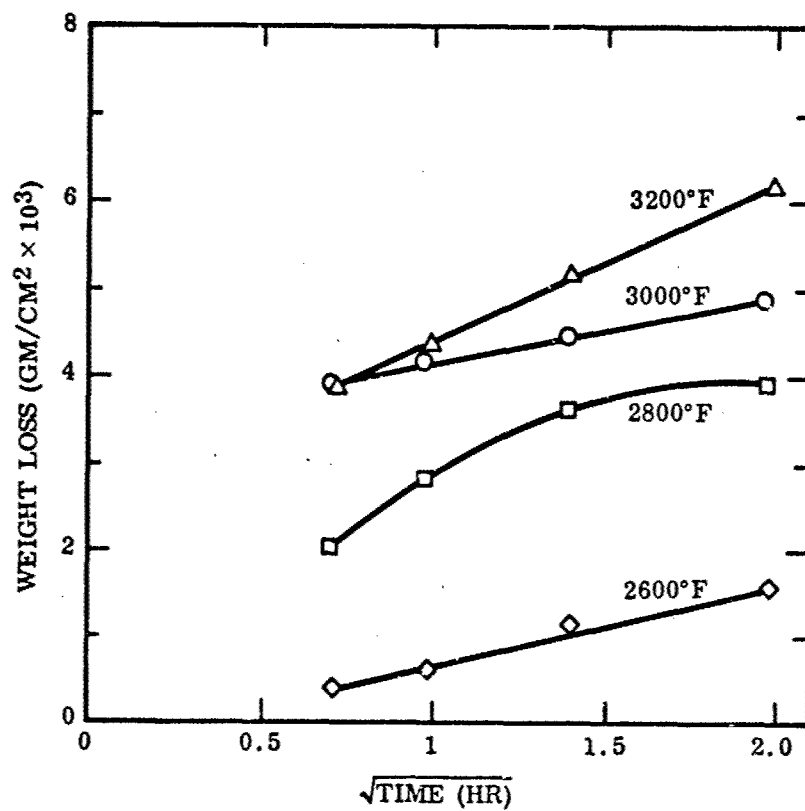
Figure 66 Vacuum Volatility Rate Curves, TZM/Durak-B

Table XXXI. Vacuum Volatility Data, TZM/Durak-B

Temp. (°F)	Pressure (mm Hg)	Time (hr)	Thickness		Thickness Change (mils/side)	Weight		Weight Change (gm/cm^2)
			Initial (mils)	Final (mils)		Initial (gm)	Final (gm)	
2600	1×10^{-5}	0.5	18.6	18.4	0.1	0.8582	0.8563	0.000388
	1×10^{-5}	1		18.4	0.1		0.8552	0.000612
	8×10^{-6}	2		18.4	0.1		0.8525	0.00116
	5×10^{-6}	4		18.4	0.1		0.8484	0.00200
2800	1×10^{-5}	0.5	19.0	18.6	0.2	0.9062	0.8963	0.00202
	7×10^{-6}	1		18.4	0.3		0.8922	0.00286
	5×10^{-6}	2		18.4	0.3		0.8885	0.00361
	3×10^{-6}	4		18.4	0.3		0.8873	0.00386
3000	1×10^{-5}	0.5	19.7	19.3	0.2	0.9736	0.9545	0.00390
	7×10^{-6}	1		19.2	0.25		0.9530	0.00421
	5×10^{-6}	2		19.2	0.25		0.9516	0.00444
	3×10^{-6}	4		19.1	0.3		0.9496	0.00490
3200	2×10^{-5}	0.5	18.4	18.0	0.2	0.8812	0.8624	0.00384
	1×10^{-5}	1		18.0	0.2		0.8601	0.00431
	9×10^{-6}	2		17.9	0.25		0.8558	0.00518
	6×10^{-6}	4		17.6	0.4		0.8510	0.00616

Average Area = 4.90 cm^2.

Temperature – Pressure Cycling

The experimental conditions and results are given in Table XXXII.

Although there was one random edge failure, no adverse effect can be attributed to cycling. It can be seen in Figure 63 that the baseline conditions of this experiment are within 40° F of the failure boundary. A temperature error of 40° F during the cycling experiments could not be considered unreasonable. The microstructure resulting from this test is presented in Figure 67 and should be compared with the structure of a specimen tested at 2800° F, 1.0 mm Hg, for 60 min (Figure 65B). The structures are similar with the notable exception that in the cracks there is less of the spongy mixture of oxides, lower silicides, and Mo characteristic of low-pressure oxidation. Apparently during the lower temperature, higher pressure phase of the cyclic process, the upper portion of the crack was widened sufficiently to allow the crack interior to reach ambient pressure during all subsequent phases of the test. It can be seen that the coating performance under these cyclic conditions may well be superior to that under baseline conditions. Again, it should be noted, however, that cycling was between two elevated temperatures and differed from the more conventional tests in which samples are cooled to room temperature after each cycle. The tendency for defect formation or propagation and growth of defects is minimized by not cooling to room temperature.

Acoustic Vibration

The microstructures of those acoustically irradiated specimens were examined and compared with the as-coated structures. No differences were evident, and it was concluded that acoustic vibration had no effect on this system.

Defect Tolerance and Repair

In simple bending at room temperature, the Durak-B coating fractured at about a 12-deg bend angle, and, as a consequence of coating fracture, the substrate fractured at the same bend angle. This indicates that care must be taken to avoid any deformation of this system at low temperature after coating. As previously mentioned, however, bends of as much as 30 deg could be made at 250° F without severe cracking and spalling of the coating or fracture of the substrate.

A specimen that was bent to about 10 deg at 75° F was oxidation-tested at 2775° F for 60 min at 1.0 mm Hg. The specimen passed, and it was concluded that any excess cracks had no significant effect on coating performance.

The results of the impact tests are presented in Table XXXIII. The results were similar to the other coated TZM systems when specimens were tested on a rubber backup to permit some deformation of the sample. However, on a steel backup the coating fractured at a lower energy level than in other systems. This may be consistent with the simple bend, slow strain rate observations. The substrate, however, did not fracture at the highest energy level used.

160
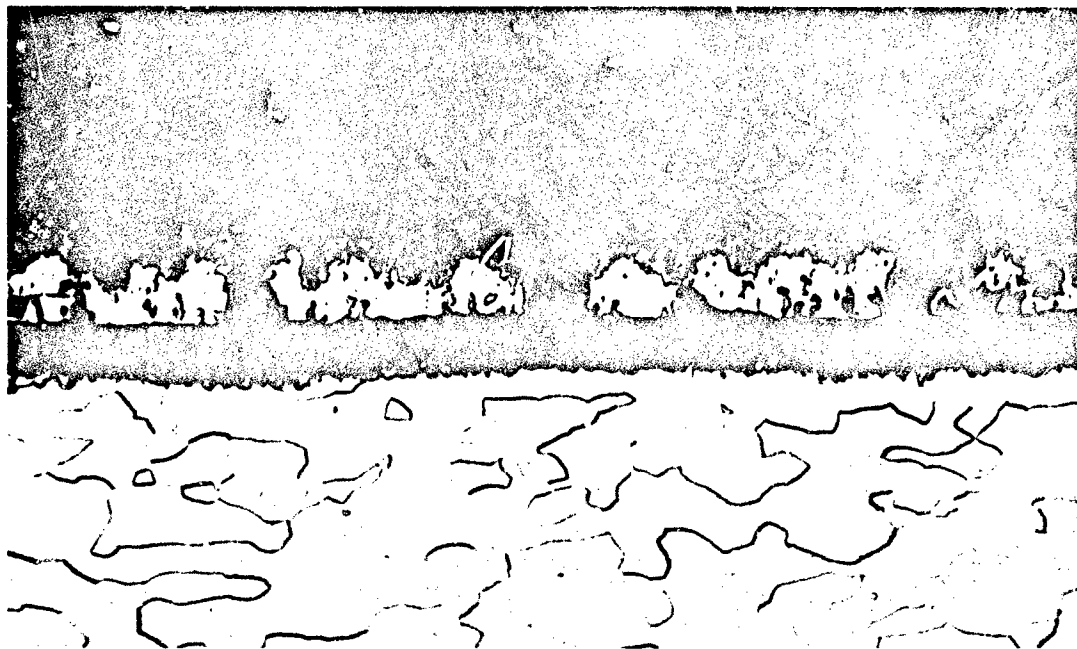
P921   ×500

Figure 67 TZM/Durak-B Structure After 4 Cycles From 2800°F, 1.0 mm Hg,
7 min, to 2200°F, 3.0 mm Hg, 21 min

161

Table XXXII. Results of Temperature-Pressure Cycling Tests, TZM/Durak-B

Phase of cycle	Temp. (°F)	Pressure (mm Hg)	Time (min)	No. of cycles	Total time (min)	Performance rating	Baseline time to failure (min)	
							Random	Total
1st (base-line)	2800	1.0	7		28		90	90
				4		Random edge failure		
2nd	2200	3.0	21		84		–	–

Table XXXIII. Results of High-Velocity Impact Tests, TZM/Durak-B

Backup material	Kinetic Energy (ft-lb)[a]					
	Spalling		Coating fracture		Substrate fracture	
	Pass	Fail	Pass	Fail	Pass	Fail
Rubber	<0.3	0.3	<0.3	0.3	<0.3	0.3
Steel	1.7	2.3	0.7	1.0	2.3	>2.3

(a)Calculated from projectile mass and velocity at time of impact.

The results of studies with specimens containing defects in the form of slots 0.05 in. by one-half or three-fourths of the coating thickness are presented in Table XXXIV. These results demonstrated the ability of this system to tolerate gross defects of a rather severe nature. The microstructure of the defective region of the specimen tested at 1.0 mm Hg is shown in Figure 68. The coating is still protective under the defect; however, it is obvious that it is near failure and would not withstand a much longer exposure. The baseline studies indicated that glass could fill the lower portions of the cracks and that it was the upper regions of cracks that were attacked and broadened. It was not surprising, therefore, that removal of the outer portions of the cracks, as was done in these defect tolerance studies, did not greatly influence the performance. In addition, and of equal importance, was the fact that a thicker layer of glass had formed in the defect region.

The few, premature random failures that were observed and noted in Table XXXIV were probably the result of variations in defect patterns of the as-coated samples or slight temperature errors.

Repair studies were not conducted with TZM/Durak-B, but it is felt that any repair processes that are successful with TZM/Disil and TZM/PFR-6 would be equally successful in this system.

Materials Compatibility

The results of the materials compatibility studies are presented in Table XXXV. The failure noted for the couple with Ta-10 W/Sn-Al was the result of liquid metal attack on the contact surface by products from the Sn-Al coating rather than any oxidation effect. Also the TZM/Durak-B surfaces not in contact with the Ta-10 W/Sn-Al were well protected from oxidation.

P919   ×1000

Figure 68   One Side of a 0.005 in. by 3/4 t Defect in TZM/Durak-B After Testing,
2850°F, 1.0 mm Hg, for 30 min

164

Table XXXIV. Defect Tolerance Results, TZM/Durak-B (Defects in the form of slots 0.005 in. by 1/2 or 3/4 of coating thickness)

Test conditions			Performance rating			Baseline time to failure (min)	
Temp. (°F)	Pressure (mm Hg)	Time (min)	1/2 t	3/4 t	Bulk specimen	Random	Total
2850	1.0	30	Passing	Passing	Random surface failure	90	90
2950	20	120	Passing	Passing	Random surface failure	>240	>240
3000	20	60	Passing	Passing	Passing	>240	>240
3050	20	60	Passing	Passing	Random surface and edge failure	40	>240

Table XXXV. Materials Compatibility With TZM/Durak-B

Contact material	Test conditions			Performance rating	Baseline time to failure (min)	
	Temp. (°F)	Pressure (mm Hg)	Time (min)		Random	Total
TZM/PFR-6	2525	1.0	45	Passing	>240	>240
Cb-752/CrTiSi	2525	1.0	60	Passing	>240	>240
Cb-752/PFR-32	2675	1.0	60	Passing	>240	>240
B-66/CrTiSi	2675	1.0	60	Passing	>240	>240
Ta-10W/Sn-Al	2700	1.0	60	Total failure[a]	>240	>240
MoSi$_2$	Compatible under all baseline conditions					
SiO$_2$	Compatible under all baseline conditions					
Al$_2$O$_3$	Compatible to 2700°F in 1 atm air					

(a) This was not an oxidation failure but a result of liquid metal attack on the TZM/Durak-B.

165

Cb-752/PFR-32

Material Evaluation

PFR-32 is a slightly modified $CbSi_2$-base coating applied by a single-cycle pack process. Details of composition and process history are proprietary (Pfaudler Corp., Rochester, N. Y.) In the initial development work by Pfaudler, a two-cycle process was used. The single-cycle process, developed recently, was selected for use in this program by mutual agreement of the Air Force Materials Laboratory, Pfaudler Corp., and LMSC.

The general appearance of the as-coated test specimens is shown in Figure 69. Each specimen was uniform in color on both sides, but color from specimen to specimen varied from light to dark gray. Surfaces were moderately smooth, but small protusions occurred in a random distribution, as shown in Figure 69B. Edge quality was variable, with wide fissures along many edges (Figure 69B). In other areas, good edge coverage was attained.

Structures representative of as-coated samples are shown in Figures 70 and 71. Edge defects (Figure 70A) tended to be moderately deep V-shaped notches. Most of these large defects ranged from one-half to three-fourths of the coating thickness in depth (to root of notch). Fine hairline cracks, however, often extended from the root to the substrate/coating interface. Numerous hairline cracks or fissures existed on all flat surfaces. These extended from surface to substrate, as shown in Figures 70 and 71. In most cases, the cracks were oriented perpendicular to the surface but branched into two or more fissures running parallel to the surface just above the substrate/coating interface. This longitudinal crack propagation occurred in the innermost 0.5- to 0.75-mil-thick region of the coating. As shown in Figure 71, this zone contained less of the fine second phase observed in the coating than did the bulk of the coating.

Structural details of the coating and substrate near the interface are shown in Figure 71B. The coating has a columnar structure with long grains oriented perpendicular to the surface. The hairline cracks extending inward from the surface are intergranular, following the vertical boundaries of the columnar grains. The zone near the substrate/coating interface also has a columnar structure but in addition shows traces of the large equiaxed grain structure of the substrate (Figure 71A). The columnar grain size in this zone is much finer than that of the bulk of the coating. A thin diffusion zone about 0.02 to 0.05 mil thick is also evident just below the substrate/coating interface (Figure 71B). In the fine columnar grain zone, the main cracks branch into two or more transgranular (cleavage) fissures running parallel to the interface. In some cases, however, the cracks extend on into the substrate, as shown in Figure 71B. As will be described later, these hairline fissures exist in the coated samples and are not the result of metallographic preparation. As one type of defect characteristic of these samples, they will be shown to play an important role in the overall performance capabilities of this system.

A qualitative spectrochemical analysis of the coating revealed Cb, Si, W, and Zr to be the major elements present. In addition, a trace of Al was found. Since the coating is formed by reaction of silicon with the alloy, it is not surprising to find both W and Zr in the coating (Cb-10W-2.5Zr alloy). Aluminum may have been an intentional addition through the pack or may be an impurity picked up in the processing The coating appears to be basically $CbSi_2$, with one or more dispersed phases.

166
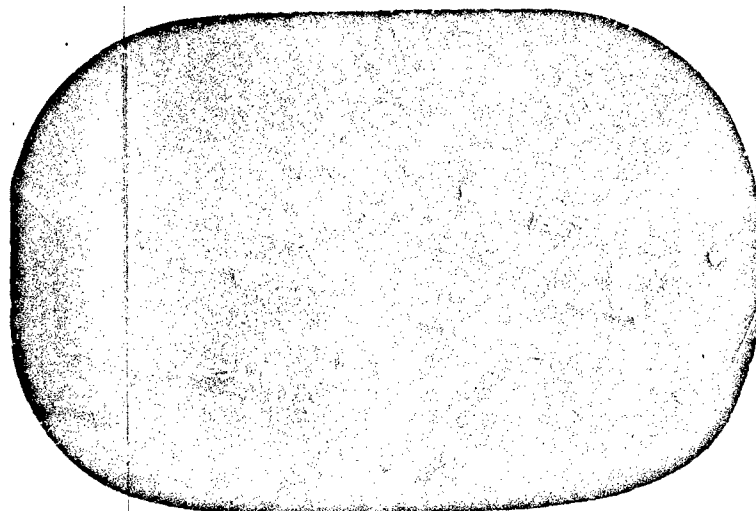
M9968   (A) Surface   ×6

M5640   (B) Edge and Surface   ×18

Figure 69   General Appearance of As-Coated Cb-752/PFR-32

M6098   (A) Edge   ×500
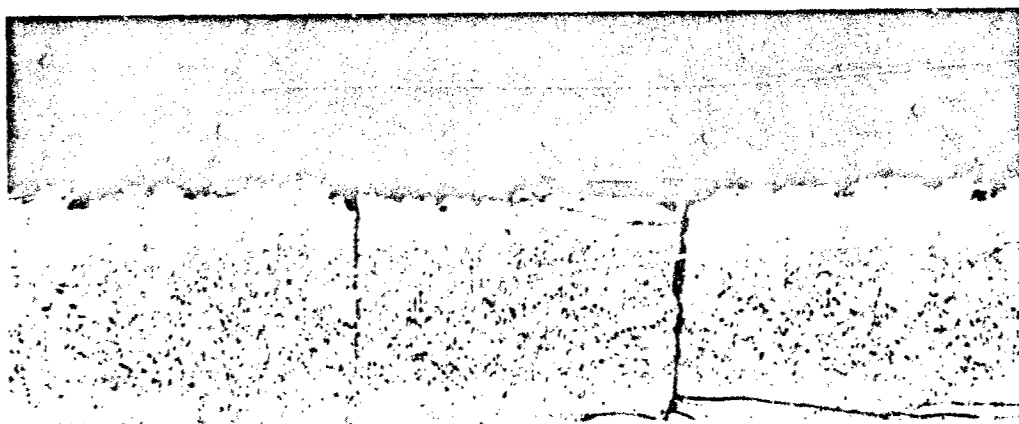
M8303   (B) Surface   × 500

Figure 70   Representative Microstructure of As-Coated Cb-752/PFR-32

168

M8850   (A) General Structure   ×1000

M8356   (B) Detail of Coating Structure   ×3000

Figure 71 Microstructural Details of As-Coated Cb-752/PFR-32, Substrate/Coating Interface

169

The microstructure of the substrate was identical to that of the uncoated sheet stock. Moderate hardening of the substrate was noted, however, as shown in Figure 72. Average substrate hardness increased by 29% from 173 DPH uncoated to 223 DPH coated. Hardness was uniform through the cross section, with no major rise in hardness above the average to within 0.5 mil of the substrate/coating interface. Lack of a hardness gradient indicates that the hardness increase was not due to contamination during coating. Diffusion rates are sufficiently low at coating temperatures to produce a hardness gradient through the cross section if contamination by O, N, or Si had occurred. It is believed that the increase was due to an aging reaction in the substrate as a result of the coating process thermal cycle. Solution-annealed Cb-752 sheet will age to over 200 DPH upon heating 1/2 hr at 1900° F (30). At 2400° F the precipitate over-aged such that hardness decreased to about 186 DPH. Resolutioning occurred upon heating above 2400° F. Since the coating process temperature is probably in the range of 1800 to 2000° F, hardening by aging could be anticipated. As shown in Figure 72, the substrate in coated samples softened on oxidation testing at 2700° F, followed by rapid cooling. This behavior also is in agreement with results of studies on the heat treatment response of the Cb-752 alloy.

Bend tests conducted on random samples early in the program indicated good room-temperature ductility. Samples were clamped in a machinist's vise and bent by hand over a 4t radius at room temperature. Ninety-degree bends were made without substrate fracture. However, 15 months later, a series of instrumented bend tests was conducted in which all samples exhibited extreme embrittlement at room temperature. Also, ductile bends could not be made at room temperature by hand bending in the vise as done previously. Heating to 250° F was necessary for ductile bending at this time. Room-temperature bend ductility was restored, however, upon heating above 2400° F for 30 min. Thus, room-temperature bend ductility after oxidation testing was a valid performance criterion for this coating system throughout the program. These aspects of bend ductility behavior are discussed in detail subsequently.

The average coating thickness, determined from 25 measurements on the cross section of each of three samples, was 2.90 mils. Thicknesses on the individual samples were 2.65 ± 0.1, 3.25 ± 0.15, and 2.80 ± 0.2 mil. Two nondestructive methods, one based on thickness increase and the other on weight increase after coating, were used to obtain a more valid indication of average coating thickness and uniformity of thickness for the overall lot of samples. Results of a statistical study based on the micrometer measurement of the thickness of 100 samples before and after coating are presented in Figure 73. Corresponding normal distribution curves calculated from $\bar{x}$ and σ values are superimposed to show the nature of distributions obtained by sampling.

Average thickness ($\bar{x}$) increased from 20.7 to 26.1 mils as a result of coating. The difference between these two values does not represent true coating thickness, however, since some of the substrate is consumed in making the coating. Assuming that the coating is essentially $CbSi_2$ of theoretical density 5.72 gm/cc, it can be calculated from the reaction

$$Cb + 2Si = 2CbSi_2 \tag{33}$$

170
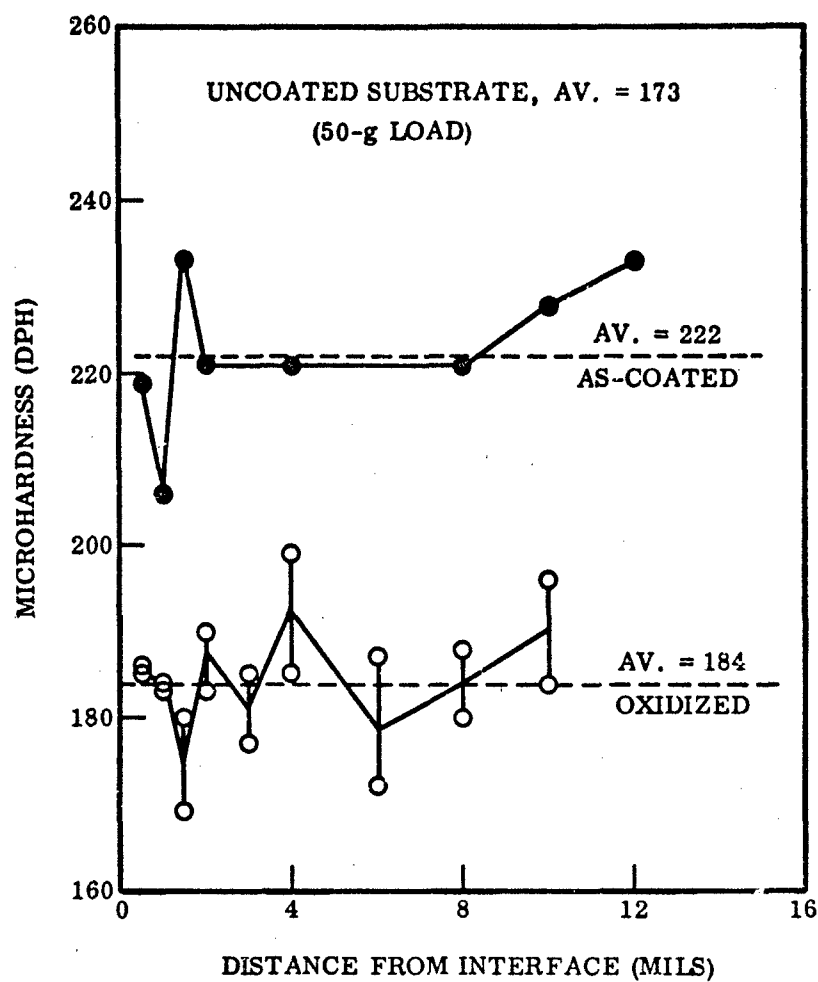
Figure 72 Substrate Hardness Traverse of As-Coated and Oxidized
(4 hr, 2700°F, 760 mm Hg) Cb-752/PFR-32

171
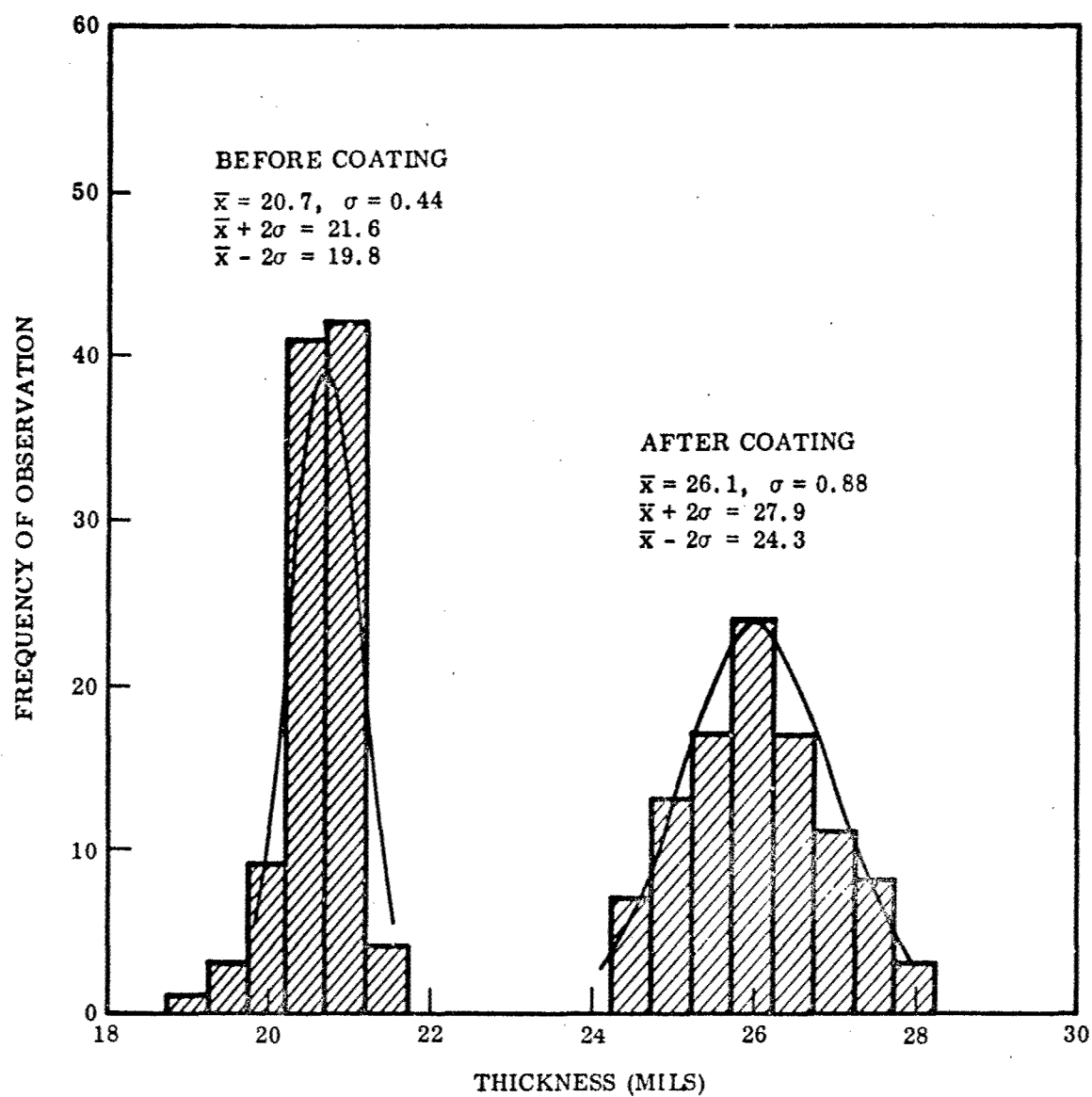
Figure 73 Statistical Analysis of Total Thickness of Cb-752/PFR-32
Before and After Coating

172

that 1 mil of Cb will be consumed in producing 2.4 mils of $CbSi_2$. Using a reasonable assumption of 1 mil/side of substrate consumed during production of the coating, average coating thickness is calculated to be 3.7 mils/side $[2.61 - (20.7-2.0)]/2$. The standard deviation in coating thickness can be calculated from the simple relation

$$\sigma_T^2 = \sigma_c^2 + \sigma_s^2 \tag{34}$$

where σ_T, σ_s, and σ_c are the standard deviation of thickness for the total sample after coating, the substrate before coating, and the coating, respectively. The value of σ_c was calculated as 0.76 mil (2 sides) or 0.38 mil/side. Based on 2σ limits, 95% of the samples would be expected to have a coating between 2.94 and 4.46 mils thick (3.7 ± 0.76).

Since these calculations are based on micrometer measurement of thickness, average and standard deviations are representative of maximum coating thickness. The surfaces are rough by nature, and the micrometer measures distance between high spots only. Maximum coating thickness from metallographic measurements on cross sections of three samples was 2.75, 3.4, and 3.0 mils, giving an average of 3.05 mils. Considering that only three samples were measured, agreement with the calculated average and deviation based on 100 samples is good.

A second estimation of average coating thickness was obtained from weight measurements. A statistical study of 100 samples weighed before and after coating yielded the following results (in grams):

Value	Before Coating	After Coating
$\bar{x}$	1.01	1.08
σ	0.0261	0.0307

Assuming the weight increase of 0.07 gm to be silicon pickup and the coating to be $CbSi_2$ of theoretical density, average coating thickness also can be calculated from Equation (33). The average sample area measured on five specimens was found to be 4.9 cm^2. Weight increase, therefore, was 0.0143 gm/cm^2. This corresponds to 0.0378 gm/cm^2 of $CbSi_2$, which when divided by density gives the average coating thickness as 0.0066 cm or 2.60 mils. This value is in very good agreement with the averaged measured thickness of 2.90 mils for three samples.

The deviation in weight increase calculated from Equation (34) is 0.0162 gm. From this figure and the same assumptions as before, standard deviation in coating thickness is calculated to be 0.6 mils. Thus, based on a 2σ limit, 95% of the samples would be expected to have a coating between 1.4 and 3.8 mils thick (2.60 ± 1.2). The standard deviation in thickness, calculated from weight change, is about 50% greater than that calculated from thickness change. Because the samples were sheared and hand ground to final dimensions, uniformity of size and hence weight of the original specimen blanks was poor, resulting in large values for sigma before and after coating. Calculated sigmas for coating thickness based on weight measurements are excessively broad as a result and do not necessarily indicate the true uniformity of coating thickness.

In summary, the following results for average coating thickness and range of values were obtained:

Direct measurement:	$2.90 \pm \genfrac{}{}{0pt}{}{0.35}{0.25}$ mils
Calculated from thickness:	3.70 ± 0.76 mils
Calculated from weight:	2.60 ± 1.2 mils

For purposes of this study, it is assumed that average coating thickness on the tabs is 2.75 ± 0.5 mils per side.

Baseline Behavior

Individual test results of baseline tests are plotted in Figure 74 and are tabulated in Appendix III. Both random and total failure boundaries for each of the six pressures from 0.01 to 50 mm Hg are shown in Figure 74. A marked change in performance capabilities is seen to occur at air pressures between 1 and 5 mm Hg. At 5 mm Hg and above, the random and total failure boundaries are widely separated and air pressure appears to have little effect on overall performance. A significant drop in performance occurs at pressures of 1 mm Hg or lower, however, and the random and total failure boundaries are comparatively close together.

These differences and trends in behavior are shown more clearly in Figure 75. Here, the random and total failure boundaries expressed as the maximum temperature for 30-, 60-, 120-, and 240-min life are described as a function of air pressure. The data also are summarized in Table XXXVI. At 5 mm Hg pressure, random failure will occur in 30 min at 2875° F. However, exposure for 240 min at this temperature and pressure is required to produce total failure. At 1 mm Hg pressure, random failure occurs in 60 min at 2700° F, and total failure occurs in 120 min. The significance of these relations is further illustrated by the following maximum temperature capabilities for a life of 1 hr:

	Failure Limit	
	Random	Total
Air — 5 mm Hg	2860° F	2940° F
Air — 1 mm Hg	2700° F	2735° F

Thus, not only is the maximum temperature capability reduced at low pressure but also the margin of safety between conditions for a random but perhaps tolerable failure and a total or catastrophic failure is greatly reduced.

The general effect of air pressure on performance capabilities is best illustrated in Figure 75. Pressure in the range of 5 to 50 mm Hg was found to have virtually no influence on performance for coating lifetimes out to 4 hr. It is likely that results in this range are the same as those that would be obtained by testing in air at 1 atm. A minimum in performance was observed at 1 mm Hg pressure. At lower pressures, little effect on temperature was observed for the longer times to failure, but for short-time use (30 min) the temperature increased. Surprisingly, at 0.01 mm Hg the temperature for a 30-min life (random failure) exceeded that for 50 mm Hg pressure by 100° F (1 mm = 2975° F, 50 mm = 2875° F).

174

Table XXXVI. Baseline Data, Cb-752/PFR-32

Air Pressure (mm Hg)	Maximum Temperature for Indicated Life (°F)			
	30 min	60 min	120 min	240 min
Random Failure Limits				
50	2875	2860	2825	2800
20	2875	2860	2825	2800
5	2875	2860	2800	2790
1	2725	2700	2675	2650
0.1	2925	2770	2710	2650
0.01	2975	2740	2680	2650
General Failure Limits				
50	2975	2940	2910	2875
20	2975	2940	2910	2875
5	2975	2940	2910	2875
1	2760	2735	2700	2675
0.1	2925	2780	2725	2675
0.01	>3000	2975	2725	2675

These changes in performance capabilities with reduced air pressure were the result of changes in the basic mechanisms of protection and failure. Two observations indicate that a marked change in oxidation behavior occurred in air at pressures between 1 and 5 mm Hg. First, at 5 mm Hg or higher, the initial failures occurred at random sites on the flat surfaces. At 1 mm Hg or lower, however, failure sites appeared first in random locations on the edges. Thus, the mode of failure shifted from random surface to random edge control with decreased pressure between 5 and 1 mm Hg. Second, a significant change in the characteristics of the oxide film occurred in this pressure range. At 5 mm Hg and above, a clear, glassy, adherent oxide was formed. The color of the specimen was light gray to tan. However, near failure boundaries, random flecks of a rust-colored phase appeared in the glassy film. At pressures of 1 mm Hg and lower, a loose, powdery, or flake-type oxide was formed. The scale tended to be blue-black and generally spalled off upon cooling to room temperature. X-ray diffraction studies of the spalled scale revealed CbO_2 to be the major constituent. As shown in Table XXXVII, lines that could be ascribed to CbO and Cb_5Si_3 were also found in the pattern. No lines identifiable with Cb_2O_5 or SiO_2 were found.

Detailed metallographic studies were conducted to provide a better understanding of the oxidation behavior of this system. The general effect of pressure on coating structure and thickness is shown in Figure 76. General microstructure of the coating was virtually identical after testing at 760, 5, and 0.1 mm Hg. The only significant differences observed at these pressures were in the relative thickness of the coating that remained and the nature of oxide scales formed. For equivalent temperatures and times (to 4 hr), no significant differences in coating thickness and oxide scale were observed in samples tested at pressures from 5 to 760 mm Hg. (Note the differences in temperature, time, and magnification in Figures 76A and 76B.) These observations support the general conclusion
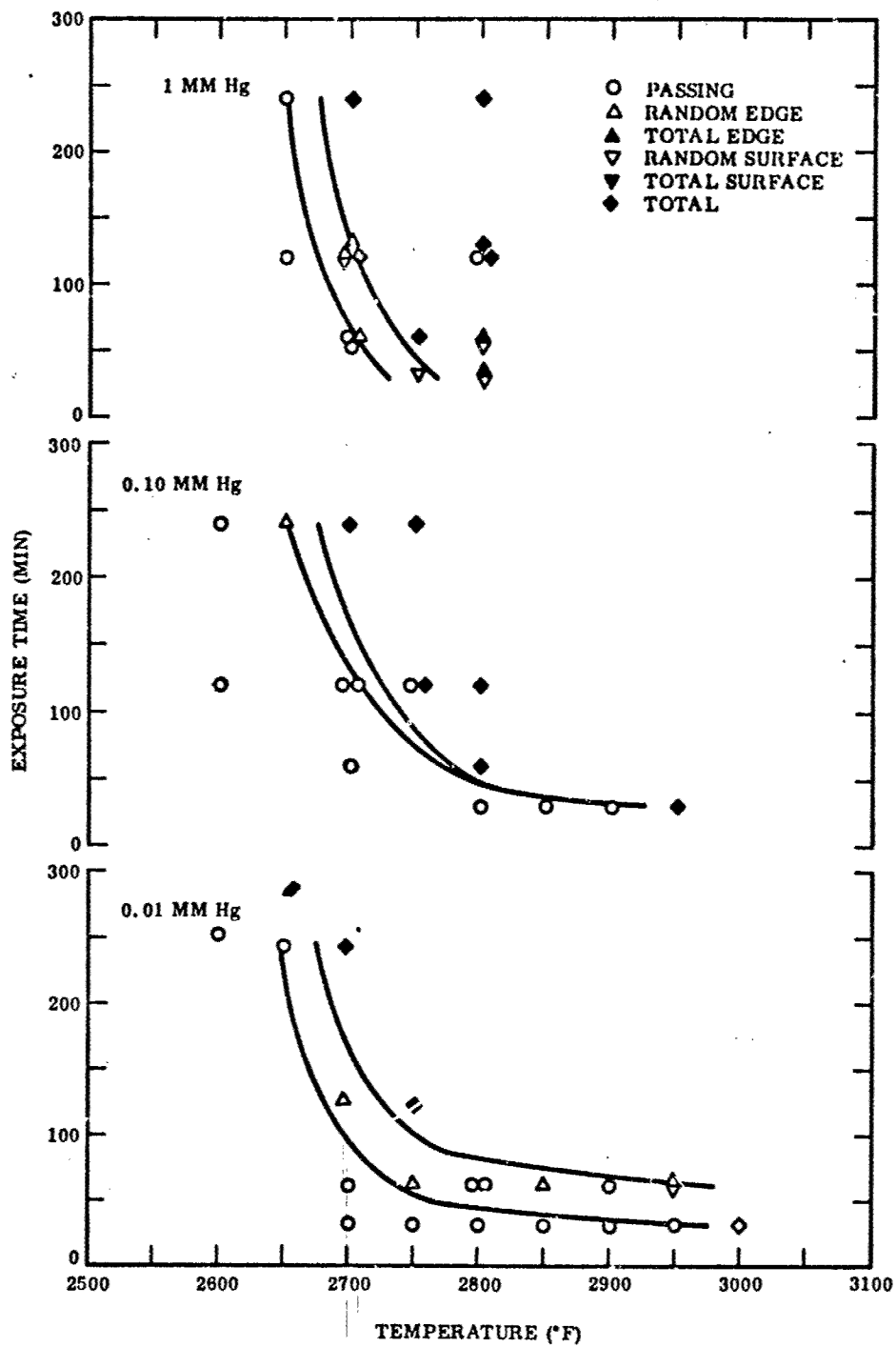
175

Figure 74 Results of Baseline Tests, Cb-752/PFR-32

176
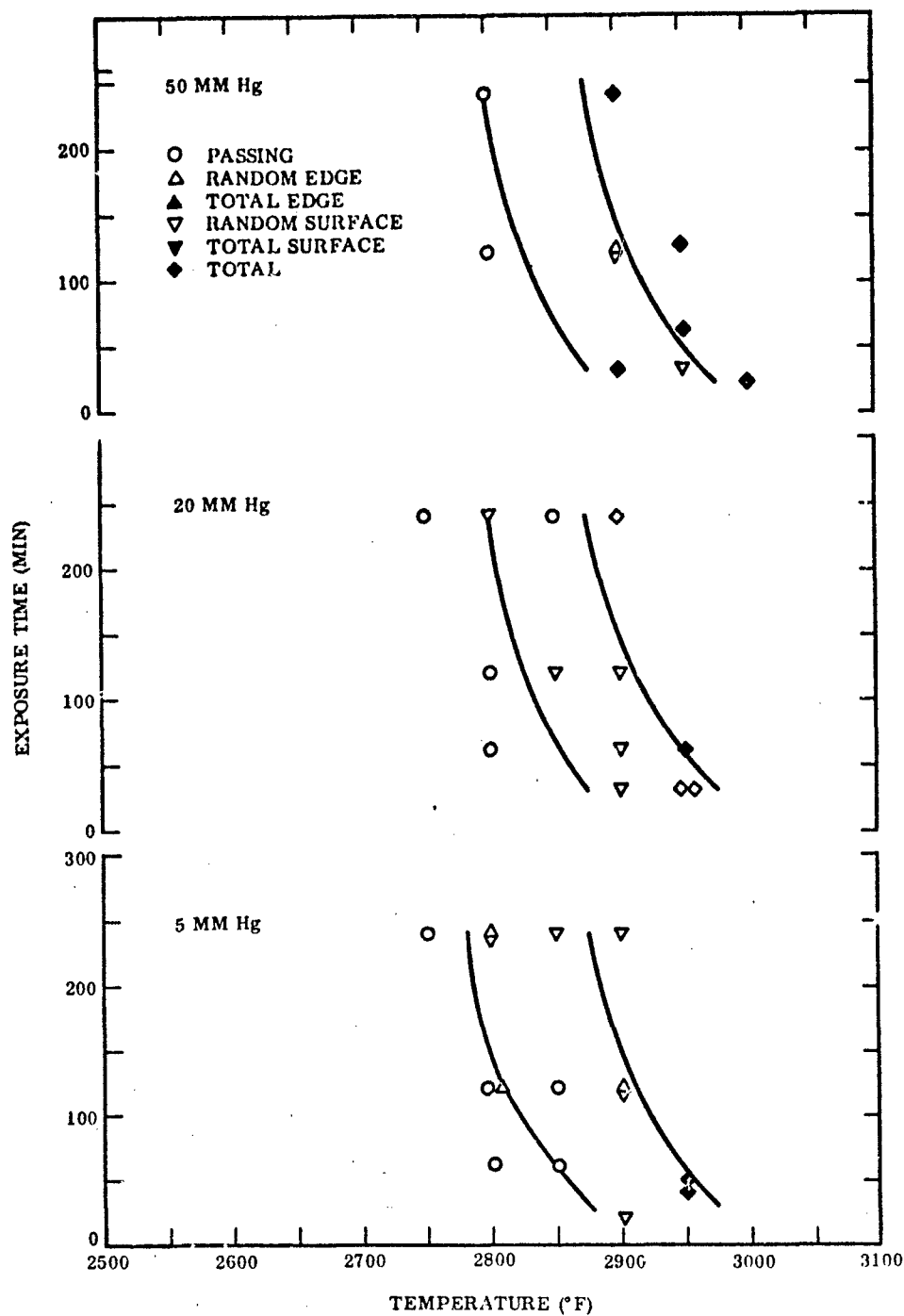
Figure 74 Results of Baseline Tests, Cb-752/PFR-32 (cont'd)

177
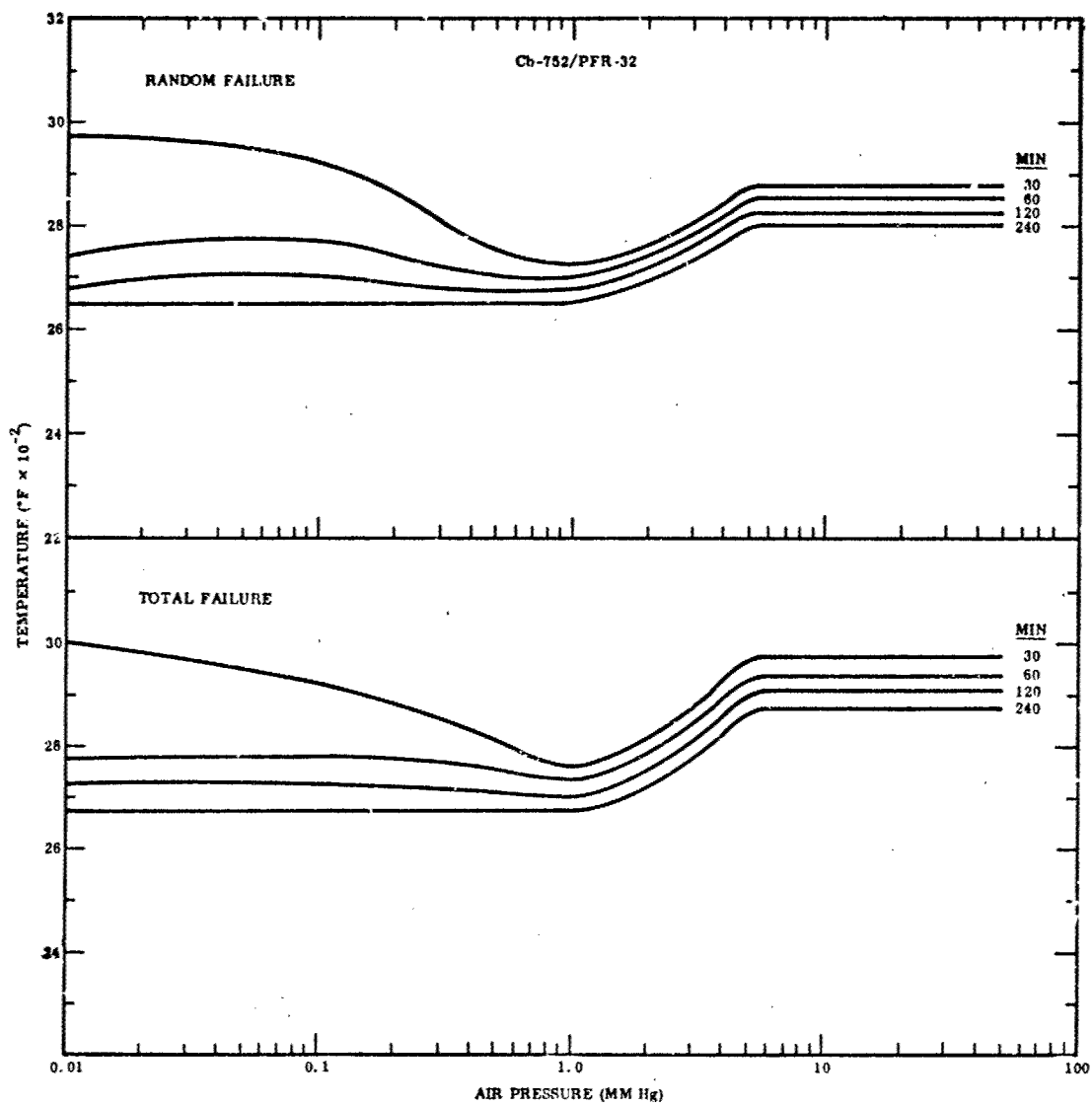
Figure 75 Baseline Failure Limits, Cb-752/PFR-32

178

Table XXXVII. X-ray Diffraction Data
(Scale from Cb-752/PFR-32 specimen exposed to air at 2800° F
and 0.10 mm Hg for 62 min)

Observed		ASTM data					
		CbO_2			Cb_5Si_3		
d	I[a]	d	I/I_1	hkl	d	I/I_1	hkl
		4.29	20	211			
		3.63	30	301			
3.74	L				3.256	30	200
3.42	H	3.42	100	400	3.045	50	111
2.54	H	3.21	30	321	2.623	10	002
2.42	M	2.91	30	411	2.460	50	210
2.25	M	2.54	80	223,520			
2.23	M	2.491	30	501,431	2.432	50	102
1.91	L	2.422	50	440	2.234	100	211
1.75	M	2.341	20	521	2.174	50	300
1.71	L	2.253	30	402	2.152	80	112
1.58	L	2.166	20	620	1.631	30	400
1.53	L	2.041	10	541	1.586	30	113
1.50	M	1.975	20	103	1.531	60	222
1.42	M	1.932	20	631	1.497	30	320
1.28	L	1.897	20	640,213	1.488	40	312
1.22	L	1.862	20	701	1.439	50	321
		1.829	20	303	1.424	80	213,410
		1.766	30	612,730,721	1.385	60	402
		1.754	80	267	1.311	50	004
		1.712	50	800			

(a) H = high; M = medium; L = low.
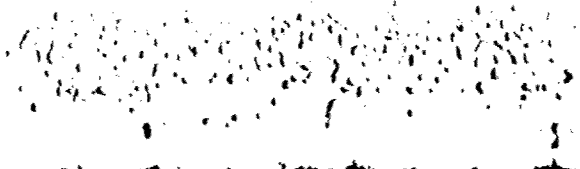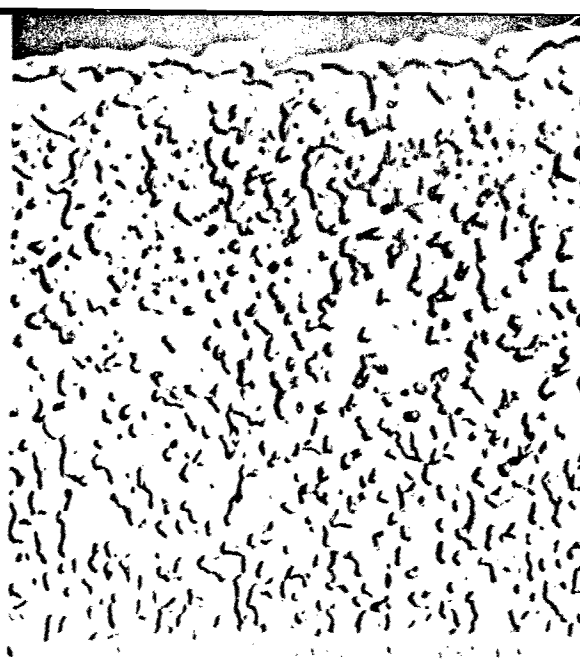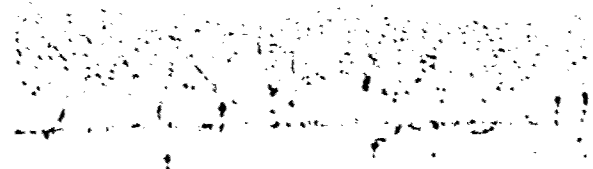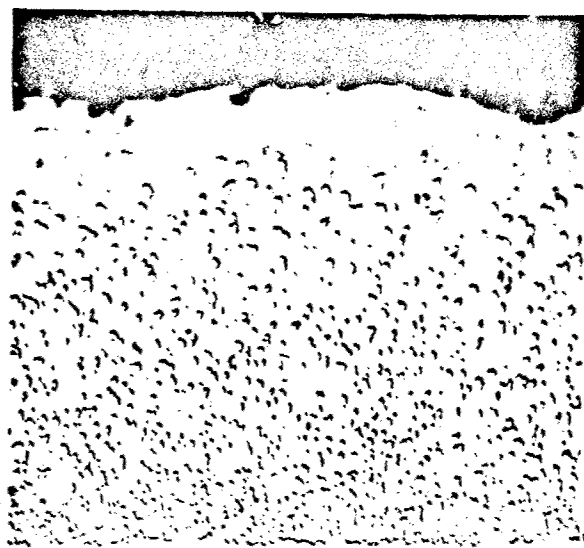
M6309 (A) 2700°F, 760 mm Hg, 240 min ×1000

M9268   (B) 2850°F, 5 mm Hg, 76 min ×1500
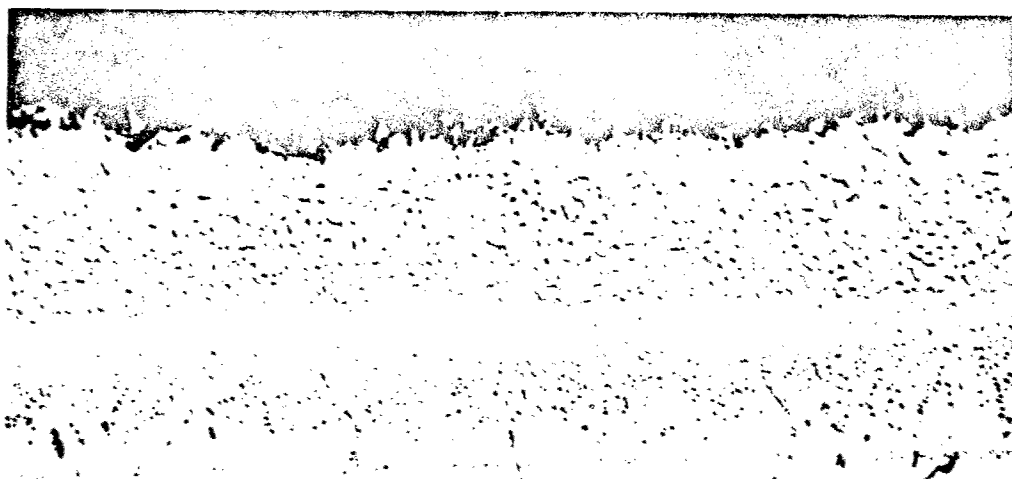
M6363   (C) 2700°F, 0.1 mm Hg, 120 min   ×1300

Figure 76 Effect of Air Pressure on Coating Structure and Thickness of Cb-752/PFR-32

180

that pressure in the range of 5 to 760 mm Hg h little, if any, effect cn oxidation behavior cf this system in exposure times to 4 hr. The major effect of pressure occurs on testing below 5 mm Hg and behavior in this region is characterized by high surface recession rates. As shown in Figures 76A and 76C, after 2 hr at 2700° F in air at 0.1 mm Hg, residual coating thickness was less than half that of a sample tested 4 hr at 2700° F in air at 760 mm Hg. (Note magnification differences.) In addition, the sample was covered with a thick black oxide scale containing a large amount of CbO_2 in a glassy matrix (Figure 76C).

Microstructural details of the PFR-32 coating on Cb-752 after exposure at reduced pressure are shown in Figure 77. The outer surface layer has been converted to Cb_5Si_3 by the selective oxidation of silicon. This layer also extends around the periphery of large fissures such as the edge defect shown in Figure 77. The bulk of the coating is $CbSi_2$ (containing some W and Zr) in which a second phase is dispersed. This phase is believed to be Cb_5Si_3, on the basis of its metallographic features and an apparent continuity with the outer Cb_5Si_3 layer. The inner diffusion layer consists of a graded mixture of Cb_5Si_3 and Cb_2Si with an underlying zone of primarily Cb_2Si. No trace of the lower silicide (Cb_3Si or Cb_4Si) was observed. These microstructural details are identical to those found for pure $CbSi_2$ coatings on Cb in diffusion studies conducted under an Air Force contract at LMSC (31). All samples of the Cb-752/PFR-32 system tested from 0.01 to 760 mm Hg at 2600−3000° F exhibited these same structural details.

This was a significant difference in behavior compared with the $MoSi_2$-base coatings on TZM or unalloyed Mo. In these systems at reduced pressure, the coating was converted completely to Mo_5Si_3 by selective oxidation of silicon after short exposure. This phase, in turn, was oxidized to a spongelike mixture of Mo, Mo_3Si, and glass. On the PFR-32 system, Cb_5Si_3 existed only as a discrete surface layer and random particles dispersed in the underlying $CbSi_2$ phase. This coating underwent a more uniform surface recession (only below 5 mm Hg pressure) and did not form the spongy mixture of coating and glass at low pressure. The slower rate of diffusion of Si in columbium silicides compared with molybdenum silicides as measured by substrate/coating diffusion studies (31) probably accounts for this significant difference in behavior.

As previously mentioned, failure was controlled by random defects in the Cb-752/PFR-32 system at pressures of 0.01 to 50 mm. However, the sites of random failure shifted from flat surfaces at pressures above 5 mm Hg to edges at pressures below 5 mm Hg. Failure at random surface sites in the higher pressure range is illustrated in Figure 78. The hairline defects previously described comprise the sites for attack. As shown in Figure 78A, attack began well below the surface of the coating by gradual widening of the hairline fissure. Oxidation also occurred along the transverse fissures that branch out along the original coating substrate interface. At the intermediate stage illustrated by Figure 78B, the main fissure broadened to a wide channel extending from the surface to the Cb_5Si_3/Cb_2Si diffusion zone. The reduced thickness of this zone beneath the transverse fissure is clear evidence that these branch cracks existed at the test temperature. Finally, the ultimate failure stage is illustrated by Figure 78C. Once the lower silicide layers were exposed, rapid oxidation occurred laterally along the substrate/coating

Cb₅Si₃

CbSi₂ + Cb₅Si₃

Cb₅Si₃

Cb₂Si + Cb₅Si₃

Cb₂Si

SUBSTRATE

M9264   ×1500
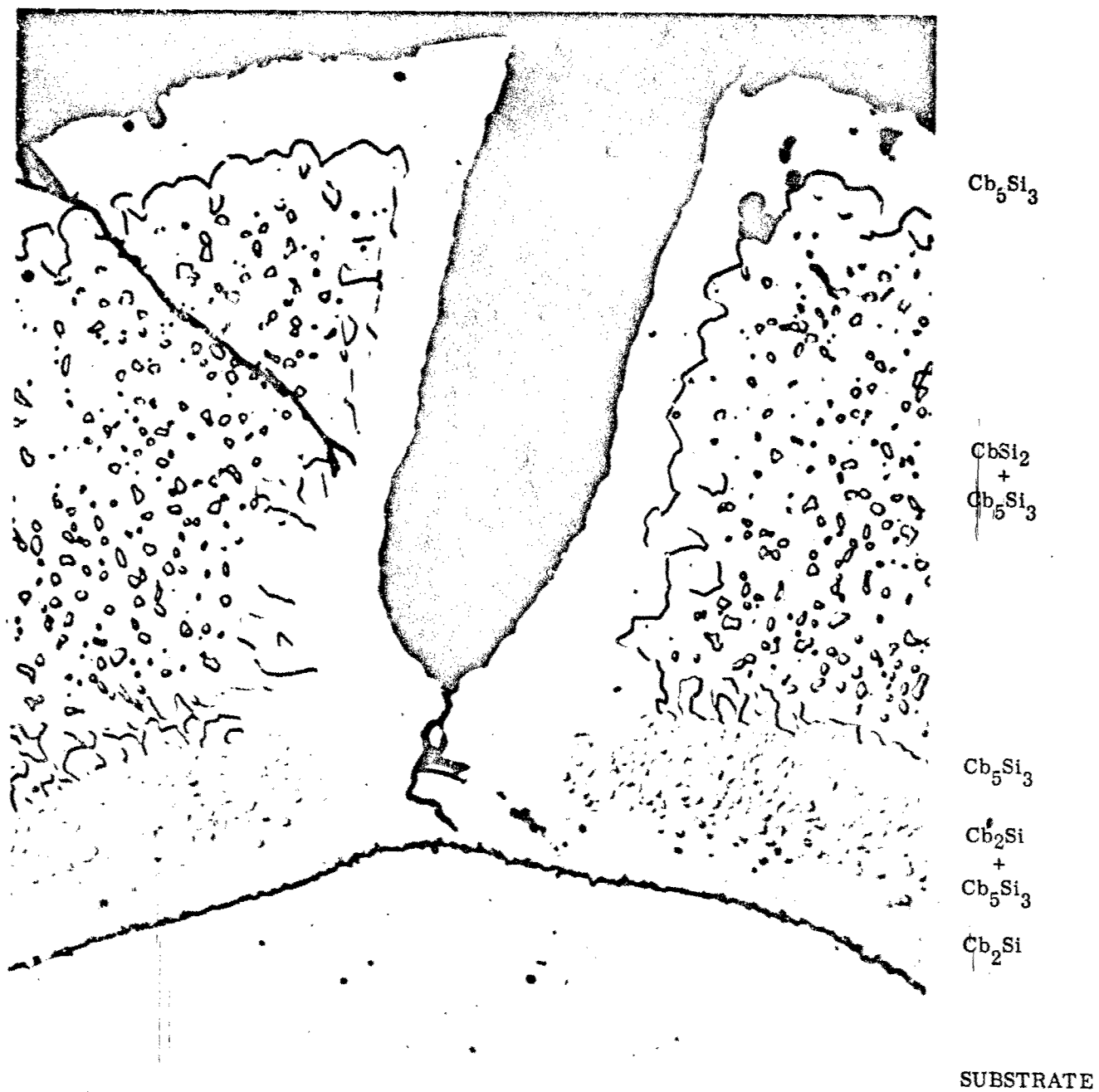
2850°F, 20 mm Hg, 19:1 N₂:O₂, 76 min

Figure 77 Structural Details of Cb-752/PFR-32 Tested in 19:1 N₂:O₂ at 20 mm Hg
(5 mm Hg Air Equivalent)

182

P326   (A) 2900° F, 20 mm Hg, 60 min   ×400

P328   (B) 2900° F, 20 mm Hg, 120 min   ×400
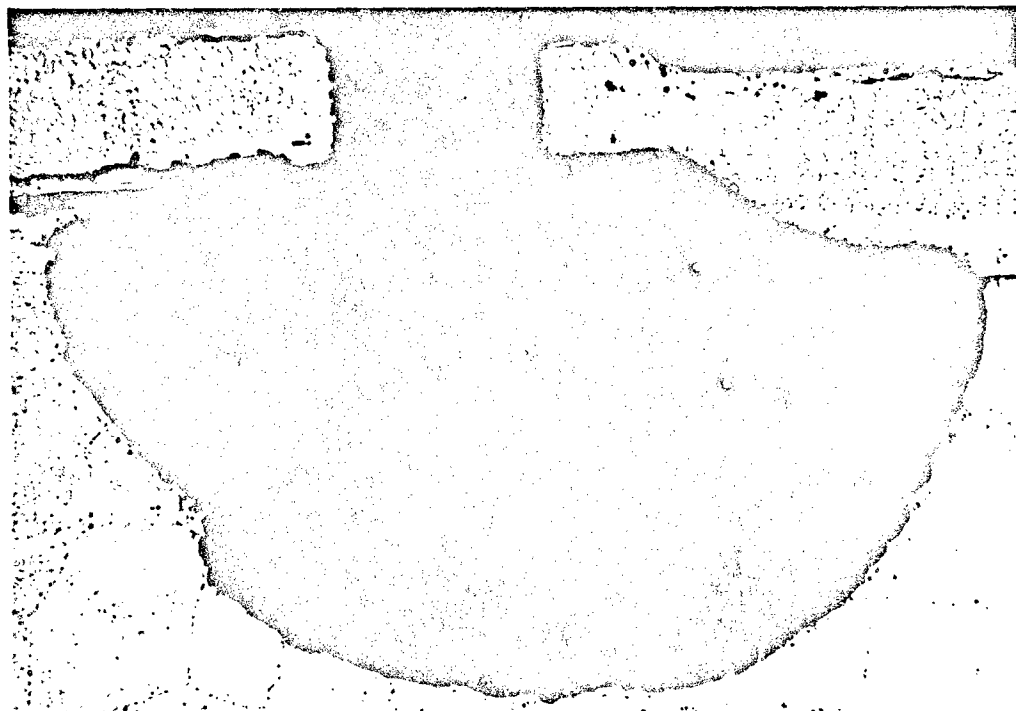
P327   (C) 2900° F, 20 mm Hg, 120 min   ×400

Figure 73 Mode of Failure (Random Surface) of Cb-752/PFR-32 in Air at
5—50 mm Hg

183

interface and the substrate was attacked. The large pit developed is particularly interesting because this behavior heretofore was believed to be characteristic only of coated Mo-base alloys. Pits of this type can be formed only if a volatile oxide exists, since the reaction products must be removed as a gas. Thus, it has been demonstrated that oxide volatilization does occur at low pressure with Cb-base alloys, and failures similar to those found in coated Mo can occur. The volatile oxide in this case is probably CbO or some stoichiometric variation of CbO. Also, since the alloy contains 10% W, formation of volatile WO_3 would be expected.

Since large defects occurred at the edges, the question arises as to why failure occurs primarily along hairline fissures on the flat surfaces. Figure 79 shows the edge condition of a sample tested in the region where random surface failures predominate. The large edge defects are filled with a clear silica glass which apparently has sufficient healing capacity to prevent excessive attack at these sites. Small patches of columbium oxides are seen in the outermost layers of the glass above the defects. Also shown in this picture is the initial phase of attack below the surface at a fine hairline fissure. The reaction products here are primarily oxides of Cb with some silica.

The differences in behavior at hairline fissures and large edge defects at pressures of 5 mm Hg or higher is believed to be related to the relative pressure of oxygen (or oxygen activity) available at the site. At large defects, sufficient oxygen was available to form a protective silica glass that effectively healed the defect, or at least greatly retarded the rate of attack along the defect. In the fine hairline cracks, however, access of oxygen was limited and correspondingly lower pressures (or activity) resulted. At lower oxygen pressure, large amounts of CbO_2 were incorporated in the oxidation products and attack of the coating was accelerated. This is shown in Figure 80 ; in air at 0.1 mm Hg pressure, severe oxidation occurred at the large edge defects. In Figure 79, little attack is evident after 76 min at 2850° F in a 19:1 N_2/O_2 mixture with an equivalent air pressure of 5 mm Hg. In Figure 80A, however, severe attack has occurred in 30 min at 2850° F in air at 0.1 mm Hg pressure. The reaction product in this case was shown to be CbO_2 dispersed as massive particles in a glassy matrix.

At pressures below 5 mm Hg, the mode of attack was one of surface recession, and life strongly depended on effective or minimum coating thickness. Since coating thickness beneath large edge defects is one-fourth to one-half of the average coating thickness, these areas were the weakest point in the system. It is not surprising, therefore, that random edge failures predominated at low pressure. Also, surface defects underwent rapid attack and overall surface recession of the coating was high below 5 mm Hg. Thus, general failure would be expected to occur shortly after the initial random failure, accounting for the close proximity of random and total failure boundaries.

M9227

×600

2850° F, 20 mm Hg 19:1 N$_2$:O$_2$, 76 min

Figure 79 Healing of Edge Defects in Cb-752/PFR-32 in Air at 5−50 mm Hg Pressure

185
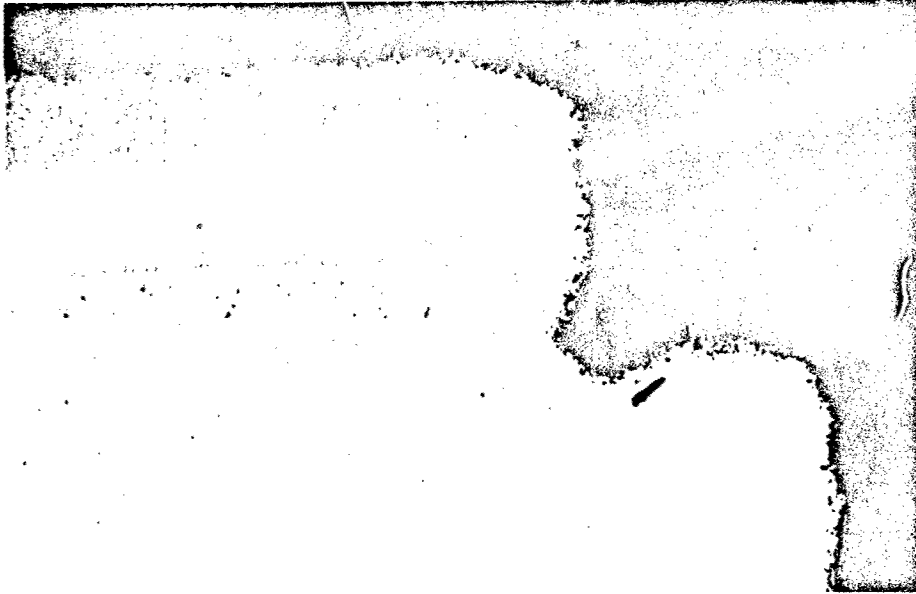
P336   (A) 2850° F, 0.1 mm Hg, 30 min   ×400
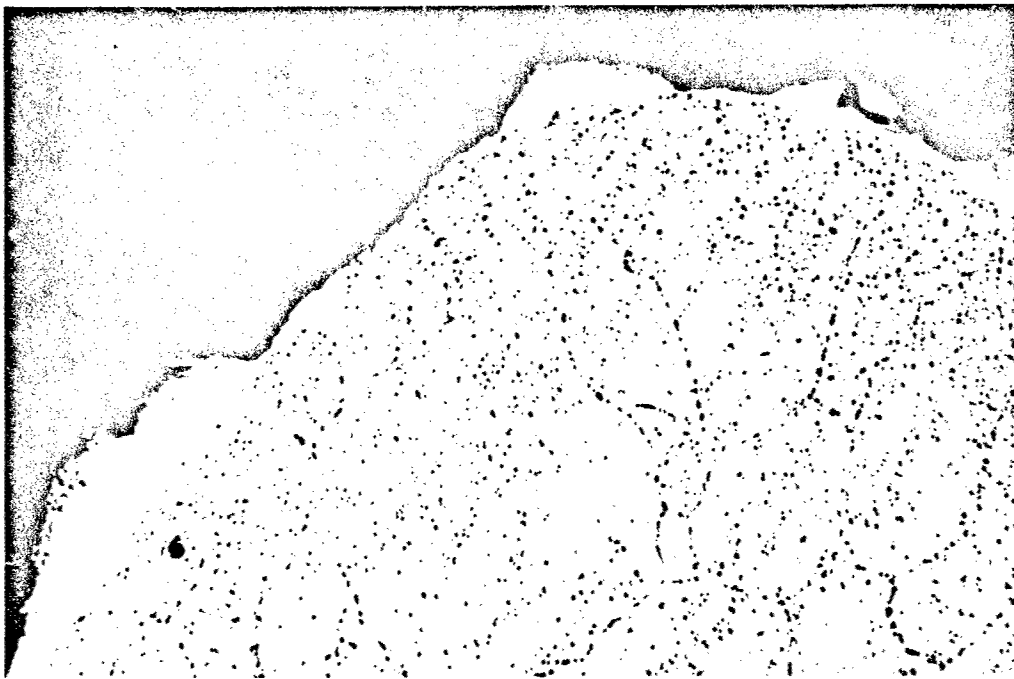
M8311   (B) 2950° F, 0.1 mm Hg, 30 min   ×500

Figure 80 Mode of Failure (Random Edge) of Cb-752/PFR-32 in Air at
0.01−1 mm Hg

186

Gas Velocity

The effect of exposure to air flowing at Mach 3 velocity on performance capabilities was evaluated at pressures of 5 and 20 mm Hg. Test temperatures were selected on the basis of the 60-min random failure limits (baseline data) for these pressures. The rate of growth of the lower silicide phases (Cb_5Si_3 + Cb_2Si) was used to determine correction factors for the optical pyrometer needed for calculation of true temperature during test. The results of these calibrations are shown in Table XXXVIII and Figure 80.

Table XXXVIII. Temperature Calibration by Diffusion Zone Method
for Cb-752/PFR-32
(30-min exposure)

Radiant heated		Resistance heated		
True temperature (°F)	Thickness Cb_5Si_3 + Cb_2Si (mils)	Estimated true temperature[a] (°F)	Thickness Cb_5Si_3 + Cb_2Si (mils)	Calculated true temperature (°F)
2500	0.217	2500	0.218	2489
2600	0.324	2600	0.290	2592
2700	0.361	2700	0.423	2741
2800	0.497	2800	0.488	2800

(a) Corrected optical reading assuming ϵ = 0.75.

A plot of zone thickness versus true temperature for the radiant-heated samples was used to calculate the true temperature from zone thickness measured on resistance-heated samples. A second plot of estimated true versus calculated true temperatures was used for selecting appropriate optical pyrometer corrections in conducting the flow tests. The results indicate that the emittance (normal spectral) during test was equal to the initial assumed value of 0.75. The value of 0.75 had previously been obtained by blackbody-hole techniques using preoxidized $Cb/CbSi_2$ rods.

An Arrhenius plot of the rate of growth of the total diffusion zone (Cb_5Si_3 + Cb_2Si) in the Cb-752/PFR-32 as a function of true temperature is presented in Figure 81. For comparison, growth rate curves for diffusion zones in $Cb/CbSi_2$ and $Mo/MoSi_2$ systems are also presented. It is significant that the rates for Cb-752/PFR-32 and $Cb/CbSi_2$ exhibit the same temperature dependency (Q = 27,150 and 29,000 cal/mol, respectively). The slightly higher rate at any temperature of the Cb-752/PFR-32 system is not particularly significant considering the limited number of tests conducted to establish the growth rate curves at each temperature. For all practical purposes, the two systems behave in the same manner. Both systems show a significantly lower growth rate and temperature dependency of rate compared with $Mo/MoSi_2$ (Q = 33,400 cal/mol) (32).

Tests at 5 mm Hg (air) pressure were conducted in a 19:1 N_2:O_2 mixture at 20 mm Hg pressure, based on the assumption that test results were more dependent on oxygen partial pressure (1 mm Hg in this case) than on total pressure. The validity of this

187
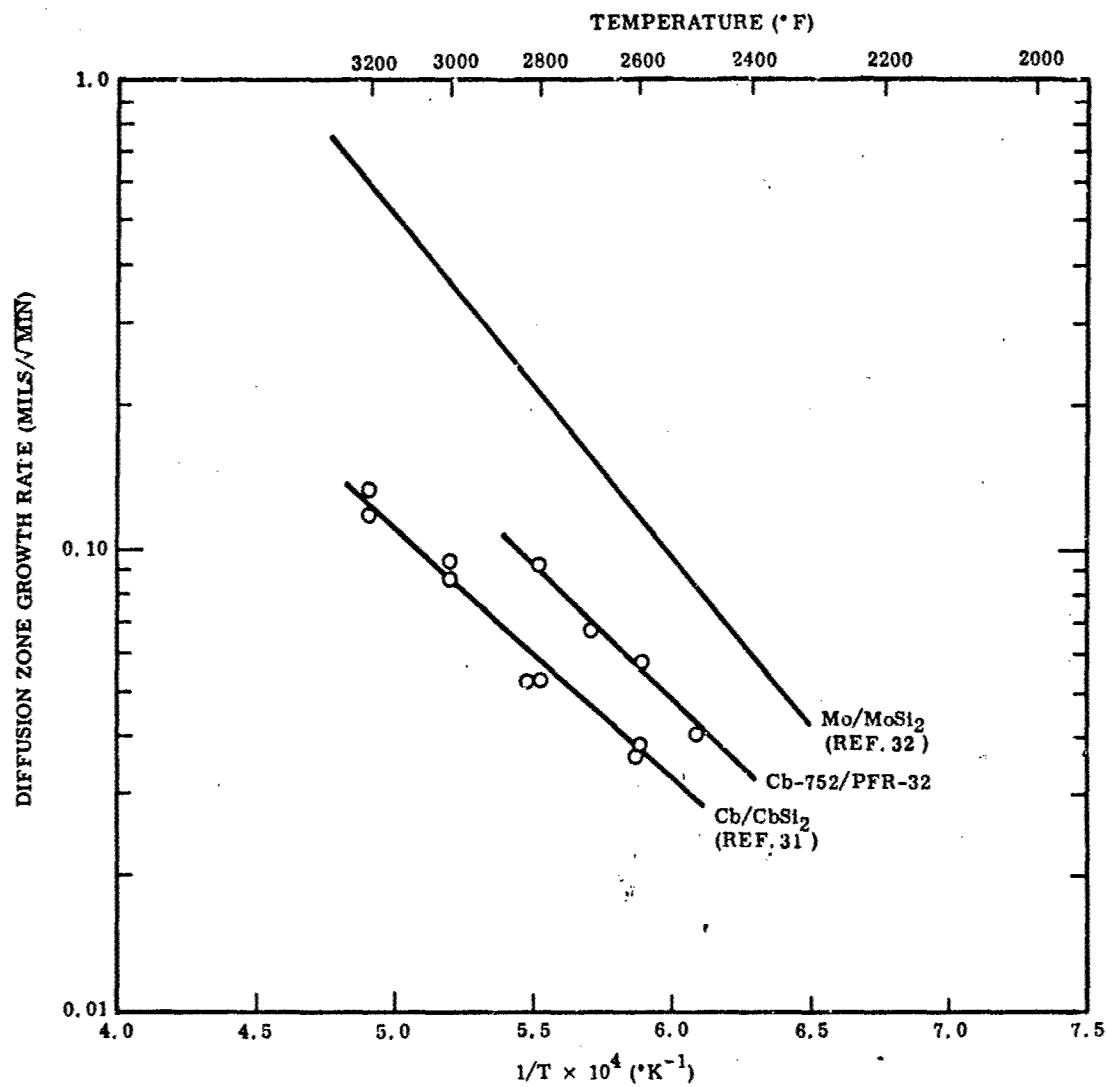
Figure 31 Arrhenius Plot of Diffusion Zone Thickness Growth Rate Versus True
Temperature for Cb-752/PFR-32

188

assumption was determined by checking baseline test results in 19:1 $N_2:O_2$ mixtures under identical test conditions (radiation heating, low velocity flow). Identical results were obtained in tests in air at 5 mm Hg and 19:1 $N_2:O_2$ at 20 mm Hg, and also in tests in air at 1 mm Hg and 19:1 $N_2:O_2$ at 5 mm Hg. Representative coating structures after testing are shown in Figures 82 and 83. The test in 19:1 $N_2:O_2$ at 5 mm Hg pressure with an assumed normal air equivalence of 1.25 mm Hg clearly showed the transition to rapid surface recession and formation of CbO_2-ric glassy scale characteristic of tests in normal air at 1 mm Hg pressure (Figure 83). Hence, it was concluded that the flow test could be conducted with the 19:1 mixture gas for simulating low air pressure conditions.

The results of the flow tests conducted, along with the corresponding performance capabilities under baseline (low-velocity) conditions, are shown in Table XXXIX. No significant effect of gas velocity at flow rates up to Mach 3 on performance capabilities is indicated.

Table XXXIX. Results of Mach 3 Flow Tests, Cb-752/FFR-32

Test conditions					Performance evaluation	Baseline time to failure	
Temp. (°F)	Total pressure (mmHg)	Atmosphere	Equivalent air pressure (mmHg)	Time (min)		Random (min)	Total (min)
2850	20	Air	20	60	Pass	65	>240
2900	20	Air	20	60	Total failure	<30	150
2850	20	19:1 $N_2:O_2$	5	60	Pass	65	>240

Samples tested to within 5 min of the time to random failure at 2850° F (baseline conditions) at 20 and 5 mm Hg pressure did not fail. A sample tested 30 min beyond the time for random failure at 2900° F and 20 mm Hg exhibited a complete failure. Since total failure occurred in about half the time predicted from baseline tests, it might be concluded that velocity did degrade performance. However, a temperature increase of only 40° F (to 2940° F) could have caused total failure in 60 min at 20 mm Hg pressure. Considering the limits of accuracy in measurement and control of true temperature after random failure occurs in resistance-heated specimens, failure in this case cannot reasonably be attributed to a gas velocity effect.

The appearance of specimens tested in high-velocity air is shown in Figure 84. The flow exposed surface was covered with a thin adherent layer of clear glass. The general appearance and microstructure were identical to those of samples tested under equivalent conditions but at low velocity in the baseline study. The mode of attack at 5 and 20 mm Hg was the same for both high and low flow conditions. No surface recession was evident, and attack was concentrated in random hairline fissures.

189
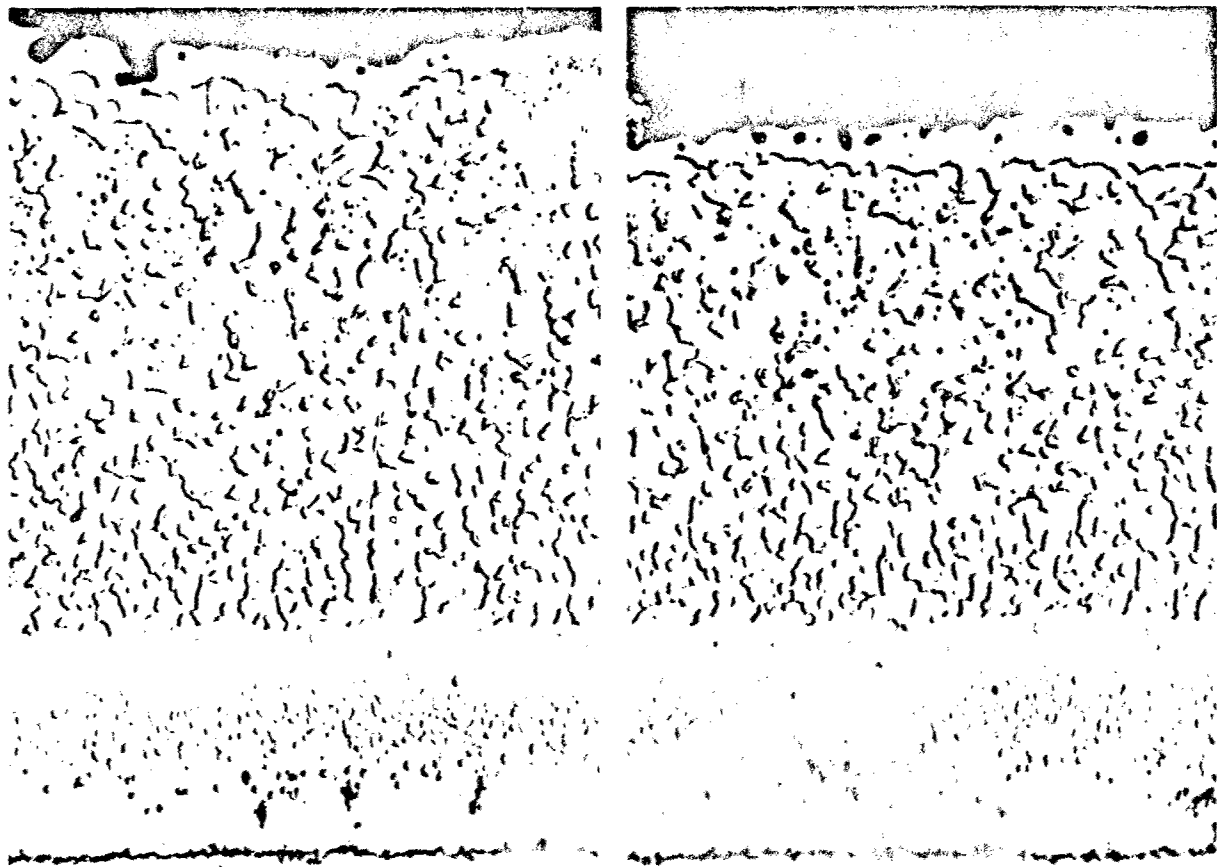
M9269   ×1500   ×1500

Air − 5 mm Hg, 2850° F, 76 min   19:1 N_2:O_2 − 20 mm Hg, 2850° F, 76 min

Figure 82 Equivalence of Tests in Air and 19:1 N_2:O_2 Mixture at Oxygen Pressure of 1 mm Hg, Cb-752/PFR-32
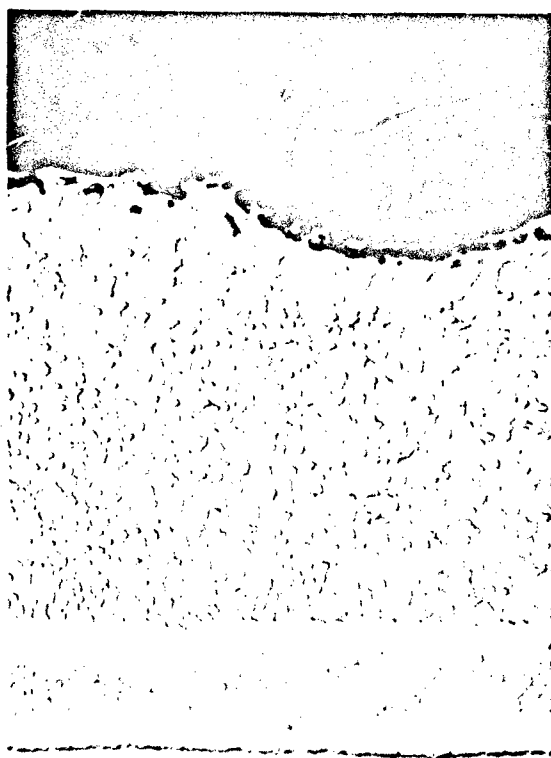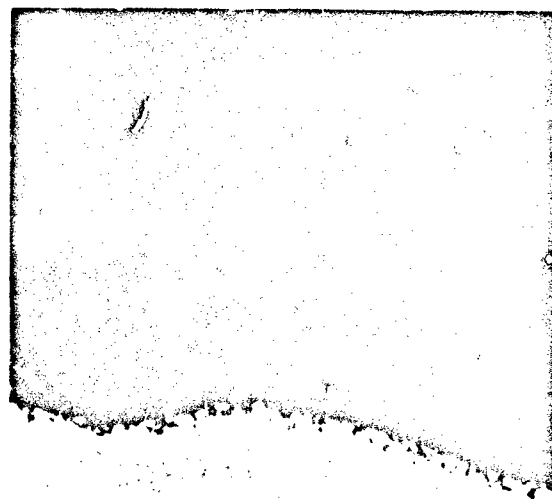
M9242   ×1000   M9244   ×1000

(A) 2850°F, 5 mm Hg 19:1 N_2:O_2, 60 min
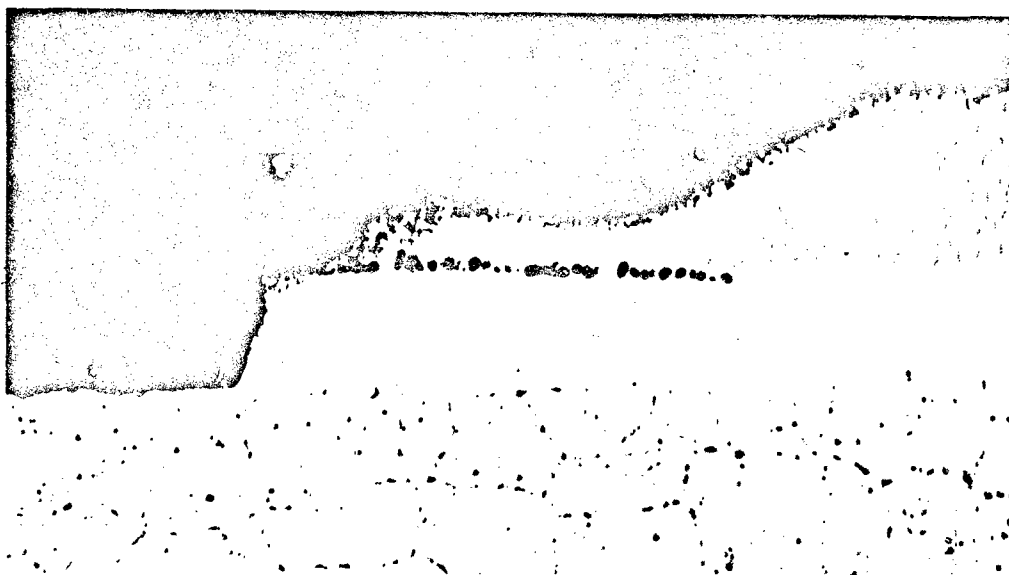
P376   (B) 2800°F, 1 mm Hg Air, 60 min   ×1000

Figure 83   Equivalence of Tests in Air and 19:1 N_2:O_2 Mixture at Oxygen Pressure of 0.2 mm Hg, Cb-752/PFR-32

191
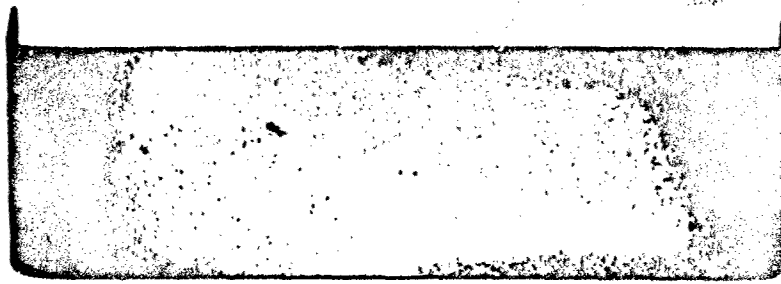
M8860   2900°F – 20 mm Hg Air, 60 min   ×1
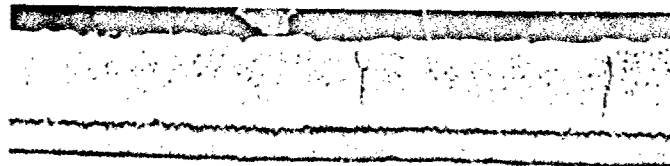
FLOW SIDE

SUBSTRATE
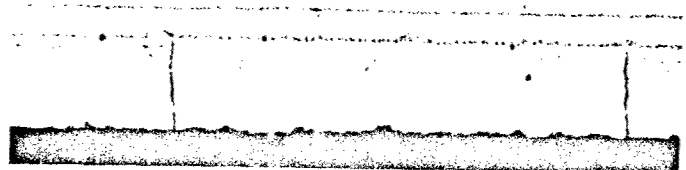
STATIC SIDE

P378 2850°F, 23–28 mm Hg 19:1 N_2:O_2, 60 min   ×250

Figure 84   Appearance and Structure of Cb-752/PFR-32
After Mach 3 Flow Tests

192

Vacuum Volatility

The results of vacuum volatility studies are summarized in Table XL. All specimens exhibited significant decreases in total thickness and weight after heating for 30 to 240 min at temperatures of 2600 − 3200° F at a pressure of less than 10^{-5} mm Hg. Weight loss per unit area of the substrate was calculated on the basis of the planar surface area measured for each sample. It should be noted that the true surface area from which material is being evaporated is much larger than the measured planar area, which does not include the contribution of surface irregularities. Thus, calculated rates are a relative indication of behavior only and cannot be used for absolute calculations of volatilization effects.

Analysis of data on weight loss as a function of time indicates a parabolic relationship. As shown in Figure 85, weight loss is a linear function of the square root of time at 2600, 2800, and 3000° F. The parabolic rate constant increases with increasing temperature. At 3000 and 3200° F, the rate behavior is high initially and low finally. These data suggest that the vacuum degradation process is governed by solid-state diffusion but that the diffusion processor rate-controlling mechanism may change with higher temperature or increased exposure time.

Metallographic studies were conducted to correlate degradation behavior with structure. As shown in Figure 86A, the coating structure after 4 hr at 2600° F is almost identical with that of samples tested in air at 0.01 to 50 mm Hg pressure. (See Figures 76 and 80.) A thick layer of Cb_5Si_3 has formed on the outer surfaces, presumably by the disproportionation of $CbSi_2$ to Cb_5Si_3 and Si, which, in turn, volatilizes as a gas. It is believed that, with such structures, the rate of silicon loss is governed primarily by the rate of diffusion of silicon through the outer Cb_5Si_3 layer.

At longer times or higher temperatures where pronounced reduction in rate of silicon loss was observed, a complete change in coating structure was observed (Figure 86B). The coating at this stage had been converted to Cb_2Si and Cb_5Si_3 by interdiffusion with the substrate and volatilization of silicon from the surface. The $CbSi_2$ no longer existed in the coating. A marked decrease in coating thickness was also evident. Based on metallographic interpretation, the outer two-thirds of the coating is Cb_2Si + Cb_5Si_3 and the inner one-third is Cb_2Si. The exact composition of the phases was not determined. Extensive porosity was evident in surface layers of all vacuum exposed samples. Also, it is interesting to note that at 3200° F, no precipitates were evident in the Cb-752 substrate. The substrate either was solution annealed or purified as a result of heating at this temperature.

Two distinct effects on defects were observed upon vacuum exposure. At low temperatures where $CbSi_2$ was present, hairline fissures perpendicular to the plane surfaces were widened and deepened. Large edge cracks, on the other hand, were not materially enlarged. At high temperatures where $CbSi_2$ was absent, virtually no defects existed on the plane surfaces. Apparently, all the hairline fissures were healed in the rapid conversion from $CbSi_2$ to Cb_2Si + Cb_5Si_3 by interdiffusion with the substrate. However, heavy attack was noted at all large edge defects, as shown in Figure 86.

Table XL. Vacuum Volatility Data, Cb-752/PFR-32

Heat treatment			Surface area (cm^2)	Total thickness		Thickness decrease (mils/side)	Weight		Weight loss (gm/cm^2)(a)
Temp. (°F)	Pressure (mm Hg)	Time (hr)		Before (mils)	After (mils)		Before (gm)	After (gm)	
2600	1×10^{-5}	1/2	4.71	25.5	—	—	1.0816	1.0776	8.51×10^{-4}
	8.0×10^{-6}	1			—	—		1.0755	13.0×10^{-4}
	6×10^{-6}	2			—	—		1.0724	1.96×10^{-3}
	6×10^{-6}	4			24.1	0.55		1.0672	3.06×10^{-3}
2800	1×10^{-5}	1/2	5.03	25.4	24.2	0.60	1.0860	1.0741	2.36×10^{-3}
	9×10^{-6}	1			23.7	0.85		1.0697	3.24×10^{-3}
	7×10^{-6}	2			23.5	0.95		1.0640	4.37×10^{-3}
	5×10^{-6}	4			23.1	1.15		1.0563	5.91×10^{-3}
3000	2×10^{-5}	1/2	4.74	25.4	24.2	0.60	1.0867	1.0676	4.03×10^{-3}
	2×10^{-5}	1			23.7	0.85		1.0609	5.41×10^{-3}
	1×10^{-5}	2			—	—		1.0530	7.12×10^{-3}
	9×10^{-6}	4			22.9	1.25		1.0445	8.90×10^{-3}
3200	1×10^{-5}	1/2	4.71	25.3	23.2	1.05	1.0894	1.0598	6.30×10^{-3}
	9.5×10^{-6}	1			22.8	1.25		1.0531	7.73×10^{-3}
	7×10^{-6}	2.16			22.7	1.30		1.0513	8.32×10^{-3}
	5×10^{-6}	4.16			22.7	1.30		1.0507	8.45×10^{-3}

(a) Per unit area of substrate.

194
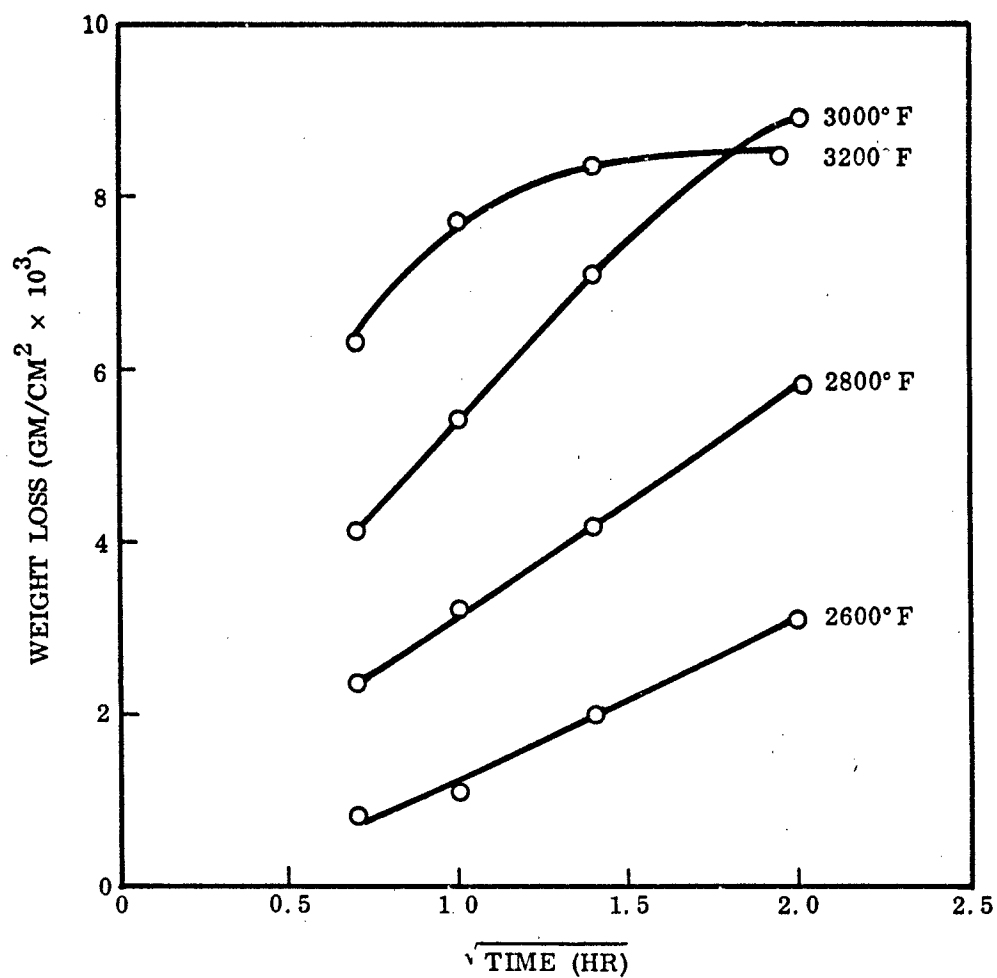
Figure 85 Vacuum Volatility of Cb-752/PFR-32 at 2600−3200° F, 10^{-5} mm Hg
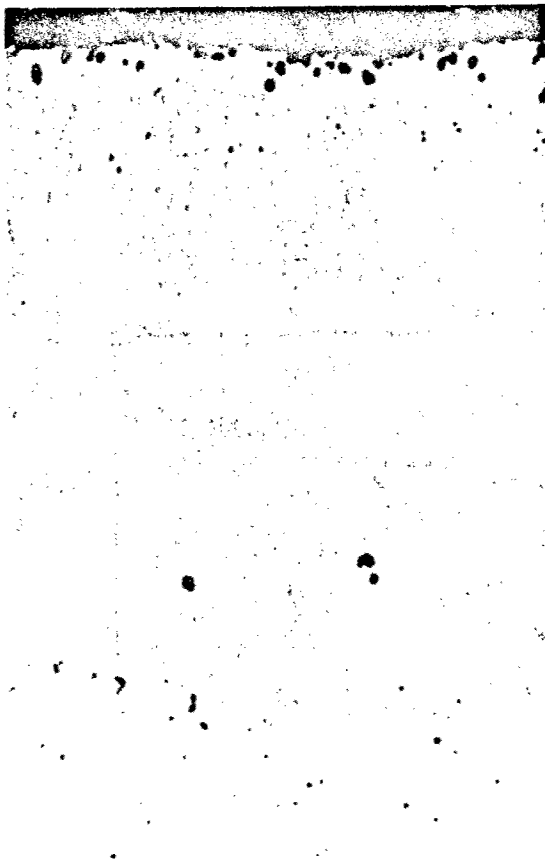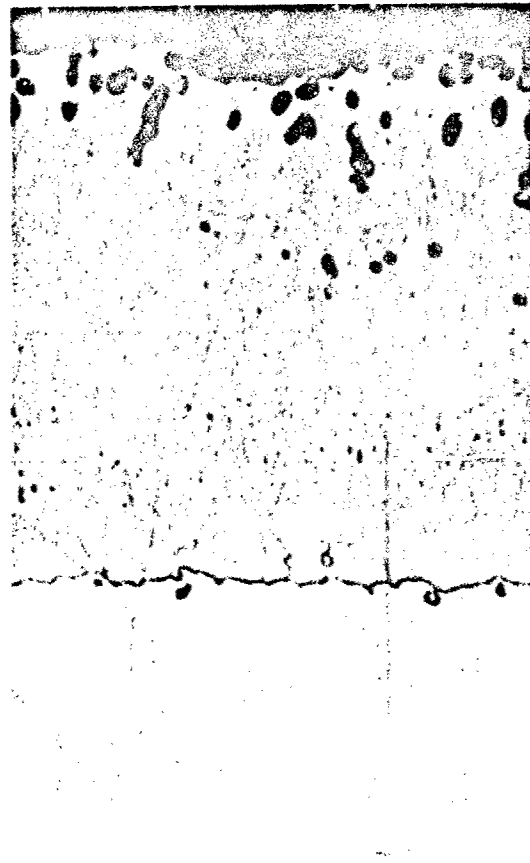
P393   ×1000   P395   ×1000

P392   (A) 4 hr, 2600°F   ×500   P394   (B) 4 hr, 3200°F   ×500

Figure 86   Microstructure of Cb-752/PFR-32 After Heating in Vacuum

196

Analysis of the data and microstructures indicates that vacuum exposure may degrade the oxidation resistance of the Cb-752/PFR-32 system in one or more of three ways. First, total coating thickness is reduced by surface recession. As shown in Table XL, approximately 1.25 to 1.30 mils/side of coating is lost by the time complete conversion to Cb_5Si_3 occurs. Thinning by recession occurs quite uniformly over the surface. Since a significant change in volume occurs upon conversion of $CbSi_2$ to Cb_5Si_3, most of the thinning may be the result of compositional change rather than physical loss of the coating. It has been calculated that 1 mil of $CbSi_2$ (ρ = 5.72 gm/cc) will, upon disproportionation, yield 0.643 mil of Cb_5Si_3 (ρ = 6.56), assuming that all silicon is lost to the vapor phase.

A second, and perhaps more important, change with respect to coating performance may be the direct result of conversion of the coating to the less oxidation-resistant, lower silicides. Thick layers of Cb_5Si_3 formed on the surface may burn off rapidly upon heating in air. With sufficient $CbSi_2$ remaining in the bulk of the coating, oxidation resistance may be restored after initial reactions expose the higher silicide phase. However, if all the $CbSi_2$ has been removed during vacuum exposure, rapid failure of the entire coating will probably occur.

The third, and most important, effect of vacuum exposure is related to the widening of cracks and fissures, as shown in Figure 86. Since performance at reduced pressure is random-defect controlled, the widening and deepening of defects upon heating in vacuum will accelerate failure at these sites upon subsequent use.

It is concluded that the limits for total failure will be lowered (shorter life at any temperature and pressure) by the surface recession and changes in coating composition. The limits for random failure, on the other hand, will be affected most by widening of cracks and fissures. Examination of weight-loss data and microstructures indicates that heating for up to 120 min at 2600° F or 60 min at 2800° F may not seriously degrade performance of this system upon subsequent use. However, longer times or higher temperatures will probably produce significant reductions in useful life. The effects of vacuum exposure may be most pronounced upon oxidation at pressures below 5 mm Hg, where high rates of surface recession occur in addition to accelerated attack at random defects.

Temperature-Pressure Cycling

The results of temperature-pressure cycling experiments are summarized in Table XLI. The first two experiments were designed to simulate the environmental changes on the internal and external surfaces of a lifting-reentry vehicle heat shield panel during reentry. The system survived four cycles under internal conditions (2800° F, 0.01 mm to 2400° F, 0.10 mm) and nine cycles under external conditions (2700° F, 1.0 mm to 2200° F, 3.0 mm) without failure. In both cases, the accumulated exposure at the high-temperature phase of the cycle (baseline phases) approached the random failure limit established in baseline tests.

It is concluded that combined temperature pressure cycling of this nature did not degrade performance and that useful life would be predicted from the baseline

Table XLI. Results of Temperature-Pressure Cycling, Cb-752/PFR-32

Phase of cycle	Temperature (°F)	Pressure (mm Hg)	Time (min)	No. of cycles	Total time (min)	Performance rating	Baseline time to failure	
							Random (min)	Total (min)
1st (baseline)	2800	0.01	7	4	28	Pass	40	80
2nd	2400	0.10	21	4	84		–	–
1st (baseline)	2700	1.0	7	9	63	Pass	65	135
2nd	2200	3.0	21	9	189		–	–
1st (vacuum)	2600	10^{-5}	30	1	30		–	–
2nd (baseline)	2600	1.0	240	1	240	Pass	>240	>240

data using accumulated exposure at the high-temperature phase of the cycle. It should be noted, however, that the specimens were not cooled to room temperature after each cycle. It appears that temperature cycling between two levels of temperature above 2000°F may have little effect on performance compared with that noted by many investigators upon cycling silicide-base coatings from high temperature to room temperature.

In a third experiment, exposure for 30 min at 2600°F to high vacuum did not degrade the performance upon subsequent heating at 2600°F in air at 1.0 mm Hg pressure. No signs of failure were noted after a 4-hr oxidation test — confirming the prediction that short-time exposure to vacuum at 2600−2800°F may not be particularly deleterious.

Acoustic Vibration

Exposure to random and sine acoustic vibration appeared to have some effect on subsequent oxidation behavior. As shown in Table XLII, no failures were detected in samples exposed to random or sine vibration upon testing to within 5 min of the random failure limit at 2800°F and 20 mm Hg. However, one sample exposed to random vibration failed in 60 min at 2650°F and 1.0 mm Hg. This is considerably below the failure limit of 4 hr for this temperature and pressure. A second sample exposed to sine vibrations did not fail in 60 min at 2650°F and 1.0 mm Hg. It is possible that vibration propagated transverse cracks along the interface in the sample that failed prematurely. As previously discussed, some samples had transverse interfacial cracks as-coated where an inadequate diffusion zone was formed. Since the severity of this type of defect varied from sample to sample, variable results might be expected in environmental tests of this type.

198

Table XLII. Results of Acoustic Vibration, Cb-752/PFR-32

| Vibration mode | Exposure conditions | Oxidation test conditions | | | Performance rating | Baseline time to failure | |
		Temperature (°F)	Pressure (mm Hg)	Time (min)		Random (min)	Total (min)
Random	60 sec, 30 – 1500 cps, 159.5 dB	2800	20	60	Pass	240	>240
		2650	1	60	Fail Random Surface	240	>240
Sine	50–1500 cps, 20 sec at 100– cps intervals, 172.5 dB peak at 510 cps	2800	20	60	Pass	240	>240
		2650	1	60	Pass	>240	>240

Defect Tolerance and Repair

Resistance to defect formation in handling, assembly, and use was evaluated by bend and impact tests. These tests were conducted about 15 months after manufacture of the test coupons. As previously indicated, the samples were ductile in bending at room temperature when received but were brittle when tested 15 months later. Samples consistently exhibited brittle fracture in instrumented bend tests over 3 to 6t radius at crosshead ratio of 0.1 to 1.0 in./min. Bending by hand in a radiused toolmaker's vise used in the original bend tests of as-received material caused similar behavior. Detailed investigations were conducted to delineate this behavior.

The ductile-brittle transition temperature in bending was established for a 3t radius at crosshead rates of 1.0 in./min. The results are shown in Table XLIII.

Table XLIII. Effect of Temperature on Bend Ductility, Cb-752/PFR-32

| Test temperature (°F) | Bend angle (deg) | |
	Coating fracture	Substrate fracture
77	18	18
85	22	22
95	31	31
161	38	44
212	39	48
227	40	>90[a]
237	39	39
245	38	74
250	40	>90[a]

(a) No substrate cracking after 90-deg bend.

The general effect of temperature on behavior in bending is illustrated by typical load-deflection curves in Figure 87. At or near room temperature, the coating fractured upon bending between 20 to 30 deg (160—150 deg included angle). At this point, large cracks developed on the tension side, and the coating spalled off the tension side. Cracks initiated in the coating propagated completely through the substrate, resulting in complete fracture of the specimen. At temperatures from about 160 to 240°F, the cracks did not propagate completely through the substrate. However, sufficient penetration occurred to result in ultimate fracture of the substrate upon continued bending short of 90 deg. The point of initial coating fracture was indicated by a pronounced drop in load as shown in Figure 87. Finally, above 250°F, crack propagation was sufficiently arrested to permit 90-deg bends without substrate fracture. It is interesting to note from Table XLIII that at temperatures of 161 to 250°F, samples could be bent 38 to 40 deg before initial fracture and spalling of the coating were observed.

Bend transition studies indicated that ductile-brittle behavior was related to the relative ability of cracks formed in the coating to propagate through the substrate. The relative contribution of coating and substrate to this behavior was investigated by conducting bend tests on samples from which the coating had been stripped. In all cases where the coating was removed completely by pickling, the substrate was found to be ductile at room temperature (90-deg bend without fracture). In the presence of the brittle coating, however, the substrate behaved in a brittle manner.

Notch toughness of the substrate appeared to be a critical factor. However, the ductile-brittle behavior was peculiar to this system and not a characteristic of the substrate per se in the presence of sharp notches produced upon crack'ng the coating. For example, the Cb-752/CrTiSi system was ductile at room temperature. Coating cracks generated upon bending were stopped at the coating-substrate interface. The Cb-752/Vought system was partially ductile at room temperature and completely ductile at 180°F. Samples of Cb-752 coated with $CbSi_2$ by pack siliconizing (15 hr at 1850°F) at LMSC also were ductile in bending at room temperature. The Cb-752 sheet used in these three systems was of the same lot as that used for the Cb-752/PFR-32 system samples.

At first, it was suspected that contamination of the substrate with oxygen, nitrogen, or perhaps silicon during processing was responsible for high ductile-brittle transition temperatures in bending. This could explain differences between the various Cb-752/coating systems. Upon further consideration, however, the aging reactions in the substrate in response to the thermal cycle characteristic of a given coating seem to be a more likely explanation. This was based on the observation that the Cb-752 substrate was hardened upon coating to 222 DPH for PFR-32, 207 DPH for Vought IV, and 188 DPH for CrTiSi. However, upon heating above 2400°F, the substrate in all systems softened to between 165 and 185 DPH, which was the base hardness range of the sheet before coating. Since Cb-752 is known to age upon heating at 1900°F and to soften upon heating above 2400°F (30), the hardness increases may well be due to the coating thermal cycle. This cycle, of course, differs for each system. It is significant, perhaps, that the ductile-brittle transition temperature in bending is directly proportional to the hardness increase upon coating. It is suspected that aging reactions during coating decrease the notch toughness of the alloy.
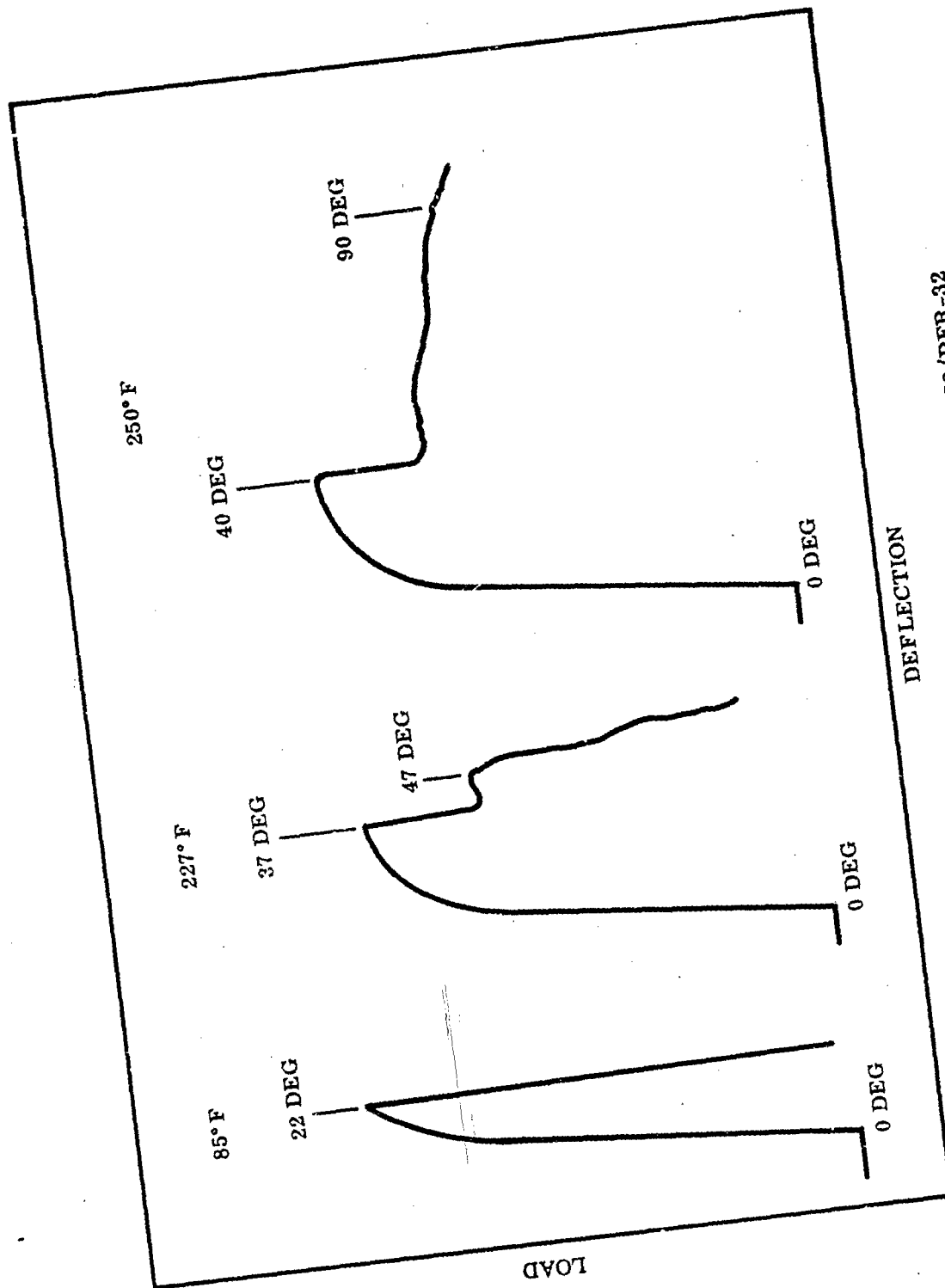
Figure 87 Load-Deflection Curves, Bending of Cb-752/PFR-32

As further proof of this hypothesis, the Cb-752/PFR-32 specimens were found to be ductile after annealing at 2500°F or higher. Ninety-degree bends were made at 75°F after annealing 30 min in argon at 2500°F. On the other hand, samples annealed several hours at 2000°F remained brittle. Thus, it appears that high ductility can be restored by re-solution of precipitates formed during coating in a subsequent short-time high-temperature anneal.

Precipitates that might be responsible for this behavior could not be resolved by light microscopy at magnifications up to 3000×. A clustering phenomenon characteristic of early stages of precipitation and growth may be involved. As shown in Figure 88, the only significant change detected in the region of the substrate/coating interface upon annealing at 2500°F was the formation of a Cb_5Si_3 + Cb_2Si interfacial zone in the coating. This zone also may play a role in bend ductility of the system. The lower silicides appear to offer some measure of resistance to crack propagation. It is possible that the velocity of crack propagation may be slowed sufficiently by this diffusion zone to be less than some critical value required for propagation into the substrate. Detailed studies beyond the scope of this program are needed to define more clearly the basic factors governing ductile-brittle behavior of coated systems such as this.

Based on original materials evaluation, it appeared that the ductile-brittle transition temperature of the Cb-752/PFR-32 system increased during 15 months of storage at room temperature. Low-temperature aging studies were conducted to determine if a slow aging reaction at room temperature was responsible. First, a new lot of 16 Cb-752/PFR-32 specimens was prepared using the same lot of Cb-752 sheet and process parameters employed for the original lot of specimens. These samples were provided through the courtesy of the Pfaudler Corp. for study of possible aging effects. Bend tests conducted at LMSC 1 week after coating revealed brittle behavior at 77 and 161°F. A ductile 90-deg bend was achieved at 212°F. Although this was lower than the 250°F temperature required for ductile bends of the original lot after 15 months' storage, the results indicate that no significant aging reactions occurred upon storage of this system. Coated specimens appear to be characterized by a generally high ductile-to-brittle transition temperature. Attempts to increase the ductile-to-brittle transition by aging for up to 1 week at 900°F also were unsuccessful, giving further indication of freedom from low-temperature aging reactions. The initial observation of room-temperature ductility, therefore, probably resulted from tests of random samples that were not representative of the overall lot of specimens.

An important discovery with respect to defect tolerance for this system resulted from the 900°F aging tests. In many samples, the coating was found to blister and peel off the surface after 8 hr exposure to air at 900°F, as shown in Figure 89. A white, powdery oxide formed in a dendritic pattern over exposed surfaces. Metallographic examination revealed that oxygen penetrated the fine hairline fissures normal to the surface and attacked the substrate through the transverse cracks extending along the substrate/coating interface (Figure 89B). As discussed previously, these cracks are observed in the as-coated specimens and branch along the interface. Significant attack occurs in less than 2 hr and the coating effectively is lifted off the substrate in 3 to 4 hr by propagation of these interfacial cracks.
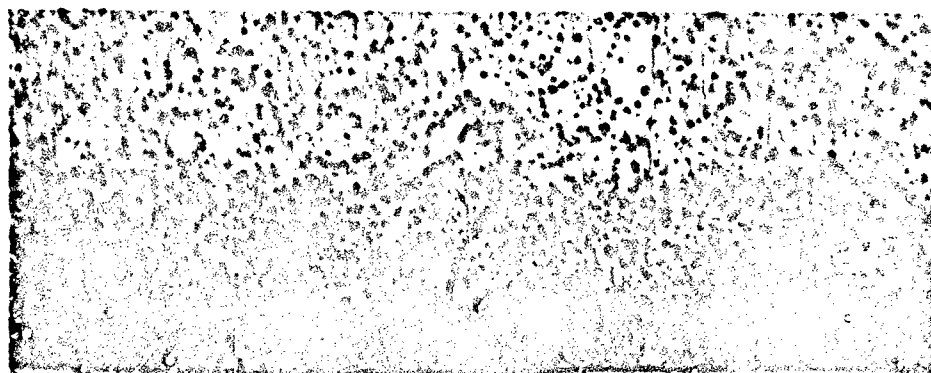
M8848   (A) As-Coated   ×3000

M8849   (B) 30 min, 2500°F   ×3000

Figure 89   Effect of Preheat Treatments on Structure of Coating and
Substrate, Cb-752/PFR-32
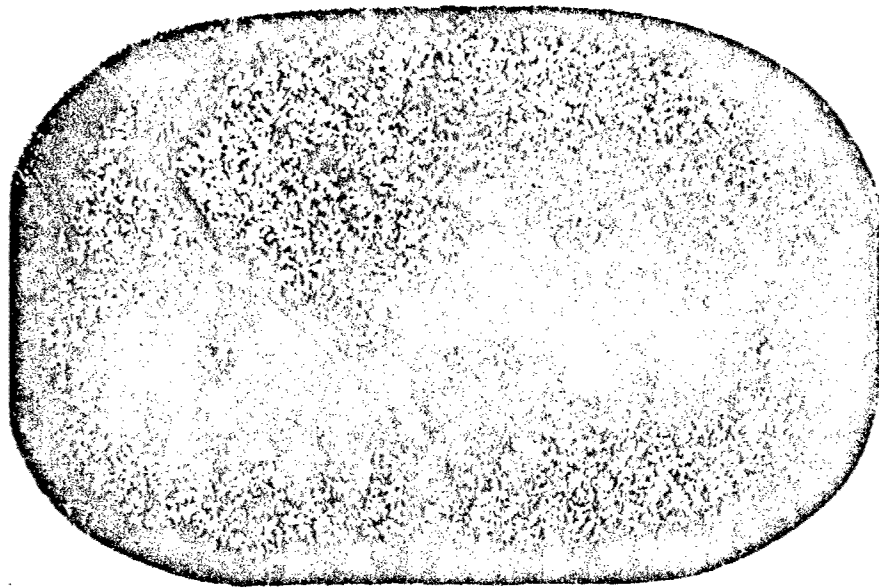
M8953   (A) 8 hr, 900°F   ×6
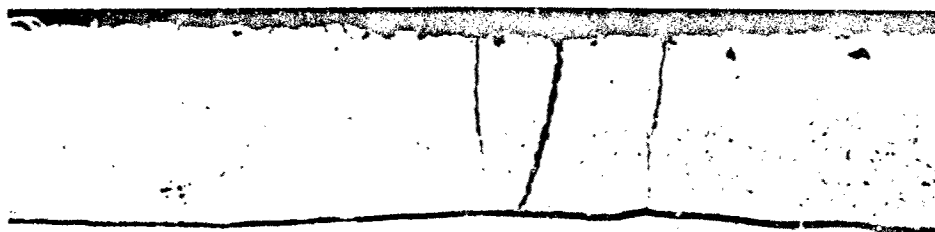
P329   (B) 2 hr, 900°F   ×400
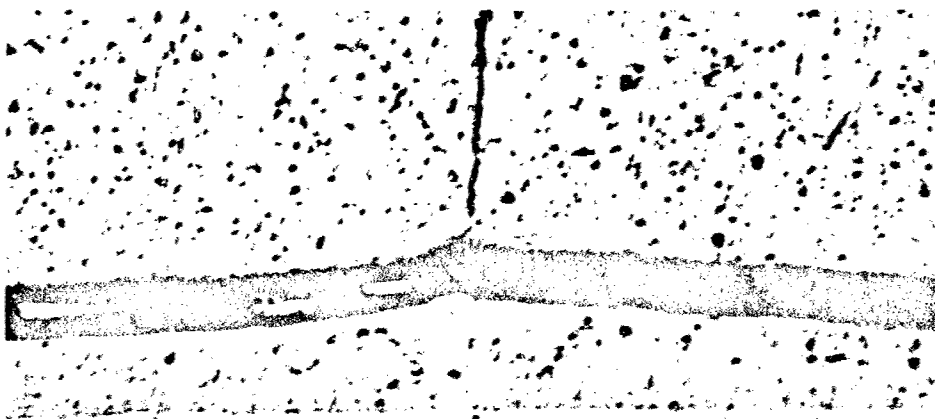
P330   (C) 2 hr, 900°F   ×3000

Figure 89   Substrate/Coating Separation Upon Heating in Air at 900°F for 5 to 8 hr, Cb-752/PFR-32

204

Samples exhibiting this behavior did not have significant or detectable amounts of a Cb_5Si_3-Cb_2Si diffusion zone at the substrate/coating (Figure 89C). It was found, however, that crack propagation and coating separation upon oxidation at low temperature could be prevented by the presence of a 0.05- to 0.1-mil-thick diffusion zone of intermediate or lower silicides. As shown in Figure 90, no propagation or separation occurred after 5 hr at 900°F in a sample previously annealed 2 hr at 2000°F to form a 0.1-mil-thick lower silicide diffusion layer. The transverse cracks terminate in or above this layer and do not expose large areas of the substrate to oxidation.

Hairline fissures in the coating represent an absolute defect that will cause complete failure of the system in a few hours at low temperature. The coating in its original condition has no tolerance for such defects. However, good defect tolerance can be assured in low temperature ranges by a simple anneal at 2000°F or higher to form a discrete diffusion zone at the substrate/coating interface.

As previously discussed, the hairline fissures also are the source of random defect failures upon oxidation at temperatures above 2400°F and pressures above 1 mm Hg. Many such defects exist in the coating as-received; others can be created by mechanical strain. Large cracks were formed by bending beyond the point of coating fracture (20 to 40 deg, depending upon temperature). In all cases, however, severe spalling occurred on the compression side and tolerance for defects formed on the tensile side could not be evaluated. Bending just short of the point of gross fracture did not appear to introduce new defects in the coating. Samples bent 25 deg at room temperature and then unloaded had a permanent set. However, the defect pattern of hairline cracks was about the same as that of undeformed specimens. Slight broadening of the fissures was evident in the region of maximum strain. Deformed samples were tested for 60 min at 2650°F in air at 1 mm Hg pressure. All samples passed, indicating no degradation of baseline performance capabilities. The ability to accommodate small plastic strain without degradation is an important characteristic of behavior in respect to assembly and use of coated parts.

Resistance to defect formation on high-velocity impact also was evaluated. Samples were tested on rubber and steel backup plates to evaluate the effects of impact when deformation was allowed in one case and prevented in the other. Results are summarized in Table XLIV.

On the rubber backup, no damage was observed with increased energy levels to 0.7 ft-lb. At levels of 1.0 ft-lb or higher, the specimens shattered as shown in Figure 91. These results parallel the bend test results in that complete fracture occurred when sufficient deformation to crack the coating was experienced. On a steel backup, more than double the impact energy was required to crack the coating, and cracks did not extend through the substrate. However, the coating spalled in addition to cracking. Since absolute defects were created in all tests on rubber or steel backup, specimens were not tested for oxidation behavior.
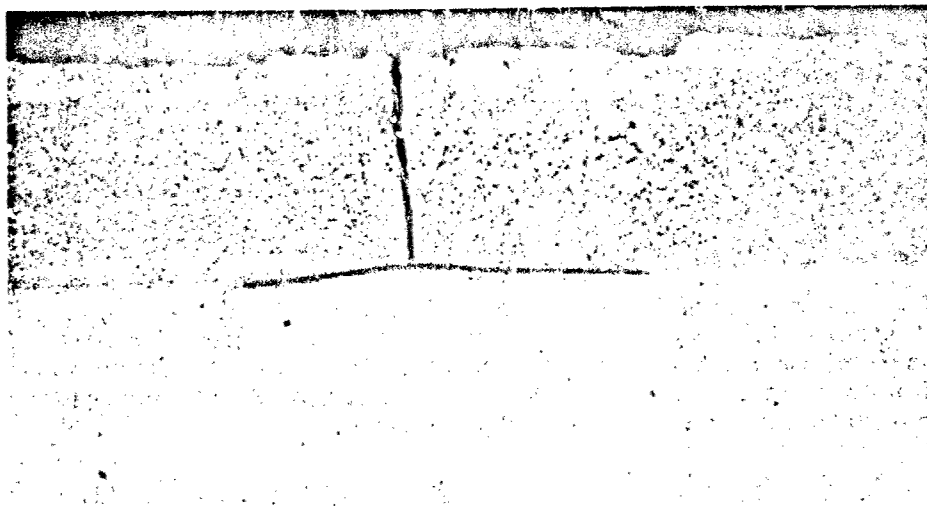
P333   (A) 2 hr, 2000°F + 5 hr, 900°F   ×400
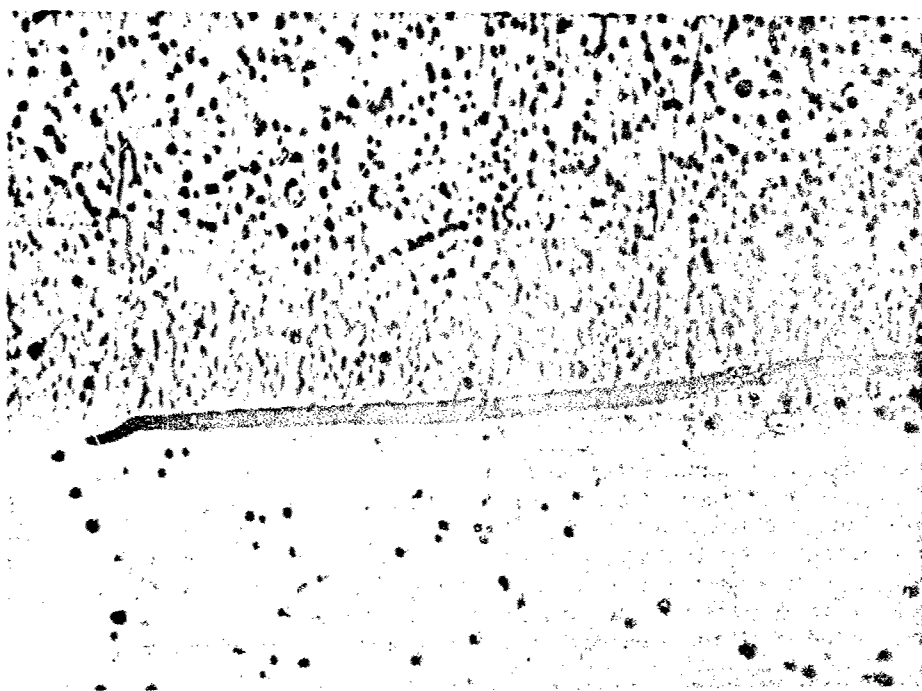
P334   (B) 2 hr, 2000°F + 5 hr, 900°F   ×3000

Figure 90   Prevention of Substrate/Coating Separation at 900°F by Cb_5Si_3
Diffusion Zone Formed at 2000°F, Cb-752/PFR-32

206
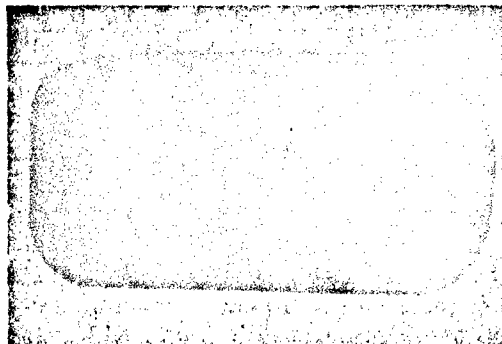
M   (A) 184 ft/sec, 1.0 ft-lb
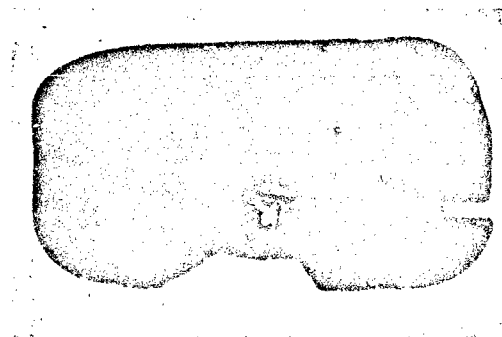
M   (B) 273 ft/sec, 2.3 ft-lb   ×3

Figure 91 Failure of Cb-752/PFR-32
           Specimens Upon Ballistic
           Impact (Rubber Backup)

Table XLIV. Results of High-Velocity Impact Tests, Cb-752/PFR-32

Backup	Kinetic energy (ft-lb)[a]					
	Spalling		Coating fracture		Substrate fracture	
	Pass	Fail	Pass	Fail	Pass	Fail
Rubber	0.7	1.0	0.7	1.0	0.7	1.0
Steel	1.5	1.7	1.5	1.7	2.3	>2.3

(a) Calculated from velocity and mass of pellet at time of impact.

The tolerance for gross defects that penetrate part way through the coating (similar to edge defects) was evaluated by means of slots 5 mils wide by specimen width in the coating. Results of tests on specimens containing defects 1/2 t and 3/4 t deep (t = coating thickness) are summarized in Table XLV. In the high-pressure range of baseline studies (20 mm Hg), a 3/4 t defect reduced coating life to less than 25% of the baseline. The 1/2 t defect also degraded performance, with an estimate of 25 to 50% of baseline life remaining. Since edge defects that extend to 1/2 or 3/4 t depths normally are healed in this pressure range, it is apparent that both width and depth of defects are critical. The 5-mil-wide slots cannot be healed effectively and result in significant degradation.

Table XLV. Defect Tolerance, Cb-752/PFR-32[a]

Test conditions			Performance rating			Baseline time to failure	
Temperature (°F)	Pressure (mm Hg)	Time (min)	1/2 t defect	3/4 t defect	Bulk specimen	Random (min)	Total (min)
2550	20	60	Pass	Fail	Pass	>240	>240
2800	20	30	Fail	Fail	Pass	240	>240
2800	20	60	Pass	Fail	Pass	240	>240
2650	1	30	Pass	Pass	Pass	240	>240
2650	1	60	Pass	Pass	Pass	240	>240
2700	1	60	Fail	Fail	Pass	60	135
2750	1	30	Fail	Fail	Fail	<30	45
2700	0.1	60	Pass	Fail	Pass	130	170
2700	0.1	120	Fail	Fail	Fail	130	170

(a) 5-mil-wide slot penetrating 1/2 or 3/4 of coating thickness (t).

In the low-pressure range (1 mm Hg or less) the 1/2 and 3/4 t defects cause less degradation. Results more closely parallel behavior with respect to normal edge defects, since such defects also are not healed and defect depth is the factor governing useful life. Results indicate that edge cracks which are the source of random defect failures in baseline tests are about 1/2 t or greater in depth. That is, performance of specimens with 1/2 t artificial defects was similar to the baseline, whereas that of specimens with 3/4 t defects was degraded.

208

It is concluded from these studies that the average tolerance for gross defects without significant degradation in baseline behavior is <1/2 t at pressures above 1 mm Hg and 1/2 t at pressures below 1 mm Hg.

The ability to restore performance by repair of absolute defects was investigated. Braze repair techniques developed on Cb/CbSi$_2$ samples were used for the Cb-752/PFR-32 system. Both the Cu-Ag-Si and Cu-Ag-CbSi$_2$ braze compositions were evaluated. Excellent wetting of the surfaces was obtained, and repaired defects appeared sound. Results of tests at 1 and 20 mm Hg are summarized in Table XLVI. The repairs were not effective at low pressure, and general failure occurred in all cases. Repairs were 75% effective at the higher pressure where 3 out of 4 defects were effectively restored to baseline capabilities (random defect limits). Results were sufficiently promising to indicate that further studies of braze repair techniques should be made.

Table XLVI. Results of Repair Studies, Cb-752/PFR-32[a]

Repair technique	Test conditions			Performance rating	Baseline time to failure	
	Temperature (°F)	Pressure (mm Hg)	Time (min)		Random (min)	Total (min)
Cu-Ag-CbSi$_2$	2700	1.0	60	2-Fail	60	135
Cu-Ag-Si	2700	1.0	60	2-Fail	60	135
Cu-Ag-CbSi$_2$	2850	20	60	2-Pass	60	>240
Cu-Ag-Si	2850	20	60	1-Fail	60	>240

(a) Repair of a 6 by 60 mil slot penetrating to substrate.

Materials Compatibility

Two aspects of materials compatibility were studied: reaction with refractory oxides (insulation materials) and reaction with other coating systems. No significant reaction was observed between the PFR-32 coating and silica, alumina, zirconia, or beryllia at temperatures to 2700°F in air at 0.01 to 50 mm Hg. At 2700°F or higher, severe reaction occurred with all oxides except silica. As shown in Table XLVII, performance both at one atmosphere and at reduced pressure was degraded. No reaction was found between PFR-32 and silica at temperatures up to 2800°F. The basic problem with other oxides was the reactions of Cb$_2$O$_5$ or CbO$_2$ with the refractory oxide. Examination of specimens at various time intervals indicated that the refractory oxides reacted with columbium oxides (and perhaps silica) formed during oxidation to produce a liquid oxide melt at points of contact. Accelerated attack and ultimate failure of the coating resulted. The problem is one of oxide-oxide incompatibility, not one of coating-oxide incompatibility.

The PFR-32 coating was found to be compatible with all other silicide-base coating on TZM and Cb-752 alloys at 2500 to 2700°F in air at 1 mm Hg pressure. As shown

209

in Table XLVII, however, PFR-32 was not compatible with the Sn-Al coating on Ta-10W alloy under these conditions. Here, liquid tin fluxed the silicide coating at points of contact, resulting in early failure.

Table XLVII. Results of Compatibility Studies, Cb-752/PFR-32

Test conditions			Contact material	Performance rating[a]	Baseline time to failure[b]	
Temperature (°F)	Pressure (mm Hg)	Time (min)			Random (min)	Total (min)
2700	760	107	Alumina	Fail	>240	>240
2700	760	319	Zirconia	Fail	>240	>240
2800	760	54	Zirconia	Fail	240	>240
2800	5	60	Beryllia	Fail	240	>240
2675	1	60	TZM/Durak	Pass	120	240
2525	1	45	TZM/PFR-6	Pass	>240	>240
2525	1	60	Cb-752/CrTiSi	Pass	>240	>240
2675	1	60	Ta-10W/Sn-Al	Fail	120	240

(a) At point of contact.
(b) $MoSi_2$ support.

Cb-752/CrTiSi

Material Evaluation

The CrTiSi coating is a complex silicide-base coating applied in a two-cycle vacuum-pack process. The basic process for coating Cb-base alloys was developed by Thompson Ramo Wooldridge, Inc. (TRW), Cleveland, Ohio. TRW also prepared the B-66/CrTiSi samples used in this investigation. In the first cycle, a Cr-Ti alloy layer was applied by heating for 8 hr at 2300° F in a pack of 60% Cr-40% Ti, and a halide activator at low pressure. Silicon was added in the second cycle by heating for 4 hr at 2050° F in a pack of silicon plus a halide activator at low pressure. Basically, the first cycle produced a chromium-rich Cr-Ti alloy overlay with a titanium-rich diffusion zone extending into the substrate. In the second or siliconizing cycle of the process, a CrTiSi coating was produced by reacting the Cr-Ti overlay with silicon. Finished coatings of this type normally have four discrete zones: (1) a Si-rich CrTiSi outer layer, (2) a Cr-rich (Si-lean) CrTiSi inner layer, (3) an intermetallic [Lave's-type phase, approximately $(Cb,Ti)Cr_2$] interfacial zone, and (4) a Ti-rich diffusion zone extending into the substrate. Details of the coating process and microstructures formed for CrTiSi on various Cb-base alloys are available in ASD-TDR publications (33 and 34).

The as-coated specimens prepared for this study had a mottled surface appearance, as shown in Figure 92. The basic color was a bright silvery gray with black islands and rivers in a random pattern on all surfaces. Figure 92 is typical of all specimens with respect to relative proportions of light and dark regions and general surface details. Light-craze cracking shown in Figure 92A was observed on all samples. Both light and dark areas were crazed. Large edge fissures were not observed, and edge coverage appeared to be very good on all samples. Surfaces were smooth textured in contrast to the normal granular texture characteristic of many silicide-base coatings.

Microstructural details of the coating system are illustrated in Figures 93 and 94. The high quality of the edge coverage is clearly evident. Few of the large V-shaped corner defects found in most silicide coatings were observed. Where present, such defects were confined to the outer Si-rich CrTiSi layer and extended to a depth of about one-third to one-half of the coating thickness. Fine hairline fissures were noted on all surfaces; these apparently are responsible for the crazing pattern observed on the surfaces. Hairline cracks terminated in the second Cr-rich CrTiSi layer of the coating. Little tendency to penetrate to the substrate or to branch into transverse fissures was observed. Although most of the coating was quite dense, a random distribution of segregated regions of high porosity in the Si-rich CrTiSi layer was noted. Where observed, porosity was confined to a depth of about one-third the total coating thickness.

The most significant feature of the coating was the nonuniformity with respect to composition and structure. As shown in Figure 93A, the $(Cb,Ti)Cr_2$ interfacial zone was not continuous. Breaks of varying length in this zone were noted on all samples. Where such breaks occurred, the coating was 0.1 to 0.3 mil thicker than where the $(Cb,Ti)Cr_2$ layer was present. Penetration of the coating into the Ti-rich diffusion zone where the $(Cb,Ti)Cr_2$ layer was absent is clearly evident.

The marked structural, and hence compositional, differences existing in the coating are revealed more clearly at high magnification. Figure 94A shows the three distinct

211

M9967   (A) Surface Details   ×6

M5534   (B) Edge and Surface   ×18

Figure 92 General Appearance of As-Coated Cb-752/CrTiSi

212
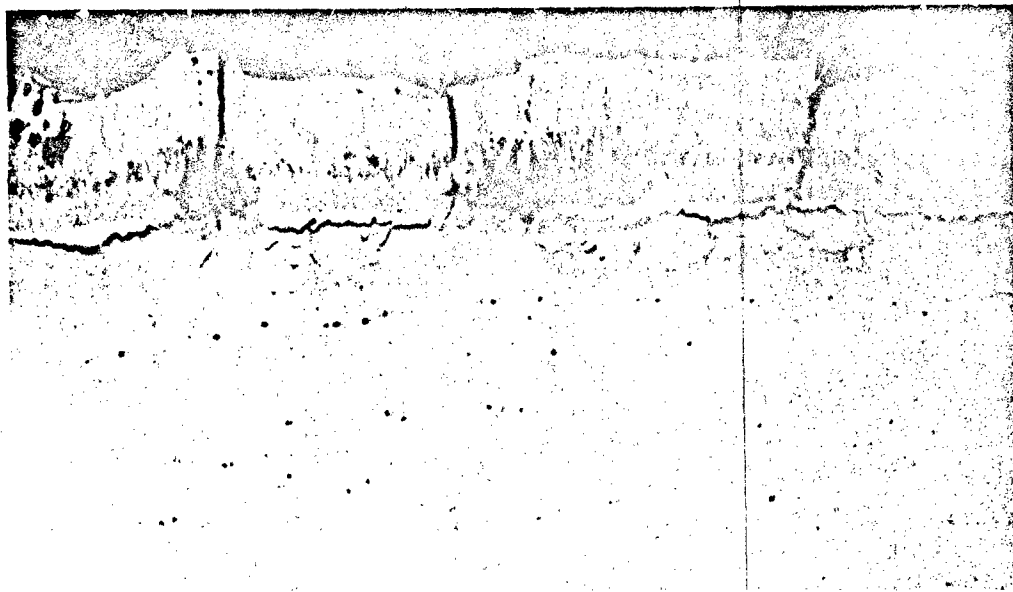
P506   (A) Surface   ×500

P505   (B) Edge   ×500

Figure 93 General Structure of As-Coated Cb-752/CrTiSi

213
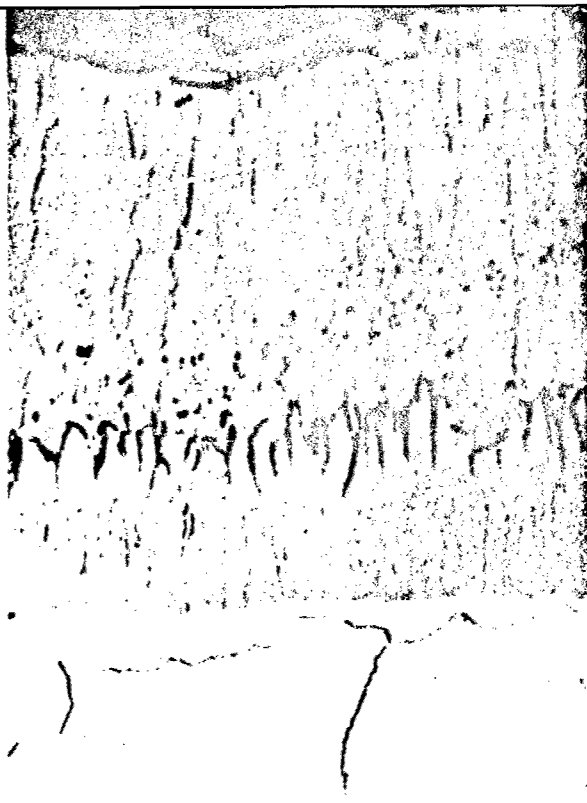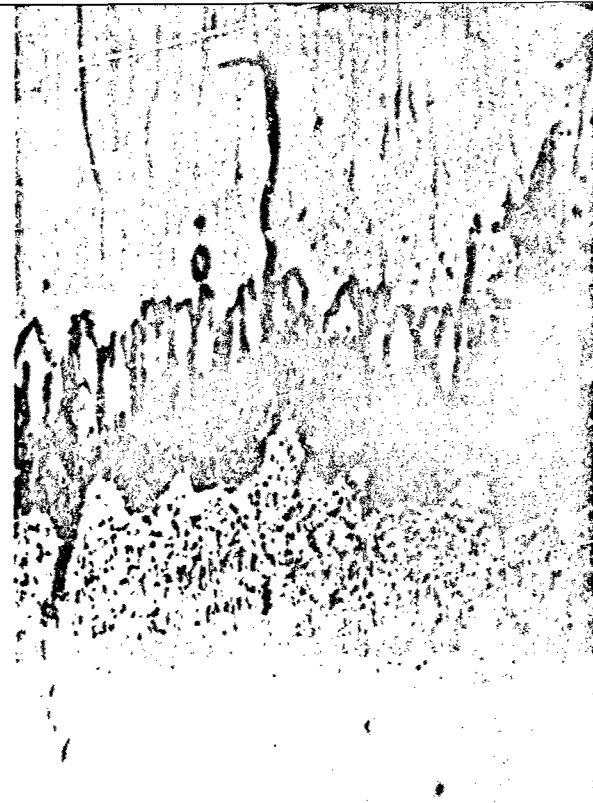
P508 (A   ight Region   ×2000 P509   (B) Dark Region   ×2000

M8360   (C) Initial Formation of Dark Region   ×3000

Figure 94 Structural Details of As-Coated Cb-752/CrTiSi

214

regions described by TRW as characteristic of the CrTiSi coating systems: (1) a Si-rich CrTiSi outer layer, (2) a Cr-rich CrTiSi inner layer, and (3) a $(Cb,Ti)Cr_2$ interfacial zone (33). Close examination of Figures 94A and C indicates that layer (2) may in turn comprise two zones: a coarse-grain outer zone and a fine-grain inner zone that grades off into the $(Cb,Ti)Cr_2$ interfacial layer. The sample has not been etched sufficiently to delineate the fourth layer, a Ti-rich diffusion zone below the $(Cb,Ti)Cr_2$. The coating region shown in Figure 94B exhibits five distinct zones, two of which have a pronounced duplex structure. The outer zone appears similar to the Si-rich CrTiSi layer of the normal structure. Below this, a second zone similar in appearance to the upper part of the Cr-rich CrTiSi layer is evident. This zone, however, grades off into a fine duplex structure which might be considered a third zone in the coating. The next lower zone has a fine precipitate in a light etching matrix. Below this, a fifth dark-etching zone is evident at the coating substrate interface. Remnants of $(Cb,Ti)Cr_2$ in the grain boundaries of the underlying Ti-rich diffusion zone can also be seen. Figures 94A and B show the relative coating thickness in each of the two areas and the extent of coating penetration into the substrate where the $(Cb,Ti)Cr_2$ zone is absent.

Detailed studies of samples before and after testing revealed that the regions of normal structure [$(Cb,Ti)Cr_2$ interfacial zone] corresponded to the light areas seen on the surface (Figure 92). Regions where the $(Cb,Ti)Cr_2$ layer was absent, on the other hand, corresponded to the dark areas of the surface. Thus, the pattern of light and dark areas on the surface shown in Figure 92 is in effect a map of the underlying structural and compositional variations in the coating. Further evidence of this correlation is presented in the section on baseline testing. The exact compositional differences between these two regions are not known. However, since substrate penetration has occurred in one case and not in the other, it is likely that the dark areas (substrate penetration) are enriched in Ti, Cb, W, and Zr compared with the light areas (no substrate penetration). It is reasonable, based on these observations and prior work, to anticipate some difference in the oxidation behavior of these regions during testing or use. Studies by TRW indicate that thickness and continuity of the $(Cb,Ti)Cr_2$ layer is a key factor controlling resistance to low-temperature (1800°F) oxidation. High-temperature (2500°F) resistance, however, was found to depend more on coating thickness than on the thickness or continuity of $(Cb,Ti)Cr_2$. However, at 2700°F, both thickness and interfacial zone characteristics seemed to be important. Melting appeared to be a factor controlling life at 2700°F, with localized fusion observed in Cr-depleted (Ti-enriched) areas of CrTiSi coatings. At this temperature, life was as much a function of coating composition as of coating thickness.

The reason for local variations in structure and composition of the CrTiSi coating on Cb-752 is not clear. Possible explanations include variations in (1) thickness or composition of the CrTi layer before siliconizing and (2) the rate of silicon deposition and conversion of the CrTi layer to CrTiSi. Electron probe studies could determine the nature of compositional variances. Investigation of compositional variations both in the CrTi overlay before siliconizing and in the completed coating should be made. It should be noted that a similar behavior was observed for the B-66/CrTiSi system. However, on B-66 alloy, fewer dark regions were observed per unit area, and the pattern of light and dark areas was markedly different from that observed on Cb-752/CrTiSi samples. Since identical procedures were followed in coating the two different

215

alloys, it follows that composition of the substrate is an important factor governing the nature and uniformity of the coating. Local variations in substrate composition (i.e., impurity or solute segregation) may play a significant role.

Spectrographic analysis of the coating revealed that Cb, Si, Cr, Ti, W, and Zr were the principal elements present. All major elements in the substrate appeared in the coating. No other trace or impurity elements were detected.

The metallurgical condition of the substrate was similar to that of the uncoated Cb-752 alloy sheet. As shown in Figure 95, the average hardness of the substrate was 188 DPH, compared with 173 DPH before coating. Hardening near the interface is the result of the Cr-Ti diffusion zone formed on coating. The depth of this zone is 1 to 1.5 mils below the interface, based on hardness measurements. After oxidation testing 4 hr at 2700° F in air at 1 atm, the average substrate hardness was 191 DPH. No hardening was found near the interface after testing, and hardness was uniform across the substrate from interface to interface. Sufficient diffusion occurred in 4 hr at 2700° F to remove any trace of the original Cr-Ti diffusion zone.

The as-coated samples were ductile in bending. Of six samples bent at room temperature, one failed with a brittle fracture while five withstood a 90-deg, 3t bend without fracture. The ductile-brittle transition appeared to be slightly below room temperature.

Coating thickness measured on the cross section of two samples averaged 1.80 mils with a range of values between 1.4 and 2.8 mils. A good correlation was found between measured thickness and thickness calculated from micrometer measurements before and after coating. As shown in Figure 96, the average thickness increased by 1.7 mils per side, from 20.6 mils before coating to 24.0 mils after coating. A very slight increase in dispersion of thickness values after coating is evident. The standard deviation of coating thickness is ±0.18 mil as calculated from the sigma values before and after coating. Thus, 95% of the samples would be expected to have a coating 1.34 to 2.06 mils thick, with the average being 1.70 mils thick. The agreement with actual measured values (cross sections) can be attributed to the smooth surface textures characteristic of this system and to the basic nature of the CrTiSi coating. Since the coating is formed by applying a CrTi layer which is converted to a complex silicide, little of the substrate is consumed in making the coating. In other systems, up to 1 mil or more of the substrate may be consumed in forming a silicide coating. Thus, for CrTiSi, the increase in total thickness provides a reasonably good measure of coating thickness. Weight change data, on the other hand, are of little value for estimating coating thickness because of the complex nature of the coating. For purposes of this study, average coating thickness exclusive of the Cr-Ti diffusion zone has been taken as 1.70 mils.

Baseline Behavior

The results of baseline tests are plotted in Figure 97, and the complete data are presented in Appendix III. Performance capabilities in slowly moving air at 0.01 to 50 mm Hg are summarized in Figure 98 and Table XLVIII. Two significant effects of reduced pressure were observed. First, the maximum temperature for a given life

216
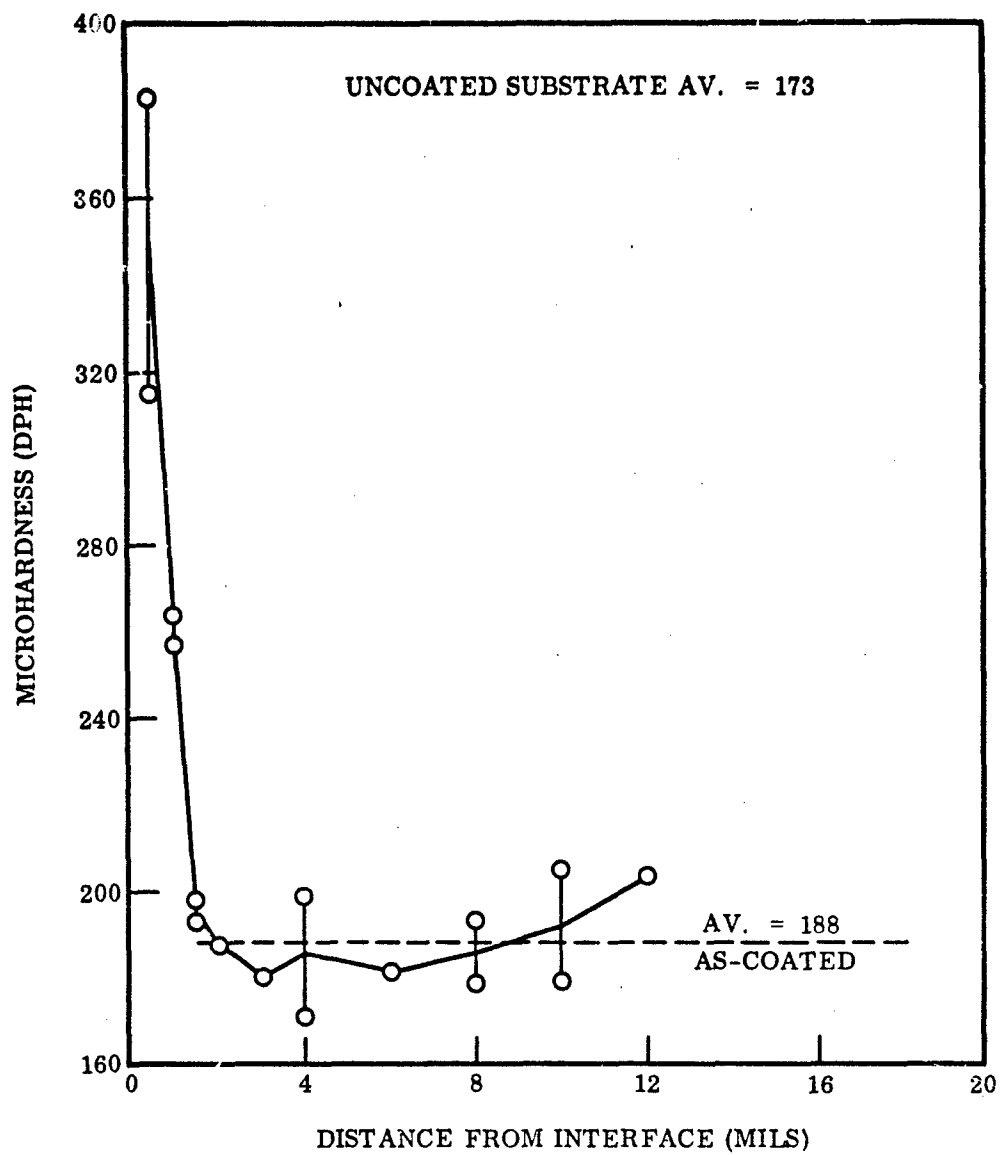
Figure 95 Results of Substrate Hardness Traverse, Cb-752/CrTiSi

217
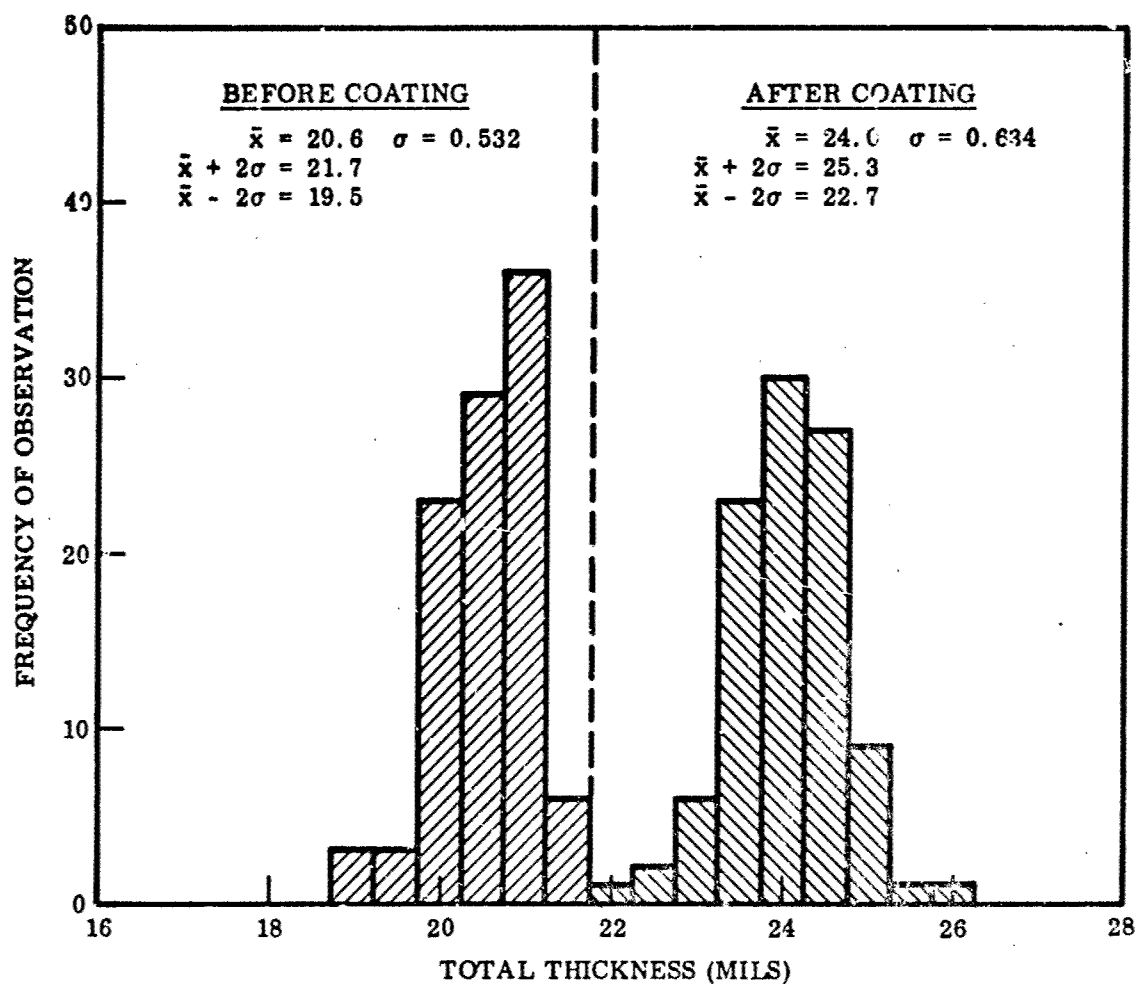
Figure 96 Frequency Histogram of Thickness Measurements of Cb-752/CrTiSi Before and After Coating

218

Table XLVIII. Maximum Temperature for Various Lifetimes, Cb-752/CrTiSi

Air pressure (mm Hg)	Maximum temperature at			
	30 min	60 min	120 min	240 min
Random failure limits				
50	2950	2925	2875	2775
20	2900	2860	2825	2775
5	2790	2780	2770	2750
1	2560	2550	2530	2510
0.1	2660	2650	2630	2610
0.01	2660	2650	2635	2610
Total failure limits				
50	2990	2970	2940	2880
20	3025	2980	2915	2825
5	2790	2780	2770	2750
1	2630	2620	2600	2575
0.1	2690	2670	2640	2610
0.01	2675	2660	2640	2610

was decreased, reaching a minimum at 1 mm Hg pressure. Second, the useful life was more strongly dependent on temperature at reduced pressure. At 1 mm Hg pressure, an increase of only 50° F resulted in an eightfold decrease of time to random failure. The most pronounced effect of pressure occurred between 20 and 1 mm Hg where a reduction of maximum temperature capability of 250−350° F for a given life without random failure was observed. The greatest sensitivity of useful life to temperature changes also was observed within this range. This behavior is of particular importance for aerospace applications, since large factors of safety may be needed to compensate for small variations in temperature or pressure.

Oxidation behavior was consistent, and a clear separation of time/temperature regimes for protection or failure could be made at each pressure level. The distinction between regions of random and total failures was also good. In the range of 1 to 50 mm Hg, the random and total failure boundaries were widely separated. At any temperature, a considerable length of exposure beyond the time for initial (random) failure was required to effect complete failure of the specimen. One notable exception was found, however, at 5 mm Hg where the random and total failure boundaries coincided. As will be shown, this was due to ignition and combustion of the samples at the time of initial coating failure. The random and total failure boundaries below 1 mm Hg also were very close together, as shown in Figure 97. In this range, rapid surface recession of the coating resulted in total failure within a few minutes after the first random failure occurred.

Random and, in many cases, total failures at pressures of 0.01 to 50 mm Hg could not be detected by visual examination. Samples rated as failing usually showed no external evidence of failure. As stated previously, the failure criteria for coated Cb-base alloys was oxidation of the substrate. This was determined by bend ductility tests and
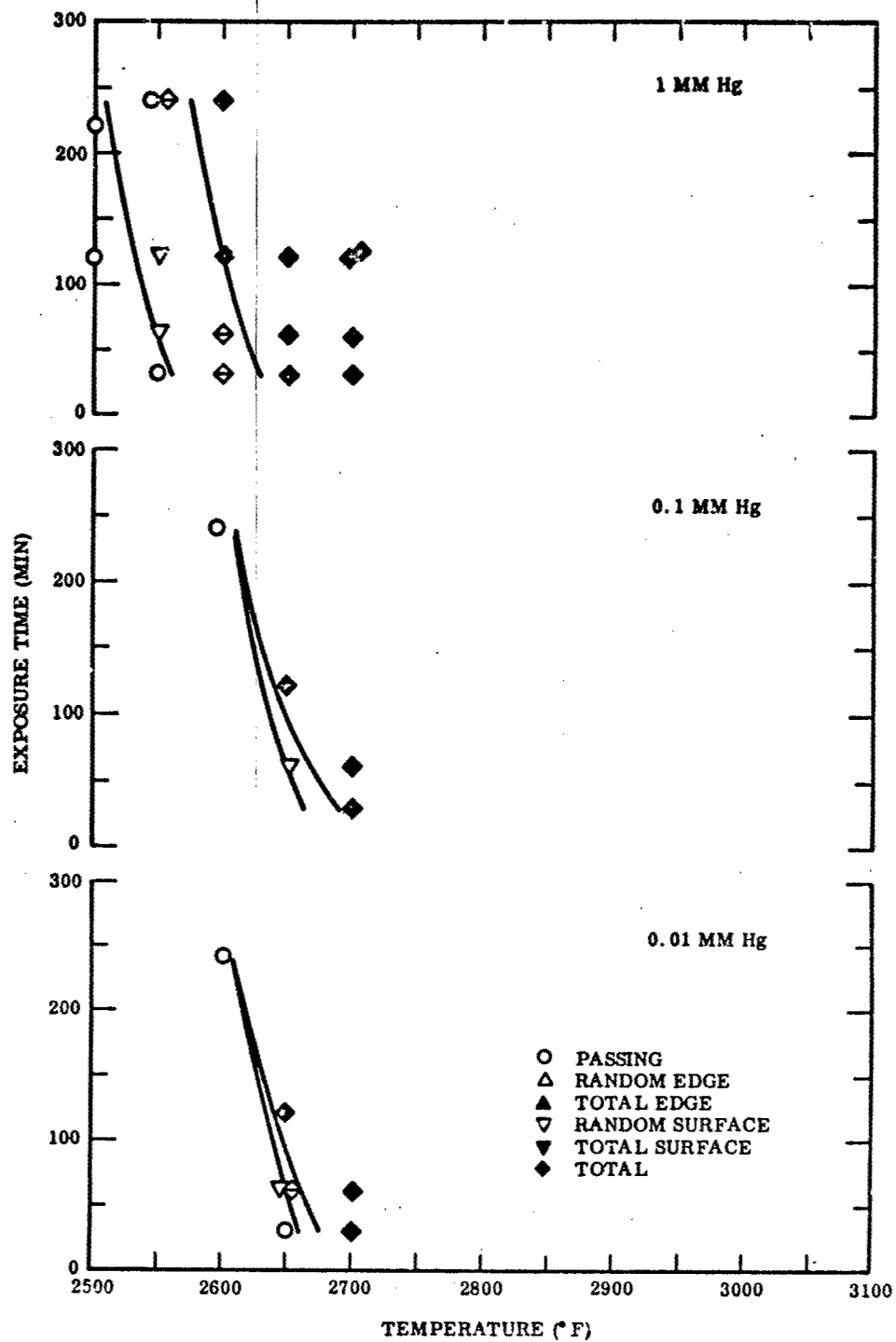
219

Figure 97 Results of Baseline Tests, Cb-752/CrTiSi

220
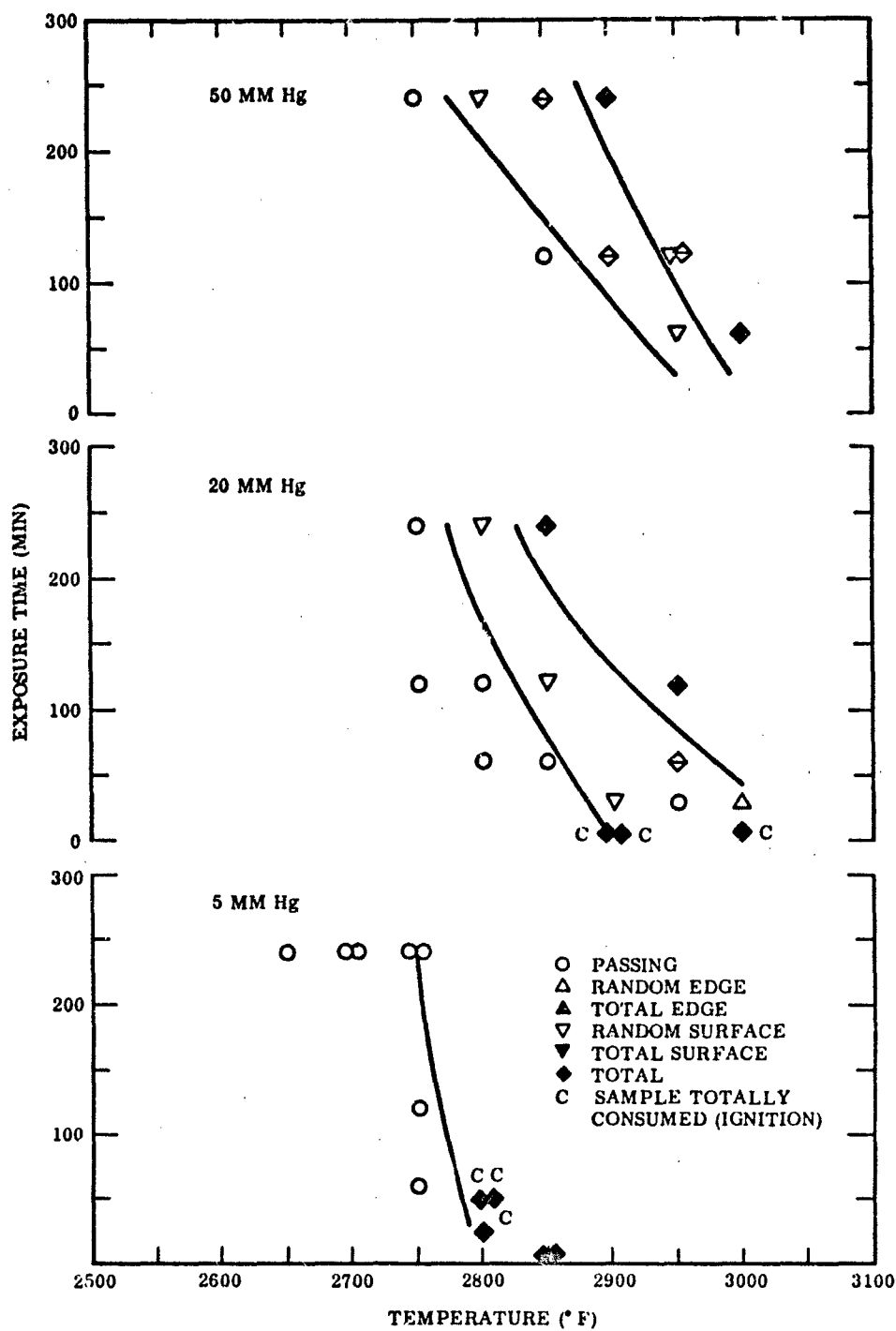
Figure 97 Results of Baseline Tests, Cb-752/CrTiSi (cont'd)

221
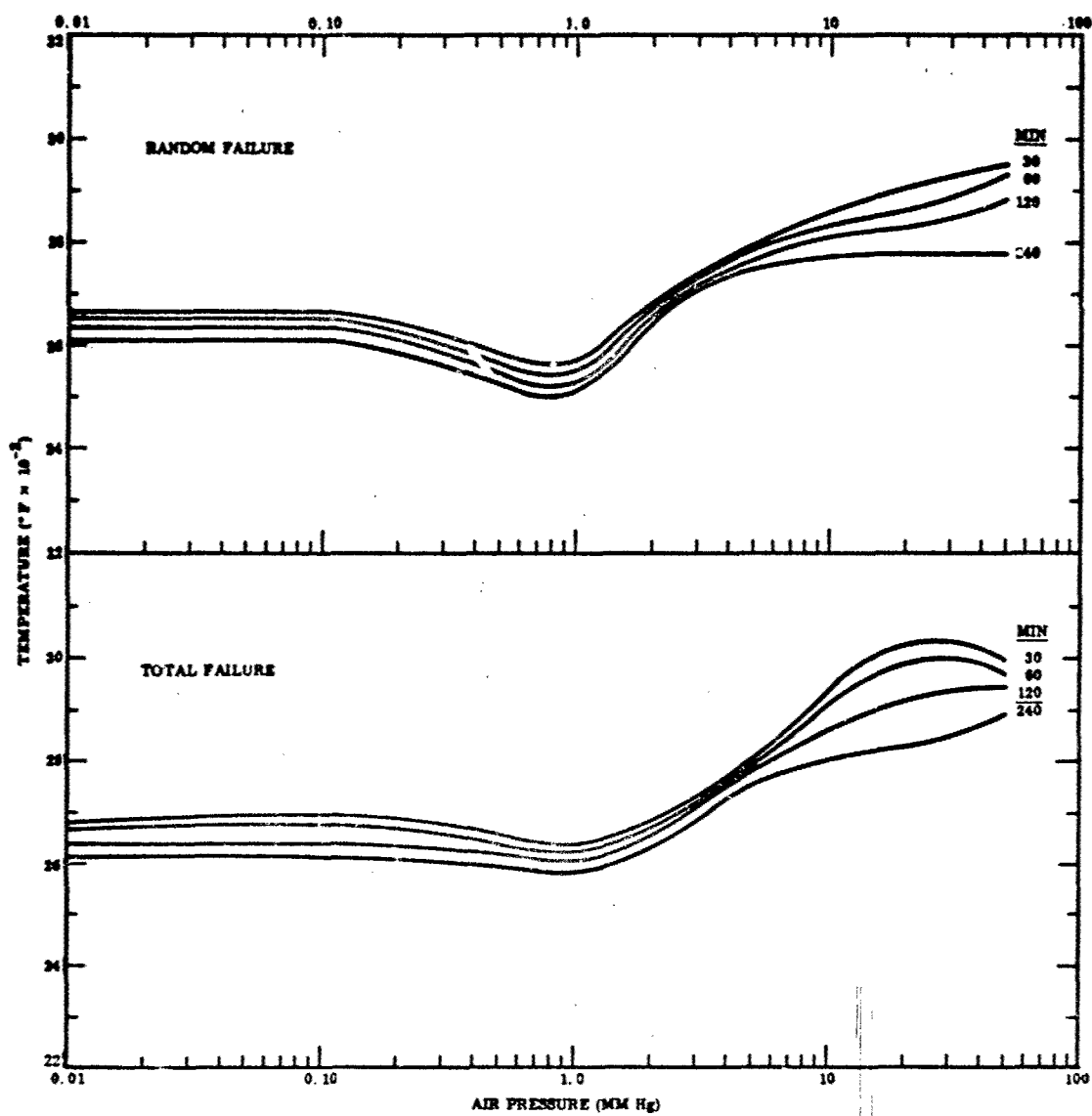
Figure 98 Baseline Failure Limits, Cb-752/CrTiSi

222

metallographic examination for oxide precipitation and substrate hardening. For many applications, good structural integrity would be retained well into the random failure region. This fact, coupled with a wide spread between random and total failures above 1 mm Hg, provides some factor of safety in utilization of the system.

One advantage cited for coated Cb-base alloys is the gradual degradation that occurs upon failure. Often, the substrate retains sufficient integrity after coating failure to prevent catastrophic destruction of the part. With coated Mo-base alloys, on the other hand, large holes or complete consumption of the substrate may occur shortly after initial failure of the coating due to the volatility of molybdenum oxides. One important exception to this generalized behavior for coated Cb-alloys was observed in tests of the Cb-752/CrTiSi system at pressures of 5 and 20 mm Hg. At these pressures, ignition and rapid combustion of the entire sample occurred after initial coating failure at temperatures of 2800 to 3000° F. The effect was most pronounced at 5 mm Hg pressure where three of five samples ignited and burned after 25 to 50 min in slowly moving air at 2800° F. Two specimens resistance heated to 2900° F burned through 2 to 8 min after reaching temperature but did not continue to burn when the heating current was cut off. At 2750° F, however, no failures were detected after 4-hr exposure in air at 5 mm Hg pressure. The effect was more random at 20 mm Hg· pressure where only three of a total of nine failed specimens ignited and burned. In these tests at 2900 and 3000° F, combustion occurred within 30 sec to 5 min at temperature. Ignition was not encountered in tests to 3000° F at 50 mm Hg pressure. Also, ignition did not occur in any tests at pressures of 0.01 to 50 mm Hg at temperatures below 2800° F. It is possible that combustion might occur at 2800° F or higher in air at pressures below 5 mm Hg. However, since total failure occurred in less than 30 min below this temperature in all cases, no tests were run at 2800° F or above. It is believed that ignition and combustion is a temperature/pressure dependent phenomenon. Based on present investigations, ignition can occur upon coating failure at temperatures above 2750° F and pressures below 20 mm Hg. Twenty mm Hg may be an upper limit of pressure for ignition failures. The speed of combustion once ignition occurs is very fast. In one test at 2800° F and 5 mm Hg pressure, a sudden drop in chamber pressure was observed. Upon looking in the furnace a few seconds later, it was found that the specimen had disappeared. In all but one case of combustion, no trace of the samples or oxide residues could be found anywhere in the furnace after test. In one case, combustion was observed in a resistance-heated test specimen. The sample parted in the middle and within a few seconds burned back to leave a stub end in each of the two water-cooled electrodes. This was not due to arcing, which may occur upon failure of resistance-heated specimens, but was a definite combustion-type reaction.

Needless to say, ignition and combustion are of critical significance in the utilization of coated Cb-base alloys. Detailed studies should be made to determine the basic cause of such behavior and the precise conditions under which ignition will occur.

First failures in the Cb-752/CrTiSi system occurred at random locations on edges and flat surfaces. Generally, edge failures occurred simultaneously or within a very short time of each other. No preference for initial failure at either edge or surface sites was indicated. Unlike other silicide-base coatings, attack was not localized at cracks or fissures in the coating. Such defects, however, may have provided paths for leakage of gases through the coating where substrate embrittlement without noticeable coating

degradation was observed. However, in no cases could random failures be correlated directly with crack-type coating defects.

Random defect failures could be correlated with local variations in coating thickness and composition. Upon testing at pressures from 0.01 to 760 mm Hg, samples developed ridged surface patterns, as shown in Figure 99. Random areas on the surface were in high relief. Micrometer measurements of total specimen thickness after testing indicated a 5 to 30% growth in thickness with an average of about a 15% increase. Areas in relief were about 1.8 mils above the original surface, and coating thickness at these points was double that of the initial average value. A marked surface recession was noted in the areas between ridges. This effect is illustrated by the cross section of a sample tested in air at 1 atm (Figure 100). After 4 hr at 2700° F, the residual coating was 3.5 mils thick in the ridged areas and about 0.9 mil thick in the depressed plateau regions. First failures at all pressure levels invariably occurred in these depressed regions. Detailed studies revealed that these regions corresponded to the light-colored areas on the as-coated samples where a continuous $(Cb, Ti)Cr_2$ layer existed at the interface. The ridged regions which were relatively unattacked and remained protective corresponded to the dark areas of the as-coated samples. As previously discussed, these areas do not have a $(Cb, Ti)Cr_2$ interfacial zone and probably are enriched in Cb, Ti, W, and Zr. The similarity of the ridged pattern after oxidation testing (Figure 99) and the original surface pattern (Figure 92) is readily apparent.

The differences in oxidation behavior of light and dark regions of the coating were more pronounced upon testing at reduced pressure. Whereas the coating was still protective after 4 hr at 2700° F in air at 760 mm Hg, it failed completely in less than 30 min at 2700° F in air at 0.10 mm Hg. As shown in Figure 101, residual coating in the ridged areas (dark regions as-coated) was 2-2.5 mils and still protective after the reduced pressure test. However, in the depressed areas (light regions as-coated), the coating was oxidized completely and total failure had occurred. The extent of substrate oxidation in the failed areas is shown by relief polishing (Figure 101A) and by the large amount of oxide precipitates in the substrate (Figure 101B). Hardness below the ridged areas was 189 DPH, the same as that of the substrate in the as-coated condition. Substrate hardness in the failed regions (relief polished areas in Figure 101A) averaged 99 DPH.

The formation of elevated ridges was observed in all samples tested from 2500 to 3000° F in air at pressures of 0.01 to 760 mm Hg. The extent of elevation above the original coating surface and general microstructure indicates that localized melting and forces of surface tension caused the ridges to be formed. Enrichment of the dark-colored regions with titanium as a result of penetration into the Ti-rich diffusion zone during coating may have lowered the melting point in these areas. Eutectic melting will occur in the Ti-Si system at 2400-2500° F, and it is reasonable to expect melting in one or more of the Ti-rich inner silicide layers of the coating upon heating at 2500° F or higher. The composition of these localized regions may change upon melting as a result of alloying with surrounding coating material. If sufficient change occurs, the areas may solidify and have a higher remelt temperature. It was not determined whether the ridged areas were liquid or solid at test temperature. However, the existence of ridged areas in samples tested in high-velocity air (Mach 3) from 2750 to 2900° F suggests that solidification occurred immediately after melting.

224
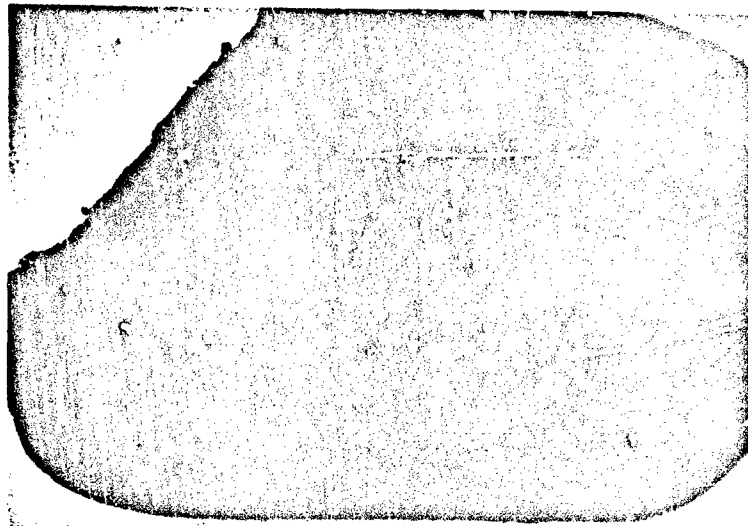
M6376   (A) 2500° F, 1 mm Hg, 240 min   ×6
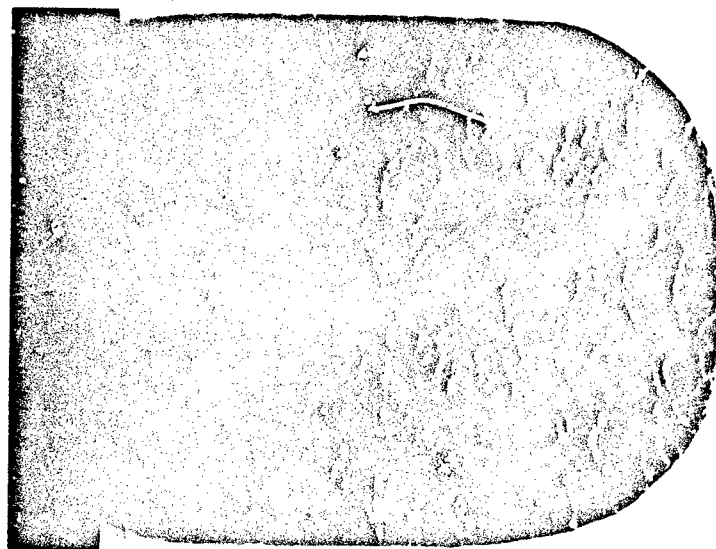
M6373   (B) 2650° F, 0.10 mm Hg, 30 min   ×6

Figure 99 Surface Topography After Oxidation Testing,
Cb-752/CrTiSi

225
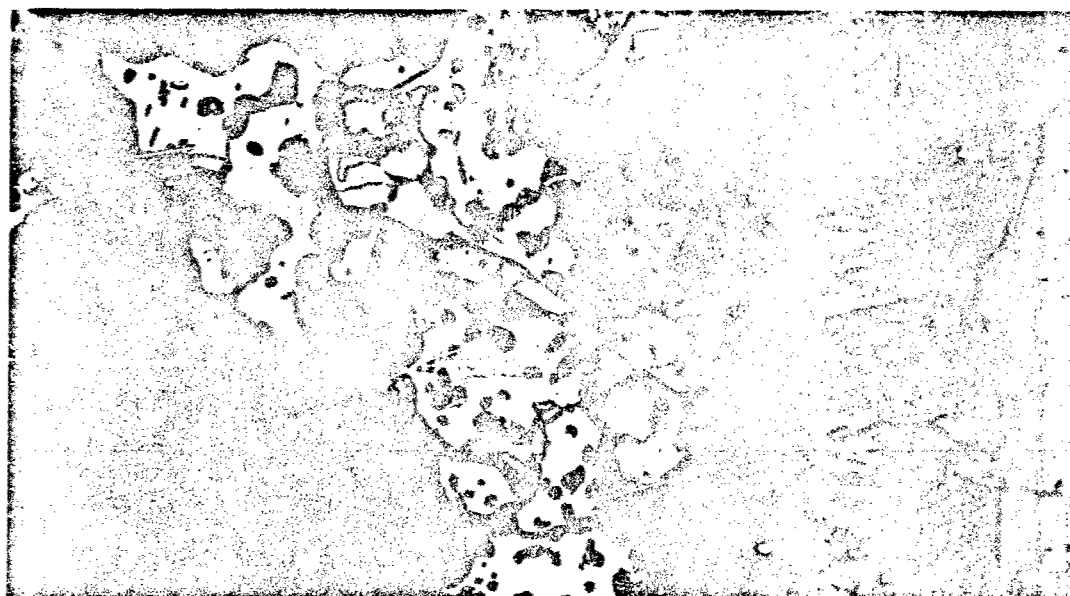
M6325   (A) Ridged Area   ×1000

M6324   (B) Plateau Area   ×1000

Figure 100 Microstructure of Cb-752/CrTiSi After Test in Air at 760 mm Hg Pressure, 2700°F, 240 min

226

M6383

(A) Failure Pattern

×50
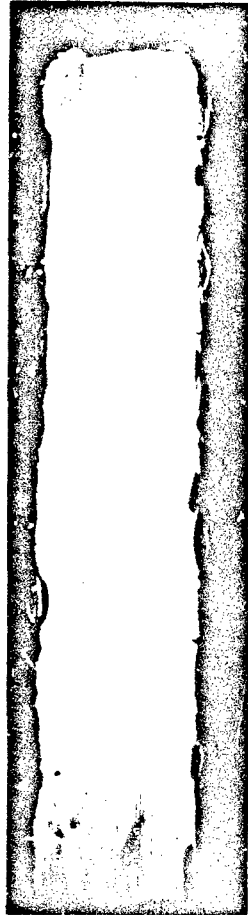
M6307, 6305 — (B) Structural Details in Good and Failed Regions

×1000

Figure 10J Microstructure of Cb-752/CrTiSi After Test in Air at 0.10 mm Hg Pressure. 2700°F, 30 min

227

Random failures in the Cb-752/CrTiSi system occurred either by leakage of oxygen and/or nitrogen through the coating or by surface recession. Leakage, and hence failure, was accelerated at reduced pressure by changes in composition of the coating and oxidation products. At pressures of 5 to 50 mm Hg, low rates of surface recession of the coating were observed. As shown in Figure 102, after 1 hr at 2750° F in air at 5 mm Hg the residual coating was 1 to 2 mils thick in plateau region and 3 to 4 mils thick in ridged regions. An adherent oxide scale had formed. The oxide on ridged areas tended to a rust color, indicating enrichment with titanium in these regions. Oxide on the plateau areas was green to gray-green in color, indicative of a high chromium content. Random failures occurred by gas leakage through the coating in thinner regions of the plateau areas. Hairline fissures might provide paths for gas leakage, or gases may diffuse through the coating. The plateau areas were gradually depleted in chromium, as evidenced by disappearance of the $(Cb, Ti)Cr_2$ interfacial zone during exposure. It is postulated that chromium was lost by a combination of direct volatilization and selective oxidation to Cr_2O_3 which subsequently evaporated from the scale. Deposits of Cr_2O_3 were found in cooler regions of the furnace after all tests. TRW (33) has concluded that the CrTiSi coating becomes more permeable to oxygen as a result of chromium loss by evaporation at low pressure (10^{-2} mm Hg). However, evidence of chromium loss at pressures up to 50 mm Hg has been found in this study of the Cb-752/CrTiSi system.

At pressures of 1 mm Hg or less, high rates of surface recession were observed. As shown in Figures 103 and 104, the coating in plateau regions was consumed completely within 1 hr at 2650° F in air at 0.1 to 1.0 mm Hg pressure. In ridged areas, however, 1 to 4 mils of coating remained. At 0.1 mm Hg, only the 0.5—0.75-mil-thick outer region of the ridges had been attacked, leaving a porous layer of oxide and coating (Figure 104A). Random failures, like those at higher pressure, were confined to the plateau regions where the $(Cb, Ti)Cr_2$ interfacial zone had existed in the as-coated condition. However, at 1 mm Hg and lower, the primary causes of failure were surface recession and loss of coating rather than leakage through the coating. The oxide scale on all samples tested at pressures below 5 mm Hg was rich in CbO_2 and was similar to that formed on the PFR-32 coating in this pressure range. The scale tended to spall upon cooling to room temperature.

Gas Velocity

Two methods for true versus apparent temperature calibration of resistance-heated specimens were employed. First, direct sightings on coated and bare substrates indicated normal emittance values of 0.75 to 0.90 in the 2500—2800° F range. Coated samples were preoxidized in air at 20 mm Hg before calibration. Second, using an estimated emittance of 0.75, coated samples were heated by direct resistance for 30 min at 2500, 2600, 2700, and 2800° F in air at 20 mm Hg pressure. A second set of samples was heated under the same conditions by radiation in a blackbody zone to provide a known true-temperature baseline. Metallographic studies of diffusion zones then were made to determine if zone thickness measurements could be used to calculate the true temperature of the resistance-heated samples. A reasonable correlation was obtained from thickness measurements of the innermost diffusion zone within the coating. This zone is shown in Figures 100A, 101A, 102A, 103A, and 104A as a single phase,

228

×1500
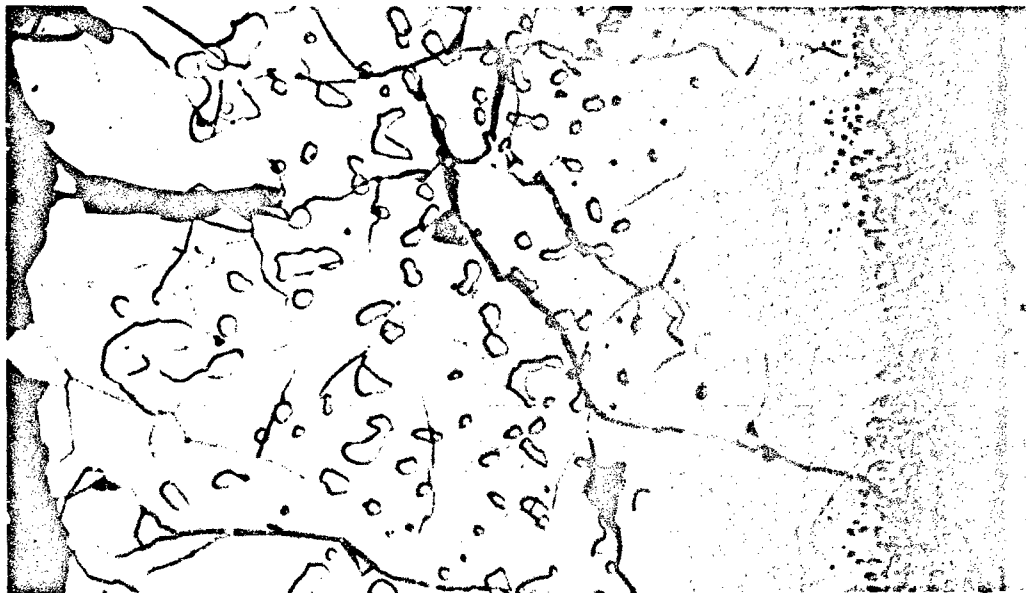
(B) Plateau Area

M9238

×1000

(A) Ridged Area

M3803

Figure 102 Microstructure of Cb-752/CrTiSi After Test in Air at 5 mm Hg pressure, 2750°F, 60 min

229

M6328 ×1000 (A) Ridged Area M6329 ×1000 (B) Plateau Area

Figure 103 Microstructure of Cb-752/CrTiSi After Test in Air at 1 mm Hg Pressure, 2650° F, 60 min

230
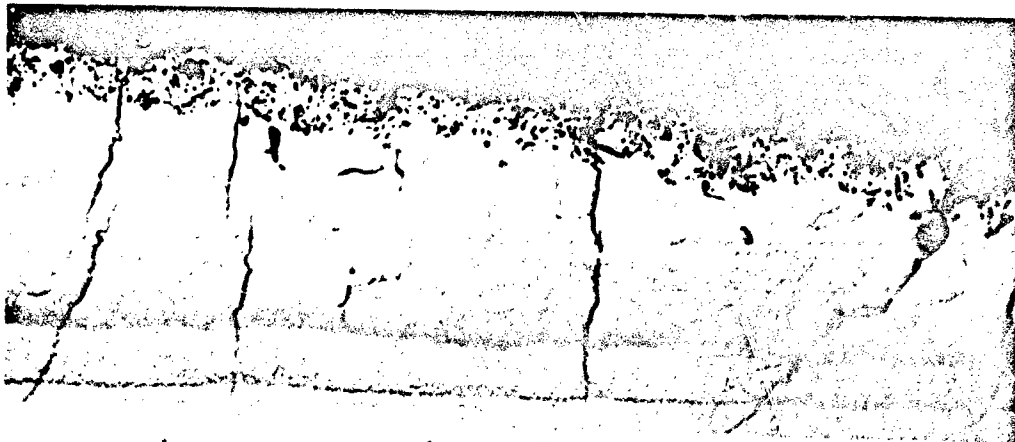
M8315   (A) Ridged Area   ×1000

M8316   (B) Plateau Area   ×1000

Figure 104 Microstructure of Cb-752/CrTiSi After Test in Air at 0.1 mm Hg
Pressure, 2650° F, 60 min

231

dark-stained layer adjacent to the coating substrate interface. A 0.05-mil-thick layer of this zone also is seen on as-coated specimens in the dark regions [(Cb, Ti)Cr_2 free, Figure 94B]. The results are presented in Table XLIX.

Table XLIX. Temperature Calibration of Cb-752/CrTiSi
by Diffusion-Zone Method

Radiant heated			Resistance heated	
True temp. (°F)	Zone thickness (mil)	Estimated true temp. (a) (°F)	Zone thickness (mil)	Calculated true temp. (°F)
2500	0.18	2500	—	—
2600	0.28	2600	0.24	2560
2700	0.38	2700	0.33	2660
2800	0.51	2800	0.46	2760

(a) Assume $\epsilon = 0.75$.

.True temperatures for resistance-heated specimens were calculated from a plot of log of zone thickness versus reciprocal absolute temperature for radiation specimens using zone thickness values measured on resistance-heated samples. These values were about 40°F less than the estimated true temperature based on an emittance of 0.75. A corrected emittance value of 0.85 was used for the gas velocity tests.

It was not determined whether measurement of this zone could be used as an index of temperature for widely varying exposure conditions. Cursory studies indicate that zone thickening may not follow a parabolic rate low and may be dependent to a large extent on environment and local variations in coating composition. Further work is required to determine if such measurements can be applied as broadly for this coating system as those for Cb-752/PFR-32 or silicide-coated Mo-base alloys.

The equivalence of tests in air and $N_2:O_2$ mixtures at the same oxygen partial pressure was studied. Performance and general appearance were found to be the same for tests in air at 5 mm Hg pressure and in a 19:1 $N_2:O_2$ mixture at 20 mm Hg pressure ($P_{O_2} = 1.0$ mm Hg). As shown in Figure 105, the microstructure of samples tested in the equivalent atmospheres was identical. The 19:1 $N_2:O_2$ mixture at 20 mm Hg pressure, therefore, was used in Mach 3 flow tests to simulate a 5 mm Hg air environment used in the baseline tests. The results of these tests are summarized in Table L.

No effect of gas velocity on performance capabilities was found. All specimens exhibited performance capabilities equivalent to those of baseline samples. Total failure at 2900°F and 20 mm Hg in about half the time predicted from baseline results was probably due to slight errors in temperature. From Figure 97, total failure would have occurred in 60 min at 2980°F, only 80°F higher than the assumed test temperature. Localized overheating often occurs in resistance specimens after one or more random failures appear,

232

M9234   ×1000

(B) 2750°F, 20 mm Hg, 30 min 19:1 N_2:O_2

M9239   ×1000

(A) 2750°F, 5 mm Hg, 30 min, Air

Figure 105 Equivalence of Tests in Air and in 19:1 N_2:O_2 Mixtures at the Same Oxygen Partial Pressure

233

and test temperature is difficult to control beyond this point. The general surface and microstructural appearance of flow-tested specimens was identical to that of equivalent baseline specimens.

Table L. Results of Mach 3 Flow Tests, Cb-752/CrTiSi

Test conditions						Baseline time to failure	
Temp. (°F)	Total pressure (mm Hg)	Atmosphere	Equivalent air pressure (mm Hg)	Time (min)	Performance rating	Random (min)	Total (min)
2850	20	Air	20	60	Pass	75	200
2900	20	Air	20	60	Total failure	< 30	135
2750	20	19:1 N_2:O_2	5	60	Pass	240	240

Vacuum Volatility

The results of vacuum exposure studies are summarized in Table LI and Figure 106. Samples lost weight but increased in thickness upon heating from 2600 to 3200° F in vacuum. Thickness increase was due to local melting and formation of ridged areas like those developed in oxidation tests. Coating thickness decreased in plateau areas, but thickness changes could not be followed by micrometer measurements. As shown in Figure 106, curves of weight loss versus square root of time were linear at low pressure and for short times at high temperature. The fit to a parabolic relation indicates diffusion control of the process. The curves shown are similar to those found for Cb-752/PFR-32 and for the coated TZM systems. The weight loss after 4 hr at 3200° F was 0.07 gm, which is the same as the average weight increase upon coating as calculated from the weight of 100 random samples. This would indicate that most of the coating is destroyed upon high-temperature exposure.

Coating structure after 4 hr at 2600 and 3200° F is shown in Figure 107. At 2600° F, degradation is confined to the outer Si-rich CrTiSi layer. About one-third to one-half of the coating has been converted to a spongy, porous layer that probably would burn off rapidly upon subsequent exposure to air. The underlying portion of the coating is dense, however, and should be protective. At 3200° F, a band of almost continuous porosity developed at the substrate/coating interface. Large voids existed in areas where the (Cb,Ti)Cr$_2$ interface had existed. The outer Si-rich CrTiSi layer was severely attacked, and only a few scattered islands of this phase remained. The coating in this condition probably would fail in oxidation tests. High-temperature vacuum exposure also affected the substrate, as indicated by the complete absence of precipitates after 4 hr at 3200° F.

Weight loss and microstructural data indicate that silicon, and perhaps some chromium, is lost by disproportionation at 2600 − 2800° F. At 3000 and 3200° F, however, both Si and Cr are lost, with a resultant marked increase in weight loss and internal degradation of Cr-rich regions of the coating. It is concluded that exposures of up to 1 hr at 2600 to 2800° F should not seriously degrade the protective capabilities of the CrTiSi coating.

234

Table LI . Results of Vacuum Volatility Studies, Cb-752/CrTiSi

Temp. (°F)	Pressure (mm Hg)	Time (min)	Surface area (cm²)	Thickness			Weight		Weight loss (gm/cm²)
				Initial (mils)	Final (mils)	decrease (mil/side)	Initial (gm)	Final (gm)	
2600	2×10^{-5}	30	4.77	24.3	25.4	+0.55	1.1165	1.1048	2.46×10^{-3}
	2×10^{-5}	60			—	—		1.0999	3.48×10^{-3}
	1×10^{-5}	120			—	—		1.0926	5.0×10^{-3}
	9×10^{-6}	240						1.0814	7.36×10^{-3}
2800	4×10^{-5}	30	4.65	—	—	—	1.1102	1.0841	5.61×10^{-3}
	2×10^{-5}	60			—	—		1.0767	7.20×10^{-3}
	9×10^{-6}	120			—	—		1.0681	9.05×10^{-3}
	7×10^{-6}	256			—	—		1.0610	1.06×10^{-2}
3000	2×10^{-5}	30	4.35	24.2	—	—	1.0509	0.9996	1.10×10^{-3}
	1×10^{-5}	60			—	—		0.9940	1.22×10^{-2}
	1×10^{-5}	120			—	—		0.9887	1.34×10^{-2}
	9×10^{-6}	240			—	—		0.9835	1.45×10^{-2}
3200	2×10^{-5}	30	4.70	24.3	—	—	1.0931	1.0255	1.35×10^{-2}
	1×10^{-5}	60			—	—		1.0271	1.40×10^{-2}
	1×10^{-5}	120			—	—		1.0249	1.45×10^{-2}
	9×10^{-6}	240			—	—		1.0224	1.50×10^{-2}

235
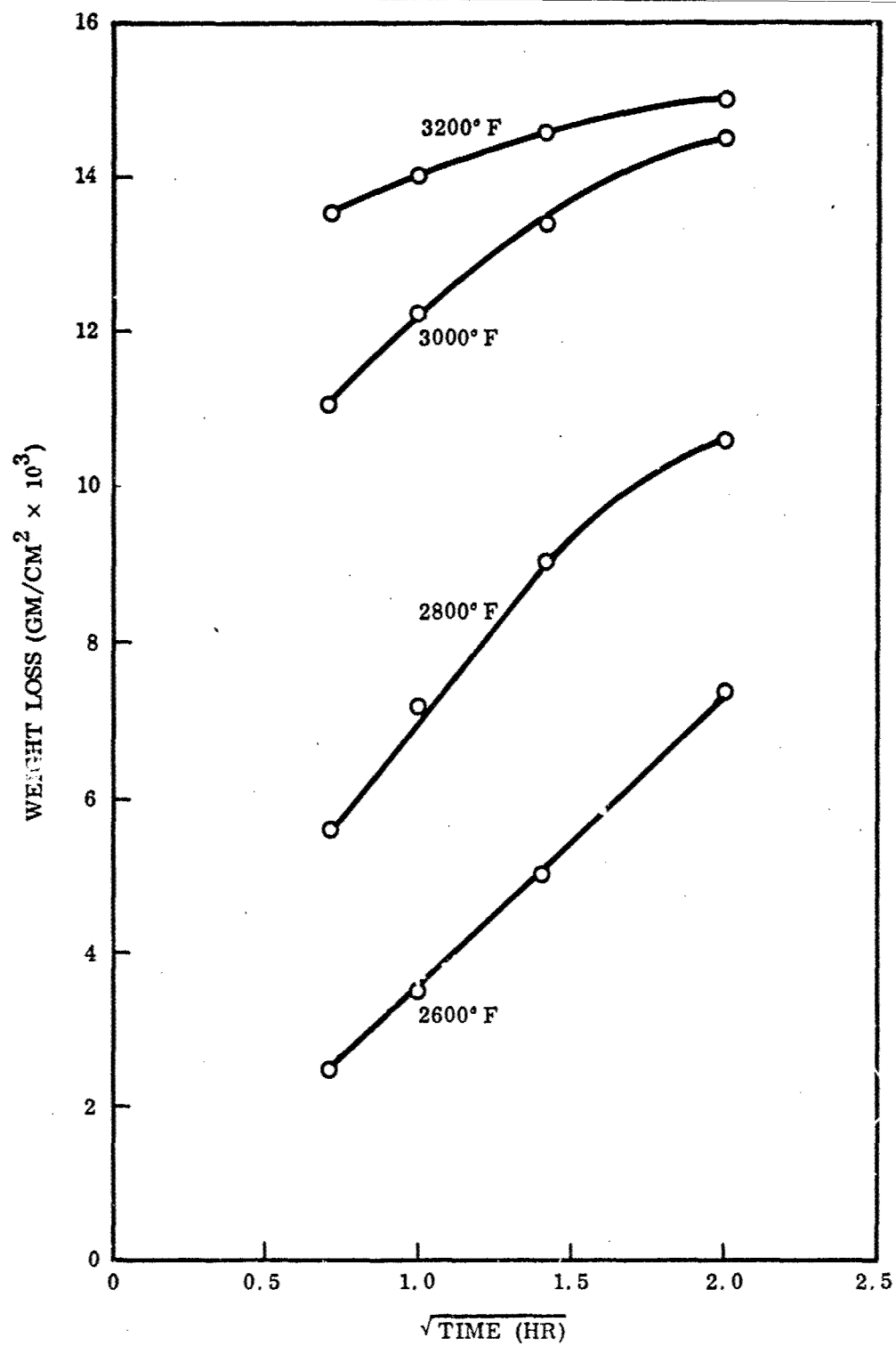
Figure 106 Vacuum Volatilization Rate, Cb-752/CrTiSi

236
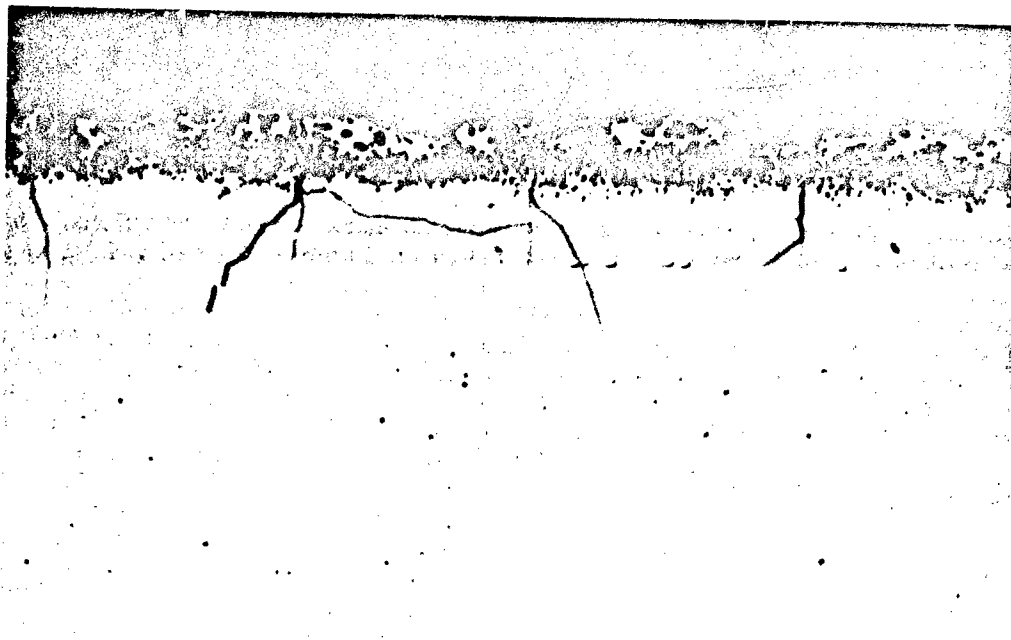
P678 (A) 2600° F, 240 min ×500

P693 (B) 3200° F, 240 min ×500

Figure 107 Structure of Cb-752/CrTiSi After Vacuum Exposure

Temperature-Pressure Cycling

The Cb-752/CrTiSi system was not significantly degraded by cyclic variations in temperature and pressure. As shown in Table LII, cyclic conditions typical of external surfaces of reentry vehicles (1-3 mm Hg range) could be tolerated. Exposure equivalent to 4 reentry cycles was tolerated, and the general condition of the sample was similar to that of samples tested under steady-state baseline conditions. In cyclic tests simulating internal surfaces (0.01 to 0.10 mm Hg), total failure occurred in one-half the time to random failure and one-third the time to total failure. However, it should be noted that at 2675° F, only 25° F above the baseline phase of the cycle, total failure would have occurred in 30 min (Figure 97). Hence, it cannot be concluded with any certainty that cyclic exposure degraded performance in this test. It is more likely that a slight temperature error resulted in early failure. This is substantiated by the fact that 30-min exposure to vacuum at 2600° F did not degrade performance in air at 1.0 mm Hg at 2600° F. Here, in fact, the sample was good, whereas baseline data would have predicted random failure.

Table LII. Results of Temperature and Pressure Cycling, Cb-752/CrTiSi

Phase of cycle	Test conditions					Performance rating	Baseline time to failure	
	Temp. (° F)	Pressure (mm Hg)	Time (min)	No. of cycles	Total time (min)		Random (min)	Total (min)
1st (Baseline)	2550	1.0	7	4	28	Pass	60	>240
2nd	2200	3.0	21		84			
1st (Baseline)	2550	0.01	7	4	28	Total failure	60	90
2nd	2200	0.10	21		84			
1st (Vacuum)	2600	10^{-5}	30	1	30			
2nd (Baseline)	2600	1.0	30		30	Pass[a]	<30	120

(a) Adherent rust-colored scale, unlike baseline 1 mm Hg test specimens.

Of interest in the vacuum preexposure test was the complete change in oxide scale characteristics. A uniform rust-colored adherent scale was formed upon oxidation at 1 mm Hg in contrast to a blue-gray oxide which formed on specimens not preexposed to vacuum and spalled upon cooling. Enrichment with Ti as a result of Si and Cr loss upon heating in vacuum was probably responsible for this change.

Acoustic Vibration

Metallographic examination of samples exposed to random and sine vibration at high-intensity levels revealed no significant effects on coating structure. As shown in Table LIII, specimens exposed to acoustic radiation did not exhibit premature failure

238

In oxidation tests at 1.0 mm Hg. Since Cb-752/CrTiSi appears to be relatively toler-ant of hairline fissures, it is unlikely that vibration would have any effect on subse-quent performance capabilities.

Table LIII. Results of Acoustic Vibration, Cb-752/CrTiSi

| Vibration mode | Exposure conditions | Test conditions | | | Performance rating | Baseline time to failure | |
		Temp. (°F)	Pressure (mm Hg)	Time (min)		Random (min)	Total (min)
Random	(a)	2525	1.0	60	Pass	150	>240
Sine	(b)	2525	1.0	60	Pass	150	>240
		2800	20	60	Pass	175	>240

(a) 30−1,500 cps, 159.5 dB, 60 sec.
(b) 50−1,500 cps, 172.5 dB peak at 510 cps, 20 sec at each of 100-cps intervals.

Defect Tolerance and Repair

Resistance to formation of crack-type defects in bending and impact was evaluated.
At temperatures of 75 to 216° F, fracture and spalling of the coating occurred at bend angles of 23 to 28 deg. Temperature had little if any effect on bend angle to coating fracture. Samples bent just short of fracture (20 deg) did not fail after 1 hr at 2525° F in air at 1.0 mm Hg pressure. From baseline results, random failure would have occurred with unstressed samples in 150 min at 2525° F or in 60 min at 2550° F.

The types of defects introduced upon bending are shown in Figure 108. Hairline fissures preexisting in the coating were widened and extended into the Ti-rich diffusion zone upon bending. It is surprising that defects of this severity did not degrade performance significantly From all indications, the Cb-752/CrTiSi system has a high tolerance for defects under selected test conditions.

The Cb-752/CrTiSi system was severely damaged in impact at relatively low velocities and energy levels. As shown in Table LIV, coating fracture and spalling occurred at energy levels of 0.6 ft-lb. Complete fracture of the specimen by shattering occurred at 0.7 ft-lb, as shown in Figure 109. Although this system is normally considered ductile, at high strain rates (impact) brittle fracture occurs when deformation is per-mitted. Conversely, when deformation is prevented (steel backup), no damage was observed at the highest energy level (2.3 ft-lb).

Samples impacted at 0.3 ft-lb (rubber backup), where coating cracking and spalling occur, failed at random surface sites in the impact area upon oxidation testing.
Failure occurred in 60 min at 2525° F in air at 1.0 mm Hg. Corresponding baseline life is 150 min; however, at 2550° F random failure would occur in 60 min. Since

239

M8359   ×500

(A) As-Coated

P507   ×500
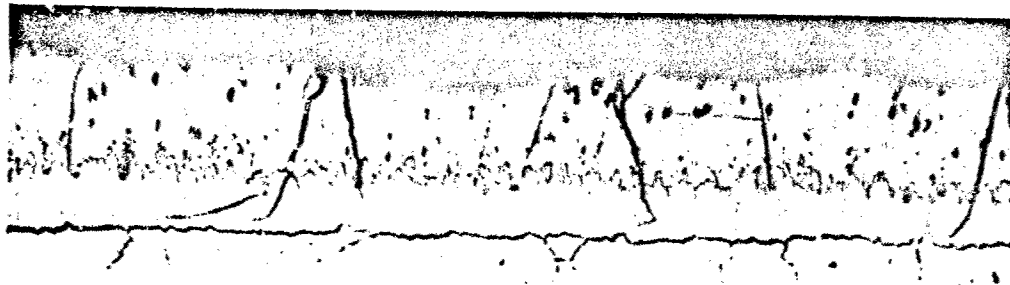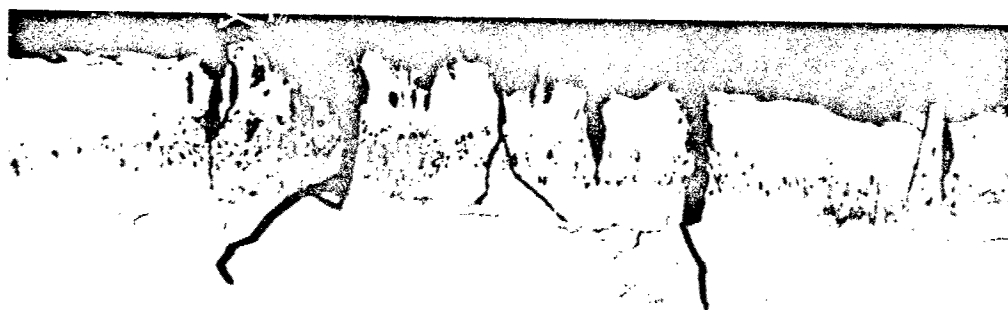
(B) Bent 20 deg at Room Temperature, Tensile Side at Point of
    Maximum Strain

Figure 108 Defects Produced on Bending Short of Coating Fracture, Cb-752/CrTiSi

240

(A) 137 ft/sec, 0.6 ft-lb — Coating
Fracture, Spalling

(B) 153 ft/sec, 0.7 ft-lb — Specimen
Fracture

Figure 109 Fracture of Cb-752/CrTiSi Upon
Ballistic Impact (Rubber Backup)

random failure was confined to the impact area, it is concluded that performance was degraded in this case. Cracks formed upon impact penetrated into but not through the substrate, resulting in premature failure. Low defect tolerance is indicated when cracks penetrate through the diffusion zone and into the substrate.

Table LIV. Results of High-Velocity Impact Tests, Cb-752/CrTiSi

Backup	Kinetic energy (ft-lb)[a]					
	Spalling		Coating fracture		Substrate fracture	
	Pass	Fail	Pass	Fail	Pass	Fail
Rubber	0.3	0.6	0.3	0.6	0.6	0.7
Steel	2.3	>2.3	2.3	>2.3	2.3	>2.3

(a) Calculated from pellet mass and velocity at time of impact.

The tolerance of this system for defects is further illustrated by rer ts of tests on samples with gross defects penetrating one-half and three-fourths o he original coating thickness (Table LV). No significant degradation was indicated, even for 3/4 t defects, in tests to 2800° F at 1.0 and 20 mm Hg. However, low tolerance for gross defects was indicated in two other regions of temperature and pressure: (1) low-pressure region (< 1 mm Hg) where surface recession controls behavior and (2) high-temperature (> 2800° F), high-pressure (> 1 mm Hg) regions where ignition and combustion can occur. In these ranges, 1/2 t defects cause a significant reduction in performance.

Table LV . Results of Defect Tolerance Studies, Cb-752/CrTiSi

Test conditions			Performance rating			Baseline time to failure	
Temp. (°F)	Pressure (mm Hg)	Time (min)	1/2 t defect	3/4 t defect	Bulk sample	Random (min)	Total (min)
2750	20	240	Pass	Pass	Pass	>240	>240
2800	20	30	Pass	Pass	Pass	175	>240
2800	20	60	Pass	Pass	Pass	175	>240
2850	20	21	Ignition and combustion			85	240
2850	20	59	Ignition and combustion			85	240
2525	1.0	30	Pass	Pass	Pass	150	>240
2525	1.0	60	Pass	Pass	Pass	150	>240
2600	1.0	30	Pass	Pass	Pass	<30	120
2650	0.1	60	Fail	Fail	Total failure	60	95

Two methods of repair of defects were studied: (1) braze repair with Cu-Ag-Si or Cu-Ag-CbSi$_2$ pastes and (2) the solar CrTiSi patch-repair techniques. As shown in Table LVI, both techniques were effective. At 20 mm Hg, performance was

242

restored completely by Cu-Ag-Si brazing and by the solar process. One speci-
men repaired with Cu-Ag-CbSi$_2$ failed by combustion, probably as a result of
ineffective repair.

In all tests, defects penetrated into the substrate prior to application of the patch
repair. The structure of a sample repaired with a Cu-Ag-Si braze and tested at
2500° F in air at 1 mm Hg is shown in Figure 110. A thin layer of silicide remained
at the bottom of the defect, but the bulk of the patch had been oxidized to a glassy
plug. Most of the protection was provided by the thick glassy patch which may
have been liquid at the test temperature.

Table LVI. Results of Repair Studies, Cb-752/CrTiSi

Repair technique	Test conditions			Performance rating	Baseline time to failure	
	Temp. (°F)	Pressure (mm Hg)	Time (min)		Random (min)	Total (min)
Cu-Ag-Si	2500	1.0	60	4-pass	>240	>240
Cu-Ag-CbSi$_2$	2500	1.0	60	4-pass	>240	>240
Solar CrTiSi	2500	1.0	60	4-pass	>240	>240
Cu-Ag-Si	2850	20	60	4-pass	85	240
Cu-Ag-CbSi$_2$	2850	20	45	Ignition and combustion	85	240
Solar CrTiSi	2850	20	60	4-pass	85	240

Materials Compatibility

The Cb-752/CrTiSi reacted mildly with ZrO$_2$, Al$_2$O$_3$, and SiO$_2$ at temperatures up
to 2600° F in air at 0.01 to 760 mm Hg pressure. Some discoloration and a tendency
for adherence occurred at contact points but in no cases did sufficient reaction occur
to cause failure. (See Figure 99A.) Severe reaction with degradation of performance
was noted upon contact with Al$_2$O$_3$ at 2700° F and SiO$_2$ at 2750° F. The coating was
not affected by contact with MoSi$_2$ at temperatures up to 3000° F.

The results of compatibility studies with other coating systems are summarized
in Table LVII. All silicide-base coatings on TZM and Cb-752 were compatible;
no tendency for interaction of coating systems was found. A potential compati-
bility problem with Ta-10W/Sn-Al was indicated, however.

As shown in Figure 111, the CrTiSi coating was attacked by liquid tin. Reaction
products penetrated three-fourths of the coating thickness on the contact side.
Reaction with tin was also noted on the opposite side. Either the tin wet
and flowed over the entire surface or tin vapor reacted with the coating. Although
the CrTiSi coating remained protective under these test conditions, it is likely
that performance may be degraded at higher temperatures as indicated by the com-
plete destruction of the CrTiSi coating on B-66 in contact with Sn-Al at 2675° F.
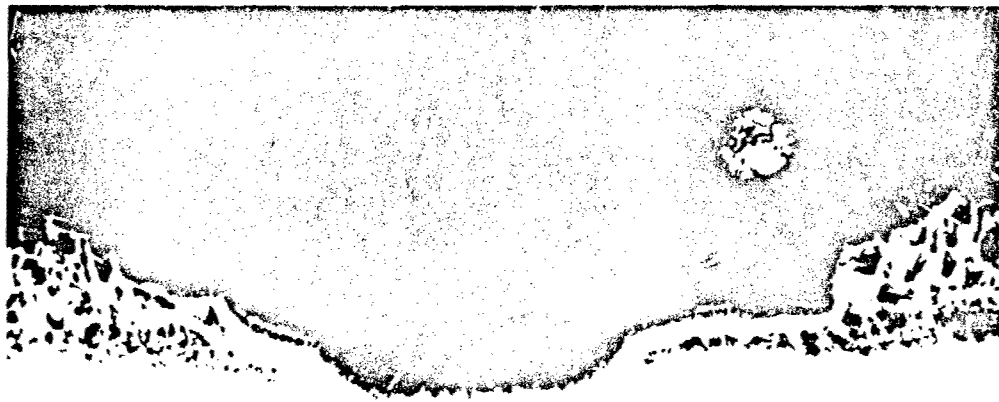
M9320   (A) Glassy Oxide Plug   ×400
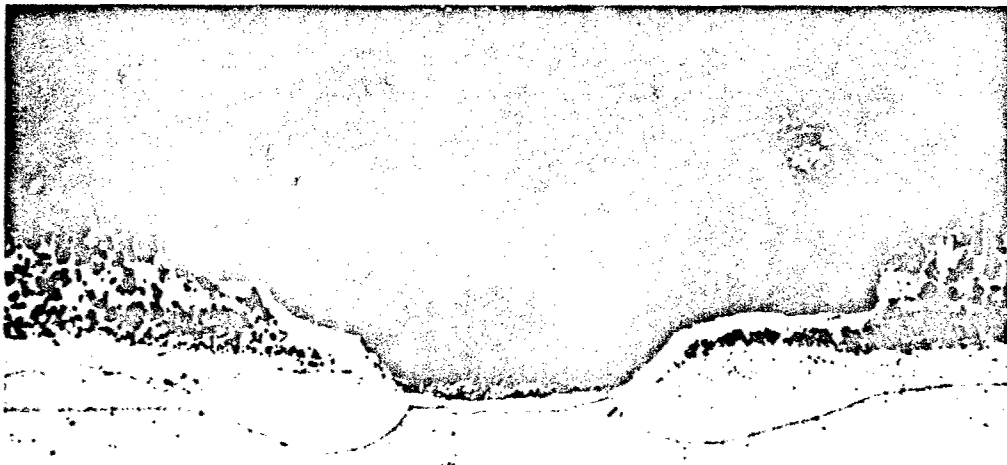
M9320   (B) Residual Coating   ×400

Figure 110 Cu-Ag-Si Repair of Cb-752/CrTiSi Tested at 2500°F, 1 mm Hg, 60 min
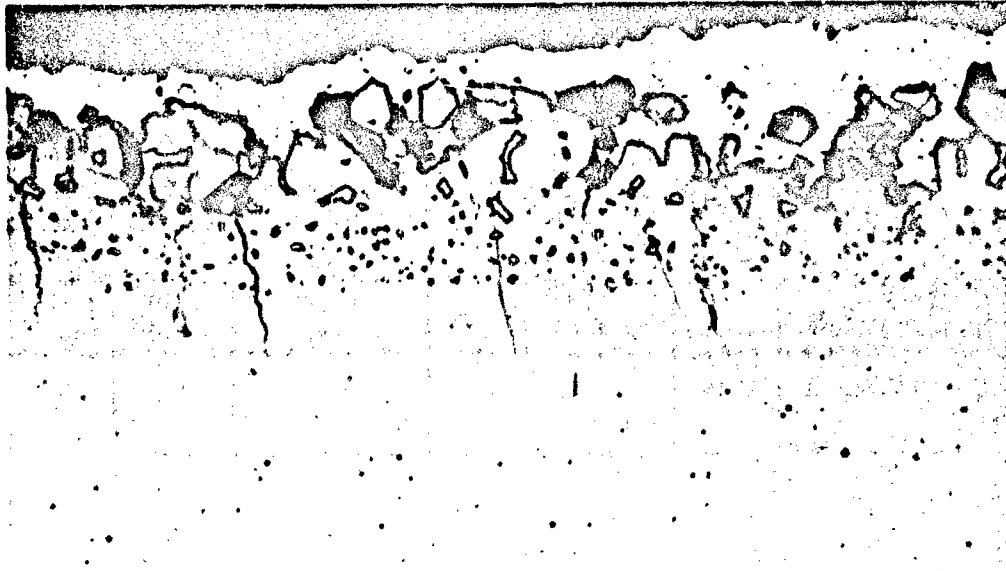
P692   ×500

(A) Contact Side
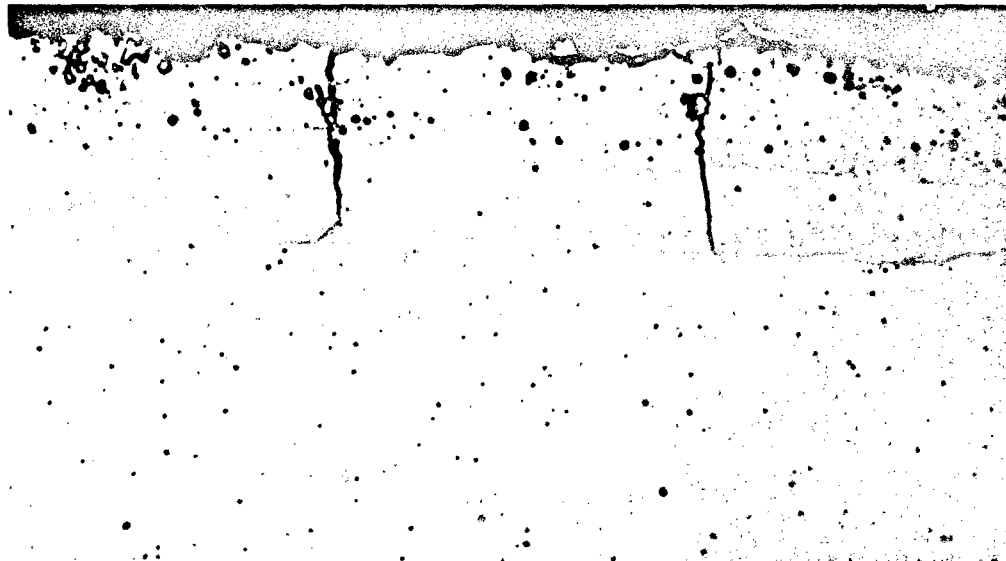
P691   ×500

(B) Noncontact Side

Figure 111 Alteration of CrTiSi Coating at 2550° F, 1.0 mm Hg, 60 min, Upon Contact With Ta-10W/Sn-Al System

245

Table LVII. Results of Compatibility Studies, Cb-752/CrTiSi

Contact material	Test conditions			Performance rating	Baseline time to failure	
	Temp. (°F)	Pressure (mm Hg)	Time (min)		Random (min)	Total (min)
TZM/Durak	2525	1.0	60	Pass	150	>240
TZM/PFR-6	2525	1.0	45	Pass	150	>240
Cb-752/PFR-32	2525	1.0	60	Pass	150	>240
Ta-10W/Sn-Al	2525	1.0	60	Pass	150	>240

B-66/CrTiSi

Material Evaluation

The CrTiSi coating was applied to the B-66 alloy by Thompson Ramo Wooldridge using the same procedures employed for coating the Cb-752 alloy. Since process history (pack composition, coating thermal cycles, etc.) was identical for the two alloys, differences in coating structure and behavior can be related directly to differences in substrate composition and properties. This permits an assessment of the relative contribution of the substrate to the overall performance capabilities of the basic CrTiSi coating. Details of the coating process and a description of the CrTiSi coating for Cb-base alloys are presented in the results section for Cb-752/CrTiSi.

The general appearance of the B-66/CrTiSi samples is shown in Figure 112. Samples were light gray in color with small dark gray to black spots or islands randomly distributed over the surface (Figure 112A). The pattern of light and dark areas on the surface was quite different from that observed on Cb-752/CrTiSi samples. Fewer dark areas existed on B-66 samples, and large areas of the surface were relatively uniform in color. Where dark areas did exist, however, they tended to be large compared with the dark regions on CrTiSi-coated Cb-752. Surfaces were smooth and free of gross defects. Fine hairline cracks could be seen in random locations on all surfaces and edges.

Microstructural details of the coating are shown in Figures 113 and 114. General features of this coating system were similar to those observed for the Cb-752/CrTiSi system. In the light gray regions, a continuous $(Cb, Ti)Cr_2$ interfacial zone existed at the coating substrate interface. In the dark gray to black regions, this interfacial phase was absent and a completely different coating in terms of structure and composition had formed (Figure 114B).

The CrTiSi coating on B-66 appeared to be more complex in terms of structure and composition compared with the same coating on Cb-752. The outer Si-rich CrTiSi layer on B-66 was less dense and appeared to contain a second phase. The surface was notably more rough or uneven than that on Cb-752/CrTiSi. The innermost layers of the coating were very similar to those observed on Cb-752/CrTiSi. Modification of the outermost layer is probably due to incorporation of Mo and V in the original Cr, Ti overlay as a result of interdiffusion with the substrate. Spectrographic analysis indicated the presence of Mo, V, Cr, Ti, Cb, and Si in the coating. No other trace elements were detected. These differences in the outer silicide layer and in the relative amount and distribution of light and dark regions for the CrTiSi coating on Cb-752 and B-66 may be sufficient to cause marked differences in performance capabilities and oxidation behavior of the two systems.

The B-66/CrTiSi samples were free of gross defects. As shown in Figure 113, edge coverage was excellent. The widest fissures extended about halfway through the coating, usually terminating at the inner Cr-rich CrTiSi layer. Fine hairline fissures extended from the surface to the $(Cb, Ti)Cr_2$ interfacial zone. Some tendency for transverse branching along the interfacial zone was noted.

247
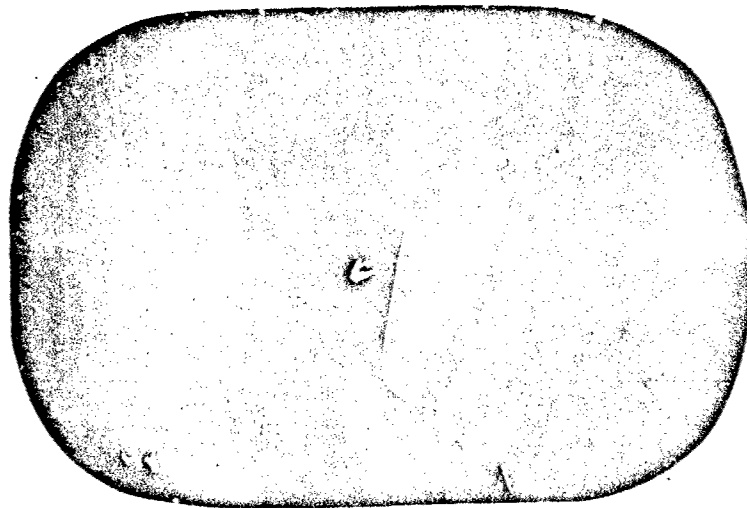
M9970   (A) Surface   ×6

M5534   (B) Edge and Surface   ×18

Figure 112 General Appearance of B-66/CrTiSi, As-Coated

248
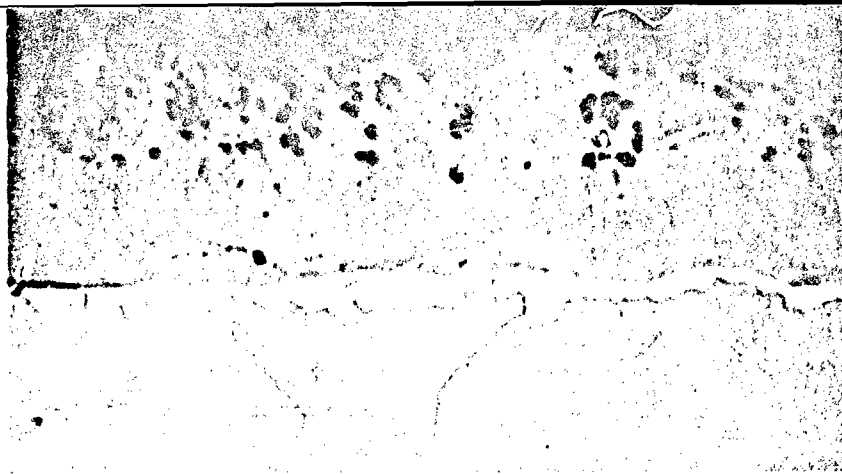
(A)
Surface
(As-Polished)

×1000
M6102

(B)
Surface
(Etched)

×1000
M6101

(C)
Edge
(Etched)

×500

Figure 113 Microstructural Details of B-66/CrTiSi, As-Coated

249

P859   ×2000   P860   ×2000
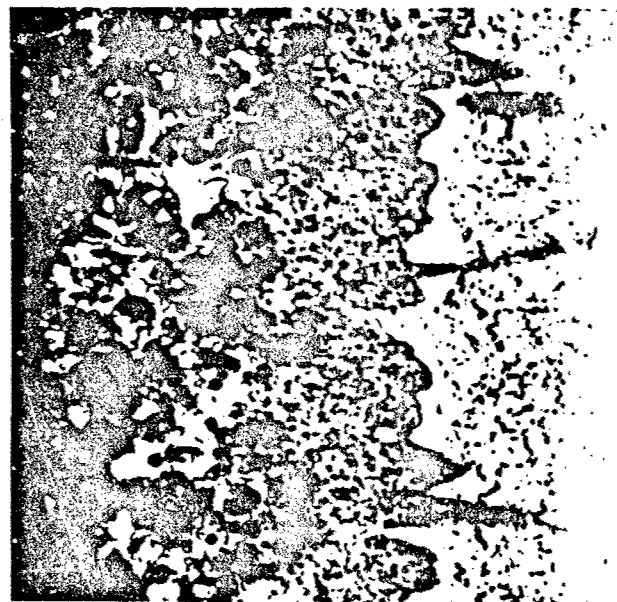
(A) Light Area   (B) Dark Area

Figure 114   Comparison of Coating Structure in Light and Dark Regions, B-66/CrTiSi

250

The B-66 substrate was recrystallized and grain coarsened by the coating thermal cycles. A slight softening occurred, as shown in Figure 115. Diffusion hardening (Cr, Ti) occurred to a depth of 1.5 to 2.0 mils below the (Cb,Ti)Cr$_2$ interfacial zone. Beyond this depth, substrate hardness was uniform across the section. After testing in air (760 mm Hg) for 4 hr at 2700° F, substrate hardness decreased further and little change was noted in the Cr,Ti diffusion zone. With the Cb-752/CrTiSi system, the hardened diffusion zone near the interface with the coating disappeared upon testing at 2700° F.

The as-coated B-66/CrTiSi samples were glass brittle in bending from room temperature to 212° F. Partial ductility was found at 248° F, and ductile 90-deg 3t bends could be made at 320° F. Heat-treatment studies revealed that embrittlement was not caused by changes in the substrate as a result of the coating thermal cycle. Uncoated sheet samples annealed in vacuum by a schedule simulating the coating thermal cycle (8 hr at 2300° F, slow cool, plus 4 hr at 2050° F, slow cool) were ductile in bending at room temperature. Hardness was 226 DPH after heat treatment, which is close to the 223 DPH value measured on the substrate of as-coated samples. No evidence of intergranular or other precipitation was found.

TRW has reported that the bend transition temperature of B-66 sheet is increased by application of the CrTiSi coating (35). The ductile-to-brittle temperature of coated sheet was 200 to 250° F compared with a value of -200° F for uncoated sheet. Subsequent heat treatment or elevated-temperature testing resulted in some recovery of ductility, with bend transition temperatures dropping to 75 to 200° F. The increase in transition temperature after coating was attributed to the combined effect of (1) grain growth, (2) intergranular precipitation of oxides, and (3) existence of a brittle surface layer (the coating). It was concluded that 250 to 300° F of the increase in transition temperature could be attributed to sensitization of the base metal (precipitation embrittlement) and that 150° F of the total increase was due to the notch effect of the brittle surface layer.

Solar (36) also found reductions in tensile and bend ductility of B-66 after coating with three different silicide systems. Hydrogen embrittlement was suspected, and ductility was improved after annealing at 2000 to 2350° F. However, annealing the B-66/CrTiSi samples prepared for this study for 1 to 4 hr at 2300 to 2600° F in vacuum or in air did not reduce the ductile-to-brittle transition temperature significantly. Brittleness, like that observed in Cb-752/PFR-32 and coated TZM systems, was believed to be the result of a brittle surface layer combined with a notch-sensitive substrate, as suggested by TRW (35).

The effect of brittle surface layers was studied by bend testing samples from which part or all of the coating had been removed by pickling. With 1.9 mils per side pickled off to remove all the coating and most of the (Cb,Ti)Cr$_2$ layer, the samples were still brittle in bending at room temperature. Cracks began in the (Cb,Ti)Cr$_2$ phase remaining in the grain boundaries of the Cr,Ti diffusion zone and propagated rapidly through the substrate. Upon removing 3.8 mils per side, partial ductility was restored but random fractures occurred where traces of the (Cb,Ti)Cr$_2$ phase still remained. Ductile 90-deg bends were made at room temperature after 4.5 mils per side had been removed. Bend ductility was restored after complete removal of the coating and the Cr,Ti diffusion layer. It was concluded that brittle behavior was the direct result of
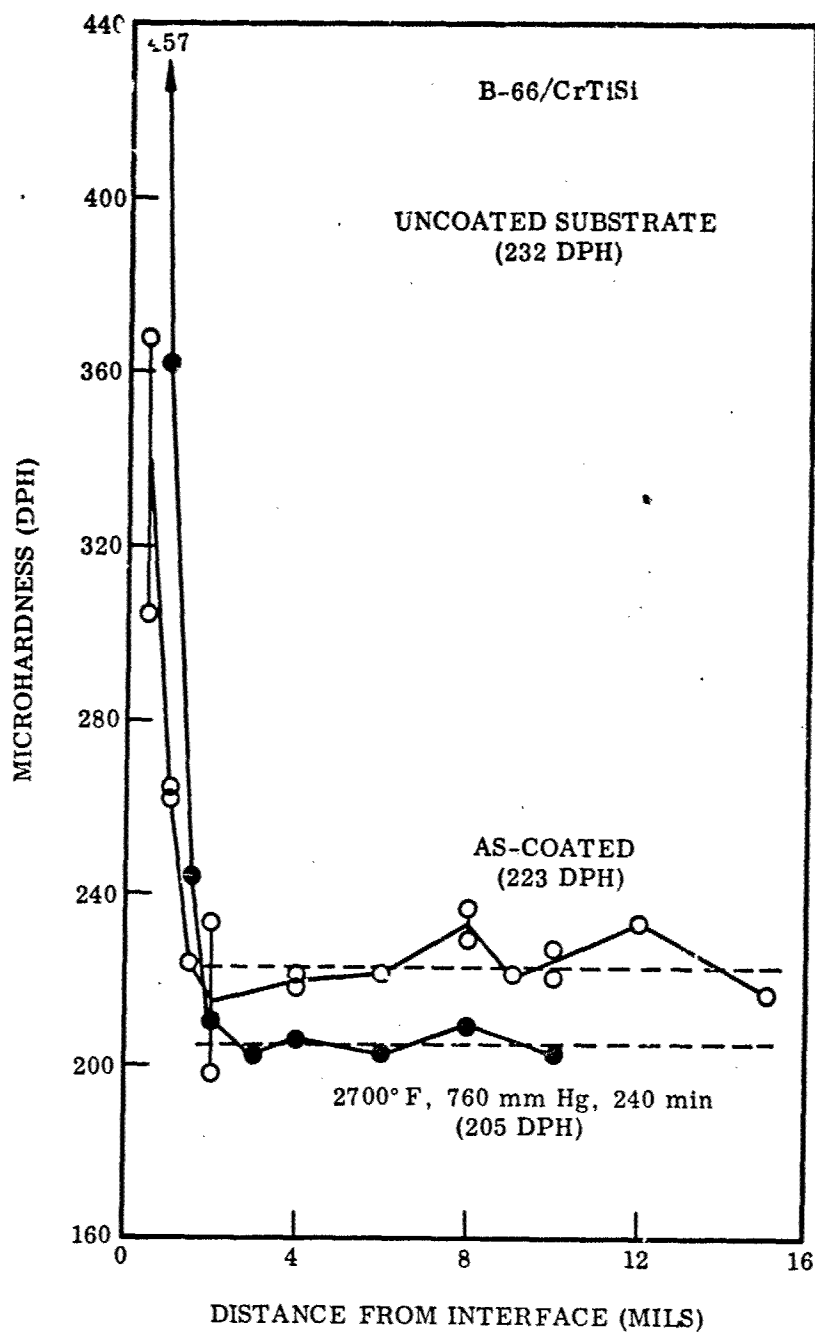
Figure 115 Results of Substrate Hardness Traverse of B-66/CrTiSi

252

notch sensitivity of the substrate. As such, the structure and composition of the substrate would be important factors, as indicated by TRW (3.). Since coated samples remained brittle at room temperature after high-temperature exposure, bend tests were conducted at 125°F to evaluate residual ductility after oxidation tests.

The coating was very uniform in thickness, both within a given sample and from sample to sample. Sample-to-sample uniformity is illustrated in Figure 116. The dispersion of thickness values σ was not increased significantly after application of the coating. As with Cb-752/CrTiSi, the thickness increase after coating was found to be a good measure of average coating thickness. From Figure 116, the average coating thickness is calculated to be 1.35 mils (one-half of the total thickness increase). The standard deviation for thickness of the coating, calculated from the data in Figure 116, is 0.135 mil. Based on 2σ limits, 95% of the samples would be expected to have a coating 1.08 to 1.62 mils thick. Direct measurement of one sample on a metallographic section gave an average thickness of 1.63 mils with a range of values between 1.5 and 1.7 mils. For purposes of this program, the average coating thickness will be taken as 1.4 mils exclusive of the (Cr, Ti) diffusion zone. This is about 0.3 mil or 20% less than the CrTiSi coating on Cb-752.

Baseline Behavior

The results of baseline oxidation tests are plotted in Figure 117 and are tabulated in Appendix III. Performance capabilities are summarized in Figure 118 and Table LVIII. Variations in pressure from 0.01 to 50 mm Hg had comparatively little effect on the maximum temperature for a given lifetime to random or total failure. For example, random failure in 30 min occurred at 2625°F in air at 50 mm Hg and at 2630°F in air at 0.01 mm Hg. For a time of 4 hr to failure, performance was improved slightly at low pressure with failure at 2525°F in air at 50 mm Hg and at 2590°F in air at 0.01 mm Hg.

Table LVIII. Maximum Temperature for Various
Lifetimes, B-66/CrTiSi

Air pressure (mm Hg)	Maximum temperature (°F) at			
	30 min	30 min	120 min	240 min
Random failure limits				
50	2625	2595	2560	2525
20	2625	2600	2560	2500
5	2650	2640	2625	2600
1	2725	2700	2650	2550
0.1	2630	2625	2610	2590
0.01	2630	2625	2610	2590
General failure limits				
50	2725	2680	2640	2610
20	2725	2680	2640	2610
5	2810	2790	2760	2725
1	2750	2720	2670	2575
0.1	2650	2640	2630	2610
0.01	2650	2640	2630	2610

253
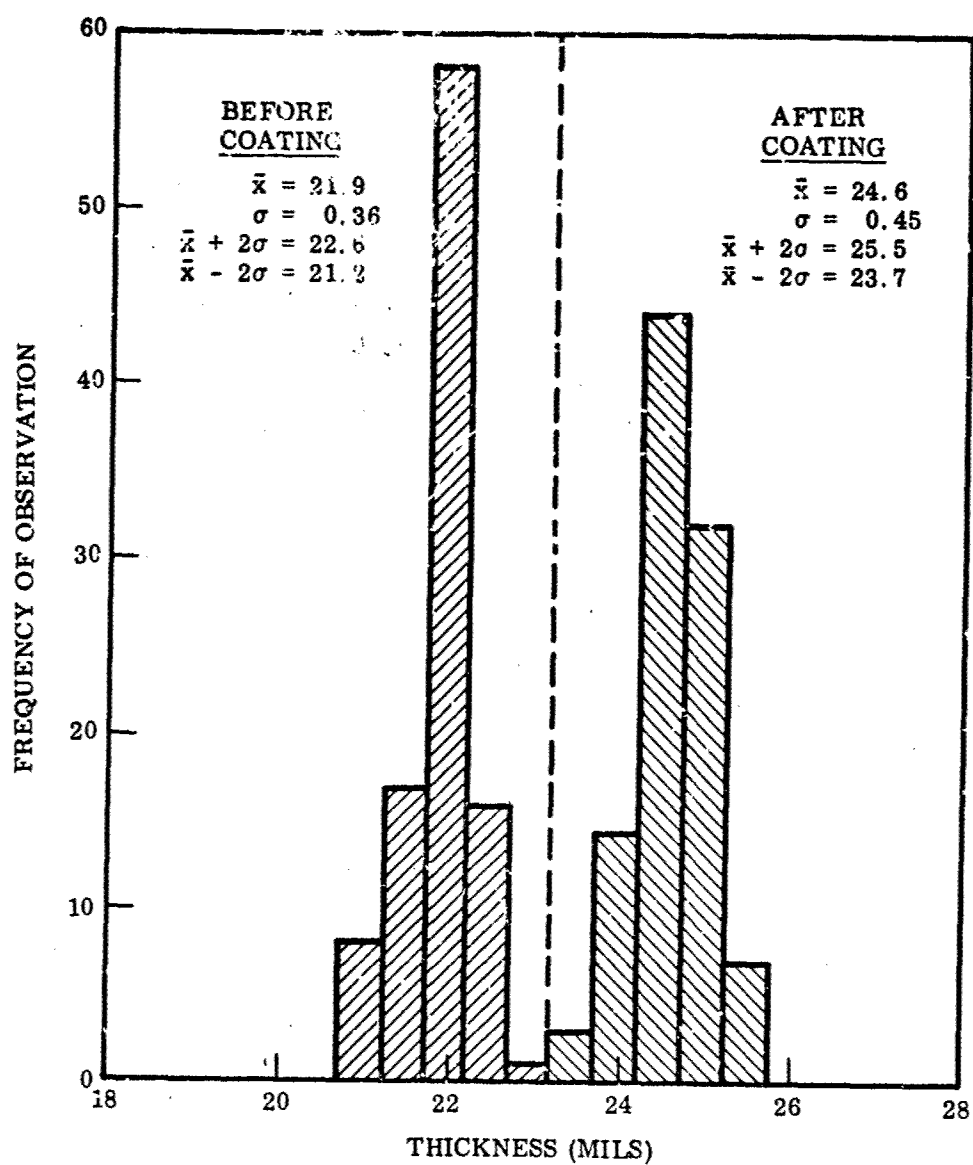
Figure 116 Frequency Histogram of Total Thickness, B-66/CrTiSi

254

This is not to say, however, that the behavior and performance capabilities of B-66/CrTiSi were insensitive to pressure. The most significant effect was an increase in the sensitivity of useful life to temperature at reduced pressure. This was exhibited in two ways. First, at pressures of 1 mm Hg or less, total failure occurred within a few minutes of the first random failures at any temperature. More important, for any time of exposure, total failure occurred at a temperature about 20°F above that at which random failure would occur. Above 1 mm Hg pressure, an increase of 100 to 150°F beyond the random failure limit was necessary to cause total failure in a given time of exposure. Second, at pressures of 0.10 mm Hg or less, the time to failure was more dependent on temperature. Here, an increase of 40°F resulted in an eightfold decrease in life. At higher pressures, an increase of 100 to 150°F was required to produce the same effect. The significance of this behavior, of course, is that a greater margin of safety is required at pressures below 5 mm Hg to prevent premature failures in service as a result of minor temperature variations.

Although the behavior of this system is very similar to that of Cb-752/CrTiSi, several marked differences are apparent. The B-66/CrTiSi system had a maximum temperature capability between 2600 and 2700°F for a 30-min life and between 2500 and 2600°F for a 4-hr life at all pressure levels. As a rule, random failures would be expected in less than 30 min at 2650°F in air at 0.01 to 50 mm Hg. The Cb-752/CrTiSi system, however, showed no failures in 4 hr at 2~50°F in air at 5 to 50 mm Hg pressure. At 1 mm Hg or less, performance was comparable to that of the B-66/CrTiSi system. The Cb-752/CrTiSi system had a minimum in performance capabilities for random or total failure at 1.0 mm Hg pressure, whereas B-66/CrTiSi had a maximum performance capability for random failure at 1.0 mm Hg and for total failure at 5.0 mm Hg. Also, ignition and combustion of Cb-752/CrTiSi occurred at 2800°F in air at 5 mm Hg, whereas B-66/CrTiSi did not ignite or burn at temperatures up to 2850°F.

These differences in behavior are due to basic changes in the chemistry and structure of the CrTiSi coating resulting from incorporation of various substrate elements in the coating. With the B-66 alloy, the presence of Mo and V in the coating had a significant effect on performance in air at pressures of 1.0 mm Hg or higher. Random failure occurred within 30 min at temperatures above 2600°F as a direct result of localized melting that occurred upon heating between 2600 and 2650°F. The dark gray to black areas of the coating where the $(Cb, Ti)Cr_2$ interfacial zone was absent melted at about 2625°F. This behavior is shown in Figure 119 where a photograph of the same surface was taken before and after testing at 2650°F. The relation between areas of local melting that stand up in relief after testing and the dark-colored surface patterns prior to test is clearly evident. These areas, of course, are enriched in Mo, Cb, Ti, and V since more of the substrate was consumed in producing the coating at these regions.

Local melting was extremely consistent in this system. It was never observed in tests at 2600°F or lower and was always observed at 2650°F or higher. Samples of B-66/CrTiSi often provided a good check on temperature calibration. Where melting did not occur at an indicated temperature of 2650°F or did occur at 2600°F, further calibration checks revealed a drift in the control thermocouple output. The effect often was masked in air at pressures below 1 mm Hg due to high surface recession rates.
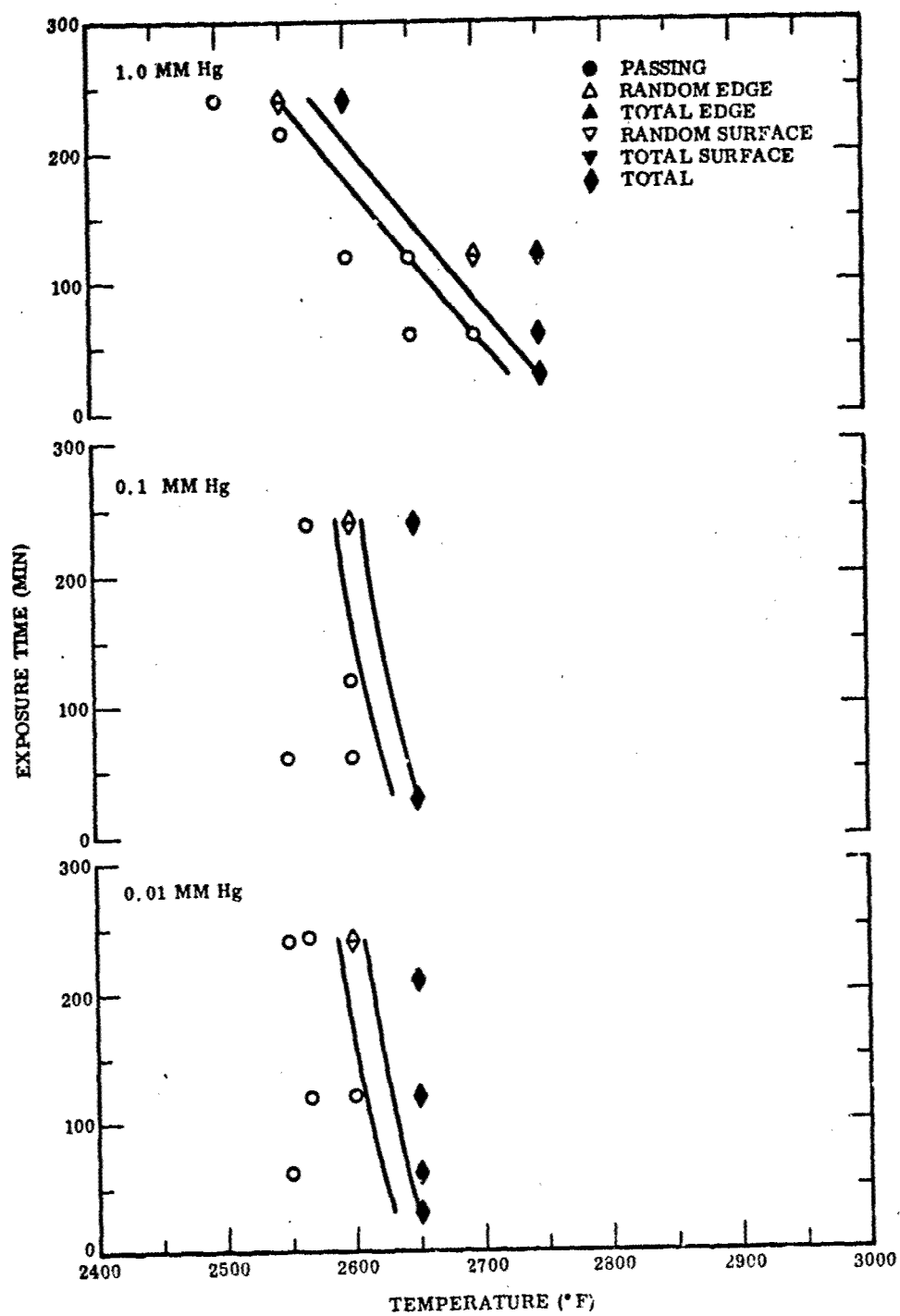
255

Figure 117 Results of Baseline Tests, B-66/CrTiSi

256
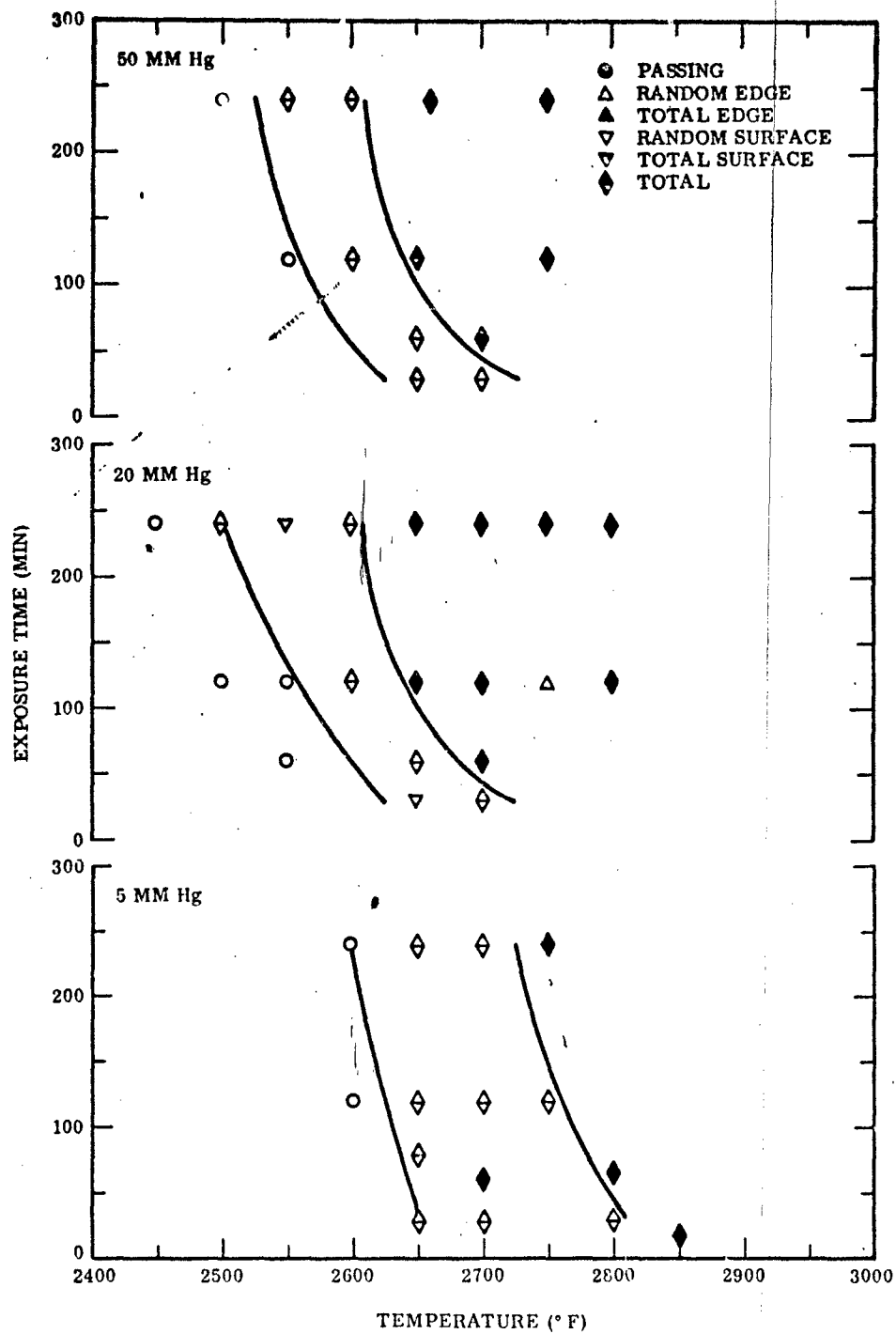
Figure 117 Results of Baseline Tests, B-66/CrTiSi (cont'd)

257
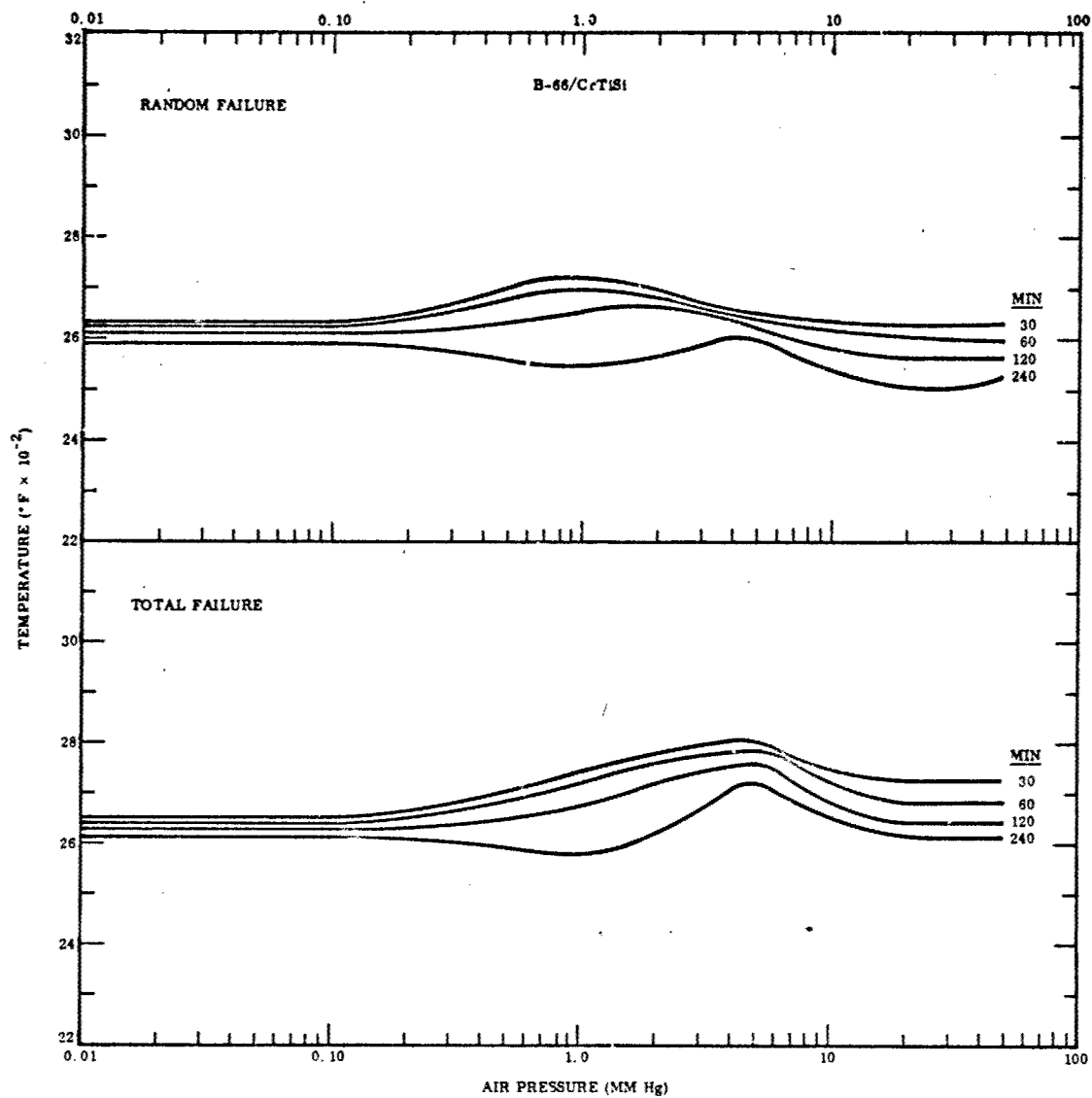
Figure 118 Baseline Failure Limits,B-66/CrTiSi

258
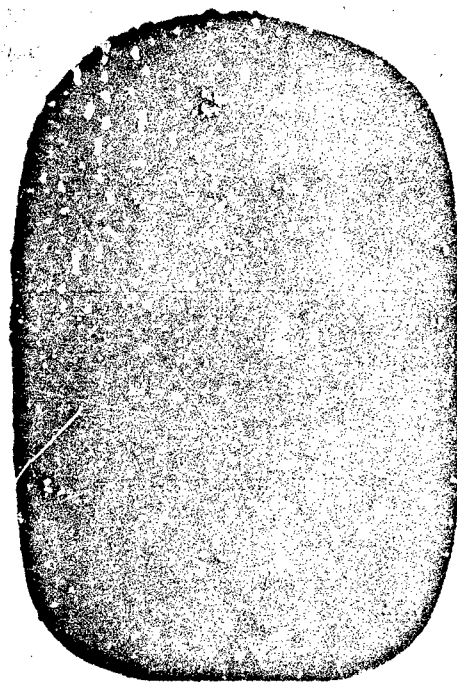
M8173   (A) As-Coated   ×6   M8407   (B) 2650° F, 20 mm Hg,   ×6
                                                    161 min
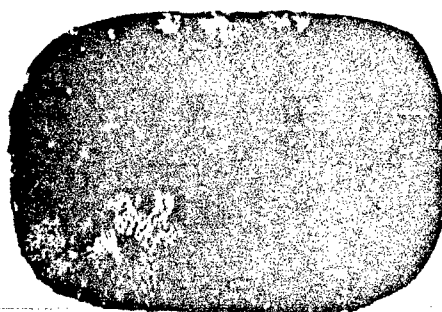
M7196   (C) 2800° F, 10^{-5} mm Hg,   ×3
                        30 min

Figure 119 Formation of Blisters at Dark Regions in Oxidation Tests of B-66/CrTiSi

As shown in Figure 119C, melting occurred in vacuum and was dependent only on temperature and coating composition.

The local melting that occurred in B-66/CrTiSi was far more severe and produced serious local defects compared with that observed after localized melting of dark areas in the CrTiSi coating on Cb-752. As shown in Figures 120 and 121, huge blisters formed in melted areas of CrTiSi on B-66. Surface tension tended to pull the melt away from the surface, creating large voids in the coating around the periphery of the molten zone. This created paths of easy leakage which proved to be sites for random failures in all tests at pressures of 1.0 to 760 mm Hg. As shown in Figure 120, the surface in a melt-free area was protected after 4 hr at 2700° F in air at 760 mm Hg, whereas an edge failure occurred due to local melting and void formation. In many cases, oxides precipitated in regions under the void areas while the substrate directly under the sound melt region was protected. Mach 3 flow tests revealed that the melt areas were liquid or at least mushy at test temperatures. No blisters were found on flow surfaces, whereas they did exist on the static side of test specimens. Regions of local melting on Cb-752/CrTiSi, on the other hand, appeared to be solidified after short times at high temperature.

At pressures of 0.1 mm Hg and less, high surface recession rates masked the effects of local melting on the B-66 alloy. As shown in Figure 121, oxidation occurred, resulting in general failure shortly after the first random failure. Heavy precipitation of oxides is evident in the Cr, Ti diffusion layer and underlying substrate. Random failures in this range occurred at the thinnest regions of the coating. CbO_2-rich oxides that spalled on cooling were formed. At 1 mm Hg or above, green- to rust-colored oxides indicative of high chromium and titanium were formed. It is significant that the transition from Cr-rich to Cb-rich and low to high surface recession oxides occurred at between 1.0 and 0.1 mm Hg for B-66 and between 5.0 and 1.0 mm Hg for Cb-752. The presence of Mo and V in the coating may have acted to stabilize the coating to lower pressure levels.

The source of random failures at pressures of 1 to 760 mm Hg and temperatures below 2650° F appeared to be leakage of gas through the coating. This occurred either by effusion along crack-type defects or by diffusion or both. Visible changes in structure in this region were confined to the outer Si-rich layer of the coating. Heavy attack and recession of this layer occurred with the extent of attack being greater as pressure was reduced to 1 mm Hg. As with Cb-752/CrTiSi, random failures occurred at both edge and surface sites with no indicated preferences. Attack was not localized at fissures but occurred uniformly over the surface and edges. Generally, failures were not visible. Oxide precipitation and substrate embrittlement characterized all failures. It should be noted, however, that many totally failed samples would be considered structurally sound in some applications. No tendency for ignition or combustion was noted in the environment of the tests conducted.

Gas Velocity

The same temperature calibration developed for Cb-752/CrTiSi was used to calibrate the B-66/CrTiSi system for Mach 3 flow tests. In addition, the 2625° F local melting

M6857   (A) Surface, Protective   ×1000

M6856   (B) Edge, Random Failure, 2700° F, 240 min   ×500

Figure 120 Structure of B-66/CrTiSi After Testing in Air at 760 mm Hg

261

M8451   (A) 2700°F, 20 mm Hg, 120 min.   Large Melted   ×50
Blister With Voids, Random Failure
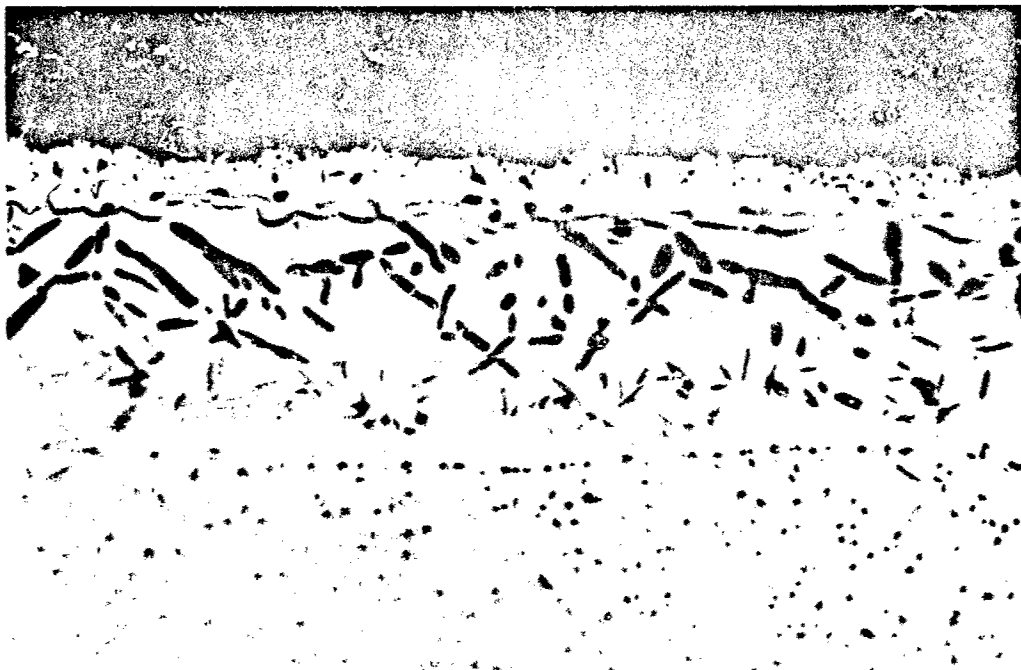
M6945   (B) 2650°F, 0.1 mm Hg, 240 min.   ×1000
Surface Recession, Total Failure

Figure 121 Structure of B-66/CrTiSi After Testing in Air at Reduced Pressure

262

behavior was used to check pyrometer calibrations. Tests conducted in 19:1 $N_2:O_2$ mixtures at 20 mm Hg yielded the same results as those conducted in air at 5 mm Hg, indicating atmosphere equivalence for use in the lower pressure tests.

The results of Mach 3 flow tests are presented in Table LIX. The data per se indicate no significant effect of gas velocity on performance. However, at the time these tests were run, baseline studies were incomplete and critical regions of performance had ..ot been clearly defined. Thus, tests above 2600°F where local melting occurs were run past the point of random failure and, in three cases, total failure. As would be predicted from baseline data, random failure and, in three cases, total failure did occur. The results, unfortunately, do not indicate if flow degraded performance when local melting occurred during tests. They do show, however, that structural integrity is retained well past the point of total failure, as defined by failure criteria based on substrate oxidation and embrittlement.

Table LIX, Results of Mach 3 Flow Tests, B-66/CrTiSi

Test conditions					Performance rating	Baseline time to failure	
Temp. (°F)	Total pressure (mm Hg)	Atmosphere	Equivalent air pressure (mm Hg)	Time (min)		Random (min)	Total (min)
2600	20	Air	20	60	Pass	60	240
2750	20	Air	20	60	Total failure	<30	<30
2900	20	Air	20	60	Total failure	<30	<30
3000	20	Air	20	44	Ignition[a] Total failure	<30	<30
2575	20	19:1 $N_2:O_2$	5	60	Pass	>240	>240
2650	20	19:1 N_2O_2	5	60	Random surface	30	>240

(a) Partial combustion; did not burn up.

Examination of test specimens indicates that high gas velocity may degrade performance at temperatures above 2600°F. In all tests, regions of local melting and blistering existed on the static underside of specimens. On the flow side, however, melted areas washed away and formed a slight buildup on the downstream end. Areas where melts formed were visible, but melted material has been washed out. Washout was not complete, however, and a small thickness of the innermost layer or diffusion products remained over the substrate. Heavy oxidation of the substrate, however, was seen below these regions, which constituted random failure sites. All test specimens were used in calibration and initial tests, and further studies of this behavior could not be made.

One specimen tested at 3000°F in air at 20 mm Hg ignited after 44 min. Failure occurred at the downstream end where a buildup of molten coating had formed.

Combustion stopped when the heating current was shut off. Total failure also was noted in the central hot zone of the specimen.

Examination of specimens tested at 2600° F or lower where melting did not occur indicated no significant effect or flow on performance. The general appearance was identical to that of baseline specimens.

Vacuum Volatility

The results of degradation studies in vacuum at 2600, 2800, and 3000° F are presented in Table LX. At 2600° F, weight loss data fitted a parabolic rate curve. Total weight loss per unit area and rate of loss were slightly less than those observed for the CrTiSi coating on Cb-752. The structure after 4 hr at 2600° F was almost identical to that of the CrTiSi coating on Cb-752 (Figure 107). Only the outer, Si-rich CrTiSi layer was attacked and the extent of degradation was less severe than that observed for Cb-752/CrTiSi. Short exposure at temperatures to 2600° F would not be expected to degrade the oxidation resistance of the system seriously.

Table LX. Vacuum Volatility Data, B-66/CrTiSi

Heat treatment			Surface area (cm^2)	Thickness		Weight		Weight change (gm/cm^2)
Temp. (°F)	Pressure (mm Hg)	Time (min)		Initial (mils)	Final(a)	Initial (gm)	Final (gm)	
2600	1×10^{-5}	30	4.9	24.5	Rough surface	1.0862	1.0776	1.75×10^{-3}
	9.5×10^{-6}	60			—		1.0740	2.49×10^{-3}
	8×10^{-6}	120			—		1.0684	3.22×10^{-3}
	6×10^{-6}	240			—		1.0582	5.71×10^{-3}
2800	9×10^{-6}	30	—	23.7	Coating melted	1.0358	0.9977	—
	8×10^{-6}	60			Coating melted		0.9923	—
3000	1×10^{-6}	120	—	24.7	Coating melted	1.1098	1.0725	—

(a) The final thickness could not be measured for the reasons stated.

At temperatures above 2600° F, where local melting occurred, severe degradation resulted. As shown in Figure 122, large voids were formed deep within the coating. The Cr-Ti diffusion layer also had melted and in many areas separated, exposing the substrate. The coating in this condition could not be expected to protect the substrate. Further studies were not conducted, since complete destruction occurred upon heating above 2600° F and little degradation occurred upon heating below this temperature.

M6886   (A) Surface   ×1000
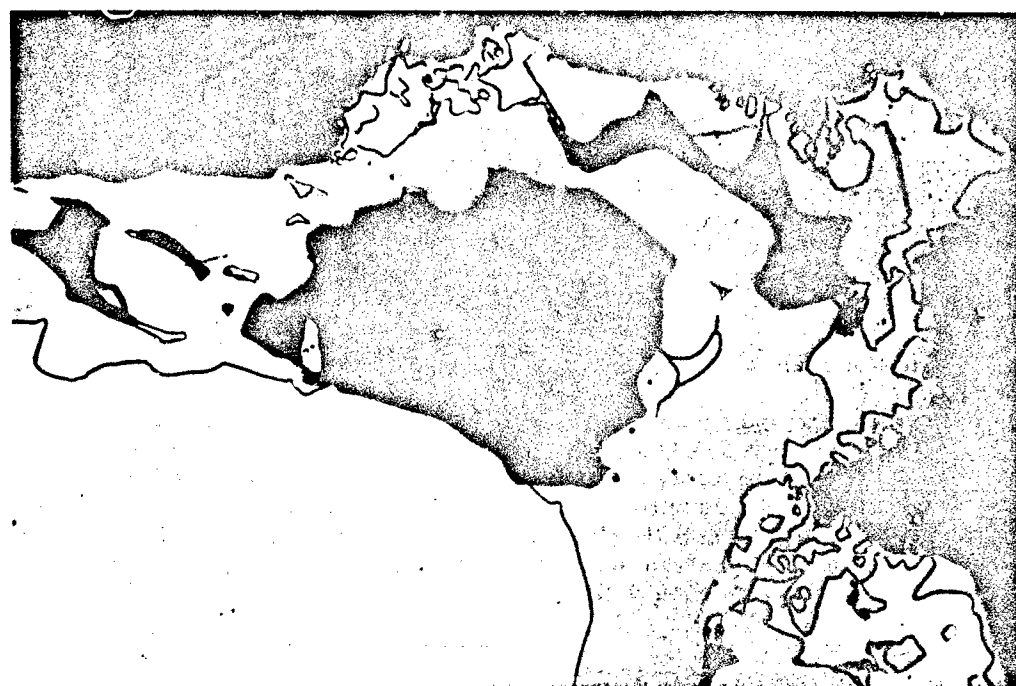
M6885   (B) Edge 2800° F, 10^{-5} mm Hg, 60 min   ×1000

Figure 122 Effect of Heating in Vacuum on Structure of B-66/CrTiSi

Temperature-Pressure Cycling

A significant reduction in performance capabilities occurred after cycling, as shown in Table LXI. The data indicate that time to random failure at 2650° F and 1 mm Hg pressure was reduced to about 25% of the baseline value by cycling to 2200° F and 3 mm Hg pressure. At 2700° F and 1 mm Hg, cycling reduced the time to total failure to less than one-third of the baseline value.

Table LXI. Results of Temperature and Pressure Cycling, B-66/CrTiSi

Phase of cycle	Test conditions					Performance rating	Baseline time to failure	
	Temp. (°F)	Pressure (mm Hg)	Time (min)	No. of cycles	Total time (min)		Random (min)	Total (min)
1st (Baseline)	2700	1.0	7	9	63	Total failure	60	85
2nd	2200	3.0	21	9	189			
1st (Baseline)	2700	1.0	7	4	28	Total failure	60	85
2nd	2200	3.0	21	4	84			
1st (Baseline)	2650	1.0	7	4	28	Random sur-face failure	120	145
2nd	2200	3.0	21	4	84			

Failures in these tests were associated with regions of local melting. These regions were alternately melted and solidified upon cycling from 2650 or 2700 to 2200° F. Spalling occurred in some cases. Cracks formed around melt areas accelerated failures in all cases. The results indicate that cooling below 2650° F after local melts have formed will accelerate failure.

Acoustic Vibration

Exposure to sine and random noise did not have a significant effect on coating structure or performance capabilities. The microstructure of the vibrated samples was identical to that of as-coated material, and no tendency for crack formation or propagation was detected. Samples were tested for 1 hr at 2650° F and 1.0 mm Hg and 1 hr at 2550° F and 20 mm Hg after vibration. All samples passed. In view of the high tolerance of this system for crack-type defects, it is not surprising that no effect of vibration was observed.

Defect Tolerance and Repair

Resistance to defect formation in bending and impact was evaluated at room temperature. In bending, simultaneous fracture of the coating and substrate occurred at a bend angle of 20 deg. Samples bent just short of this point were tested for 1 hr at 2650° F in air at 1 mm Hg. Random failure occurred in the bend region near the edges of the sample. The center section remained ductile. Baseline data would predict random failure in 120 min, indicating a 50% or greater reduction in useful life. Metallographic examination indicated that hairline cracks in the coating had propagated through the Cr, Ti diffusion zone and into the substrate along fingers of the $(Cr, Ti)Cr_2$ phase extending down the grain boundaries. Some cracks also propagated into but not through the Cr, Ti diffusion zone. The results indicate low resistance to defect formation upon straining and low tolerance for crack-type defects extending into or through the diffusion zone. Use of elevated temperatures (above 300° F) may be necessary to prevent system degradation in any attempts to straighten or align parts.

As would be expected from the notch sensitivity characteristics of the system, severe degradation occurred upon impact. Pellet velocities of 137 ft/sec (0.6 ft-lb impact) did not cause visual damage (Table LXII). However, at 153 ft/sec (0.7 ft-lb), fracture and spalling of the coating occurred. At 184 ft/sec (1.0 ft-lb) the entire specimen shattered like glass. The impact was damaging, however, only when deformation was permitted. On steel backups, no damage was indicated at velocities of 235 ft/sec (2.3 ft-lb). Samples impacted on a rubber backup at 137 ft/sec (0.6 ft-lb) failed in 1 hr at 2650° F in air at 1 mm Hg. Again, this 50% or more reduction in life was due to propagation of coating cracks into and through the Cr, Ti diffusion zone.

Table LXII. Results of High-Velocity Impact Tests, B-66/CrTiSi

Backup	Kinetic energy (ft-lb)[a]					
	Spalling		Coating fracture		Substrate fracture	
	Pass	Fail	Pass	Fail	Pass	Fail
Rubber	0.6	0.7	0.6	0.7	0.7	1.0
Steel	2.3	>2.3	2.3	>2.3	2.3	>2.3

(a) Calculated from pellet mass and velocity at time of impact.

This system also has good tolerance for gross coating defects. As shown in Table LXIII, performance was not seriously degraded by defects consisting of slots 5 mils wide that penetrated one-half and three-fourths of the coating thickness. In fact, in one test at 2600° F and 20 mm Hg, the substrate was protected under both the 1/2 t and 3/4 t slots but failed at a random-defect site elsewhere on the bulk sample. Failure in this case was probably caused by leakage along fissures that penetrated deeper than 3/4 t of the thickness. The results indicate that cracks or fissures must be greater than 3/4 t depth to cause random failure in regions where local melts do not form. Less tolerance for gross defects would be expected at pressures less than 1 mm Hg where high surface recession rates prevail.

267

Table LXIII. Defect Tolerance, B-66/CrTiSi

Test conditions			Performance rating			Baseline time to failure	
Temp. (°F)	Pressure (mm Hg)	Time (min)	1/2 t defect	3/4 t defect	Bulk sample	Random (min)	Total (min)
2600	20	60	Pass	Pass	Random edge failure	60	240
2600	20	120	Fail	Pass	Pass	60	240
2600	1.0	60	Pass	Pass	Pass	180	210
2700	1.0	30	Pass	Fail	Pass	60	85

In evaluating the feasibility of in-field or patch repair of coating defects, the Cb-752/CrTiSi system was selected as a representative model for the two systems using CrTiSi coatings. The results of the study on Cb-752/CrTiSi should be equally applicable to B-66/CrTiSi at temperatures up to 2600° F. Both coatings are similar with respect to structure, composition and general behavior up to this temperature. Above 2600° F, B-66/CrTiSi has limited utility due to local melting. Baseline data indicate that meaningful evaluations of repair techniques could not be made beyond this point.

Materials Compatibility

As previously shown, random areas of the CrTiSi coating on B-66 melt between 2600 and 2650° F. When one or more of these molten regions was in contact with a dissimilar material, accelerated failure occurred. $MoSi_2$, silicide coatings on TZM, SiO_2, and Al_2O_3 fused with the local melt regions and caused failure of B-66/CrTiSi in less than 1 hr at temperatures above 2600° F, and pressures of 1.0 to 50 mm Hg. Where contact with molten regions did not occur, no significant degradation was noted for couples with $MoSi_2$, SiO_2, and silicide coatings on TZM at temperatures up to 2800° F. A severe reaction with Al_2O_3 occurred at 2550 – 2600° F where local melting of the CrTiSi coating was not observed. The Sn-Al coating on Ta-10W severely attacked the CrTiSi coating on B-66. At 2675° F, liquid tin fluxed the entire coating on B-66, causing total failure within a few minutes. A lesser reaction at lower temperatures is likely, as indicated by the fact that the CrTiSi coating on Cb-752 reacted with Sn-Al at 2525° F but still protected the substrate in a 1-hr exposure.

Cb-752/Vought IV

Material Evaluation

Vought IV is a complex Si-Cr-B coating that is quite different in structure and composition from the other silicide-base coatings for Mo and Cb alloys. The coating process was developed by Vought Astronautics Division, Chance Vought Corporation, Dallas, Texas, under Air Force contract(37). A duplex pack cementation process is used. In the first cycle, a $CbSi_2$ coating is formed by siliconizing for 16 hr at 2100° F. Chromium and boron are co-deposited on the silicide in a second cycle of 16 hr at 2200° F. A pack of 30% Cr, 30% ferroboron, 4% halide activator, and the balance 325-mesh Al_2O_3 is used to deposit Cr and B. Iron is also deposited from this pack.

The inner regions of a coating produced by this method are $CbSi_2$ and lower silicides such as Cb_5Si_3 and Cb_2Si. The outer layers are lean in silicon and rich in Cr and B. They contain a complex mixture of compounds such as CrB, FeB, $CbCr_2$, Cr_3Si, CrB_2, and $CbSi_2$. All the elements in the substrate alloy also appear in the coating. For Cb-752 alloy, Cb, W, and Zr therefore will be present. Spectrographic analysis of the coated Cb-752 samples prepared by Vought Astronautics showed the presence of Cb, Si, W, Zr, Fe, Al, Cr, Mg, B, and Ni. Needless to say, exact identification of phases observed in the coating is next to impossible.

This coating might be expected to perform quite differently from the CrTiSi coating or other silicide-base coatings in low-pressure environments. The fact that other coatings have a silicon-rich surface and a silicon-lean inner region whereas Vought IV has just the opposite may be significant. The high boron content also should lead to formation of boron-modified glasses that may be more stable at low pressures but may also be more fluid at high temperature. It was this combination of unique characteristics that prompted the selection of Vought IV for study in this program.

The general appearance of as-coated specimens is shown in Figure 123. Most of the tabs had a whitish-gray, powdery coating on the surface. This was soft and nonadherent and could easily be scraped off. In many areas the powdery deposit was absent and the underlying coating was a dark gray to black color, as shown in Figure 123A. Surfaces were smooth but had a moderately granular texture.

Edge coverage appeared to be excellent, and no cracks or fissures were evident upon examination at low-power magnifications. Plane surfaces also appeared to be free of cracks and fissures. However, on metallographic cross sections, large subsurface cracks or voids were evident. As shown in Figure 124, these extended from a fraction of a mil below the surface of the coating to within 0.2–0.3 mil of the coating substrate interface. The width of the defects varied from 0.1 to 0.5 mil. They were found in random locations on flat surfaces and edges, but generally tended to be near an edge (Figure 124B).

This is an insidious type of defect since it is buried just beneath the surface and cannot be detected readily by visual examination. After a few minutes of oxidation, however, the defect can be open to the atmosphere, providing a source for premature failure of the coating. Aside from these defects, the coating was very sound and relatively free of cracks. Edge coverage was excellent in many cases, with no tendency for V-shaped fissure formation or "unicorn" growth. It is believed that, with slight modification of the basic coating process, the large subsurface defects could be eliminated or greatly

269
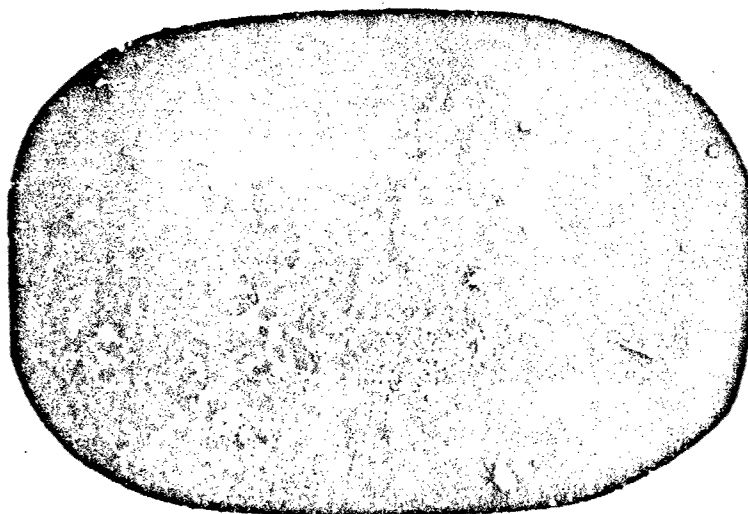
M9966   (A) Surface   ×6

M6118   (B) Edge and Surface   ×18

Figure 123   General Appearance of Cb-752/Vought IV, As-Coated

270

M6103   ×1000

(A) Surface

M6104   ×500
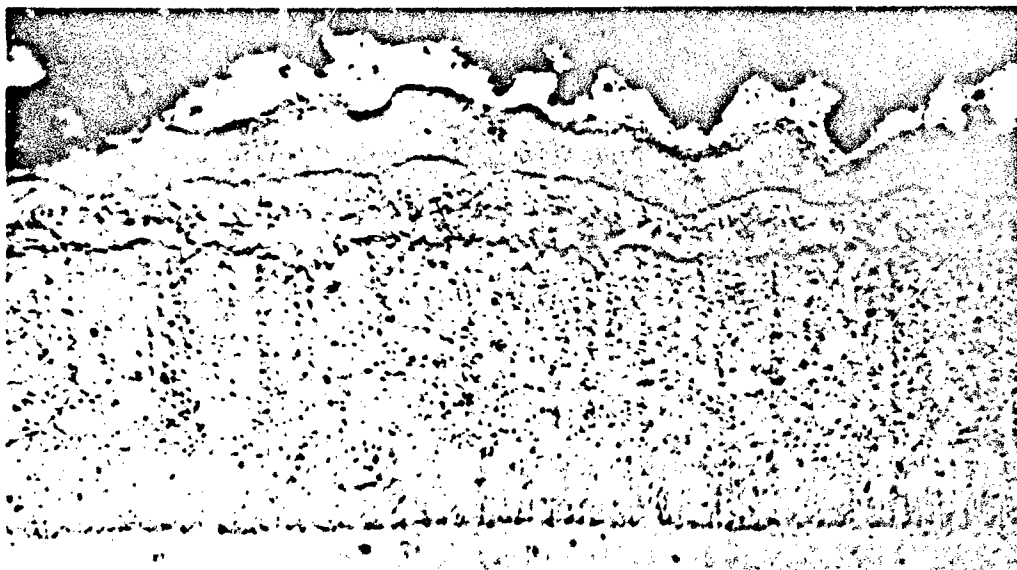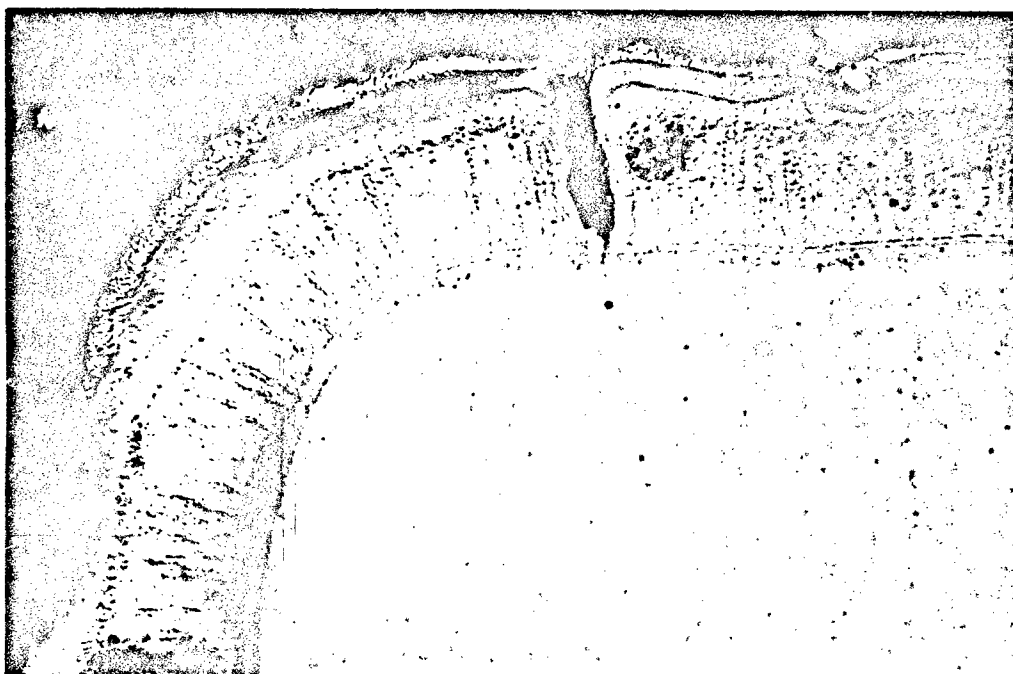
(B) Edge

Figure 124   Microstructure of Cb-752/Vought IV, As-Coated

271

reduced in size. Basically, the system would appear to have potential for developing a comparatively sound coating with few defects.

The complex structure of the coating is shown in Figure 124A. The innermost layer is probably a lower silicide of columbium, such as Cb_5Si_3 or Cb_2Si. From this layer upward, the composition would grade into $CbSi_2$ and then into a complex mixture of silicon-lean silicides and borides. No attempt was made to identify the various layers or phases in the coating. The outermost white layer corresponds to the powdery whitish-gray deposit on the surface. This may be finely divided Al_2O_3 from the pack or a mixture of silicon-lean, metal-rich material deposited from the pack.

The hardness of the substrate was increased from an initial value of 176 DPH to an as-coated value of 208 DPH. As discussed for Cb-752/PFR-32, this increase is probably the result of an aging effect in the substrate in response to the coating thermal cycle. After testing for 142 min at 2700° F in air at 1 atm, substrate hardness decreased to 166 DPH. Hardness as-coated was uniform across the section, indicating freedom from contamination and diffusion effects during coating. The hardness was 213 DPH 0.5 mil below the coating and 202 DPH 10 mils below the interface.

Bend ductility behavior was quite similar to that of the Cb-752/PFR-32 system. Initially, samples were ductile at room temperature and could be bent 90 deg over a 3t radius without substrate fracture. However, some 15 months later the samples were found to be brittle in bending at room temperature. Results of a bend transition study made after 15 months' storage at room temperature are shown in Table LXIV.

Table LXIV. Bend Transition, Cb-752/Vought IV[a]

Temperature (°F)	Bend Angle to Coating Fracture (deg)	Bend Angle to Substrate Fracture (deg)
85	20	53
95	28	36
115	24	43
130	24	53
160	32	72
180	18	>90
227	37	>90

(a) 3t radius, 1.0 in./min RAM speed.

The system was partially ductile at room temperature, but heating to over 160° F was required to make a ductile 90-deg bend. Bend ductility behavior of coated Cb-752 is discussed in the section on Cb-752/PFR-32. The Vought IV coating system behaved in much the same manner. After heating above 2400° F in oxidation tests, samples without coating failure were ductile in bending at 75°F. Failed samples, on the other hand, were glass brittle. Room-temperature bend ductility was a valid criterion for coating failure.

The average coating thickness measured on a metallographic cross section was
2.65 mils, with a range of values between 2.5 and 2.8 mils along plane surfaces.
Based on measurement of 100 random samples, the total sample thickness increased
by 2.55 mils per side after coating (Figure 125). Because of the complex nature of
the coating, correlations between increase in total thickness (part growth) and result-
ant coating thickness could not be made. The Vought IV coating deposited on Cb-base
alloys by the same process as used in this program ranged between 2.0 and 2.5 mils
in thickness (37). For purposes of this program, the average coating thickness was
assumed to be 2.5 mils. The increase in dispersion of total thickness values after
coating (Figure 125) indicates a large variability in thickness of the coating from sample
to sample.

Baseline Behavior

The Vought IV coating was originally developed for service to 2600° F. Average coat-
ing life on a variety of Cb-base alloys at this temperature was about 11 hr in air at
1 atm (37). The results of baseline tests at 2500 to 2800° F in air at 0.01 to 5 mm Hg
pressure are shown in Figure 126. Complete data are tabulated in Appendix III. The
results show a general inconsistency of behavior at the four pressure levels studied.
Total failures often occurred at lower temperatures or shorter times than those at
which good performance had been observed. For example, at 0.01 mm Hg, one sample
was good after 4 hr at 2600° F whereas others failed in 4 hr at 2600° F and 4 hr at
2550° F. Running duplicate or triplicate check tests also revealed inconsistent behavior,
with one sample passing and one or two samples failing under identical test conditions.
Performance at 1 atm was also variable, with samples failing at 38, 119, and 194 min
and passing at 142 min at 2700° F.

This behavior led to a general lack of confidence in single or even duplicate test
results. The data were such that well-defined boundaries separating regions of pro-
tection or failure could not be constructed. Further testing of the samples did not
appear to be warranted, and all other aspects of the overall evaluation of this system
were curtailed. It should be noted, however, that the results of tests conducted on
each and every coating system studied in this program characterize the particular
set of samples prepared for the program; they characterize the performance capabili-
ties of a given coating system only to the extent to which the samples are representa-
tive of the overall or average quality of that system. It was important, therefore, to
determine what characteristics of the Vought IV coating contributed to variable per-
formance. By delineating mechanisms of failure or protection, some indication may
be gained of whether behavior was characteristic of the basic substrate/coating com-
bination or of some peculiar feature of the samples themselves. Most of the effort
beyond original baseline tests, therefore, was limited to metallurgical evaluations
of the effects of pressure on coating structure and modes of attack. This analysis
also provides some insight into whether the unique structure and composition of the
Vought IV coating presented any advantages over more conventional silicide coating
systems for aerospace environments.
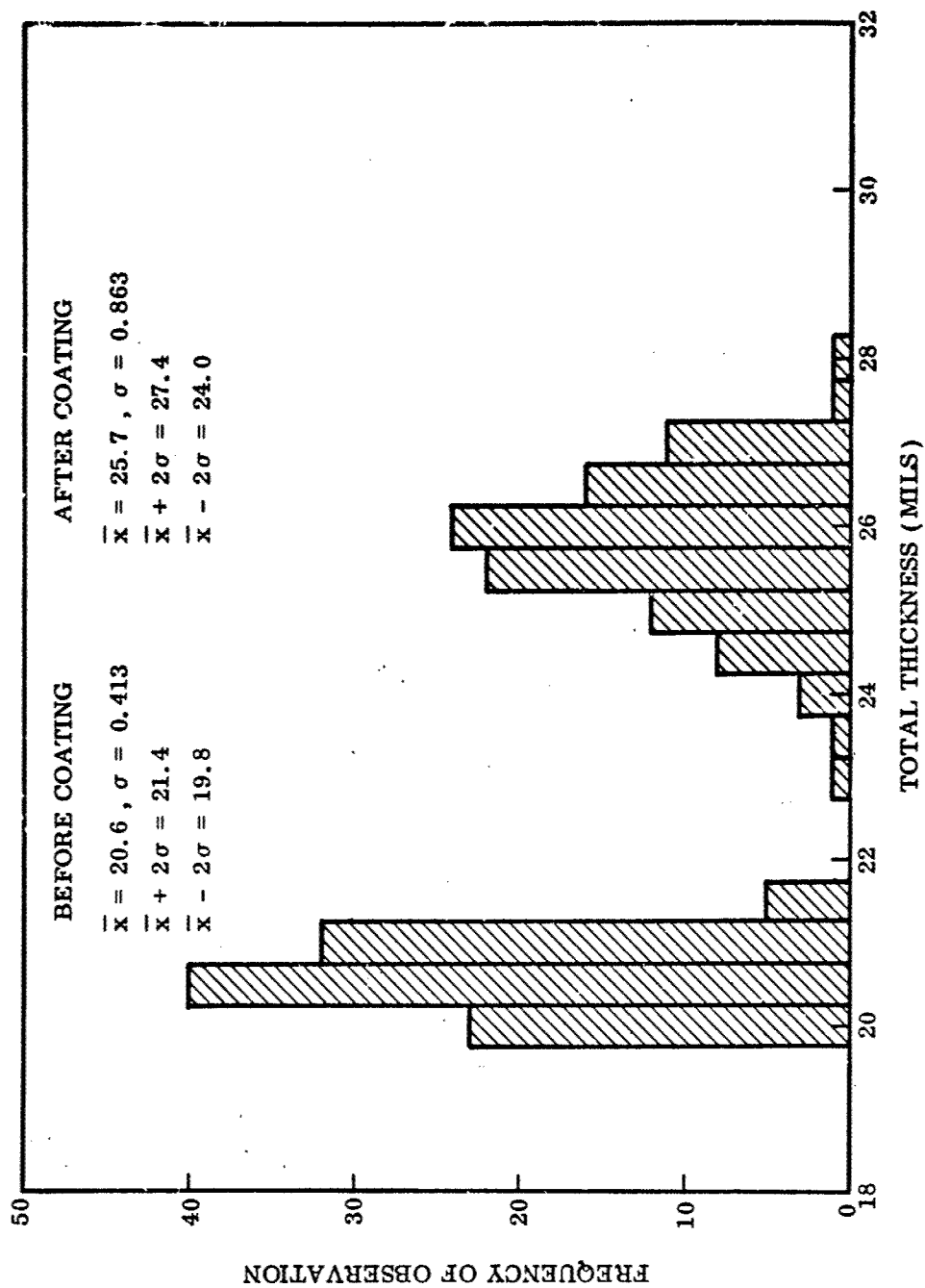
Figure 125   Frequency Histogram of Total Thickness, Cb-752/Vought IV

274

As might be expected, the large subsurface defects were a major source of random defect failures. As shown in Figure 127, these defects reached to within a fraction of a mil of the substrate. Here, in 31 hr at 900° F, leakage through the coating along these defects has resulted in heavy oxidation and complete embrittlement of the substrate. At higher temperatures, where more oxidation products (glass) can form, many of these defects were healed. This is shown in Figure 128A, where after 142 min at 2700°F in air at 1 atm a subsurface defect is completely filled with a dark glassy oxide. However, when the defects extended close to the substrate, as in Figure 127, oxidation of the substrate occurred before sufficient glass could form to heal the defect.

Normally, a random defect failure would develop in the region immediately surrounding such a site. However, as shown in Figure 126 and in the tabulated data (Appendix III), most failures were total rather than random. This indicates a somewhat more complex mechanism of attack and failure. Metallographic studies of specimens revealed two distinct regions of behavior dependent on pressure.

At 1 mm Hg or above, little surface recession occurred. A thick dark gray to black oxide scale was found which spalled off upon cooling to room temperature. The surface of the samples appeared to be liquid during the test, with vigorous bubbling or boiling occurring immediately upon reaching temperature. Only the oxide was liquid and, as will be shown, the coating did not melt at temperatures up to and including 3200° F. Failure at 2600 to 2800° F at pressures above 1 mm Hg started at the large subsurface defects. Columbium and perhaps tungsten oxides formed from oxidation of the substrate alloyed with the liquid glass formed on the coating to create a very corrosive nonprotective oxide. Upon continued heating, the sample was rapidly consumed by what might be called a slow combustion process. As indicated in Figure 126, one-fourth to one-half of the entire sample often was burned away. At 1 mm Hg, eight of ten failed samples had large sections that were consumed. One of these samples was completely consumed within 4 hr at 2700° F; no trace of it was found. Combustion was not self-sustaining, however, and the rapid burning observed with Cb-752/CrTiSi did not occur.

Variable performance at 1 mm Hg or above was due to variations in severity of defects from sample to sample. However, it was the combination of a severe defect and corrosive reaction product from coating and substrate that caused catastrophic failures. The extent of substrate damage after failure was far worse than that observed after failure of coated TZM-Mo at even higher temperatures. Although fewer and less severe defects might be realized by process modifications or new controls, nonetheless any one defect can lead to catastrophic failure in short times at temperatures above 2600° F in air at 1 mm Hg or higher. This is believed to be an inherent characteristic of the complex chemistry of the Vought IV coating.

At pressures below 1 mm Hg, the oxidation products at the time of local failure appeared to be noncorrosive. Although oxides were liquid at 2500° F and above, far less bubbling or blistering occurred and no portion of any of the failed specimens was consumed at temperatures up to 2800° F. Totally failed specimens were glass brittle and often crumbled as the result of straining. The oxide formed was less glassy in appearance than that at 1 mm Hg and often adhered to the substrate upon cooling.

As shown in Figures 128B and 129, pronounced surface recession of the coating occurred after testing at 0.01 to 0.1 mm Hg. Random failure in this range occurred both by attack at local defects and by loss of coating due to accelerated oxidation. In many
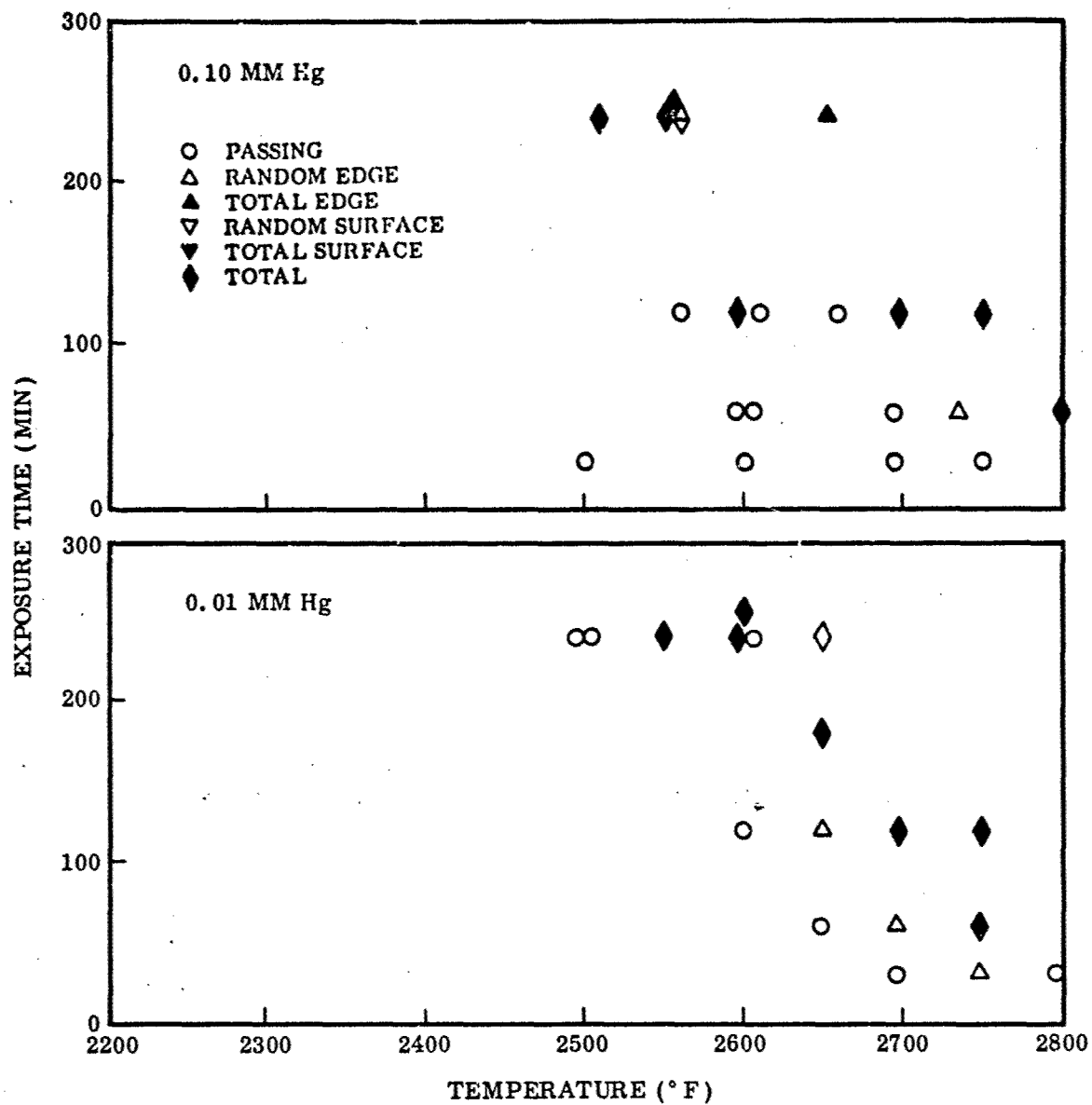
275

Figure 126 Results of Baseline Tests, Cb-752/Vought IV

276
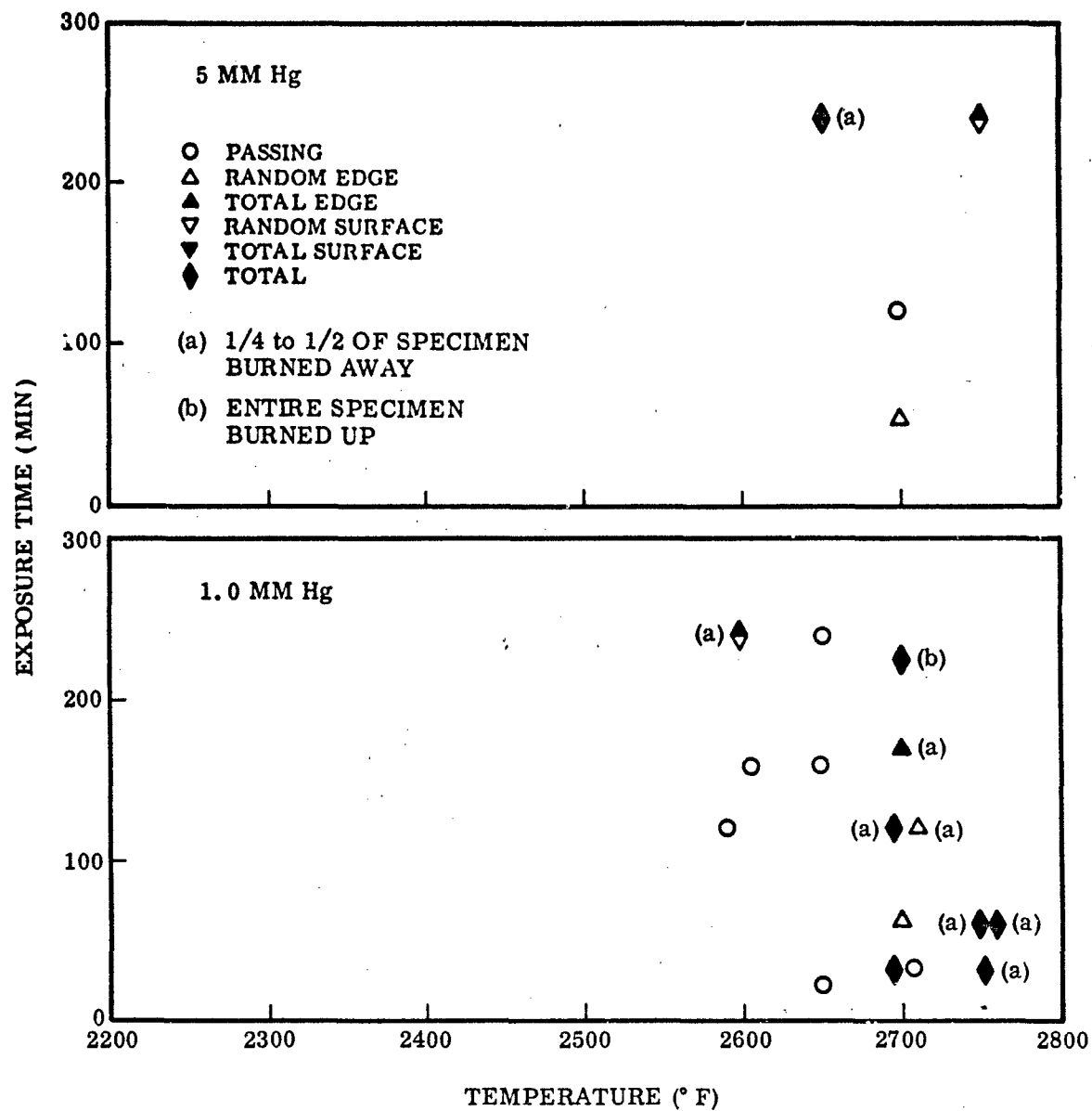
Figure 126 Results of Baseline Tests, Cb-752/Vought IV (cont'd)

277
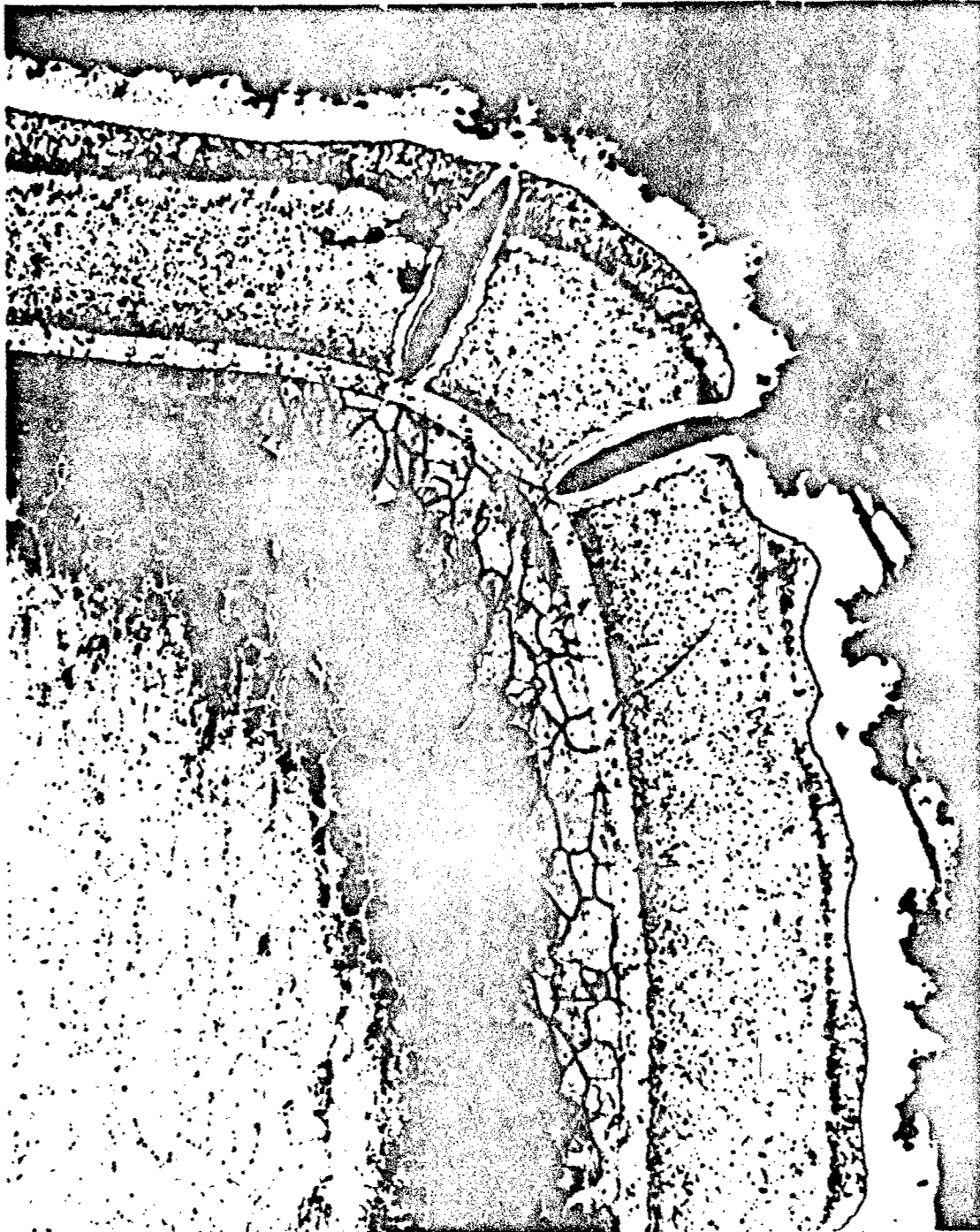
31 hr-900° F

Figure127   Low Temperature Degradation of Cb-752/Vought IV

M6326   (A) 2700° F, 760 mm Hg, 142 min   ×1000
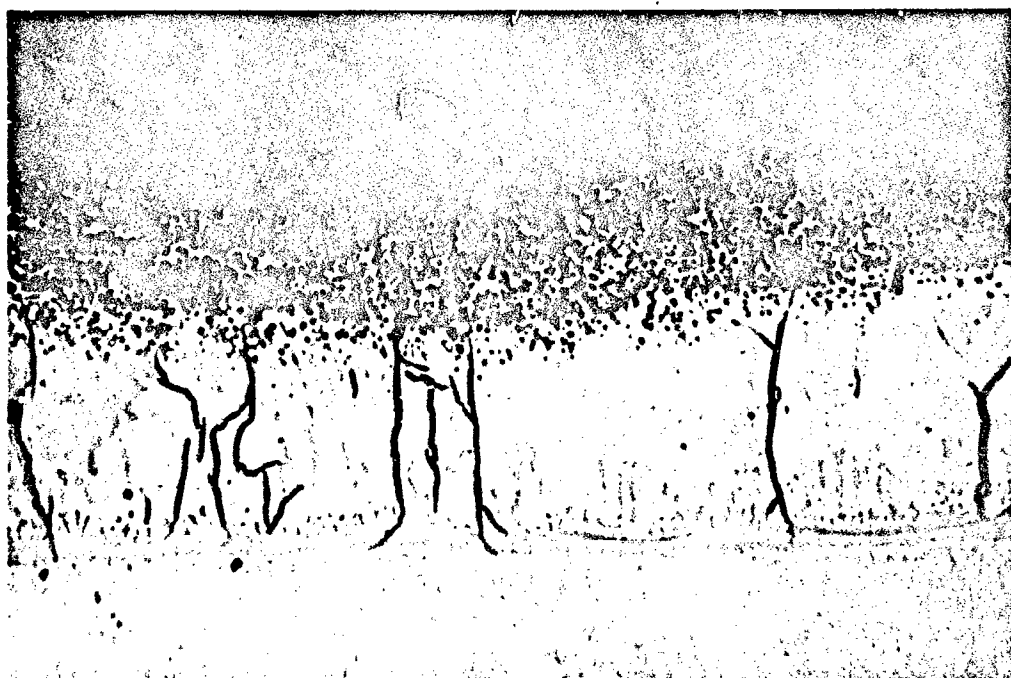
M6441   (B) 2700° F − 0.1 mm Hg − 60 min   ×1000

Figure 128   Effect of Pressure on Structure of Cb-752/Vought IV

279

P917   ×500

(A) Protected Area

P916   ×500
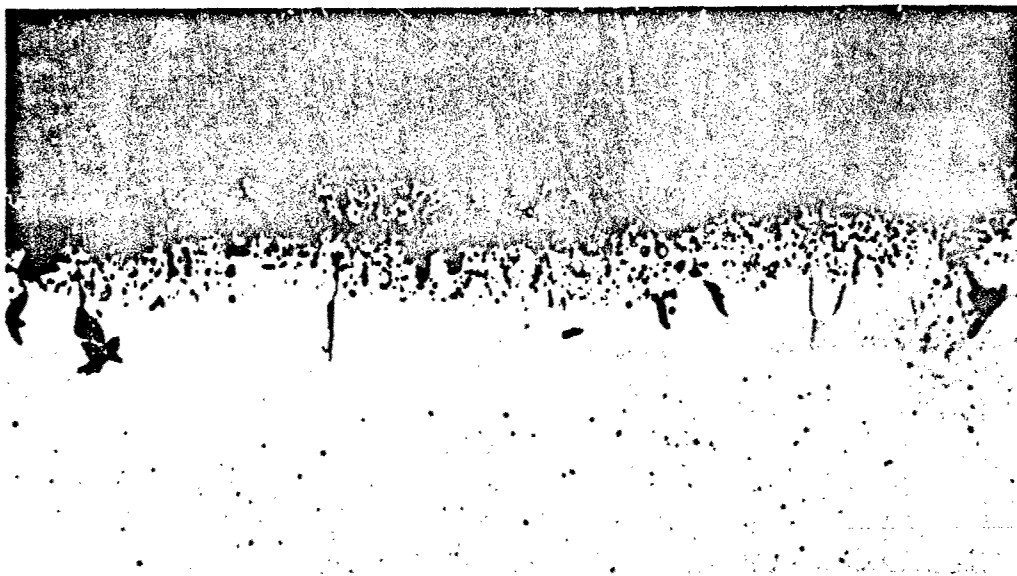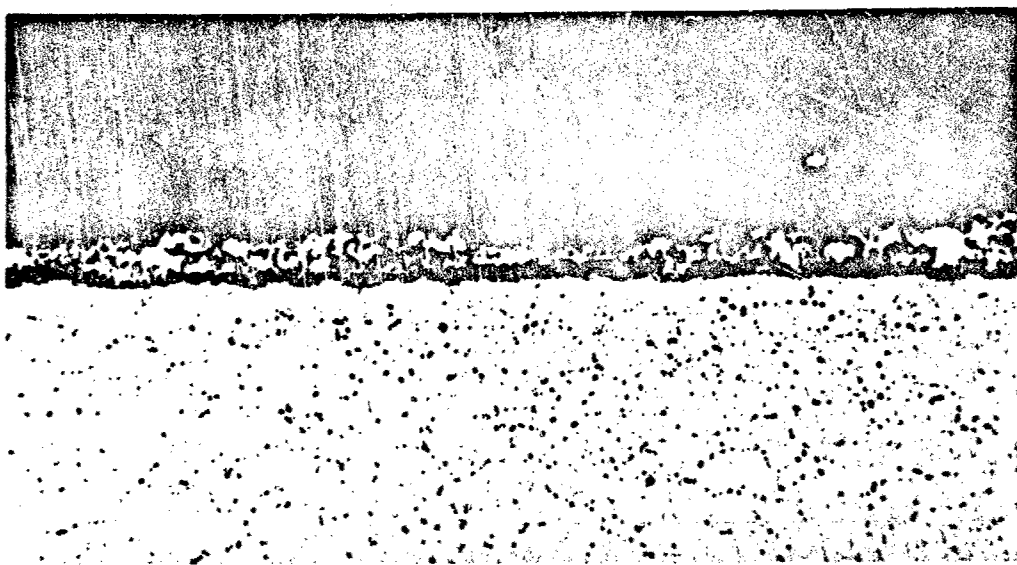
(B) Failed Area

Figure 129   Range of Surface Recession Observed in One Sample
              of Cb-752/Vought IV, Tested at 2650° F, 0.01 mm Hg,
              240 min

cases, failures at local defects were masked by general surface recession failures. Variable performance in this region was due not only to variations in number and severity of coating defects but also to variations in coating thickness and composition. As shown in Figure 129, surface recession was not uniform over the surface of a given specimen. In one region, all the coating was destroyed, resulting in oxidation of the substrate (Figure 129B). In another region, at least 50% of the coating remained and the substrate was protected (Figure 129A). Considering the complex chemistry of this system (at least nine major elements in the coating), local variations in composition probably account for this behavior. Large variations in thickness could also be significant.

A significant result of this analysis is that, in spite of the unique characteristics and complex structure of the Vought IV coating, it exhibits an oxidation behavior at low pressure similar to that of simple or somewhat less complex silicide coatings on Cb alloys. High boron and low silicon in the outer regions of the coating did not help materially to prevent or retard accelerated oxidation at reduced pressures. In fact, at pressures above 1 mm Hg it promoted catastrophic failure of the specimen after local breakdown of the coating. Temperatures at which good performance was observed for 30 min to 4 hr in air at 0.01 to 0.1 mm Hg were in the same range as those determined for the PFR-32 and CrTiSi coatings on Cb-752. However, with this set of Cb-752/Vought IV samples, the temperatures at which consistently good performance was exhibited appeared to be lower than those determined for the other systems.

Gas Velocity

Flow tests were not conducted because of the variable performance capabilities of the samples. Since the oxide formed at temperatures above 2500° F is liquid or semiliquid, it is likely that high gas velocity would increase rates of surface recession by physical removal of protective scales.

Vacuum Volatility

Degradation of the coating after vacuum heating was evaluated to determine if the complex chemistry of Vought IV affected stability. The results are presented in Table LXV, and rate curves based on weight loss per unit area of planar surface are shown in Figure 130. All samples lost weight, and thickness decreased by 0.5 to 1.5 mils per side after heating at 2600 to 3200° F. A parabolic rate behavior similar to that for the other silicide coatings on Mo and Cb alloys was found. However, direct comparison of weight loss data with that of simple silicide systems is misleading, since a heavy element such as chromium constitutes a large portion of the loss from Vought IV. A more valid comparison can be made with the CrTiSi coatings on Cb-752 and B-66. The total weight loss per unit area (discounting minor differences in true surface area) for the three chromium-modified coatings is given in Table LXVI.

Table LXV. Vacuum Volatility Data, Cb-752/Vought IV

Temp.	Pressure	Time (hr)	Thickness		Weight		Thickness Decrease (mils/side)	Weight Loss (gm/cm²)
			Initial (mils)	Final (mils)	Initial (gm)	Final (gm)		
2600	1×10^{-5}	0.5	25.6	–	1.0991	1.0943	–	0.000931
	1×10^{-5}	1		24.6		1.0927	0.5	0.00124
	7×10^{-6}	2		–		1.0899	–	0.00178
	5×10^{-6}	4		24.5		1.0847	0.5	0.00279
2800	2×10^{-5}	0.5	25.8	–	1.0849	1.0730	–	0.00131
	1×10^{-5}	1		24.2		1.0690	0.8	0.00398
	9×10^{-6}	2		23.7		1.0621	1.0	0.00442
	8×10^{-6}	4		23.4		1.0553	1.2	0.00574
3000	2×10^{-5}	0.5	25.6	23.6	1.0985	1.0773	1.0	0.00411
	1×10^{-5}	1		23.0		1.0702	1.3	0.00548
	8×10^{-6}	2		–		1.0634	–	0.00680
	6×10^{-6}	4		22.6		1.0600	1.5	0.00746
3200	2×10^{-5}	0.5	25.4	23.8	1.0874	1.0619	0.8	0.00494
	1×10^{-5}	1		23.3		1.0529	1.0	0.00668
	9×10^{-6}	2		23.1		1.0455	1.2	0.00812
	7×10^{-6}	4		23.0		1.0444	1.2	0.00833

Average Area = 5.16 cm².
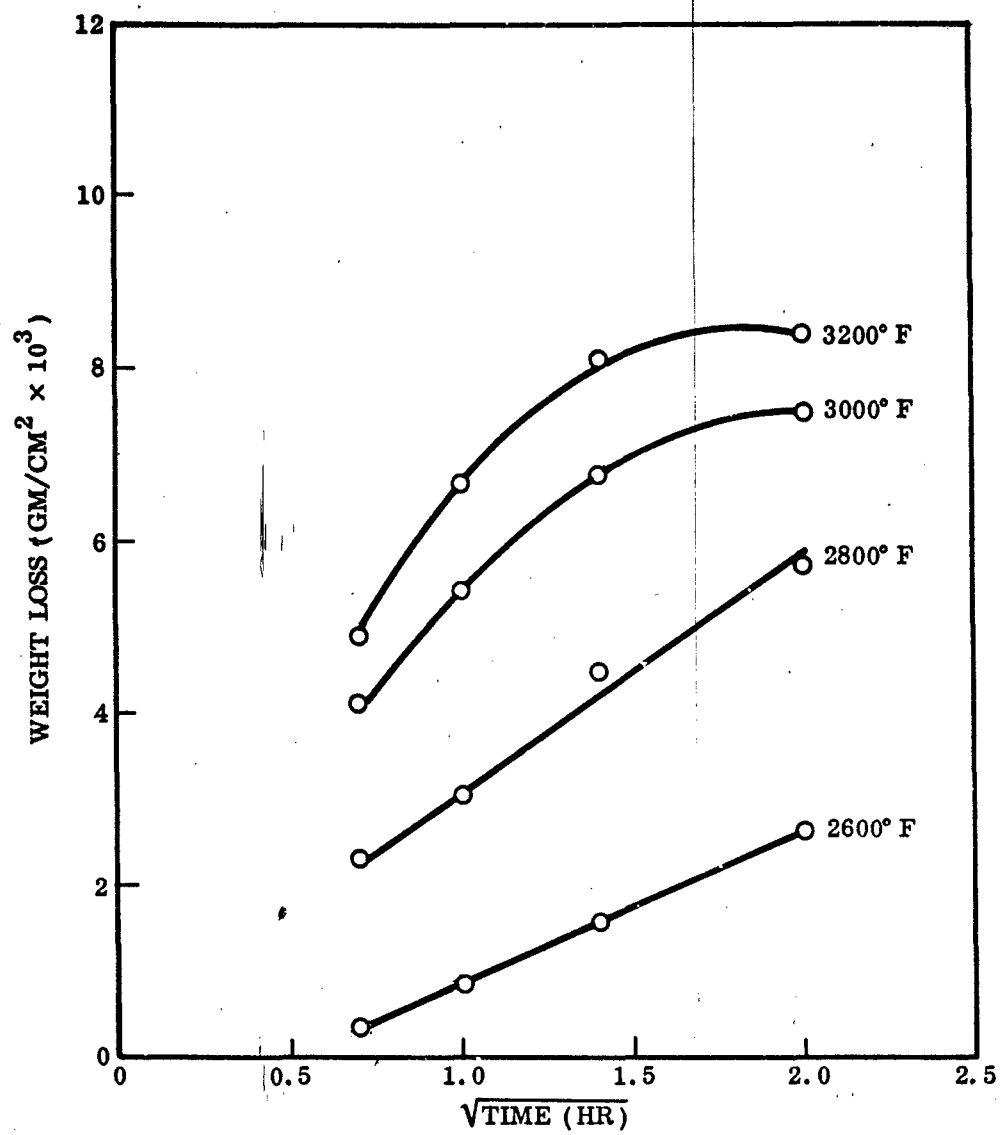
Figure 130 Weight Loss Upon Heating in Vacuum, Cb-752/Vought IV

Table LXVI. Weight Loss After 4 hr in Vacuum, Cb-752/Vought IV

Coating	Loss (gm/cm^2)			
	2600° F	2800° F	3000° F	3200° F
Cb-752/CrTiSi	7.36×10^{-3}	10.6×10^{-3}	14.5×10^{-3}	15.0×10^{-3}
B-66/CrTiSi	5.71×10^{-3}	—	—	—
Cb-752/Vought IV	2.79×10^{-3}	5.74×10^{-3}	7.46×10^{-3}	8.33×10^{-3}

The comparatively low weight loss for the Vought IV coating indicates greater compositional stability at reduced pressure. Metallographic studies revealed that structural damage to the coating was minimal. As shown in Figure 131, the coating was intact except for minor porosity near the surface, even after 4 hr at 3200° F in high vacuum. Although 0.5 to 1.5 mils of surface recession was observed, residual coating thickness was about 4 mils — almost double that of the initial thickness. Considerable interdiffusion with the substrate had occurred. Most of the measured thickness decrease was due to loss of the outer Cr-B-rich layers of the coating. The balance of the coating was little affected. This undoubtedly will change oxidation behavior, but reasonably good resistance to oxidation should remain. The only deleterious effect observed was a widening of the subsurface defects due to loss of the thick Cr-B layer which had formed on the inside surfaces of these voids. Although the bulk coating should be protective after vacuum exposure, random defect failures would be expected on all samples due to enlargement of existing defects.

It is interesting that no evidence of melting in the coating was found at temperatures up to 3200° F. Considering the complex chemistry of this system, it is rather surprising that eutectic melting did not occur. It is suggested that studies of oxidation behavior after vacuum heat treatment be made, provided that samples with greatly reduced defect levels could be produced for such investigations. The high melting point and good structural stability of the coating warrant further study and development.

Temperature-Pressure Cycling

No tests were made because of the variable performance of the available specimens.

Acoustic Vibration

No structural damage was found after exposure to random and sine vibration. Samples were not tested for oxidation resistance after vibration because of the variable performance of the as-coated samples.

Defect Tolerance and Repair

As shown previously, Cb-752/Vought IV samples could be bent 20 to 25 deg over a 3t radius before cracking and spalling of the coating and fracture of the substrate occurred. At bends less than this value, minor fissures were created but no serious damage resulted. None of the deformed specimens were tested for oxidation resistance.

284
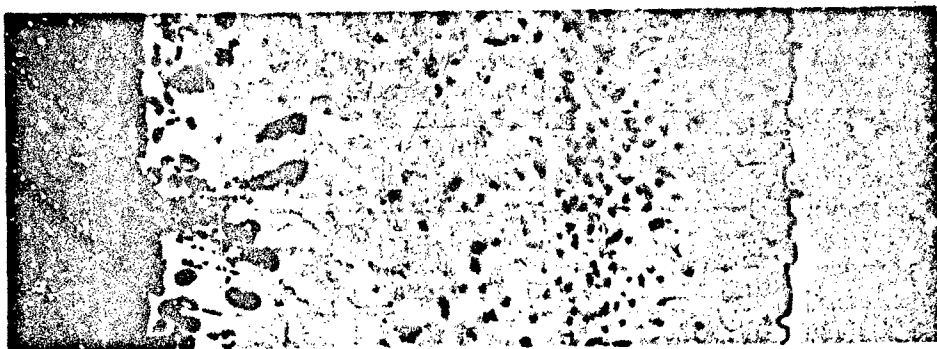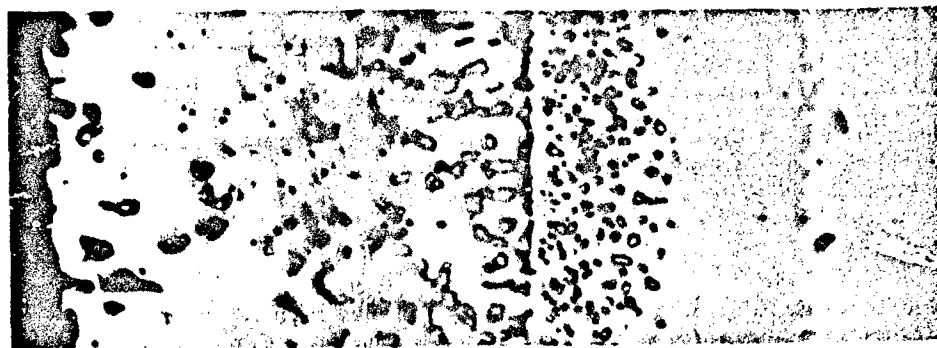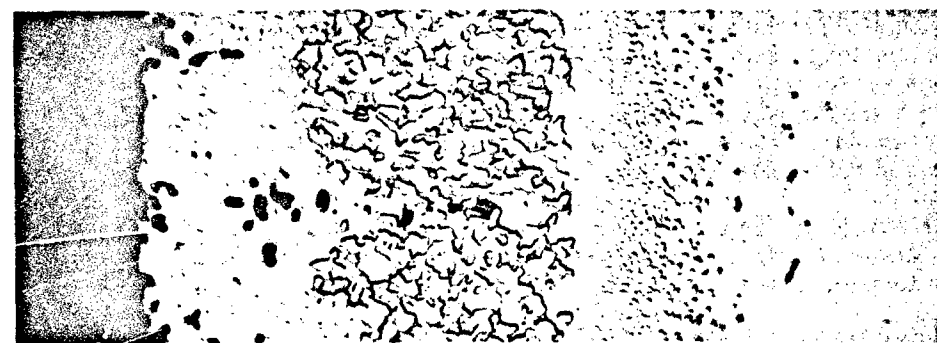
M7703   2600° F   M7704   2800° F   M7702   3000° F   M7705   3200° F

10^{-5} mm Hg — 240 min

Figure 131   Effect of Heating in Vacuum on Structure and Thickness
of Vought IV on Cb–752 (×1000)

285

The Cb-752/Vought IV samples proved to have the greatest resistance to damage by impact of all the silicide-base coatings on Mo and Cb alloys. As shown in Table LXVII, substrate fracture did not occur at the highest level of velocity (273 ft/sec) and impact (2.3 ft-lb), even though deformation was permitted by use of a rubber backup. Some spalling of the coating did occur at this velocity. However, at 235 ft/sec (1.7 ft-lb) no physical damage to the coating was evident.

Table LXVII. Results of High-Velocity Impact Tests, Cb-752/Vought IV

Backup	Kinetic Energy (ft-lb)					
	Spalling		Coating Fracture		Substrate Fracture	
	Pass	Fail	Pass	Fail	Pass	Fail
Rubber	1.7	2.3	1.7	2.3	2.3	> 2.3
Steel	2.3	>2.3	2.3	>2.3	2.3	> 2.3

No oxidation tests for defect tolerance or repair studies were conducted because of the variable performance of as-coated samples.

Materials Compatibility

As might be expected, liquid or semiliquid boron-rich oxides formed above 2500° F caused compatibility problems with refractory oxides. Alumina, thoria, zirconia, and silica all reacted with and fused to the samples during tests. The effect was most pronounced at 1 mm Hg and above, where several failures occurred at contact points. Below 1 mm Hg, less reaction occurred and samples frequently did not fuse to contact materials. Silica appeared to present the least compatibility problem in terms of causing failures at contact points but did tend to fuse to the specimens. With all oxides, severe reaction occurred upon failure of the coating. Oxides of columbium reacted with the coating, glass, and refractory oxides to form a low-melting complex glass.

Compatibility of the Vought IV coating with other refractory metal/coating systems was not evaluated. However, similar reactions would be expected between the boron-rich semifluid glass formed on Vought IV and the oxidation products formed on other coatings.

Ta-10W/Sn-Al

Material Evaluation

The tin-aluminum coating for tantalum alloys was developed by General Telephone and Electronics (GT&E), Bayside, Long Island. The composition of the coating as applied is 90% of a mixture of 75% tin–25% aluminum and 10% of $TaAl_3$ intermetallic. Elemental powders are mixed with a suitable lacquer and are applied to the surface by dipping or spraying. After drying, the coated tabs are sintered 1/2 hr at 1900° F. This forms a tantalum aluminide diffusion layer ($TaAl_2$ and $TaAl_3$) on the substrate with an overlay of a tin-aluminum alloy containing $TaAl_3$ as a dispersed phase. The coating is unique in that the Sn-Al overlay is liquid at temperatures above 1200° F. The underlying $TaAl_2$ + $TaAl_3$ layer, however, is solid at temperatures over 3000° F.

The Ta-10W/Sn-Al samples were coated by GT&E for use in this program. The majority of samples were dip-coated, which was the major process in use at the time. Since spray coating was under development, 25 of the baseline specimens were coated by this procedure for comparative evaluation. The major advantage of the spray coat is the ability to apply a more uniform coating in terms of thickness. Coatings applied by dipping tend to run and form local buildups of coating, particularly at the lower end of the samples.

The general appearance of the coated tabs is shown in Figure 132. The rough, uneven surface and excess coating formed by gravity draining on the lower end of dip-coated samples is readily apparent. Spray-coated samples had a much smoother surface and were more uniform in thickness. Results of thickness measurements made on cross-sectional samples are shown below:

Table LXVIII. Coating Thickness Measurements, Ta-10W/Sn-Al

Process	Total coating (mils)			Aluminide layer (mils)		
	Min.	Max.	Av.	Min.	Max.	Av.
Dip Coat	2.7	5.7	4.2	1.0	1.7	1.3
Spray Coat	3.6	5.2	4.6	1.2	2.0	1.4

Thicknesses of the $TaAl_3$ diffusion layer and total coating thickness were about the same on flat surfaces. The spray-coated tabs, as expected, had less variation in total thickness but about the same variation in thickness of the $TaAl_3$ zone. The microstructures are compared in Figure 133.

As shown in Figures 132 and 134, the most striking difference was at the bottom of specimens where large buildup of coating formed on dipped specimens. Edge coverage was variable on these tabs, and large variations in both total thickness and $TaAl_3$ thickness occurred at the corners. The corners on spray-coated tabs had a much more uniform coating, with thickness and variations in thickness about the same as on flat surfaces. The $TaAl_3$ zone was continuous and free of large defects around the edges of all samples.

287
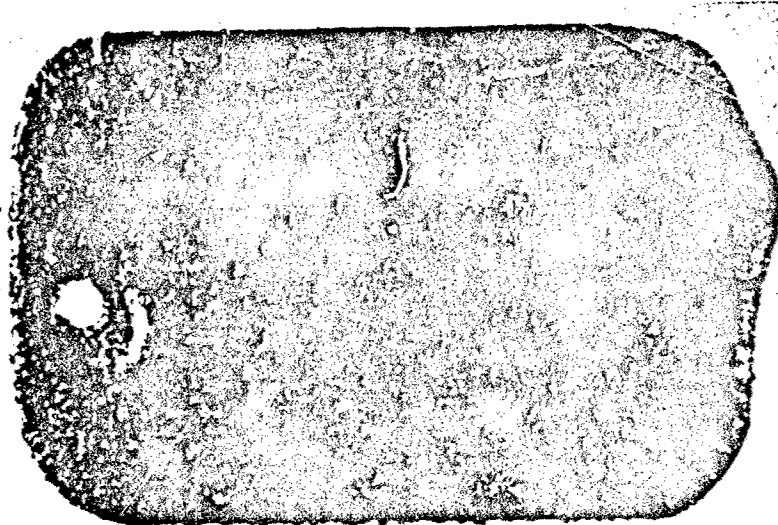
M9963   ×6
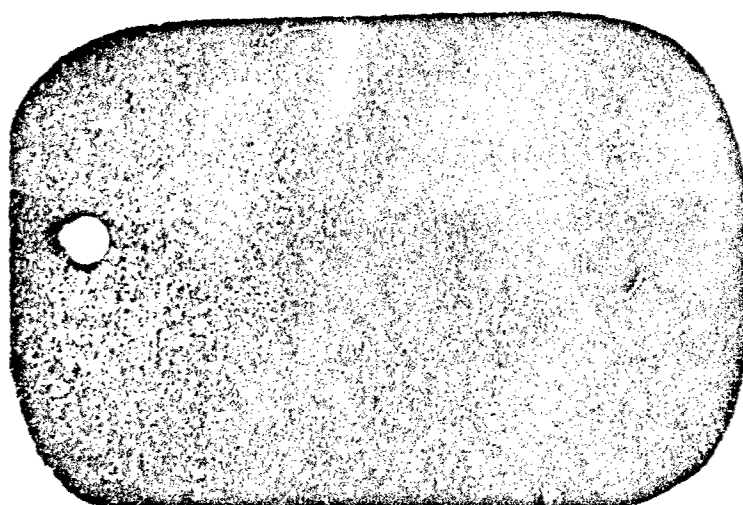
(A) Dip Coated

M9965   ×6

(B) Spray Coated

Figure 132 Surface of As-Coated Ta-10W/Sn-Al Specimens

M8309   ×500

(A) Dip Coated

M9891   ×500

(B) Spray Coated

Figure 133 Structure on Flat Surfaces of As-Coated Ta-10W/Sn-Al

M6148   ×500

(A) Dip Coated

M9892   ×500

(B) Spray Coated

Figure 134 Structure at Edges of As-Coated Ta-10W/Sn-Al

The microstructural details of the coating are shown in Figure 135. The outer layer appeared to be nearly pure tin in which large particles were dispersed. The absence of primary crystals of aluminum in the outer layer indicates a fairly low aluminum content. The particles that were present are made up of two phases. The darker inner core probably is $TaAl_3$. The lighter outer core may be $TaAl_2$ formed by loss of aluminum to the melt or may be a ternary Ta-Al-Sn compound formed by reaction with liquid tin. The inner aluminide diffusion layer also was found to be a complex mixture of two or more phases. It is believed to consist primarily of a mixture of $TaAl_2$ and $TaAl_3$. Compounds of Ta and Sn (Ta_3Sn) may also be present.

No evidence of a diffusion zone extending into the substrate was found by metallographic observation and hardness test. Hardness at 0.5 mil below the interface was 275 DPH and averaged 282 DPH across the section. Substrate hardness before coating was 286 DPH, indicating no effect of the coating process or thermal cycle on the substrate. The microstructure of the substrate was similar to that of uncoated sheet. Samples were ductile at room temperature and were bent 90 deg over a 3t radius without substrate fracture.

Measured values of thickness and weight before and after coating could not be used to calculate average coating thickness or uniformity. Due to the rough surface and uneven distribution of the Sn-Al on each tab, micrometer and weight measurements were of little value. Total thickness increase (maximum, based on micrometer readings) averaged 7 mils per side. The standard deviation after coating ($\sigma = 1.33$ mils) was about four times that of uncoated sheet ($\sigma = 0.36$ mil). This gives some indication of sample-to-sample variability but includes contributions of variation in surface roughness as well as in coating thickness.

Spectrographic analysis indicated Ta, W, Al, and Sn to be the principal elements in the coatings. Traces of Mo, Fe, Ni, and Cu also were found.

Baseline Behavior

The results of baseline oxidation tests are plotted in Figure 136 and tabulated in Appendix III.

The evaluation of baseline oxidation behavior at reduced pressure proved to be a difficult task for two reasons. First, performance criteria based on visual appearance and room temperature bend ductility often were misleading. Second, high-temperature tests for which resistance heating was required often were inconclusive due to localized recession of the substrate and consequent overheating and burnout of samples before failure of the coating occurred.

Unlike coated Cb-base alloys, room temperature bend ductility could not be used as a measure of coating performance. Samples were found to be embrittled to varying degrees on heating in air at pressures of 0.01 to 50 mm Hg for times of 30−240 min at temperatures of 2400−3100° F. Small fissures to large cracks were formed on making 3t-90 deg bends at room temperature after test. The degree of cracking could be correlated to some extent with time and temperature. Small to medium fissures formed on testing at 2500−2800° F and medium to large cracks formed at 2850−3100° F. Longer time at

291

M8310   ×3000

(A) Outer Surface Layer

M8358   ×3000
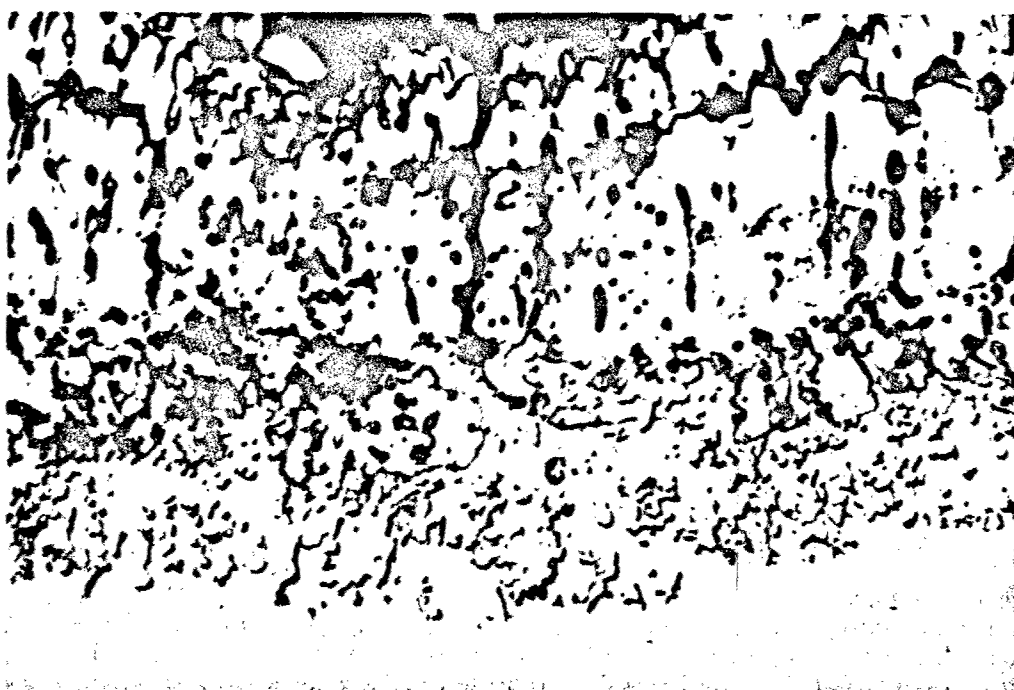
(B) Substrate/Coating Interface

Figure 135 Microstructural Details of Dip-Coated Ta-10W/Sn-Al

292

temperature tended to produce more severe cracks on bend testing. Pressure in the range of 1−50 mm Hg did not seem to have an effect on severity of cracking after equivalent time and temperature.

Metallographic examination indicated that cracking was associated with the formation of a diffusion zone below the $TaAl_2$-$TaAl_3$ intermetallic layer. As shown in Figure 137, a continuous and uniformly thick diffusion zone was formed in the surface of the substrate. It graded into the alloy substrate without a clear interface with the substrate. Also, penetration along grain boundaries of the substrate was observed. The zone had a hardness of 520 DPH. Cracks formed in the coating on bending propagated into and through this zone, continuing on in the substrate. Hardness of substrate grains was the same as the hardness of the original substrate alloy (av. = 286 DPH). No evidence of oxide precipitation in substrate grains was observed, even in samples where large cracks formed on bending. Conversely, when oxide precipitation resulting from coating failure was observed, the substrate was hardened to 400−600 DPH and glass brittle fracture occurred on bending.

It is believed that this effect was due to diffusion of aluminum or tin into the substrate. Samples heated in vacuum for 4 hr at 2600 to 2800° F did not crack on bending. Since all of the tin was lost by evaporation in these tests, the absence of substrate embrittlement suggests that diffusion of tin into the alloy may be the cause of brittle behavior. Although the possibility of oxygen or nitrogen leakage through the coating has not been excluded as a cause, it seems to be an unlikely one. The diffusion zone is too uniform in thickness to be attributed solely to gas leakage through a complex coating. Also, no hardening of substrate grains or formation of precipitates was observed. Furthermore, when samples were tested at pressures where tin boiled out of the coating, no diffusion zone such as that shown in Figure 137 was formed even though severe oxidation of the substrate occurred. Detailed electron probe studies would help to clarify the exact cause of substrate embrittlement where oxidation was not evident.

In view of this behavior, bend ductility, other than glass brittle fracture, was not used as a performance criterion. Samples were rated as failing to protect from oxidation only if glass brittle fracture occurred or if excessive substrate hardening and oxide precipitation were noted. This required extensive metallographic study to evaluate the performance of samples. Consequently, some of the less important aspects of the test program on this system were abridged slightly.

Failure boundaries could not be established at pressures of 1, 5, 20, and 50 mm Hg. The maximum temperature for a 30-min to 4-hr life at these pressures was above 2900° F. This required the use of resistance heating for tests. However, surface recession of the substrate due to interdiffusion with the coating was not uniform, and local regions of heavy recession of the substrate developed (Figure 138). This, in turn, caused localized overheating which accelerated the process and eventually caused localized failure of the sample. As shown in Figure 138, the coating still protected the substrate from oxidation. The substrate hardness immediately below the large pit in Figure 138A was 240 DPH. In some areas of this sample, one-fourth to one-third of the substrate thickness had been consumed by diffusional process in localized regions.
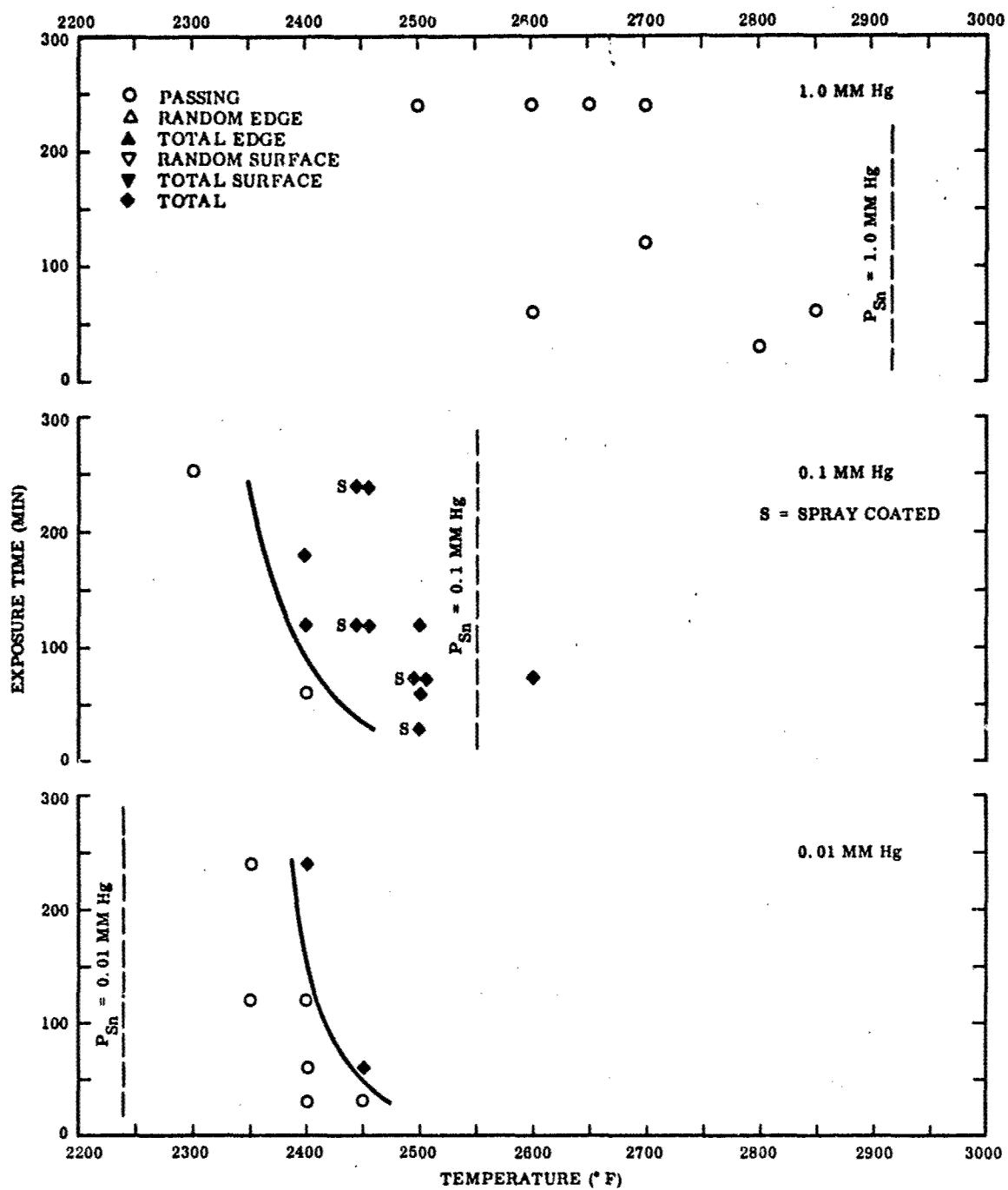
293

Figure 136 Results of Baseline Tests, Ta-10W/Sn-Al

294
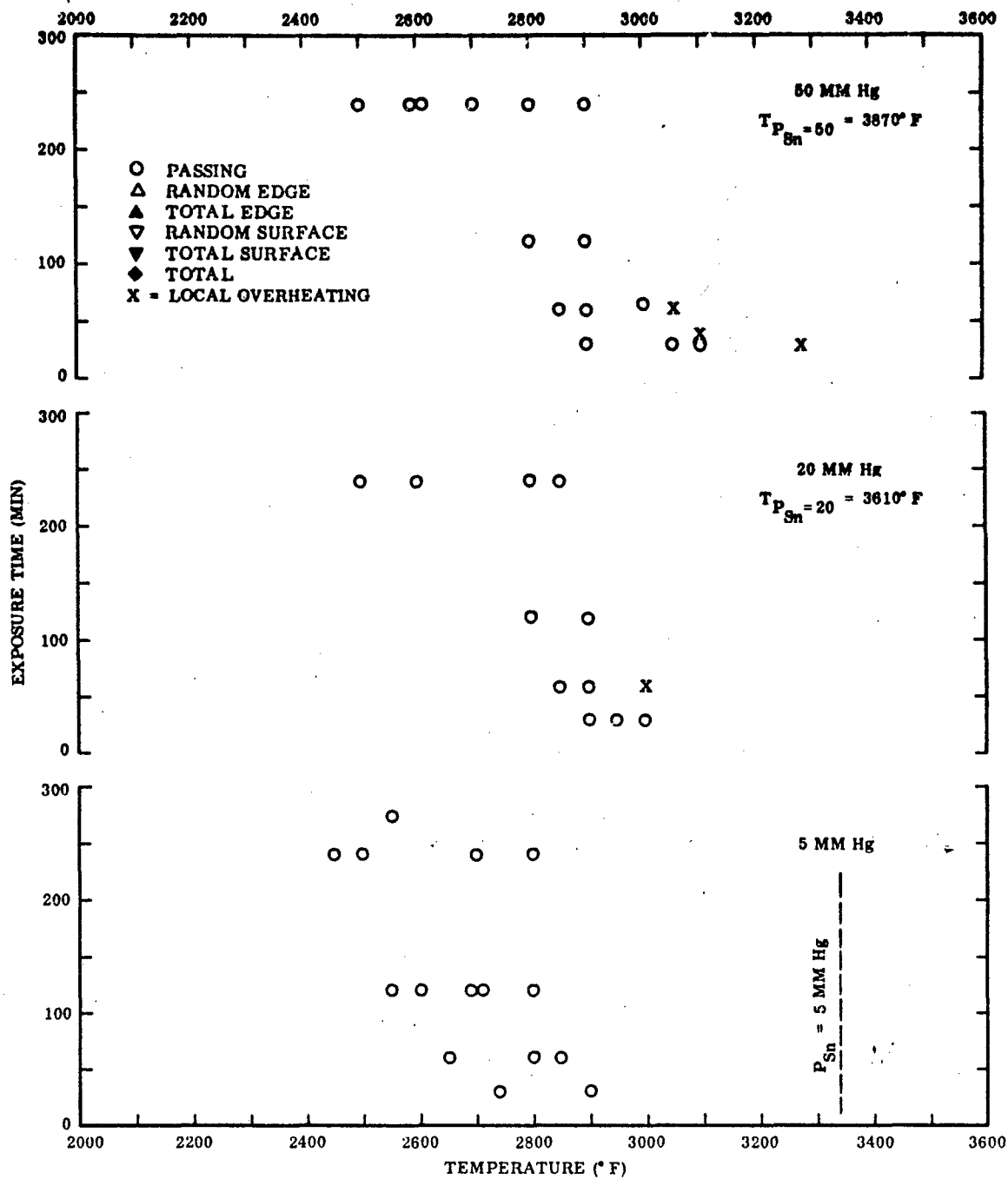
Figure 136 Results of Baseline Tests, Ta-10W/Sn-Al (cont'd)

M9810   ×2300

(A) Unstrained Region, No Etch

M9805   ×2300
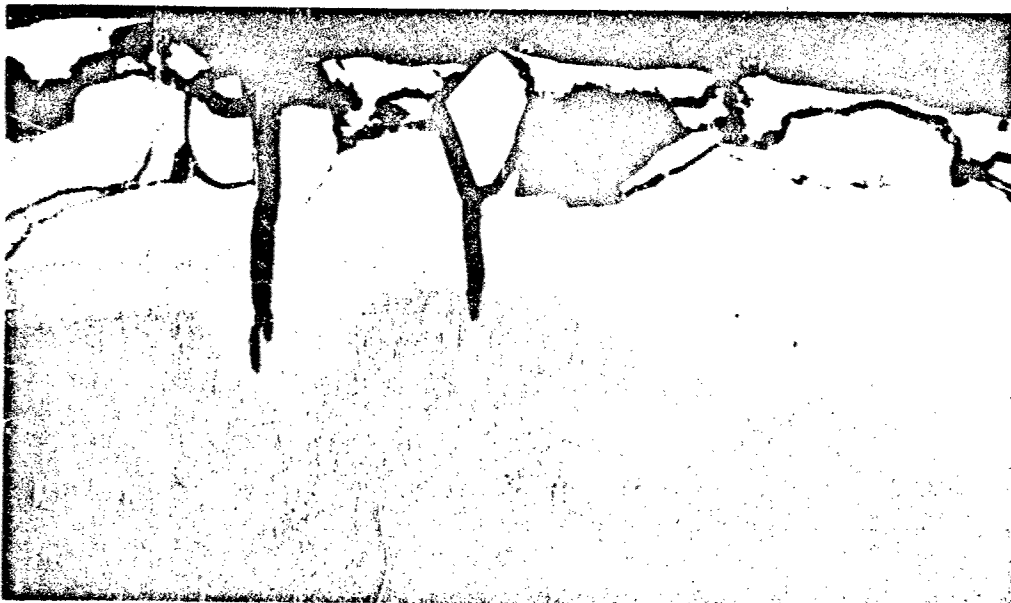
(B) Strained Region, Etched, 2850° F, 20 mm Hg, 240 min

Figure 137 Substrate Embrittlement Resulting From Interdiffusion With the Coating

P927   ×100
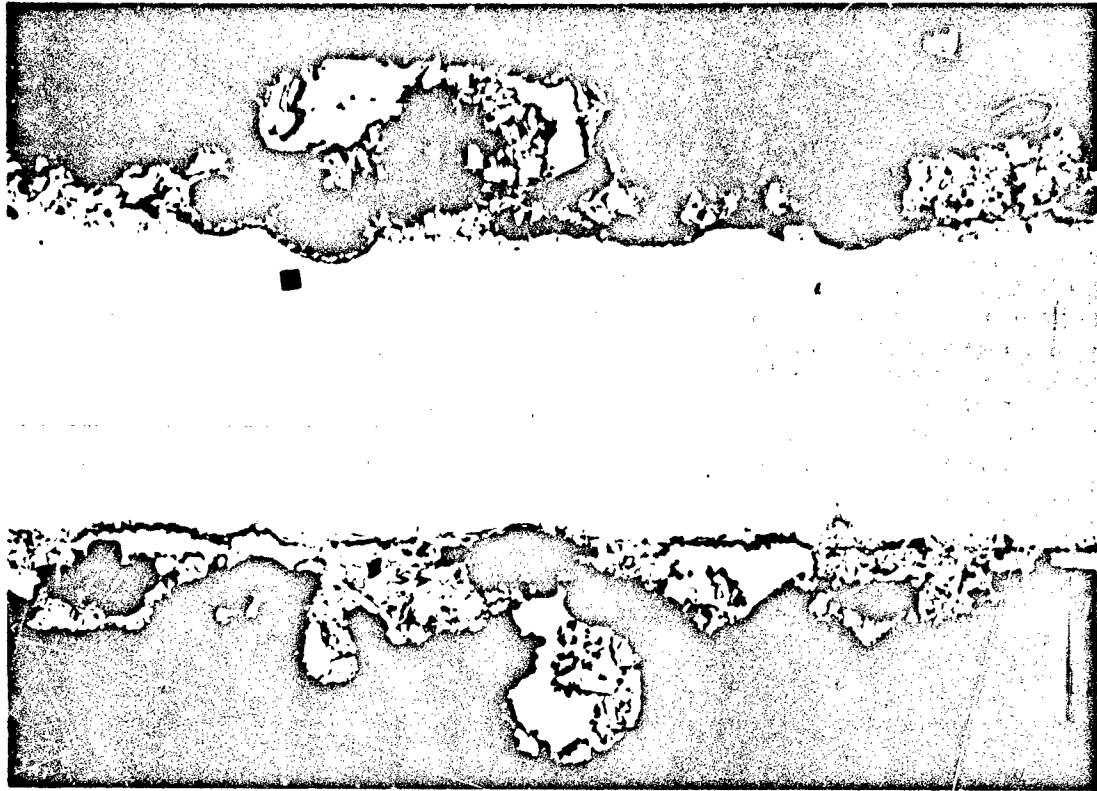
(A) 2800° F, 50 mm Hg, 240 min
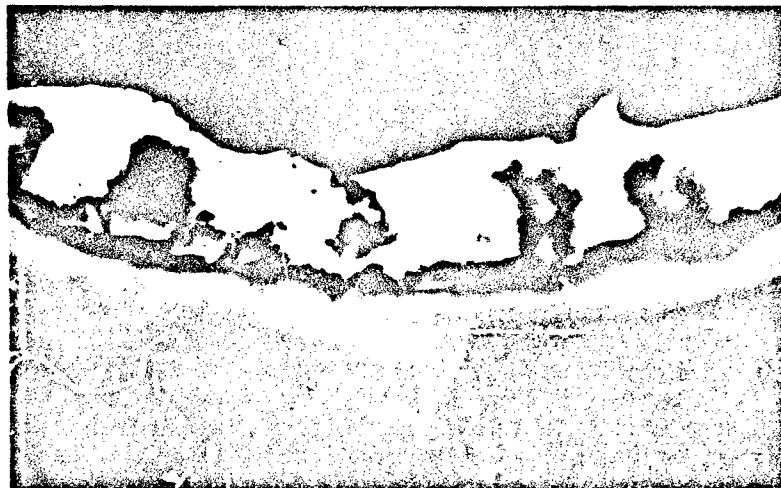
P928   ×2000

(B) Region Above Hardness Indentation Shown in (A)

Figure 138 Localized Substrate Recession From Reaction With Sn-Al Coating

297

This behavior was not observed in samples heated to 2800° F by radiation. Recession of substrate by diffusion in these samples was comparatively uniform. The severe local recession in resistance-heated samples was probably due to thermal gradients and fluctuations within the sample.

Although the Sn-Al coating protected the substrate from oxidation for up to 4 hr at 2850° F or above at pressures of 1–50 mm Hg, appreciable surface recession of the substrate occurred at these temperatures and pressures. Failure of the system could result from destruction of the substrate in sheet structures by diffusion and liquid alloy attack, even though resistance to oxidation had been provided. The mechanism involved is worthy of more detailed study. The structures in Figure 138 suggest that liquid tin has attacked the $TaAl_2$-$TaAl_3$ intermetallic. This may transport tantalum (and tungsten) to the surface from which they are oxidized. Aluminum, in turn, may diffuse into the substrate and form more $TaAl_2$-$TaAl_3$ intermetallic. Thus, although the substrate is protected from oxidation, tantalum and tungsten essentially are transported to the surface of the coating from which they are lost by oxidation. Analogous processes are known to occur for certain noble metal coatings on refractory metals. Cursory studies at LMSC have shown, for example, that liquid platinum protects Mo from oxidation but transports Mo to the surface from which it is lost by oxidation.

The basic oxidation-resistant characteristics of the Sn-Al coating appear to be governed by both the molten Sn alloy outer layer and the $TaAl_2$-$TaAl_3$ inner layer at reduced pressure. In effect, oxidation resistance is dependent upon a "coating on a coating" in that the phase that is rich in liquid tin protects the aluminide layer from low-pressure oxidation. Excellent protection from oxidation is afforded at all temperatures and pressures where tin is stable on the surface (little vaporization). The coating structure after 1 hr at 2400° F in air at 0.1 mm Hg is shown in Figure 139. The test temperature was about 200° F below the temperature at which the vapor pressure of tin is 0.1 mm Hg. Tin is stable on the surface but is evaporating. The structure is similar to that of samples tested at 1 atm except for some loss of tin by volatilization. The $TaAl_2$-$TaAl_3$ zone has thickened, with a corresponding reduction in substrate thickness. The two-phase nature of this zone is revealed after etching (Figure 139B). The zone shows no evidence of low-pressure oxidation attack and is highly protective.

With continued heating, all the tin is lost by vaporization. Within 2 hr, the $TaAl_2$-$TaAl_3$ layer is exposed to the atmosphere, and rapid degradation by low-pressure attack occurs. This is illustrated by Figure 140A, where a spongy layer of oxides and tantalum alumi-nides remains. Once the layer is totally consumed, rapid oxidation of the substrate occurs, as shown in Figure 140B.

In summary, the life of the Sn-Al coating at temperatures below the temperature at which the vapor pressure of tin equals the system pressure is governed by the rate at which tin evaporates or is consumed by oxidation plus the rate at which the $TaAl_2$-$TaAl_3$ is con-sumed by oxidation after the tin has been lost. At temperatures above the boiling point of tin for any given pressure, the tin flashes off the coating in a few seconds and useful life is governed only by the oxidation rate of the aluminide coating. In all such tests, sample weight decreased by 10% and thickness decreased by 20% immediately after loss of the tin. Baseline data at 0.1 and 0.01 mm Hg are representative of these two types

298
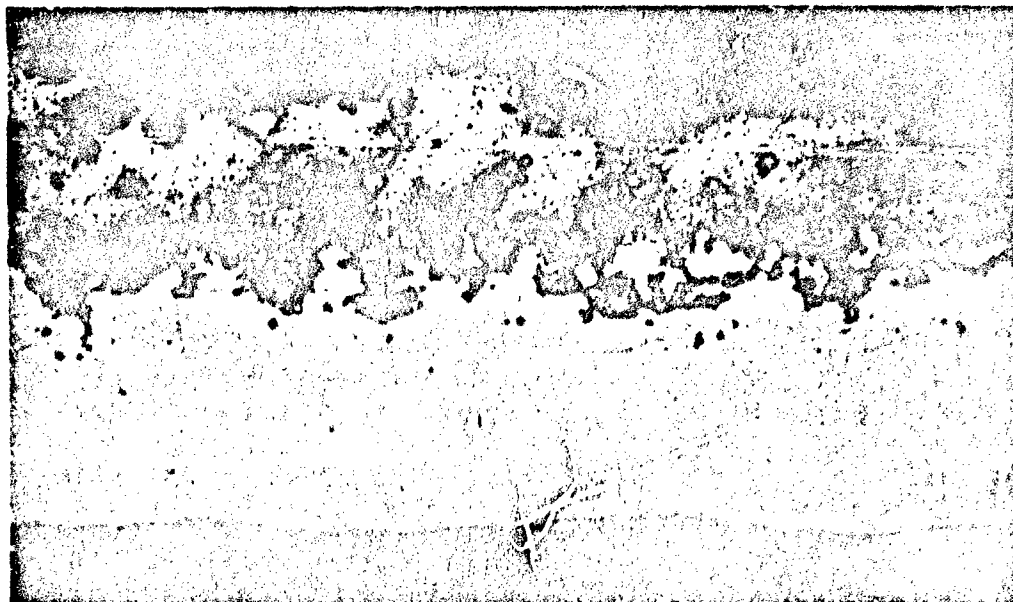
M8361   ×500

(A) As-Polished
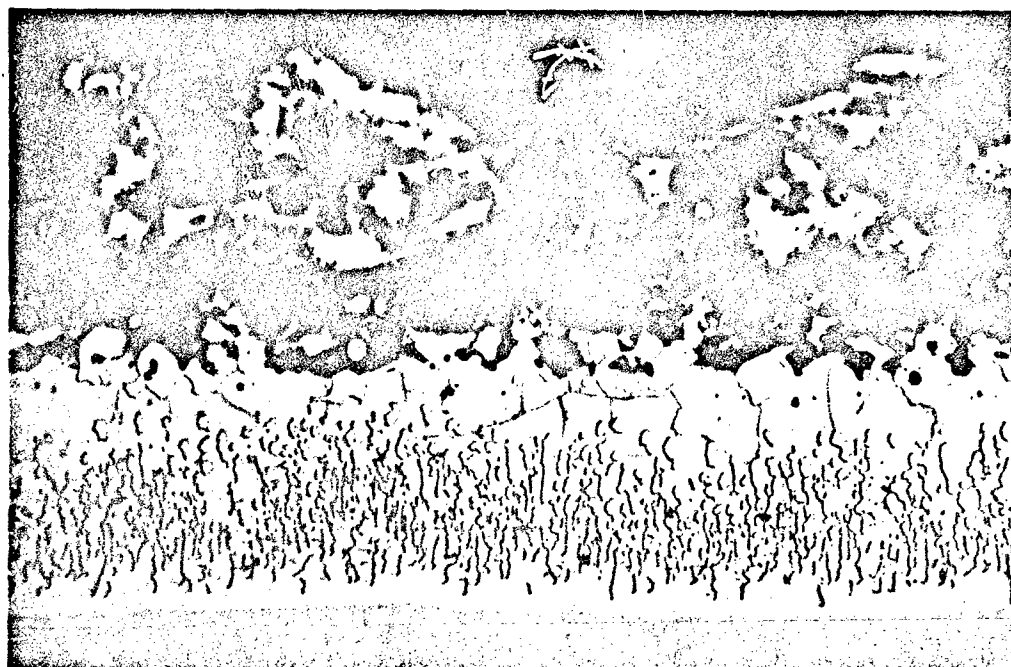
M8362   ×500

(B) Etched

Figure 139 Coating Structure After Test, 2400° F, 0. 1 mm Hg, 60 min,
No Tin Loss, Ta-10W/Sn-Al

299
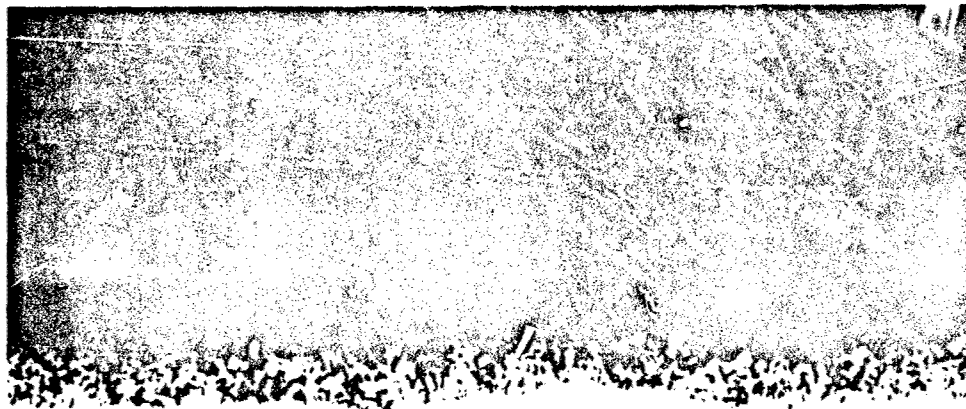
P979   ×500

(A) Protected Region, 2450° F, 0.01 mm Hg, 60 min
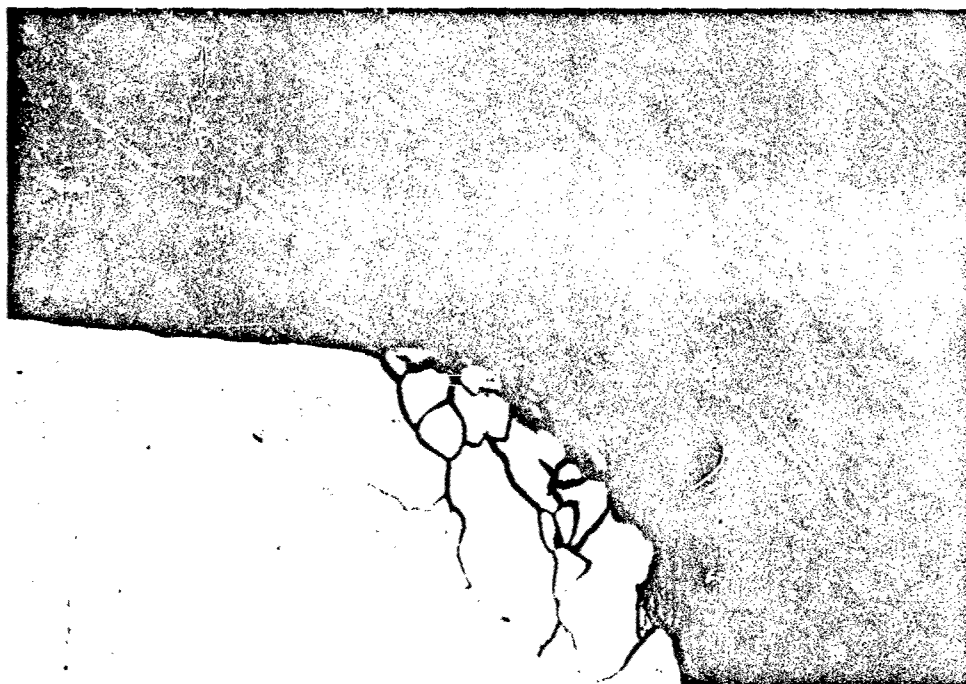
M9804   ×500

(B) Total Failure, 2500° F, 0.1 mm Hg, 75 min

Figure 140 Coating Failure After Vaporization of Tin, 2500° F, 0.1 mm Hg,
            75 min, Ta-10W/Sn-Al

300

of behavior. The rate of degradation of the aluminide layer appears to be quite sensitive to temperature and is very rapid above 2400° F in air at low pressure.

It is significant that at pressures of 1 to 50 mm, where very high temperatures are needed to evaporate tin, the Sn-Al coating probably has a higher temperature capability than silicide-base coatings on Mo and Cb alloys. Thus, this coating can be considered more resistant to low-pressure degradation at pressures down to 1 mm Hg and temperatures up to 2900° F. However, at pressures below 1 mm Hg where tin evaporates at low temperature, the Sn-Al coating has less capability than silicide-base coatings. At these pressures, silicide coatings can be used at temperatures 200 to 300° F higher than the Sn-Al coating for equivalent lifetime. The performance at reduced pressures is governed largely by the vapor pressure of tin as a function of temperature and could be improved by alloying to reduce vapor pressure or by using a metal other than tin to give stability at low pressure.

The Sn-Al coating appears to be relatively insensitive to minor crack-type defects, and performance was governed primarily by tin evaporation rates and surface recession of aluminide layers at all pressures. Thus, few random failures occurred, and those that did occur were due largely to variations in coating thickness.

Check tests of spray- and dip-coated samples at 1 atm and at 0.1 mm Hg revealed no significant differences in performance. The general appearance and structure were the same for both materials after test. It is possible that some differences might occur at high temperature (> 2800° F) where substrate loss by surface recession occurs. The more uniform spray-coated samples may be more resistant to localized recession effects. However, none of the resistance-type specimens were spray coated, so this behavior could not be studied.

Gas Velocity

The results of the gas velocity studies with Ta-10W/Sn-Al are presented in Table LXIX. These results are not conclusive because there was again localized surface recession due to interdiffusion between the substrate and the coating. The effect was more severe in the flow tests than in baseline studies, and consequently it was impossible to reach temperatures where flow might grossly affect coating performance. In some cases, specimens were thinned to the point that holes were formed and localized overheating occurred. There was surface recession on both sides of the specimens, although the effect was greater on the flow side. There was heavy oxidation around severely overheated regions of the substrate, and some intergranular oxide formation was observed under recessed regions on the flow side.

Apparently the temperature was not uniform across transverse sections of the flow test samples, since the liquid tin tended to flow toward the specimen centerline and accumulate there in depths up to about 1/8 in. This was at first believed to be an effect of flow, but an experiment was conducted in which a flow specimen was heated to about 2800° F in air at 1 atm for a few minutes under nonflow conditions. The coating material flowed to the center, and the surface pattern was similar to that observed on flow-tested specimens. This, of course, is evidence of a nonuniform temperature across the specimen.

301

Table LXIX. Results of Mach 3 Flow Tests, Ta-10W/Sn-Al

Temp. (°F)	Total pressure	Atmos- phere	Equivalent air pressure	Time (hr)	Comments
2650	20	19:1 N_2:O	5	1	Redistribution of coating material; thinning of substrate
2700	20	19:1 N_2:O_2	5	1	Redistribution of coating material; thinning of substrate
2850	20	19:1 N_2:O_2	5	1	Redistribution of coating material; holes in substrate; oxide precipitate in grain boundaries; thinning of substrate
2700	20	Air	20	1	Redistribution of coating material; thinning of substrate
2800	20	Air	20	1	Redistribution of coating material; some oxide precipitate in grain boundaries; thinning of substrate
2850	20	Air	20	1	Redistribution of coating material on flow side; thinning of substrate
2900	20	Air	20	1	Redistribution of coating material on flow side; severe oxidation in regions of severe overheating

302

Usually, some tin and aluminides were left in regions where the coating was thinner on flow-tested samples, and areas of surface recession were more predominant in those regions. Some segregation of phases occurred during testing, with the result that in areas of thinner coating the Ta and/or W were more soluble in those phases existing at the surface. Also, those phases may leak oxygen more readily, which could account for the observation of oxides underlying some recessed regions. It is not entirely clear whether the aggravated surface recession in the flow tests, as compared with baseline studies, was due to flow or to the additional temperature gradient that resulted from a difference in geometry. There were insufficient specimens to evaluate this thoroughly.

Significantly, the tin generally was not washed from the surface, and consequently the aluminide layer was protected from low-pressure oxidation. However, the residual layer of tin was less on the flow side than on the static side. The tin may be retained on the surface by a tenacious aluminum oxide layer which probably exists on the surface of the tin. Large crystals of Al_2O_3 were found on the surface of some samples after test. These were identified by x-ray diffraction.

It must be concluded that the specimens tested under flow conditions were failures; however, the failures were not the result of substrate oxidation but of excessive thinning of the substrate. This effect should not be regarded simply as an artifact of testing; it may result from a combination of flow and thermal diffusion. In many applications of coated refractory metals, temperature gradients and flow conditions will exist and a similar behavior may be encountered.

Vacuum Volatility

The results of the vacuum volatility studies with Ta-W/Sn-Al are presented in Table LXX. Thickness data are omitted because of variations in thickness from specimen to specimen and on single specimens.

The boiling point of tin at 10^{-5} mm Hg is about 1600° F. Therefore, the weight losses recorded reflect the loss of tin. Since the amount of tin present on specimens varied appreciably from specimen to specimen, the results of single-specimen experiments at various temperatures cannot be realistically compared and consequently the data are not plotted.

It is apparent from the data that the tin was evaporated rapidly and then the weight remained fairly constant throughout the exposure. A weight increase was noted after 2 hr at 3000° F and after 1 hr at 3200° F, probably as the result of tungsten diffusing from the specimen support into the specimens.

Probably coating performance subsequent to high-temperature (> 1600° F) vacuum exposure will be degraded seriously. The aluminide layer will be unprotected and subject to rapid oxidation, especially at reduced pressures.

303

Table LXX. Vacuum Volatility Data, Ta-10W/Sn-Al

| Temp. (°F) | Pressure (mm Hg) | Time (hr) | Weight | | Weight change (gm/cm^2) |
			Initial (gm)	Final (gm)	
2600	2.2×10^{-5}	0.5	2.1857	1.9489	0.0465
	1.4×10^{-5}	1		1.9461	0.0469
	1.0×10^{-5}	2		1.9441	0.0474
	8×10^{-6}	4		1.9424	0.0477
2800	1.5×10^{-5}	0.5	2.2837	2.0292	0.0489
	1.0×10^{-5}	1		2.0285	0.0491
	9.0×10^{-6}	2		2.0279	0.0492
	8×10^{-6}	4		2.0279	0.0492
3000	1×10^{-5}	0.5	2.2796	2.0131	0.0523
	9×10^{-6}	1		2.0124	0.0524
	8×10^{-6}	2		2.0124	0.0524
	1×10^{-5}	4		2.0140	0.0521
3200	2×10^{-5}	0.5	2.1917	1.9585	0.0471
	1×10^{-5}	1		1.9579	0.0472
	8×10^{-6}	2		1.9600	0.0467
	8×10^{-6}	4		1.9626	0.0461

304

Temperature-Pressure Cycling

Meaningful tests in terms of the utility of the data could not be conducted within the scope of this program for two reasons:

(1) In the temperature and pressure range where liquid tin is a stable phase in the coating, definition of baseline performance limits was not possible. To be of value, cyclic experiments must indicate deviations from baseline limits.

(2) Under cyclic conditions where liquid tin is unstable, performance is governed by the behavior of the residual tantalum aluminide layer. Any assessment of the effect of cycling would necessarily entail a comparison of cyclic performance with extensive baseline data for a tin-free aluminide coating at all pressure levels.

As will be discussed in Section V of this report, a kinetic model test was conducted with this system. After eight reentry cycles at temperatures and pressures where liquid tin remains as a stable phase, the specimen was not significantly different from comparable baseline test samples.

Acoustic Vibration

Specimens of Ta-10W/Sn-Al that were acoustically irradiated were examined metallographically and found to be unaffected. The structure of this coating system is such that it would be expected to be resistant to vibration damage. Furthermore, even if the aluminide layer, which is probably the more susceptible part of the coating, were to be damaged during exposure to vibration, it is likely that the coating would be capable of readily rehealing itself.

Defect Tolerance and Repair

Specimens were bent to an angle of 25 to 30 deg — just short of total fracture of the aluminide layer. One specimen was oxidation tested at 2700° F for 60 min in air at 1 mm Hg. As might be expected with this system, any cracks in the aluminide layer were healed, the substrate was well-protected, and the performance of the coating was not degraded.

During impact testing, no coating spalling, coating fracture, or specimen fracture occurred at the highest kinetic energy, 2.3 ft-lb, on either a rubber or steel backup. Considering the nature of the coating (it is likely that the tin absorbed a large fraction of the energy) and the ductility of the substrate, this outstanding impact resistance is not surprising. One of the specimens impacted on a rubber backup with a projectile having a kinetic energy of 2.3 ft-lb was oxidation tested. The specimen was rated as passing after 1 hr at 2700° F in air at 1.0 mm Hg.

Defects in the form of slots 50 by 250 mils by coating thickness were introduced, and the specimens were oxidation tested for 1 hr at 2700° F in air at 1 mm Hg. If the defect

305

penetrated the entire coating including the aluminides, the coating was incapable of self-repair and failure occurred. If, however, the defect did not penetrate the aluminide layer completely, there was self-repair and performance was not hindered. (See Figure 141.) The liquid tin alloy would not wet the Ta-10W surface, which was initially only slightly oxidized, but would wet the aluminide surface. In fact, it wetted so well and repair was so good that the structure of defective regions was nearly identical to that of nondefective regions and was difficult to distinguish under high-power microscopy.

Gross defects in the Sn-Al coating can be simply and effectively repaired. The repair technique recommended by Sylcor entailed reapplication of the slurry mix and a subsequent diffusion anneal in a vacuum or inert atmosphere. This restores the coating to the original condition and is typical of repair techniques for slurry-type coatings. The portable furnace technique used by Solar should be directly applicable to "in-field" repairs of this system. It was concluded that this technique was adequate and that further development or evaluation for use in low-pressure environments was not needed. That is, as long as the tin-rich phase exists at low pressures, pressure has little, if any, effect on the performance capabilities of this system. Hence, this repair process where the original coating structure is restored should be entirely suitable. Since this process is simple and effective, exploration of alternate repair methods was considered unnecessary.

Materials Compatibility

The effect of the Sn-Al coating in contact with other coated refractory materials was described in the results sections for the other materials. On the basis of these results, it could be concluded that high-temperature contacts between Ta-10W/Sn-Al and other coating systems should be avoided. The effects on the Ta-10W/Sn-Al system are presented in Table LXXI. In couples with other coating systems, the Ta-10W was protected from oxidation. However, the Sn-Al coating became exceedingly complex in its structure. More important, there was severe surface recession of the Ta-10W substrate in contact areas. This was the only evidence of the local substrate recession effect found in radiation-heated samples. The compatibility of this system with other high-temperature coating materials was inconsistent in the degree of adversity of effects on the substrate. This was probably dependent on the intimacy of the contact between the materials of a couple as well as composition of the contact system.

A severe reaction was found between the Sn-Al coating and SiO_2 at low pressure where tin was lost by vaporization. As shown in Figure 142, the residual aluminide coating failed at contact points with SiO_2. Severe reaction was found at a temperature as low as 2300° F. Compatibility with SiO_2 was good, however, under test conditions where liquid tin remained as a stable phase in the coating.

The Sn-Al coating was found to be incompatible with $MoSi_2$ at 2500−2700° F at 1 mm Hg. This was expected, of course, since the alloy is incompatible with silicide-base coatings in this temperature-pressure range.

306
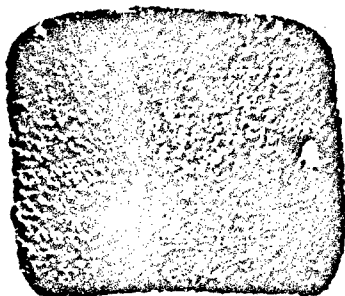
(A) Defect Extended Into Ta-Aluminide Zone,
No Failure
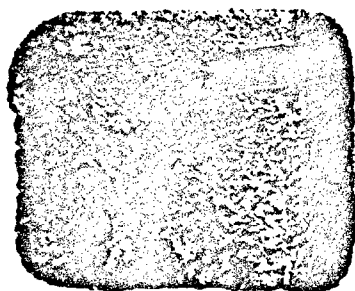
(B) Defect Extended to Substrate,
Total Failure

M9711   ×3

Figure 141 Comparative Performance of Defects in Ta-10W, Sn-Al,
2700° F, 1.0 mm Hg, 30 min

Table LXXI. Results of Compatibility Studies, Ta-10W/Sn-Al

Contact material	Test conditions			Performance rating
	Temp. (°F)	Pressure (mm Hg)	Time (min)	
TZM/PFR-6	2525	1.0	45	Failure[a]
TZM/Durak-B	2700	1.0	60	Failure[a]
Cb-752/PFR-32	2675	1.0	60	Failure[a]
Cb-752/CrTiSi	2525	1.0	60	Failure[a]
B-66/CrTiSi	2675	1.0	60	Failure[a]
$MoSi_2$	Incompatible at 2500−2700° F and probably at still higher temperatures			
SiO_2	Incompatible under all baseline conditions where tin is not stable in the coating (evaporated)			

(a) Using oxidation as a criterion, the specimen passed, but there was gross modification of the coating by Si and considerable surface recession occurred along the contact surface; in service, the properties of a coated structure might be seriously affected.

M9613   ×5

Contact Region
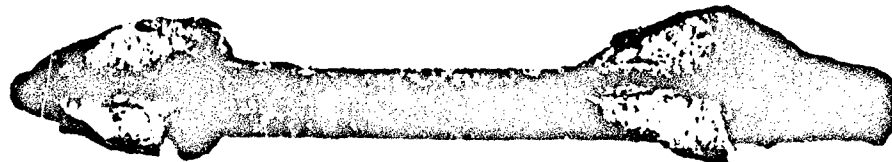
M9614   ×6

Figure 142 Local Failure of Ta-10W/Sn-Al Due to Contact With SiO$_2$, 2400° F, 0.1 mm Hg, 180 min

Section V

SUMMARY

EFFECT OF REDUCED PRESSURE (BASELINE BEHAVIOR)

The effect of air pressure on the performance capabilities of seven different refractory metal/coating systems is summarized in Figures 143 and 144. Data are not presented for the eighth system, Cb-752/Vought IV, because of inconsistencies in performance of specimens obtained for this investigation. The curves show the maximum temperature at which specimens will not fail within 4 hr as a function of air pressure. At temperatures above the defined limits for each system, random (Figure 143) or total (Figure 144) failure will occur in less than 4 hr.

Two different regions of behavior exist: (1) a range from 1 to 50 mm Hg, where performance capabilities are sensitive to pressure changes and (2) a range from 0.01 to 1 mm Hg, where pressure changes have comparatively little effect.

1-50 mm Hg Range

Coating performance in this range for silicide-base systems is controlled by random defects. PFR-6, Disil, and Durak-B coatings on TZM and the PFR-32 coating on Cb-752 behave in a similar manner. Fine hairline fissures in these coatings are sites for attack, and local surface failures tend to predominate. The wide edge fissures that penetrate through as much as three-fourths of the coating thickness are more effectively healed in this pressure range. Glassy protective oxides are formed, and surface recession of the coating is slight. Oxidation of the coating is more rapid than that at 1 atm, however, and some silicon is lost to the atmosphere, probably as SiO. The intermediate (Me_5Si_3-type) silicide is formed at the surface by selective oxidation of silicon. Thickness of the outer Me_5Si_3 layer becomes greater as pressure is reduced, indicating an increase in rate of oxidation of the coating with decreasing pressure.

The fact that performance of these four systems (PFR-6, Disil, Durak-B, and PFR-32) at 1-50 mm Hg is governed by fine hairline fissures in the coating is a significant discovery. Localized attack occurs by internal widening of these fissures. It appears that the partial pressure of oxygen in these defects is sufficiently low to cause greatly accelerated oxidation. Oxygen partial pressure on the surface or in wide edge cracks is probably the same as that of the atmosphere and is sufficiently high at gas pressures above 1 mm Hg to provide adequate protection in these areas. Critical defects are those in which free access of oxygen is restricted but in which low partial pressures (< 0.2 mm Hg P_{O_2}) can exist. Differences in performance capabilities of these systems at 1-50 mm Hg are probably related to the number, size, and location of hairline defects and to minor variations in glass composition that affect the softening point and viscosity and the general protective capabilities of the glassy oxide films that are formed.

311
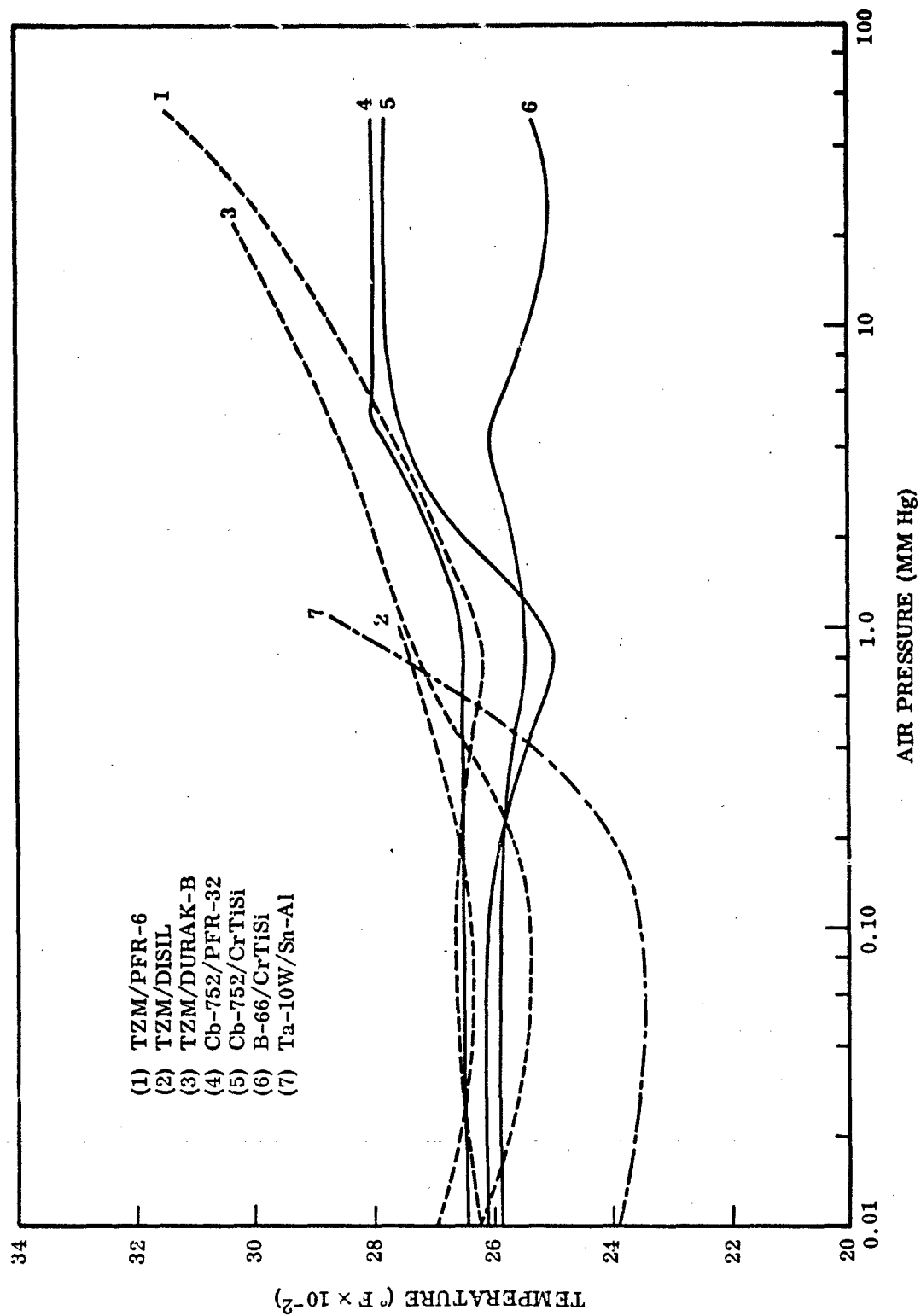
Figure 143 Comparison of 4-hr Random Failure Limits, Baseline Results

(1) TZM/PFR-6
(2) TZM/DISIL
(3) TZM/DURAK-B
(4) Cb-752/PFR-32
(5) Cb-752/CrTiSi
(6) B-66/CrTiSi
(7) Ta-10W/Sn-Al

AIR PRESSURE (MM Hg)

TEMPERATURE ($^{\circ}$F × 10^{-2})
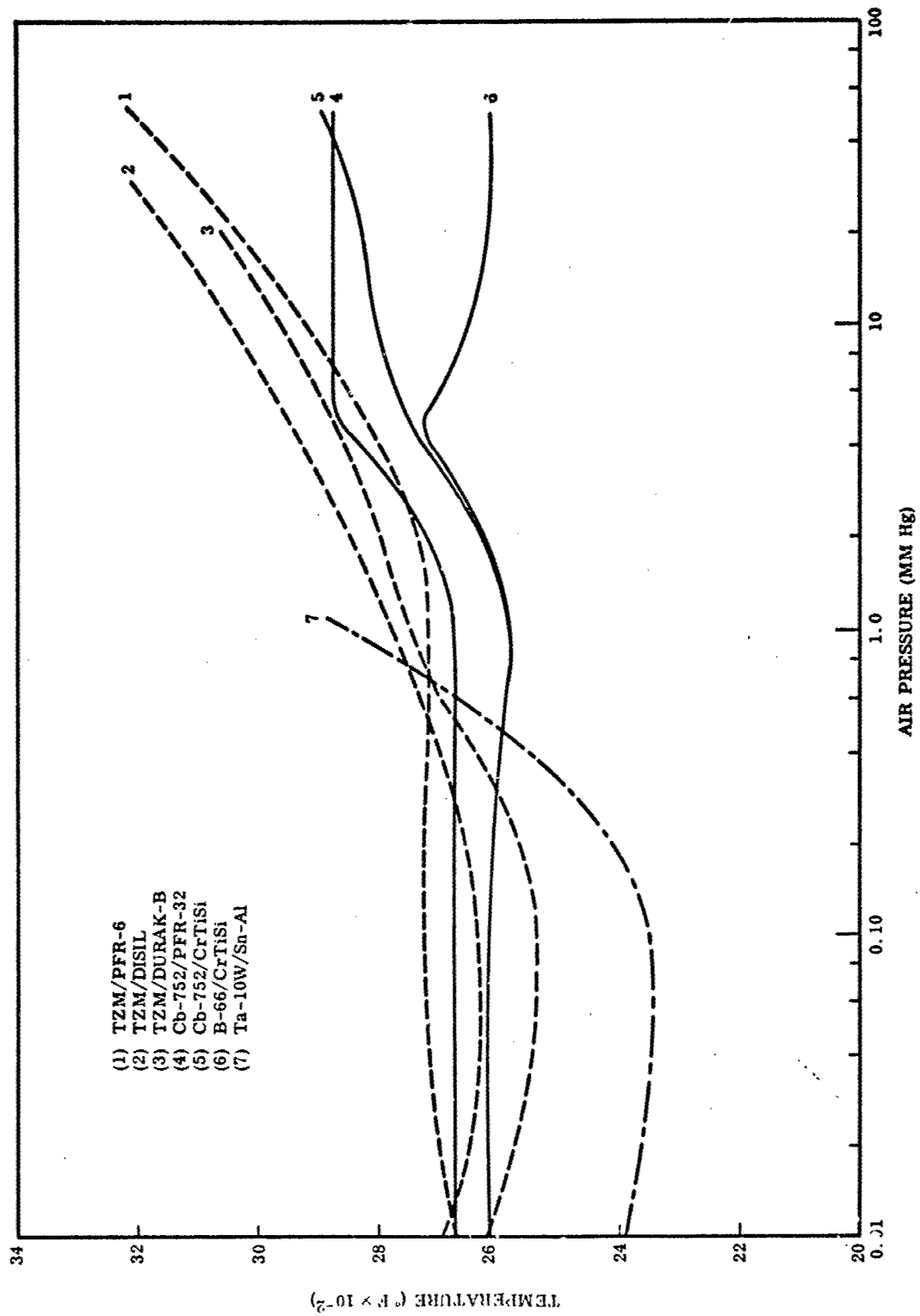
Figure 144 Comparison of 4-hr Total Failure Limits, Baseline Results

Legend:
(1) TZM/PFR-6
(2) TZM/DISIL
(3) TZM/DURAK-B
(4) Cb-752/PFR-32
(5) Cb-752/CrTiSi
(6) B-66/CrTiSi
(7) Ta-10W/Sn-Al

Y-axis: TEMPERATURE ($^\circ$F $\times 10^{-2}$)
X-axis: AIR PRESSURE (MM Hg)

313

The CrTiSi coatings on Cb alloys exhibit a behavior in this pressure range different from that of more conventional $MoSi_2$- or $CbSi_2$-base coatings. These coatings are more tolerant of cracks and fissures, and failures do not appear to be related to defects of a mechanical nature. In these systems, performance is governed by compositional variations in the coating that cause localized melting upon heating above 2600° F. Random failures (and, ultimately, total failure) occur by leakage of oxygen through the coating in regions that did not melt or through local defects created as a result of local melting. Loss of chromium at reduced pressure may be a factor contributing to increased gas leakage through the coating. Coating thickness, composition, and compositional uniformity appear to be critical factors governing performance and reliability.

Performance of the Sn-Al coating on Ta-10W is governed by the stability of the liquid tin alloy. At pressures above 1 mm Hg, temperatures over 3000° F are needed to cause rapid evaporation or boiling of tin. Hence, at 1—50 mm Hg, the useful life of this system was relatively insensitive to pressure variations at temperatures below 3000° F. The coating behaved much the same as it did at 1 atm. Performance capabilities were equal to or better than those of silicide-base coatings on Mo and Cb alloys. All defects were healed effectively by the liquid tin alloy surface layer.

As a rule, the limits of time and temperature for random and total failure were widely separated at 1—50 mm Hg pressure for all systems. This provides a safety factor in that catastrophic failure does not follow shortly after the first random failure. Also, even when total failure has occurred, most systems still retain a large measure of structural integrity for some time. Rates of substrate oxidation after coating failure are lower than would be the case in air at 1 atm. One notable exception was noted for the Cb-752 alloy. With some coating systems, rapid oxidation or ignition and combustion of the substrate occurred at pressures of 5—20 mm Hg after the first coating failure. In the Cb-752/CrTiSi system, samples were observed to ignite and burn with a self-sustaining combustion reaction after initial coating failure at temperatures above 2800° F in air at 5—20 mm Hg pressure. With the Vought IV and PFR-32 coatings on this alloy, rapid substrate oxidation (but not self-sustaining combustion) was noted in many cases after coating failure.

An unusual effect was noted with the Sn-Al coating on Ta-10W. Loss of substrate occurred by interdiffusion with the coating at rapid rates above 2800° F. In some cases, one-fourth to one-half of the substrate was consumed in local areas. In areas locally overheated (probably > 3000° F) the substrate was completely consumed. It appears that Ta may be oxidized selectively from the surface of the coating. The coating may transport tantalum from the substrate to the surface in a manner similar to that observed with some of the noble metal coatings on refractory metals. Although the coating protects from oxidation, loss and structural failure of the substrate can occur. Of course, with all silicide-base coatings, substrate loss also occurs by interdiffusion with the coating. However, rates of substrate loss at temperatures above 2800° F appear to be very high for the Sn-Al coating on Ta-10W.

314

0.01 – 1.0 mm Hg Range

PFR-6, Disil, and Durak-B on TZM; PFR-30 and CrTiSi on Cb-752; and CrTiSi on B-66 can be considered to have essentially the same performance capabilities in this pressure range. It is surprising, considering the wide variations in coating and substrate compositions, that the behavior of these systems is so similar. All systems have a useful life of 4 hr at temperatures of 2550 to 2650° F but will experience random or total failure in less than 1 hr at temperatures above 2650° F. Useful life is strongly temperature dependent above 2550° F, and limits of time-temperature for random or total failure are close together. In most cases, total failure occurs within a few minutes after the first random failure.

The basic reason for this type of behavior and for the similarity of behavior for these systems is that all silicide-base coatings exhibit high rates of surface recession at pressures below 1 mm Hg. Oxygen partial pressure on all surfaces is sufficiently low to cause rapid attack of the entire coating. The contribution of coating defects is masked, and life is governed primarily by effective coating thickness. Effective thickness often may be established by large V-shaped cracks that penetrate one-half to three-fourths of the coating in depth. Hence, edge failures tend to predominate at pressures below 1 mm Hg. Because of the variations in coating thickness on flat surfaces and rapid rates of recession, however, total surface failures may occur at the same time or within a few minutes of edge failure.

The maximum temperature for a given lifetime is relatively insensitive to pressure changes in the 0.01 to 1.0 mm Hg range. This region probably represents a minimum or plateau in performance capabilities for all systems. It is possible that increased rates of reaction (formation of SiO, suboxides of the substrate, etc.) are offset by reduced amounts of oxygen available for reaction as pressure is decreased. With further reduction in pressure below 0.01 mm Hg, an increase in useful life at any temperature would be expected due to lack of sufficient oxygen for reaction.

At pressures below 1 mm Hg, tin evaporates rapidly or boils at temperatures above 2200° F. The marked decrease in performance capabilities of the Ta-10W/Sn-Al system in this pressure range is due to loss of tin by evaporation. The inner tantalum aluminide layers which protect the substrate are exposed to the atmosphere and undergo accelerated oxidation at reduced pressure. In this respect, behavior is similar to that of silicide coatings. The utility of the Sn-Al system at reduced pressure, therefore, is governed largely by vapor pressure considerations for the liquid tin layer. At low pressures where tin evaporates readily, this system has much lower temperature capabilities than silicide-base coatings for Mo or Cb alloys.

The fact that performance of silicide-base coatings at pressures below 1 mm Hg is governed by surface recession behavior is an important discovery. The similarity of behavior of six widely different coating systems indicates that improved performance capabilities are not likely to be achieved by continuing efforts to modify existing systems. A radically new approach to coating technology will be needed to make significant improvements. Primary consideration must be given to stabilization of composition at reduced pressure. The use of overlay coatings designed to protect the

315

silicide-base coating at reduced pressure or development of an entirely new base for coating systems may be required. Another alternative would be to pressurize internal regions or to provide inert atmospheres for protection of structures.

It should be noted that internal surfaces in reentry vehicles are exposed to static environments at pressures below 1 mm Hg during periods of peak heating. Thus, structures designed only from considerations of external (higher pressure) oxidation behavior can fail from the inside out. The temperature limitations imposed by the low-pressure regime are likely to govern design in the final analysis. This means that silicide-base coatings for both Mo- and Cb-base alloys may be limited to 2550−2650° F maximum operating temperature where multiple mission use and reasonably long life (1 to 4 hr) are needed. Consequently, efforts to improve capabilities should be directed to performance in the 0.01 to 1.0 mm Hg range.

GAS VELOCITY EFFECTS

Results of tests with air flowing over the surface at a velocity of Mach 3 indicate a significant effect on performance only when liquid or semiliquid (viscous) conditions exist on the flow exposed surface. When all portions of the coating and oxidation products are solid, performance capabilities are similar to those determined in slowly moving air (baseline behavior).

With silicide-coated TZM, viscosity of glassy oxide films as a function of temperature and minor compositional variations appears to govern behavior. If the glass is sufficiently fluid to be thinned by flow, surface recession of the coating occurs at pressures above 1 mm Hg. However, recession rates are low, and life by and large is still governed by low-pressure attack within fine hairline fissures. Thus degradation, if any, by flow is not very marked. The effect was most pronounced for TZM/PFR-6 where flow conditions removed glass bubbles forming above fissures in the coating. This accelerated attack within the fissures and reduced life. For all systems with TZM, no effect of flow was noted at temperatures below 2900° F and pressures of 5 to 20 mm Hg.

Behavior for silicide-coated Cb-base alloys was similar to that of coated TZM in most respects. One notable exception, however, was indicated with the B-66/CrTiSi system. Local areas of this coating melted above 2600° F and were washed off by the flowing gas. Degraded performance would be expected above 2600° F in flowing air; however, the extent of degradation was not defined due to lack of test samples.

Since the liquid tin layer of the Sn-Al coating on Ta-10W protects the underlying tantalum aluminide coating from low-pressure attack, loss of this layer by high-velocity flow should degrade performance. Results of flow studies show that parallel flow at Mach 3 thinned the liquid tin layer but did not completely remove it. Thus, resistance to oxidation was not materially different from that determined by tests in slowly moving air. However, local surface recession of the substrate due to interdiffusion with the coating was accelerated in flow tests. Several samples failed by physical loss of substrate from reaction with the coating. Flow may have accelerated loss of substrate elements by transport through the coating. Further studies are needed to understand more completely the behavior of this system. The basic mechanism of protection,

however, indicates that under flow conditions where tin would be removed completely, rapid failure of the underlying aluminide coating would occur in air at reduced pressure.

GAS TEMPERATURE EFFECTS

Results of tests with TZM/PFR-6 at reduced pressure in plasma arc facilities indicate that the temperature of the air does not have a significant effect on performance. Identical results have been obtained at given temperatures and pressures using direct resistance (cool gas), radiation (warm gas), and plasma (hot gas) methods of heating.

VACUUM VOLATILITY EFFECTS

Exposure to vacuum ($\sim 10^{-5}$ mm Hg) at high temperature alters both the structure and the composition of coatings. In all systems, elements with high vapor pressures (Si, Cr, Sn, Al, and B) are lost by evaporation upon heating in vacuum. The effect on coating systems is manifested in three ways:

(1) Less-oxidation-resistant compounds are formed, first on the surface and eventually throughout the entire coating.

(2) Surface recession of the coating occurs.

(3) Cracks and fissures in the coating are widened and deepened. Porous areas may be formed.

The results may be partial or complete degradation of the coating, depending on the system and the length and temperature of exposure.

Silicide-base coatings on Mo and Cb can withstand 30 min to 1 hr heating in vacuum at 2600 to 2800° F without serious effect on subsequent ability to resist oxidation at low pressure (little if any change from baseline behavior). In fact, the widening or opening-up of hairline fissures that occurs upon heating in vacuum may be beneficial to performance in the 1−50 mm Hg pressure range. Opening of these defects may facilitate more effective healing above 1 mm Hg and actually improve performance capabilities. However, performance below 1 mm Hg may be seriously degraded by opening and deepening of fissures. This causes a reduction in effective coating thickness which will degrade life in the region where surface recession controls performance. At higher temperatures or longer times, more complete conversion of disilicides to less-oxidation-resistant Me_5Si_3 or Me_3Si compounds will greatly reduce life at all pressures and temperatures. Also, with CrTiSi coatings, excessive loss of Cr will occur, destroying much of the coating.

The Sn-Al coating on Ta-10W poses the greatest problem with respect to vacuum exposure. At 10^{-5} mm Hg, tin will boil at 1600° F; at 10^{-7} mm Hg, it will boil at 1325° F. All the tin is lost in a few seconds upon very low temperature heating. As previously discussed, the residual tantalum aluminide layer will not provide adequate resistance to oxidation in air at reduced pressures and high temperature. Hence, the

317

coating system is severely degraded by vacuum heating. Temperature, not time, is the critical factor with respect to this system.

TEMPERATURE-PRESSURE CYCLING

These experiments were designed to simulate the basic cycles of temperature, pressure, and time that are characteristic of lifting reentry heat-shield panels. Basically, this cycle is a short-time, high-temperature pulse at low pressure followed by a longer time, lower temperature soak at higher pressure. Cycles characteristic of both internal and external surfaces (in terms of pressure) were studied.

It was found that the performance of PFR-6, Disil, and Durak-B on TZM and PFR-32 and CrTiSi on Cb-752 was not degraded by cyclic exposure. Performance could be predicted from baseline curves on the basis of the total accumulated time at the high-temperature, low-pressure phase of the cycle. The lower temperature, higher pressure phase of the cycle had little effect and could be ignored for all practical purposes.

This would not have been true if the second phase of the cycle had been conducted in a temperature-pressure region where continuing rapid low-pressure attack or oxidation would occur. In most cases of reentry, however, temperatures after the peak pulse are below 2600°F, where low-pressure oxidation effects on silicide-base coatings are minimal. Hence, further degradation would not be likely to occur in the second phase, and only the initial high-temperature pulse would control behavior. Results indicate that useful life at a given temperature and pressure is the same for continuous or intermittent exposure. Effects of cyclic exposure appear to be simply additive.

In these tests, samples were cycled from high to low temperature without cooling to room temperature. Some degradation might be expected if cracking or spalling of oxide or coating occurred upon cooling to room temperature between cycles. Also, it should not be tacitly assumed that short exposure to high temperature at low pressure will not degrade oxidation behavior at high temperatures and high pressure. In fact, many systems which are protected at low pressure fail instantly upon exposure to higher pressure air. These relationships are very complex and cannot be reduced to simple mathematical expressions or graphs that will predict behavior for all possible combinations of cumulative exposure. The prediction of capabilities under dynamically changing conditions must be based largely on a knowledge of the general structural and compositional changes that occur in a coating as a function of temperature, pressure, and time. The mechanism of protection and failure at various temperatures and pressures also should be known. Hence, considerable attention has been given to these details in the evaluation of baseline behavior for each system. This provides a better foundation for using the results of the program.

The B-66/CrTiSi system was the only silicide system tested for which useful life under cyclic exposure was not the same as that under continuous exposure conditions. For this system, cyclic life was about 25% of the continuous exposure life at temperatures above 2600° F. This was found to be due to cracking and spalling of the coating in local regions as a result of alternate melting and solidification upon cycling above and below 2600° F. It is quite likely that the system would behave like the others in cycling at

318

temperatures below the 2600—2650° F range, where local melting of the coating would not occur.

The baseline oxidation behavior of PFR-6, Disil, ard Durak-B on TZM and of PFR-32 and CrTiSi on Cb-752 was not changed significantly after a 30-min exposure at 2600° F in high vacuum. In fact, Durak-B on TZM appeared to have somewhat better performance in air at 1 mm Hg pressure after the vacuum exposure. The upper portion of fissures responsible for random defect failures in the 1—50 mm Hg range was widened by the vacuum treatment, and less tendency for attack at fissures during oxidation was noted. A similar behavior for this system was observed in all the temperature-pressure cycling tests.

ACOUSTIC VIBRATION EFFECTS

None of the eight refractory metal coating systems was damaged by exposure to sine or random vibration at high intensity levels. There was an indication of lateral branching of cracks along the substrate/coating interface in the Cb-752/PFR-32 system in one sample, but the effect was not consistent.

Vibration damage of coated structures would be geometry dependent and is difficult to evaluate on small test samples. Because the degree of restraint was too great to permit flexure of the samples, few if any defects were generated. Evaluation of large structural elements would provide more meaningful data.

DEFECT TOLERANCE AND REPAIR

PFR-6 and Disil coatings on TZM could be bent 25 to 30 deg at room temperature before major cracking and spalling of the coating occurred. Bends in TZM/Durak-B were limited to 10 to 12 deg. The PFR-32 and CrTiSi coatings on Cb-752 sustained 15- to 20-deg bends before coating fracture. An increase in the number of fine hairline fissures occurred on the tension side of samples bent short of these coating fracture limits. Baseline oxidation behavior, however, was not degraded for any of these systems after bending. This behavior is of importance in assembly and handling of coated parts and indicates a good tolerance for defects that might be introduced during manufacture.

The only system in which a low tolerance was indicated was B-66/CrTiSi. In this system, coating fracture occurred at about a 20-deg bend. In bending short of major fracture, fine hairline fissures propagated deep into the substrate, and premature oxidation failure occurred in subsequent tests. This was also true of all the coatings on TZM and Cb-752 in which hairline cracks were introduced by impact. All systems had a low tolerance for impact where deflection of the sample was permitted. Cracks formed in the coating propagated deep into the substrate and caused early failure. All of the coated TZM and all but one of the coated Cb-base alloys shattered upon impact at low velocities and energy levels when deflection was allowed. Resistance to impact damage was high, however, when samples were rigidly supported. The Cb-752/Vought IV system had the highest resistance to impact damage of the coated Mo- and Cb-base alloys. Of course, the Sn-Al coating on Ta-10W had the highest resistance to defect

319

formation and the greatest tolerance for defects produced by bending and impact of all the eight systems studied.

Resistance to defect formation by bending (strain) or impact and tolerance for defects produced was dependent on both coating and substrate. Notch sensitivity of the substrate was a critical factor. High notch sensitivity resulted in deep propagation of the cracks formed in the coating into the substrate. Notch sensitivity of Cb-752 was found to be increased by coating thermal cycles due to an aging reaction. This resulted in brittle behavior of coated Cb-752 in bending and impact. Notch sensitivity of all coating systems decreased with increasing temperature, and resistance to defect formation for TZM and Cb-752 systems was high above 200° F.

In general, increasing the number of fine hairline fissures in the coating per se did not degrade baseline oxidation behavior. Only the number of available sites for random failure increased. Since the coatings contain a large number of such sites as-coated, the effect, if any, of additional sites was small. However, fine hairline fissures in the coating are in general an undesirable type of defect. In air at $1-50$ mm Hg pressure, they constitute sites for random failure of the coating. Also, with some systems they can cause catastrophic failure of the coating in air at very low temperature. In $MoSi_2$- and $CbSi_2$-base coatings, these fissures may branch and run laterally along the substrate/coating interface. At low temperature, oxygen penetrates the fissure and attacks the substrate/coating interface. Large sections of the PFR-32 coating on Cb-752 were separated from the substrate in as little as 4 hr at 900° F in air at 1 atm by this type of attack. PFR-6 coatings on TZM exhibited a similar tendency for interfacial attack.

It was found that low-temperature failures of this type occurred when little if any intermediate Me_5Si_3 was formed between the $MeSi_2$ coating and the substrate. Lateral branching of cracks and interfacial separation did not occur if $0.03-0.05$ mil of Me_5Si_3 existed as an interfacial zone. The tolerance for hairline fissures in a given system, therefore, is quite dependent on coating structure. The performance and reliability of all systems would be upgraded significantly if hairline cracks could be eliminated. In many respects, these are far more insidious defects than the wide edge cracks that normally are considered detrimental to quality and reliability.

The tolerance for large defects was evaluated by means of 6-mil-wide slots cut to various depths. None of the coating systems, including Sn-Al, were capable of healing wide defects that penetrated to the substrate. With Sn-Al, it was found that the liquid tin alloy did not wet the exposed substrate, probably because of formation of an oxide film during heating to test temperature. When a trace of the aluminide layer was left over the substrate, however, wetting and complete healing of the defect occurred.

Baseline performance of the three TZM systems at 0.01 to 50 mm Hg was not degraded by wide defects that penetrated three-fourths of the coating thickness. At pressures above 1 mm Hg, performance is governed by narrow fissures, and wide defects are healed effectively. At pressures below 1 mm Hg, surface recession controls. In this range, the naturally occurring wide defects that cause premature failure must penetrate beyond three-fourths of the thickness, since the artificial 3/4 t defects did not reduce life. For coated Cb alloys, 3/4 t defects could be tolerated above 1 mm Hg but caused

early failure below 1 mm. At lower pressures, defect tolerance was about 1/2 t. Defects of any depth except those that penetrated to the substrate were healed in the Ta-10W/Sn-Al system at pressures above 1 mm Hg. However, under temperature-pressure conditions where tin will boil, it is likely that defects penetrating into the residual aluminide coating would degrade performance.

The feasibility of local repair of absolute coating defects was demonstrated for the silicide-base coatings. For coated TZM, use of Cu-Ag-Si braze alloys restored 100% of performance at 1 mm Hg pressure. The Boeing $MoSi_2$-Synar repair was 100% effective at 1 mm Hg but gave inconsistent performance at higher pressures. The Cu-Ag-Si repair restored performance to the PFR-32 coating at 20 mm Hg but was not effective at lower pressures. Performance of CrTiSi coatings on Cb alloys was completely restored both by Cu-Ag-Si braze alloys and by the Solar patch repair process at all pressure levels.

The critical factor in all repair processes is conditioning of the substrate to promote wetting or bonding of the patch. For the braze alloys, incorporation of NaOH into the normal brazing flux was needed to promote wetting of exposed substrate metals. The Solar repair, of course, is made under an inert atmosphere and uses fluoride activators to provide wetting and bonding. Partial effectiveness of the $MoSi_2$/Synar repair probably was due to poor bonding as a result of incomplete protection of the substrate during initial heatup. Results of these studies indicate good feasibility for patch repair of local defects. The use of Cu-Ag-Si braze alloys for this purpose is a new approach that shows sufficient promise to warrant further study.

COMPATIBILITY PROBLEMS

All the coating systems present compatibility problems with refractory oxides or other coating systems when liquid or semiliquid material is present. Thus, the Sn-Al coating which has a liquid tin surface above 1200° F tends to react with virtually all materials over its entire temperature range of intended use. Liquid tin fluxes silicide coatings from Mo or Cb alloys at 2500−2600° F, degrading performance of these materials. It reacts with silica at temperatures as low as 2300° F, causing premature failure of the Sn-Al coating at points of contact. Use of this system in any type of multicomponent or insulated structure will cause serious compatibility problems.

B-66/CrTiSi presents problems in contact with other silicide-base coating systems at temperatures above 2600° F. Where regions of local melting on B-66/CrTiSi contact other materials, both systems are degraded.

All the silicide coatings on Mo and Cb alloys react with refractory oxides such as Al_2O_3, ZrO_2, BeO, and SiO_2 at temperatures above 2600° F. The reaction, however, is between the refractory oxide and the glassy oxide formed on the coating − not between the refractory oxide and the coating per se. Reaction is severe only at temperatures where the glassy oxides on coatings soften or melt and form low melting eutectics with the refractory oxide. The least problems are found with silicide-coated TZM in contact with silica. More serious problems are found with silicide (including CrTiSi)

coatings on Cb alloys in contact with any refr⁓   Cb₂O₅ and CbO₂ formed
during oxidation react with Al₂O₃, SiO₂, and   ⌐° F or higher and cause
contact failure of the coating. The most stable ⌐ ...act material for all systems at
temperatures to 3000° F was found to be MoSi₂.

KINETIC MODEL TESTS

One of the program objectives was to obtain sufficient data to permit reasonably confident
forecasts of performance and reliability under varying conditions of exposure. The
preceding general summary presented a review of basic performance capabilities and
factors likely to govern performance in the use of refractory metal coating systems.
Using this analysis, and, of course, detailed data on each system as presented in earlier
sections of this report, the performance of a heat-shield panel for a lifting reentry
vehicle on a model reentry mission was analyzed. A high L/D (3.0) suborbital flight
trajectory was used. (See Table XIV in the Test Procedures section.)

The basic elements of the reentry environment are (1) a 7-min heat pulse with tempera-
tures from 2300 to 2750° F at a mean external pressure of 1.4 mm Hg, followed by (2) a
17-min cooldown at temperatures of 2550 to 2050° F at pressures of 1.8 to 3.0 mm Hg.
Baseline and temperature-pressure cycling data indicate that the low temperature cool-
down phase of reentry would have little if any effect on the eight coating systems. Hence,
this phase was neglected and the analysis based on cyclic exposure to the 7-min heat
pulse. As shown in Table LXXII, the baseline time to random failure was taken from
baseline curves for various average temperatures in the heat pulse cycle. These values
were taken as, first, the peak temperature and, subsequently, lower average tempera-
tures computed from Table XIV. Next, the length of time at peak and each lower
average temperature per cycle was combined with the baseline time to failure to deter-
mine the probable number of cycles that could be run before random failure would occur.
A straight addition of cyclic exposure times was used. Since cyclic tests for B-66/CrTiSi
indicated only 25% of baseline life on cycling above and below 2600° F, the baseline time
to failure for this system was corrected to 25% of the static value in computing cycles
to failure.

From Table LXXII, the least number of cycles to failure indicated for the various
combinations of time and temperature in the heat pulse was used as the basis for pre-
dicting performance in kinetic model tests.

It should be noted that the overall average temperature for the 7-min pulse does not
necessarily govern behavior. For example, with B-66/CrTiSi, a 5-min exposure to an
average temperature of 2655° F was a more severe condition (5 cycles to failure) than
a 7-min exposure to 2582° F (7 cycles to failure). Thus, the environment must be
analyzed to find the life-limiting combination of time and average temperature in this
manner for each system if reasonable predictions are to be made.

Samples of each system were tested for a total of 8 reentry cycles or until an obvious
failure occurred (less than 8 cycles). The results are shown in Table LXXIII. The
most significant results are for the CrTiSi coating on Cb-752 and B-66. For Cb-752,

Table LXXII. Prediction of Behavior in Kinetic Model Test

Av. temp. (°F)	Av. pressure (mm Hg)	Time (min)	Coating system						
			TZM/ PFR-6	TZM/ Disil	TZM/ Durak-B	Cb-752/ PFR-32	Cb-752/ CrTiSi	B-66/ CrTiSi	Ta-10W/ Sn-Al
			Time to random failure (min)[a]						
2750	1.4		40	240	240	<30	<30	<30	>240
2683	1.4		80	>240	>240	95	<30	75	>240
2655	1.4		120	>240	>240	240	<30	110	>240
2630	1.4		190	>240	>240	>240	<30	140	>240
2582	1.4		>240	>240	>240	>240	<30	200	>240
			Cycles to random failure[b]						
2750	1.4	1	40	240	240	<30	<30	<8	>240
2683	1.4	3	27	>80	>80	32	<10	6	>80
2655	1.4	5	24	>58	>58	48	<6	5	>58
2630	1.4	6	32	>40	>40	>40	<5	6	>40
2582	1.4	7	>34	>34	>34	>34	<4	7	>34

(a) Baseline failure limits at 1 mm Hg pressure.
(b) Corrected for any degradation due to temperature-pressure cycling; B-66/CrTiSi figured at 25% of baseline.

the analysis predicted random failure in less than 4 cycles. One sample did not fail after 3 cycles; a second sample developed a random edge failure in 5 cycles. Similarly, for B-66, failure was predicted after 5 cycles and random edge and surface failures were found after 8 cycles of testing. These failures may have occurred in an earlier cycle but were not detected until the sample was evaluated by bend test and metallographic study.

The results for these two systems indicate that confident forecasts of performance and reliability can be made on the basis of the analyses and data obtained in this environmental test program. All other systems passed after 25% of the predicted number of omissions, which can also be considered a reasonable forecast of performance. None of the systems failed way short of predicted behavior.

Table LXXIII. Results of Kinetic Model Tests

Coating system	Predicted number of missions	Number of missions run	Performance
TZM/PFR-6	24	6	Pass
TZM/Disil	>34	8	Pass
TZM/Durak-B	>34	8	Pass
Cb-752/PFR-32	<30	8	Pass
Cb-752/CrTiSi	<4	3	Pass
		5	Fail, random edge
B-66/CrTiSi	5	8	Fail, random edge and surface
Ta-10W/Sn-Al	>34	8	Pass

Section VI

CONCLUSIONS AND RECOMMENDATIONS

CONCLUSIONS

(1) Coa⁺ ᵭ refractory metals have good utility for a broad range of aerospace applications. Commercially available silicide-base coatings for Mo- and Cb-base alloys can be exposed to slowly moving or high-velocity air at pressures of 0.01 to 50 mm Hg for 4 hr at 2550−2650° F without random failure. This capability is based on the performance of good-quality samples that were representative of optimum manufacturing practices for each system.

(2) The oxidation resistance of all silicide-base coatings (including CrTiSi) is degraded in air at reduced pressure. Minimum performance capabilities exist for all systems at pressures of 0.01 to 1.0 mm Hg. The maximum temperature for a given life to failure in this range is essentially the same for all systems, irrespective of wide variations in coating and substrate composition and in manufacturing processes. Thus, in many cases, selection of materials systems can be based on factors other than oxidation behavior in aerospace environments.

(3) In lifting reentry applications, temperature limits will probably be determined by the performance capabilities of the interior surfaces of heat shields and leading edges. Structures designed on the basis of external environmental considerations are likely to fail from the inside out.

(4) Performance capabilities at pressures above 1 mm Hg can be upgraded by removal or mitigation of fine hairline cracks and fissures in the coating. Gross defects that expose the substrate can be healed effectively by a variety of in-field repair techniques. Below 1 mm Hg, high rates of surface recession mask the contribution of defects. It is doubtful if performance can be upgraded by continuing efforts to modify existing coating compositions. An entirely new approach to coating technology is needed to improve performance in this critical low-pressure range.

(5) All coating systems retain structural integrity for a considerable length of time beyond random or even total failure of the coating in air at reduced pressure. With Cb-base alloys, however, rapid oxidation or self-sustaining combustion of the substrate can occur in critical temperature-pressure regions after the first random failure.

(6) The data obtained in this investigation can be used to make reasonable forecasts of performance capabilities and reliability under varying conditions of exposure. However, because of the complex nature of coating system behavior, results cannot be reduced to

325

simple mathematical expressions or charts that will describe completely the performance under all possible combinations of environments or events. Knowledge of the structural and compositional changes that occur in use and of the factors that govern protection or failure provides a means, however, by which available data can be used to make reasonable predictions under dynamic conditions. The overall utility of data obtained in this investigation is enhanced by the understanding of behavior that was developed in detail for each coating system. Furthermore, this understanding provides a useful basis for guiding future efforts to develop improved coating systems.

RECOMMENDATIONS FOR FUTURE WORK

(1) Coating systems with improved performance capabilities in the pressure range of 0.01 to 1.0 mm Hg should be developed. Consideration should be given to completely new coating formulations that are more stable in terms of structure and composition in this range at temperatures above 2400° F. As an alternate approach, development of coatings that will protect existing silicide-base formulations from accelerated attack at pressures below 1 mm Hg might be considered. The Sn-Al coating on Ta-10W can be viewed as such a system wherein a liquid tin alloy is in effect a "coating" that protects an underlying aluminide coating from accelerated attack in air at reduced pressure. The only current alternative to permit utilization of the high-temperature capabilities of silicide-base systems in reentry vehicles would be to pressure internal regions above 1 mm Hg at time of peak heating.

(2) The Sn-Al coating for Ta alloys is very promising for aerospace applications and is worthy of more detailed study and development. Four factors limiting performance are (1) the vapor pressure of tin, (2) low-pressure oxidation of tantalum aluminides, (3) substrate embrittlement by interdiffusion, and (4) substrate recession by interdiffusion. Consideration should be given to alloying or replacement of tin to improve low-pressure stability. Substrate/coating interdiffusion processes should be investigated in detail. Also, baseline data at pressures of 0.01 to 50 mm Hg should be obtained for tin-free coatings to define more completely the performance capabilities after loss of tin by vaporization at low pressure. Consideration might be given to modification of the aluminide layer to improve resistance to oxidation at low pressure.

(3) Ignition and self-sustaining combustion of coated columbium alloys at time of coating failure present a serious problem in using these materials. Detailed studies should be made to clearly define the limits of temperature and pressure within which combustion can occur for various substrate/coating combinations. Factors controlling this process should be studied in detail.

(4) The contribution of fine hairline fissures and intermediate silicide interfacial zones to performance capabilities and reliability has largely been overlooked in coating development programs. Methods for eliminating, reducing, or sealing of hairline defects in coatings for Mo and Cb alloys should be investigated. Immediate and significant improvements in performance and reliability at pressures above 1 mm Hg could be realized by

effective elimination of such defects. Basic studies of deposition processes are needed to determine factors contributing to formation and growth of such defects. Also, the role of interfacial ⸱ ⸱ ⸱ ⸱ ⸱ (Mo, h) type) should be studied in more detail, and ⸱ ⸱ ⸱ ⸱ ⸱ ⸱ ⸱ ⸱ ⸱ ⸱ to provide optimum coating structures.

(5) Local variations in composition of the CrTiSi coating are undesirable. Considering the overall utility and advantages of this system, concerted efforts should be made to produce more uniform coatings. First, structure and composition (which can vary between wide limits) should be correlated with oxidation behavior at reduced pressure. For example, some regions of this coating on Cb-752 appeared very resistant to oxidation at pressures down to 0.01 mm Hg. Other regions were rapidly attacked. Subsequently, process controls should be developed to make uniform coatings of optimum composition. It is believed that this basic system has far greater potential than that realized to date.

(6) The use of simple gas torch brazing techniques to repair small coating defects by fusion of alloy pastes shows sufficient promise to warrant further development. The Cu-Ag-Si or MeSi$_2$ alloy paste compositions developed under this program are but one example of a broad class of materials that can be used. This approach provides a simple low-cost method for in-field repair that was effective on a wide range of silicide-base systems. Consideration should be given to the formulation of low-melting alloys that upon fusion with the coating will change sufficiently in composition to have a high remelt temperature. Also, in parallel approach, the use of thin low-melting metallic overlays to heal fine fissures or small cracks in silicide-base coatings should be considered. It is possible that many natural defects could be healed and coating performance upgraded by surface fusion and penetration of defects with liquid alloys.

Section VII

REFERENCES

1. R. A. Perkins, L. A. Reidinger, and S. Sokolsky, "Problems in the Oxidation Protection of Refractory Metals in Aerospace Applications," Trans. 7th Symposium on Ballistic Missile and Space Technology, Aerospace Corp.—USAF, Vol. 1, 1962. pp. 429—450 (also, Space/Aeronautics, Vol. 6, 1963, pp. 107—114)

2. L. A. McKellar, "Ascent Aerodynamics Environment," Space Materials Handbook, Contract AF 04(647)-673, Lockheed Missiles & Space Co., 1962

3. R. E. Gaumer et al., "Thermal Control Materials," Space Materials Handbook, Contract AF 04(647)-673, Lockheed Missiles & Space Co., 1962

4. E. G. Czarnecki and M. T. Braun, "Development and Evaluation of Coatings for Earth Re-Entry Systems," Proc. AGARD Conference on Refractory Metals, Oslo University, Jun 1963 (Pergamon Press, London)

5. J. Cobb, "The Ascent Vibration Environment," Space Materials Handbook, Contract AF 04(647)-673, Lockheed Missiles & Space Co., 1962

6. R. E. Gaumer and A. I. Funai, Determination of the Thermal Emittance Stability of Spacecraft Radiator Coatings, ASD-TDR 63-429, Lockheed Missiles & Space Co., May 1963

7. Materials Problems Associated With the Thermal Control of Space Vehicles, Materials Advisory Board, MAB-155-M, National Research Council, Oct 1959

8. M. Kornhauser, "Predictions of Cratering by Meteoroid Impacts," Advances in Astronautical Sciences, Vol. 2, 4th Annual Meeting AAS, Plenum Press, 1958

9. R. W. Chittenden, Extraterrestrial Factors Influencing Performance of a Passive Spherical Satellite, RADC-TN-60-224, Melpar, Inc., Aug 1960

10. J. E. Gilligan and H. T. Sumsion, "Physical Impact Phenomena," Space Materials Handbook, Contract AF 04(647)-673, Lockheed Missiles & Space Co., 1962

11. H. T. Sumsion, "Structural Materials — Metallic," Space Materials Handbook, Contract AF 04(647)-673, Lockheed Missiles & Space Co., 1962

12. M. R. Licciardello et al., Development of Frontal Section for Super Orbital, Lifting Re-Entry Vehicle, Solar Div. of International Harvester Co., Contract AF 33(616)-8494, May 1964

13. F. S. Johnson, "Structure of the Upper Atmosphere," Space Materials Handbook, Contract AF 04(647)-673, Lockheed Missiles & Space Co., 1962

14. H. W. Woolley, Effect of Dissociation on Thermodynamic Properties of Pure Diatomic Gases, NACA-TN-3270, National Advisory Committee for Aeronautics, Apr 1955

15. R. A. Perkins, "High Temperature Materials for Chemical Rockets," AIME, High Temperature Materials II, Vol. 18, Metallurgical Conferences, Wiley, 1963

16. L. Lees, "Laminar Heat Transfer Over Blunt Bodies at Hypersonic Flight Speeds," Jet Propulsion, Vol. 26, Apr 1956

17. R. W. Detra, N. H. Kemp, and F. R. Riddel, "Addendum to Heat Transfer to Satellite Vehicles Re-entering the Atmosphere," Jet Propulsion, pp. 1256, 1257, Dec 1957

18. W. L. Hankey, Jr., R. D Neumann, and E. H. Flinn, Design Procedures for Computing Aerodynamic Heating at Hypersonic Speeds, WADC-TR-59-610, Wright Air Development Div., Jun 1960

19. S. M. Bogdonoff and I. E. Vas, The Effect of Sweep Back Angle on the Pressure Distribution of a Blunt Flat Plate at Hypersonic Speeds, ARDC-TR-57-121, Bell Aircraft Corp., Jun 1957

20. E. R. G. Eckert, Survey of Boundary Layer Heat Transfer at High Velocities and High Temperatures, WADC-TR-59-624, Univ. of Minnesota, Apr 1960

21. M. O. Creager, "High Altitude Hypervelocity Flow Over Swept Blunt Glider Wings," Paper No. 59-113, presented at IAS National Summer Meeting, Los Angeles, 16-19 Jun 1959

22. E. R. Van Driest, Investigation of Laminar Boundary Layer in Compressible Fluids Using the Crocco Method, NAC TN 2597, North American Aviation, Inc., Jan 1952

23. N. G. Kulgein, "Heat Transfer From a Nonequilibrium Turbulent Boundary Layer to Catalytic Surfaces," AIAA J., Vol. 3, Feb 1965

24. P. J. Chao, G. J. Dormer, and B. S. Bayne, Advanced Development of PFR-6, ML TDR 64-84, Pfaudler Co., May 1964

25. L. G. Wyckoff, Refractory Coating Repair Processes, BOAC-D2-81116, The Boeing Co., Dec 1963

26. V. S. Moore and A. R. Stetson, Evaluation of Coated Refractory Metal Foils, RTD-TDR-63-4006-PT. 2, Solar Div. of International Harvester Co., Dec 1964

27. R. W. Bartlett and P. R. Gage, Investigation of Mechanisms for Oxidation Protection and Failure of Intermetallic Coatings for Refractory Metals, ASD-TDR-63-753-PT. 2, Aeronutronic Applied Research Lab., Jul 1964

28. W. K. Stratton et al., Advances in the Materials Technology Resulting From the X-20 Program, AFSC-ML-TR-64-396, The Boeing Co., Mar 1965

29. K. H. Kim and F. A. Hummel, "Studies in Lithium Oxide Systems, XII: $Li_2O - B_2O_3 - Al_2O_3$," J. Am. Ceram. Soc., Vol. 45, 1962, pp. 487-489

30. J. G. Bewley and M. Schussler, Final Report on Process Improvement of Columbium (Cb-752) Alloy, AFSC-ML-TR-65-63, Union Carbide Corp., Mar 1965

31. Investigation of Modified Silicide Coatings for Refractory Metal Alloys With Improved Low-Pressure Oxidation Behavior, Contract AF 33(615)-1732, Final Report, Lockheed Missiles & Space Co. (to be published)

32. R. A. Perkins, "Status of Coated Refractory Metals," J. Spacecraft and Rockets, Vol. 2, Jul—Aug 1965, p. 520

33. D. B. Warmuth, J. D. Gadd, and R. A. Jeffreys, Advancement of High Temperature Protective Coatings for Columbium Alloys (II), ASD-TDR-62-934-PT. 2, Thompson Ramo Wooldridge, Inc., Apr 1964

34. J. D. Gadd and H. J. Tolchinsky, Advancement of Protective Coating Systems for Columbium and Tantalum Alloys, First Quarterly Progress Report, Contract AF 33(615)-1525, TRW TM-3975, Thompson Ramo Wooldridge, Inc., Jul 1964

35. J. D. Gadd and R. A. Jeffreys, Advancement of High Temperature Protective Coatings for Columbium Alloys, ASD-TDR-62-934, Thompson Ramo Wooldridge, Inc., Nov 1962

36. V. S. Moore and A. R. Stetson, Evaluation of Coated Refractory Metal Foils, RTD-TDR-63-40006-PT. 1, Solar Div. of International Harvester Co., Sep 1963

37. W. L. Aves et al., Diffusion Coating Process for Columbium Base Alloys, AFSC-ML-TDR-64-71, Chance Vought Corp., Jun 1964

Appendix I

METALLOGRAPHIC TECHNIQUES

The details of the specimen pre ... ... performed in this program are presented here to provide a basis for similar endeavors by other investigators

When possible, samples were mounted without sectioning to prevent damage to the coatings. When sectioning was required, it was accomplished with a small diamond cutoff wheel at slow speeds using plenty of lubricating coolant.

MOUNTING

The mounting of coated specimen cross sections is performed as follows;

(1) Linen-phenolic rod material 3/4 in. in diameter is cut into discs approximately 1/8 to 1/4 in. thick.

(2) Slots are cut into each disc. The slots are only slightly wider than the thickness of the samples.

(3) A layer about 1/4 in. thick of finely ground red bakelite is placed on the bottom of the mold after assembling the bottom and side of the mold.

(4) The slot in a linen-phenolic disc is filled with the ground bakelite (by simply placing the disc in a beaker of ... ... relite) and is then lowered into the mold assembly ... ... s onto the layer of bakelite already in ... ...

(5) A sample is then put ... ... to the slot in the ... ... (again using tweezers), taking care not to push the sample into and ... ough the underlying bakelite. About 1/2 in. mo ... the bakelite is added.

(6) Ordinary bakelite is then added to fill the ... old ... ... out 1/4 in. from the top.

(7) The top part of the mold is plac ... ... assembly is heated, pressed, and cured in nor ... ... r 13 min, starting with a cold heater. After curing, the ... ... owed to cool under pressure in an air blast for 10 min.

These procedures will provide a mount wherein shrinkage of bakelite will be minimized and the close proximity of the linen-phenolic will provide abrasion resistance for good edge retent ...

GRINDING

Initial grinding is performed on 240-grit SiC wet or dry paper until contact is made with the linen-phenolic. If the mount is made properly, the specimen is not visible.

Final grinding is done on 600-grit SiC wet or dry paper until intact coatings are obtained. The coatings may be slightly chipped, but this may be ignored because a chip-free coating is virtually impossible to obtain by grinding.

POLISHING

Coated tantalum and columbium alloy specimens are put directly into a final automatic polishing operation using a slurry of "Cer-Cre" Metallographic Polishing Abrasive and several milliliters of a solution consisting of 10 gm of NaOH, 35 gm of $K_3Fe(CN)_6$, and 100 ml of distilled H_2O on Microcloth or Gamol. This procedure is not advised if vibratory-type polishers are used. Grit is embedded in the tantalum and columbium from the 600-grit grind, and removal of this grit during vibratory polishing will cause contamination of the abrasive slurry and will produce scratches. The use of rotary-type polishers is recommended.

Polishing should be continued until all grit is removed and a flat, clear substrate sur-face is obtained. Dishing will not occur on tantalum specimens but may occur on columbium. If so, the slurry should be diluted with distilled water.

Molybdenum samples are polished initially on slipper satin cloth impregnated with 1μ diamond paste, using no more than about 350 gm. This step is also performed auto-matically. Polishing is continued until all effects of the 600-grit grind are eliminated.

Final polishing of molybdenum specimens is performed on Microcloth or Gamol using a slurry of Cer-Cre abrasive to which no more than 6 to 10 drops of a 10% solution of chromic acid (chromium trioxide) is added.

ETCHING

Etching of the tantalum and columbium specimens is done in a solution consisting of 7.5 ml HF, 2.5 ml HNO_3, and 100 ml H_2O.

A 5-min etch will produce sufficient detail, assuming that a perfect polish is obtained. If lower silicides are to be etched, 2 hr are required, but then any disilicide will be severely attacked. Little or no etching of the substrate will occur. When coatings have been modified and contain titanium, etching should be limited to about 20 sec.

Etching of the molybdenum specimens is performed as follows:

(1) Prepare a stock solution consisting of 1 gm NaOH, 35 gm $K_3Fe(CN)_6$, and 100 ml H_2O.

(2) Prepare etchant by adding 1 to 2 ml of stock solution to 100 ml H_2O.

(3) Etch for 30 sec or as desired.

All polishing conducted in this program was performed on automatic polishing equip-ment novel to the LMSC laboratory. The equipment is not available commercially.

334

Thus, the polish-etch techniques described here may be difficult to perform by hand polishing or on automatic polishing equipment wherein the abrasive and added solutions are thrown from the wheels. If vibratory polishers are employed, preparation may take 10 times longer or may not even be possible because of differences in the rates of etching and subsequent metal removal.

Results cannot be predicted if other preparation materials are substituted for those recommended.

Appendix II

PREPARATION OF CONTROLLED DEFECT SPECIMENS
FOR ASSET VEHICLE TEST

As described in the Procedures section of this report, LMSC developed a method for producing precision defects in coatings by electrical spark discharge machining. At the request of the Air Force, this process was used to prepare 59 standard defect samples for testing and evaluation in the Asset Program.

The samples were 3/4 by 1-1/2 by 0.060 in. thick Cb-752 alloy sheet coated with CrTiSi. The average coating thickness was about 2.2 mils per side. Two 3/4-in.-long parallel defects were placed in each specimen. Defects were spaced 1/4 in. apart. The following samples were prepared:

C9−12	Defects transverse to specimen axis; one defect 6 mils wide b.· 1 mil deep, and one defect 6 mils wide by 3 mils deep. Samples for testing at University of Dayton.
C13A,B,C and 14A,B,C	Defects parallel to specimen axis; both defects 6 mils wide by 1 mil deep. Samples for flight test.
C17A,B,C and 18A,B,C	Defects parallel to specimen axis; both defects 6 mils wide by 4 mils deep. Samples for flight test.
C19A,B,C and 20A,B,C	Defects transverse to specimen axis; both defects 6 mils wide by 4 mils deep. Samples for flight test.
C53−70	Defects transverse to specimen axis; both defects 6 mils wide by 4 mils deep. Samples for testing at University of Dayton.
C71−89	Defects parallel to specimen axis; both defects 6 mils wide by 4 mils deep. Samples for testing at University of Dayton.

The appearance of typical defects is shown in Figure 24 of the Procedures section. The measured values of width and depth at three locations in each defect are presented in Table LXXIV. The defects produced were very uniform in width and depth and close to target values. Low values of width or depth obtained near an edge or in the center were due to the presence of a slight bow in most of the samples. With flat specimens, defects were uniform along the entire 3/4-in. length.

337

Table LXXIV. Measured Width and Depth of Defects Cut in Asset Test Samples

Sample no.	Defect direction[a]	Width (μ)			Depth (μ)		
		End	Center	End	End	Center	End
C9	T	151	0	153	25	0	22
		137	180	175	60	30	55
C10	T	0	170	153	0	13	12
		137	179	153	22	40	33
C11	T	350	0	340	24	0	30
		320	288	300	25	62	40
C12	T	300	268	260	28	30	38
		300	276	264	56	50	62
C13A	L	143	142	135	24	20	16
		140	137	142	24	28	16
B	L	145	147	148	30	28	21
		146	145	151	32	20	31
C	L	141	136	136	28	23	20
		145	140	141	2'.	23	22
C14A	L	142	137	125	20	20	13
		146	143	125	31	31	17
B	L	138	125	128	24	14	15
		142	125	140	22	18	15
C	L	125	142	143	17	25	22
		0	140	145	0	17	34
C17A	L	152	157	152	'01	95	90
		161	158	155	93	100	97
B	L	150	157	155	98	91	90
		155	158	153	90	100	96
C	L	156	161	160	87	96	104
		157	160	157	96	85	100
C18A	L	156	159	157	90	90	85
		157	159	156	80	91	90
B	L	157	160	157	94	98	94
		156	159	160	95	100	104
C	L	159	162	164	93	93	90
		158	161	160	90	94	92
C19A	T	157	165	158	90	150	80
		155	163	159	90	110	108
B	T	156	158	155	106	98	90
		157	160	155	100	94	96
C	T	159	163	162	110	85	100
		158	164	163	110	92	93
C20A	T	158	164	159	120	92	100
		156	161	159	110	90	96
B	T	165	160	158	125	90	80
		159	160	160	111	93	89
C	T	158	164	160	94	95	110
		160	165	160	96	99	105
C53−70	L	152 AIM			25 AIM		
C71−89	L	152 AIM			100 AIM		

(a) L = longitudinal and T = transverse relative to the long axis of the specimen.

338

Appendix III

TABULATED BASELINE DATA

Table LXXV. TZM/PFR-6 Baseline Data

Test no.	Furnace	Support material	Pressure (mmHg)	Flow rate (cfh)	Temp (°F)	Time (min)	Weight change (%)	Thickness change (%)	Support reaction	Rating	Edge failure	Surface failure	Remarks
001	Resistance	Copper	50	–	3090	430	–	–	–	Pass	–	–	Glassy, blistered
002				–	3137	240	–	–	–	Pass	–	–	Glassy, blistered
003				–	3450	–	–	–	–	–	–	–	Glassy, blistered, melting point estimate
004				–	3235	176	–	–	–	Fail	Random	Random	Glassy, blistered, failed at 160 min
005				–	3235	120	–	–	–	Fail	–	Random	Glassy, blistered
011		↓	↓	–	3284	60	–	–	–	Pass	–	–	
082	Radiation	MoSi₂		–	2950	120	-1.50	+5.19	Nil	–	–	–	
083				–	2950	240	-0.82	+37.34		–	–	–	
086				3.0	3000	240	-0.62	+7.33		–	–	–	
092				3.0	3000	120	-0.04	+13.08	↓	–	–	–	
096	Resistance	Copper		6.0+	3100	45	–	–	–	–	–	Random	Glassy, blistered, failed at 235 min
097					3150	240	-2.01	+1.92	–	Fail	–	Random	Glassy, blistered, failed at 187 min
098					3200	192	–	–	–	Fail	Total	Total	Glassy, blistered
101					3200	30	-3.12	+0.80	–	Pass	–	–	Glassy, blistered
102					3250	60	–	+12.90	–	Pass	–	–	Glassy, blistered
110					3100	215	–	–	–	Pass	–	–	Glassy, blistered
127					3300	41	–	–	–	Fail	Random	Random	Glassy, blistered, failed at 30 min
128					3250	15	–	–	–	Fail	Random	Random	Glassy, blistered, failed at 15 min
008		↓		–	3235	12	–	–	–	Fail	Random	Random	Glassy, blistered, failed at 12 min
070	Radiation	MoSi₂	20	2.5	2850	120	-1.21	+9.20	Nil	Pass	–	–	Glassy, blistered
071					2850	240	+0.80	+7.63			–	–	
074					2900	120	+0.23	+9.15			–	–	
075					2900	240	-0.09	+16.80			–	–	
079					2950	240	-0.03	+14.77			–	–	
080					2950	120	+0.09	+4.88		↓	–	–	
084					3000	120	+1.74	+13.82		Fail	Random	–	
085					3000	120	-0.10	+13.33		Pass	–	–	
091		↓			3000	240	-5.02	+6.72	↓	Fail	Random	–	
094	Resistance	Copper		6.0+	3130	7	–	-2.21	–	Fail	Total	Total	
095					3150	33	–	+1.85	–	Fail	Total	Total	
103					3100	30	–	+0.80	–	Pass	–	–	
104					3100	120	-2.34	+6.50	–	Fail	Total	Total	
041	Radiation	SiO₂	5	1.6	2740	240	+0.04	-0.30	Nil	Pass	–	–	Glassy, smooth
042		SiO₂			2740	121	-0.07	+2.00			–	–	Glassy, smooth
057		SiO₂			2800	120	-0.50	+3.70			–	–	Glassy, blistered
061		MoSi₂			2815	30	+0.10	+4.20			–	–	
062					2800	240	-2.80	+3.20		Fail	Random	–	
063					2850	120	+1.60	+1.50		Pass	–	–	
064					2850	240	-1.60	+28.40		Fail	Total	Total	
072				1.5	2900	120	-1.34	+16.54			Total	Total	
073					2900	240	-4.06	+23.07			Total	Total	
076					2900	30	-1.02	+5.51			Random	–	Glassy, matte
077					2900	60	-1.03	+7.11			Random	Random	Glassy, smooth
078					2950	60	-5.03	+1.89			Total	Total	Glassy, blistered
041					2950	120	–	–			Total	Total	
090					2950	30	-1.68	-1.78			Random	Random	
093					3000	30	-1.95	+22.87			Total	Total	
100		↓			2950	60	-0.67	+0.35		Pass	–	–	Matte
111	Resistance	Copper		6.0+	3050	20	–	–	↓	Fail	Total	Total	Disintegrated
030	Radiation	Al₂O₃	1	0.40	2600	241	-1.80	-14.50	Nil	Fail	Random	–	Glassy, matte
031		Al₂O₃		0.40	2600	122	-1.20	-4.00			–	–	
033		SiO₂		0.07	2650	121	+0.02	-1.50		↓	–	–	
034				0.07	2650	240	-0.40	-2.30			–	–	
040				0.07	2900	230	–	–		Pass	–	–	
043				0.40	2750	250	–	–		Fail	Total	Total	
044					2750	120	–	–		Fail	Random	Random	
049					2750	60	-1.10	-1.20		Fail	–	Random	
051					2750	30	-1.10	0		Pass	–	–	
052					2700	60	-1.90	-0.70		Pass	–	–	
055					2650	30	-6.70	-14.20		Pass	–	–	
056					2900	60	-6.60	-10.00		Fail	Total	Total	
058					2900	60	-7.40	-11.20			–	–	
069		MoSi₂		–	2650	30	-5.10	-9.00		↓	–	–	
059	Resistance	Copper		1.50	2600	30	–	+1.36	↓		–	–	
012	Radiation	Al₂O₃	0.10	–	2670	210	-10.7	–	Nil	Fail	Total	Random	Matte, powdery
013				–	2600	134	–	–		Pass	–	–	
017				–	2595	60	-3.10	-11.10			–	–	
019				–	2595	120	-4.13	-9.93			–	–	
022				–	2595	210	-8.00	-8.25		↓	–	–	
023				0.15	2700	120	-8.70	-19.00			–	–	
024				0.05	2700	210	-5.2	-18.00		Fail	Random	Random	
026				–	2650	240	-10.3	-17.00	↓	Pass	–	–	
025				0.02	2700	240	-11.0	-10.00	Mild	Fail	Random	Random	
036		SiO₂		0.02	2700	121	-10.4	-8.40	Nil	Pass	–	–	
037				0.13	2700	120	-7.8	-3.50		Fail	Random	–	
038				0.05	2750	130	-10.4	-16.8		Pass	–	–	
049					2750	240	-14.3	-14.8		Fail	Total	Total	
053					2800	120	3.2	+2.6		Fail	Total	Total	Matte, powdery, crumbled
054					2800	60	-11.3	-27.9		Fail	Total	–	Matte, powdery
060		MoSi₂			2800	62	-4.5	-17.2		Pass	–	–	
068		MoSi₂			2800	30	-4.5	-10.2		Pass	–	–	
088		MoSi₂		0.15	2850	30	-9.71	-17.29		Fail	Total	Random	
089				0.15	2850	60	-22.96	-29.55		Fail	Total	Total	No coating left
018	Radiation	Al₂O₃	0.01	–	2595	30	-2.80	-15.0	Nil	Pass	–	–	Matte, powdery
020				–	2595	120	-4.45	-7.12			–	–	
021				–	2595	210	-7.35	-11.90			–	–	
027				0.10	2600	63	-6.70	-9.00		↓	–	–	
028					2600	124	-9.60	-12.00		Fail	Random	–	
032		SiO₂			2700	210	-20.00	–			Total	Total	
045					2750	60	-9.70	-16.5			Random	–	
046					2750	120	-17.00	-15.0			Total	Total	
047					2750	60	-5.70	-4.1		Pass	–	–	
048				0.01	2750	120	-13.00	-15.00		Fail	Total	–	
050				0.10	2800	60	-2.30	-6.80		Pass	–	–	
065		MoSi₂		0.15	2650	30	-5.90	-10.50		Fail	Random	Random	
066				0.15	2650	60	-13.00	-7.80	↓	Fail	Total	Total	
067				0.05	2600	30	-7.94	-0.84		Pass	–	–	
067		↓	↓	0.01	2650	210	-7.20	-12.30		Fail	Random	–	

Table LXXVI. TZM/Disil Baseline Data

Test no.	Process	Support material	Pressure (mmHg)	Flow rate (cfh)	Temp. (°F)	Time (min)	Weight change (%)	Thickness change (%)	Support reaction	Rating	Edge failure	Surface failure	Remarks
061	Radiation	MoSi₂	90	3.0	2500	120	-0.06	+0.33	Nil	Fail	Random	–	Smooth, matte, with dark stripes
062					2500	240	-0.13	+0.41	Nil	Fail		–	Smooth, matte, with dark stripes
007					2900	120	-0.79	-0.86	Mild			–	Smooth, glassy, with dark stripes
068					2900	240	-2.33	+3.65	Nil			–	Smooth, glassy, with dark stripes
069					2950	120	–	–				Random	Smooth, glassy, failure in stripe
070					2950	240	–	–				–	Smooth, glassy, with dark stripes
075					2950	120	-0.18	+2.37				–	
076					2950	240	-7.62	+2.12		↓	↓	–	
063	Resistance	Copper		>6	3200	240	–	–	–	Pass		–	
063	Radiation	MoSi₂	30	2.5	2500	120	-0.20	0	Nil	Fail	Random	–	Smooth, matte, with dark stripes
064					2500	240	+0.02	-0.44				–	
065					2600	120	-0.75	+0.43				–	
066					2590	240	-1.55	+3.54				–	
063					2750	120	-0.55	+0.43				–	
064					2750	240	-3.62	+1.33				–	
038					2800	120	-3.3	+0.9				–	
039					2800	240	-3.1	+0.9				–	
030					2850	120	-3.1	+0.5				–	
037					2850	240	-0.9	+0.5				–	
048					2900	120	-3.94	+2.06				–	
046					2900	240	-9.87	+0.43				–	
073					2950	120	+0.07	+0.44		Pass	–	–	Smooth, glassy, with dark stripes
073					2950	240	+0.08	+1.69		Pass	–	–	Smooth, glassy, with dark stripes
062	Resistance	Copper		>6	3050	180	–	–	–	Pass	–	–	Smooth, glassy, with dark spots
065	Radiation	MoSi₂	5	1.5	2500	120	-0.06	0	Nil	Pass	Random	–	Smooth, matte, with dark stripes
066		MoSi₂		1.5	2500	240	-0.71	+0.84		Fail	Random	–	
040		SiO₂		1.0	2650	240	-1.50	-0.42		Fail	Random	–	
036		MoSi₂		1.5	2700	240	-0.6	+1.3		Fail	Random	–	
019				1.0	2750	120	+3.4	0		Pass	–	–	
020					2750	240	-0.3	-10.7		Fail	Random	–	
006				↓	2800	120	-0.7	-0.9				–	
007					2800	240	-3.5	+1.7		↓	↓	–	
033				1.5	2850	60	+0.1	-0.4	Mild			–	
034				1.5	2850	120	-0.5	+0.9	Nil			–	
035				1.5	2850	240	-0.3	+0.9				–	
067				–	2900	30	+0.02	+0.86		Pass	–	–	
068				1.5	2900	30	+0.29	+0.29		Pass	–	–	
066				–	2900	60	-0.60	+0.86		Pass	–	–	
069				1.5	2900	60	-0.38	-0.87		Fail	Random	Random	
047				↓	2900	120	-0.03	+1.34				–	
048					2900	240	-0.5	+2.17				–	
074					2950	120	-5.20	+0.88		↓	↓	–	
078	Resistance	Copper		6.0	2950	124	–	–			Total	–	
077				7.0	3000	<13	–	–			Total	Total	Failed at 13 min
080				0	3000	<22	–	–	–		Total	Total	Failed at 22 min
081	↓	↓	↓	0	3050	30	–	–	–	↓	Total	Total	Rough, matte
011	Radiation	MoSi₂	1.0	1.0	2750	60	-0.4	+2.1	Nil	Pass	–	–	Smooth, matte, with stripes
012				1.0	2750	120	-0.9	+0.5			–	–	
018				1.0	2750	240	+0.4	+0.4		↓	–	–	
028				1.0	2800	30	-0.7	+2.6			–	–	
005				0.4	2800	60	-0.6	+0.9		Fail	Random	–	
008				0.4	2800	120	-1.5	-0.9			Total	–	
019				1.0	2850	30	-1.2	+3.8			Random	–	
037					2850	60	-1.0	+0.9			Total	–	
041					2900	30	-3.18	+0.42	↓		Total	Random	
042					2900	60	-7.58	+7.11			Total	Total	
071	Radiation	MoSi₂	0.1	0.15	2600	240	-2.16	-0.45	Nil	Pass	–	–	Smooth, matte, with stripes
040		SiO₂		0.06	2650	120	-2.41	-2.78		Pass	–	–	Smooth, matte, with stripes
043		SiO₂		0.06	2650	120	-2.31	-4.50		Pass	–	–	Smooth, matte, with stripes
044		SiO₂		0.06	2650	240	-3.30	-2.44		Fail	Total	Total	Crazed, matte, with stripes
023		MoSi₂		0.05	2700	120	-7.4	-6.0	Mild	Pass	–	–	Smooth, matte, with stripes
024				0.05	2700	240	-0.2	-6.4		Fail	Total	–	Smooth, matte, with stripes
013				0.07	2750	120	-3.3	-3.5		Pass	–	–	Crazed, matte, with stripes
014				0.07	2750	240	-4.5	-5.0			Total	Random	Crazed, matte, with stripes
004				0.05	2800	30	-3.5	-5.2	Nil		–	–	Smooth, matte, with stripes
003				0.05	2800	60	-10.7	-6.9	Mild		–	–	Crazed, matte, with stripes
010				0.05	2800	120	-16.7	-12.0		Fail	Total	Random	Smooth, matte, with stripes
009				0.05	2800	240	-20.0	-14.4		Fail	Total	Total	Severe failure in stripes
021				0.05	2850	30	-1.8	-4.0		Pass	–	–	Smooth, matte, with stripes
022				0.05	2850	60	-3.4	-5.2		Pass	–	–	Smooth, matte, with stripes
060	↓	↓	0.10	0.10	2900	30	-12.85	-17.18	Nil	Fail	Total	Total	Rough, matte, with stripes
061			0.10	0.10	2900	60	-21.16	-10.22	Nil	Fail	Total	Total	Rough, matte, with stripes
070	Radiation	MoSi₂	0.01	0.17	2650	240	-2.24	-2.21	Nil	Pass	–	–	Smooth, matte
027				0.10	2700	240	-2.6	-1.3		Fail	Total	–	Smooth, matte
025					2750	240	-6.0	+3.1		Fail	Total	Total	Rough, matte, crazed
002					2800	30	-2.0	-4.9		Pass	–	–	Smooth, matte, crazed
001					2800	60	-4.0	-6.0		Pass	–	–	
017				0.13	2800	120	-2.3	-2.2		Pass	–	–	
018				0.13	2800	240	-3.0	-2.5		Fail	Total	Random	
052				0.07	2850	30	-10.86	-12.22				Total	Smooth, metallic
051				0.10	2850	60	-10.2	-7.8				–	Smooth, matte, crazed
032	↓	↓	↓	0.10	2850	120	-19.4	-8.0	↓	↓	↓	Total	Smooth, metallic

341

Table LXXVII. TZM/Durak-B Baseline Data

Test no.	Furnace	Support material	Pressure (mmHg)	Flow rate (cfh)	Temp. (°F)	Time (min)	Weight change (%)	Thickness change (%)	Support reaction	Rating	Edge failure	Surface failure	Remarks
048	Radiation	MoSi$_2$	50	3.9	2950	120	-7.1	0	Nil	Fail	Random	-	Glassy, smooth
049	Radiation	MoSi$_2$		3.0	2950	240	-4.66	+3.92	Nil	Fail	Random	-	Glassy, smooth
057	Resistance	Copper		6.0	3050	240	-	-	-	Pass	-	-	Glassy, smooth, crazed
063					3100	240	-	-	-	Pass	-	-	Glassy, smooth
056					3150	38	-	-	-	Fail	Random	-	Glassy, smooth, crazed
065					3200	37	-	-	-	Fail	-	Random	Glassy, smooth, crazed
046	Radiation	MoSi$_2$	20	2.5	2950	120	+0.25	+2.69	Nil	Pass	-	-	Glassy, smooth, crazed
047	Radiation	MoSi$_2$		2.5	2950	240	+0.29	+0.97	Nil	Pass	-	-	
054	Resistance	Copper		6.0	3050	58	-	-	-	Fail	-	Random	
059					3050	209	-	-	-		Random	-	
053					3100	42	-	-	-		Total	Total	
052					3150	24	-	-	-		Total	Total	
039	Radiation	MoSi$_2$	8	1.0	2800	120	+0.4	-0.5	Nil	Pass	-	-	Smooth, matte
040				1.0	2800	240	+0.1	+1.0		Pass	-	-	Smooth, matte
034				1.0	2820	240	-0.2	-1.0		Fail	Random	-	Smooth, matte
041				1.5	2850	120	+0.4	-1.5		Pass	-	-	Smooth, matte, crazed
042				1.5	2850	240	+1.4	-1.9		Pass	-	-	Smooth, matte, crazed
004	Resistance	Copper		6.0	2900	30	-	-	-	Fail	Total	Total	Smooth, matte, crazed
058	Resistance	Copper		6.0	2900	69	-	-	-	Fail	Total	Total	Rough, matte
051	Resistance	Copper		6.0	2950	49	-	-	-	Fail	Total	Total	Rough, matte
038	Radiation	SiO$_2$	1.0	0.4	2700	240	-	-	Nil	Pass	-	-	Smooth, matte, crazed
015		SiO$_2$			2750	120	-1.8	-1.1		Pass	-	-	
014		SiO$_2$			2750	240	-1.5	-1.0		Fail	Random	-	
035		MoSi$_2$			2800	30	-1.5	-0.5		Pass	-	-	
036		MoSi$_2$			2800	60	-1.0	0		Pass	-	-	
031		SiO$_2$			2800	132	-4.0	+1.5		Fail	Total	Total	
030		SiO$_2$			2800	240	-14.9	+0.5			Total	Random	
044		MoSi$_2$		1.0	2850	30	-0.96	+1.0			Random	Total	
045		MoSi$_2$		1.0	2850	60	-1.37	0			Total	Total	
050		MoSi$_2$		1.5	2950	30	-4.73	+9.05			Total	Total	Rough, matte
022	Radiation	SiO$_2$	0.10	-	2500	240	-5.4	-17.8	Nil	Pass	-	-	Matte, smooth, crazed
023				-	2500	240	-5.9	-14.0		Pass	-	-	Matte, smooth, crazed
028				-	2550	245	-6.2	-5.7		Fail	Total	Total	Matte, pitted, crazed
03A				-	2600	240	-7.7	-2.5		Fail	Total	Total	Matte, smooth, crazed
017				-	2600	240	-13.2	-7.7		Fail	Total	Total	
010				-	2650	120	-8.2	-0.5		Pass	-	-	
009				-	2650	240	-1.7	-6.3		Fail	Total	Total	
027				0.05	2700	60	-	-5.0		Pass	-	-	
006				-	2700	120	-3.5	-		Fail	Total	Total	
005				-	2700	240	-3.9	+2.5		Fail	Total	Total	
016				0.05	2750	30	-4.8	-6.2		Pass	-	-	
019					2750	60	-6.9	-6.5		Fail	-	Total	
002					2750	120	-6.2	-		Fail	Total	Total	
003					2750	240	-41.3	-		Fail	Total	Total	Matte, rough
029					2800	30	-4.1	-3.2		Pass	-	-	Matte, smooth, crazed
033				0.05	2800	30	-5.0	-1.0		Pass	-	-	Matte, smooth, crazed
043		MoSi$_2$		0.15	2850	30	-4.8	-1.5		Fail	Total	Total	Matte, smooth, crazed
001	Radiation	SiO$_2$	0.01	-	2600	210	-5.4	+0.5	Nil	Pass	-	-	Matte, rough, barely passing
018				-	2600	220	-9.0	+2.5			-	-	Matte, rough, barely passing
011				-	2650	60	-4.2	-0.5			-	-	Matte, smooth, crazed
012				-	2650	120	-8.5	+0.1			-	-	Matte, smooth, crazed
013				-	2650	240	-12.0	-5.0		Fail	Total	Total	Matte, rough
024				0.1	2700	30	-2.8	-3.3		Pass	-	-	Matte, smooth, crazed
025					2700	60	-3.2	-0.6		Pass	-	-	
026					2700	120	-6.8	+0.5		Fail	Total	Total	
021					2750	30	-4.1	-1.1		Pass	-	-	
020					2750	60	-6.2	-2.6		Fail	Total	Total	
032					2800	30	-1.4	-2.4		Pass	-	-	Matte, smooth, crazed, light gray

342

Table LXXIX. Cb-752/PFR-32 Baseline Data

Test No.	Furnace	Support Material	Pressure (mmHg)	Flow Rate (cfh)	Temp. (°F)	Time (min)	Weight Change (%)	Thickness Change (%)	Support Reaction	Rating	Edge Failure	Surface Failure	Remarks
072	Radiation	MoSi₂	90	–	2900	120			Nil	Fail	Random	Random	Glassy, gray
073				–	2900	240			Nil		General	General	
075				2	2950	60			Slight		General	General	
076					2950	135			Slight		General	General	
080					2800	120			Nil	Pass	–	–	
081					2800	340			Nil	Pass	–	–	
086					2950	30			Nil	Fail	–	Random	
067	Resistance	Copper		8.0	3000	21			–	Fail	General	General	
068	Resistance	Copper		8.0	2900	30			–	Fail	General	General	
053	Radiation	MoSi₂	20	2.5	2850	120	+0.3	-1.1	Nil	Fail	–	Random	Glassy, gray
054					2850	240	+0.3	-2.0		Pass	–	–	Glassy, gray
055					2900	120	-0.50	+1.1		Fail	–	Random	Glassy, brown, black spots
056					2900	240	+2.93	-0.30		Fail	General	General	
062					2800	120	+0.14	-3.80		Pass	–	–	
063					2800	240	+0.16	-1.15		Fail	–	Random	
064					2900	30		-1.16		Fail	–	Random	
065					2900	60		-4.23		Fail	–	Random	
066					2750	240		-3.20		Pass	–	–	Glassy, gray
074					2950	33			Slight	Fail	Random	Random	Glassy, gray, yellow, blue, red
077					2950	30			Slight	Fail	Random	Random	Glassy, gray
078					2950	60			Nil	Fail	General	General	Glassy, gray
093					2800	60			Nil	Pass	–	–	Glassy, gray, brown spots
033	Radiation	SiO₂	5	1.0	2750	240	+0.16	+2.0	Nil	Pass	–	–	Glassy, gray, black spots
035		SiO₂			2800	129	–	-0.4	Severe	Fail	Random	–	Glassy, gray-tan
038		FeO			2800	60	–	-2.0	Severe	Pass	–	–	
039		SiO₂			2800	60	+0.10	-4.0	Slight	Pass	–	–	
040		MoSi₂			2800	120	–	-0.80	Slight	Pass	–	–	
046				2.0	2800	240		+10.30	–	Fail	Random	Random	
048				1.5	2850	120	+0.20	-1.90	Nil	Pass	–	–	
049					2850	240	+0.40	-2.00		Fail	–	Random	
057					2900	120	+2.47	-1.90			Random	Random	Glassy, gray-tan, dark spots
058					2900	240	+1.83	-5.00			–	Random	Glassy, gray-tan, dark spots
067					2950	<54	–	–	–		General	General	Disintegrated, possible contact with Al₂O₃
068					2950	<45	–	–	–		General	General	Disintegrated, possible contact with Al₂O₃
091					2850	60	–	–	Nil	Pass	–	–	Glassy, gray
089	Resistance	Copper		8.0	2900	22	–	–	–	Fail	–	Random	Glassy, gray
010	Radiation	Al₂O₃	1	0.40	2698	120	-1.0	+16.0	Severe	Fail	Random	Random	Fused to support
011					2698	240	–	–		Fail	General	General	Fused to support, most of sample gone
012					2700	69	-0.75	+10.0		Pass	–	–	Glassy, dark spots
013					2700	60	-0.75	+8.0		Fail	Random	–	Glassy, dark spots, loose scale
014					2700	123	-0.24	–		Fail	General	General	Sampled crumbled
015					2700	125	-4.6	–		Fail	Random	Random	Fused to support
024				0.07	2650	120	-1.5	+9.0		Pass	–	–	Gray-gold
025		SiO₂		0.07	2650	240	-0.6	+2.8	Nil	Pass	–	–	Gray
031				0.40	2750	60	-4.8	+5.5	Nil	Fail	General	General	Glassy, blue-gray
032				0.40	2755	30	-2.3	-0	Nil	Fail	–	General	Matte, silver gray
043				0.40	2800	60	-14.1	+9.1	Mild	Fail	General	Random	Matte-glassy, gray-black
047		MoSi₂		1.0	2700	60	-2.2	+9.2	Mild	Pass	–	–	Glassy, gray-blue
082				0.15	2800	120	–	–	–	Fail	General	General	Disintegrated
083				1.0	2800	120	–	–	Nil	Pass	–	–	Glassy, gray
084				1.0	2800	120	–	–	–	Fail	General	General	
085				1.0	2800	240	–	–	–	Fail	General	General	
090	Resistance	Copper		1.5	2800	30	–	–	–	Fail	General	General	Matte
001	Radiation	Al₂O₃	0.10	–	2600	120	-2.6	+6.8	Mild	Pass	–	–	Oxide spalled, black glassy oxide
003				–	2670	240	-2.5	+1.5		Pass	–	–	
008				0.05	2700	120	-10.0	-11.0		Pass	–	–	
009					2700	240	-21.0	-16.0		Fail	General	General	
016					2700	60	-5.0	+6.0		Pass	–	–	
017					2700	120	-12.0	-10.0		Pass	–	–	
022		ZrO₂			2650	242	–	–		Fail	Random	–	
026		SiO₂			2750	120	-11.3	-5.2	Nil	Pass	–	–	
029					2750	240	-24.0	-27.0		Fail	General	General	
041					2800	62	+2.9	-19.6		Fail	General	General	
042					2800	120	-21.0	-15.6		Fail	General	General	
044					2800	30	-4.4	-1.5		Pass	–	–	
052		MoSi₂			2850	30	-3.7	-2.0		Pass	–	–	
061				0.15	2900	30	-7.9	+9.8		Pass	–	–	
071				0.15	2930	30	–	–		Fail	General	General	
109				0.06	2750	120	–	–		Fail	General	General	
002	Radiation	Al₂O₃	0.01	–	2593	250	-3.5	+9.7	–	Pass	–	–	Oxide spalled, black glassy oxide
004				0.10	2695	60	-6.0	+6.3	Mild	Pass	–	–	
005					2695	30	-2.9	-4.8	Nil	Pass	–	–	
006					2695	124	-8.2	-12.0	Mild	Fail	Random	–	
007					2695	240	-16.0	-20.0	Mild	Fail	General	General	
023					2650	240	-2.5	+2.0	Mild	Pass	–	–	
027		SiO₂			2750	60	-8.4	+6.8	Nil	Fail	Random	–	
028					2750	30	-2.1	+4.4		Pass	–	–	
030					2750	120	-11.0	+6.7		Fail	General	General	
036					2800	30	-1.5	-6.2		Pass	–	–	
037					2800	60	-1.7	-4.0			–	–	
045		MoSi₂		0.15	2800	60	-7.6	+5.0	Mild		–	–	
050				0.10	2850	30	-3.0	-0.8	Mild		–	–	
051				0.10	2850	60	–	–	Nil	Fail	Random	–	
059				0.07	2900	30	-6.60	-0		Pass	–	–	
060				0.07	2900	60	-2.54	+3.2		Pass	–	–	
069				–	2950	30	–	–		Pass	–	–	
070				–	2950	60	–	–		Fail	Random	Random	
079				0.05	3000	30	–	–		Fail	Random	Random	

343

Table LXXX. Cb-752/CrTiSi Baseline Data

Test no.	Furnace	Support material	Pressure (mmHg)	Flow rate (cfh)	Temp. (°F)	Time (min)	Weight change (%)	Thickness change (%)	Support reaction	Rating	Edge failure	Surface failure	Remarks
055	Radiation	$MoSi_2$	50	3.0	2850	120			Nil	Pass	-	-	Matte, brown-gray
056					2850	240			Nil	Fail	Random	Random	Spongy, rust-green
058					2900	120					Random	Random	
059					2900	240					Total	Total	
060					2950	120					Random	Random	
061					2950	60					-	Random	
062					2950	120					-	Random	
072				6.0	3000	60			-		Total	Total	Matte, brown
073				6.0	2800	240			-		-	Random	Matte, brown
074				6.0	2750	240				Pass	-	-	Matte, rust-green
047	Radiation	$MoSi_2$	20	2.5	2800	240	-0.8	+16.0	Nil	Fail	-	Random	Matte, rust-yellow
048					2750	120	+0.3	+0.8	Nil	Pass	-	-	Matte, rust-green
049					2750	240	-0.2	+0.3	Nil	Pass	-	-	
050					2850	120	-0.5	+17.7	Nil	Fail	-	Random	
051					2850	60	-0.4	+23.7	Mild	Pass	-	-	
052					2650	240	-2.0	+34.2	Mild	Fail	Total	Total	Blue crystalline oxide
053					2900	5	-	-	-	Fail	Total	Total	Melted
054					2900	5	-	-	-	Fail	Total	Total	Melted
057					2800	120			Mild	Pass	-	-	Matte, rust-blue
063	Resistance	Copper		8.0	2900	30	-	-	-	Fail	-	Random	Matte-sponge, rust
064					2950	30	-	-	-	Pass	-	-	Matte-sponge, rust
065					3000	<1	-	-	-	Fail	Total	Total	Melted
066					2950	60	-	-	-	Fail	Random	Random	Matte-sponge, rust
067					2950	119	-	-	-	Fail	Total	Total	Matte-sponge, rust
069	Radiation	$MoSi_2$		2.5	2900	60	-	-	Nil	Pass	-	-	Matte, rust-green
075	Resistance	Copper		6.0	3000	30	-	-	-	Fail	Random	-	Matte-sponge, rust
023	Radiation	Al_2O_3	5	0.40	2650	240	-	+23.0	-	Pass	-	-	Matte, green-gray
038		SiO_2		1.0	2707	240	-	-	Nil	Pass	-	-	Matte, rust-green
041		SiO_2			2750	240	-35.0	+19.0	Severe	Pass	-	-	Fused with SiO_2 support
042		SiO_2			2750	120	-0.44	+9.2	Nil	Pass	-	-	Matte, green-gray
044		$MoSi_2$			2800	50	-	-	-	Fail	Total	Total	Burned up
045					2800	50	-	-	-	Fail	Total	Total	Burned up
046					2800	24	-	-	Nil	Fail	Total	Total	75% consumed
071				1.5	2750	60				Pass	-	-	Matte, green
070				1.5	2750	240				Pass	-	-	Matte, green-gray
060a				1.5	2700	240				Pass	-	-	Matte, green-gray
076	Resistance	Copper		6.0	2900	8	-	-	-	Fail	Total	Total	Burned through
077	Resistance	Copper		6.0	2900	2	-	-	-	Fail	Total	Total	Burned through
008	Radiation	Al_2O_3	1	0.40	2700	123			-	Fail	Total	Total	
009					2700	120	-2.3	+15.0	-				Oxide spalled
011					2700	60	-2.5	+18.0	-				Oxide spalled
012					2700	30	-1.8	-	-				
026		SiO_2		0.07	3050	120	-8.0	-7.0	Mild				Oxide spalled, gray scale
027					2650	60	-1.2	+13.6					
028					2650	30	-1.1	+14.7					
029					2600	240	-0.1	-					
030					2600	60	-0.15	+11.9			Random	Random	
031					2800	120	-0.90	+13.7			Total	Total	
032					2600	30	-0.4	+13.5			Random	Random	
033					2550	120	-0.6	+0.4			-	Random	
034					2550	60	-0.7	-0.4			-	Random	
035					2550	240	-0.1	+3.0		Pass	-	-	
037					2550	240	-0.7	+7.9		Fail	Random	Random	
039					2550	220	+0.25	+3.5		Pass	-	-	Matte, green-gray
040					2500	120	+0.17	+1.3		Pass	-	-	Matte, green-gray
043					2550	32	-1.0	-0-		Pass	-	-	Matte, tan-gray
006	Radiation	Al_2O_3	0.10	-	2695	240	-2.5	+3.0	Mild	Pass	-	-	
010		Al_2O_3		0.05	2700	60	-2.3	+15.0		Fail	Total	Total	
013		Al_2O_3			2700	30	-3.4	+13.0			Total	Total	Matte, gray adherent scale
021		SiO_2			2650	122	-8.5	+3.0			Total	Total	Oxide spalled, gray
022		SiO_2			2646	60	-3.0	+19.0			-	Random	Gray adherent scale
007	Radiation	Al_2O_3	0.01	-	2605	240	-2.5	+3.0	Mild	Pass	-	-	
017		Al_2O_3		0.10	2704	30	-3.0	+11.0	Severe	Fail	Total	Total	Gray adherent scale
018		Al_2O_3			2704	60	-2.2	+16.0	Severe	Fail	Total	Total	Gray adherent scale
020		SiO_2			2650	120	-8.5	+3.0	Mild	Fail	Total	Total	Oxide spalled, gray
024					2653	30	-3.1	+13.5	Nil	Pass	-	-	
025					2650	60	-8.6	+8.2	Nil	Fail	-	Random	
036					2630	60	-	-	Nil	Fail	Random	Random	

344

Table LXXXI. B-66/CrTiSi Baseline Data

Test no.	Furnace	Support material	Pressure (mmHg)	Flow rate (cfh)	Temp (°F)	Time (min)	Weight change (%)	Thickness change (%)	Support reaction	Rating	Edge failure	Surface failure	Remarks
054	Radiation	MoSi₂	50	3.0	2750	120			Mild	Fail	Total	Total	Matte, green-gray, blistered
055					2750	240							Matte, brown-gray, blistered
056					2650	120							Matte, green-gray, blistered
059					2060	240							Matte, rust-gray, blistered
060					2600	120			Nil		Random	Random	Matte, green-gray, smooth
061					2600	240					Random	Random	
062					2550	120				Pass	-	-	
063					2550	240				Fail	Random	Random	
066					2500	240				Pass	-	-	
073					2650	30				Fail	Random	Random	Matte, green-gray, blistered
074					2650	60					Random	Random	
077					2700	30					Random	Random	
078					2700	60					Total	Total	
041	Radiation	MoSi₂	20	2.5	2800	120			Mild	Fail	Total	Total	Matte, rust-green, blistered
042					2800	210					Total	Total	Matte, brown, blistered
043					2750	120					Random	-	Matte, rust-brown, blistered
044					2750	240					Total	Total	Matte, brown-green, blistered
045					2700	120							Matte, brown-green, blistered
046					2700	240							Matte, brown-green, blistered
048					2650	240							Matte, brown-gray, blistered
049					2650	120							Matte, green, blistered
050					2600	120					Random	Random	Matte, gray, smooth
051					2600	210					Random	Random	Matte, rust-gray, smooth
064					2550	120			Nil	Pass	-	-	Matte, green-gray, smooth
065					2550	240				Fail	-	Random	
067					2500	120				Pass	-	-	
068					2500	240				Fail	Random	Random	
069					2450	240				Pass	-	-	
071					2650	30				Fail	-	Random	Matte, green, blistered
072					2650	60					Random	Random	Matte, green-gray, blistered
079					2700	60					Total	Total	Matte, green-gray, blistered
080					2700	30					Random	Random	Matte, green-gray, blistered
081					2550	60				Pass	-	-	Matte, green-gray, smooth
007	Radiation	MoSi₂	5.0	1.0	2800	66	-1.6	+31.0	Severe	Fail	Total	Total	Matte, rust-gray, blistered
026				1.5	2700	120	-0.16		Mild		Random	Random	Matte, rust-green, blistered
027					2700	240	+0.07				Random	Random	Matte, rust, blistered
030					2750	120	-0.16				Random	Random	Matte, rust, blistered
031					2750	210	-0.26				Total	Total	Matte, rust, blistered
034					2650	120	-0.06				Random	Random	Matte, gray, smooth
035					2650	240	-0.21				Random	Random	Matte, gray, smooth
036					2600	120	+0.21	---	Nil	Pass	-	-	Matte, blue-gray, smooth
037					2600	210	-0.04		Mild	Pass	-	-	Matte, blue-gray, smooth
040				2.0	2800	30				Fail	Random	Random	Matte, green-gray, blistered
047				1.5	2850	19					Total	Total	Matte, black, blistered
052					2700	30					Random	Random	Matte, green-gray, blistered
053					2700	60					Total	Total	Matte, green-rust, blistered
057					2600	81					Random	Random	Matte, green-gray, blistered
058					2600	30					Random	Random	Matte, green-gray, blistered
012	Radiation	SiO₂	1.0	-	2600	120	-0.4	+3.7	Nil	Pass	-	-	Matte, blue-gray, smooth
013				-	2600	240	-0.2	+12.6	Nil	Fail	Total	Total	Matte, rust-green, smooth
016				0.05	2550	215	-0.4	+2.9	Mild	Pass	-	-	Matte, rust-green, smooth
017				0.05	2550	240	-0.3	-0-	Nil	Fail	Random	Random	Matte, green-gray, smooth
018				0.05	2500	240	+0.1	+2.5	Mild	Pass	-	-	
023		MoSi₂		1.0	2650	120	-0.35	-0-			-	-	
024					2650	60	-0.22				-	-	
028					2700	60	-0.26				-	-	
029					2700	120	-0.26			Fail	Random	Random	
032					2750	60	+0.10				Total	Total	Matte, green-gray, blistered
033					2750	120	-4.80				Total	Total	Matte, green-gray, blistered
039					2750	30	+1.05				Total	Total	Matte, green-gray, blistered
001	Radiation	Al₂O₃	0.10	-	2567	240	-1.45		Mild	Pass	-	-	Matte, oxide spalled
003		SiO₂		0.01	2650	240			Mild	Fail	Total	Total	Matte, oxide spalled
004		MoSi₂		0.10	2650	30			Mild	Fail	Total	Total	Matte, oxide spalled
011				0.06	2550	60	-0.9	-0-	Nil	Pass	-	-	Matte, violet, smooth
014				0.07	2600	60	-0.7	+1.7	Mild	Pass	-	-	Matte, gray, smooth
015				0.01	2600	120	-0.6	+3.7	Mild	Pass	-	-	Matte, gray-blue, smooth
025				0.10	2600	240	-0.44		Mild	Fail	Random	Random	Matte, rust, smooth
002	Radiation	Al₂O₃	0.01	-	2566	120	-1.34		Severe	Pass	-	-	Matte, oxide spalled
007		Al₂O₃		-	2566	242	-1.0		Mild	Pass	-	-	Matte, oxide spalled
006		SiO₂		0.01	2650	210	-2.0	-5.93	Nil	Fail	Total	Total	Matte, blue-gray, blistered
009		SiO₂		0.01	2550	60	-2.0	-0-	Nil	Pass	-	-	Matte, blue, smooth
010		SiO₂		0.01	2550	240	-2.0	+3.5	Nil	Pass	-	-	Matte, blue, smooth
019		MoSi₂		0.10	2650	60	-1.4	+10.0	Mild	Fail	Total	Total	Matte, blue, oxide spalled
020				0.01	2650	120	-1.0	+10.0		Fail	Total	Total	Matte, blue, oxide spalled
021				0.10	2600	120	-0.8	+0.8		Pass	-	-	Matte, gray, smooth
022				0.10	2600	240	-1.0	+3.2		Fail	Random	Random	Matte, gray, oxide spalled
038				0.10	2650	30	-1.10			Fail	Total	Total	Matte, blue-green, smooth

345

Table LXXXII. Cb-752/Vought IV Baseline Data

Test no.	Furnace	Support material	Pressure (mmHg)	Flow rate (cfh)	Temp (°F)	Time (min)	Weight change (%)	Thickness change (%)	Support reaction	Rating	Edge failure	Surface failure	Remarks
067	Radiation	SiO₂	5.0	>0.4	2650(a)	240	–	–	Severe	Fail(a)	Total	Total	Glassy, black scale, spalled
061	↓	↓	↓	1.0	2700	56	+2.2	+26.8	Nil	Fail(a)	Random	–	Glassy, black scale, spalled
062				1.0	2700	120	-1.0	+7.1	Nil	Pass	.	–	Glassy, black scale, spalled
058				1.0	2750	240	-11.8	+12.8	Severe	Fail	Total	Random	Matte, gray-black scale, spalled
008	Radiation	Al₂O₃	1.0	0.4	2599	120	-1.5	+2.2	Nil	Pass	–	–	Glassy, black scale, spalled
009	↓	↓			2598	240	+5.4	–	Nil	Fail(a)	Total	Random	
012					2600	240	-0.28	+12.0	Nil	Pass	–	–	
016					2697	30	–	–	Severe	Pass	–	–	
019					2698	120	–	–	↓	Fail(a)	Total	Total	Glassy, gray-black scale, spalled
020					2698	120	–	–		Fail(a)	Random	.	Glassy, black scale, spalled
021					2697	60	-2.0	–		Fail(a)	Random	–	Glassy, black scale, spalled
037		SiO₂			2650	121	-2.0	+17.0	Nil	Pass	–	–	Glassy, gray-black scale, spalled
040					2655	240	-0.4	+7.8	Nil	Pass	–	–	Glassy, blue-black scale, spalled
045					2700	168	–	–	Nil	Fail(a)	Total	–	
052					2755	60	–	–	Severe	Fail(a)	.	Total	
053					2650	60	–	–	Severe	Fail(a)	↓	↓	
056					2750	30	-6.4	+31.0	Nil	Fail			Total consumption, no remains
037					2700	226	-10.0	–	.	Fail(a)			
059	↓	↓			2750	30	-0.2	–	Nil	Fail(a)	↓	↓	Glassy, black scale, spalled
001	Radiation	Al₂O₃	0.10	0.01	2502	30	-3.5	-7.5	Mild	Pass	–	–	Matte, gray-black scale, adherent
002	↓	↓			2600	120	-12.0	-17.0		Fail	Total	Total	Matte, gray-black scale, spalled
003					2600	60	-3.8	-0.9		Pass	–	–	Matte, gray-black scale, adherent
004					2600	60	-3.4	-3.6			–	–	Matte, gray-black scale, adherent
010					2695	30	-4.6	-0.8			–	–	Matte, gray-black scale, adherent
011					2695	60	-3.2	+3.5			–	–	Glassy, gray-black scale, spalled
015					2603	120	-3.4	-2.4		↓	–	–	Matte, gray-black scale, adherent
017				0.05	2697	120	-2.4	+2.3		Fail	Total	–	Glassy, gray-black scale, spalled
022				0.01	2602	120	-3.5	+1.2		Pass	–	–	Matte, gray-black scale, adherent
024					2558	240	-1.3	+10.0		Fail	Random	Random	Glassy, gray-black scale, spalled
026					2658	120	-0.9	+5.4		Pass	–	–	Glassy, black scale, adherent
038		SiO₂			2650	240	-2.0	+17.0	Nil	Fail	Total	–	Glassy, gray-black scale, spalled
042				0.05	2710	60	-3.8	+7.0		↓	Random	–	
044				0.01	2550	240	–	–			Total	Total	
046				0.01	2550	240	-4.7	+8.1			Total	Total	
048				0.05	2750	30	-4.2	-3.5		Pass	–	–	
054					2750	120	-2.5	+2.2		Fail	Total	Total	
060					2595	240	-8.3	–		Fail	Total	Total	
064					2800	60	-3.6	+5.2		Fail	Total	Total	Glassy, gray-black scale, adherent
065	↓	↓	↓	↓	2800	30	-4.2	+4.6	↓	Pass	–	–	Glassy, gray-black scale, adherent
005	Radiation	Al₂O₃	0.01	0.10	2600	254	-3.3	–	Nil	Fail	Total	Total	Glassy, gray-black scale, spalled
006	↓	↓			2660	170	-3.2	–		Pass	–	.	Glassy, gray-black scale, adherent
013					2695	120	5.9	–		Fail	Total	Total	Glassy, gray-black scale, spalled
014					2695	60	-1.8	–		Fail	Random	–	
027					2650	60	-4.6	-1.5		Pass	–	–	
028					2657	120	-4.6	+6.6		Fail	Random	–	
035		SiO₂			2650	240	-5.6	-17.0		Fail	Random	Random	
041					2598	240	-9.0	-13.0		Fail	Total	Total	Glassy, yellow-white scale, spalled
043					2550	240	-4.1	-20.0			Total	Total	Glassy, gray-black scale, spalled
047					2750	30	-12.0	+5.4			Random	–	↓
049					2750	60	-6.7	+11.5			Total	Total	
050					2750	120	-17.4	-9.1			Total	Total	
051					2500	240	-3.8	-2.3		Pass	–	–	Glassy, gray-black scale, adherent
055					2500	242	-1.9	+4.2			–	–	
063					2795	30	+2.9	+4.7			–	–	
066					2600	240	-3.8	+4.1			–	–	
023		Al₂O₃			2698	30	-2.0	+0.9		↓	–	–	Glassy, gray-black scale, spalled
025	↓	Al₂O₃	↓	↓	2650	180	-4.9	-1.6	↓	Fail	Total	Total	Glassy, gray-black scale, spalled

(a) One-fourth to one-half of sample totally consumed.

Table LXXXIII. Ta-10W/Sn-Al Baseline Data

Test no.	Furnace	Support material	Pressure (mmHg)	Flow rate (cfh)	Temp. (°F)	Time (min)	Weight change (%)	Thickness change (%)	Bond ductility	Substrate hardness	Surface color	Performance rating	Remarks
011	Resistance	Copper	60	6+	3100	36	Nil	+53.7	Large cracks	–	Gray	Pass	Local overheating
012					3280	30	–	–	Glass brittle	–	Black	Total failure	Local overheating
013					3100	37	–	–	Glass brittle	–	Black	Total failure	Local overheating
016					3050	30	-6.2	+56.2	Medium cracks	–	Gray	Pass	Local substrate recession
018					3050	60	–	–	Glass brittle	–	Black	Total failure	Local overheating
019					3000	65	–	–	–	–	–	Total failure	Burned through
020					2900	120	+0.5	+28.1	Large cracks	233–282	Gray	Pass	Local substrate recession
022					2900	60	-0.5	+1.9	Large cracks	–			Local substrate recession
025					2900	30	–	–	Small cracks	–			
030					2850	60	–	–	Small cracks	–			
043					2800	120	–	–	Small cracks	–			
044					2700	240	–	–	Medium cracks	231–254			Local substrate recession
045					2600	240	–	–	Small cracks	–			
058					2600	240	+0.3	+1.0	Medium cracks	–			
059					2500	240	Nil	+1.0	Medium cracks	–			
063					2400	240	–	–	Small cracks	241–266			Local substrate recession
073					2900	240	+1.1	+72.9	Large cracks	–			Local substrate recession
014	Resistance	Copper	20	6+	3000	30	Nil	+43.0	Large cracks	–	Gray	Pass	
017					2900	30	–	–	Medium cracks	–			No local substrate recession
021					2900	120	+0.4	+35.4	Large cracks	284–334			Local substrate recession
023					2900	60	+0.4	+31.0	Large cracks	233–313			Local substrate recession
024					2600	120	+0.2	+22.3	Medium cracks	–			No local substrate recession
026					2500	240	–	–	Medium cracks	207–295			Local substrate recession
027					2850	240	–	–	Large cracks	234–308			
028					2950	30	–	–	Medium cracks	–			
029					2550	60	–	–	Large cracks	195–285			No local substrate recession
079					2500	240	+0.1	+11.4	Medium cracks	–			
080					2600	240	+0.4	+33.9	Medium cracks	–			
081					3000	55	–	–	Glass brittle	–	Black	Total failure	Burned through
009	Resistance	Copper	5	6+	2700	30			No cracks	–	Gray	Pass	
015					2900	30			Large cracks	–			
031					2850	60			Large cracks	250–324			Local substrate recession
032					2800	60			Medium cracks	–			No local substrate recession
033					2700	120			Medium cracks	–			
034					2650	60			Small cracks	–			
035					2600	120			Small cracks	–			
036					2550	120			Small cracks	–			
037					2550	274			Large cracks	199–274			No local substrate recession
042					2450	240			No cracks	–			
057	Radiation	SiO2		1.5	2500	240			Large cracks				
074				1.0	2400	120			No cracks				
075					2600	240			No cracks				
076					2700	120			No cracks				
077					2700	240			Small cracks				
002	Radiation	SiO2	1.0	–	2600	60	+0.1	+5.8	Small cracks		Gray	Pass	
003				–	2650	240	+0.2	+7.0	Medium cracks				
004				–	2700	120	-7.6	-9.2					
007				–	2600	240	+0.4	+7.2					
008				–	2700	240	+0.4	+31.5		210–278			
010	Resistance	Copper		1.5	2800	30	–	–		277–364	Black		No local substrate recession
056	Radiation	SiO2		0.8	2500	240	Nil	+4.3			Gray		
078	Resistance	Copper		1.5	2650	60	-9.2	-29.8	No cracks		Gray		
001	Radiation	SiO2	0.10	0.10	2600	77	–	–	Glass brittle		Black	Total failure	
005					2500	60	-12.0	-7.9	Glass brittle		Black	Total failure	
006					2400	60	+0.1	+3.4	Small cracks		Gray	Pass	
054					2500	75	-8.5	-0.2	Glass brittle	355–618	Black	Total failure	Severe attack of SiO_2
055					2500	120	-8.8	-45.7					Severe attack of SiO_2
082					2400	120	-8.6	-14.2					Severe attack of SiO_2
083					2450	120	–	-23.2					Mild attack of SiO_2
084					2450	240	–	-25.4					Severe attack of SiO_2
085					2300	251	-0.1	+3.6	No cracks		Gray	Pass	No attack of SiO_2
086					2400	180	–	–	Glass brittle	369–672	Black	Total failure	Severe attack of SiO_2
S-1*	Radiation	SiO2	0.01	0.08	2500	30	-12.3	-9.4	Glass brittle	–	Black	Total failure	Mild attack of SiO_2
S-2*					2500	75	-10.5	-11.7					
S-3*					2450	120	-11.7	-12.8					
S-4*					2450	240	-12.7	-14.9					
046					2400	30	-10.3	-19.2	No cracks	–	Gray	Pass	
047					2400	60	-7.7	-21.4	No cracks	–	Gray	Pass	Severe attack of SiO_2
048					2400	240	-9.4	-21.8	Glass brittle	–	Black	Total failure	Severe attack of SiO_2
049					2400	120	-8.8	-17.4	Large cracks	–	Gray	Pass	Severe attack of SiO_2
050					2450	30	-9.0	-21.8	Large cracks	–	Gray	Pass	Mild attack of SiO_2
051					2450	60	-9.5	-23.2	Glass brittle	–	Black	Total failure	No attack of SiO_2
052					2350	120	Nil	Nil	No cracks	–	Gray	Pass	No attack of SiO_2
053					2350	240	Nil	+7.0	No cracks	–	Gray	Pass	No attack of SiO_2

*Spray coated

347

DOCUMENT CONTROL DATA - R&D

(Security classification of title, body of abstract and indexing annotation must be entered when the overall report is classified)

1. ORIGINATING ACTIVITY (Corporate author)	2a. REPORT SECURITY CLASSIFICATION
Lockheed Missiles & Space Company Palo Alto, California	Unclassified
	2b. GROUP N/A

3. REPORT TITLE

Coatings for Refractory Metals in Aerospace Environments

4. DESCRIPTIVE NOTES (Type of report and inclusive dates)

Final Report, 1 June 1963 - 20 Sept 1965

5. AUTHOR(S) (Last name, first name, initial)

R. A. Perkins
C. M. Packer

6. REPORT DATE	7a. TOTAL NO. OF PAGES	7b. NO. OF REFS
Sept 1965	347 p.	37

8a. CONTRACT OR GRANT NO.	9a. ORIGINATOR'S REPORT NUMBER(S)
AF 33(657)-11150	AFML TR-65-351
b. PROJECT NO. 7312	AF-7312
c. Task No.	9b. OTHER REPORT NO(S) (Any other numbers that may be assigned this report)
d. 731201	LMSC-2-04-65-1

10. AVAILABILITY/LIMITATION NOTICES "This document is subject to special export controls and each transmittal to foreign governments or foreign nationals may be made only with prior approval of the Metals and Ceramics Division (MAM). Air Force Materials Laboratory, Wright-Patterson AFB, Ohio."

11. SUPPLEMENTARY NOTES	12. SPONSORING MILITARY ACTIVITY
	AF Materials Laboratory Wright-Patterson AFB, Ohio

13. ABSTRACT The behavior of 8 commercially coated refractory metal systems in various aerospace conditions was evaluated: PFR-6, Disil, and Durak-B coated TZM; PFR-32, CrTiSi, and Vought IV coated Cb-752; CrTiSi coated B-66; and Sn-Al coated Ta-10W. Environmental and performance requirements for aerospace applications of coated refractory metals were analyzed. Model environmental conditions for typical lifting reentry missions were derived, and the results used in determining time, temperature, and pressure for experimental phases of the program. Experimental equipment and evaluation procedures for studying the behavior of coated refractory metal systems in aerospace environments were developed. Initially, the maximum temperature for a given useful lifetime up to 4 hr in slowly moving air was determined for each system at pressures of 0.01 to 50 mm Hg. Subsequently, the effects of such variables as Mach 3 air flow, vacuum exposure, temperature and pressure cycling, and acoustic irradiation were evaluated in terms of deviation from the performance in slowly moving air. The tolerance of the systems to various defects was studied, and in-field patch repair processes and compatibility with other high-temperature materials were explored. A detailed metallographic study was also conducted for each coating system. The behavior under various conditions was thus explained, and recommendations for additional applications and development were made. The following conclusions were drawn: the 8 coating systems have good utility over a broad range of aerospace applications; the oxidation resistance of all silicide-base coatings (including CrTiSi) and Sn-Al coatings is degraded at reduced pressure; in lifting reentry applications, temperature limits will probably be determined by the performance capabilities of the interior surfaces, where pressures will be lower.

DD FORM 1473 (1 JAN 64)

210 115

14. KEY WORDS	LINK A		LINK B		LINK C	
	ROLE	WT	ROLE	WT	ROLE	WT

INSTRUCTIONS

1. **ORIGINATING ACTIVITY:** Enter the name and address of the contractor, subcontractor, grantee, Department of Defense activity or other organization (corporate author) issuing the report.

2a. **REPORT SECURITY CLASSIFICATION:** Enter the overall security classification of the report. Indicate whether "Restricted Data" is included. Marking is to be in accordance with appropriate security regulations.

2b. **GROUP:** Automatic downgrading is specified in DoD Directive 5200.10 and Armed Forces Industrial Manual. Enter the group number. Also, when applicable, show that optional markings have been used for Group 3 and Group 4 as authorized.

3. **REPORT TITLE:** Enter the complete report title in all capital letters. Titles in all cases should be unclassified. If a meaningful title cannot be selected without classification, show title classification in all capitals in parenthesis immediately following the title.

4. **DESCRIPTIVE NOTES:** If appropriate, enter the type of report, e.g., interim, progress, summary, annual, or final. Give the inclusive dates when a specific reporting period is covered.

5. **AUTHOR(S):** Enter the name(s) of author(s) as shown on or in the report. Enter last name, first name, middle initial. If military, show rank and branch of service. The name of the principal author is an absolute minimum requirement.

6. **REPORT DATE:** Enter the date of the report as day, month, year; or month, year. If more than one date appears on the report, use date of publication.

7a. **TOTAL NUMBER OF PAGES:** The total page count should follow normal pagination procedures, i.e., enter the number of pages containing information.

7b. **NUMBER OF REFERENCES:** Enter the total number of references cited in the report.

8a. **CONTRACT OR GRANT NUMBER:** If appropriate, enter the applicable number of the contract or grant under which the report was written.

8b, 8c, & 8d. **PROJECT NUMBER:** Enter the appropriate military department identification, such as project number, subproject number, system numbers, task number, etc.

9a. **ORIGINATOR'S REPORT NUMBER(S):** Enter the official report number by which the document will be identified and controlled by the originating activity. This number must be unique to this report.

9b. **OTHER REPORT NUMBER(S):** If the report has been assigned any other report numbers (either by the originator or by the sponsor), also enter this number(s).

10. **AVAILABILITY/LIMITATION NOTICES:** Enter any limitations on further dissemination of the report, other than those imposed by security classification, using standard statements such as:

(1) "Qualified requesters may obtain copies of this report from DDC."

(2) "Foreign announcement and dissemination of this report by DDC is not authorized."

(3) "U. S. Government agencies may obtain copies of this report directly from DDC. Other qualified DDC users shall request through
_____ ."

(4) "U. S. military agencies may obtain copies of this report directly from DDC. Other qualified users shall request through
_____ ."

(5) "All distribution of this report is controlled. Qualified DDC users shall request through
_____ ."

If the report has been furnished to the Office of Technical Services, Department of Commerce, for sale to the public, indicate this fact and enter the price, if known.

11. **SUPPLEMENTARY NOTES:** Use for additional explanatory notes.

12. **SPONSORING MILITARY ACTIVITY:** Enter the name of the departmental project office or laboratory sponsoring (paying for) the research and development. Include address.

13. **ABSTRACT:** Enter an abstract giving a brief and factual summary of the document indicative of the report, even though it may also appear elsewhere in the body of the technical report. If additional space is required, a continuation sheet shall be attached.

It is highly desirable that the abstract of classified reports be unclassified. Each paragraph of the abstract shall end with an indication of the military security classification of the information in the paragraph, represented as (TS), (S), (C), or (U).

There is no limitation on the length of the abstract. However, the suggested length is from 150 to 225 words.

14. **KEY WORDS:** Key words are technically meaningful terms or short phrases that characterize a report and may be used as index entries for cataloging the report. Key words must be selected so that no security classification is required. Identifiers, such as equipment model designation, trade name, military project code name, geographic location, may be used as key words but will be followed by an indication of technical context. The assignment of links, rules, and weights is optional.

GPO 886-551